

Anders Nilsson · Bilong Liu

Vibro- Acoustics, Volume 2

Second Edition



Science Press
Beijing



Springer

Vibro-Acoustics, Volume 2

Anders Nilsson · Bilong Liu

Vibro-Acoustics, Volume 2

Second Edition

 Science Press
Beijing

 Springer

Anders Nilsson
MWL-Marcus Wallenberg Laboratory
for Sound and Vibration Research
KTH, The Royal Institute of Technology
Stockholm
Sweden

Bilong Liu
Key Laboratory of Noise and Vibration
Research
Institute of Acoustics, Chinese Academy
of Sciences
Beijing
China

Supported by National 973 Program of China (2012CB720204)

ISBN 978-3-662-47933-9 ISBN 978-3-662-47934-6 (eBook)
DOI 10.1007/978-3-662-47934-6

Jointly published with Science Press, Beijing
ISBN: 978-7-03-039150-6 Science Press, Beijing

Library of Congress Control Number: 2015946068

Springer Heidelberg New York Dordrecht London

1st edition: © Science Press 2013

2nd edition: © Science Press, Beijing and Springer-Verlag Berlin Heidelberg 2016

This work is subject to copyright. All rights are reserved by the Publishers, whether the whole or part of the material is concerned, specifically the rights of translation, reprinting, reuse of illustrations, recitation, broadcasting, reproduction on microfilms or in any other physical way, and transmission or information storage and retrieval, electronic adaptation, computer software, or by similar or dissimilar methodology now known or hereafter developed.

The use of general descriptive names, registered names, trademarks, service marks, etc. in this publication does not imply, even in the absence of a specific statement, that such names are exempt from the relevant protective laws and regulations and therefore free for general use.

The publishers, the authors and the editors are safe to assume that the advice and information in this book are believed to be true and accurate at the date of publication. Neither the publishers nor the authors or the editors give a warranty, express or implied, with respect to the material contained herein or for any errors or omissions that may have been made.

Printed on acid-free paper

Springer-Verlag GmbH Berlin Heidelberg is part of Springer Science+Business Media
(www.springer.com)

Preface

The vibration of simple structures like beams and plates was discussed in Volume I of Vibro-Acoustics. Various wave types and their propagation in simple structures were investigated. The coupling effects between the basic wave types propagating in real constructions were demonstrated in the first volume.

In Volume II the response and dynamic characteristics of more complicated structures like shells, composite panels and frame reinforced plates typical of many types of vehicles are derived. The acoustic coupling between these structures and the energy flow between them are important parts of Volume II. The interaction between structures and fluids is also highlighted.

Volume II of the text includes a chapter on variational methods. The technique is used for the derivation of equations governing the vibration of sandwich and other composite elements and some simple shell elements. In the following chapter the coupling between mechanical systems is explored. This includes an introduction to the vibration of rubber mounts, resilient mountings and the design of engine foundations. Then follow chapters on waves in fluids including outdoor sound propagation and room acoustics. Coupling effects between vibrating structures and a surrounding fluid or quite simply sound radiation and sound transmission loss and fluid loading of structures are the subjects of the next chapter. Discussions on random excitation of structures follow. Finally, some methods, including Statistical Energy Analysis, for the prediction of excitation and propagation of structure-borne sound in large built-up structures are investigated.

A number of problems are formulated at the end of each chapter. Solutions to the problems are given in Volume III. A summary of some basic equations presented in the first two volumes are summarized in Volume III. Many results discussed in Volume II are verified by model and full-scale measurements.

Genova, Italy
August 2015

Anders Nilsson

Contents

9	Hamilton’s Principle and Some Other Variational Methods	1
9.1	Hamilton’s Principle	2
9.2	Flexural Vibrations of Slender Beams	4
9.3	Equation of Motion for Honeycomb Beams in Flexure	7
9.4	Plates with Constrained Viscoelastic Layer.	14
9.5	Timoshenko Beams	20
9.6	Mindlin Plates	21
9.7	Cylindrical Shells	26
9.8	Lagrange’s Equation	32
9.9	Garlekin’s Method	33
9.10	An Example Using Garlekin’s Method.	36
	Problems.	39
10	Structural Coupling Between Simple Systems.	41
10.1	Introduction	41
10.2	Coupled Mass–Spring Systems	43
10.3	Coupled Systems with Losses.	47
10.4	Example	49
10.5	Rubber Mounts, Some Material Parameters	53
10.6	Wave Propagation in Rubber Mounts, Approximate Solutions	58
10.7	Equivalent Stiffness of Simple Mounts—Approximate Methods.	61
10.8	Static Deflection of Cylindrical Rubber Mounts	65
10.9	Wave Propagation in Circular Rods, Exact Solutions.	66
10.10	Measurements of Effective Stiffness of Mounts.	75
10.11	Structural Coupling Via Resilient Mounts	80
10.12	Simple Transmission Model	85
10.13	Multi-point Coupling	94

10.14	Multi-point Coupling, Low and High Frequency Limits	96
10.15	Source Strength	97
	Problems	100
11	Waves in Fluids	103
11.1	Wave Equation	103
11.2	Energy and Intensity	109
11.3	Losses	110
11.4	Basic Solutions to Wave Equation.	113
11.5	Green's Function.	118
11.6	Dipole and Other Multipole Sources	121
11.7	Additional Sources and Solutions	123
11.8	Moving Monopole Sources.	129
11.9	Reflection from a Plane Surface	133
11.10	Reflection from a Water Surface	141
11.11	Influence of Temperature and Velocity Gradients	143
11.12	Acoustic Fields in Closed Rooms	146
11.13	Geometrical Acoustics	151
11.14	Near and Reverberant Acoustic Fields in a Room	155
11.15	Measurement of the Sound Transmission Loss of a Wall	157
	Problems	159
12	Fluid Structure Interaction and Radiation of Sound	163
12.1	Radiation and Fluid Loading of Infinite Plates	163
12.2	Radiation—General Formulation	169
12.3	Green's Function—Rigid Plane Boundary	171
12.4	Spatial Fourier Transforms—Several Variables	174
12.5	Radiation from Infinite Point-Excited Plates	177
12.6	Mobilities of Fluid-Loaded Infinite Plates.	181
12.7	Discussion of Results—Infinite Fluid-Loaded Plates	184
12.8	Radiation from Finite Baffled Plates	186
12.9	Radiation Ratios—Finite Baffled Plates	192
12.10	Radiation from Point-Excited Plates.	197
12.11	Sound Radiation Ratios—Cylinders.	200
12.12	Losses Due to Radiation	202
12.13	Radiation from Fluid-Loaded Finite Plates	204
	Problems	212
13	Sound Transmission Loss of Panels	215
13.1	Sound Transmission Through Infinite Flat Panels	216
13.2	Plate Velocity Induced by an Acoustic Field.	223
13.3	Sound Transmission Between Rooms Separated by a Single Leaf Panel.	226
13.4	Sound Transmission Between Equal Rooms	234

13.5	Sound Transmission Between Irregular Rooms	236
13.6	Effect of Boundary Conditions of Plate on Sound Transmission Loss.	237
13.7	Effect of a Baffle on Sound Transmission Loss.	243
13.8	Measurement Results.	248
13.9	Loss Factors and Summary.	253
13.10	Sound Transmission Through Complex Structures.	256
13.11	Flanking Transmission.	260
13.12	Sound Transmission Through Fluid Loaded Plates	261
	Problems.	262
14	Waveguides	265
14.1	Introduction	265
14.2	Structural Waveguides	267
14.3	Coupled Structural Waveguides	270
14.4	Measurements and Predictions	276
14.5	Composite, Sandwich, and Honeycomb Plates	289
14.6	Flexural Vibrations of Honeycomb/Sandwich Beams.	294
14.7	Wavenumbers, Sandwich/Honeycomb Beams	296
14.8	Displacement	298
14.9	Dynamic Properties of Sandwich Beams	302
14.10	Bending Stiffness of Sandwich Plates	305
14.11	Response of Sandwich Beams	307
14.12	Energy Flow in Sandwich Beams	312
14.13	Energy Flow Across Pinned Junctions	314
14.14	Wave Propagation on Infinite Cylinders.	316
14.15	Vibration of Open Circular Cylindrical Shells.	322
14.16	Sound Transmission Loss of Shallow Shell Segments	324
14.17	Comparison Between Measured and Predicted TL.	329
	Problems.	337
15	Random Excitation of Structures.	339
15.1	Introduction	339
15.2	Excitation of Plates	342
15.3	Rain on the Roof Excitation of Plates	346
15.4	Turbulent Boundary Layers	350
15.5	TBL Models.	352
15.6	Plate Response Due to TBL Excitation	356
15.7	Measurements of TBL-Induced Vibrations	362
15.8	Comparison Between Measured and Predicted Velocity Levels Induced by TBL	366
15.9	Parameter Study	371
15.10	Flow Noise Induced in Ships	373
	Problems.	378

16	Transmission of Sound in Built-Up Structures	379
16.1	Introduction	380
16.2	Statistical Energy Analysis, SEA.	382
16.3	Energy Flow Between Continuous Systems	387
16.4	Coupling Between Acoustic Fields and Vibrating Structures.	390
16.5	Prediction of Sound Transmission Through a Panel Using SEA	393
16.6	Sound Transmission Through Double Walls.	395
16.7	Limitation of SEA-Derived Sound Transmission Loss	398
16.8	Coupling Between Vibrating Structures	400
16.9	Energy Flow in Large Structures, SEA	402
16.10	SEA Parameters	406
16.11	Ship Noise	409
16.12	Waveguide Model.	411
16.13	Noise Levels in Accommodation Spaces	415
16.14	Source Data	417
16.15	Measured and Predicted Results	418
16.16	Conclusions—Noise Prediction on Ships	423
	Problems.	424
	Appendix A: Sound Transmission Loss of Single Leaf Panels	425
	Appendix B: Velocity Level of Single Leaf Panels Excited by an Acoustic Field	429
	Appendix C: Input Data for Noise Prediction on Ships	433
	References	437
	Index	449

Chapter 9

Hamilton's Principle and Some Other Variational Methods

Many problems in mathematical physics and thus in vibro-acoustics cannot be solved exactly. However, a variational technique can often be used to sufficiently well formulate the equations governing the response of a structure excited by external forces. The technique ensures that errors are minimized. Variational techniques are excellent tools for solving dynamic problems for which exact solutions cannot be formulated.

The widely used Finite Element Method is based on Hamilton's principle, which is a very powerful variational method. The principle can be proved based on Newton's law of motion. Inversely Newton's law can be derived using Hamilton's principle. However, Hamilton's principle is much more general than Newton's law and for this reason, it has survived the revolution in mechanics brought by Einstein.

The key problem for the successful application of any variational technique is the mathematical formulation of the kinetic and potential energies of a system. This formulation also requires a physical understanding of the mechanisms governing the motion of a system. This can be illustrated by considering two different types of three-layered beams. In one case, the structure consists of a beam with a constrained viscoelastic layer. For the vibrating beam, the shear forces in the viscoelastic layer along the axis of the beam are of importance. In the other case, the core of a three-layered beam consists of a honeycomb structure. In this case, the shear forces perpendicular to the axis of the beam are of major importance for the deflection of the beam. For the two cases, the energies are modeled in different ways resulting in two different equations as discussed in Sects. 9.3 and 9.4. In each case, the results are only valid as long as the basic physical assumptions are satisfied.

Hamilton's principle is in this chapter used to derive the equations, which up to certain frequencies govern the flexural vibrations of thick beams or plates and of cylindrical shells. The Lagrange and Galerkin methods are also discussed. The longitudinal vibration of thick beams or rods is examined in Chap. 10 in connection with discussions on various models describing the axial vibration of cylindrical rubber mounts.

9.1 Hamilton's Principle

The most general formulation of the law governing the motion of a mechanical system is Hamilton's principle. In formulating the principle, it is assumed that the potential energy \mathcal{U} is a known function of some generalized coordinates q_1, q_2, \dots, q_n and time t . The potential energy is symbolically written as $\mathcal{U} = \mathcal{U}(q, t)$. The kinetic energy \mathcal{T} of the same system is also assumed to be a known function of the coordinates q_1, q_2, \dots, q_n , the velocities $\dot{q}_1, \dot{q}_2, \dots, \dot{q}_n$ and time t . Thus, the kinetic energy is written as $\mathcal{T} = \mathcal{T}(q, \dot{q}, t)$.

The Hamilton's principle states: between two instants of time, t_1 and t_2 , the motion of a mechanical system is such that for the coordinates defining the system to be described by the functions $q_i(t)$ the integral

$$\mathcal{J} = \int_{t_1}^{t_2} (\mathcal{T} - \mathcal{U}) dt \quad (9.1)$$

is stationary. It is assumed that the coordinates or displacements of the system at $t = t_1$ and $t = t_2$ are known.

Hamilton's principle can also be written in the form

$$\delta \int_{t_1}^{t_2} (\mathcal{T} - \mathcal{U}) dt = 0 \quad (9.2)$$

The expression states that the variation of the integral is zero when the system is given a virtual displacement if the virtual displacement is zero at $t = t_1$ and $t = t_2$. During time period t_1 to t_2 the system will move in such a way that the time average of the difference between the kinetic and potential energies is an extremum or in most cases a minimum.

The difference between the kinetic and potential energies is called the Lagrangian of the system and is defined as (or sometimes as $-\mathcal{L}$)

$$\mathcal{L} = \mathcal{T} - \mathcal{U} \quad (9.3)$$

The influence of an external field or force can also be incorporated in the variational expression. By defining the potential energy for the conservative external forces as \mathcal{A} and by including this in the original expression (9.2) Hamilton's principle reads

$$\delta \int_{t_1}^{t_2} (\mathcal{T} - \mathcal{U} - \mathcal{A}) dt = 0 \quad (9.4)$$

For a conservative (no losses) and external force described by the vector \mathbf{F} acting on a particle and moving the particle along a path given by the vector \mathbf{s} the potential energy of the external force is reduced and giving the energy as

$$\mathcal{A} = - \int \mathbf{F} ds \tag{9.5}$$

Hamilton's principle as a tool for deriving the governing equations describing the motion of a simple beam and some more complicated structures are discussed in the following sections.

One proof of Hamilton's principle can, as suggested by Petyt [63], be illustrated by considering a simple system shown in Fig. 9.1. Let the vector \mathbf{F} describe a conservative force acting on the point mass m . The work \mathcal{W} done by a conservative force, defined by the vector \mathbf{F} , when moving the mass m from a position \mathbf{r}_1 to \mathbf{r}_2 is independent of the path taken. The work \mathcal{W} done along any path s is

$$\mathcal{W} = \int \mathbf{F} ds$$

During the process the mass or the system has lost the potential energy \mathcal{U} , thus $\mathcal{U} = -\mathcal{W}$. The conservative vector force \mathbf{F} can thus be expressed as a function of the potential energy \mathcal{U} of the symbol

$$\mathbf{F} = -\mathbf{grad} \mathcal{U} \tag{9.6}$$

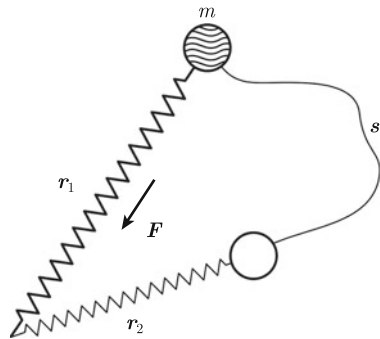
Consider now a simple mass m subjected to a conservative force defined by the vector \mathbf{F} . According to the principle of virtual displacement, it follows that

$$\mathbf{F} \cdot \delta \mathbf{r} - m \ddot{\mathbf{r}} \cdot \delta \mathbf{r} = 0 \tag{9.7}$$

The vector \mathbf{r} defines the position of the mass. The virtual work $\delta \mathcal{W} = \mathbf{F} \cdot \delta \mathbf{r}$ done by the conservative force is also given by $\delta \mathcal{U} = -\mathbf{F} \cdot \delta \mathbf{r}$ when \mathcal{U} is the potential energy of the system. Considering this, Eq. (9.7) is written as

$$\delta \mathcal{U} = -m \ddot{\mathbf{r}} \cdot \delta \mathbf{r} \tag{9.8}$$

Fig. 9.1 A simple mass system moved by a force between two positions



The kinetic energy \mathcal{T} of the mass or in fact the system is $\mathcal{T} = m \cdot \dot{\mathbf{r}}^2/2$. Thus

$$\delta\mathcal{T} = m \cdot \dot{\mathbf{r}} \cdot \delta\dot{\mathbf{r}} \quad (9.9)$$

By subtracting the expression (9.8) from (9.9) the result is

$$\delta\mathcal{T} - \delta\mathcal{U} = m \cdot \dot{\mathbf{r}} \cdot \delta\dot{\mathbf{r}} + m\ddot{\mathbf{r}} \cdot \delta\mathbf{r} = \frac{d}{dt} (m\dot{\mathbf{r}} \cdot \delta\mathbf{r}) \quad (9.10)$$

Integration with respect to time from t_1 to t_2 gives

$$\int_{t_1}^{t_2} (\delta\mathcal{T} - \delta\mathcal{U}) dt = [m\dot{\mathbf{r}} \cdot \delta\mathbf{r}]_{t_1}^{t_2} \quad (9.11)$$

Assuming that the virtual displacement $\delta\mathbf{r}$ is equal to zero for $t = t_1$ and $t = t_2$ it follows that

$$\delta \int_{t_1}^{t_2} (\mathcal{T} - \mathcal{U}) dt = 0$$

This is Hamilton's result as given by Eq. (9.2).

Hamilton's principle is discussed in for example Refs. [58, 77, 78].

9.2 Flexural Vibrations of Slender Beams

The flexural vibrations of "thin" or slender beams were discussed in Chap. 7 (Volume I). Again, a "thin" beam under flexure is considered to demonstrate how Hamilton's principle can be used to derive the equations governing the motion of the beam as well as to formulate the boundary conditions of the beam.

A simple homogeneous and slender beam is shown in Fig. 9.2. The bending stiffness of the beam is D' and its mass per unit length is m' . The beam is extended along the x -axis from $x = 0$ to $x = L$ and is excited by a force $F'(x, t)$ per unit length. The resulting displacement of the beam is $w(x, t)$ defined positive, as the force, along the

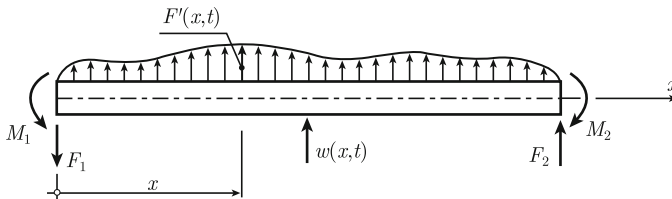


Fig. 9.2 Forces and bending moments acting on a beam

positive y -axis. The forces and bending moments at the boundaries are F_1 , F_2 , M_1 , and M_2 as defined in Fig. 9.2.

The potential energy \mathcal{U}_l induced by bending is per unit length of the beam given by Eq. (3.84) as

$$\mathcal{U}_l = \frac{D'}{2} \cdot \left(\frac{\partial^2 w}{\partial x^2} \right)^2$$

The kinetic energy per unit length of the beam is

$$\mathcal{T}_l = \frac{m'}{2} \cdot \left(\frac{\partial w}{\partial t} \right)^2$$

The potential energy \mathcal{A}_1 per unit length induced by the external force F' is according to the definition (9.5) given by

$$\mathcal{A}_1(t) = - \int_0^L w(x, t) F'(x, t) dx$$

The potential energy \mathcal{A}_2 induced by the external forces and moments is

$$\begin{aligned} \mathcal{A}_2(t) &= -F_2(t)w(L, t) + F_1(t)w(0, t) + M_2(t) \left[\frac{\partial w}{\partial x} \right]_{x=L} - M_1(t) \left[\frac{\partial w}{\partial x} \right]_{x=0} \\ &= - \left[Fw - M \cdot \frac{\partial w}{\partial x} \right]_0^L \end{aligned} \quad (9.12)$$

The total potential energy invoked by all external forces is consequently

$$\mathcal{A}(t) = - \int_0^L w(x, t) F'(x, t) dx - \left[Fw - M \cdot \frac{\partial w}{\partial x} \right]_0^L \quad (9.13)$$

According to Hamilton's principle the kinetic and potential energies should satisfy Eq. (9.4). Thus

$$\delta \int_{t_1}^{t_2} (\mathcal{T} - \mathcal{U} - \mathcal{A}) dt = \delta \int_{t_1}^{t_2} dt \left[-\mathcal{A} + \int_0^L dx (\mathcal{T}_l - \mathcal{U}_l) \right] = 0 \quad (9.14)$$

By inserting Eqs. (9.4), (9.5), and (9.13) in Eq. (9.14) the result is

$$\begin{aligned} &\delta \int_{t_1}^{t_2} dt \left[\int_0^L dx \left\{ \frac{m'}{2} \cdot \left(\frac{\partial w}{\partial t} \right)^2 - \frac{D'}{2} \cdot \left(\frac{\partial^2 w}{\partial x^2} \right)^2 + w F' \right\} \right] \\ &+ \left[Fw - M \cdot \frac{\partial w}{\partial x} \right]_0^L = 0 \end{aligned} \quad (9.15)$$

Effecting the variation the expression (9.15) is written as

$$\begin{aligned} & \int_{t_1}^{t_2} dt \left[\int_0^L dx \left\{ m' \cdot \left(\frac{\partial w}{\partial t} \right) \left(\frac{\partial \delta w}{\partial t} \right) - D' \cdot \left(\frac{\partial^2 w}{\partial x^2} \right) \left(\frac{\partial^2 \delta w}{\partial x^2} \right) + F' \delta w \right\} \right] \\ & + \int_{t_1}^{t_2} dt \left[F \delta w - M \cdot \frac{\partial \delta w}{\partial x} \right]_0^L = 0 \end{aligned} \quad (9.16)$$

Next, integration by parts is carried out. For simplicity, each part of the integrand is treated separately. The first part of the double integral of (9.16) gives

$$X_1 = \int_0^L dx \int_{t_1}^{t_2} dt \cdot m' \frac{\partial w}{\partial t} \frac{\partial \delta w}{\partial t} = \int_0^L dx \left\{ \left[m' \frac{\partial w}{\partial t} \delta w \right]_{t_1}^{t_2} - \int_{t_1}^{t_2} dt \cdot m' \frac{\partial^2 w}{\partial t^2} \delta w \right\}$$

However, as required, the displacement w is fixed at the initial and final time limits. Thus $\delta w = 0$ at $t = t_1$ and $t = t_2$. The integral X_1 is consequently reduced to

$$X_1 = - \int_{t_1}^{t_2} dt \cdot m' \frac{\partial^2 w}{\partial t^2} \delta w \quad (9.17)$$

The second part X_2 of the integral (9.16) is integrated by parts as

$$\begin{aligned} X_2 &= \int_{t_1}^{t_2} dt \left\{ \int_0^L dx \left[-D' \cdot \left(\frac{\partial^2 w}{\partial x^2} \right) \left(\frac{\partial^2 \delta w}{\partial x^2} \right) \right] \right\} \\ &= -D' \int_{t_1}^{t_2} dt \left[\left(\frac{\partial^2 w}{\partial x^2} \right) \left(\frac{\partial \delta w}{\partial x} \right) \right. \\ &\quad \left. - \left(\frac{\partial^3 w}{\partial x^3} \right) \delta w \right]_0^L - D' \int_0^L dx \int_{t_1}^{t_2} dt \cdot \frac{\partial^4 w}{\partial x^4} \cdot \delta w \end{aligned} \quad (9.18)$$

By introducing the expressions (9.17) and (9.18) in Eq. (9.16) the result is

$$\begin{aligned} & \int_{t_1}^{t_2} dt \int_0^L dx \delta w \left[-m' \frac{\partial^2 w}{\partial t^2} - D' \frac{\partial^4 w}{\partial x^4} + F' \right] \\ & + \int_{t_1}^{t_2} dt \left[\delta w \left(D' \frac{\partial^3 w}{\partial x^3} + F \right) - \frac{\partial \delta w}{\partial x} \left(D' \frac{\partial^2 w}{\partial x^2} + M \right) \right]_0^L = 0 \end{aligned} \quad (9.19)$$

For the result to be zero for any δw or $\partial \delta w / \partial x$, it follows that the expressions inside the brackets must be zero. Setting the expression inside the first bracket equal to zero gives

$$D' \frac{\partial^4 w}{\partial x^4} + m' \frac{\partial^2 w}{\partial t^2} = F' \quad (9.20)$$

This is the equation of motion of a slender and homogeneous beam in flexure as already discussed in Sect. 3.7.

By setting the second square bracket equal zero, the boundary conditions for $x = 0$ and $x = L$ are obtained as

$$\delta w \left(D' \frac{\partial^3 w}{\partial x^3} + F \right) = 0 \quad (9.21)$$

$$\frac{\partial \delta w}{\partial x} \left(D' \frac{\partial^2 w}{\partial x^2} + M \right) = 0 \quad (9.22)$$

For the first condition (9.21) to be satisfied at a boundary, it follows that

$$F = -D' \frac{\partial^3 w}{\partial x^3} \quad \text{or} \quad \delta w = 0 \quad (9.23)$$

The second condition requires

$$M = -D' \frac{\partial^2 w}{\partial x^2} \quad \text{or} \quad \frac{\partial \delta w}{\partial x} = 0 \quad (9.24)$$

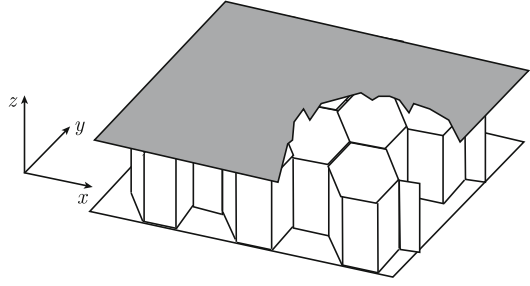
The results give the expressions for force and bending moment as given by the displacement w of the beam as already derived in Chap. 3, Eqs. (3.73) and (3.75). The conditions $\delta w = 0$ and $\delta(\partial w/\partial x) = 0$ are equivalent to w and $\partial w/\partial x$ being constant at the boundaries. For most practical purposes a coordinate system can be oriented in such a way that the boundary conditions can be written $w = 0$ and $\partial w/\partial x = 0$.

For one end of the beam simply supported, it follows that $w = 0$ to satisfy the first requirement (9.23). For a simply supported beam, the bending moment is zero at the boundary. The second requirement gives $\partial^2 w/\partial x^2 = 0$. For a beam clamped at both ends, $w = 0$ and $\partial w/\partial x = 0$ to satisfy both Eqs. (9.23) and (9.24).

Thus, by defining the kinetic and potential energies for a beam in flexure not only the equation of motion but also a set of boundary conditions are derived from Hamilton's principle.

9.3 Equation of Motion for Honeycomb Beams in Flexure

The so-called sandwich panel, discussed in Sect. 4.7, is a structure, which can satisfy requirements to low weight and high strength. Another such structure is shown in Fig. 9.3. The core of the panel is a honeycomb structure. Thin laminates are bonded to each side of the core as shown in Fig. 9.3. The core is primarily acting as a spacer between the high strength laminates to give a sufficiently high bending stiffness to the entire structure. In general, the stiffness of the core is high enough to ensure that

Fig. 9.3 Honeycomb panel

the laminates move in-phase in the frequency range of interest. Typical materials used for honeycombs are aluminum or Nomex, an aramid fiber paper coated by a phenolic resin. Aluminum cores are often used in combination with aluminum laminates. Various types of composite laminates are used with Nomex cores. These laminates typically consist of a number of layers of fibers, which form part of a supporting matrix. The orientation of the fibers and their properties determine the macro-mechanical behavior of the laminates. Often, not only the laminates but also the cores are orthotropic. The acoustic and dynamic properties of various types of sandwich and honeycomb elements are discussed in Sects. 14.5 through 14.13.

In general, the core is stiff in the direction perpendicular to the laminates. For a stiff core, it can be assumed that the laminates move in-phase as shown in Fig. 4.4a. However, this requires that the dilatation frequency or double wall resonance f_d be well outside the frequency range for which the structure is designed, compare the discussion in Sect. 7.9. For a sandwich or honeycomb element, one element having the mass per area μ_1 and the other μ_2 , with a lightweight core having the thickness H and the Young's modulus E perpendicular to the laminates the dilatation frequency f_d is

$$f_d = \frac{1}{2\pi} \left[\frac{E(\mu_1 + \mu_2)}{H\mu_1\mu_2} \right]^{1/2}$$

The equations governing the flexural motion of a honeycomb or sandwich beam can be formulated based on Hamilton's principle as discussed in Refs. [79–82]. Consider a beam element shown in Fig. 9.4. The thickness of the core is H . The core has a density ρ_c and effective shear stiffness G_e with respect to lateral forces. The E -modulus of the core in the axial direction is denoted E_{cx} . The laminates are assumed to be identical and have the thickness h and density ρ_l and E -modulus E_{lx} in the x -direction.

According to Hamilton's principle, the equation of motion governing the lateral motion of the structure can be derived once expressions defining the kinetic and potential energies of the structure have been formulated. However, certain assumptions have to be made with respect to the motion of the structure. The laminates are assumed to move in-phase having the same lateral displacement. The lateral displacement is modeled as a combination of pure bending of the entire beam and by shear in the core as shown in Fig. 9.5a, b, respectively.

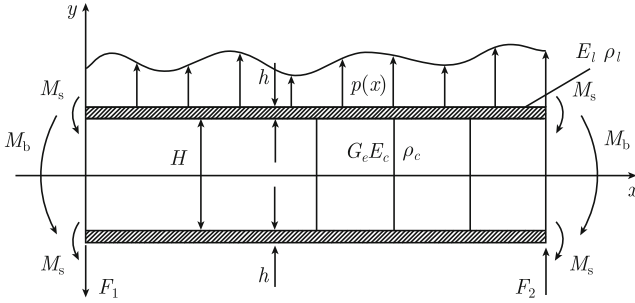
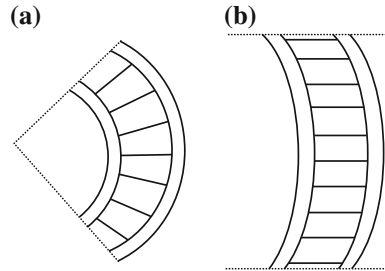


Fig. 9.4 A sandwich beam

Fig. 9.5 Displacement of a beam, **a** pure bending, **b** shear deformation



The lateral displacement of the beam is w . The angular displacement $\partial w / \partial x$ is caused by pure bending, defined by the angular displacement β , and by shear in the core given by the angular displacement γ . Thus,

$$\frac{\partial w}{\partial x} = \beta + \gamma \tag{9.25}$$

The potential energy \mathcal{U}_{II} due to pure bending of the beam is per unit length obtained from Eq. (3.84) as

$$\mathcal{U}_{II} = \frac{D'_1}{2} \left(\frac{\partial \beta}{\partial x} \right)^2 \tag{9.26}$$

The bending stiffness D'_1 of the entire beam, width b , is

$$\begin{aligned} D'_1 &= 2b \int_0^{H/2} E_{cx} y^2 dy + 2b \int_{H/2}^{H/2+h} E_{lx} y^2 dy \\ &= E_{cx} \frac{bH^3}{12} + E_{lx} b \left[\frac{H^2 h}{2} + Hh^2 + \frac{2h^3}{3} \right] \end{aligned} \tag{9.27}$$

In general $E_{lx} \gg E_{cx}$ and $H \gg h$.

The potential energy \mathcal{U}_{2l} induced by the shear deformation of the core is per unit length obtained from Eq. (3.41) as

$$\mathcal{U}_{2l} = SG_e \gamma^2 / 2; \quad S = Hb \quad (9.28)$$

The cross section area of the beam is S . The laminates will bend due to the shear deformation of the core. The potential energy \mathcal{U}_{3l} per unit length due to the shear deformation γ of the core is for each laminate

$$\mathcal{U}_{3l} = \frac{D'_2}{2} \left(\frac{\partial \gamma}{\partial x} \right)^2; \quad D'_2 = E_{lx} \frac{bh^3}{12} \quad (9.29)$$

where D'_2 is the bending stiffness of one of the two identical laminates.

The kinetic energy is assumed to be determined by the lateral motion of the entire beam and the rotation of vertical segments of the beam. In the first case the kinetic energy \mathcal{T}_{1l} per unit length is

$$\mathcal{T}_{1l} = \frac{m'}{2} \left(\frac{\partial w}{\partial t} \right)^2; \quad m' = b(H\rho_c + 2h\rho_l) \quad (9.30)$$

The mass per unit length of the beam is m' . The kinetic energy \mathcal{T}_{2l} due to rotation $\partial\beta/\partial t$ is per unit length

$$\begin{aligned} \mathcal{T}_{2l} &= \frac{I'_\omega}{2} \left(\frac{\partial \beta}{\partial t} \right)^2 \\ I'_\omega &= 2b \int_0^{H/2} \rho_c y^2 dy + 2b \int_{H/2}^{H/2+h} \rho_l y^2 dy \\ &= \rho_c \frac{bH^3}{12} + \rho_l b \left[\frac{H^2 h}{2} + Hh^2 + \frac{2h^3}{3} \right] \end{aligned} \quad (9.31)$$

where I'_ω is the mass moment of inertia of the beam.

The beam is excited by a force $F'(x, t)$ per unit length. The forces F_1 and F_2 are defined in Fig. 9.4. The shear deformation of the core induces a bending of each laminate resulting in a bending moment M_s of the laminate and giving it an angular displacement γ . The total bending moment of the entire beam is M_b caused by pure bending, or rather by the angular displacement β . The total potential energy of the external loading is in accordance with Eq. (9.13) equal to

$$\mathcal{A}(t) = - \int_0^L w(x, t) F'(x, t) dx - [Fw - M_b \cdot \beta - 2M_s \cdot \gamma]_0^L \quad (9.32)$$

Hamilton's principle, Eq. (9.4), yields

$$\delta \int_{t_1}^{t_2} (\mathcal{T} - \mathcal{V} - \mathcal{A}) dt = \delta \int_{t_1}^{t_2} dt \left[-\mathcal{A} + \int_0^L dx (\mathcal{T}_{1l} + \mathcal{T}_{2l} - \mathcal{V}_{1l} - \mathcal{V}_{2l} - 2\mathcal{V}_{3l}) \right] = 0$$

This expression in combination with the Eqs. (9.26), (9.28)–(9.31) results in

$$\begin{aligned} \delta \int_{t_1}^{t_2} dt \left\{ \frac{1}{2} \int_0^L dx \left[m' \left(\frac{\partial w}{\partial t} \right)^2 + I'_w \left(\frac{\partial \beta}{\partial t} \right)^2 - D'_1 \left(\frac{\partial \beta}{\partial x} \right)^2 - S G_e \gamma^2 \right. \right. \\ \left. \left. - 2D'_2 \left(\frac{\partial \gamma}{\partial x} \right)^2 + 2wF' \right] + [Fw - M_b \beta - 2M_s \gamma]_0^L \right\} = 0 \end{aligned} \quad (9.33)$$

The angular displacement γ , which is due to shear, is according to Eq. (9.25) equal to $\gamma = \partial w / \partial x - \beta$. Considering this and effecting the variation and after integrating by parts and by observing that $\delta w = \delta \beta = 0$ for $t = t_1$ and $t = t_2$ the result reads

$$\begin{aligned} \iint dx dt \delta w \left[-G_e S \left\{ \frac{\partial^2 w}{\partial x^2} - \frac{\partial \beta}{\partial x} \right\} + 2D'_2 \left\{ \frac{\partial^4 w}{\partial x^4} - \frac{\partial^3 \beta}{\partial x^3} \right\} + m' \frac{\partial^2 w}{\partial t^2} - F' \right] \\ + \iint dx dt \delta \beta \left[-G_e S \left\{ \frac{\partial w}{\partial x} - \beta \right\} - D'_1 \frac{\partial^2 \beta}{\partial x^2} + 2D'_2 \left\{ \frac{\partial^3 w}{\partial x^3} - \frac{\partial^2 \beta}{\partial x^2} \right\} + I'_w \frac{\partial^2 \beta}{\partial t^2} \right] \\ + \int dt \delta w \left[G_e S \left\{ \frac{\partial w}{\partial x} - \beta \right\} - 2D'_2 \left\{ \frac{\partial^3 w}{\partial x^3} - \frac{\partial^2 \beta}{\partial x^2} \right\} - F' \right]_0^L \\ + \int dt \delta \beta \left[D'_1 \frac{\partial \beta}{\partial x} - 2D'_2 \left\{ \frac{\partial^2 w}{\partial x^2} - \frac{\partial \beta}{\partial x} \right\} + M_b - 2M_s \right]_0^L \\ + 2 \int dt \frac{\partial \delta w}{\partial x} \left[D'_2 \left\{ \frac{\partial^2 w}{\partial x^2} - \frac{\partial \beta}{\partial x} \right\} + M_s \right]_0^L = 0 \end{aligned} \quad (9.34)$$

For the entire expression to equal zero for any virtual displacement along the total length of the beam, the displacement w and the angular displacement β , pure bending, must satisfy two differential equations obtained by setting the first two large brackets equal to zero. Thus

$$-G_e S \left\{ \frac{\partial^2 w}{\partial x^2} - \frac{\partial \beta}{\partial x} \right\} + 2D'_2 \left\{ \frac{\partial^4 w}{\partial x^4} - \frac{\partial^3 \beta}{\partial x^3} \right\} + m' \frac{\partial^2 w}{\partial t^2} - F' = 0 \quad (9.35)$$

$$-G_e S \left\{ \frac{\partial w}{\partial x} - \beta \right\} - D'_1 \frac{\partial^2 \beta}{\partial x^2} + 2D'_2 \left\{ \frac{\partial^3 w}{\partial x^3} - \frac{\partial^2 \beta}{\partial x^2} \right\} + I'_w \frac{\partial^2 \beta}{\partial t^2} = 0 \quad (9.36)$$

For the last three integrals of Eq. (3.34) to equal zero the boundary conditions at $x = 0$ and $x = L$ must satisfy

$$F = G_e S \left\{ \frac{\partial w}{\partial x} - \beta \right\} - 2D'_2 \left\{ \frac{\partial^3 w}{\partial x^3} - \frac{\partial^2 \beta}{\partial x^2} \right\} \quad \text{or} \quad w = 0 \quad (9.37)$$

$$M_b - 2M_s = -D'_1 \frac{\partial \beta}{\partial x} + 2D'_2 \left\{ \frac{\partial^2 w}{\partial x^2} - \frac{\partial \beta}{\partial x} \right\} \quad \text{or} \quad \beta = 0 \quad (9.38)$$

$$M_s = -D'_2 \left\{ \frac{\partial^2 w}{\partial x^2} - \frac{\partial \beta}{\partial x} \right\} \quad \text{or} \quad \frac{\partial w}{\partial x} = 0 \quad (9.39)$$

By substituting Eq. (9.36) into (9.37) the first boundary condition is written as

$$F = -D'_1 \frac{\partial^2 \beta}{\partial x^2} + I'_\omega \frac{\partial^2 \beta}{\partial t^2} \quad \text{or} \quad w = 0$$

The differential equation governing the lateral displacement $w(x, t)$ of the honeycomb beam is obtained by eliminating the angular displacement β from Eq. (9.35) by means of Eq. (9.36). One way to execute this operation is to introduce the expression $w(x, t) = W \cdot \exp[i(\omega t - k_x x)]$ and $\beta(x, t) = B \cdot \exp[i(\omega t - k_x x)]$ in Eqs. (3.35) and (3.36). The two unknown amplitudes W and B are solved. Thereafter expressions of the form $(-ik_x)^n W$ are interpreted as $\partial^n w / \partial x^n$ and $(i\omega)^n W$ as $\partial^n w / \partial t^n$. The details are left for Problem 9.4. The procedure, a direct and inverse Fourier transform, leads to the result:

$$\begin{aligned} & -2D'_1 D'_2 \frac{\partial^6 w}{\partial x^6} + 2D'_2 I'_\omega \frac{\partial^6 w}{\partial x^4 \partial t^2} + G_e S D'_1 \frac{\partial^4 w}{\partial x^4} \\ & - [(D'_1 + 2D'_2)m' + G_e S I'_\omega] \frac{\partial^4 w}{\partial x^2 \partial t^2} \\ & + G_e S m' \frac{\partial^2 w}{\partial t^2} + m' I'_\omega \frac{\partial^4 w}{\partial t^4} = G_e S F' - (D'_1 + 2D'_2) \frac{\partial^2 F'}{\partial x^2} + I'_\omega \frac{\partial^2 F'}{\partial t^2} \end{aligned} \quad (9.40)$$

$$\begin{aligned} & -2D'_1 D'_2 \frac{\partial^6 \beta}{\partial x^6} + 2D'_2 I'_\omega \frac{\partial^6 \beta}{\partial x^4 \partial t^2} + G_e S D'_1 \frac{\partial^4 \beta}{\partial x^4} \\ & - [(D'_1 + 2D'_2)m' + G_e S I'_\omega] \frac{\partial^4 \beta}{\partial x^2 \partial t^2} \\ & + G_e S m' \frac{\partial^2 \beta}{\partial t^2} + m' I'_\omega \frac{\partial^4 \beta}{\partial t^4} = G_e S \frac{\partial F'}{\partial x} - 2D'_2 \frac{\partial^3 F'}{\partial x^3} \end{aligned} \quad (9.41)$$

Once w and β are determined, the angular displacement γ is obtained from Eq. (9.25) as $\gamma = \partial w / \partial x - \beta$. Except for the source terms, w and β satisfy the same differential equation.

By letting the shear modulus G_e approach infinity and by setting I'_ω equal zero and thus neglecting shear and rotation, Eq. (9.40) is reduced to $D'_1 \partial^4 w / \partial x^4 +$

$m' \partial^2 w / \partial t^2 = F'$ or the standard equation governing flexural vibrations of a slender beam with the bending stiffness D'_1 and mass m' per unit length.

If on the other hand the core is soft, G_e tends to zero, and neglecting rotation, Eq. (9.40) is reduced to

$$2D'_1 D'_2 \frac{\partial^6 w}{\partial x^6} + [(D'_1 + 2D'_2)m'] \frac{\partial^4 w}{\partial x^2 \partial t^2} = (D'_1 + 2D'_2) \frac{\partial^2 F'}{\partial x^2}$$

which for $D'_1 \gg D'_2$ is approximated by

$$D'_2 \frac{\partial^4 w}{\partial x^4} + \frac{m'}{2} \frac{\partial^2 w}{\partial t^2} = F'/2$$

This is the equation of motion of one laminate assuming the weight of the two identical laminates being equal to the total weight of the beam. Since the distance between the beams is constant, each beam is supporting the force $F'/2$.

The boundary conditions for a honeycomb beam are given in Eq. (9.37) through (9.39). For a clamped beam, the displacement is zero at the boundaries. This requirement satisfies Eq. (9.37). Since at the boundaries the bending moments M and M_s are different from zero it follows that the remaining requirements, (9.38) and (9.39), only are satisfied if $\beta = 0$ and $\partial w / \partial x = 0$. Thus, the boundary conditions to be satisfied at a clamped edge are as follows: $w = 0$, $\beta = 0$ and $\partial w / \partial x = 0$.

For a simply supported beam, it must be assumed that the beam is “hinged” at the center of the end section as shown in Fig. 9.6. The displacement w and the bending moments M and M_s are zero at the end section. The expressions to be satisfied at a boundary are given by (9.38) and (9.39) as $\partial \beta / \partial x = 0$ and $\partial^2 w / \partial x^2 - \partial \beta / \partial x = 0$ or quite simply $w = \partial^2 w / \partial x^2 = \partial \beta / \partial x = 0$.

For a free edge, the boundary conditions must satisfy $F = M = M_s = 0$. The bending moments are zero when $\partial^2 w / \partial x^2 = \partial \beta / \partial x = 0$. The force, (9.37), can by means of Eq. (9.36) be written as

$$F = -D'_1 \frac{\partial^2 \beta}{\partial x^2} + I'_w \frac{\partial^2 \beta}{\partial t^2}$$

Fig. 9.6 A simply supported edge



Table 9.1 Boundary conditions for a honeycomb/sandwich beam

End condition			
Simply supported	$w = 0$	$\partial\beta/\partial x = 0$	$\partial^2 w/\partial x^2 = 0$
Clamped	$w = 0$	$\beta = 0$	$\partial w/\partial x = 0$
Free	$\partial\beta/\partial x = 0$	$\partial^2 w/\partial x^2 = 0$	$D'_1 \partial^2 \beta/\partial x^2 - I'_\omega \partial^2 \beta/\partial t^2 = 0$

For a free edge $F = 0$. Often $I'_\omega \ll 1$ which simplifies the boundary condition for a free edge to $\partial^2 \beta/\partial x^2 = 0$.

The three boundary conditions are summarized in Table 9.1.

The vibrations of sandwich and honeycomb beams are discussed further in Sects. 14.5 through 14.13.

9.4 Plates with Constrained Viscoelastic Layer

The loss factor of a structure is an important parameter. By increasing the loss factor of a structure its vibration energy can be reduced close to a resonance. Various methods to increase the losses of a system were discussed in Sect. 5.5. In particular, the so-called constrained viscoelastic layers can be quite effective. An example of a constrained layer is shown in Fig. 9.7. The constraining layer induces shear and longitudinal waves in the viscoelastic material. The losses due to shear typically dominate and determine the total losses of the structure. The deformation due to the bending of a plate with a constrained viscoelastic layer is also shown in Fig. 9.7.

The addition of a constraining layer and a viscoelastic layer to a structure not only changes the loss factor but also the dynamic properties of the structure. It is therefore essential to formulate the equations governing the vibrations of the structure. These equations can again be derived by means of Hamilton's principle as discussed in Refs. [83, 84]. The result also gives the total bending stiffness, loss factor, and boundary conditions for the damped element.

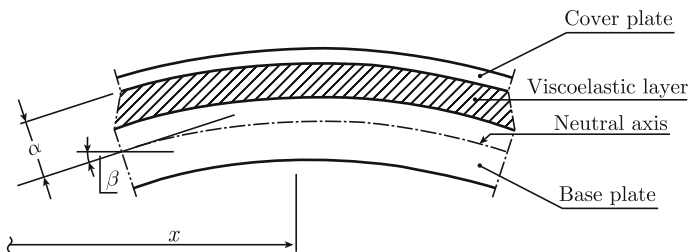


Fig. 9.7 Deformation of a beam with a constrained viscoelastic layer

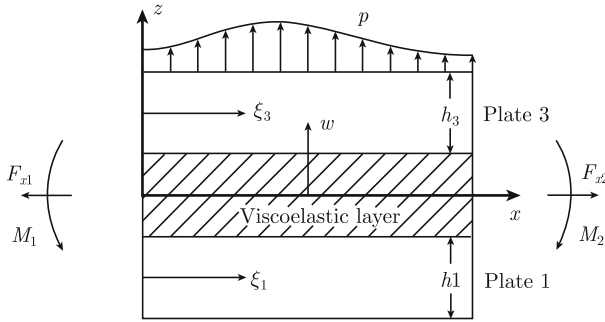


Fig. 9.8 Forces and moments acting on a plate element having a constrained viscoelastic layer

Certain assumptions have to be made concerning the bending of the structure for estimating its kinetic and potential energies. Consider a plate element under bending as shown in Fig. 9.8.

The length of the plate along the x -axis is L . The displacement of the plate is assumed to depend only on its x -coordinate. The base plate, denoted 1, has the Young's modulus E_1 , density ρ_1 , Poisson's ratio ν_1 , and thickness h_1 . The corresponding parameters for the cover or constraining plate are E_3 , ρ_3 , ν_3 , and h_3 . The bending stiffness or rather its real part is

$$D_{0n} = \frac{E_{0n} h_n^3}{12(1 - \nu_n^2)}; \quad n = 1 \text{ for base plate and } n = 3 \text{ for cover plate}$$

It is assumed that the loss factors η_1 and η_3 of the base and cover plates are small as compared to the loss factor η_2 of the viscoelastic material. The thickness of the viscoelastic layer is h_2 and its complex shear modulus is $G = G_0(1 + i\eta_2)$. Its density is ρ_2 . The E -modulus of the viscoelastic material is assumed to be small as compared to E_1 and E_3 . However, the properties of the viscoelastic material should be such that the distance h_2 between the base and the cover plates is constant under flexure.

Consider a plate with a constrained viscoelastic layer oriented in the x - y -plane of a coordinate system. The displacement $w(x, t)$ of the plate due to flexure is along the z -axis. The in-plane displacements in the x -direction of the plates 1 and 3 are given by ξ_1 and ξ_3 , respectively. The mass $\mu_2 = \rho_2 h_2$ per unit area of the viscoelastic layer is assumed small as compared to $\mu_1 = \rho_1 h_1$ and $\mu_3 = \rho_3 h_3$, the masses per unit area of the base and cover plates.

The kinetic energy \mathcal{T}_w per unit width of the plate is

$$\mathcal{T}_w = \int_0^L \frac{1}{2} (\mu_1 \dot{\xi}_1^2 + \mu_3 \dot{\xi}_3^2 + \mu_0 \dot{w}^2) dx \quad (9.42)$$

The mass per unit area of the entire plate is μ_0 or

$$\mu_0 = \mu_1 + \mu_2 + \mu_3 \approx \mu_1 + \mu_3 \quad (9.43)$$

The potential energy \mathcal{U}_w per unit width of the plate is determined by the base plate and the cover plate, longitudinal vibrations of the base and cover plates and by shear in the viscoelastic layer. Thus

$$\begin{aligned} \mathcal{U}_w = \int_0^L \frac{1}{2} \left[D_1 \left(\frac{\partial^2 w}{\partial x^2} \right)^2 + D_3 \left(\frac{\partial^2 w}{\partial x^2} \right)^2 + E_1 h_1 \left(\frac{\partial \xi_1}{\partial x} \right)^2 \right. \\ \left. + E_3 h_3 \left(\frac{\partial \xi_3}{\partial x} \right)^2 + G h_2 \gamma^2 \right] dx \end{aligned} \quad (9.44)$$

The shear angle γ depends on the bending of the beam and the horizontal displacements of the plates. Based on the geometry shown in Fig. 9.9 the shear angle γ_1 due to bending and γ_2 caused by sliding is

$$\begin{aligned} h_2 \gamma_1 = x_3 - x_1 = (R + h_e - R) \cdot \frac{\partial w}{\partial x} = h_e \frac{\partial w}{\partial x}; \\ h_e = h_2 + (h_1 + h_3)/2; \quad h_2 \gamma_2 = \xi_3 - \xi_1 \end{aligned}$$

Thus

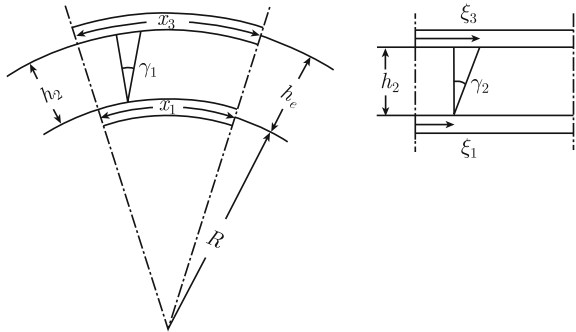
$$\gamma = \gamma_1 + \gamma_2 = \frac{h_e}{h_2} \frac{\partial w}{\partial x} + \frac{\xi_3 - \xi_1}{h_2} \quad (9.45)$$

Following the discussion leading up to Eq. (9.13) in Sect. 9.2, it follows that the potential energy \mathcal{A}_w per unit width induced by the external loading is

$$\mathcal{A}_w = - \int_0^L w p dx - \left[(h_1 \xi_1 + h_3 \xi_3) F'_x / (h_1 + h_3) + F'_z w - M' \frac{\partial w}{\partial x} \right]_0^L \quad (9.46)$$

where p is the external pressure acting on the plate, F'_z is the force per unit width of the plate acting in the z -direction and F'_x is the force per unit width of the plate acting in the x -direction and M' is the external bending moment per unit width acting on the plate. The external pressure is positive in the direction of the positive z -axis.

Fig. 9.9 Shear angles in viscoelastic layer



The force acting on plate 1 in the x -direction is assumed to be $F'_x h_1 / (h_1 + h_3)$. The corresponding force on plate 3 is $F'_x h_3 / (h_1 + h_3)$.

The differential equations governing the flexural vibration of the plate are obtained from Hamilton's principle

$$\delta \int_{t_1}^{t_2} (\mathcal{T}_w - \mathcal{U}_w - \mathcal{A}_w) dt = 0 \quad (9.47)$$

By inserting the expressions (9.42) through (9.46) in (9.47) and effecting the variation the result is

$$\begin{aligned} & \int_{t_1}^{t_2} dt \int_0^L dx [\mu_1 \dot{\xi}_1 \delta \dot{\xi}_1 + \mu_3 \dot{\xi}_3 \delta \dot{\xi}_3 + \mu_0 \dot{w} \delta \dot{w}] \\ & - \int_{t_1}^{t_2} dt \int_0^L dx \left[(D_1 + D_3) \frac{\partial^2 w}{\partial x^2} \cdot \frac{\partial^2 \delta w}{\partial x^2} + E_1 h_1 \frac{\partial \xi_1}{\partial x} \cdot \frac{\partial \delta \xi_1}{\partial x} + E_3 h_3 \frac{\partial \xi_3}{\partial x} \cdot \frac{\partial \delta \xi_3}{\partial x} \right] \\ & - \int_{t_1}^{t_2} dt \int_0^L dx \left[G h_2 \left[\frac{h_e}{h_2} \frac{\partial w}{\partial x} + \frac{1}{h_2} (\xi_3 - \xi_1) \right] \cdot \left[\frac{h_e}{h_2} \frac{\partial \delta w}{\partial x} + \frac{1}{h_2} (\delta \xi_3 - \delta \xi_1) \right] - p \delta w \right] \\ & - \int_{t_1}^{t_2} dt \left[F'_x \frac{h_1 \delta \xi_1 + h_2 \delta \xi_2}{h_1 + h_2} + F'_z \delta w - M' \frac{\partial \delta w}{\partial x} \right]_0^L = 0 \end{aligned} \quad (9.48)$$

Integrating by parts and considering the requirements δw , $\delta \xi_1$ and $\delta \xi_3$ equal to zero at $t = t_1$ and $t = t_2$ the result reads

$$\begin{aligned} & \int_{t_1}^{t_2} dt \int_0^L dx \delta w \left[-\mu_0 \ddot{w} - (D_1 + D_3) \frac{\partial^4 w}{\partial x^4} + G \frac{h_e^2}{h_2} \frac{\partial^2 w}{\partial x^2} + G \frac{h_e}{h_2} \left(\frac{\partial \xi_3}{\partial x} - \frac{\partial \xi_1}{\partial x} \right) + p \right] \\ & + \int_{t_1}^{t_2} dt \int_0^L dx \delta \xi_1 \left[-\mu_1 \ddot{\xi}_1 + E_1 h_1 \frac{\partial^2 \xi_1}{\partial x^2} + G \frac{h_e}{h_2} \frac{\partial w}{\partial x} + G \frac{1}{h_2} (\xi_3 - \xi_1) \right] \\ & + \int_{t_1}^{t_2} dt \int_0^L dx \delta \xi_3 \left[-\mu_3 \ddot{\xi}_3 + E_3 h_3 \frac{\partial^2 \xi_3}{\partial x^2} - G \frac{h_e}{h_2} \frac{\partial w}{\partial x} - G \frac{1}{h_2} (\xi_3 - \xi_1) \right] \\ & + \int_{t_1}^{t_2} dt \left[\delta w \left[(D_1 + D_3) \frac{\partial^3 w}{\partial x^3} + F'_z \right] - \frac{\partial \delta w}{\partial x} \left[(D_1 + D_3) \frac{\partial^2 w}{\partial x^2} + M' \right] \right]_0^L \\ & + \int_{t_1}^{t_2} dt \left[\delta \xi_1 \left(h_1 E_1 \frac{\partial \xi_1}{\partial x} - F'_x \frac{h_1}{h_1 + h_3} \right) + \delta \xi_3 \left(h_3 E_3 \frac{\partial \xi_3}{\partial x} - F'_x \frac{h_3}{h_1 + h_3} \right) \right]_0^L = 0 \end{aligned} \quad (9.49)$$

For the result to be zero for any δw , $\delta \xi_n$, $\partial \delta w / \partial x$ and $\partial \delta \xi_n / \partial x$, it follows that the expressions inside the brackets must equal zero. The first three expressions inside the large brackets give

$$(D_1 + D_3) \frac{\partial^4 w}{\partial x^4} + \mu_0 \ddot{w} - G \frac{h_e^2}{h_2} \frac{\partial^2 w}{\partial x^2} - G \frac{h_e}{h_2} \left(\frac{\partial \xi_3}{\partial x} - \frac{\partial \xi_1}{\partial x} \right) = p \quad (9.50)$$

$$E_1 h_1 \frac{\partial^2 \xi_1}{\partial x^2} - \mu_1 \ddot{\xi}_1 + G \frac{h_e}{h_2} \frac{\partial w}{\partial x} + G \frac{1}{h_2} (\xi_3 - \xi_1) = 0 \quad (9.51)$$

$$E_3 h_3 \frac{\partial^2 \xi_3}{\partial x^2} - \mu_3 \ddot{\xi}_3 - G \frac{h_e}{h_2} \frac{\partial w}{\partial x} - G \frac{1}{h_2} (\xi_3 - \xi_1) = 0 \quad (9.52)$$

In order to solve these equations in a simple way certain approximations have to be made. The wavenumber k_x governing the flexure of the plate is mainly determined by the first two terms of the first equation, (9.50). Considering this, the second term of the second expression, (9.51), can be neglected as compared to the first term as long as

$$\left[\frac{12E_i}{h_i \mu_i \omega^2} \right]^{1/2} \gg 1 \quad \text{for } i = 1 \text{ and } 2$$

By neglecting the second term in the expressions (9.51) and (9.52) the functions ξ_1 and ξ_3 are readily eliminated from (9.50). The resulting differential equation reads

$$\frac{\partial^6 w}{\partial x^6} - \mathcal{Z}(1 + \Upsilon) \frac{\partial^4 w}{\partial x^4} + \frac{\mu_0}{D_1 + D_3} \left[\frac{\partial^2 \ddot{w}}{\partial x^2} - \ddot{w} \mathcal{Z} \right] = 0 \quad (9.53)$$

where

$$\mathcal{Z} = \frac{G}{h_2} \left[\frac{E_1 h_1 + E_3 h_3}{E_1 h_1 E_3 h_3} \right]; \quad \Upsilon = \frac{[h_2 + (h_1 + h_3)/2]^2}{(D_1 + D_3)} \left[\frac{E_1 h_1 E_3 h_3}{E_1 h_1 + E_3 h_3} \right] \quad (9.54)$$

The details are left for Problem 9.5.

For a wave propagating along the positive x -axis the displacement is written as

$$w(x, t) = A \cdot \exp[i(\omega t - k_x x)]; \quad k_x = \left[\frac{\mu_0 \omega^2}{D_x} \right]^{1/4} \quad (9.55)$$

where D_x is the bending stiffness of the composite panel. The bending stiffness is complex and is written $D_x = D_{x0}(1 + i\eta_{\text{tot}})$ where η_{tot} is the total loss factor of the composite structure and D_{x0} the real part of the bending stiffness D_x . The wavenumber and thus also the bending stiffness are obtained by inserting Eq. (9.55) in (9.53). The result is

$$-k_x^6 - \mathcal{Z}(1 + \Upsilon)k_x^4 + \frac{\mu_0 \omega^2}{D_1 + D_3} (k_x^2 + \mathcal{Z}) = 0 \quad (9.56)$$

This third-order equation in k_x^2 is readily solved by means of some standard numerical program. For a propagating wave the real part of k_x^2 must be positive. However, the expression (9.56) can be modified to make it possible to use a simple iterative method to estimate the bending stiffness and the loss factor of the plate. Thus, divide Eq. (9.56) by k_x^4 and use the definition of k_x given in (9.55). The result is

$$D_x = (D_1 + D_3) \left[1 + \frac{\Upsilon \mathcal{Z}}{k_x^2 + \mathcal{Z}} \right] \quad (9.57)$$

The total loss factor η_{tot} of the plate is defined as

$$\eta_{\text{tot}} = \frac{\text{Im}(D_x)}{\text{Re}(D_x)}$$

By assuming that $\eta_2 \gg \eta_1$ and $\eta_2 \gg \eta_3$ and by introducing \mathcal{X} as $\mathcal{X} = \mathcal{Z}/k_x^2$ the total loss factor is obtained as

$$\eta_{\text{tot}} = \frac{\eta_2 \mathcal{X}_0 \Upsilon}{1 + (2 + \Upsilon) \mathcal{X}_0 + (1 + \Upsilon)(1 + \eta_2^2) \mathcal{X}_0^2} \quad (9.58)$$

The real part of \mathcal{X} is defined as \mathcal{X}_0 . The expression (9.58) is the same as that given in Eq. (5.101). A simple iterative method to solve k_x^2 the equation is presented in Sect. 5.5.

The limiting wavenumbers for a composite plate with an intermediate layer having either a very low or very high shear modulus can be obtained from Eq. (9.56). For $G = 0$ the parameter \mathcal{Z} , defined in (9.55), is also equal to zero. The wavenumber for a propagating wave is for $\mathcal{Z} = 0$ obtained from (9.56) as

$$k_x = \left[\frac{\mu_0 \omega^2}{D_1 + D_3} \right]^{1/4}$$

This solution represents the wavenumber for a flexural wave propagating along two plates, which can slide against each other without inducing any shear forces along the sliding surfaces. One plate has the bending stiffness D_1 and the other has the bending stiffness D_3 .

For the other limiting case, the shear modulus of the interlayer of the composite structure is assumed to be high. For G large or rather for the ratio G/h_2 being large, the parameter \mathcal{Z} , Eq. (9.54), is also large. If for simplicity it is assumed that $E_1 = E_3 = E$ and $h_1 = h_3 = h$ and $h_2 \ll h$ Eq. (9.54) gives $\Upsilon \approx 3$. In the limiting case as $\mathcal{Z} \rightarrow \infty$ the expression (9.56) is reduced to

$$4k_x^4 = \left[\frac{\mu_0 \omega^2}{D_1 + D_3} \right]; \quad D_1 = D_3 = \frac{Eh^3}{12(1 - \nu^2)}$$

The wavenumber is thus

$$k_x = \left[\frac{\mu_0 \omega^2}{D_0} \right]^{1/4} \quad \text{where} \quad D_0 = \frac{E(2h)^3}{12(1-\nu^2)}$$

This is the wavenumber for flexural waves propagating along a plate with the thickness $2h$. Thus in limiting case as $G/h_2 \rightarrow \infty$ the plates vibrate as if they were firmly bonded to each other.

The boundary conditions for a plate with a constrained viscoelastic layer are obtained from the last two integrals of Eq. (9.49). As before, it is assumed that the motion of the plate only depends on the x -coordinate. For the last two integrals to be zero the following boundary conditions at $x = 0$ and $x = L$ must be satisfied

$$\begin{aligned} \text{(i)} \quad & w = 0 \text{ or } (D_1 + D_3) \frac{\partial^3 w}{\partial x^3} + F'_z = 0 \\ \text{(ii)} \quad & \frac{\partial w}{\partial x} = 0 \text{ or } (D_1 + D_3) \frac{\partial^2 w}{\partial x^2} + M' = 0 \\ \text{(iii)} \quad & \xi_1 = 0 \text{ or } h_1 E_1 \frac{\partial \xi_1}{\partial x} - F'_x \frac{h_1}{h_1 + h_3} = 0 \\ \text{(iv)} \quad & \xi_3 = 0 \text{ or } h_3 E_3 \frac{\partial \xi_3}{\partial x} - F'_x \frac{h_3}{h_1 + h_3} = 0 \end{aligned} \quad (9.59)$$

9.5 Timoshenko Beams

Flexural vibrations of thick beams were discussed in Chap. 4. For the bending of thick beams rotation as well as shear can be considered as suggested by Timoshenko [85, 86]. A differential equation governing the lateral vibrations of a so-called Timoshenko beam is given without proof in Sect. 4.4. However, this equation can be obtained directly from Eq. (9.40), which governs the vibration of sandwich beam, by setting the thicknesses of the laminates equal zero. Consequently, the bending stiffness D'_2 of the laminates as well as the bending moment M_s acting on the laminates should also equal zero. The mass m' per unit length of the beam is $m' = \rho S$ where S is the cross section area of the beam and ρ the density of the core. Further, for a homogeneous beam, width b and thickness h , the mass moment of inertia is $I'_\omega = \rho I' = \rho b h^3 / 12 = \rho S h^2 / 12$. Considering these notations, Eq. (9.40) is for $D_2 = 0$ and $F' = 0$ reduced to

$$G_e S D'_1 \frac{\partial^4 w}{\partial x^4} - [D'_1 m' + G_e S I'_\omega] \frac{\partial^4 w}{\partial x^2 \partial t^2} + G_e S m' \frac{\partial^2 w}{\partial t^2} + m' I'_\omega \frac{\partial^4 w}{\partial t^4} = 0 \quad (9.60)$$

The effective shear modulus G_e is written $G_e = T_b G$ where T_b is the so-called Timoshenko constant discussed in Sect. 4.4.

Table 9.2 Boundary conditions for a Timoshenko beam

End condition		
Simply supported	$w = 0$	$\partial\beta/\partial x = 0$
Clamped	$w = 0$	$\beta = 0$
Free	$\partial\beta/\partial x = 0$	$\beta = \partial w/\partial x$

The boundary conditions are obtained from Eq. (9.34) by again setting $D'_2 = 0$. This means that the last integral of Eq. (9.34) always is equal to zero. Consequently, there are only two conditions to be satisfied at each end of a beam. The force F and bending moment M resulting from the bending of the beam as defined in Fig. 3.14 are

$$F = G_e S \left[\frac{\partial w}{\partial x} - \beta \right] = G T_b S \left[\frac{\partial w}{\partial x} - \beta \right]; \quad M = -D'_1 \frac{\partial \beta}{\partial x} \tag{9.61}$$

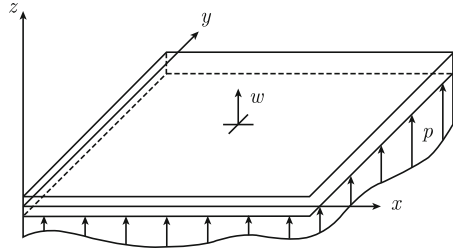
The resulting boundary conditions are given in Table 9.2. The displacement w and angular displacement β should also satisfy Eq. (9.36) for $D'_2 = 0$. Eigenfrequencies for various boundary conditions are derived as discussed in Sect. 14.8 and Problem 9.9.

In Sect. 4.12 the bending of I-beams was discussed. The wavenumbers etc. were derived using the Euler and Timoshenko theories as well an exact model. Resulting wavenumbers are shown in Fig. 4.16. It is evident that the Timoshenko theory gives a better agreement with respect to the exact solution than the Euler theory in the low and mid frequency regions. For high frequencies using the Timoshenko model, the wavenumber for the first propagating wave is proportional to the frequency. However, based on the exact solution the wavenumber is proportional to the square root of the frequency. Consequently, in the high frequency range there is a big discrepancy between the exact wavenumber and the wavenumber calculated by means of the Timoshenko theory. However, for homogeneous beams with rectangular or circular cross sections the Timoshenko theory can yield very good results even in the very high frequency region if the Timoshenko constant is properly chosen as discussed in Sect. 4.4.

9.6 Mindlin Plates

The Euler equation governs the flexural vibrations of slender beams. The equation is only valid up to certain frequencies as discussed in Sect. 4.4. Timoshenko added terms to include shear in as well as rotation of the beam. The result was the so-called Timoshenko beam equation discussed in Sect. 9.5. In a similar way, Mindlin in Ref. [73] extended the basic Kirchhoff theory which describes the flexural vibrations of thin plates. The extension included shear in and rotation of the plate. The Mindlin theory is thus an extension in the frequency domain of the Kirchhoff theory. Again, as

Fig. 9.10 Plate excited by a pressure



in the case of the Timoshenko beam, the governing equations for a so-called Mindlin plate can be derived using Hamilton's principle.

As a starting point consider a plate oriented in the x - y -plane as shown in Fig. 9.10. The displacement w along the z -axis is caused by bending and shear. The local change of slope along the x -axis is due to pure bending of the plate is defined as $\beta_x(x, y, t)$ at time t and at the position (x, y) on the plate. The resulting displacement ξ along the x -axis is $\xi = -\beta_x \cdot z$ where z is the distance from the neutral axis of the plate. In the same way, the displacement η in the y -direction is given by $\eta = -\beta_y \cdot z$ where $\beta_y(x, y, t)$ is the change of slope of the plate due to pure bending along the y -axis. The displacements along the three main axes are

$$\begin{aligned} \xi(x, y, t) &= -\beta_x(x, y, t) \cdot z && \text{along the } x\text{-axis} \\ \eta(x, y, t) &= -\beta_y(x, y, t) \cdot z && \text{along the } y\text{-axis} \\ w(x, y, t) &&& \text{along the } z\text{-axis} \end{aligned} \quad (9.62)$$

The resulting strains in the plate are according to the definitions (3.11) and the assumptions (9.62) obtained as

$$\begin{aligned} \varepsilon_x &= \frac{\partial \xi}{\partial x} = -z \cdot \frac{\partial \beta_x}{\partial x}; \quad \varepsilon_y = \frac{\partial \eta}{\partial y} = -z \cdot \frac{\partial \beta_y}{\partial x} \\ \gamma_{xy} &= \frac{\partial \xi}{\partial y} + \frac{\partial \eta}{\partial x} = -z \cdot \frac{\partial \beta_x}{\partial y} - z \cdot \frac{\partial \beta_y}{\partial x}; \\ \gamma_{xz} &= \frac{\partial w}{\partial x} + \frac{\partial \xi}{\partial z} = \frac{\partial w}{\partial x} - \beta_x; \quad \gamma_{yz} = \frac{\partial w}{\partial y} + \frac{\partial \eta}{\partial z} = \frac{\partial w}{\partial y} - \beta_y, \end{aligned} \quad (9.63)$$

The last two expressions can also be written as

$$\frac{\partial w}{\partial x} = \beta_x + \gamma_{xz} \quad \text{and} \quad \frac{\partial w}{\partial y} = \beta_y + \gamma_{yz}$$

The slope $\partial w / \partial x$ of the plate is caused by pure bending β_x and shear determined by γ_{xz} . The slope $\partial w / \partial y$ is given a corresponding interpretation. The same type

of assumptions was introduced describing the lateral displacement of sandwich and Timoshenko beams. This was discussed in Sect. 9.3, Eq. (9.25), and in Sect. 9.5.

The kinetic and potential energies of a plate element can now be defined as functions of the strains. In Eq. (3.14) the potential energy per unit volume of a homogeneous and isotropic solid was given as

$$\mathcal{U}_v = \int (\sigma_x d\varepsilon_x + \sigma_y d\varepsilon_y + \sigma_z d\varepsilon_z + \tau_{xy} d\gamma_{xy} + \tau_{xz} d\gamma_{xz} + \tau_{yz} d\gamma_{yz}) \quad (9.64)$$

Although the plate is not necessarily thin, it is assumed that the normal stress σ_z is equal to zero not only on the two surfaces of the plate but also in the interior of the plate. This assumption, $\sigma_z = 0$, and the basic stress-strain relationships (3.5) and (3.6) give

$$\sigma_x = \frac{E}{1-\nu^2} \cdot (\varepsilon_x + \nu\varepsilon_y); \quad \sigma_y = \frac{E}{1-\nu^2} \cdot (\varepsilon_y + \nu\varepsilon_x) \quad (9.65)$$

The shear stress τ_{xy} is according to Eq. (3.12) defined as $\tau_{xy} = G \cdot \gamma_{xy}$. The other shear stresses are defined accordingly. Thus by setting $\sigma_z = 0$ and by inserting (9.65) and the appropriate shear stresses in Eq. (9.64) the result is

$$\begin{aligned} \mathcal{U}_v &= \frac{E}{1-\nu^2} \int (\varepsilon_x d\varepsilon_x + \nu\varepsilon_y d\varepsilon_x + \varepsilon_y d\varepsilon_y + \nu\varepsilon_x d\varepsilon_y) \\ &\quad + G \int (\gamma_{xy} d\gamma_{xy} + \gamma_{xz} d\gamma_{xz} + \gamma_{yz} d\gamma_{yz}) \end{aligned} \quad (9.66)$$

The first integral is rewritten as

$$\begin{aligned} &\int [(1-\nu)(\varepsilon_x d\varepsilon_x + \varepsilon_y d\varepsilon_y) + \nu(\varepsilon_x + \varepsilon_y)d(\varepsilon_x + \varepsilon_y)] \\ &= (1-\nu) \left(\varepsilon_x^2 + \varepsilon_y^2 \right) / 2 + \nu (\varepsilon_x + \varepsilon_y)^2 / 2 = \frac{1}{2} \left(\varepsilon_x^2 + \varepsilon_y^2 + 2\nu\varepsilon_x\varepsilon_y \right) \end{aligned} \quad (9.67)$$

The potential energy per unit volume of the plate is from (9.66) and (9.67) obtained as

$$\mathcal{U}_v = \frac{E}{2(1-\nu^2)} \left(\varepsilon_x^2 + \varepsilon_y^2 + 2\nu\varepsilon_x\varepsilon_y \right) + \frac{G}{2} \left(\gamma_{xy}^2 + \gamma_{xz}^2 + \gamma_{yz}^2 \right) \quad (9.68)$$

The energy \mathcal{U}_S per unit area of the plate is

$$\mathcal{U}_S = \int_{-h/2}^{h/2} dz \mathcal{U}_v$$

Since the bending stiffness D of the plate is $Eh^3/[12(1-\nu^2)]$ and $G = E/[2(1+\nu)]$, it follows from Eqs. (9.68) and (9.63) that the potential energy per unit area of the plate is

$$\begin{aligned}
\mathcal{U}_S = & \frac{D}{2} \left[\left(\frac{\partial \beta_x}{\partial x} \right)^2 + \left(\frac{\partial \beta_y}{\partial y} \right)^2 + 2\nu \left(\frac{\partial \beta_x}{\partial x} \right) \left(\frac{\partial \beta_y}{\partial y} \right) \right] \\
& + \frac{Gh}{2} \left[\left(\frac{\partial w}{\partial x} - \beta_x \right)^2 + \left(\frac{\partial w}{\partial y} - \beta_y \right)^2 + 2\nu \frac{\partial \beta_x}{\partial x} \frac{\partial \beta_y}{\partial y} \right] \\
& + \frac{Gh^3}{24} \left[\frac{\partial \beta_x}{\partial x} + \frac{\partial \beta_y}{\partial y} \right]^2
\end{aligned} \tag{9.69}$$

The kinetic energy \mathcal{T}_v per unit volume of the plate is the sum of the kinetic energy caused by the lateral motion of the plate plus the kinetic energies caused by rotation around the x and y -axes. Hence,

$$\mathcal{T}_v = \frac{1}{2} \left[\rho \left(\frac{\partial w}{\partial t} \right)^2 + \rho z^2 \left(\frac{\partial \beta_x}{\partial t} \right)^2 + \rho z^2 \left(\frac{\partial \beta_y}{\partial t} \right)^2 \right] \tag{9.70}$$

The kinetic energy \mathcal{T}_S per unit area of the plate is thus

$$\mathcal{T}_S = \int_{-h/2}^{h/2} dz \mathcal{T}_v = \frac{1}{2} \left[\mu \left(\frac{\partial w}{\partial t} \right)^2 + I_\omega \left(\frac{\partial \beta_x}{\partial t} \right)^2 + I_\omega \left(\frac{\partial \beta_y}{\partial t} \right)^2 \right] \tag{9.71}$$

In this equation the mass per unit area of the plate is $\mu = \rho h$. The mass moment of inertia is $I_\omega = \rho h^3/12$. The pressure p acting on the plate induces a potential energy \mathcal{A}_S per unit area of the plate. The resulting energy is $\mathcal{A}_S = -pw$. It is assumed that the work done by the forces and moments along the boundaries is equal to zero. The Lagrangian \mathcal{L} of the system is obtained from Eqs. (9.69) and (9.71) as

$$\begin{aligned}
\mathcal{L} = \mathcal{T}_S - \mathcal{U}_S - \mathcal{A}_S = & \frac{1}{2} \left[\mu \left(\frac{\partial w}{\partial t} \right)^2 + I_\omega \left(\frac{\partial \beta_x}{\partial t} \right)^2 + I_\omega \left(\frac{\partial \beta_y}{\partial t} \right)^2 \right] \\
& - \frac{D}{2} \left[\left(\frac{\partial \beta_x}{\partial x} \right)^2 + \left(\frac{\partial \beta_y}{\partial y} \right)^2 + 2\nu \left(\frac{\partial \beta_x}{\partial x} \right) \left(\frac{\partial \beta_y}{\partial y} \right) \right] \\
& - \frac{Gh}{2} \left[\left(\frac{\partial w}{\partial x} - \beta_x \right)^2 + \left(\frac{\partial w}{\partial y} - \beta_y \right)^2 + 2\nu \frac{\partial \beta_x}{\partial x} \frac{\partial \beta_y}{\partial y} \right] \\
& - \frac{Gh^3}{24} \left[\frac{\partial \beta_x}{\partial x} + \frac{\partial \beta_y}{\partial y} \right]^2 + pw
\end{aligned} \tag{9.72}$$

The resulting variational expression is from Eq. (9.4) obtained as

$$\delta \int dx dy dt (\mathcal{T}_S - \mathcal{U}_S - \mathcal{A}_S) = 0$$

The result after effecting the variation with respect to w , β_x and β_y is three differential equations:

$$\begin{aligned} & -\mu \frac{\partial^2 w}{\partial t^2} + Gh \left[\frac{\partial^2 w}{\partial x^2} + \frac{\partial^2 w}{\partial y^2} \right] - Gh \left[\frac{\partial \beta_x}{\partial x} + \frac{\partial \beta_y}{\partial y} \right] = -p \\ & -I_\omega \frac{\partial^2 \beta_x}{\partial t^2} + D \frac{\partial^2 \beta_x}{\partial x^2} + \frac{D(1-\nu)}{2} \frac{\partial^2 \beta_x}{\partial y^2} + \frac{D(1+\nu)}{2} \frac{\partial^2 \beta_y}{\partial x \partial y} + Gh \left[\frac{\partial w}{\partial x} - \beta_x \right] = 0 \\ & -I_\omega \frac{\partial^2 \beta_y}{\partial t^2} + D \frac{\partial^2 \beta_y}{\partial y^2} + \frac{D(1-\nu)}{2} \frac{\partial^2 \beta_y}{\partial x^2} + \frac{D(1+\nu)}{2} \frac{\partial^2 \beta_x}{\partial x \partial y} + Gh \left[\frac{\partial w}{\partial y} - \beta_y \right] = 0 \end{aligned} \quad (9.73)$$

The functions β_x and β_y are eliminated by means of the last two expressions of (9.73). The result is a differential equation, including shear and rotational effects, governing the displacement w of a homogeneous plate. The result is

$$D \nabla^2 (\nabla^2 w) - \left[\frac{D\mu}{Gh} + I_\omega \right] \nabla^2 \left(\frac{\partial^2 w}{\partial t^2} \right) + \mu \frac{\partial^2 w}{\partial t^2} + \frac{\mu I_\omega}{Gh} \frac{\partial^4 w}{\partial t^4} = p + \frac{D}{Gh} \nabla^2 p - \frac{I_\omega}{Gh} \frac{\partial^2 p}{\partial t^2} \quad (9.74)$$

This result is consistent with the Timoshenko beam equation (9.60). If it is assumed that w is a function of x and t , Eq. (9.74) is reduced to Eq. (9.60) if the shear modulus is interpreted as an effective modulus or as $T_p G$ where T_p is a parameter comparable to the Timoshenko constant discussed in Sect. 4.3. For the case that shear and rotation are neglected, Eq. (9.74) is reduced to the so-called Kirchhoff equation (3.115). No shear implies that $G \rightarrow \infty$. The rotational effects are neglected by setting I_ω equal to zero in Eq. (9.74).

For free plate vibrations, $p = 0$, and assuming $w = A \cdot \exp[i(\omega t - kx)]$ the wavenumber k should satisfy the dispersion equation

$$Dk^4 - \left[\frac{D\mu}{G_e h} + I_\omega \right] \omega^2 k^2 - \mu \omega^2 + \omega^4 \frac{\mu I_\omega}{G_e h} = 0 \quad (9.75)$$

This expression can be somewhat rearranged resulting in

$$k^4 - \left[k_1^2 + \left(\frac{k_t}{T_p} \right)^2 \right] k^2 - \kappa^4 + \frac{(k_1 k_t)^2}{T_p^2} = 0 \quad (9.76)$$

where k_1 is the wavenumber for longitudinal waves propagating in the plate, k_t the wavenumber for transverse waves and κ the wavenumber for flexural waves propagating in a thin Kirchhoff plate. Thus

$$k_1 = \omega \sqrt{\frac{\rho(1-\nu^2)}{E}}; \quad k_t = \omega \sqrt{\frac{\rho}{G}}; \quad \kappa = \left[\frac{\mu \omega^2}{D} \right]^{1/4}$$

The solutions to Eq. (9.76) are obtained from the expression

$$k^2 = \frac{1}{2} \left[k_1^2 + \left(\frac{k_t}{T_p} \right)^2 \right] \pm \frac{1}{2} \left\{ \left[k_1^2 - \left(\frac{k_t}{T_p} \right)^2 \right]^2 + 4\kappa^4 \right\}^{1/2} \quad (9.77)$$

As the frequency approaches zero $\kappa \gg k_t > k_1$ and the solutions to Eq. (9.77) tend to $k = \pm\kappa$ and $k = \pm i\kappa$ corresponding to the solutions for a Kirchhoff plate. For increasing frequencies the solutions to Eq. (9.77) can be written

$$k = \pm\kappa(1 + \Delta) \quad \text{and} \quad k = \pm i\kappa(1 + \Delta); \quad \Delta = \frac{1}{4\kappa^2} \left[k_1^2 + \left(\frac{k_t}{T_p} \right)^2 \right] \quad (9.78)$$

For the error in the wavenumber to be less than 10% the Kirchhoff theory to be applicable, the parameter Δ should be less than 1/10. This requires that $\kappa h < 1$. This is in agreement with the discussion in Sect. 4.4. The details are left for problem 9.6.

In the high frequency region $k_t > k_1 \gg \kappa$ the solutions to (9.77) tend to $k = \pm k_1$ and $k = \pm k_t/T_p$. The first solution corresponds to a quasi-longitudinal wave propagating along the axis of the plate. The displacement due to this wave corresponds to an anti-phase motion of the upper and lower surfaces of the plate as illustrated in Fig. 4.4. The second solution depends on the shear in the plate and corresponds to a transverse wave propagating in the plate along its axis, the displacement perpendicular to the plane of the plate. This corresponds to an in-phase motion of the plate. As discussed in Sect. 4.4 the wavenumber for the in-phase motion of the plate should tend to the Rayleigh wavenumber k_r as the frequency approaches infinity. In order to satisfy this requirement it follows that $k_t/T_p \rightarrow k_r$ as $f \rightarrow \infty$. In the limit $T_p = k_t/k_r$. For $\nu = 0.3$ Table 4.2 gives the ratio between the speeds of propagation of the waves as $c_r/c_t = k_t/k_r = 0.93$. Thus in order to satisfy the asymptotic behavior of the wavenumber the parameter T_p should equal 0.93 for $\nu = 0.3$.

9.7 Cylindrical Shells

Most "flat" plates have a slight curvature. Typical plate elements of a car construction are not completely flat but exhibit a slight curvature. In ships and trains, frames and stringers strengthen plate elements resulting in those plates having a certain curvature. The fuselage of an aircraft can be compared to a cylinder. The cylindrical shape increases the strength of the structure. In fact, the strength of a plate is increased by giving it a curvature and making it into a shell. As stated by Leissa, Ref. [87], "Shells are the most efficient structures available to mankind, and they should be used more in design than they are."

The influence of a slight curvature on the vibration pattern of a plate was mentioned in Sect. 8.8. The added characteristic of a curvature makes it more complex to derive

the differential equations governing the vibrations of shells as compared to flat plates. Again, Hamilton’s principle is a very efficient tool for deriving the basic equations for vibrating shells. A large number of cases are discussed in Leissa’s much used reference book [87]. Soedel also discusses the dynamic behavior of shells extensively in Ref. [88].

The general procedure of finding the equations governing the vibrations of a shell can be illustrated by an example, which can be considered simple in comparison with problems that are more general. The example, the vibration of a thin cylindrical shell, is of great importance for many vibro-acoustic problems in the field of aeronautics and naval architecture. The fuselage of an aircraft or certain ship structures can be compared to cylindrical shells. Pipes constitute another important class of shells.

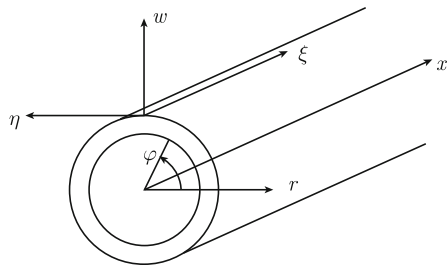
A cylindrical shell is shown in Fig. 9.11. The shell is oriented along the positive x -axis of a cylindrical coordinate system. The thickness of the shell is h . The radius, or the distance from the center of the shell to the midplane of the shell, is R . The coordinate in the radial direction is z . The rotational angle is φ as shown in Fig. 9.11. The displacement of the shell is ξ in the x -direction, η in the tangential direction, and w in the radial direction. The density, Young’s modulus, shear modulus, and Poisson’s ratio are defined as ρ , E , G , and ν , respectively.

In formulating classical theory on small displacements of thin shells, Love [89] made the following assumptions as summarized by Leissa [87]:

- (i) The thickness of the shell is small compared to the radius of the shell.
- (ii) Second and higher order magnitude of strain displacement can be neglected in comparison with first-order terms.
- (iii) The transverse normal stress is small compared to other normal stress components and can be neglected.
- (iv) Normals to the undeformed middle surface of the shell remain straight and normal to the deformed middle surface.

The last assumption is often referred to as the Kirchhoff hypothesis and discussed in Sect. 3.9. Because of the last assumption on geometry it follows that the shear angles γ_{xz} and $\gamma_{\varphi z}$ and the strain σ_z can be set to equal zero. In accordance with the Kirchhoff hypothesis, rotary inertia of the shell is neglected.

Fig. 9.11 A cylindrical shell with coordinates and displacements



For a flat and thin plate, oriented in the x - y -plane, and for which the shear angles γ_{xz} and γ_{yz} and the strain σ_z are set to equal zero the potential energy per unit volume is given by Eq. (3.123) as

$$\mathcal{U}_V = \frac{E}{2(1-\nu^2)} \left[\varepsilon_x^2 + \varepsilon_y^2 + 2\nu\varepsilon_x\varepsilon_y + (1-\nu)\gamma_{xy}^2/2 \right]$$

For a thin cylindrical shell shown in Fig. 9.11 the corresponding potential energy is

$$\mathcal{U}_V = \frac{E}{2(1-\nu^2)} \left[\varepsilon_x^2 + \varepsilon_\varphi^2 + 2\nu\varepsilon_x\varepsilon_\varphi + (1-\nu)\gamma_{x\varphi}^2/2 \right] \quad (9.79)$$

where as before ε_x is the tension in the x -direction of the cylinder. The tension in the tangential direction is ε_φ . The shear angle between the x and the tangential directions on the surface of the shell is $\gamma_{x\varphi}$.

For a thin and flat plate, the tensions in the x - y -plane due to bending and displacement ξ in the x -direction and η in the y -direction are from Eqs. (3.2) and (3.104) obtained as

$$\varepsilon_x = \frac{\partial\xi}{\partial x} - z \frac{\partial^2 w}{\partial x^2}; \quad \varepsilon_y = \frac{\partial\eta}{\partial y} - z \frac{\partial^2 w}{\partial y^2} \quad (9.80)$$

The corresponding shear angle γ_{xy} is according to (3.11) and (3.111)

$$\gamma_{xy} = \frac{\partial\xi}{\partial y} + \frac{\partial\eta}{\partial x} - 2z \frac{\partial^2 w}{\partial x \partial y} \quad (9.81)$$

For a cylindrical shell, Fig. 9.11, the y -coordinate is replaced by $r\varphi$. Due to the curvature of the shell the added tension in the tangential direction of the cylinder caused by its displacement w is

$$\varepsilon_\varphi = \frac{\Delta\eta}{r\Delta\varphi} = \frac{(r+w-r)\Delta\varphi}{r\Delta\varphi} = \frac{w}{r} \quad (9.82)$$

Considering the results (9.80) through (9.82) the tensions and the shear angle of the shell are, as expressed in cylindrical coordinates

$$\varepsilon_x = \frac{\partial\xi}{\partial x} - z \frac{\partial^2 w}{\partial x^2}; \quad \varepsilon_\varphi = \frac{w}{r} + \frac{1}{r} \frac{\partial\eta}{\partial\varphi} - \frac{z}{r^2} \frac{\partial^2 w}{\partial\varphi^2}; \quad \gamma_{x\varphi} = \frac{1}{r} \frac{\partial\xi}{\partial\varphi} + \frac{\partial\eta}{\partial x} - 2z \frac{\partial^2 w}{r \partial x \partial\varphi} \quad (9.83)$$

The potential energy per unit volume of the shell is defined in Eq. (9.79). Taking the variation of the total potential energy gives

$$\begin{aligned} \delta\mathcal{U} = \int \delta\mathcal{U}_V dV = \frac{E}{(1-\nu^2)} \int dV \left[\delta\varepsilon_x(\varepsilon_x + \nu\varepsilon_\varphi) + \delta\varepsilon_\varphi(\varepsilon_\varphi + \nu\varepsilon_x) \right. \\ \left. + \delta\gamma_{x\varphi} \cdot \gamma_{x\varphi}(1-\nu)/2 \right] \end{aligned} \quad (9.84)$$

where $dV = r dr d\varphi dx$. The angle φ varies between 0 and 2π and the radius r between $R - h/2$ and $R + h/2$ and x over the length L of the cylinder. Writing r as $r = R + z$ and dr as $dr = dz$ the first part of the integral (9.84) after introducing (9.83) reads

$$\begin{aligned}\delta\mathcal{U}_1 &= \frac{E}{(1-\nu^2)} \int dV [\delta\varepsilon_x(\varepsilon_x + \nu\varepsilon_\varphi)] \\ &= \frac{ER}{(1-\nu^2)} \int_0^L dx \int_{-h/2}^{h/2} dz \int_0^{2\pi} d\varphi \left[\frac{\partial\delta\xi}{\partial x} - z \frac{\partial^2\delta w}{\partial x^2} \right] \\ &\quad \times \left[\frac{\partial\xi}{\partial x} - z \frac{\partial^2 w}{\partial x^2} + \frac{\nu w}{r} + \frac{\nu}{r} \frac{\partial\eta}{\partial\varphi} - \frac{\nu z}{r^2} \frac{\partial^2 w}{\partial\varphi^2} \right]\end{aligned}$$

For $h \ll R$ the coordinate r is set to equal R in this equation since $R - h/2 \leq r \leq R + h/2$. After integration with respect to z the result is

$$\begin{aligned}\delta\mathcal{U}_1 &= \frac{ERh}{(1-\nu^2)} \int_0^L dx \int_0^{2\pi} d\varphi \left\{ \frac{\partial\delta\xi}{\partial x} \left[\frac{\partial\xi}{\partial x} + \frac{\nu w}{R} + \frac{\nu}{R} \frac{\partial\eta}{\partial\varphi} \right] \right. \\ &\quad \left. + \frac{h^2}{12} \frac{\partial^2\delta w}{\partial x^2} \left[\frac{\partial^2 w}{\partial x^2} + \frac{\nu}{R^2} \frac{\partial^2 w}{\partial\varphi^2} \right] \right\}\end{aligned}$$

After partial integration and assuming the boundary conditions to be satisfied, the integral is written as

$$\begin{aligned}\delta\mathcal{U}_1 &= \frac{ERh}{(1-\nu^2)} \int_0^L dx \int_0^{2\pi} d\varphi \left\{ -\delta\xi \left[\frac{\partial^2\xi}{\partial x^2} + \frac{\nu}{R} \frac{\partial w}{\partial r} + \frac{\nu}{R} \frac{\partial^2\eta}{\partial x\partial\varphi} \right] \right. \\ &\quad \left. + \delta w \frac{h^2}{12} \left[\frac{\partial^4 w}{\partial x^4} + \frac{\nu}{R} \frac{\partial^4 w}{\partial x^2\partial\varphi^2} \right] \right\}\end{aligned}\quad (9.85)$$

In a similar way the second part of Eq.(9.84) is

$$\begin{aligned}\delta\mathcal{U}_2 &= \frac{E}{(1-\nu^2)} \int dV [\delta\varepsilon_\varphi(\varepsilon_\varphi + \nu\varepsilon_x)] \\ &= \frac{ERh}{(1-\nu^2)} \int_0^L dx \int_0^{2\pi} d\varphi \left\{ \delta w \left[\frac{\nu}{R} \frac{\partial\xi}{\partial x} + \frac{w}{R^2} + \frac{1}{R^2} \frac{\partial\eta}{\partial\varphi} \right. \right. \\ &\quad \left. \left. + \frac{h^2}{12} \left(\frac{1}{R^4} \frac{\partial^4 w}{\partial\varphi^4} + \frac{\nu}{R^2} \frac{\partial^4 w}{\partial x^2\partial\varphi^2} \right) \right] \right\} \\ &\quad - \frac{ERh}{(1-\nu^2)} \int_0^L dx \int_0^{2\pi} d\varphi \left\{ \delta\eta \left[\frac{1}{R^2} \frac{\partial w}{\partial\varphi} + \frac{1}{R^2} \frac{\partial^2\eta}{\partial\varphi^2} + \frac{\nu}{R} \frac{\partial^2\xi}{\partial x\partial\varphi} \right] \right\}\end{aligned}\quad (9.86)$$

The final part of the expression (9.84) is obtained as

$$\begin{aligned}\delta\mathcal{U}_3 &= \frac{E}{(1-\nu^2)} \int dV [\delta\gamma_{x\varphi} \cdot \gamma_{x\varphi} (1-\nu)/2] \\ &= \frac{ERh}{(1-\nu^2)} \int_0^L dx \int_0^{2\pi} d\varphi \frac{(1-\nu)}{2} \left\{ \delta\xi \left[-\frac{1}{R^2} \frac{\partial^2 \xi}{\partial \varphi^2} - \frac{1}{R} \frac{\partial^2 \eta}{\partial x \partial \varphi} \right] \right. \\ &\quad \left. + \delta\eta \left[-\frac{1}{R} \frac{\partial^2 \xi}{\partial x \partial \varphi} - \frac{\partial^2 \eta}{\partial x^2} \right] + \delta w \frac{4h^2}{12R^2} \frac{\partial^4 w}{\partial x^2 \partial \varphi^2} \right\}\end{aligned}\quad (9.87)$$

The kinetic energy of the structure is

$$\mathcal{T} = \int_0^L dx \int_{-h/2}^{h/2} dz \int_0^{2\pi} d\varphi R \frac{\rho}{2} [(\dot{\xi})^2 + (\dot{\eta})^2 + (\dot{w})^2]$$

Thus,

$$\begin{aligned}\delta \int dt \mathcal{T} &= \iiint R dx d\varphi dt \mu [\delta \dot{\xi} (\dot{\xi}) + \delta \dot{\eta} (\dot{\eta}) + \delta \dot{w} (\dot{w})] \\ &= - \iiint R dx d\varphi dt \mu [\delta \xi (\ddot{\xi}) + \delta \eta (\ddot{\eta}) + \delta w (\ddot{w})]\end{aligned}\quad (9.88)$$

Finally using Hamilton's principle $\delta \int dt (\mathcal{T} - \mathcal{U}_1 - \mathcal{U}_2 - \mathcal{U}_3) = 0$, the Eqs. (9.85) through (9.88) give

$$\frac{ERh}{(1-\nu^2)} \int_0^L dx \int_0^{2\pi} d\varphi \int_{t_1}^{t_2} dt (\delta \xi \cdot F_1 + \delta \eta \cdot F_2 + \delta w \cdot F_3) = 0 \quad (9.89)$$

where

$$\begin{aligned}F_1 &= \frac{\partial^2 \xi}{\partial x^2} + \frac{\nu}{R} \frac{\partial w}{\partial x} + \frac{\nu}{R} \frac{\partial^2 \eta}{\partial x \partial \varphi} + \frac{1-\nu}{2} \left(\frac{1}{R^2} \frac{\partial^2 \xi}{\partial \varphi^2} + \frac{1}{R} \frac{\partial^2 \eta}{\partial x \partial \varphi} \right) - \frac{1-\nu^2}{Eh} \mu \ddot{\xi} \\ F_2 &= \frac{1}{R^2} \frac{\partial w}{\partial \varphi} + \frac{1}{R^2} \frac{\partial^2 \eta}{\partial \varphi^2} + \frac{\nu}{R} \frac{\partial^2 \xi}{\partial x \partial \varphi} + \frac{1-\nu}{2} \left(\frac{1}{R} \frac{\partial^2 \xi}{\partial x \partial \varphi} + \frac{\partial^2 \eta}{\partial x^2} \right) - \frac{1-\nu^2}{Eh} \mu \ddot{\eta} \\ F_3 &= -\frac{h^2}{12} \left(\frac{\partial^4 w}{\partial x^4} + \frac{1}{R^4} \frac{\partial^4 w}{\partial \varphi^4} + \frac{2}{R^2} \frac{\partial^4 w}{\partial x^2 \partial \varphi^2} \right) - \frac{\nu}{R} \frac{\partial \xi}{\partial x} - \frac{w}{R^2} - \frac{1}{R^2} \frac{\partial \eta}{\partial \varphi} - \frac{1-\nu^2}{Eh} \mu \ddot{w}\end{aligned}\quad (9.90)$$

For the integral (9.89) to be zero the functions F_1 , F_2 , and F_3 must equal zero. The resulting equations can be written in matrix form as

$$\mathbf{L} \cdot \mathbf{r} = 0; \quad \mathbf{r} = \begin{Bmatrix} \xi \\ \eta \\ w \end{Bmatrix} \quad (9.91)$$

The elements of the 3×3 operator \mathbf{L} are

$$\begin{aligned}
 L_{11} &= \frac{\partial^2}{\partial x^2} + \frac{1-\nu}{2} \frac{1}{R^2} \frac{\partial^2}{\partial \varphi^2} - \frac{1-\nu^2}{Eh} \mu \frac{\partial^2}{\partial t^2}; \quad L_{12} = \frac{(1+\nu)}{2R} \frac{\partial^2}{\partial x \partial \varphi}; \quad L_{13} = \frac{\nu}{R} \frac{\partial}{\partial x} \\
 L_{21} &= \frac{1+\nu}{2R} \frac{\partial^2}{\partial x \partial \varphi}; \quad L_{22} = \frac{1-\nu}{2} \frac{\partial^2}{\partial x^2} + \frac{1}{R^2} \frac{\partial^2}{\partial \varphi^2} - \frac{1-\nu^2}{Eh} \mu \frac{\partial^2}{\partial t^2}; \quad L_{23} = \frac{1}{R^2} \frac{\partial}{\partial \varphi} \\
 L_{31} &= \frac{\nu}{R} \frac{\partial}{\partial x}; \quad L_{32} = \frac{1}{R^2} \frac{\partial}{\partial \varphi}; \\
 L_{33} &= \frac{1}{R^2} + \frac{h^2}{12} \left(\frac{\partial^4}{\partial x^4} + \frac{1}{R^4} \frac{\partial^4}{\partial \varphi^4} + \frac{2}{R^2} \frac{\partial^4}{\partial x^2 \partial \varphi^2} + \frac{\mu}{D} \frac{\partial^2}{\partial t^2} \right)
 \end{aligned} \tag{9.92}$$

The bending stiffness D is $D = Eh^3 / [12(1 - \nu^2)]$. The operator \mathbf{L} is often referred to as the Donell-Mushtari operator.

In the limiting case as R tends to infinity and as $R\partial\varphi$ tends to ∂y or rather as the shell approaches the shape of a flat plate the governing equations (9.91) and (9.92) are reduced to

$$\begin{aligned}
 \frac{\partial^2 \xi}{\partial x^2} + \frac{1-\nu}{2} \frac{\partial^2 \xi}{\partial y^2} + \frac{1+\nu}{2} \frac{\partial^2 \eta}{\partial x \partial y} - \frac{1-\nu^2}{Eh} \mu \ddot{\xi} &= 0 \\
 \frac{1+\nu}{2} \frac{\partial^2 \xi}{\partial x \partial y} + \frac{1-\nu}{2} \frac{\partial^2 \eta}{\partial x^2} + \frac{\partial^2 \eta}{\partial y^2} - \frac{1-\nu^2}{Eh} \mu \ddot{\eta} &= 0 \\
 \nabla^2(\nabla^2 w) + \frac{\mu}{D} \ddot{w} &= 0
 \end{aligned} \tag{9.93}$$

The first two equations of (9.93) govern in-plane waves, or longitudinal and transverse waves, propagating in a flat plate. This is demonstrated by introducing the velocity and vector potentials discussed in Sect. 4.1, Eqs. (4.10) through (4.12). Compare Problem 9.8. The last equation of (9.93) is the wave equation for flexural waves propagating in a thin plate.

The Donell-Mushtari operator (9.92) can be modified by adding higher order terms of $(h/R)^2$ as suggested by Flügge, Byrne and Lur'ye. Returning to Eq. (9.83) and the expression $1/r$ and remembering that this quantity was approximated by $1/R$ across the thickness of the cylinder a somewhat better result would be achieved by writing $1/r$ as

$$\frac{1}{r} = \frac{1}{R+z} = \frac{1}{R(1+z/R)} \approx \frac{1}{R} \left(1 - \frac{z}{R} \right) \quad \text{for } R \gg z$$

An operator L_f including this correction term can be written as

$$L_f = L + \chi \cdot \Delta L; \quad \chi = \frac{h^2}{12R^2} \quad (9.94)$$

The operator L is defined in Eq.(9.92). The correction terms ΔL_{ij} of the operator ΔL are

$$\begin{aligned} \Delta L_{11} &= \frac{1-\nu}{2} \frac{1}{R^2} \frac{\partial^2}{\partial \varphi^2}; \quad \Delta L_{12} = 0; \quad \Delta L_{13} = -R \frac{\partial^3}{\partial x^3} + \frac{1-\nu}{2R} \frac{\partial^3}{\partial x \partial \varphi^2} \\ \Delta L_{21} &= 0; \quad \Delta L_{22} = \frac{3(1-\nu)}{2} \frac{\partial^2}{\partial x^2}; \quad \Delta L_{23} = -\frac{(3-\nu)}{2} \frac{\partial^3}{\partial x^2 \partial \varphi} \\ \Delta L_{31} &= -R \frac{\partial^3}{\partial x^3} + \frac{1-\nu}{2R} \frac{\partial^3}{\partial x \partial \varphi^2}; \quad \Delta L_{32} = -\frac{3-\nu}{2} \frac{\partial^3}{\partial x^2 \partial \varphi}; \quad \Delta L_{33} = \frac{1}{R^2} + \frac{2}{R^2} \frac{\partial^2}{\partial \varphi^2} \end{aligned} \quad (9.95)$$

Leissa discusses in Ref. [87] a number of additional models describing the vibration of cylinders. Some solutions to the Eqs. (9.94) and (9.95) are discussed in Sects. 14.14 through 14.17. In certain cases, also the tension in a shell must be considered. For example, there is typically an overpressure inside an aircraft when in flight. This overpressure induces a tension in the plates of the fuselage. The tension will influence the vibration of the structure as discussed in Chaps. 14 and 15.

9.8 Lagrange's Equation

The equations governing the motion of a mechanical system or rather a system of particles can be derived from Lagrange's equations. These equations were formulated before Hamilton presented his principle. However, Lagrange's equations can be derived from Hamilton's principle. Thus, let the potential energy of a mechanical system be \mathcal{U} . The potential energy \mathcal{U} is a known function of some generalized coordinates q_1, q_2, \dots, q_n and time t . The coordinates identify the positions of n particles. The potential energy is symbolically written $\mathcal{U} = \mathcal{U}(q, t)$. The kinetic energy \mathcal{T} of the same system is also assumed to be a known function of the coordinates q_1, q_2, \dots, q_n , the velocities $\dot{q}_1, \dot{q}_2, \dots, \dot{q}_n$ and time t . The kinetic energy is written $\mathcal{T} = \mathcal{T}(q, \dot{q}, t)$. The Lagrangian operator \mathcal{L} of the system is defined as $\mathcal{L} = \mathcal{T} - \mathcal{U}$. According to Hamilton's principle, Eq. (9.2), it follows that

$$\delta \int_{t_1}^{t_2} \mathcal{L} dt = 0 \quad (9.96)$$

The Lagrangian \mathcal{L} is $\mathcal{L} = \mathcal{L}(q, \dot{q}, t)$. A variation of the expression (9.96) gives

$$\int_{t_1}^{t_2} dt \left[\frac{\partial \mathcal{L}}{\partial q} \cdot \delta q + \frac{\partial \mathcal{L}}{\partial \dot{q}} \cdot \delta \dot{q} \right] = 0 \quad (9.97)$$

The last expression inside the bracket is integrated by parts resulting in

$$\int_{t_1}^{t_2} dt \frac{\partial \mathcal{L}}{\partial \dot{q}} \cdot \delta \dot{q} = \left[\frac{\partial \mathcal{L}}{\partial \dot{q}} \cdot \delta q \right]_{t_1}^{t_2} - \int_{t_1}^{t_2} dt \left(\frac{\partial \mathcal{L}}{\partial t} \right) \delta q dt \quad (9.98)$$

However, $\delta q = 0$ for $t = t_1$ and t_2 as discussed in Sect. 9.1. Thus for Eq. (9.97) to be equal to zero it follows that

$$\frac{d}{dt} \left(\frac{\partial \mathcal{L}}{\partial \dot{q}} \right) - \frac{\partial \mathcal{L}}{\partial q} = 0 \quad (9.99)$$

This is Lagrange's equation for a conservative system. For a conservative force acting on the mechanical system a resulting potential energy can be defined as in Eq. (9.5) to write the Lagrangian as $\mathcal{L} = \mathcal{T} - \mathcal{V} - \mathcal{A}$. Some applications of Lagrange's equations are discussed in Sects. 10.2 through 10.4. Even systems having losses can to a certain extent be described by means of Lagrange's equations as discussed in Sect. 10.3

9.9 Garlekin's Method

The forced response of plates was discussed in Chap. 8. It was concluded that analytical solutions to this type of problems only could be formulated for certain boundary conditions. For rectangular plates two opposite sides must be simply supported for a solution to be found. Another possibility is that two opposite sides are described as "sliding" as illustrated in Fig. 8.2. However, good but approximate solutions can be formulated as suggested for example by Garlekin and discussed in Refs. [16, 25]. Garlekin's original papers were written in Russian. The variational method proposed by Garlekin can be used to find the best possible solution to a problem provided the differential equation describing the response of the structure and its boundary conditions are known. The method is a generalized and simplified application of the virtual work principle. The solution to the problem is set to be a linear combination of a number of shapes or trial functions $\phi_k(\mathbf{r})$ where \mathbf{r} are some coordinates for which the structure is defined. The amplitude of the trial functions is chosen so as to minimize the errors.

In order to describe the method assume that a structure is excited by a pressure $p(\mathbf{r}) \cdot \exp(i\omega t)$. The resulting response of the plate, $w(\mathbf{r}) \cdot \exp(i\omega t)$, is governed by the differential equation

$$\mathbf{L}w - p = 0 \quad (9.100)$$

where \mathbf{L} is some operator. For example, for a homogeneous beam under flexure and oriented along the x -axis the operator \mathbf{L} is defined as $D' \cdot \partial^4 / \partial x^4 - m' \omega^2$ using standard notations. The solution to Eq. (9.100) is according to the Galerkin technique approximated by the expression

$$w_N(\mathbf{r}) = \sum_{k=1}^N C_k \phi_k(\mathbf{r}) \quad (9.101)$$

where $\phi_k(\mathbf{r})$ are functions satisfying some set of boundary conditions but not necessarily the differential equation (9.100) governing the displacement of the structure. The number of trial functions is N . The error $\varepsilon_N(\mathbf{r})$ resulting from introducing the approximate solution (9.101) in Eq. (9.100) is defined as

$$\varepsilon_N(\mathbf{r}) = \mathbf{L}w_N(\mathbf{r}) - p(\mathbf{r}) \quad (9.102)$$

Whenever w_N satisfies both boundary conditions and governing differential equation the error function $\varepsilon_N(\mathbf{r})$ is zero and $w(\mathbf{r}) = w_N(\mathbf{r})$. Galerkin states that any error is minimized by orthogonalizing the error function with respect to the given trial functions. This condition is formulated as

$$\int d\mathbf{r} \cdot \phi_n(\mathbf{r}) \cdot \varepsilon_N(\mathbf{r}) = 0 \quad (9.103)$$

The integration is carried out over the coordinates for which the structure is defined. The Eqs. (9.101) through (9.103) give

$$\int d\mathbf{r} \cdot \phi_n(\mathbf{r}) \sum_{k=1}^N C_k \mathbf{L}\phi_k(\mathbf{r}) - \int d\mathbf{r} \cdot \phi_n(\mathbf{r}) \cdot p(\mathbf{r}) = 0 \quad (9.104)$$

The unknown amplitudes C_k are the solutions to Eq. (9.104) which also can be written in matrix form as

$$\begin{bmatrix} A_{11} & A_{12} & \cdots & A_{1N} \\ A_{21} & A_{22} & \cdots & A_{2N} \\ \cdots & \cdots & \cdots & \cdots \\ A_{N1} & A_{N2} & \cdots & A_{NN} \end{bmatrix} \cdot \begin{Bmatrix} C_1 \\ C_2 \\ \cdots \\ C_N \end{Bmatrix} = \begin{Bmatrix} B_1 \\ B_2 \\ \cdots \\ B_N \end{Bmatrix} \quad (9.105)$$

where

$$A_{ij} = \int d\mathbf{r} \phi_i(\mathbf{r}) \mathbf{L}\phi_j(\mathbf{r}); \quad B_i = \int d\mathbf{r} \phi_i(\mathbf{r}) p(\mathbf{r}) \quad (9.106)$$

Thus, Galerkin's method results in N linear equations giving the amplitudes or expansion coefficients C_i .

The Garlekin condition (9.103) can be shown to have a minimum. This can be illustrated by considering a simple problem—a finite beam under flexure. Thus, let a homogeneous beam of length L be oriented along the x -axis of a coordinate system. The mass per unit length of the beam is m' and its bending stiffness D' . The beam is excited by a force $F'(x) \exp(i\omega t)$ per unit length. The differential equation governing the bending or lateral displacement $w(x) \exp(i\omega t)$ of the beam is given by Eq. (7.45) as

$$D' \frac{d^4 w}{dx^4} - \omega^2 m' w = F' \quad (9.107)$$

Assume that the beam is clamped at both ends at $x = 0$ and at $x = L$. Let the response $w(x)$ of the beam be approximated by

$$w_N(x) = \sum_{k=1}^N C_k \phi_k(x) \quad (9.108)$$

The trial functions $\phi_k(x)$ satisfy the boundary conditions for a clamped beam but not necessarily the differential equation (9.107). The error introduced by using the approximate solution (9.108) is according to Eq. (9.102) defined as

$$\varepsilon_N = D' \frac{d^4 w_N}{dx^4} - \omega^2 m' w_N - F' \quad (9.109)$$

The error function $\varepsilon_N(x)$ is now multiplied by $\phi_n(x)$. The result is integrated over the length of the beam. Thus,

$$\int_0^L dx \phi_n(x) \varepsilon_N(x) = \int_0^L dx \phi_n(x) \left[D' \frac{d^4 w_N(x)}{dx^4} - \omega^2 m' w_N(x) - F'(x) \right] \quad (9.110)$$

In Sect. 9.2 the flexural vibrations of a slender beam were discussed. A variational expression based on Hamilton's principle was given by Eq. (9.19). For a time dependence $\exp(i\omega t)$ of displacement and force this expression is reduced to

$$\int_{t_1}^{t_2} dt \int_0^L dx \delta w \left[m' \omega^2 \frac{\partial^2 w}{\partial t^2} - D' \frac{\partial^4 w}{\partial x^4} + F' \right] + \int_{t_1}^{t_2} dt \left[\delta w \left(D' \frac{\partial^3 w}{\partial x^3} + F \right) - \frac{\partial \delta w}{\partial x} \left(D' \frac{\partial^2 w}{\partial x^2} + M \right) \right]_0^L = 0 \quad (9.111)$$

For a beam satisfying any of the natural boundary conditions, for example free, simply supported or clamped ends, the last bracket is equal to zero. By replacing w by w_N as defined in Eq. (9.101) where all the trial functions $\phi_n(x)$ satisfy one of the natural boundary conditions it follows that (9.111) is reduced to

$$\int_0^L dx \delta w \varepsilon_N = 0 \quad (9.112)$$

Since the response is approximated by (9.108) it follows that

$$\delta w(x) = \delta w_N(x) = \sum_{k=1}^N \phi_k(x) \delta C_k \quad (9.113)$$

This result in combination with (9.112) yields

$$\sum_{k=1}^N \delta C_k \int_0^L dx \phi_k(x) \varepsilon_N(x) = 0 \quad (9.114)$$

The equation has to be satisfied for any small variation of δC_k . The variations of the coefficients δC_k are arbitrary and not interrelated. For Eq. (9.114) to be satisfied, it follows that

$$\int_0^L dx \phi_k(x) \varepsilon_N(x) = 0 \quad (9.115)$$

This result is in accordance with the Garlekin condition (9.103).

9.10 An Example Using Garlekin's Method

Analytical solutions for the forced excitation of homogeneous and rectangular plates can only be formulated for some simple boundary conditions as previously discussed. For other boundary conditions, FEM calculations or some variational technique must be used to find the response and natural frequencies of the structure. As an example, the Garlekin's method will be used to determine the response of a clamped and rectangular homogeneous plate.

A condition for using Garlekin's method is that some trial functions can be defined. The trial functions must satisfy the boundary conditions but not necessarily the differential equation governing the vibration of the plate. The displacement of a rectangular plate with all four sides clamped is written as

$$w_N(x, y) = \sum_m \sum_n A_{mn} \varphi_m(x) \varphi_n(y) \quad (9.116)$$

The functions $\varphi_m(x)$ and $\varphi_n(y)$ can for example be represented by the eigenfunctions for clamped beams oriented in the x and y directions, respectively. Consequently, the function $w_N(x, y)$ satisfies the boundary conditions for the plate but not the differential equation governing the vibration of the plate. The mode numbers are represented by m and n . The beam eigenfunctions for clamped boundary conditions

are listed in Table 7.2. The subscript N of w_N in Eq. (9.116) is equal to the number of possible combinations of the beam functions to be included in the summation. A similar approach can be followed to describe the functions of plates having other boundary conditions. For a plate with three sides clamped and one side free along the line $x = L_x$, the function $\varphi_m(x)$ is obtained from Table 7.5 and $\varphi_n(y)$ as before from Table 7.2.

However, the functions listed in Tables 7.2 through 7.5 are somewhat cumbersome to handle in particular when calculating the matrix elements A_{ij} defined in (9.106). It can therefore be more convenient to use alternative trial functions, which do not approximate the actual displacement as well as the so-called simple beam functions listed in Tables 7.1–7.5. For a clamped beam under flexure and of length L such trial functions can be written as

$$X_m(x) = \sin \frac{m\pi x}{L} \sin \frac{\pi x}{L} = \frac{1}{2} \left(\cos \frac{\pi x(m+1)}{L} - \cos \frac{\pi x(m-1)}{L} \right) \quad (9.117)$$

These trial functions satisfy the boundary conditions for a clamped beam, i.e., $X_m(x) = X'_m(x) = 0$ for $x = 0$ and $x = L$. The advantage of these trial functions as compared to the beam functions is that they are the sum of two cosine functions, which are orthogonal and easy to derivate. It is therefore straightforward to calculate the matrix elements of (9.106). For a plate or for that matter a beam, which is exposed to a load symmetric with respect to its center the resulting response of the structure is also symmetric requiring $X_m(x) = X_m(L-x)$. This condition is only satisfied for m odd in Eq. (9.117).

As a numerical example consider a quadratic and homogeneous plate, side L , with clamped boundaries. The mass per unit area of the plate is μ and its bending stiffness D . The plate is exposed to a pressure $p_0 \cdot \exp(i\omega t)$ across its entire surface, p_0 being constant. The frequency of the pressure is low or of the order of the natural frequency of the plate resulting in that only the first few modes of the plate are necessary for describing the motion of the plate. Therefore, consider only the first three symmetric modes of the panel. These modes are

$$\phi_1(x, y) = X_1(x)X_1(y); \quad \phi_2(x, y) = X_2(x)X_1(y); \quad \phi_3(x, y) = X_1(x)X_2(y)$$

Neglecting a constant, $1/2$, the trial functions are written

$$\begin{cases} \phi_1(x, y) = \left(1 - \cos \frac{2\pi x}{L}\right) \cdot \left(1 - \cos \frac{2\pi y}{L}\right) \\ \phi_2(x, y) = \left[\cos \left(\frac{4\pi x}{L}\right) - \cos \left(\frac{2\pi x}{L}\right)\right] \cdot \left[1 - \cos \left(\frac{2\pi y}{L}\right)\right] \\ \phi_3(x, y) = \left[1 - \cos \left(\frac{2\pi x}{L}\right)\right] \cdot \left[\cos \left(\frac{4\pi y}{L}\right) - \cos \left(\frac{2\pi y}{L}\right)\right] \end{cases} \quad (9.118)$$

The operator L in Eq. (9.106) is for this plate given by

$$L = D \left(\frac{\partial^4}{\partial x^4} + 2 \frac{\partial^4}{\partial x^2 \partial y^4} + \frac{\partial^4}{\partial y^4} \right) - \mu \omega^2 \quad (9.119)$$

The response of the plate is approximated by

$$w_N = C_1 \phi_1 + C_2 \phi_2 + C_3 \phi_3 \quad (9.120)$$

Defining α as $\alpha = L \cdot [\mu \omega^2 / D]^{1/4}$ the matrix elements A_{ij} defined in (9.106) are obtained as

$$\begin{aligned} A_{11} &= D/L^2 \left(32\pi^4 - 9\alpha^4/4 \right); & A_{12} &= A_{21} = A_{13} = A_{31} = D/L^2 \left(24\pi^4 - 3\alpha^4/4 \right) \\ A_{22} &= A_{33} = D/L^2 \left(252\pi^4 - 3\alpha^4/2 \right); & A_{23} &= A_{32} = D/L^2 \left(16\pi^4 - \alpha^4/4 \right) \end{aligned} \quad (9.121)$$

The elements B_i are obtained from (9.106) as

$$B_1 = p_0 L^2; \quad B_2 = B_3 = 0 \quad (9.122)$$

The resulting amplitudes C_i of the trial functions are the solutions to the matrix equation $A \cdot C = B$. Thus

$$C_1 = \frac{B_1(A_{22} + A_{23})}{A_{11}(A_{22} + A_{23}) - 2A_{12}^2}; \quad C_2 = C_3 = -\frac{B_1 A_{12}}{A_{11}(A_{22} + A_{23}) - 2A_{12}^2} \quad (9.123)$$

There are resonances when the denominator is equal to zero or when $\alpha = L \cdot [\mu \omega^2 / D]^{1/4}$ is the solution to

$$(45/16)\alpha^8 - 587\pi^4\alpha^4 + 7424\pi^8 = 0$$

The parameter α should be real and positive. There are two possible solutions corresponding to the first two natural frequencies of the plate. The solutions are

$$f_{11} = 5.7765 \cdot \frac{1}{L^2} \left(\frac{D}{\mu} \right)^{1/2}; \quad f_{13} = f_{31} = 21.9455 \cdot \frac{1}{L^2} \left(\frac{D}{\mu} \right)^{1/2} \quad (9.124)$$

Based on more accurate numerical methods the natural frequencies f_{11} and f_{13} are, with four accurate decimals, obtained as $f_{11} = 5.7272/L^2 \cdot \sqrt{D/\mu}$ and $f_{13} = 20.9417/L^2 \cdot \sqrt{D/\mu}$. The error using the approximate trial functions given in (9.119) is for f_{11} 0.9% and for f_{13} 4.8%.

The amplitudes of the trial functions are

$$C_1 = \frac{p_0 L^4 (268\pi^4 - 7\alpha^4/4)}{D(7424\pi^8 - 587\pi^4\alpha^4 + 45\alpha^8/16)}$$

$$C_2 = C_3 = -\frac{p_0 L^4 (24\pi^4 - 3\alpha^4/4)}{D(7424\pi^8 - 587\pi^4\alpha^4 + 45\alpha^8/16)}$$

The static deflection of the plate at its center, i.e., for $x = y = L/2$ and $\alpha = 0$, is obtained from Eqs. (9.121) and (9.118) as $0.00122 \cdot p_0 L^4 / D$. Numerical results with five accurate decimals give $0.00126 \cdot p_0 L^4 / D$.

If only one term or trial function is used to approximate the displacement of the plate, then (9.85) is reduced to $w_N = C_1 \phi_1$. The resulting amplitude C_1 is obtained as

$$C_1 = \frac{B_1}{A_{11}} = \frac{p_0 L^4}{D(32\pi^4 - 9\alpha^4/4)}$$

The first natural frequency using only one trial function is the solution to $\alpha^4 = 128\pi^4/9$ giving $f_{11} = 5.92/L^2 \cdot \sqrt{D/\mu}$. This frequency is 3.4% higher than the accurate value.

The natural frequencies predicted using the Garlekin method are always higher or equal to the exact values. This is also the case whenever the Rayleigh-Ritz technique, Eq. (8.87), is used as discussed in Sect. 8.6. The Rayleigh-Ritz technique gives the same natural frequency as the Garlekin method if the same trial functions are used. See Problem 9.7. However, the Garlekin method gives the amplitudes at forced excitation. The Rayleigh-Ritz technique can only be used for free vibrations.

Problems

- 9.1 Prove Newton’s law $F_x = m\ddot{x}$ by using Hamilton’s principle.
- 9.2 A particle, mass m , is at time $t = 0$ at the height z_0 above ground. The mass is released at $t = 0$. Determine the equation governing the motion of the mass using Hamilton’s principle and give its height at any t before it hits the ground.
- 9.3 Derive the wave equation for longitudinal waves propagating in a slender beam. Formulate also the boundary conditions. Use Hamilton’s principle.
- 9.4 Prove Eq. (9.40) by using Eqs. (9.35) and (9.36).
- 9.5 Prove Eq. (9.53) by using the Eqs. (9.50)–(9.52).
- 9.6 Use (9.78) to show that $\kappa h < 1$ for the error of the wavenumber to be less than 10% using the Kirchhoff theory.

9.7 Show that the Rayleigh–Ritz technique and the Galerkin method give the same natural frequencies for a vibrating plate. In both cases use two trial functions. Assume that the displacement is zero along the edges of the plate. Assume that the displacement of a plate is approximated by

$$w = C_1\phi_1 + C_2\phi_2$$

This function satisfies some boundary conditions. The displacement along the edges of the plate is zero.

9.8 Show that the first two expressions of Eq. (9.93) govern longitudinal and transverse waves.

9.9 Determine the natural frequencies for a simply supported Timoshenko beam.

Chapter 10

Structural Coupling Between Simple Systems

Transfer of vibrations from excitation zones to supporting and adjoining structures mainly determines noise emission from vehicles, machines, and other sources of noise. The radiated noise can be reduced effectively by minimizing the vibration transfer between sources and supporting structures. A simple example of this is the insertion of resilient mounts between structures. These mounts offer cheap solutions to many problems. Today it is more or less standard procedure to mount any type of machinery on resilient mounts. Initially this type of mountings was used to prevent the energy transfer of low frequency vibrations from an engine to a supporting structure or from a vibrating supporting structure to sensitive equipment. Simple design criteria were developed to optimize these types of mountings. The methods used described the coupling between simple mass–spring systems with several degrees of freedom. With respect to noise, a resilient mounting must be effective in a wide frequency range, usually from 20 to 2000 Hz or even higher. In this frequency range, coupled dynamic systems can no longer be considered as coupled rigid masses and ideal springs.

This chapter starts with an investigation of the vibration of systems of point masses and ideal springs. Thereafter follows a survey of dynamic properties of some simple resilient mounts. Finally, there is a discussion on the transfer of energy from a vibrating source to a receiving structure.

10.1 Introduction

Resilient mountings are used to reduce the energy flow from a vibrating source, for example an engine, to its foundation. The reduction of the energy flow depends on the frequency contents of the forces exciting the mass of the source, the “stiffness” of the mounts and the mobility of the foundation. In general, the stiffness of the mounts should be such that the fundamental resonance frequencies of the entire resilient system, considering all six degrees of freedom, are well below the fundamental frequency of the internal or external forces exciting the mass corresponding

to the engine. Resilient mounts are usually designed in such a way that the first few resonances of say a mounted engine are in the very low frequency range. For typical mounting systems for internal combustion engines or even very large Diesel engines, the first fundamental resonances of the mounted engine should be well below 10 Hz. In this low frequency range resilient mounts can, to a certain extent, be modeled as ideal and mass less springs or alternatively as a rod. A simple case, a mass mounted on a spring modeled as a rod, was discussed in Sect. 6.6. However, the dynamic stiffness of a rubber mount is more complicated than revealed by a simple rod model. The stiffness of the mount also depends on the amplitude of the displacement, frequency, temperature, configuration, and preload. For large amplitudes, the behavior of a rubber mount is non-linear.

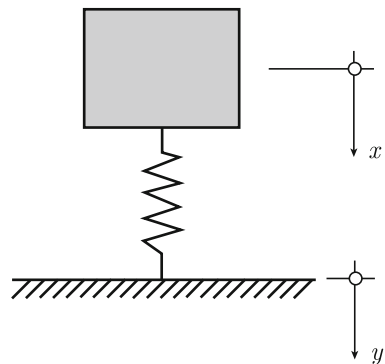
A source like an engine is built up of a number of beam- and plate- like structures. In the very low frequency range, below the first few natural frequencies for the individual substructures, the engine vibrates as an almost rigid mass.

The response of a rigid mass excited by an external force and mounted on an ideal spring to a foundation with the point mobility Y was discussed in Sect. 2.8. The FT of the displacement \hat{y} of the foundation as compared to the FT of the displacement \hat{x} of the mass is

$$\hat{y} = \frac{\hat{x}}{1 + i\omega/(kY)}$$

The stiffness of the spring is given by k . The mobility of the foundation is often such that the displacement y is much smaller than x . If the mobility of the foundation is not sufficiently small so as to neglect the displacement, the foundation can be modeled as yet another simple mass–spring system as indicated in Fig. 10.1. In the low frequency range, the result is again that the entire system can, for small amplitudes, be described as a system of rigid masses coupled by ideal springs.

Fig. 10.1 Mass–spring system mounted on a not completely rigid foundation



10.2 Coupled Mass–Spring Systems

Some simple systems with one degree of freedom were discussed in Chap. 1. The motion of mass–spring systems mounted on foundations, which are not necessarily infinitely stiff, was introduced in Sect. 2.8. Real systems have several or in fact an infinite number of degrees of freedom. A machine or vibrating source should always be mounted to a foundation or supporting structure in such a way that the first few natural frequencies of the system do not coincide with any of the major peaks in the spectrum of the forces exciting the system. For a simple 1-DOF system, the ratio between the frequency f_0 of the first harmonic of the exciting force and the first natural frequency f_r of the simple mass–spring system should satisfy the inequality $f_0/f_r > \sqrt{2}$ to avoid any amplification effects. The first few natural frequencies of a mounting system should therefore always be calculated during the design phase. These first few natural frequencies are very often within the very low frequency range. If this is the case, coupled systems can be modeled as an assembly of simple mass–spring systems. The prediction of the first few natural frequencies of the entire system can therefore often be carried out in a fairly simple way.

The basic equations governing the motion of simple multi-degree of freedom systems are in most cases readily derived by the use of energy methods. The methods require that the kinetic energies of the masses and the potential energies stored in the springs are defined for the system. The equations governing the motion of the masses are thereafter obtained from Lagrange’s equation. The procedure leads to a system of equations. The resulting system can be transformed to make the equations uncoupled.

For continuous systems like beams and plates, the forced response of a structure was obtained by means of the appropriate eigenfunctions. The response was derived as an infinite sum of these eigenfunctions and their corresponding amplitudes. This was discussed in Chap. 6 through 8. A similar approach can be followed to describe the forced motion of coupled discrete systems.

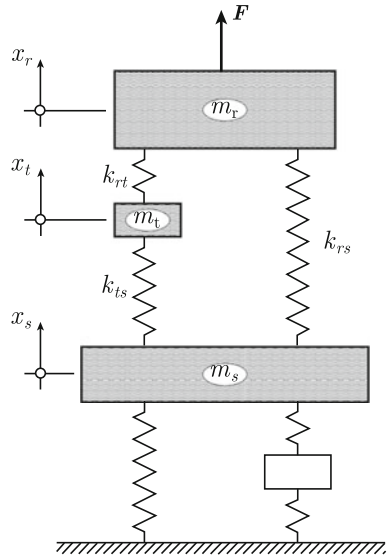
As an example, consider the coupled system shown in Fig. 10.2. All masses are rigid and the springs are ideal and thus mass less. Losses are not included. In this particular case, the masses can move in one direction only. The displacement of the mass m_r is denoted x_r . The kinetic energy \mathcal{T} of the entire system is

$$\mathcal{T} = \sum_r \frac{m_r \dot{x}_r^2}{2} \quad (10.1)$$

The kinetic energies for all masses are included. The spring constant for a resilient element connecting the masses r and s is denoted k_{rs} . For such a spring, compressed as shown in Fig. 10.2, the reacting force at one end of the spring is

$$F_{rs} = k_{rs}(x_r - x_s)$$

Fig. 10.2 An assembly of rigid masses coupled by ideal springs



The potential energy stored in the spring, which connects the masses r and s , is

$$\mathcal{U}_{rs} = \int F_{rs} dx_r - \int F_{rs} dx_s = \int k_{rs}(x_r - x_s) d(x_r - x_s) = \frac{k_{rs}(x_r - x_s)^2}{2} \tag{10.2}$$

The coordinates x_r and x_s define the displacements with respect to the static case of the two ends of the spring connecting the masses r and s . The total stored potential energy in the springs is

$$\mathcal{U}^s = \sum k_{rs}(x_r - x_s)^2/2 \tag{10.3}$$

The summation is made for all possible combinations of r and s for which k_{rs} is defined. Each spring should only be included once.

The external forces exciting the system also contribute to the potential energy of the system. For force and displacement defined positive in the same direction, as shown in Fig. 10.2, the potential energy is converted into kinetic energy as the mass moves in the direction of the force. The potential energy decreases as the mass moves in the direction of the force vector. In a similar way the potential energy for a free mass decreases as the mass accelerates in the direction of the force of gravity. A conservative force, like the force of gravity close to the surface of the earth, is independent of moderate variations of the coordinates x_r and velocities \dot{x}_r . The potential energy of all masses excited by external conservative forces defined positive as in Fig. 10.2 is thus

$$\mathcal{U}^f = \mathcal{U}_0 - \sum_r F_r \cdot x_r \tag{10.4}$$

The parameter \mathcal{U}_0 corresponds to the potential energy of the system when initially at rest. The total potential energy of the system is

$$\mathcal{U} = \mathcal{U}^s + \mathcal{U}^f = \sum_{r,s} k_{rs}(x_r - x_s)^2/2 + \mathcal{U}_0 - \sum_r F_r \cdot x_r \quad (10.5)$$

The equations governing the motion of the masses can now be obtained by means of the procedure developed by Lagrange. This method, Lagrange's equation, is discussed in Sect. 9.8. The Lagrangian function \mathcal{L} is defined as the difference between the kinetic and potential energies of the system. Thus

$$\mathcal{L} = \mathcal{T} - \mathcal{U} \quad (10.6)$$

Lagrange's equation requires, as discussed in Sect. 9.8, that

$$\frac{d}{dt} \left[\frac{\partial \mathcal{L}}{\partial \dot{x}_r} \right] - \frac{\partial \mathcal{L}}{\partial x_r} = 0 \quad (10.7)$$

The Lagrangian function \mathcal{L} for the system shown in Fig. 10.2 is obtained from Eqs. (10.1), (10.5) and (10.6) as

$$\mathcal{L} = \sum_r \frac{m_r \dot{x}_r^2}{2} - \sum_{r,s} k_{rs}(x_r - x_s)^2/2 - \mathcal{U}_0 + \sum_r F_r x_r \quad (10.8)$$

This expression inserted in Eq. (10.7) yields

$$m_r \ddot{x}_r + \sum_{r,s} k_{rs}(x_r - x_s) = F_r \quad (10.9)$$

The result is a system of coupled equations. These equations can be written in matrix form as

$$\mathbf{M} \cdot \ddot{\mathbf{X}} + \mathbf{K} \cdot \mathbf{X} = \mathbf{F} \quad (10.10)$$

For a system built up of N masses, each allowed to move in one direction only as defined by the coordinates x_r , \mathbf{M} and \mathbf{K} are $N \times N$ symmetric matrices. \mathbf{X} and \mathbf{F} are column vectors, each with N elements.

For free motion of the system, the external forces are equal to zero. For this case, the eigenvalues λ or eigenfrequencies $f = \omega/(2\pi)$ are obtained from Eq. (10.10) by setting

$$\mathbf{F} = 0; \quad \ddot{\mathbf{X}} = -\lambda \mathbf{X} \quad \text{or} \quad \ddot{\mathbf{X}} = -\omega^2 \mathbf{X} \quad (10.11)$$

According to standard procedure, the eigenvalues are obtained by setting the determinant of $\mathbf{K} - \lambda \mathbf{M}$ equal to zero, i.e.,

$$\text{Det}[\mathbf{K} - \lambda\mathbf{M}] = 0 \quad (10.12)$$

There are N eigenvalues for a system with N degrees of freedom. Each eigenvalue λ_r corresponds to an eigenvector \mathbf{X}_r . This vector defines the relative displacements between the masses for that particular eigenvalue or at that particular eigenfrequency. This is in analogy with eigenfunctions and eigenfrequencies derived for continuous systems as discussed in Chap. 6 through 8. The eigenvector \mathbf{X}_r should satisfy the equation

$$(\mathbf{K} - \lambda_r\mathbf{M}) \cdot \mathbf{X}_r = 0 \quad (10.13)$$

The eigenvectors \mathbf{X}_r are orthogonal if the matrices \mathbf{M} and \mathbf{K} are symmetric. For the r -th mode the governing equation is obtained from Eq. (10.13) as

$$\mathbf{K} \cdot \mathbf{X}_r = \lambda_r\mathbf{M} \cdot \mathbf{X}_r$$

This expression is multiplied by the transposed vector of \mathbf{X}_s . The result is

$$\mathbf{X}_s^T \cdot \mathbf{K} \cdot \mathbf{X}_r = \lambda_r \mathbf{X}_s^T \cdot \mathbf{M} \cdot \mathbf{X}_r \quad (10.14)$$

By interchanging the subscripts r and s , the following equation is obtained

$$\mathbf{X}_r^T \cdot \mathbf{K} \cdot \mathbf{X}_s = \lambda_s \mathbf{X}_r^T \cdot \mathbf{M} \cdot \mathbf{X}_s \quad (10.15)$$

If the matrices \mathbf{M} and \mathbf{K} are symmetric, it is readily verified that

$$\mathbf{X}_s^T \cdot \mathbf{K} \cdot \mathbf{X}_r = \mathbf{X}_r^T \cdot \mathbf{K} \cdot \mathbf{X}_s; \quad \mathbf{X}_r^T \cdot \mathbf{M} \cdot \mathbf{X}_s = \mathbf{X}_s^T \cdot \mathbf{M} \cdot \mathbf{X}_r \quad (10.16)$$

By subtracting Eq. (10.15) from (10.14) and using Eq. (10.16) it follows that

$$(\lambda_r - \lambda_s) \cdot \mathbf{X}_r^T \cdot \mathbf{M} \cdot \mathbf{X}_s = 0$$

Since $\lambda_r \neq \lambda_s$ for $r \neq s$ the orthogonality condition is obtained as

$$\mathbf{X}_r^T \cdot \mathbf{M} \cdot \mathbf{X}_s = 0; \quad \mathbf{X}_r^T \cdot \mathbf{K} \cdot \mathbf{X}_s = 0 \quad \text{for } r \neq s \quad (10.17)$$

The forced response of a continuous system can be determined by means of the mode summation technique as described in Chap. 6 through 8. For discrete systems a similar approach can be followed. The general solution describing the forced excitation of a discrete system is in vector form defined as

$$\mathbf{X} = \sum_r A_r(t) \cdot \mathbf{X}_r \quad (10.18)$$

The eigenvectors are given by \mathbf{X}_r . The time-dependent amplitude for each eigenvector is given by $A_r(t)$. For harmonic excitation with the time dependence $\exp(i\omega t)$

the resulting forced response must have the same time dependence, i.e., $\exp(i\omega t)$. The time-dependent amplitudes $A_r(t)$ are consequently of the form $A_r \cdot \exp(i\omega t)$. The equation of motion of the system is, in matrix form, given by Eq. (10.10). For $\ddot{\mathbf{X}} = -\omega^2 \mathbf{X}$, Eq. (10.10) can be rewritten as

$$(\mathbf{K} - \omega^2 \cdot \mathbf{M}) \cdot \mathbf{X} = \mathbf{F} \quad (10.19)$$

The general solution, Eq. (10.18), is inserted in Eq. (10.19), thus

$$(\mathbf{K} - \omega^2 \cdot \mathbf{M}) \cdot \sum_r A_r \cdot \mathbf{X}_r = \mathbf{F}$$

This general expression is multiplied by the transposed vector \mathbf{X}_r^T . Considering the orthogonality of the eigenvectors, Eq. (10.17), the result after the multiplication, is

$$(\mathbf{X}_r^T \cdot \mathbf{K} \cdot \mathbf{X}_r - \omega^2 \cdot \mathbf{X}_r^T \cdot \mathbf{M} \cdot \mathbf{X}_r) \cdot A_r = \mathbf{X}_r^T \cdot \mathbf{F}$$

The amplitudes A_r and the response are consequently

$$A_r = \frac{\mathbf{X}_r^T \cdot \mathbf{F}}{\mathbf{X}_r^T \cdot \mathbf{K} \cdot \mathbf{X}_r - \omega^2 \mathbf{X}_r^T \cdot \mathbf{M} \cdot \mathbf{X}_r}; \quad \mathbf{X} = \sum_r A_r \cdot \mathbf{X}_r \cdot e^{i\omega t} \quad (10.20)$$

It is assumed that the time-dependent force vector is given by $\mathbf{F} \cdot \exp(i\omega t)$.

In analogy with the discussion in Sect. 7.4, the concepts of modal mass M_r and modal stiffness K_r for mode r can be introduced as

$$M_r = \mathbf{X}_r^T \cdot \mathbf{M} \cdot \mathbf{X}_r; \quad K_r = \mathbf{X}_r^T \cdot \mathbf{K} \cdot \mathbf{X}_r$$

However, as previously mentioned, modal mass, modal stiffness, etc., are not absolute measures but depend on how the eigenvector is normalized. However, the angular eigenfrequency for mode r is always obtained as $\omega_r = \sqrt{K_r/M_r}$.

10.3 Coupled Systems with Losses

All systems have losses. However, the natural frequencies of a system are often predicted while neglecting the losses. In Chap. 1 the eigenfrequency of a simple mass–spring system is given in Eq. (1.14) as function of the losses. For small and moderate losses, the shift, with respect to the loss free case, is small or moderate.

At frequencies close to a natural frequency, the forced response of a system very much depends on the energy dissipated. These losses can be included in Lagrange's equation as suggested by Rayleigh and described in for example Ref. [90].

The damping forces at each end of the types of mounts shown in Fig. 10.2 are assumed to be proportional to the relative velocity $\dot{x}_r - \dot{x}_s$ between the masses r and s . The damping forces are

$$Q_r = c_{rs}(\dot{x}_r - \dot{x}_s); \quad Q_s = c_{sr}(\dot{x}_s - \dot{x}_r); \quad c_{rs} = c_{sr} \quad (10.21)$$

The dissipation function \mathcal{D} is defined through

$$Q_r = -\frac{\partial \mathcal{D}}{\partial \dot{x}_r}$$

For the system shown in Fig. 10.2 with a damping defined by Eq. (10.21) the dissipation function \mathcal{D} is obtained as

$$\mathcal{D} = \sum_{r,s} c_{rs}(\dot{x}_r - \dot{x}_s)^2/2 \quad (10.22)$$

The summation is made over all possible combinations of r and s for which c_{rs} is defined. However, each damper should only be included once. Lagrange's equation can, when including dissipation, be written as

$$\frac{d}{dt} \left[\frac{\partial \mathcal{L}}{\partial \dot{x}_r} \right] - \frac{\partial \mathcal{L}}{\partial x_r} + \frac{\partial \mathcal{D}}{\partial \dot{x}_r} = 0 \quad (10.23)$$

For the system in Fig. 10.2 the motion of the masses is, in matrix form and based on the results (10.1), (10.5), (10.22), and (10.23), obtained as

$$\mathbf{M} \cdot \ddot{\mathbf{X}} + \mathbf{C} \cdot \dot{\mathbf{X}} + \mathbf{K} \cdot \mathbf{X} = \mathbf{F} \quad (10.24)$$

For a system without losses, i.e., for \mathbf{C} equal to zero, a solution can be found as described in the preceding section. The same procedure can be used to solve Eq. (10.24) for certain cases or rather for certain types of damping. A necessary condition is that the matrix \mathbf{C} is defined as a linear combination of the matrices \mathbf{M} and \mathbf{K} . For α and β constants and $\mathbf{C} = \alpha \cdot \mathbf{M} + \beta \cdot \mathbf{K}$, the orthogonal eigenvectors \mathbf{X}_r , which satisfy the orthogonality conditions in (10.17), are also orthogonal with respect to the matrix \mathbf{C} . Consequently

$$\mathbf{X}_r^T \cdot \mathbf{C} \cdot \mathbf{X}_s = 0 \quad \text{for } r \neq s \quad \text{and} \quad \mathbf{C} = \alpha \cdot \mathbf{M} + \beta \cdot \mathbf{K} \quad (10.25)$$

The solution to equation (10.24) is thus

$$X = \sum_r A_r \cdot X_r \cdot e^{i\omega t};$$

$$A_r = \frac{X_r^T \cdot F}{X_r^T \cdot K \cdot X_r + i\omega X_r^T \cdot C \cdot X_r - \omega^2 X_r^T \cdot M \cdot X_r} \tag{10.26}$$

Again, it is assumed that the time-dependent force vector is given by $F \cdot \exp(i\omega t)$.

The eigenvectors X_r are for certain cases also eigenvectors to the damped system described in Eq. (10.24). For structural or hysteric damping, the parameter c is inversely proportional to the angular frequency as discussed in Sect. 1.1. For this type of damping, the matrix C can be written as $C = H/\omega$. The new matrix H is assumed to be independent of ω . It can be shown that the eigenvectors X_r to the undamped system also are eigenvectors to the damped system defined by Eq. (10.24) if

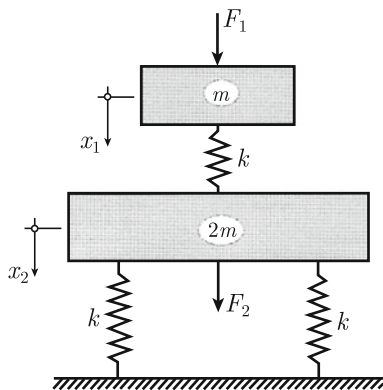
$$C = H/\omega \quad \text{and} \quad H = \gamma \cdot M + \varepsilon \cdot K$$

The parameters γ and ε and the matrices M and K are assumed to be independent of ω . However, the resulting eigenvectors are complex. This type of damping is often assumed based on numerical rather than on physical considerations. Some more general cases are discussed in for example Refs. [25, 63].

10.4 Example

The general procedure of solving a forced problem can be illustrated by a simple example. A two degree of freedom system is shown in Fig. 10.3. Two masses m and $2m$ are coupled by means of a resilient mount, spring constant k , and damping coefficient c . The damping is defined as in Eq. (10.21).

Fig. 10.3 A simple 2-DOF system



The bigger mass is connected by two identical springs to an infinitely stiff foundation. The dynamic properties for each spring are defined by k and c . Each mass can only move in the vertical direction. No rotation is allowed. The kinetic and potential energies and the dissipation function are

$$\begin{aligned} T &= m(\dot{x}_1^2 + 2\dot{x}_2^2)/2; \quad \mathcal{U} = k[(x_1 - x_2)^2 + 2x_2^2]/2 - F_1x_1 - F_2x_2 + \mathcal{U}_0 \\ \mathcal{D} &= c[(\dot{x}_1 - \dot{x}_2)^2 + 2\dot{x}_2^2]/2 \end{aligned} \quad (10.27)$$

Based on Eqs. (10.6) and (10.23) the resulting equations governing the displacements of the masses are

$$m\ddot{x}_1 + c(\dot{x}_1 - \dot{x}_2) + k(x_1 - x_2) = F_1; \quad 2m\ddot{x}_2 + c(3\dot{x}_2 - \dot{x}_1) + k(3x_2 - x_1) = F_2$$

In matrix form this is equivalent to

$$\begin{aligned} \mathbf{M} \cdot \ddot{\mathbf{X}} + \mathbf{C} \cdot \dot{\mathbf{X}} + \mathbf{K} \cdot \mathbf{X} &= \mathbf{F} \\ \mathbf{M} = m \begin{bmatrix} 1 & 0 \\ 0 & 2 \end{bmatrix}; \quad \mathbf{K} = k \begin{bmatrix} 1 & -1 \\ -1 & 3 \end{bmatrix}; \quad \mathbf{C} = c \begin{bmatrix} 1 & -1 \\ -1 & 3 \end{bmatrix} \end{aligned} \quad (10.28)$$

The damping matrix is proportional to the stiffness matrix. The eigenvalues for the undamped system, i.e., for $c = 0$, are obtained from Eq. (10.12) as

$$\text{Det} \begin{bmatrix} k - m\lambda & -k \\ -k & 3k - 2m\lambda \end{bmatrix} = 0$$

By introducing $\omega_0^2 = k/m$, the result is

$$\lambda_1 = \omega_0^2/2 \quad \text{and} \quad \lambda_2 = 2\omega_0^2 \quad (10.29)$$

The eigenvectors \mathbf{X}_r corresponding to λ_r are obtained from Eq. (10.13) as

$$[\mathbf{K} - \lambda_r \mathbf{M}] \mathbf{X}_r = [\mathbf{K} - \lambda_r \mathbf{M}] \begin{Bmatrix} x_1 \\ x_2 \end{Bmatrix}_r = 0$$

Inserting the appropriate values for the matrices \mathbf{K} and \mathbf{M} and the eigenvalue $\lambda_1 = \omega_0^2/2$, the result is

$$k \begin{bmatrix} 0.5 & -1 \\ -1 & 2 \end{bmatrix} \begin{Bmatrix} x_1 \\ x_2 \end{Bmatrix}_1 = 0$$

The equation is satisfied by

$$\mathbf{X}_1 = \begin{Bmatrix} x_1 \\ x_2 \end{Bmatrix}_1 = \begin{Bmatrix} 2 \\ 1 \end{Bmatrix} \quad (10.30)$$

or in fact, by any vector which is proportional to X_1 . However, it is often convenient to set the last element in the column vector to equal unity. In a similar way the eigenvectors X_2 corresponding to $\lambda_2 = 2\omega_0^2$ are obtained as

$$X_2 = \begin{Bmatrix} -1 \\ 1 \end{Bmatrix} \tag{10.31}$$

The modes of vibration are illustrated in Fig. 10.4. At the first resonance, the amplitude of the displacement of the smaller mass is twice the amplitude of the bigger mass. At the second resonance, the masses are moving out of phase. For a force vector with the time dependence $\exp(i\omega t)$ the response of the system is obtained from Eqs. (10.20) and (10.26) as

$$X = \frac{(2F_1 + F_2)e^{i\omega t}}{3k + 3i\omega c - 6\omega^2 m} \cdot \begin{Bmatrix} 2 \\ 1 \end{Bmatrix} + \frac{(-F_1 + F_2)e^{i\omega t}}{6k + 6i\omega c - 3\omega^2 m} \cdot \begin{Bmatrix} -1 \\ 1 \end{Bmatrix} \tag{10.32}$$

The result is also written

$$X = \frac{(2F_1 + F_2)e^{i(\omega t + \varphi_1)}}{[(3k - 6\omega^2 m)^2 + (3\omega c)^2]^{1/2}} \cdot \begin{Bmatrix} 2 \\ 1 \end{Bmatrix} + \frac{(-F_1 + F_2)e^{i(\omega t + \varphi_2)}}{[(6k - 3\omega^2 m)^2 + (6\omega c)^2]^{1/2}} \cdot \begin{Bmatrix} -1 \\ 1 \end{Bmatrix}$$

$$\tan \varphi_1 = -\frac{\omega c}{k - 2m\omega^2}; \quad \tan \varphi_2 = -\frac{2\omega c}{2k - m\omega^2}$$

The frequencies at which the amplitudes have maxima are readily obtained from Eq. (10.32). A maximum is obtained when the absolute value of one of the denominators is minimum. Thus, resonances are obtained for $\omega = \sqrt{\omega_0^2/2 - (c/2m)^2}$ and $\omega = \sqrt{2\omega_0^2 - 2(c/m)^2}$

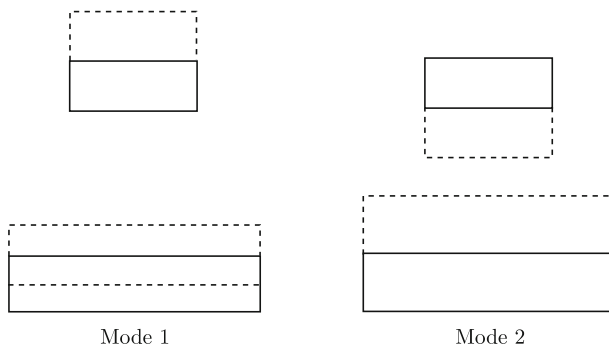


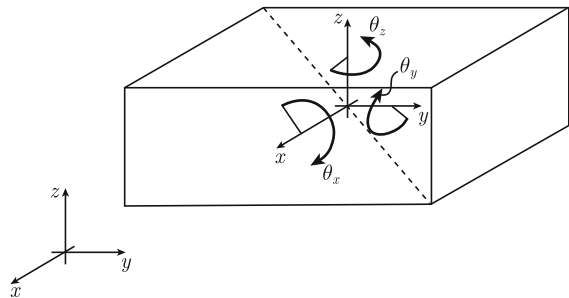
Fig. 10.4 Modes of vibration for the 2-DOF system shown in Fig. 10.3

The same problem could be solved in a very straightforward way without the use of the methods described above. However, the methods are well suited for solving numerically the motion of large complicated systems. In fact, every type of Finite Element Method calculation is first based on a Hamilton description of the coupled elements of the entire system. Thereafter, the resulting system of equations can be solved as discussed above. The accuracy and efficiency of any FEM code depend on how well the displacements of the various continuous elements are described and how well large matrices are inverted and data stored.

In the example discussed each mass was allowed one degree of freedom. In general, all six degrees of freedom must be considered for each mass. Figure 10.5 illustrates a simple case of a resiliently mounted engine. The engine is modeled as a rigid mass. Each corner of the engine is supported by a simple spring. The foundation is assumed to be infinitely stiff. The displacement of the center of gravity with respect to the state of equilibrium is defined by the vector (x, y, z) . The angles of rotation with respect to the main coordinate axes are θ_x , θ_y , and θ_z . The displacements of each corner of the engine and thus the potential energy can be expressed as functions of x , y , and z and the three angles of rotation. The stiffness of the identical springs can be defined as k_x , k_y , and k_z along the three coordinate axes. The kinetic energy of the system can be derived as function of \dot{x} , \dot{y} , \dot{z} , $\dot{\theta}_x$, $\dot{\theta}_y$, and $\dot{\theta}_z$ as well as the mass m of the engine and its moments of inertia J_x , J_y , and J_z . The six equations governing the motion of the mass are obtained by means of Lagrange's equation. The generalized coordinates x_r are x , y , z , θ_x , θ_y , and θ_z . In most practical cases, it can be assumed that the rotational angles are small. This allows the sine and cosine functions to be approximated by the first term of their respective Taylor expansion.

In practice, many types of resilient mounts are used to reduce the transmission of structure-borne sound from a mechanical source to its foundation and its supporting structure [98]. The efficiency of the mounting depends on many parameters including the vibrational characteristics of the source, the stiffness of the coupling points between source and mounts, the dynamic properties of the mount, and on the mobility of the foundation. Some of these aspects are discussed in the following sections, which include an introduction concerning the material properties of rubber, modeling

Fig. 10.5 A resiliently mounted rigid mass, six degrees of freedom



of simple mounts, mobility of foundations, and source strength. Finally a method for the modeling of coupling between source, mount, and receiver or foundation is discussed.

10.5 Rubber Mounts, Some Material Parameters

There are many different reasons for using resilient mounts. In vehicles, resilient mounts are used extensively to reduce low frequency and large amplitude vibrations induced for example by road-tyre or wheel-rail contacts. The purpose of the mounts is to improve ride comfort. Resilient mounts can also be used for the protection of sensitive equipment or engines from excessive vibrations. On a standard truck, there are hundreds of various types of resilient mounts. One important application for resilient mounts is the reduction, in the audible frequency range, of the transmission of structure-borne sound from sources to receivers. Consequently, the noise radiated from the receiving structure is also reduced.

In the very low frequency region, resilient mounts are used to reduce large amplitude vibrations. These low frequency often non-linear vibrations are typically noticeable even by the naked eye. This is no longer the case in the audible frequency range. For example, the vibrational displacement of a huge ship Diesel engine is of the order 10^{-7} m at 1 kHz. Therefore, the modeling of the low and high frequency behavior of resilient mounts is different.

There is a great variety of springs used for the resilient mounting of engines etc. Most mounts are made of rubber or rubber-like materials. The spring models discussed in the preceding sections and also in Chap. 1 are idealized and in fact assumed to be mass less. In Chap. 6 the “Thin Rod” model was introduced. Internal resonances are included in the “Thin Rod” model, which is not the case for the ideal mass-less spring. The “Thin Rod” model assumes that the deflection of a mount due to a varying axial force is due to quasi-longitudinal waves propagating along the axis of the mount. Even this model is inadequate since for typical rubber mounts diameter and height are of the same magnitude. This means that not only waves propagating in the axial direction but also in the radial direction of the mount must be included in any theoretical model describing the compression of a rubber mount. The addition of more complex modes of vibration of the mount depends on the frequency of the disturbance as well as the cross section dimensions of the mount. The dynamic behavior of a rubber mount depends on its geometry and material properties.

To a certain extent natural rubber can be considered as an almost incompressible material. The Poisson’s ratio for natural rubber is almost equal to 0.5. The total volume of a rubber element is therefore more or less constant during compression—just like a volume of water in a thin plastic bag. The compression ΔV due to a pressure p on the surface of a volume, which initially is V , is given as

$$\frac{\Delta V}{V} = -\frac{\Delta p}{K} \quad (10.33)$$

The parameter K is the bulk modulus defined in Sect. 3.1 as

$$K = \frac{E}{3(1 - 2\nu)}$$

For $\nu \approx 0.5$ the ratio $\Delta V/V$ is obviously small as given by Eq. (10.33).

Considering that the shear modulus G is given as $G = E/[2(1 + \nu)]$ and the definition of the bulk modulus, the E -modulus can, after the elimination of ν , be written as

$$E = \frac{9KG}{3K + G} \quad (10.34)$$

For $K \gg G$ or $\nu \approx 0.5$ the expression (10.34) is simplified to $E \approx 3G$. The shear modulus of rubber is a function of frequency as discussed in Sect. 3.2 and shown in Fig. 10.8.

The resilience of a rubber mount depends on how the shape of the mount can be deformed during compression. If only a small deformation is allowed, the resulting stiffness is very high. One example of such a case is shown in Fig. 10.6a. A continuous layer of rubber is mounted in between two large plates. The plates are exposed to an external pressure. The rubber material can only expand along the perimeter of the plates. The resilience of the construction is therefore very small. In order to improve the resilience, the rubber material must be allowed to expand. Two possibilities are shown in Fig. 10.6b, c. The stiffness of a rubber mount depends on the area of the free surface as compared to the area under pressure.

There is a simple so-called engineering method to describe the stiffness as the function of geometry for some rubber mounts. The technique is described in a classic book by Gödel [91]. Further developments are presented in an often-quoted review

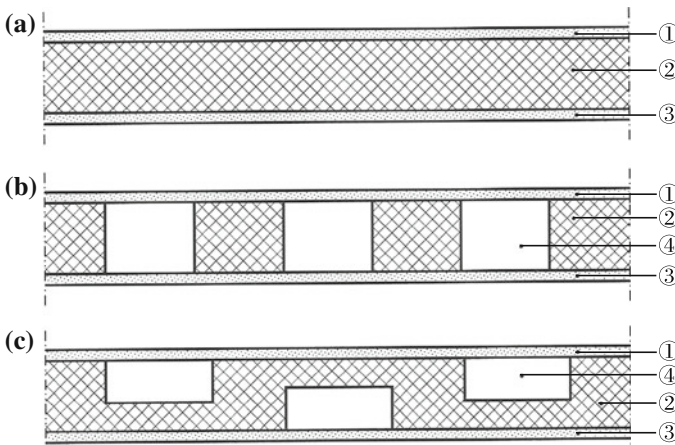


Fig. 10.6 Rubber mount with a large shape function (a) and two alternative configurations, (b, c). 1 and 3, plates; 2, rubber; 4, air cavity

paper by Snowdon [92]. The apparent stiffness or modulus E_a of a rubber mount depends on a so-called shape function and a parameter \mathcal{B} , which in turn depends on the hardness of the rubber material. For rubbers unfilled by carbon black the parameter \mathcal{B} is equal to 2. The shape function for a symmetric mount is defined as the ratio between the areas of one loaded surface to the total force free area. For a cylinder with the radius r and height h , the shape function \mathcal{S} is defined as

$$\mathcal{S} = \frac{\pi r^2}{2\pi r h} = \frac{r}{2h} \quad (10.35)$$

For a rectangular block with the sides a and b and height h the shape function is

$$\mathcal{S} = \frac{ab}{2h(a+b)} \quad (10.36)$$

Measured values of E , G , and K and values for \mathcal{B} are listed in Table 10.1 for rubber with increasing hardness. The degree of hardness, IRHD—International Hardness degree, depends on the amount of carbon black in the rubber. IRH and Shore Durometer readings are approximately the same.

The apparent E modulus, defined as E_a , of the rubber material of mount with the shape function \mathcal{S} is according to Ref. [92] given as

$$E_a = \frac{E(1 + \mathcal{B}\mathcal{S}^2)}{1 + E/K \cdot (1 + \mathcal{B}\mathcal{S}^2)} \quad (10.37)$$

For $K \gg G$ the approximate result of (10.37) is $E_a = E(1 + \mathcal{B}\mathcal{S}^2)$. For a mount with a geometry as shown in Fig. 10.6a, the shape factor is very large. According to Eq. (10.37), the apparent stiffness is also very large for this particular case. Since for large shape functions,

$$\lim_{\mathcal{S} \rightarrow \infty} E_a = K = \frac{E}{3(1 - 2\nu)}$$

For natural rubber $\nu \approx 0.5$, which makes the bulk modulus K very large. The shear modulus G and the loss factor η of natural rubber are also functions of temperature and frequency as described in Ref. [92]. The shear modulus for filled natural rubber increases above 1kHz as the temperature is decreased. In a similar way the losses increase already at 100Hz as the temperature is decreased. The non-linear temperature-dependent stiffness of precompressed rubber cylinders is discussed extensively by Kari [93]. For rubber-like materials with a very high internal damping, the shear modulus shows a strong dependence on frequency. Unfilled and lightly filled rubbers are fairly linear for increasing strain. The stiffness of moderately and heavily filled rubber materials strongly depends on amplitude in the low frequency region as illustrated in Ref. [94].

Table 10.1 Hardness and stiffness parameters for natural rubber, IRHD < 48, and rubber with carbon black filler, IRH° > 48. From Ref. [95]

IRH°	B	E MPa	G MPa	K MPa
30	1.86	0.92	0.3	1000
35	1.78	1.18	0.37	1000
40	1.70	1.50	0.45	1000
45	1.60	1.80	0.54	1000
50	1.46	2.20	0.64	1030
55	1.28	3.25	0.81	1090
60	1.14	4.45	1.06	1150
65	1.08	5.85	1.37	1210
70	1.06	7.35	1.73	1270
75	1.04	9.40	2.22	1330

Although the stiffness parameters of rubber materials depend on a number of parameters like shape, frequency, amplitude, and temperature, it is still of interest to list a number of hardness and stiffness parameters as in Table 10.1.

There are many rubber-like materials, which are commercially available. Some of these are listed in Table 10.2. In general, the hardness of each material can vary considerably as indicated in the table.

The static and dynamic stiffnesses of rubber mounts are in general different. From the static to the dynamic state there is a rapid change of stiffness and loss factor as discussed in Ref. [96]. The frequency dependence of the stiffness in the transition region is not sufficiently well known. In practice, the static and dynamic stiffnesses are considered as two different parameters. The ratio between the dynamic stiffness

Table 10.2 Rubber spring materials

Trade name	Density kg/m ³	Hardness IRH°	Working temperature °C
Natural rubber	950	30–98	–50 to 140
Polystyrene rubber			
Buna S	920	40–95	–50 to 140
Nitrile rubber			
Perbunan N	980	40–95	–50 to 140
Chloroprene rubber			
Neoprene, Sowprene	1230	40–95	–50 to 140
Butyl rubber	930	40–90	–50 to 150
Silicon rubber	1190	40–90	–100 to 220
Polyurethane	1260	65–95	–30 to 80

From Ref. [91]

and the static stiffness of a rubber mount is often in many product catalogs stated to be of the order 1.3. However it has been shown that this ratio can be as large as 5.

In addition, the stiffness of a resilient mount depends not only on shape, temperature, and frequency but also on the amplitude of the excitation as discussed in Ref. [94]. In particular, in the low frequency region, the stiffness of a mount is strongly dependent on the amplitude when the mount is exposed to harmonic excitation. In Ref. [94] it is shown that the dynamic stiffness of a hard mount, excited at 0.05 Hz, is decreased by a factor 4 when the amplitude was increased from 0.05 to 3 mm. For a soft mount, the difference is somewhat less dramatic. The amplitude of an operating engine is very small in the high frequency region. The stiffness of engine mounts can therefore be considered as independent of amplitude in the audio frequency range.

In Sect. 3.2 some simple models describing the dependence of E –modulus and loss factor on frequency were discussed. Expressions for frequency-dependent E –modulus and loss factor are given by the Eqs. (3.29) through (3.31). These results are based on the so-called Maxwell model. Some other models are discussed in Ref. [97]. In particular, the Zener model is emphasized in Ref. [97]. The Zener model is given by a simple spring element coupled in parallel to a Maxwell element. The Zener model gives the stress–strain ratio σ/ε as

$$\frac{\sigma}{\varepsilon} = E \cdot \frac{1 + (\omega\tau)^2 + g(i\omega\tau)}{1 + (\omega\tau)^2}$$

The relative amount of relaxation is denoted g . Using the Maxwell model the corresponding result is, from Eq. (3.29), of the form

$$\frac{\sigma}{\varepsilon} = E \cdot \frac{1 + A(\omega\tau)^2 + B(i\omega\tau)}{1 + C(\omega\tau)^2}$$

However, the models discussed in Ref. [97] are with respect to angular frequency of the same form as (3.30) and (3.31).

The so-called fractional derivative model gives an alternative description of the shear modulus as function of frequency. The model has certain computational advantages.

This so-called fractional derivate model of the shear modulus of rubber materials is introduced by Kari and presented in Ref. [112] as

$$G = \gamma G_{st}[1 + (i\omega\tau)^\beta]; \quad E = 3G \quad \text{for } \omega > 0$$

$$G \rightarrow \gamma G_{st} \quad \text{for } \omega \rightarrow 0 \quad (10.38)$$

The fractional order β is given by $0 < \beta \leq 1$ and the coefficient γ by $5 > \gamma \geq 1$ and the factor τ by $\tau > 0$. The angular frequency is ω . The rubber material is assumed linear, non-aging, isotropic, homogeneous, viscoelastic, and incompressible while being confined to isothermal rubber region conditions excluding low-temperature crystallization, glass hardening, and strain dependence. The parameter G_{st} is the

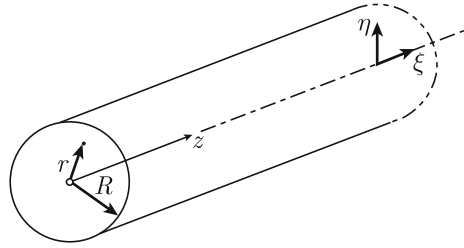
so-called static shear stiffness of the material. If the mount is exposed to a static load, the eventual deflection of the structure is determined by G_{st} or $E = 3G_{st}$. However, if the dynamic stiffness is measured for decreasing frequencies it is found that $G \rightarrow \gamma G_{st}$ as $\omega \rightarrow 0$. The parameter γ has been found to vary between 1 and 5 depending on the amount of carbon black filling in the rubber material. Occasionally the parameter γ is given in product catalogs as 1.3 or 1.4. However measurement results reveal that this value of γ is not necessarily correct.

It is suggested in Ref. [110] that β should be set to equal $1/2$. The fractional derivative model is found by Kari to give better agreement with experimental data than the Maxwell and Zener models. The fractional derivative model is reduced to the Kelvin–Voigt model (3.27) for $\beta = 1$ and harmonic displacement. It is shown by Kari [100] that predictions based on the Kelvin–Voigt model tend to overestimate the material damping in the high frequency region. A frequency-independent model of the material parameters is likely to underestimate the losses. The purpose of all these models is to define a scheme describing the frequency dependence of shear modulus and loss factor of rubber materials in the isothermal rubber region or quite simply in the frequency range of importance in vibro-acoustics, i.e., from 50 Hz up to 5 kHz.

10.6 Wave Propagation in Rubber Mounts, Approximate Solutions

The type of idealized springs discussed in the first few sections of this chapter and in Chap. 1 is assumed to be massless. Consequently, this type of idealized mount has no internal natural frequencies. A somewhat more realistic spring model was discussed in Chap. 6. The spring was modeled as a rod. This rod has a certain density, E –modulus, and loss factor. However, only longitudinal waves propagating in the direction of the axis of the rod were considered. For a “thin” rod, this is a valid assumption. The transmissibilities through an ideal spring and a rod-type spring are compared in Fig. 6.9. In the low frequency range, well below the first mass–spring resonance, the two models give comparable results. At higher frequencies, the results deviate considerably.

A typical rubber mount cannot be considered as thin. A characteristic cross dimension of a rubber mount is often of the same order as its length. Not only the displacement in the axial direction but in the plane perpendicular to the axis must therefore be considered. For “bending waves” propagating along thick beams or in thick plates, the so-called Timoshenko and Mindlin approximations were formulated. This was discussed in Sects. 9.5 and 9.6, respectively. In a similar way, different models have been developed to correct the wavenumber for “longitudinal waves” propagating in circular beams with a large diameter as compared to the wave length of the disturbance.

Fig. 10.7 Circular bar or rod

The basis for one approximate model has already been introduced in Sect. 4.5. The result, as presented in Eq. (4.60), is a first approximation of the wave number for longitudinal waves propagating in a thick plate. This basic theory can be extended to include L-waves propagating in the axial direction of beams or bars of cylindrical or rectangular cross sections. In the first case, consider the bar of Fig. 10.7 of length L , radius R and oriented along the x -axis. The displacement in the axial direction is ξ and in the radial direction η . Considering a transfer from Cartesian to cylindrical coordinates, the strain ε_r in the radial direction is, according to Eq. (3.1), given by

$$\varepsilon_r = \frac{\partial \eta}{\partial r} = -\frac{\nu \sigma_x}{E} = -\nu \frac{\partial \xi}{\partial x} \quad (10.39)$$

The displacement η in the radial direction is obtained from Eq. (10.39) as

$$\eta = -r\nu \frac{\partial \xi}{\partial x} \quad (10.40)$$

The velocities in the axial and radial directions are for harmonic excitation, time dependence $\exp(i\omega t)$, given by

$$\dot{\xi} = i\omega \xi; \quad \dot{\eta} = i\omega \eta = -i\omega r\nu \frac{\partial \xi}{\partial x} \quad (10.41)$$

For a wave propagating along the axis of the bar, the axial displacement can be defined as

$$\xi = A \cdot \exp[i(\omega t - kx)]$$

The amplitude of the wave is A and its wavenumber k . Considering this assumption and Eq. (10.41), the radial velocity is obtained as

$$\dot{\eta} = -k\omega r\nu \xi$$

The time average of the kinetic energy per unit length of the rod is

$$\begin{aligned}\bar{T}_l &= \frac{\rho}{4} \int_0^R (|\dot{\xi}|^2 + |\dot{\eta}|^2) 2\pi r dr = \frac{\omega^2 \rho}{4} |\xi|^2 \int_0^R [1 + (\nu r k)^2] 2\pi r dr \\ &= \frac{\pi R^2 \omega^2 \rho}{4} |\xi|^2 \left[1 + \frac{(\nu R k)^2}{2} \right]\end{aligned}\quad (10.42)$$

The result can also be written as

$$\bar{T}_l = \frac{\pi R^2 \omega^2 \rho_a}{4} |\xi|^2; \quad \rho_a = \rho \left[1 + \frac{(\nu R k)^2}{2} \right] \quad (10.43)$$

For a rod of quadratic cross section, the parameter R in Eq.(10.43) is set to equal $R = a\sqrt{2}$, where a is length of one of the sides. The wavenumber can be written as $k = \omega\sqrt{\rho_a/E}$. This expression in combination with the apparent density of Eq.(10.43) gives an equation in k . The solution to this equation is

$$k = \omega \sqrt{\frac{\rho}{E}} \cdot \left[1 - \frac{\omega^2 \rho \nu^2 R^2}{2E} \right]^{-1/2} \quad (10.44)$$

This approximate expression is only valid as long as the second term inside the bracket is much smaller than unity. This requirement drastically restricts the usefulness of the expression. In addition and as previously discussed, k can not exceed the wavenumber for Rayleigh waves.

The wave number given in Eq. (10.44) is frequently referred to as the Love approximation. Adding lateral inertia, according to Love's approximate theory, the basic differential equation (6.1) governing the displacement ξ due to L- waves propagating in a beam is modified to

$$\frac{\partial^2 \xi}{\partial x^2} - \frac{\rho}{E} \cdot \frac{\partial^2 \xi}{\partial t^2} + \frac{\rho \nu^2 r_p^2}{E} \cdot \frac{\partial^4 \xi}{\partial x^2 \partial t^2} = 0 \quad (10.45)$$

In this expression, the parameter r_p is equal to the radius of gyration. For a circular cross section with radius R , the radius of gyration is $r_p = R/\sqrt{2}$. For a rectangular cross section, height H and width B , the result is $r_p = \sqrt{(B^2 + H^2)/12}$. The expression (10.43) can also be obtained by first calculating kinetic and potential energies of a system. Thereafter Hamilton's principle is applied, see Chap. 9. The wave number previously given in Eq. (10.44) is again obtained by assuming a solution $\xi = A \exp[i(\omega t - kx)]$ and substituting this expression into Eq. (10.45). As in the previous case, the solution is only valid in the low frequency range or rather when $(r_p k)^2 \ll 1$.

In 1952 R.E.D. Bishop, Ref. [101] added terms to the Love model taking into account the effect of shear. For a beam of rectangular cross section, height H and width B , the resulting approximate differential equation governing the axial displacement in the beam is

$$\frac{\partial^2 \xi}{\partial x^2} - \frac{\rho}{E} \cdot \frac{\partial^2 \xi}{\partial t^2} + \frac{\rho \nu^2}{E} \cdot \frac{(H^2 + B^2)}{12} \frac{\partial^4 \xi}{\partial x^2 \partial t^2} - \left(\frac{\rho}{E}\right)^2 \left[\frac{\nu^2(1 - \nu^2)(H^4 + B^4)}{120} - \frac{\nu^2(1 + \nu)H^2 B^2}{72} \right] \frac{\partial^6 \xi}{\partial x^2 \partial t^4} = 0 \quad (10.46)$$

The corresponding result for a beam of circular cross section, radius a , is

$$\frac{\partial^2 \xi}{\partial x^2} - \frac{\rho}{E} \cdot \frac{\partial^2 \xi}{\partial t^2} + \frac{\rho \nu^2 a^2}{2E} \cdot \frac{\partial^4 \xi}{\partial x^2 \partial t^2} - \left(\frac{\rho}{E}\right)^2 \frac{\nu^2 a^4}{6} (2\nu^2 + \nu - 1) \frac{\partial^6 \xi}{\partial x^2 \partial t^4} = 0 \quad (10.47)$$

There are a number of additional approximate methods. Some are similar and even identical but referred to by different names. The most common methods are summarized in Ref. [15]. In particular the Method of Internal Constraints makes it possible to study longitudinal vibrations of bars with different boundary conditions. The method can also be a very powerful tool for predicting the vibration of structures like stiffened plates or structures with a complicated cross sections.

For all the models discussed, not only the wavenumber but also the axial stress must be estimated in order to determine the stiffness of a mount. In the absence of shear, the normal stress σ_x related to the axial displacement ξ of a beam is, according to Chap. 3, defined as

$$\frac{\partial \sigma_x}{\partial x} = \rho \frac{\partial^2 \xi}{\partial t^2} \quad (10.48)$$

The inertia force per unit volume defined in (10.48) is obtained from Eq. (10.45) as

$$\frac{\partial \sigma_x}{\partial x} = \rho \frac{\partial^2 \xi}{\partial t^2} = E \frac{\partial^2 \xi}{\partial x^2} + \nu^2 r_p^2 \rho \cdot \frac{\partial^4 \xi}{\partial x^2 \partial t^2}$$

A straightforward integration with respect to x yields

$$\sigma_x = E \frac{\partial \xi}{\partial x} + \nu^2 r_p^2 \rho \cdot \frac{\partial^3 \xi}{\partial x \partial t^2} \quad (10.49)$$

The axial stresses, calculated based on the other approximate results, are obtained in a similar way.

10.7 Equivalent Stiffness of Simple Mounts—Approximate Methods

For an ideal spring mounted to an infinitely stiff foundation the so-called spring constant k is equal to the ratio between the resulting force on the foundation and the displacement of the free end of the spring. See Fig. 10.8a and compare the discussion in Sect. 6.6.

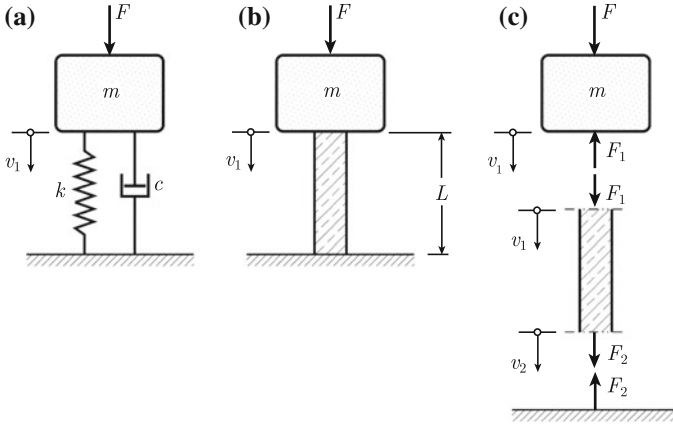


Fig. 10.8 Mass mounted on **a** an ideal spring and, **b** on a resilient mount. Resulting forces and velocities shown in (c)

For a real spring or resilient mount, the equivalent stiffness k_{eq} can be defined in a similar way. For harmonic excitation the FT of velocities and forces defined in Fig. 10.8c, are according to Eq. (6.95) related as

$$\hat{v}_1 = i\omega\hat{x}_1 = \hat{F}_1 Y_{11} + \hat{F}_2 Y_{21}; \quad \hat{v}_2 = i\omega\hat{x}_2 = \hat{F}_2 Y_{22} + \hat{F}_1 Y_{12} \quad (10.50)$$

The FT of the displacements at the two ends of the mount are \hat{x}_1 and \hat{x}_2 . For an infinitely stiff foundation $\hat{x}_2 = 0$. For this case Eq. (10.50) yields $\hat{F}_1 = -\hat{F}_2 Y_{22} / Y_{12}$ and

$$i\omega\hat{x}_1 = \hat{F}_2 \left(\frac{Y_{12}Y_{21} - Y_{11}Y_{22}}{Y_{12}} \right) \quad (10.51)$$

Defining the equivalent stiffness k_{eq} as the ratio between the FT of the resulting force on the foundation and the FT of the displacement of the free end of the spring or following the notations of Fig. 10.8 as $k_{\text{eq}} = -\hat{F}_2 / \hat{x}_1$. According to this definition, Eq. (10.50) gives

$$k_{\text{eq}} = \frac{i\omega Y_{12}}{Y_{11}Y_{22} - Y_{12}Y_{21}} \quad (10.52)$$

For the simple rod model discussed in Sect. 6.5 and defined by the mobilities Y_{ij} in Eq. (6.96) the equivalent stiffness is obtained as

$$k_{\text{eq}} = \frac{SEk_l}{\sin(k_l L)} \quad (10.53)$$

The cross section area of the rod is S , its length L and Young's modulus E . The wavenumber for longitudinal waves is k_l . In the low frequency region, i.e., for $k_l \rightarrow 0$,

the equivalent stiffness k_{eq} is approaching the static stiffness SE/L of a rod, compare Eq. (3.4).

The equivalent mobility of the rod is defined as the ratio between the FT of the velocity at the driving end of the mount and the FT of the force on the foundation. The equivalent mobility is thus equal to

$$Y_{\text{eq}} = \frac{i\omega}{k_{\text{eq}}} = \frac{Y_{11}Y_{22} - Y_{12}Y_{21}}{Y_{12}} \quad (10.54)$$

In a similar way, the driving point stiffness k_{dp} can be derived. This is the stiffness felt by a force acting at the top end of a mount when the velocity of the bottom end is blocked, i.e., $\hat{v}_2 = 0$. This driving point stiffness is obtained from (10.49) as

$$k_{\text{dp}} = \frac{i\omega Y_{22}}{Y_{11}Y_{22} - Y_{21}Y_{12}} \quad (10.55)$$

The corresponding driving point mobility is

$$Y_{\text{dp}} = \frac{Y_{11}Y_{22} - Y_{21}Y_{12}}{Y_{22}} \quad (10.56)$$

Expressions defining mobilities and equivalent stiffness are readily modified to include the so-called Love correction. For harmonic excitation, time dependence $\exp(i\omega t)$, the expression (10.49) relating stress and strain, including lateral inertia according to Love, yields

$$\sigma_x = E \left(1 - \frac{\omega^2 \nu^2 \rho r_p^2}{E} \right) \frac{\partial \xi}{\partial x} = E_x \frac{\partial \xi}{\partial x} \quad (10.57)$$

Mobilities and equivalent stiffness due to longitudinal waves in a beam are, when including the Love correction, obtained by replacing E by E_x and consequently $k_1 = \omega\sqrt{\rho/E}$ by $k_1 = \omega\sqrt{\rho/E_x}$ in the Eq. (6.96) which define the mobilities. The equivalent stiffness is obtained as

$$k_{\text{eq}} = \frac{SEk_1}{\sin(k_1L)}; \quad k_1 = \omega\sqrt{\rho/E_x}; \quad E_x = E \left(1 - \frac{\omega^2 \nu^2 \rho r_p^2}{E} \right) \quad (10.58)$$

It is assumed throughout that $1 \gg \omega^2 \nu^2 \rho r_p^2 / E$.

The equivalent stiffness k_{eq} calculated first according to the simple rod model and then from Eq. (10.56) are shown in Fig. 10.9. In the low frequency region, well below the first natural frequency of the rod, the two models give similar results. The frequencies for the first natural frequencies differ considerably. According to Eq. (10.43), the apparent mass of the beam is increased due to the inclusion of lateral inertia. The magnitude of the stiffness predicted by means of the rod theory is over

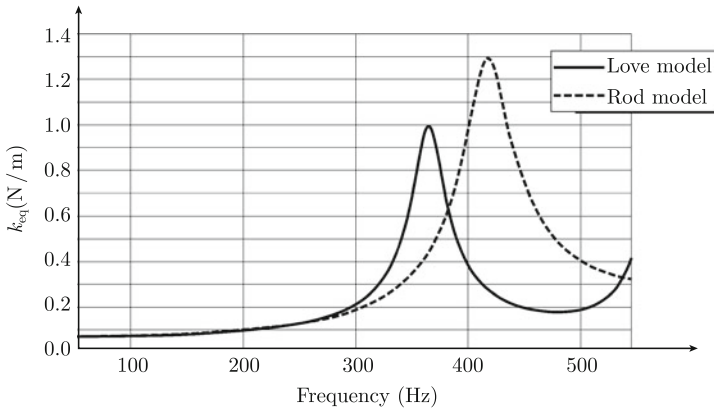


Fig. 10.9 The equivalent stiffness k_{eq} . Rod model and Love model

estimated at the first natural frequency. The natural frequency is also too high as predicted by the rod theory.

In general, resilient mounts are exposed to both static and dynamic forces. The static force or load compresses the mount. The shape factor as defined in Eqs. (10.35) or (10.36) is increased due to the load. The mount stiffens as predicted by Eq. (10.37). Wavenumber and the height of the mount decrease, resulting in the first natural frequency being shifted upwards. This is illustrated in Fig. 10.10. The results are predicted using the Love model. The equivalent stiffness of one resilient mount is shown for three static loads. A static load increases the stiffness of a mount in the low frequency region. The first natural frequency is increased as the static load is increased. Although, as later discussed in Sect. 10.10, the Love model does not

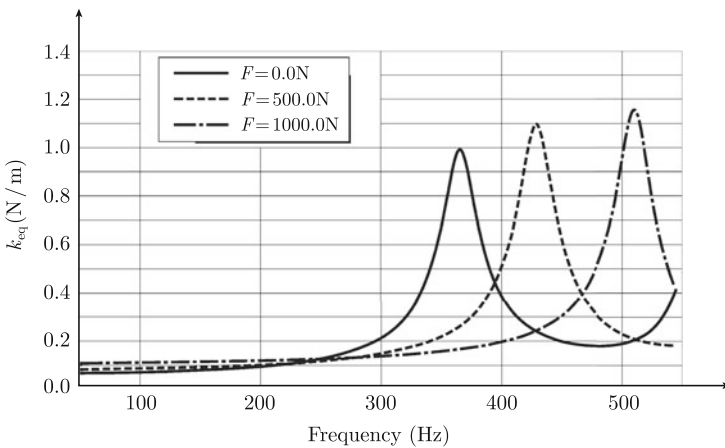


Fig. 10.10 The equivalent stiffness of a mount with different static loads. Love model

agree well with measurements, the model can indicate certain trends resulting from changed static load, shape, etc.

The applicability of the Love model is very limited since the inequality $1 \gg \omega^2 \nu^2 \rho r_p^2 / E$ must be satisfied. Some additional limitations of the Love and other models are discussed in Sects. 10.9 and 10.10. However, general trends can to a certain extent be explained by means of this very simple model. Even if sophisticated theoretical models are preferred, accurate material data as well as an in detail description of the geometry of a mount must be available. The alternative to predictions is measurements.

10.8 Static Deflection of Cylindrical Rubber Mounts

The apparent stiffness or rather modulus of elasticity E_a of a rubber mount is given by Eq. (10.37). For rubber, unfilled with carbon black, the parameter \mathcal{B} is equal to 2. For Poisson’s ratio close to 0.5 the bulk modulus is much larger than G as discussed in Sect. 10.5. Considering these specific conditions Eq. (10.37) is reduced to

$$E_a = E \cdot (1 + 2 \cdot S^2) \tag{10.59}$$

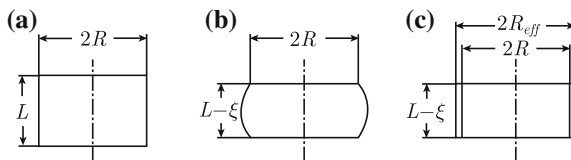
where E is the static modulus of elasticity of the rubber material. The shape factor S is equal to the ratio between the loaded area of the mount and the free surface of the same structure as discussed in Sect. 10.7.

When compressed a cylindrical mount with the radius R and height L will change shape as illustrated in Fig. 10.11. The performance of the deformed mount can according to Refs. [93, 112] be modeled as if the mount had a shape of a uniform cylinder with the radius R_{eff} and height $L - \xi$ where ξ is the distance the mount is compressed. Since the rubber is almost incompressible the volume of the material is the same before and after compression. Thus,

$$\pi R^2 L = \pi R_{\text{eff}}^2 (L - \xi); \quad R_{\text{eff}} = \frac{R\sqrt{L}}{\sqrt{L - \xi}} \tag{10.60}$$

The loaded area S_1 of the mount is approximated by the expression $S_1 = \pi R_{\text{eff}}^2$ given by the cross section area of the equivalent compressed mount of Fig. 10.11c. The free surface S_2 of the mount is set to equal the free surface of the uncompressed mount

Fig. 10.11 Uncompressed and compressed rubber mounts. **a** Initial shape. **b** Compressed shape. **c** Equivalent shape



or $S_2 = 2\pi RL$. The shape function is obtained from (10.35) as

$$S = \frac{S_1}{S_2} = \frac{\pi R_{\text{eff}}^2}{2\pi RL} = \frac{R}{2(L - \xi)} \quad (10.61)$$

The expressions (10.59) and (10.60) give the apparent modulus of elasticity E_a as

$$E_a = E \left[1 + \frac{R^2}{2(L - \xi)^2} \right] \quad (10.62)$$

The compression ξ of a rubber mount, modulus of elasticity E , length L , and cross section area S due to a force F is according to Eq.(3.4) equal to $\xi = FL/(SE)$. Thus, $dF/d\xi = SE/L$. For the compressed rubber mount $E \rightarrow E_a$ and $L \rightarrow L - \xi$ and $S \rightarrow \pi R_{\text{eff}}^2$. Consequently

$$\frac{dF}{d\xi} = \frac{\pi ER^2L}{(L - \xi)^2} \left[1 + \frac{R^2}{2(L - \xi)^2} \right] \quad (10.63)$$

For a compression d of the mount the force F required is obtained by integrating Eq.(10.63). Hence

$$\begin{aligned} F &= \int_0^d d\xi \frac{\pi ER^2L}{(L - \xi)^2} \left[1 + \frac{R^2}{2(L - \xi)^2} \right] \\ &= \frac{\pi ER^2d}{(L - d)} \left\{ 1 + \frac{R^2(3L^2 - 3Ld + d^2)}{6L^2(L - d)^2} \right\} \end{aligned} \quad (10.64)$$

This expression gives the deflection d as function of the force F compressing the mount. For small deflections, $d \ll L$, the approximate result is

$$d \approx \frac{FL}{\pi ER^2 \left(1 + \frac{R^2}{2L^2} \right)} \quad (10.65)$$

Thus, a force F acting on a circular rubber mount with the initial radius R and height L is compressing the mount the distance d given by the expression (10.65).

10.9 Wave Propagation in Circular Rods, Exact Solutions

Longitudinal waves propagating in thick plates were discussed in Sect.4.5. It was shown that contraction and shear had to be considered in the high frequency range. For longitudinal waves propagating in a thick plate, the wavenumber derived from the thin plate theory must be corrected with respect to plate thickness, Poisson's ratio

and frequency. The result can be interpreted by identifying an apparent density ρ_a of the structure. This apparent density increases with frequency, plate thickness, and Poisson's ratio. The wavenumber k_x for longitudinal waves propagating in a plate was given in Eq. (4.59). The exact wavenumber for longitudinal waves propagating in a thick plate is the solution to the dispersion Eq. (4.49). Approximate and exact wavenumbers can in a similar way be derived for longitudinal waves propagating in infinite bars of circular cross sections. The exact solution, valid for circular bars only, is often referred to as the Pochhammer–Chree solution. As in the case with the infinite thick plate, the wavenumber for longitudinal waves propagating in a circular but not necessarily thin rods is derived using the general wave equation discussed in Chap. 4.

In Sect. 4.5 the wavenumber for quasi-longitudinal waves propagating in an infinite thick plate was discussed. The wavenumber was derived starting from the general wave equation (4.4) which governs all elastic oscillatory motions in the interior of a solid. Any type of linear displacement of a solid can be described by means of longitudinal and transverse waves satisfying the equations in (4.8). The dispersion equation for quasi-longitudinal waves propagating in an infinite plate as shown in Fig. 4.4 b is given in Eq. (4.49). In a similar way, it is possible to derive the dispersion equation giving the wavenumbers for quasi-longitudinal waves propagating along the axis of an infinite, circular, and homogeneous bar with a constant cross section area. The same is not possible for a bar with a rectangular cross section.

Again, as in Sect. 4.1, the displacement in an infinitely long cylinder is described by means of the scalar potential ϕ and the vector potential ψ . The potentials should satisfy the equations given by (4.8). Thus

$$\nabla^2 \phi - \frac{1}{c_l^2} \frac{\partial^2 \phi}{\partial t^2} = 0; \quad \nabla^2 \psi - \frac{1}{c_t^2} \frac{\partial^2 \psi}{\partial t^2} = 0 \quad (10.66)$$

where c_l and c_t are the speed of sound of longitudinal and transverse waves respectively or

$$c_l = \left[\frac{E(1-\nu)}{\rho(1+\nu)(1-2\nu)} \right]^{1/2}; \quad c_t = \left[\frac{E}{2\rho(1+\nu)} \right]^{1/2} \quad (10.67)$$

The displacement vector is again defined as

$$\mathbf{r} = \mathbf{grad}\phi + \mathbf{curl}\psi$$

In cylindrical coordinates and writing $\psi = (\psi_r, \psi_\varphi, \psi_z)$ the expressions $\nabla^2 \phi$ and $\nabla^2 \psi$ are

$$\nabla^2 \phi = \frac{1}{r} \frac{\partial}{\partial r} \left(r \frac{\partial \phi}{\partial r} \right) + \frac{1}{r^2} \frac{\partial^2 \phi}{\partial \varphi^2} + \frac{\partial^2 \phi}{\partial z^2}$$

$$\nabla^2 \psi = \left(\nabla^2 \psi_r - \frac{\psi_r}{r^2} - \frac{2}{r^2} \frac{\partial \psi_\varphi}{\partial \varphi} \right) \mathbf{e}_r + \left(\nabla^2 \psi_\varphi - \frac{\psi_\varphi}{r^2} + \frac{2}{r^2} \frac{\partial \psi_\varphi}{\partial \varphi} \right) \mathbf{e}_\varphi + \left(\nabla^2 \psi_z \right) \mathbf{e}_z \quad (10.68)$$

The unit vectors \mathbf{e}_r , \mathbf{e}_φ and \mathbf{e}_z correspond to the directions along r , φ , and z , see Fig. 10.7. The second expression of Eq. (10.68) is derived in for example, Ref. [131]. For axi-symmetric displacement the functions ϕ and ψ_j sufficiently prescribe the motion of the cylinder. Compare the discussion in Sect. 4.1. The functions ϕ and ψ_j are for axi-symmetric displacement independent of the angle φ . Consequently the functions $\phi = \phi(r, z, t)$ and $\psi_j = \psi(r, z, t)$ must satisfy

$$\begin{aligned} \frac{\partial^2 \phi}{\partial r^2} + \frac{1}{r} \frac{\partial \phi}{\partial r} + \frac{\partial^2 \phi}{\partial z^2} - \frac{1}{c_l^2} \frac{\partial^2 \phi}{\partial t^2} &= 0 \\ \frac{\partial^2 \psi}{\partial r^2} + \frac{1}{r} \frac{\partial \psi}{\partial r} + \frac{\partial^2 \psi}{\partial z^2} - \frac{\psi}{r^2} - \frac{1}{c_t^2} \frac{\partial^2 \psi}{\partial t^2} &= 0 \end{aligned} \quad (10.69)$$

Assuming a wave propagating along the axis of the cylinder, wavenumber k_z , and with the time dependence $\exp(i\omega t)$ the functions ϕ and ψ are written

$$\phi = F(r) \cdot \exp[i(\omega t - k_z z)]; \quad \psi = H(r) \cdot \exp[i(\omega t - k_z z)] \quad (10.70)$$

The expressions (10.67) inserted in (10.66) yield

$$\begin{aligned} \frac{\partial^2 F}{\partial r^2} + \frac{1}{r} \cdot \frac{\partial F}{\partial r} + \lambda_1^2 F &= 0; \quad \lambda_1 = \sqrt{k_l^2 - k_z^2} \\ \frac{\partial^2 H}{\partial r^2} + \frac{1}{r} \cdot \frac{\partial H}{\partial r} - \frac{H}{r^2} + \lambda_2^2 H &= 0; \quad \lambda_2 = \sqrt{k_t^2 - k_z^2}. \end{aligned} \quad (10.71)$$

The wavenumbers k_l and k_t for pure longitudinal waves and transverse waves respectively are defined as $k_l = \omega/c_l$ and $k_t = \omega/c_t$. The expressions (10.71) governing F and H are Bessel's equations. The Bessel equation is given as

$$y'' + \frac{1}{r} y' + \left(1 - \frac{m^2}{r^2} \right) y = 0$$

The general solutions to these equations are a combination of Bessel $J_m(r)$ and Neumann $Y_m(r)$ functions. The displacement in the cylinder is finite everywhere. However, the Neumann functions tend to infinity as r tends to zero. The functions $J_m(r)$ are finite for $r = 0$. Thus, finite solutions to Eq. (10.71) require

$$F(r) = A \cdot J_0(\lambda_1 r); \quad H(r) = B \cdot J_1(\lambda_2 r) \quad (10.72)$$

where A and B are constants. Consequently, from (10.70) the potentials are obtained as

$$\begin{cases} \phi(r, z, t) = A \cdot J_0(\lambda_1 r) \cdot \exp[i(\omega t - k_z z)]; \\ \psi(r, z, t) = B \cdot J_1(\lambda_2 r) \cdot \exp[i(\omega t - k_z z)] \end{cases} \quad (10.73)$$

The displacement $\mathbf{r} = (u_r, 0, u_z)$ in the cylinder is obtained from Eq. (4.5) as $\mathbf{r} = \mathbf{grad}\phi + \mathbf{curl}\psi$. As previously discussed $\psi_r = \psi_z = 0$ and $\psi_\varphi = \psi$ reducing the displacement components to

$$\begin{cases} u_r = \frac{\partial\phi}{\partial r} - \frac{\partial\psi}{\partial z} = \left[A \frac{\partial}{\partial r} [J_0(\lambda_1 r)] + ik_z B J_1(\lambda_2 r) \right] \cdot \exp[i(\omega t - k_z z)] \\ u_z = \frac{\partial\phi}{\partial z} + \frac{1}{r} \frac{\partial(r\psi)}{\partial r} = \left[-ik_z A J_0(\lambda_1 r) + \frac{B}{r} \frac{\partial}{\partial r} [r J_1(\lambda_2 r)] \right] \cdot \exp[i(\omega t - k_z z)] \end{cases} \quad (10.74)$$

The Bessel functions $J_0(x)$ and $J_1(x)$ satisfy the following expressions

$$[J_0(x)]' = -J_1(x) \quad \text{and} \quad [xJ_1(x)]' = xJ_0(x)$$

Considering these relationships, Eq. (10.74) is modified to

$$\begin{cases} u_r = [-A\lambda_1 J_1(\lambda_1 r) + ik_z B J_1(\lambda_2 r)] \cdot \exp[i(\omega t - k_z z)] \\ u_z = [-ik_z A J_0(\lambda_1 r) + B\lambda_2 J_0(\lambda_2 r)] \cdot \exp[i(\omega t - k_z z)] \end{cases} \quad (10.75)$$

For an infinite cylinder with a free surface, the normal stress σ_r and the shear stresses $\tau_{r\varphi}$ and τ_{rz} must equal zero on the surface. The normal stress caused by the displacement $\mathbf{r} = (u_r, 0, u_z)$ is obtained from Eq. (3.6) as

$$\sigma_r = \frac{E}{1-\nu} \left[\frac{\partial u_r}{\partial r} + \frac{\nu}{1-2\nu} \left(\frac{\partial u_r}{\partial r} + \frac{u_r}{r} + \frac{\partial u_z}{\partial z} \right) \right] \quad (10.76)$$

The shear stress τ_{rz} is considering (3.11) and (3.12)

$$\tau_{rz} = G \left(\frac{\partial u_r}{\partial z} + \frac{\partial u_z}{\partial r} \right) \quad (10.77)$$

Due to axial symmetry of the displacement the shear stress $\tau_{r\varphi}$ is always identical to zero.

The parameters A and B of Eq. (10.72) are interrelated. By inserting (10.75) in (10.77) and by setting $\tau_{rz} = 0$ for $r = R$ it is found that

$$A = \frac{(\lambda_2^2 - k_z^2) J_1(\lambda_2 R)}{2ik_z \lambda_1 J_1(\lambda_1 R)} B = P \cdot B \quad (10.78)$$

The normal stress and the shear stresses being zero for $r = R$ leads to a system of two homogeneous equations in the unknown constants A and B . For nontrivial solutions

the determinant of the coefficients equals zero. Thus, by inserting Eq. (10.74) in (10.76) and setting the stresses equal to zero on the surface of the cylinder for $r = R$, gives the dispersion equation

$$\left[2\lambda_1^2 J_0''(\lambda_1 R) - \frac{\nu k_t^2}{1-\nu} J_0(\lambda_1 R) \right] (2k_z^2 - k_t^2) J_1(\lambda_2 R) = 4k_z^2 \lambda_1 \lambda_2 J_0'(\lambda_1 R) J_1'(\lambda_2 R) \quad (10.79)$$

The dispersion equation (10.79) was obtained by Pochhammer [104], in 1876 and somewhat later by Chree [105]. The numerical solutions were carried out almost 70 years later by Bancroft and Davies [106, 107].

Some useful relations with respect to the Bessel functions in (10.79) are, Ref. [43],

$$J_0'(x) = -J_1(x); \quad J_1'(x) = J_0(x) - \frac{J_1(x)}{x}; \quad J_0''(x) = -J_0(x) + \frac{J_1(x)}{x}$$

Using these formulas and the identities

$$k_1^2 = k_t^2 \frac{(1-2\nu)}{2(1-\nu)}; \quad k_z^2 = k_t^2 - \lambda_2^2$$

the Pochhammer dispersion equation (10.79) is rewritten as

$$(k_1^2 - 2\lambda_2^2)^2 \cdot \theta(\lambda_1 R) + 4\lambda_1^2 (k_1^2 - \lambda_2^2) \cdot \theta(\lambda_2 R) = 2\lambda_1^2 k_t^2 \quad (10.80)$$

The function $\theta(x)$ is defined as $\theta(x) = x J_0(x)/J_1(x)$. The expression is known as the Oneo function.

The low frequency solution to (10.80) is readily obtained using the expansion formulas for small x , Ref. [43],

$$J_0(x) = 1 - \frac{x^2}{4} + \frac{x^4}{64} + \dots; \quad J_1(x) = \frac{x}{2} + \frac{x^3}{16} + \dots$$

Thus for $x \ll 1$, $\theta(x) \approx 2 - \frac{3x^2}{4}$.

In the low frequency region or for R small the expansions inserted in (10.80), the resulting wavenumber for a propagating wave is obtained as

$$k_z = \omega \sqrt{\frac{\rho}{E}}$$

This is the wavenumber for quasi-longitudinal waves propagating in a slender bar as discussed in Sect. 3.4. In the high frequency limit or as $R \rightarrow \infty$, one possible solution to (10.80) is $\lambda_1 = 0$ which gives $k_z = k_1$, which is the wavenumber for a longitudinal wave propagating in an infinite solid.

There are also approximate expansions for Bessel functions with large arguments. Thus, from Ref. [43] or any standard text book on mathematics, the functions $J_0(x)$ and $J_1(x)$ are for large x approximated by

$$\begin{aligned} J_0(x) &\approx \sqrt{\frac{2}{\pi x}} \cdot \cos(x - \pi/4) = \sqrt{\frac{2}{\pi x}} \cdot \sin(x - 3\pi/4); \\ J_1(x) &\approx \sqrt{\frac{2}{\pi x}} \cdot \cos(x - 3\pi/4) \end{aligned}$$

For large x the function $\theta(x)$ is then written

$$\theta(x) = x J_0(x)/J_1(x) \approx x \cdot \tan(x - 3\pi/4) \quad (10.81)$$

For solutions where k_z is larger than the wavenumbers k_l for longitudinal waves and k_t for transverse waves the parameters λ_1 and λ_2 are imaginary as given by (10.71). The real parameters α and β are defined as

$$\alpha = \sqrt{k_z^2 - k_l^2}; \quad \beta = \sqrt{k_z^2 - k_t^2} \quad (10.82)$$

For large R the expression on the right hand side of Eq. (10.80) can be neglected as the left hand side expression tends to infinity for large R . Thus in the limit for large R , Eq. (10.80) is written

$$(k_t^2 - 2\lambda_2^2)^2 \cdot \theta(\lambda_1 R) + 4\lambda_1^2(k_t^2 - \beta^2) \cdot \theta(\lambda_2 R) = 0$$

By using Eqs. (10.81) and (10.82) and $k_0 = \omega\sqrt{\rho/E}$ this expression is rewritten as

$$\tan(\lambda_1 R - 3\pi/4)[k_z^2 - k_0^2(1 + \nu)]^2 + \tan(\lambda_2 R - 3\pi/4)k_z^2\lambda_1\lambda_2 = 0$$

For solutions where k_z is larger than the wavenumbers k_l for longitudinal waves and k_t for transverse waves the parameters λ_1 and λ_2 are imaginary and equal to $\lambda_1 = i\alpha$ and $\lambda_2 = i\beta$, where α and β are defined in (10.82). Based on the definitions of trigonometric functions $\tan z = i \cdot \tanh x$ for $z = ix$ and x real. For large x , $\tanh x$ tends to 1. Thus for R or α and β large the asymptotic value of $\theta(\lambda_1 R)$ and $\theta(\lambda_2 R)$ are

$$\lim_{\lambda_1 R \rightarrow \infty} \theta(\lambda_1 R) = -\alpha R; \quad \lim_{\lambda_2 R \rightarrow \infty} \theta(\lambda_2 R) = -\beta R \quad (10.83)$$

As the radius tends to infinity and after using these results, the dispersion equation is reduced to

$$[k_z^2 - k_0^2(1 + \nu)]^2 + k_z^2\alpha\beta = 0; \quad k_0 = \omega\sqrt{\rho/E} \quad (10.84)$$

The solutions to this equation were discussed in Sect. 4.4. Equation (10.84) is identical to the result given in Sect. 4.4. The resulting wavenumber for a propagating wave is equal to k_r , the Rayleigh wavenumber, given in (4.57) and listed in Table 4.2. See

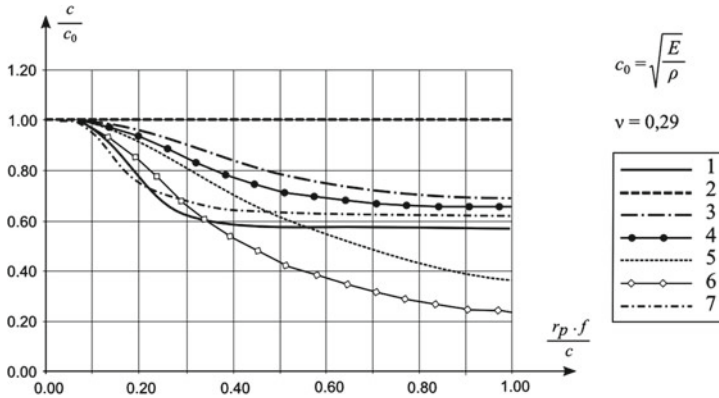


Fig. 10.12 Predicted phase velocities of L-waves propagating in the axial direction of a cylindrical beam. 1 Exact solution; 2 Elementary theory; 3 Bishop theory; 4 Bishop improved theory; 5 Love theory; 6 Love theory improved by Bishop. 7 Method of internal constraints. The ratio c/c_0 is shown as function of $r_p \cdot f/c$ where r_p is the radius of gyration and f the frequency. From Ref. [15]

also Fig. 4.9. Thus in a circular bar the wavenumber, in the axial direction, for the first propagating mode varies from k_0 , Eq. (10.84), in the low frequency region to k_r , (4.51), in the high frequency region.

Results derived from some approximate models are compared in Fig. 10.12. Phase velocities, $c = \omega/k$, calculated according to the exact and approximate wavenumber models are compared in the figure. All models are derived for predicting the axial displacement of cylindrical beams. The results are from Ref. [15]. Curve 1 in the figure corresponds to the first propagating longitudinal wave mode in an infinite cylinder. The result is the solution to Eq. (10.80). Curve 2, from elementary theory, gives $c_0 = \sqrt{E/\rho}$, which is the phase velocity for quasi-longitudinal waves. Curve 3 represents results based on the Bishop theory, Curve 4 is Bishops improved theory, Curve 5 Love theory, Curve 6 is Love theory improved by Bishop, and Curve 7 is derived from the method of internal constraints, Ref. [15]. It is evident that the approximate solutions rather poorly predict the exact result as the quantity $r_p \cdot f/c$ is increasing. However, as long as $r_p \cdot f/c < 0.1$ the possible errors are rather small. Compare also Fig. 4.9, which illustrates the wavenumber for longitudinal waves propagating in thick plates. Definition of r_p is found in p. 60.

The dispersion Eq. (10.80) has an infinite number of solutions, real and complex. The solutions can be found by means of the Newton–Raphson method. The initial values are obtained by a winding integral method as proposed by Ivansson and Karasalo [108] and discussed in Refs. [100, 102, 112]. The axial displacement in a cylinder is given by a sum of all possible modes. In a finite cylinder, waves can travel in both directions along the axis. Neglecting the time-dependent function the axial and radial displacements of the cylinder are of the form

$$\begin{aligned}
 u_z &= \sum_n \left\{ [-ik_{zn}A_n^+ J_0(\lambda_{1n}r) + B_n^+ \lambda_{2n} J_0(\lambda_{2n}r)] \cdot e^{-ik_{zn}z} \right. \\
 &\quad \left. + [ik_{zn}A_n^- J_0(\lambda_{1n}r) + B_n^- \lambda_{2n} J_0(\lambda_{2n}r)] \cdot e^{ik_{zn}z} \right\} \\
 u_r &= \sum_n \left\{ [-\lambda_{1n}A_n^+ J_1(\lambda_{1n}r) + ik_{zn}B_n^+ J_1(\lambda_{2n}r)] \cdot e^{-ik_{zn}z} \right. \\
 &\quad \left. + [-\lambda_{1n}A_n^- J_1(\lambda_{1n}r) - ik_{zn}B_n^- J_1(\lambda_{2n}r)] \cdot e^{ik_{zn}z} \right\} \tag{10.85}
 \end{aligned}$$

where k_{zn} are solutions to (10.80). The amplitudes A_n^+ and B_n^+ are related as $A_n^+ = P_n B_n^+$, where P_n is obtained from (10.78), as

$$A_n^+ = \frac{(\lambda_{2n}^2 - k_{zn}^2)J_1(\lambda_{2n}R)}{2ik_{zn}\lambda_{1n}J_1(\lambda_{1n}R)} B_n^+ = P_n \cdot B_n^+ \tag{10.86}$$

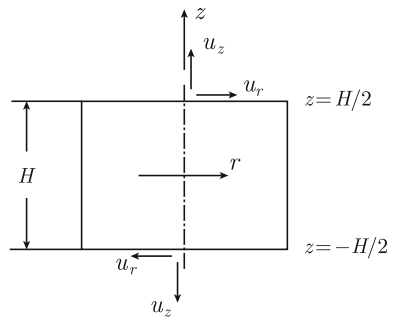
where k_{zn} are solutions to the dispersion equation and $\lambda_{1n} = \sqrt{k_1^2 - k_{zn}^2}$ and $\lambda_{2n} = \sqrt{k_t^2 - k_{zn}^2}$. In a similar way the amplitudes A_n^- and B_n^- are found to be related as

$$A_n^- = -\frac{(\lambda_{2n}^2 - k_{zn}^2)J_1(\lambda_{2n}R)}{2ik_{zn}\lambda_{1n}J_1(\lambda_{1n}R)} B_n^- = -P_n \cdot B_n^- \tag{10.87}$$

The negative sign is due to that the wavenumbers for waves traveling in the positive and negative direction of the z -axis have opposite signs.

As an example, consider a circular rubber mount of height H and with a radius R as shown in Fig. 10.13. The mount is compressed by the distance d along its axis. The displacement in the radial direction at the two end surfaces is zero. At the top end, $z = H/2$, the axial displacement is $-d$ and at the bottom end zero for $z = -H/2$. At the top end, the displacement in the radial direction is zero and the axial displacement

Fig. 10.13 Circular rubber mount



is equal to $-d$. Thus $u_r(H/2, r) = 0$ and $u_z(H/2, r) = -d$. Eq.(10.85) through (10.87) gives

$$\sum_{n=1}^{\infty} \left[C_n^+ \cdot e^{iq_n} + C_n^- \cdot e^{-iq_n} \right] U_n^r = 0; \quad \sum_{n=1}^{\infty} \left[C_n^+ \cdot e^{iq_n} - C_n^- \cdot e^{-iq_n} \right] U_n^z = -d \quad (10.88)$$

where $q_n = Hk_{zn}/2$ and

$$\begin{aligned} U_n^r &= -\lambda_{1n}(\lambda_{2n}^2 - k_{zn}^2)J_1(\lambda_{2n}R)J_1(\lambda_{1n}r) - 2\lambda_{1n}k_{zn}^2J_1(\lambda_{1n}R)J_1(\lambda_{2n}r) \\ U_n^z &= -ik_{zn}(\lambda_{2n}^2 - k_{zn}^2)J_1(\lambda_{2n}R)J_0(\lambda_{1n}r) + 2i\lambda_{1n}\lambda_{2n}J_1(\lambda_{1n}R)J_0(\lambda_{2n}r) \\ C_n^+ X_n &= B_n^+; \quad -C_n^- X_n = B_n^-; \quad X_n = 2i\lambda_{1n}k_{zn}J_1(\lambda_{1n}R) \end{aligned} \quad (10.89)$$

At $z = -H/2$ the boundary conditions are $u_r(-H/2, r) = 0$ and $u_z(-H/2, r) = 0$. Eq.(10.85) through (10.87) give

$$\sum_{n=1}^{\infty} \left[C_n^+ \cdot e^{-iq_n} + C_n^- \cdot e^{iq_n} \right] U_n^r = 0; \quad \sum_{n=1}^{\infty} \left[C_n^+ \cdot e^{-iq_n} - C_n^- \cdot e^{iq_n} \right] U_n^z = 0 \quad (10.90)$$

The notations are defined in Eq.(10.89). As stated by Kari [100], the most straightforward way to determine the coefficients of Eqs.(10.88) and (10.90) is probably through a point-matching technique. More accurate results are achieved by the sub region method which is presented in Ref. [100]. The series of Eq.(10.90) are truncated after M terms. The number of terms required is discussed in Ref. [102]. As stated in this reference $M = 64$ is sufficient for most engineering applications.

The results so far discussed in this section are only valid for mounts with no preload. For a preloaded mount, the entire mount is deformed and can no longer be described as a uniform cylinder. This problem has been addressed in Ref. [112]. It is found that a deformed or compressed mount can be described as a uniform cylinder with a radius R_{eff} slightly larger than the radius R of the undeformed mount i.e., of the mount without a preload. The volume of the rubber is the same with and without the preload. Thus if the mount of the length L is compressed the distance d by the preload the effective radius is

$$R_{\text{eff}} = R \cdot \sqrt{\frac{L}{L-d}} \quad (10.91)$$

This model is discussed in Sect. 10.10.

10.10 Measurements of Effective Stiffness of Mounts

The geometry and general construction of resilient elements can often be fairly complicated. Mounts for heavy equipment are, to ensure stability, frequently mounted at a certain angle with respect to a vertical line through the mount. A possible mounting of a ship Diesel is shown in Fig. 10.14. A straightforward calculation of the elasticity of mounts with complicated geometries cannot be carried out even if material parameters and geometries can be well specified. Numerical methods like FEM including non-linear modules are best suited for this type of calculation. A FEM prediction can in general be made up to sufficiently high frequency limits to include the first few resonances in the spring.

An alternative to numerical calculations is to make direct measurements of the dynamical properties of the mount. However, a certain number of practical difficulties must be solved to make these measurements. Some of these problems are discussed in Refs. [109, 110]. There are two predominant measurement techniques. The first, the direct method, was proposed by Snowdon [92]. The test specimen is mounted on a stiff foundation. The top end of the mount is excited by a shaker. The displacement at the top end and the force at the blocked end are measured to determine the transfer stiffness of the mount. However, a force transducer mounted between mount and a stiff foundation can easily brake in particular as the preload is increased. The alternative is the so-called indirect method, see for example, Refs. [102, 111]. The measurements should preferably be carried out in a test rig especially designed for this particular purpose. One such rig, proposed and tested by Leif Kari [109, 110], is illustrated in Fig. 10.15.

The test object is mounted between a force distribution plate and a motion reducing blocking mass. The two masses are “stiff” to ensure that their first few natural frequencies are outside the frequency range of interest. This is also true for the frame of the rig. The lower blocking mass is mounted to the frame by means of very soft springs. The test objects can be preloaded and thus compressed by a static force. A hydraulic oil pressure transducer measures the static load on the mount. A dynamic

Fig. 10.14 Mounting of a ship Diesel

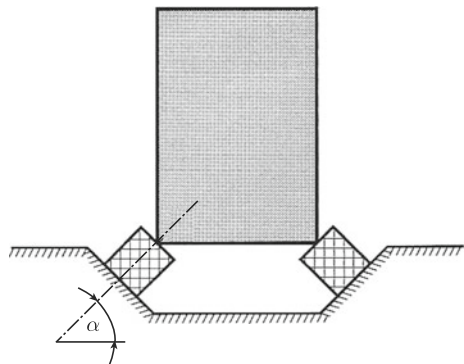
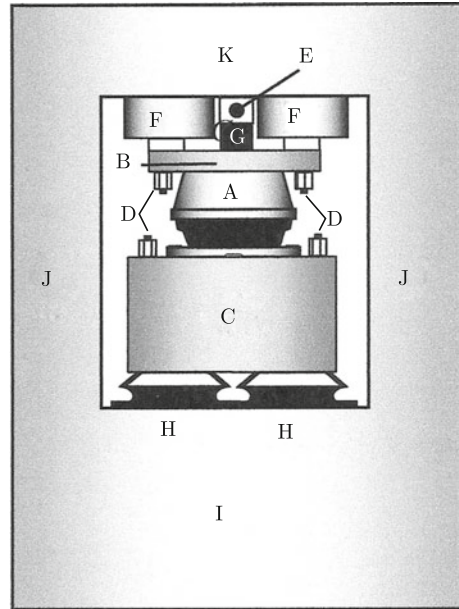


Fig. 10.15 Test rig for the measurement of the dynamic stiffness of resilient mounts. *B* Test object; *B* Force distribution plate; *C* Blocking mass; *D* Accelerometer; *E* Hydraulic piston with strain gauge; *F* Shaker; *G* Upper isolator; *H* Lower isolator; *I* Rigid body; *J* Supporting column; *K* Cross bar. From Kari



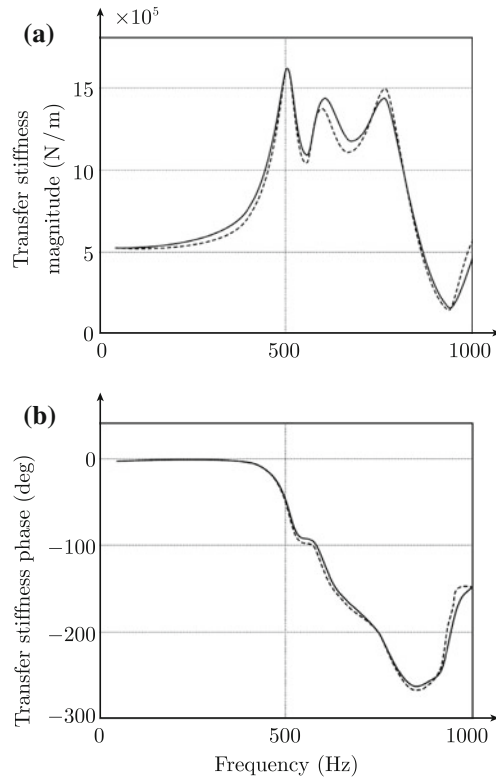
force can be superimposed by means of two electro-dynamic exciters. Forces and velocities at the top and bottom ends of the test mounts are measured. In principle, the four pole or two port parameters relating forces and velocities are determined based on these measurements. The point and transfer mobilities Y_{11} , Y_{12} , Y_{21} , and Y_{22} defined in Sect. 6.5 could thus be obtained.

However, it is not straightforward to measure the forces at the top and bottom ends of the mount by means of force transducers. As mentioned before, there is a tendency for the transducers to break when mounted between a test object and a stiff mass. The lower mass of the test rig shown in Fig. 10.15 is mounted on very soft springs. For sufficiently high frequencies, the mass is vibrating as if it were disconnected from the spring. Consequently, the force induced by the mount or the test object on the mass M is for sufficiently high frequencies and harmonic excitation given by $F_2 = i\omega M v_2$ where v_2 is the velocity of the mass. The equivalent or transfer stiffness k_{eq} of a mount is in Eq. (10.92) defined as the ratio between the FT of the force induced by the mount at its lower end and the FT of the displacement of the upper part of the mount or

$$k_{\text{eq}} = \frac{\hat{F}_2}{\hat{x}_1} = \frac{\omega^2 M \hat{x}_2}{\hat{x}_1} = \frac{\omega^2 M G_{v_2 v_1}}{G_{v_1 v_1}} = |k_{\text{eq}}| e^{i\varphi} \quad (10.92)$$

Here $G_{v_1 v_2}$ is the one-sided cross-power spectral density between the velocities at the two ends of the mount. The one-sided autospectrum of the velocity at the upper end is defined as $G_{v_1 v_1}$. Both the magnitude of the stiffness parameter and the phase

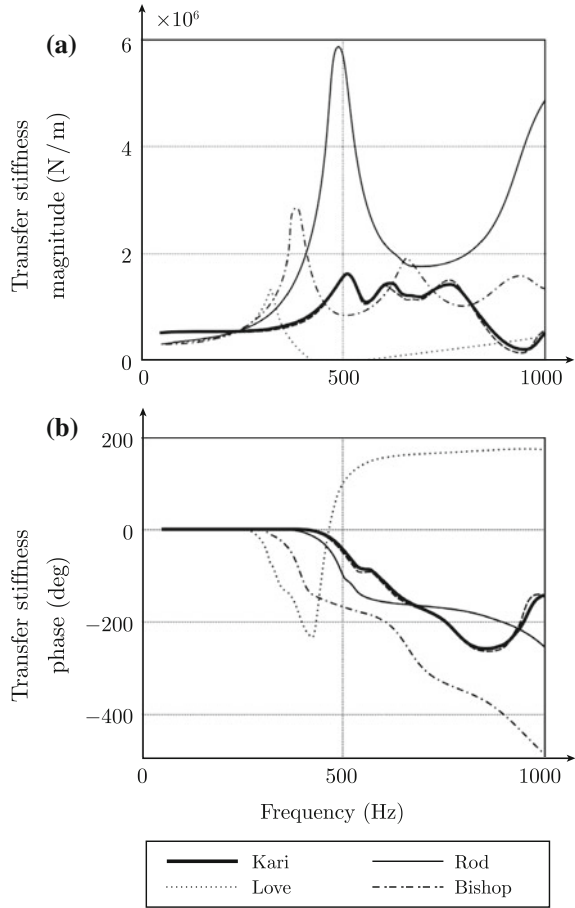
Fig. 10.16 Calculated (*solid*) and predicted (*dashed*) transfer stiffness of a cylindrical rubber mount. From Ref. [100]



angle are determined. Two piezo-electric accelerometers are mounted on the top mass and two on the lower blocking mass. The weight of the blocking mass is of the order 500 kg. For typical mounts, measurements of the equivalent stiffness can be carried out in the frequency range 100–1000 Hz. The preload or static load can vary up to 60 kN. In addition to measurements of the axial transfer stiffness of mounts also measurements of transverse transfer stiffness, torsional transfer stiffness and moment and cross coupling transfer stiffness are reported in Ref. [102].

The prediction model developed by Leif Kari is discussed in Ref. [100] and summarized in Sect. 10.9. In Ref. [100], measured and predicted results are compared. One such comparison is shown in Fig. 10.16. The test object was a cylindrical vibration isolator, length 50 mm and radius 50 mm. The nominal hardness of the rubber material is 40° IRH and the density 1050 kg/m³. The measured and predicted magnitude of the transfer stiffness and its phase angle are shown in Fig. 10.16. The agreement is very good between predicted and measured results. In Ref. [102] predictions of the transfer stiffness of mounts based on various models discussed in Sect. 10.6 are compared. First, a mount with a length of 5000 mm is considered. Otherwise radius and material parameters are the same as in the previous case, i.e., radius 50 mm, nominal hardness 40° IRH and the density 1050 kg/m³. In principal

Fig. 10.17 Transfer stiffness. The Kari results and the measurements are almost identical. From Ref. [102]



the test object is a long rod structure. The various models show very good agreement for this particular case. However, in the second example, where again the length of the mount is 50 mm as in the very first example, the various models give very different results. Only the Kari model successfully predicts the transfer stiffness. The long rod model predicts well the frequency for the first resonance though the magnitude of the stiffness is overestimated. The other more elaborate models like those of Love and Bishop fail to predict the frequency response of the transfer stiffness as shown in Fig. 10.17.

Yet some other measurements are presented in Fig. 10.18. The results show how the transfer stiffness of a mount is varying as function of frequency and preload. In the low frequency range, the stiffness of the mount is increasing with increasing preload. The first resonance frequency is also shifting with the preload. There is a tendency that the frequency is increasing with increasing preload. For this particular mount, the stiffness at resonance is approximately six times the stiffness in the low

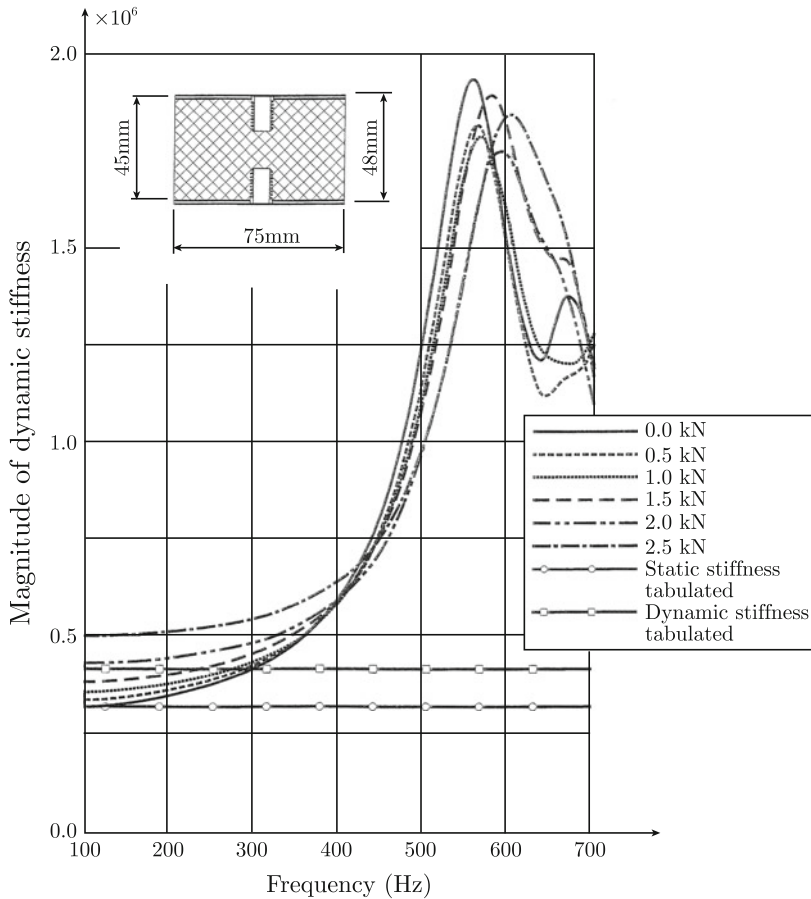


Fig. 10.18 Transfer stiffness as function of preload. From Ref. [102]

frequency region. The dynamic stiffness is given by manufacturer as 30% higher than the static stiffness. However, this value agrees poorly with the measurements.

In the second example, measurements are made on a more complex element than the first. The mount consists of two rubber elements mounted at an angle of 45° with respect to the horizontal plane. This type of mount is often used for the installation of Diesel engines on ships as shown in Fig. 10.14. The mounts are mainly exposed to shear and compression. Figure 10.19 shows the absolute value of the equivalent stiffness in the vertical direction. The stiffness varies dramatically in the audio frequency range. From 270 to 420 Hz the stiffness of the mount is increased by a factor 60. For real resilient mounts there is no such thing as a spring constant!

It should be evident that a resilient mounting system can only be optimized if the dynamical properties of the mount are properly measured or otherwise carefully

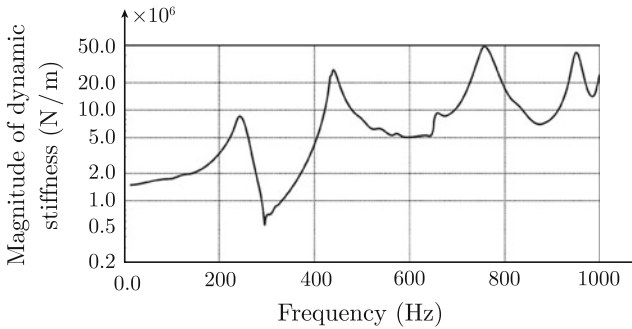


Fig. 10.19 Measured absolute value of equivalent stiffness of two rubber elements mounted at an angle of 45° . From Kari

predicted. The influence of such parameters as frequency, temperature, amplitude, static load must be estimated.

Predictions of the transfer stiffness of bushings and of shear mounts are reported in Ref. [112].

10.11 Structural Coupling Via Resilient Mounts

The prediction and reduction of energy flow from a source to supporting structures and from these to adjoining structures are often the basis for a successful noise reduction. A mechanical source is often mounted to a supporting structure at a certain number of discrete points. A typical example is an engine resiliently mounted to a so-called sub frame in a car or a washing machine supported on a floor in a building. The energy flow from source to foundation depends on the dynamic and geometric properties of source, mounts, and supporting structure. As long as the area of the contact points between structures and mounts are small, the point and transfer mobility concepts can be used to describe coupling effects and energy flow from the source. The characteristic dimension a of the contact surface and the wave number κ for flexural waves in supporting structure should satisfy the condition $\kappa a \ll 1$.

The mobility concept has already been used for describing the coupling between structures. The coupling of finite beams exposed to axial excitation was discussed in Sect. 6.5. The field parameters, force and velocity, at each end of a beam are related by means of the four mobility functions Y_{11} , Y_{12} , Y_{21} , and Y_{22} . As shown in Sect. 6.6, velocity and force at one end of the axially excited beam can be determined by means of a 2×2 transfer matrix and the velocity and force at the other end. When the number of degrees of freedom at each end of the beam is increased larger transfer matrices are required. For the inplane bending of a thin beam, a 4×4 transfer matrix is required for relating the field parameters at each end. This was discussed in Sect. 7.6. For a complete description of a beam, allowing six degrees of freedom at each end, a

12×12 transfer matrix is necessary. Clearly, it can be formidable task to measure or calculate all the 144 transfer functions for one element since in general, the resilient element cannot be described as a simple thin beam or rod.

A full mobility matrix for a single point on a structure relating velocities v_x , v_y , and v_z to forces F_x etc., and moments M_x etc., includes 36 elements. Or,

$$\begin{bmatrix} \hat{v}_x \\ \hat{v}_y \\ \hat{v}_z \\ \hat{\omega}_x \\ \hat{\omega}_y \\ \hat{\omega}_z \end{bmatrix} = \begin{bmatrix} Y_{F_x v_x} & Y_{F_y v_x} & Y_{F_z v_x} & Y_{M_x v_x} & Y_{M_y v_x} & Y_{M_z v_x} \\ Y_{F_x v_y} & Y_{F_y v_y} & Y_{F_z v_y} & Y_{M_x v_y} & Y_{M_y v_y} & Y_{M_z v_y} \\ Y_{F_x v_z} & Y_{F_y v_z} & Y_{F_z v_z} & Y_{M_x v_z} & Y_{M_y v_z} & Y_{M_z v_z} \\ Y_{F_x \omega_x} & Y_{F_y \omega_x} & Y_{F_z \omega_x} & Y_{M_x \omega_x} & Y_{M_y \omega_x} & Y_{M_z \omega_x} \\ Y_{F_x \omega_y} & Y_{F_y \omega_y} & Y_{F_z \omega_y} & Y_{M_x \omega_y} & Y_{M_y \omega_y} & Y_{M_z \omega_y} \\ Y_{F_x \omega_z} & Y_{F_y \omega_z} & Y_{F_z \omega_z} & Y_{M_x \omega_z} & Y_{M_y \omega_z} & Y_{M_z \omega_z} \end{bmatrix} \begin{bmatrix} \hat{F}_x \\ \hat{F}_y \\ \hat{F}_z \\ \hat{M}_x \\ \hat{M}_y \\ \hat{M}_z \end{bmatrix}$$

The main contribution to the power flow to a structure is, in general, the result of the mobilities along the diagonal of the mobility matrix. The point mobility for thin plates was discussed in Sects. 5.3 and 8.5. In these examples the force was perpendicular to the infinite plate. The point mobility for a finite simply supported plate was derived in Sect. 8.5 and for a simply supported finite beam in Sect. 7.4. For an infinite plate, density ρ , E-modulus E and thickness h , Poisson's ratio ν , the point mobility perpendicular to the plate is $Y_{F_z v_z} = 1/(8\sqrt{\mu D}) = \sqrt{3(1-\nu^2)}/[4h^2\sqrt{E\rho}]$ and tangential to the plate approximately $Y_{F_x v_x} \approx 2\omega/(Eh)$. For an infinite steel plate, thickness h (m), the ratio between the point mobilities is

$$\frac{Y_{F_z v_z}}{Y_{F_x v_x}} \approx \frac{1}{16\pi fh} \sqrt{\frac{3E}{\rho}} \approx \frac{180}{fh} \quad (10.93)$$

Thus, for steel plates with a thickness of less than 10 mm the point mobility perpendicular to the plate dominates completely for $f < 2$ kHz, i.e., $Y_{F_z v_z} \gg Y_{F_y v_y}$.

The moment mobility $Y_{M_y \omega_y}$ is defined as the ratio between the FT of the rotational velocity ω_y around one axis, in this case y , and the FT of the bending moment M_y around the same axis. Thus

$$\omega_y = \frac{d}{dt} \left(\frac{\partial w}{\partial x} \right); \quad \hat{\omega}_y = i\omega \frac{\partial \hat{w}}{\partial x}; \quad Y_{M_y \omega_y} = \frac{\omega_y}{M_y} \quad (10.94)$$

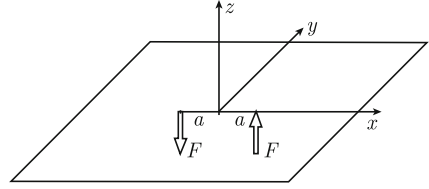
The time average of the power Π induced by the a bending moment $M_y e^{i\omega t}$ is consequently

$$\bar{\Pi} = \frac{1}{2} \text{Re} (M_y \omega_y^*) = \frac{|\omega_y|^2}{2} \text{Re} (Y_{M_y \omega_y}) = |\bar{\omega}_y|^2 \text{Re} (Y_{M_y \omega_y}) \quad (10.95)$$

Alternatively, the power spectrum of the induced power is given as

$$G_\Pi = G_{\omega_y \omega_y} \text{Re}(Y_{M_y \omega_y})$$

Fig. 10.20 Two point forces exciting an infinite plate



The moment mobility of an infinite and homogeneous beam, width b and height h , is as discussed in Problem 10.3 found to be

$$Y_{M\omega_y} = \frac{\kappa^3(1+i)}{4\omega m'}; \quad \kappa = \left(\frac{m'\omega^2}{D'}\right)^{1/4} = \left(\frac{12\rho\omega^2}{Eh^2}\right)^{1/4}; \quad m' = \rho bh \quad (10.96)$$

The moment mobility of an infinite thin plate can be derived using the results from Sect. 5.3. It was found in Sect. 5.3 that the FT of the displacement $w(r, t)$ of a plate excited by a point force $F(t)$ at $r = 0$ is described by

$$\hat{w}(r, \omega) = \hat{w}_0[H_0^{(2)}(\kappa r) - H_0^{(2)}(-i\kappa r)]; \quad \hat{w}_0 = \frac{i\hat{F}}{8\kappa^2 D} \quad (10.97)$$

If the plate is excited by a pair of forces in opposite directions as shown in Fig. 10.20 the displacement along the x -axis in between the excitation points is

$$\hat{w}_x(x, \omega) = \hat{w}(r_1, \omega) - \hat{w}(r_2, \omega); \quad r_1 = a - x; \quad r_2 = a + x \quad \text{for} \quad -a \leq x \leq a \quad (10.98)$$

The distances between a point x on the x -axis and the two forces are defined as r_1 and r_2 . The distances r_1 and r_2 are small. The solutions $\hat{w}(r_1, \omega)$ and $\hat{w}(r_2, \omega)$ can be expanded in MacLaurin series, thereafter the rotation along the x -axis is calculated and the bending mobility derived. Following the discussions in Sect. 5.3, Eqs. (5.43) and (5.50), the function $\hat{w}(r_1, \omega)$ is also written

$$\hat{w}(r_1, \omega) = \hat{w}_0(\omega)[J_0(z) - iY_0(z) - J_0(-iz) + iY_0(-iz)]; \quad z = \kappa r_1 \quad (10.99)$$

For $z \ll 1$ the Bessel and Neuman functions can according to Ref. [43] be expanded as

$$J_0(z) = 1 - \frac{z^2}{4} + \frac{z^4}{64} \dots; \quad Y_0 = \frac{2}{\pi} \left[\ln\left(\frac{z}{2}\right) + \gamma \right] J_0(z) + \frac{2z^2}{4\pi} - \frac{3z^4}{2 \cdot 64} \dots \quad (10.100)$$

The Euler constant γ is equal to 0.577... For $|z| \ll 1$, $\hat{w}(r_1, \omega)$ is, neglecting terms of z^3 and higher orders, approximated by

$$\hat{w}(r_1, \omega) = \hat{w}_0(\omega) \left\{ 1 - \frac{z^2}{4} - \frac{iz^2}{\pi} \left[1 - \left(\ln\left(\frac{z}{2}\right) + \gamma \right) \right] \right\}; \quad z = \kappa(a - x)$$

$$\hat{w}(r_2, \omega) = \hat{w}_0(\omega) \left\{ 1 - \frac{z^2}{4} - \frac{iz^2}{\pi} \left[1 - \left(\ln \left(\frac{z}{2} \right) + \gamma \right) \right] \right\}; \quad z = \kappa(a + x) \quad (10.101)$$

The FT of the rotational velocity is from (10.101) obtained as

$$\hat{\omega}_y = i\omega \frac{\partial}{\partial x} [\hat{w}(r_2, \omega) - \hat{w}(r_1, \omega)]_{x=0} = \frac{\omega a \hat{F}}{8D} \left\{ 1 + \frac{4i}{\pi} \left[1 - \ln \left(\frac{\kappa a}{2} \right) - \gamma \right] \right\} \quad (10.102)$$

However, the bending moment acting on the plate is $\hat{M}(\omega) = 2a\hat{F}(\omega)$. Thus, from (10.102),

$$Y_{M_y \omega_y} = \frac{\omega}{16D} \left\{ 1 + \frac{4i}{\pi} \left[1 - \ln \left(\frac{\kappa a}{2} \right) - \gamma \right] \right\} \quad (10.103)$$

The imaginary part of the moment mobility approaches infinity as a tends to zero. However, the power input induced in a structure by a bending moment is proportional to the real part of the moment mobility and is consequently finite even as the parameter a tends to zero.

It is often necessary to reduce the number of transmission mechanisms in order to formulate a workable model describing the coupling between a source and a receiver. Mechanisms which are considered the least likely to contribute to the energy transfer to the foundation or receiver are eliminated. All such simplifications should be verified by measurements on real and representative structures. However, over simplifications can be disastrous as demonstrated by Pavic [113]. In general, it is often assumed that the one-dimensional often vertical motion of the source predominately causes the energy flow from a source to its supporting structure. The second most important transmission mechanism is typically induced by the horizontal motion of the source. In this case, the energy transfer is mainly caused by shear in the resilient mounts. Although the forces exciting a foundation in the vertical and horizontal directions can be of the same magnitude the mobilities perpendicular and tangential to a standard foundation can be quite different as for example given by Eq. (10.93). The mobility perpendicular to the foundation tends often to be the higher. A consequence of this is that the transmission path perpendicular to the foundation generally dominates, though the construction of a foundation determines which path is dominant. The energy flow through a mount also depends on the stiffness of the mount in directions other than the axial. The radial and axial stiffness of mounts can also vary considerably.

The geometry and construction of typical mounts are often such that the energy transfer through the mounts caused by rotation is negligible. If the total energy flow from source to receiver is dominated by transmission along one path then the acoustical coupling can be adequately described by means of the simplified mobility concept. This means that each mount can be characterized by a 2×2 matrix only.

For a real construction, the couplings between source and mounts and mounts and supporting structure are via a contact area rather than a contact point. The distribution of the pressure over the contact surface determines the effective mobility of the structure. The pressure distribution on for example a foundation depends not only

on the material and geometrical parameters describing the supporting structure but also on the stiffness of the mount or indenter. A number of cases are analyzed and discussed in for example Ref. [44]. It is concluded in this reference that the simple mobility concept can be applied as long as:

- (i) Coupled systems are linear systems.
- (ii) One dominating transmission path through each mount.
- (iii) The wave number κ for flexural waves in plates or beams connected to supports satisfies the condition $h\kappa < 1$, where h is the characteristic thickness of the structure.
- (iv) The characteristic dimension a of the contact surface and the wave number κ for flexural waves in supporting structure satisfy the condition $\kappa a \ll 1$.

The accuracy of the mobility procedure depends on how well the conditions listed can be satisfied. The ultimate answer is obtained by comparing predicted and measured results.

However, not only mobilities but also impedances can be used to describe the coupling between different systems. In general, the mobility concept is much preferred. Some basic differences between the two concepts can be illustrated by means of the beam element discussed in Sect. 6.6. The beam is excited by an axial force at each end. The resulting FTs of the forces are in matrix form given by

$$\begin{Bmatrix} \hat{v}_1 \\ \hat{v}_2 \end{Bmatrix} = \begin{bmatrix} Y_{11} & Y_{12} \\ Y_{21} & Y_{22} \end{bmatrix} \cdot \begin{Bmatrix} \hat{F}_1 \\ \hat{F}_2 \end{Bmatrix} \quad \text{or} \quad \mathbf{v} = \mathbf{Y} \cdot \mathbf{F} \quad (10.104)$$

Alternatively, the forces can be expressed as functions of the velocities as

$$\begin{Bmatrix} \hat{F}_1 \\ \hat{F}_2 \end{Bmatrix} = \begin{bmatrix} Z_{11} & Z_{12} \\ Z_{21} & Z_{22} \end{bmatrix} \cdot \begin{Bmatrix} \hat{v}_1 \\ \hat{v}_2 \end{Bmatrix} \quad \text{or} \quad \mathbf{F} = \mathbf{Z} \cdot \mathbf{v} \quad (10.105)$$

It follows that $\mathbf{Z} = \mathbf{Y}^{-1}$.

By exciting one end of the beam by F_1 and letting $F_2 = 0$ and measuring the velocities v_1 and v_2 the mobilities Y_{11} and Y_{21} are determined. Thereafter the other end is excited by a force F_2 and again the velocities v_1 and v_2 are measured and the mobilities Y_{21} and Y_{22} determined while $F_1 = 0$. The measurements are carried out by means of an impedance hammer, an accelerometer, and a two-channel analyser. The technique is often referred to as the blocked force method.

In order to determine the impedance matrix of Eq. (10.105), first the velocity v_2 must be blocked while the forces at the two ends and the velocity at end 1 are measured. The measurements are repeated with the velocity v_1 blocked and v_2 measured. In general, this technique, the blocked velocity method, is more difficult than the first. In particular, it must be ensured that the velocity at one end really is blocked. Further the force required to keep one end blocked must be determined.

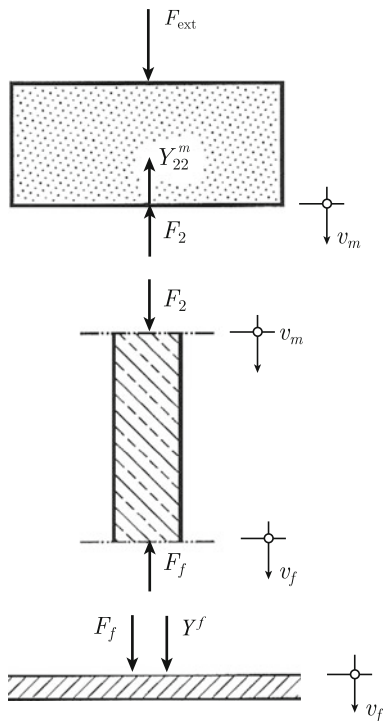
10.12 Simple Transmission Model

For obtaining stability, a real source, like an engine, is mounted to its foundation by three or more mounts. However, some of the basic concepts with respect to resilient mounting can be demonstrated by means of the primitive single mount model shown in Fig. 10.21. Some aspects on multi-point junctions are discussed in next section. The mass or rather the source in Fig. 10.21 is excited by a harmonic force F_{ext} . The mass, not necessarily rigid, is allowed one degree of freedom only as defined by the coordinate x . The foundation has the point mobility Y^f at the junction of the mount. The mobility of the mass at the junction to the mount is $Y^m = Y_{22}^m$. The transfer mobility between a hypothetical excitation point and the point connecting the mass and the mount is defined as Y_{12}^m . The index m refers to the mass or source. To start with, let the coupling element between the source and the foundation be completely stiff. Forces and displacements are allowed in one direction only i.e., perpendicular to the horizontal foundation as shown in Fig. 10.21.

The velocity \hat{v}_m of the mass at a point directly above the mount is given by

$$\hat{v}_m = \hat{F}_{ext} Y_{12}^m - \hat{F}_2 \cdot Y_{22}^m \tag{10.106}$$

Fig. 10.21 Mass/source, mount, and foundation receiver



The product $\hat{F}_{\text{ext}} Y_{12}^m$ can be interpreted as a velocity \hat{v}_0 . This quantity is equal to the “free velocity” at the junction to the mount when the source is disconnected from the mount but still excited by the external source.

For a source with only one contact point to the foundation, the FT of the velocity \hat{v}_m between source and foundation is

$$\hat{v}_m = \hat{v}_f = \hat{v}_0 - \hat{F}_2 Y^m; \quad \hat{F}_f = \hat{F}_2 \quad (10.107)$$

The FT of the velocity of the foundation is given by $\hat{v}_f = \hat{F}_f Y^f$. Thus

$$\hat{v}_m = \frac{\hat{v}_0}{1 + Y^m/Y^f} \quad (10.108)$$

For $Y^f \gg Y^m$ the resulting velocity on the foundation and at the contact point on the source is approximately equal to \hat{v}_0 . Consequently, the velocity in the coupling point can be considered as independent of the mobility of the foundation. Thus, for $Y^f \gg Y^m$ the foundation is said to be excited by a constant velocity source.

In a similar way the FT of the force acting on the foundation is given by

$$\hat{F}_f = \frac{\hat{v}_0}{Y^m + Y^f} = \frac{\hat{v}_0}{Y^m(1 + Y^f/Y^m)} \quad (10.109)$$

For $Y^m \gg Y^f$ the force on the foundation is approximately independent of the point mobility of the foundation. The foundation is said to be excited by a constant force source.

The real part of the spectrum of power transmitted to the foundation through a completely stiff mount is

$$\text{Re}G_{\Pi} = \lim_{T \rightarrow \infty} 2\text{Re} \left(\hat{F}_f \hat{v}_f^*/T \right) = \lim_{T \rightarrow \infty} 2\text{Re} \left(\hat{F}_f \hat{F}_f^* Y^f*/T \right) = G_{F_f F_f} \text{Re}(Y^f) \quad (10.110)$$

In combination with (10.109) the result is

$$\text{Re}G_{\Pi} = G_{v_0 v_0} \frac{\text{Re}(Y^f)}{|Y^f + Y^m|^2} \quad (10.111)$$

It can be shown that the maximum energy transfer from source/mass to receiver/foundation is when $Y^f = (Y^m)^*$ as demonstrated in Problem 10.8. This is the worst case, which should always be avoided. The minimum flow is for $Y^f = 0$. For a constant velocity source, the power spectrum of the transmitted power to the foundation/receiver is

$$\text{Re}G_{\Pi} \approx G_{v_0 v_0} \frac{\text{Re}(Y^f)}{|Y^f|^2} \quad \text{for } Y^f \gg Y^m \quad (10.112)$$

The corresponding expression for a constant force source, $Y^m \gg Y^f$, is

$$\operatorname{Re}G_{\Pi} \approx G_{v_0 v_0} \frac{\operatorname{Re}(Y^f)}{|Y^m|^2} \quad \text{for } Y^m \gg Y^f \quad (10.113)$$

A source of structure-borne sound is, or should be, resiliently mounted to its foundation. If the resilient mounts are considered as integral parts of the source, the condition $Y^m \gg Y^f$ would often be satisfied. In general, resiliently mounted machinery can therefore be considered as sources inducing a constant force on the foundation irrespective of the characteristics of the foundation. Heavy machinery mounted on weak foundations tend to behave like constant velocity sources in the high frequency region. An example of this is a big ship Diesel engine mounted on a foundation build up of beam and plate elements.

The transfer mobilities defining the dynamic properties of a spring are formulated following the procedure outlined in Sect. 6.4. These mobilities are defined as Y_{11} , Y_{12} , Y_{21} , and Y_{22} . The forces acting on each element are illustrated in Fig. 10.21. The velocity at the junction between spring and mass is given by v_m . The corresponding velocity at the junction between spring and foundation is v_f . The FT of the velocity v_m of the mass directly above the mount is given by Eq. (10.107) as $\hat{v}_m = \hat{v}_0 - \hat{F}_2 Y^m$. Based on the definitions of the transfer mobilities defined in Sect. 6.4 the FT of the velocities v_m and v_f at the ends of the mount are obtained as

$$\hat{v}_m = \hat{F}_2 Y_{11}^s - \hat{F}_f Y_{21}^s; \quad \hat{v}_f = \hat{F}_2 Y_{12}^s - \hat{F}_f Y_{22}^s \quad (10.114)$$

On the foundation, at the junction to the mount, the FT of the velocity v_f is

$$\hat{v}_f = \hat{F}_f Y^f \quad (10.115)$$

Eliminating the quantities \hat{F}_2 , \hat{v}_m and \hat{v}_f by means of Eqs. (10.107), (10.114), and (10.115) the FT of the force on the foundation is found to be

$$\hat{F}_f = \frac{\hat{v}_0 \cdot Y_{12}^s}{Y^m \cdot Y_{22}^s + Y^m \cdot Y^f + Y^f \cdot Y_{11}^s + Y_{\text{eq}}^s \cdot Y_{12}^s}; \quad Y_{\text{eq}}^s = \frac{Y_{11}^s \cdot Y_{22}^s - Y_{12}^s \cdot Y_{21}^s}{Y_{12}^s} \quad (10.116)$$

For a sufficiently soft mount the mobility Y_{11}^s at the top end of the spring should be much higher than the point mobility Y^m of the source. The point mobility Y_{22}^s at the bottom end could also be expected to be much higher than the point mobility Y^f of the foundation. In either case, the second term in the denominator in the expression defining \hat{F}_f in Eq. (10.116) can be neglected. For the case the source is rigidly connected to the foundation \hat{v}_m is equal to \hat{v}_f and \hat{F}_2 equal to \hat{F}_f . For this case Eqs. (10.112) and (10.107) give the FT of the resulting force F_f^0 on the foundation as

$$\hat{F}_f^0 = \frac{\hat{v}_0}{Y^m + Y^f} \quad (10.117)$$

The power spectrum of the power transmitted to the foundation is

$$\text{Re}G_{\Pi} = G_{F_f F_f} \cdot \text{Re} \left(Y^f \right)^*$$

The insertion loss IL due to the resilient mount is thus

$$IL = 10 \log \left(\text{Re}G_{\Pi^0} / \text{Re}G_{\Pi} \right) = 10 \log \left| G_{F_f^0 F_f^0} / G_{F_f F_f} \right| = 10 \log \left| \hat{F}_f^0 / \hat{F}_f \right|^2 \quad (10.118)$$

where G_{Π^0} is the power spectrum of the acoustic power transmitted to the foundation when the source is mounted without resilient coupling and G_{Π} is the corresponding result with resilient coupling.

In the low frequency region, the expression giving the insertion loss can be simplified considerably. The transfer mobilities for a rod like spring are defined in Eq. (6.96). For low frequencies, the corrected or uncorrected wavenumbers for longitudinal waves in a rod are both smaller than unity. A simple expansion of the mobilities with respect to the wave number lead to $Y_{11}^s \approx Y_{12}^s \approx Y_{21}^s \approx Y_{22}^s \approx 1/(i\omega\rho S)$ and $Y_{\text{eq}} = i\omega L/(SE)$. The transfer mobilities are consequently all large in the low frequency region and are quite simply set to be equal. As discussed above the term $Y^m \cdot Y^f / Y_{12}^s$ can normally be neglected in Eq. (10.116). Based on these assumptions the force on the foundation with and without a resilient mount is obtained as

$$\hat{F}_f = \frac{\hat{v}_0}{Y^m + Y^f + Y^s}; \quad \hat{F}_f^0 = \frac{\hat{v}_0}{Y^m + Y^f}; \quad \frac{\hat{F}_f^0}{\hat{F}_f} = \frac{Y^m + Y^f + Y^s}{Y^m + Y^f} \quad (10.119)$$

Considering these simplifications the insertion loss as defined in Eq. (10.118) is consequently given by

$$IL = 20 \log \left| \frac{Y^m + Y^f + Y^s}{Y^m + Y^f} \right| \quad (10.120)$$

Although approximate and valid in the low frequency range only, the result (10.120) clearly demonstrates the relative importance of the mobilities of source, mount, and foundation with respect to the insertion loss. For obtaining a high insertion loss, the effective mobility of the spring should be much larger than the sum of the mobilities of source and foundation. If on the other hand the foundation is very resilient, i.e., the mobility Y^f of the foundation is very high, the resulting insertion loss is small.

For the same simple case shown in Fig. 10.21, the ratio between the FT of the velocity v_m of the top end of the mount and the FT of the velocity v_f of the bottom end is

$$\frac{\hat{v}_m}{\hat{v}_f} = \frac{Y_{\text{eq}}^s + Y^f}{Y^f} \quad (10.121)$$

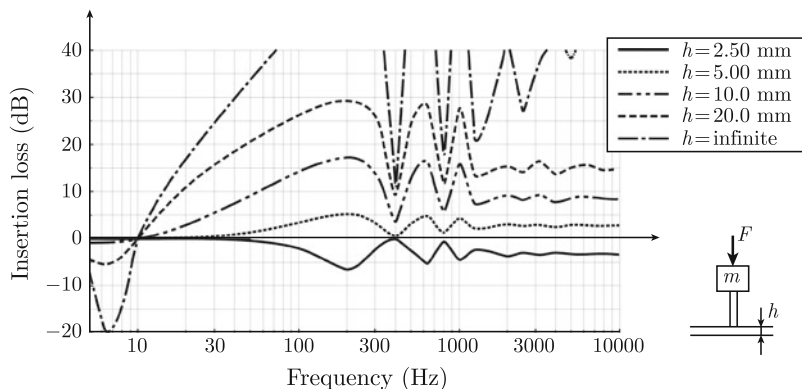


Fig. 10.22 Stiff mass mounted to a rod coupled to a steel plate, thickness h Predicted insertion loss

Thus, the ratio \hat{v}_m/\hat{v}_f is different from the ratio \hat{F}_f^0/\hat{F}_f given in Eq. (10.119). The insertion loss due to a resiliently mounted source cannot directly be determined by measuring the velocities v_m and v_f of a system when in operation.

The importance of the dynamical properties of a foundation with respect to the insertion loss for a resiliently mounted source can be demonstrated by means of the simple example illustrated in Fig. 10.22. A rigid mass is mounted to a homogeneous steel plate of thickness h . The mount is modeled as a thin rod. The transfer mobilities are determined as described in Sect. 6.5. For an infinitely stiff foundation the first resonance frequency for the mass–spring system would be 6 Hz. The insertion loss is predicted from the unabbreviated expressions (10.116) and (10.118). Resulting insertion losses predicted for four different thicknesses of the foundation plate are presented in Fig. 10.22. Close to the first resonance for the plate-mass-system the resulting insertion loss is typically negative. Even for fairly thick foundation plates the insertion loss is very limited even in the high frequency range. The poor result is due to the high mobility of the foundation or rather the steel plate to which the mount is coupled. In order to increase the insertion loss it would be necessary to stiffen the plate, for example by adding a beam underneath the coupling point between plate and mount.

Engine foundations on ships are build up of a number of plate elements. Similar types of engine foundations or engine supports can be found on trucks and trains. The structures between the coupling points between bogies and train carriages can also have a similar construction. In the very low frequency range, the foundation can be modeled as a stiff mass. The mobility of a stiff mass is $Y = 1/(i\omega M)$. The mobility is consequently decreasing with increasing frequencies. In a certain frequency range, the mobility of the built-up structure is mainly determined by its local stiffness. The mobility is increasing with increasing frequency up to a frequency range where the various plate elements start to vibrate to more or less determine the point mobility of the foundation. The real part of the mobility of a finite plate is given in Eq. (8.78) as

$$\text{Re}(Y) = \sum_{m,n} \frac{4\omega\omega_{mn}^2\eta\varphi_{mn}^2(x_0, y_0)}{m_p[(\omega_{mn}^2 - \omega^2)^2 + (\eta\omega_{mn}^2)^2]}$$

where φ_{mn} is some eigenfunction satisfying the boundary conditions of the plate element. The coordinates for the excitation point are (x_0, y_0) . In the frequency range below the first natural frequency f_{11} of the plate the real part of the point mobility is approximately given by

$$\text{Re}Y \approx \frac{fC_1}{(f_{11}^2 - f^2)^2 + (\eta f_{11})^2} + C_2$$

where C_1 and C_2 are two constants. For $f > f_{11}$ the mobility varies rapidly with frequency and tend to level out for increasing frequencies. In the high frequency region, the point mobility of the structure is more or less determined by the thickness and density of the plate elements and given by $1/(8\sqrt{\mu D})$ as discussed in Sect. 8.5. In the high frequency region the mobility will decrease with increasing frequency caused by the size of the contact area as compared to the wavelength of bending waves as discussed in Refs. [115, 116]. The result is summarized in Fig. 10.23. The mobility level in the figure is defined as $20 \log |\text{Re}Y/Y_{\text{ref}}|$ where $Y_{\text{ref}} = 1\text{m}/(\text{Ns})$. In the frequency domain B, the mobility is approximated by the expression above obtained from a simple plate model. The horizontal line in frequency domain C corresponds to the mobility of an infinite plate. The last domain is determined by plate dimensions and the finite size of the engine feet. According to Ref. [115], the mobility is decreasing with increasing frequency as in domain D for $\kappa a > 1/3$ where κ is the wavenumber for bending waves propagating in the foundation and a is a characteristic dimension of an engine foot.

Fig. 10.23 Schematic plot of mobility of engine foundation build up of plate elements. From Ref. [116]

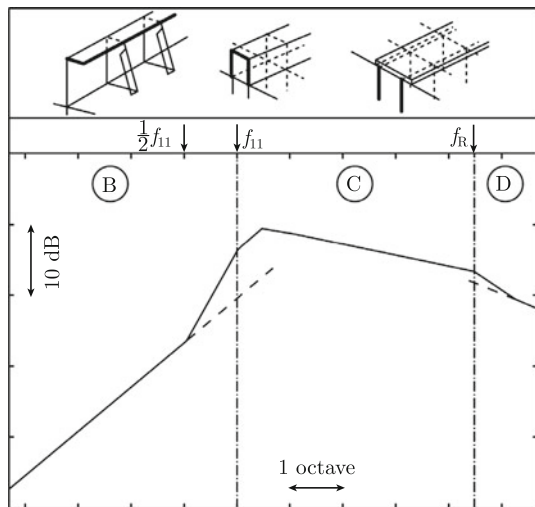


Fig. 10.24 Scale model of a catamaran



For the insertion loss of a mount to be high, the mobility of the foundation must be as low as possible. This has been demonstrated on a scale model of a catamaran, Fig. 10.24. The noise levels in the passenger compartment of this type of fast passenger vessel built of aluminum are mainly determined by structure-borne sound induced by the main engines.

The insertion losses for five different mounts were measured using the scale model. The locations of the engine feet on the foundation were the same as in full scale, i.e., in fairly weak points on the foundation plate. The measured insertion losses due to the mounts were very small or negligible for frequencies above 200 Hz corresponding to a full-scale model as shown in Fig. 10.25.

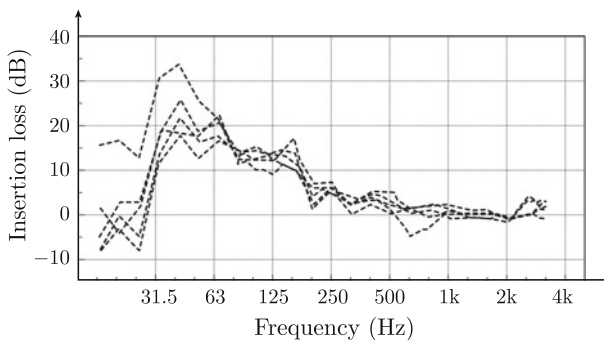


Fig. 10.25 Measured insertion loss for various mounts on the foundation of a catamaran

With respect to the A-weighted noise level in the passenger compartment, hardly any reduction of the noise level was achieved due to the various resilient mounts. The simple formula (10.120) predicting the insertion loss due to a resilient mount indicate that the effective mobility of the mount must be much higher than the mobility of the foundation to ensure a satisfactory insertion loss. However as demonstrated by the results shown in Fig. 10.16 the stiffness of mounts tends to increase with increasing frequencies or rather the point mobility of the mount is decreasing as the frequency is increased in the low frequency region. At the same time the point mobility of the foundation is increasing, Fig. 10.23. The net effect, as given by Eq. (10.120), is a decrease of the insertion loss in the high frequency region as illustrated in Fig. 10.25.

The point mobility of a foundation of the type shown in Fig. 10.25 very much depends on the location of the excitation point on the foundation plate. Consequently, the insertion loss can vary with the location of for example the engine feet on the foundation. The point mobility of a plate element is higher at the center of the plate than along its supported boundaries. It can therefore be expected that by moving a point of excitation on a foundation from unsupported to a supported position the point mobility would be reduced. Tests reported in Ref. [117] show that the transfer mobility from a point on an engine foundation to the supporting hull plating depends on the position of the excitation point. The model used for the measurements was built in scale 1:4. A frequency f in model scale corresponds to a frequency $f/4$ in full scale. Compare Problem 10.9. The measurement positions are shown in Fig. 10.26. The point F_3 is above a junction of frames along the x - and y -directions. Point F_0 is completely unsupported and the weakest point of all.

The measurement results shown in Fig. 10.27 indicate that the transfer mobility can decrease by 5 dB or more in a wide frequency range by moving the excitation point from a weak to a stiff point. The velocity v on the hull plate is given as $\hat{v} = \hat{F} Y_{tr}$, where Y_{tr} is the transfer mobility and F the force on the foundation. Thus, the velocity

Fig. 10.26 Measurement positions on foundation and hull plates. The point F_3 is above a junction of frames in the x - and y -directions. Point F_0 is completely unsupported and the weakest point of all. From Ref. [117]

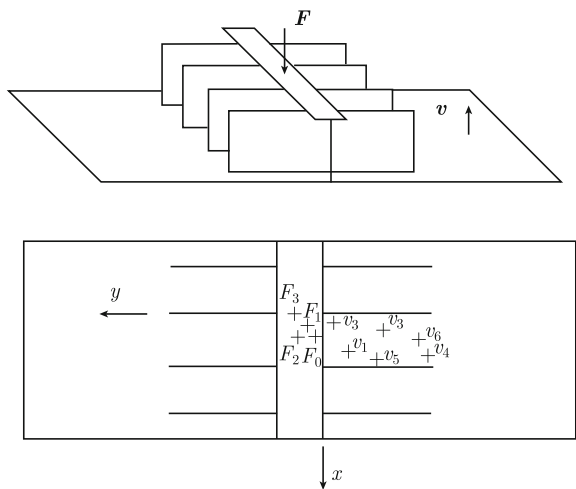
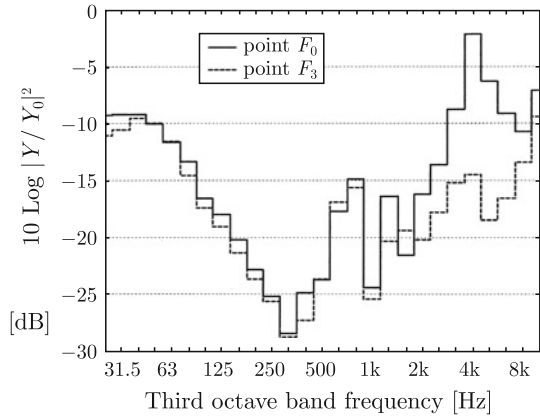


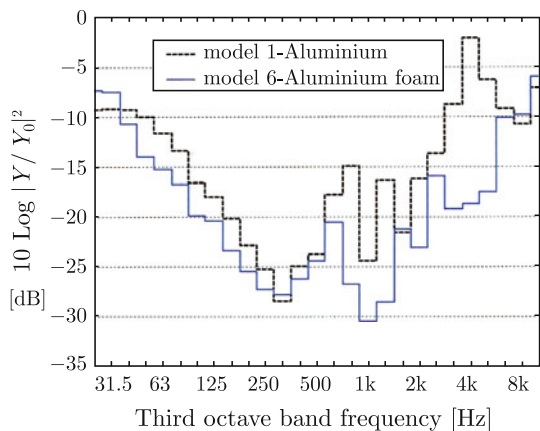
Fig. 10.27 Transfer mobilities measured on a foundation in a weak point F_0 and a stiff point F_3 . From Ref. [117]



level $20 \log |v/v_{ref}|$ of the foundation varies as $20 \log |Y_{tr}|$. The frequency response for a full-scale structure corresponds $1/4$ of the model scale frequency. Thus, 1 kHz in Fig. 10.25 corresponds to 250 Hz in full scale. Since the noise levels in the passenger compartment for this type of vessel are mainly determined by structure-borne sound induced by the main engines, a noise reduction in the area above the engine room could also be reduced by approximately 5 dB by moving the position of the engine feet from a weak to a stiff point. In practice, the feet of engines are often located in weak points for the simple reason that it is more straightforward to get access for the mounts at positions far from girders or vertical frames.

An alternative noise reducing measure is to stiffen the foundation itself. In one case reported in Ref. [117] lightweight concrete or aluminum foam were used to increase the stiffness of the engine foundation. Again, as shown in Fig. 10.28, a substantial decrease of the transfer mobility between the foundation and the hull could be achieved. Yet another method to decrease the energy transmission from

Fig. 10.28 Transfer mobilities measured on a standard foundation and a stiffened foundation. From Ref. [117]



engine to the hull structure is to increase the damping of the foundation. However, the natural damping of a foundation with an engine mounted is quite high. To increase the damping could therefore be difficult if at all possible.

The mobility of a foundation can also be decreased if the thickness of the plate elements constituting the foundation is increased. The effect of adding a solid mass or a tuned damper to foundation plates is discussed in Sect. 8.9.

10.13 Multi-point Coupling

For stability reasons a vibrating source like an engine must be coupled to its foundation by means of several mounts. A general mounting configuration is schematically illustrated in Fig. 10.29. A mass m is supported by N identical mounts. A force excites the mass at a point denoted o in Fig. 10.29. The force could be an external or an internal force or in fact a hypothetical force resulting for example from a combustion process. Whatever the case the force is henceforth denoted F_{ext} . As in the example discussed in the previous section, the mass is only allowed one degree of freedom. The mass is, in addition to the external force, also exposed to the reacting forces of the N springs. For a linear system, the principle of superposition can be applied. The velocity v_i^m at junction i on the mass results partly from the external force F_{ext} and partly from the reacting spring forces.

The contribution from the external force to FT of the velocity \hat{v}_i^m at junction i on the mass is $\hat{F}_{ext} \cdot Y_{0i}^m$, where Y_{0i}^m is the transfer mobility between the excitation point o and the junction i on the mass. The contribution from the FT of the reacting force \hat{F}_j^m from spring j is $\hat{F}_j^m \cdot Y_{ji}^m$ where Y_{ji}^m is the transfer mobility between the junctions j and i on the mass. Adding the contributions from all forces, the velocity at junction i is

$$\hat{v}_i^m = \hat{F}_{ext} \cdot Y_{0i}^m - \sum_{j=1}^N \hat{F}_j^m \cdot Y_{ji}^m \quad \text{for } i = 1 \text{ to } N \quad (10.122)$$

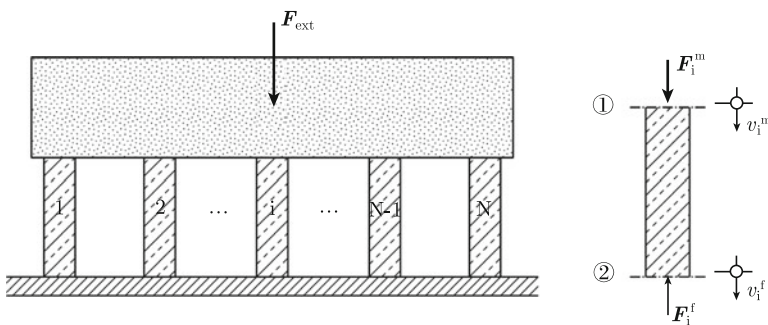


Fig. 10.29 Multi-point coupling

For spring i the velocity of the top end, denoted 1 in Fig. 10.29, is equal to the velocity of junction i on the mass. The corresponding force from the mass on the spring is F_i^m with a direction as shown in Fig. 10.29. At the bottom end, denoted 2, of the spring the velocity at the foundation at junction i is v_i^f . The reacting force from the foundation is F_i^f . According to standard procedure and as discussed in Sect. 6.5, Eq. 6.95, the velocities at the two ends of the spring can be written as

$$\hat{v}_i^m = \hat{F}_i^m \cdot (Y_{11}^s)_i - \hat{F}_i^f \cdot (Y_{21}^s)_i; \quad \hat{v}_i^f = \hat{F}_i^m \cdot (Y_{12}^s)_i - \hat{F}_i^f \cdot (Y_{22}^s)_i \quad (10.123)$$

The point mobility at the top end, 1 in Fig. 10.29, for spring i is defined as $(Y_{11}^s)_i$. The transfer mobility between the ends 1 and 2 for spring i is $(Y_{12}^s)_i$ etc. The velocity v_i^f at the junction i on the foundation depends on the forces induced by all the springs and the point mobility at junction i on the foundation and the transfer mobilities Y_i^f to all their junctions on the foundation. Thus, the FT of the velocity at the junction i on the foundation is obtained as

$$\hat{v}_i^f = \sum_{j=1}^N \hat{F}_j^f \cdot Y_{ji}^f \quad (10.124)$$

The field parameters \hat{F}_i^m , \hat{v}_i^m and \hat{v}_i^f can, by means of the expressions (10.123) and (10.124) be eliminated from Eq. (10.122). Introducing \hat{v}_{0i}^m as $\hat{v}_{0i}^m = \hat{F}_{\text{ext}} \cdot Y_{0i}^m$ the N unknown forces \hat{F}_j^f acting on the foundation are obtained from N equations defined as

$$\begin{aligned} \hat{v}_{0i}^m = \sum_{j=1}^N \left\{ \frac{Y_{ij}^m}{(Y_{12}^s)_j} \left[\sum_{k=1}^N \hat{F}_k^f \cdot Y_{kj}^f + \hat{F}_j^f \cdot (Y_{22}^s)_j \right] \right\} \\ + \frac{(Y_{11}^s)_i}{(Y_{12}^s)_i} \left[\sum_{j=1}^N \hat{F}_j^f \cdot Y_{ji}^f + \hat{F}_i^f \cdot (Y_{22}^s)_i \right] - \hat{F}_i^f \cdot (Y_{21}^s)_i \end{aligned} \quad (10.125)$$

If all point and transfer mobilities are known, from either predictions or measurements, the unknown field parameters can be solved. Once the forces have been determined, the velocities at each junction can be derived. However, the problem can be simplified considerably in both the low and high frequency regions.

10.14 Multi-point Coupling, Low and High Frequency Limits

Engine foundations are frequently build up by means of a number of beams and plates. In the low frequency region, well below the first natural frequency of any subsystem, global vibrations mainly determine the motion of the foundation. This means that the displacement at each engine foot is approximately the same. If all points on the foundation moves in phase when excited by an arbitrary force the point and transfer mobilities of the supporting structure are identical. For a real structure the mobilities are assumed to be equal, or $Y_{ij}^f \approx Y^f$. In the very low frequency region, an engine can be considered as a rigid mass, consequently $Y_{ij}^m \approx Y^m$. For a single and symmetric mounting arrangement, all mounts identical, the reacting forces from the identical springs are assumed to be the same on the foundation in the low frequency range. All these assumptions can be formulated as

$$Y_{ij}^f \approx Y^f; \quad Y_{ij}^m \approx Y^m; \quad F_i^f \approx F^f; \quad (Y_{kl}^s)_j = Y_{kl}^s \quad (10.126)$$

These simplifications and Eq. (10.125) yield

$$\begin{aligned} \hat{v}_0^m &= \frac{Y^m}{Y_{12}^s} \left(N^2 \cdot \hat{F}^f \cdot Y^f + N \cdot \hat{F}^f \cdot Y_{22}^s \right) \\ &+ \frac{Y_{11}^s}{Y_{12}^s} \left(N \cdot \hat{F}^f \cdot Y^f + \hat{F}^f \cdot Y_{22}^s \right) - \hat{F}^f \cdot Y_{21}^s \end{aligned} \quad (10.127)$$

Following the arguments in Sect. 10.12 the transfer mobilities for a spring are approximately equal in the low frequency region. This means that $Y_{ij}^s \approx Y^s$. Further, it can be assumed that $Y_{ij}^s \gg Y^m$ and $Y_{ij}^s \gg Y^f$ as also discussed in Sect. 10.12. This additional simplification in combination with Eq. (10.127) leads to

$$\hat{v}_0^m = (N \hat{F}^f)(Y^m + Y^f + Y^s/N); \quad N \hat{F}^f = \frac{\hat{v}_0^m}{Y^m + Y^f + Y^s/N} \quad (10.128)$$

The force induced by each mount on the foundation is F^f . The total force is consequently $N F^f$. This result, valid for N identical springs between mass and foundation, can be compared to the previously obtained solution derived for the single mount case. A system with N identical springs can be treated as a single mount system having the transfer mobility Y/N . The power spectrum of the acoustic power transmitted to the foundation is for $Y^s = Y_{\text{eq}}^s$ (compare Eq. (10.54))

$$G_{\Pi} = G_{v_0 v_0} \cdot \frac{\text{Re} Y^f}{\left| Y^m + Y^f + Y_{\text{eq}}^s/N \right|^2} \approx G_{v_0 v_0} \cdot \frac{\text{Re} Y^f}{\left| Y_{\text{eq}}^s/N \right|^2} = N^2 G_{v_0 v_0} \cdot \frac{\text{Re} Y^f}{\left| Y_{\text{eq}}^s \right|^2} \quad (10.129)$$

for $Y^s \gg Y^m$ and Y^f .

For increasing frequencies, the displacements on foundation and source are determined not only by global but also by local vibrations. The importance of the local vibrations increases as the frequency approaches the first natural frequencies of the subsystems. Well above the first natural frequencies for all subsystems the local vibration pattern dominates. This means that the correlation between displacements of points sufficiently well spaced is weak or insignificant. This can be expected when the distance between two observation points is of the same order of magnitude as the wavelength for bending waves in the structure. Using the same arguments, it can also be assumed that the forces from the springs reacting on source and foundation are uncorrelated. If the displacements of the various joints are uncorrelated the expressions defining the energy flow from source to foundation can be simplified considerably.

Returning to Eq. (10.125) and assuming N large, sums on the form $\sum_{k=1}^N \hat{F}_k Y_{kj}^f$ tend to zero due to the random phase of forces and mobilities. Thus, for high frequencies and N Eq. (10.125) is reduced to

$$\hat{v}_{0i}^m = \hat{F}_i^f \cdot \frac{(Y_{22}^s)_i (Y_{11}^s)_i - (Y_{21}^s)_i (Y_{12}^s)_i}{(Y_{12}^s)_i} = \hat{F}_i^f (Y_{\text{eq}}^s)_i; \quad \hat{F}_i = \frac{\hat{v}_{0i}^m}{(Y_{\text{eq}}^s)_i} \quad (10.130)$$

The definition of Y_{eq}^s given in Eq. (10.54) has been used. The power spectrum of the acoustic power transmitted to the foundation is

$$G_{\Pi} = \sum_{i=1}^N G_{v_{0i} v_{0i}} \cdot \frac{\text{Re} Y_i^f}{|(Y_{\text{eq}}^s)_i|^2} \approx N G_{v_0 v_0} \cdot \frac{\text{Re} Y^f}{|Y_{\text{eq}}^s|^2} \quad (10.131)$$

where Y^f is some average value of Y_i^f . The autospectrum of the velocity and the mobility of the foundation are defined in a similar way. In the high frequency region, the forces on the foundation are uncorrelated, whereas in the low frequency region the forces are correlated. The power transfer to the foundation is higher for the correlated than the uncorrelated forces.

10.15 Source Strength

In the previous sections some characteristics of receivers/foundations, mounts, and sources have been discussed. However well these structures are modelled also of the vibrational power of the source must be determined. For an acoustic source there are some straight forward techniques to determine its acoustic power. The output power of an acoustic source is only marginally dependent on surroundings. The acoustic power can readily be measured in free field or in a closed room as discussed in

Chap. 11. For a source of structure-borne sound, the measurement of its power is much more complicated than for an acoustic source. The vibration and operation of a structure-borne source depend on its mechanical coupling to other structures as previously discussed. For the very simple case investigated in Sect. 10.12, it was found that if the so called free velocity at a coupling point between a source and receiver was known then also the transmission of power to the foundation could be predicted once the point mobility of the source and the point mobility of the receiver at the coupling point had been determined. For the simple case illustrated in Fig. 10.21, the free velocity v_0 at the coupling point could be determined by decoupling the source/mass from any structural coupling. The free velocity could thereafter be measured while the source is in operation. There is a standard for the measurement of free velocities of sources Ref. [118]. The standard requires that the source can be decoupled from its foundation. Other methods are discussed in for example Ref. [119]. The free velocity can also be measured indirectly and determined based on the Eqs. (10.107) and (10.114) to (10.116). However, for this type of analysis mobilities for source, receiver, and mount must be known. Some inverse methods are discussed and summarized in Ref. [120]. In situ measurements of the blocked force of structure-borne sound are reported in Refs. [121, 122].

The free velocity of a source could be determined by an inverse technique. Assuming the point mobilities are known at the coupling point between source and receiver the free velocity could be determined by measuring the velocity at the coupling and using the expression (10.107). The source strength, or the free velocity v_0 , could also be determined based on the blocked velocity technique. Equation (10.107) gives the FT of the velocity v_m at a coupling point as function of the FT of the external force F_2 and the FT of the free velocity v_0 as

$$\hat{v}_m = \hat{v}_0 - \hat{F}_2 \cdot Y^m$$

Thus by applying an external force at the coupling point and by adjusting the force so that the FT of the velocity v_m is zero the FT of the free velocity is obtained as $\hat{v}_0 = \hat{F}_2 \cdot Y^m$. Both v_m and F_2 must be measured. Here the obvious problem is to measure the force while the velocity is zero or blocked.

For the very simple case illustrated in Fig. 10.21 it is possible, at least in theory, to determine the free velocity of a source in operation once the mobilities Y^m , Y^f , and Y_{eq}^s are known and the velocity v_m is measured. The FT of the free velocity v_0 is

$$\hat{v}_0 = \hat{v}_m \left(\frac{Y^f + Y_{\text{eq}}^s + Y^m}{Y^f + Y_{\text{eq}}^s} \right) \quad (10.132)$$

Alternatively, the velocity v_f of the foundation can be measured. In this case the free velocity reads

$$\hat{v}_0 = \hat{v}_f \left(\frac{Y^f + Y_{\text{eq}}^s + Y^m}{Y^f} \right) \quad (10.133)$$

In the first case, using the blocked force technique, it might not be possible to decouple the source in operation from its foundation. Furthermore, the energy flow from source to receiver is not only determined by the vertical motion at one point. In a real case, with N coupling points between source and receiver, $(6 \times N)^2$ mobilities must be determined. In addition, the free velocities and bending moments, velocities and rotations in three directions at each coupling point should be measured. Clearly, this is not realistic. Models have to be simplified. In practice this simplification can often be justified based on some knowledge of the characteristics of source and receiver. For example, machinery in buildings like electric motors for elevators are likely to be mounted on concrete slabs, a ship Diesel is mounted on a foundation build up of plate elements etc. Due to certain rules and regulations for buildings, ships, etc., supporting structures for machinery have certain characteristics in common. Thus by making measurements on a typical installation many transmission paths can be eliminated. So for example for a ship Diesel the velocities of the engine feet in the horizontal and vertical directions are typical of the same magnitude. However, the point mobility of the foundation is considerably higher in the vertical as compared to the horizontal directions. Energy transfer by means of bending moments is of less importance than by vertical forces. This type of observations for any class of equipment can drastically simplify any type of prediction. However, what is valid for one class of sources and receivers could be completely different from the coupling properties of another system.

This type of strategy has been exercised successfully by for example Moorhouse and Gibbs (Refs. [123, 124]) who demonstrate that the source strength, free velocity, and mobility of source could be measured in situ. However, the properties of the mounts supporting the machine must be known. The general technique can be illustrated by again considering the simple system of Fig. 10.21. If possible, the point mobility of the source at the coupling point between mount and source is measured in situ while the source is turned off. As discussed in Problem 10.6 the measured point mobility $(Y^m)_{\text{measured}}$ is

$$(Y^m)_{\text{measured}} = \frac{Y^m(Y^f + Y_{\text{eq}}^s)}{Y^f + Y_{\text{eq}}^s + Y^m} \quad (10.134)$$

In a similar way the measured point mobility of the foundation is obtained as

$$(Y^f)_{\text{measured}} = \frac{Y^f(Y^f + Y_{\text{eq}}^s)}{Y^f + Y_{\text{eq}}^s + Y^m} \quad (10.135)$$

If Y_{eq}^s is known the parameters Y^m and Y^f are determined from $(Y^m)_{\text{measured}}$ and $(Y^f)_{\text{measured}}$.

It may be preferable to obtain forces and moments acting on connections using inverse methods as discussed in Refs. [125, 126]. General techniques for the characterisation of structure-borne noise sources are for example presented in Refs. [119, 127, 128]. In practice, free or blocked boundary conditions can be difficult or

impossible to reproduce. In situ measurements can be the only possible alternative. Some examples are given in Refs. [123, 128–130]. Special cases like structure-borne sources in buildings and on ships are discussed in [115, 116, 119].

Problems

10.1 Two masses and three ideal springs are coupled as shown in Fig. 10.30. The masses 1 and 2 are excited by the forces $F_1 e^{i\omega t}$ and $F_2 e^{i\omega t}$, respectively. Determine the eigenfrequencies, eigenmodes, and displacement of the system.

10.2 A resilient mount is described as a simple rod. The mobilities of the rod are given by Eq. 6.96 as $Y_{11}^s = Y_{22}^s = -i\omega/[SEk_l \tan(k_l L)]$ and $Y_{12}^s = Y_{21}^s = -i\omega/[SEk_l \sin(k_l L)]$. Show that $Y_{12}^s/Y_{11}^s \rightarrow 1$ as the mass of the mount tends to zero. Determine also the limiting value of Y_{eq} as frequency or mass tends to zero.

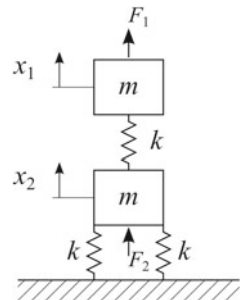
10.3 Determine the moment mobility for a homogeneous and infinite beam.

10.4 A cylindrical and symmetric rubber mount has the point and transfer mobilities $Y_{11} = Y_{22}$ and $Y_{12} = Y_{21}$. A stiff mass M is mounted to each end of the rubber element. The rubber element plus the two stiff masses constitute a symmetric mount with the point and transfer mobilities $Y'_{11} = Y'_{22}$ and $Y'_{12} = Y'_{21}$. These quantities are measured for the complete mount, mass-rubber-mass. Determine based on these measured quantities the point and transfer mobilities $Y_{11} = Y_{22}$ and $Y_{12} = Y_{21}$ for the rubber mount without the masses.

10.5 A stiff mass M is mounted on a resilient mount, which in turn is mounted on an infinite steel plate with the thickness h . Determine the insertion loss of the mount as function of the plate thickness h . Model the spring as a rod, length L and wavenumber $k_l = k_{l0}(1 - i\eta/2)$.

10.6 A source–receiver system is shown in Fig. 10.21. The source is turned off. The point mobility of the source is measured at the coupling point between the mount and the source. This point mobility is denoted $(Y_m)_{\text{measured}}$. In a similar way the point

Fig. 10.30 Two coupled masses mounted on a stiff foundation



mobility $(Y_f)_{\text{measured}}$ on the foundation at the coupling point between mount and foundation is measured. Determine $(Y_m)_{\text{measured}}$ and $(Y_f)_{\text{measured}}$.

10.7 A source–receiver system is shown in Fig. 10.21. The source is turned off. The point mobility of the source is measured at the coupling point between the mount and the source. This point mobility is denoted $(Y_m)_{\text{measured}}$. In a similar way the point mobility $(Y_f)_{\text{measured}}$ on the foundation at the coupling point between mount and foundation is measured. With the source in operation the velocities v_m and v_f are measured. Determine the free velocity v_0 of the source as function of the four measured properties.

10.8 Equation (10.110) gives the power input to the foundation as function of the mobility of the source Y^m and the mobility Y^f of the foundation as

$$\text{Re}G_{\Pi} = G_{v_0 v_0} \frac{\text{Re}(Y^f)}{|Y^f + Y^m|^2}$$

Show that the maximum energy transfer from source/mass to receiver/foundation is when $Y^f = (Y^m)^*$.

10.9 Show that if a model is built to scale 1:Z then the frequency ratio between full scale and model scale is also 1:Z.

10.10 Use the Bishop model to determine the wavenumber for displacement along the axis of a rubber mount. Determine also σ_x along the axis.

Chapter 11

Waves in Fluids

Vibrating structures radiate noise. The radiated power is determined by the acoustical coupling between the vibrating structure and the surrounding fluid. The resulting acoustic field induced by the vibrating structure is also influenced by reflecting surfaces and variations, for example, temperature and velocity in the fluid. These problems are encountered when making outdoor noise measurements. For example, the noise generated by a traveling car is reflected on the road surface. In addition to reflection effects, the measured noise from the car is influenced by a certain noise attenuation in air and over ground. Wind and temperature can influence the direction of the propagation of the sound waves and the recorded noise level. For indoor measurements, the acoustical field induced by a source in a closed room depends on the acoustical characteristics of the room as well the distance to the source.

These problems are discussed in this chapter. First, the equation governing the propagation of waves in fluids is introduced. Noise radiation from elementary sources as well as the effects of reflecting boundaries is discussed. The interactions between vibrating plates and fluids are investigated in Chaps. 12 and 13.

11.1 Wave Equation

The basic equation describing the propagation of waves in a fluid is based on a number of assumptions. An idealized nonviscous fluid is initially assumed to be at rest. The ambient temperature T_0 , pressure p_0 , and density ρ_0 are constant with respect to time and space. A disturbance caused, for example, by a vibrating solid will cause a certain motion or waves in the fluid, which in turn will cause pressure fluctuations. The resulting wave motion in the fluid has certain similarities with the motion of masses and springs coupled along a straight line. The motion of a mass in the chain creates a tension in the springs in the same way as the displacement of a particle in a fluid will cause a pressure fluctuation. The equation governing the propagation of waves in gases is based on the principles of conservation of mass and momentum as well as the equation of state for a perfect gas.

Conservation of Mass

The conservation of mass within a volume V implies that the variation of mass as function of time is equal to the mass flow out of the control volume. Initially, it is assumed that no mass is created within the control volume. The total density ρ_t of the fluid is equal to the sum of the initial density ρ_0 and any small perturbations $\rho(\mathbf{r}, t)$, which can vary in time and space. The conservation of mass within the control volume requires that

$$\frac{\partial}{\partial t} \int_V \rho_t dV + \int_S \rho_t \mathbf{v} \cdot \mathbf{n} dS = 0 \quad (11.1)$$

The particle velocity is given by the vector \mathbf{v} . The unit vector \mathbf{n} is perpendicular to the surface S of the control volume and pointing outwards. Equation (11.1) in combination with Gauss' Integral Theorem gives

$$\frac{\partial}{\partial t} \int_V \rho_t dV + \int_S \rho_t \mathbf{v} \cdot \mathbf{n} dS = \int_V \left[\frac{\partial \rho_t}{\partial t} + \text{div}(\rho_t \mathbf{v}) \right] dV = 0 \quad (11.2)$$

These expressions lead to the equation of continuity for a fluid free of sources. For the integral (11.2) to be zero, the expression inside the bracket must also be equal to zero. Thus

$$\frac{\partial \rho_t}{\partial t} + \text{div}(\rho_t \mathbf{v}) = 0 \quad (11.3)$$

The density fluctuation $\rho(\mathbf{r}, t)$ caused by some disturbance, is small as compared to the steady-state density ρ_0 . It follows that $\rho_0 \gg \rho$. The particle velocity is caused by a disturbance in the fluid, which initially is at rest. This means that the field parameters v and ρ are of the same order of magnitude with respect to ρ_0 . The second part of Eq. (11.3) can, when neglecting second-order terms, be written as

$$\text{div}(\rho_t \mathbf{v}) = \mathbf{grad}(\rho_0 + \rho) \cdot \mathbf{v} + (\rho_0 + \rho) \text{div} \mathbf{v} = \mathbf{grad}(\rho) \cdot \mathbf{v} + (\rho_0) \text{div} \mathbf{v} \approx \rho_0 \text{div} \mathbf{v}$$

The linearized equation of continuity is thus

$$\frac{\partial \rho}{\partial t} + \rho_0 \cdot \text{div}(\mathbf{v}) = 0 \quad (11.4)$$

Conservation of Momentum

Returning to the control volume. The pressure on the surface S of the volume is $p(\mathbf{r}, t)$. The density of the fluid inside the volume is as before $\rho_0 + \rho(\mathbf{r}, t)$ and the particle velocity is defined by $\mathbf{v}(\mathbf{r}, t)$. In the absence of external forces Newton's second law yields

$$\frac{d}{dt} \int_V \rho_t \mathbf{v} dV + \int_S p \mathbf{n} dS = 0$$

The vector \mathbf{n} is pointing out from the control volume. The pressure p is positive in compression. The divergence theorem in combination with the integral equation leads to

$$\int_V dV \left[\frac{d}{dt}(\rho_t \mathbf{v}) + \mathbf{grad} p \right] = 0 \quad (11.5)$$

The total or material time derivative of a function $f(\mathbf{r}, t)$ is, in Cartesian coordinates, defined as

$$\frac{df}{dt} = \frac{\partial f}{\partial t} + \frac{\partial f}{\partial x} \frac{dx}{dt} + \frac{\partial f}{\partial y} \frac{dy}{dt} + \frac{\partial f}{\partial z} \frac{dz}{dt} = \frac{\partial f}{\partial t} + \mathbf{grad} f \cdot \mathbf{v}$$

This expression in combination with Eq. (11.5) yields

$$\frac{\partial}{\partial t}(\rho_t \mathbf{v}) + \mathbf{v} \cdot \text{div}(\rho_t \mathbf{v}) + \mathbf{grad} p = 0 \quad (11.6)$$

A linearization by neglecting higher order terms gives

$$\rho_0 \frac{\partial}{\partial t}(\mathbf{v}) + \mathbf{grad} p = 0 \quad (11.7)$$

In the absence of a flow, this is the equation of motion relating the particle velocity \mathbf{v} and the fluctuating pressure p in a nonviscous fluid.

The curl of Eq. (11.7) gives

$$\rho_0 \frac{\partial}{\partial t}(\nabla \times \mathbf{v}) + \nabla \times \mathbf{grad} p = 0$$

However, $\nabla \times \mathbf{grad} p$ is always equal to zero if p is a continuous function. Consequently, the term $\nabla \times \mathbf{v}$ must also be equal to zero. Therefore, the particle velocity, as given by the vector \mathbf{v} , can be defined by means of a velocity potential as

$$\mathbf{v} = \mathbf{grad} \Phi \quad (11.8)$$

The curl of the velocity vector or of the gradient of a scalar is equal to zero as required. The definition (11.8) of the velocity potential leads to that the pressure p can be derived directly from the velocity potential. In the absence of a flow, the definition (11.8) and the basic equation (11.7) give the pressure as

$$p = -\rho_0 \frac{\partial \Phi}{\partial t} \quad (11.9)$$

It is often convenient to describe an acoustic field by means of a velocity potential rather than by the pressure function or particle velocity vector.

Compressibility

Any fluid or solid has a certain volume or bulk elasticity. For solids, the bulk elasticity K was defined in Sect. 3.1. The bulk elasticity was also discussed for rubber like materials in Sect. 10.5. However, for fluids the compressibility concept is generally preferred. The compressibility is the inverse of the bulk modulus K . A volume V of a fluid is changed by the amount ΔV when exposed to an external small pressure Δp as

$$\frac{\Delta V}{V} = -\Delta p \cdot \kappa_T \quad (11.10)$$

The parameter κ_T is the isothermal compressibility of the fluid. The compression is assumed to be adiabatic, i.e., the entropy of the fluid is constant. Equation (11.10) can also be interpreted in an alternative way. Thus, if a closed volume V is changed by the amount ΔV , the pressure inside the control volume is increased by Δp . For compression, ΔV is negative resulting in a pressure increase inside the volume.

The volume V of the fluid is equal to the mass M of the control volume divided by the total density ρ_t of the fluid or $V = M/\rho_t$. Since $\rho_t = \rho_0 + \rho$ and $\rho \ll \rho_t$ it follows that

$$\Delta V = -\frac{M}{\rho_t^2} \Delta \rho_t = -\frac{V}{\rho_t} \Delta \rho_t \approx -\frac{V}{\rho_0} \Delta \rho \quad (11.11)$$

The increase $\Delta \rho$ of the density is caused by the reduction ΔV of the control volume. The Eqs. (11.10) and (11.11) lead to

$$\frac{\partial \rho}{\partial p} = \rho_0 \cdot \kappa_T \quad (11.12)$$

For an adiabatic process and no flow, the equation of continuity (11.4) is, by introducing Eq. (11.12), obtained as

$$\kappa_T \cdot \frac{\partial p}{\partial t} + \operatorname{div} \mathbf{v} = 0 \quad (11.13)$$

The compressibility for a perfect gas can be obtained from the equations of state. For frequencies less than approximately 10^9 Hz, adiabatic compression in a gas can be assumed. For this condition, there is no heat exchange within the gas. Expressed in another way; in a section where the gas is compressed and therefore, the temperature increased, the heat transfer to an adjoining area with decompressed gas is neglected. For this particular type of process, the total pressure p_t and the total density ρ_t of the gas are related as

$$p_t = C \cdot \rho_t^\gamma \quad (11.14)$$

In this expression C is a constant and the ratio between the specific heat for the gas under constant pressure and the specific heat for constant volume, i.e., $\gamma = c_p/c_v$. Since $p_t = p + p_0$ and $\rho_t = \rho + \rho_0$ it follows from (11.14) that

$$\frac{\partial \rho}{\partial p} = \frac{1}{\gamma} \left[\frac{\rho + \rho_0}{p + p_0} \right] = \frac{1}{\gamma} \cdot \frac{\rho_t}{p_t} \quad (11.15)$$

For a perfect one atomic gas, He, the ratio γ between the specific heats is equal to 5/3. For air γ is 7/5 and for gases with several atoms γ is 4/3. The compressibility κ_T for an ideal gas is obtained from the Eqs. (11.12) and (11.15) as $\kappa_T = 1/(\gamma p_t)$. For a perfect gas temperature T , density ρ_t , and pressure p_t are related as

$$p_t = \frac{\rho_t \cdot T \cdot R}{\mathcal{M}} \quad (11.16)$$

In this expression T is the absolute temperature of the gas in degrees Kelvin, R is the universal gas constant, which is equal to 8.314 J/(degree mol), and \mathcal{M} the molecular mass (kg) of the gas, i.e., the mass of one molecule. The compressibility $\kappa_T = 1/(\gamma p_t)$ for an ideal gas is from (11.16) obtained as

$$\kappa_T = \frac{\mathcal{M}}{\gamma R T \rho_0} \quad (11.17)$$

Again, the total density is approximated by ρ_0 .

Conservation of momentum and conservation of mass led to the Eqs. (11.17) and (11.13), which are

$$\rho_0 \frac{\partial \mathbf{v}}{\partial t} + \mathbf{grad} p = 0; \quad \kappa_T \frac{\partial p}{\partial t} + \text{div} \mathbf{v} = 0$$

The velocity dependent terms can be canceled by taking the divergence of the first expression and subtracting the time derivative of the second expression. The result is the wave equation

$$\nabla^2 p - \frac{1}{c^2} \frac{\partial^2 p}{\partial t^2} = 0; \quad c = \sqrt{\frac{1}{\kappa_T \rho_0}} = \sqrt{\frac{\gamma R T}{\mathcal{M}}} \quad (11.18)$$

Equations (11.15), (11.16) and (11.18) give $\partial \rho / \partial p = 1/c^2$.

In a flow, the vector velocity of the fluid being \mathbf{u} , the simple wave equation has to be modified. In a flow, stationary observer, the time derivate $\partial p / \partial t$ has to be replaced by $\partial p / \partial t + \mathbf{u} \cdot \mathbf{grad} p$ as discussed above. The resulting wave equation giving the pressure p in a fluid moving with the vector velocity \mathbf{u} is given as

$$\nabla^2 p - \frac{1}{c^2} \left(\frac{\partial}{\partial t} + \mathbf{u} \cdot \mathbf{grad} \right)^2 p = 0$$

Since the pressure can be defined by means of the velocity potential the wave equation can, in a fluid with no flow, be written as

Table 11.1 Acoustic properties of some fluids at 0°C and 1 atm.

Fluid	Density (kg/m ³)	Velocity (m/s)
	ρ_0	c_0
Air	1.29	331
Argon	1.78	319
CO ₂	1.98	258
He	0.18	970
H ₂	0.09	1270
O ₂	1.43	317
Pure water	1000	1430
Sea water	1023	1447
Benzene	880	1320
Glycerine	1260	1920

$$\nabla^2 \Phi - \frac{1}{c^2} \frac{\partial^2 \Phi}{\partial t^2} = 0; \quad c = \sqrt{\frac{1}{\kappa_T \rho_0}} = \sqrt{\frac{\gamma RT}{\mathcal{M}}}$$

$$p = -\rho_0 \frac{\partial \Phi}{\partial t}; \quad \mathbf{v} = \mathbf{grad} \Phi \quad (11.19)$$

According to the discussions in Chap. 3, the parameter c can be identified as the speed of acoustic waves in the fluid. Some properties of fluids are listed in Table 11.1.

For moderate ranges of atmospheric pressure P in atm. and temperature T in degrees Kelvin, the density of and the velocity in a gas are approximately equal to $\rho = \rho_0 P(273/T)$ and $c = c_0 \sqrt{T/273}$.

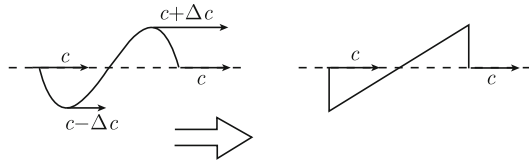
The speed of sound inside a shock wave is a special case. The speed of sound c is also influenced by a high pressure inside the wave. The speed of sound for this type of wave is according to Ref. [23]

$$c = c_0 \sqrt{1 + \frac{(\gamma + 1)(P - P_0)}{2\gamma P_0}}$$

where P_0 is the ambient pressure. For an overpressure inside the shock wave, the speed of sound is increased. For a pressure lower than the ambient, the speed is decreased. Consequently, the shape of the wave is deformed into an N-wave as indicated in Fig. 11.1. Eventually, due to losses, the sharp front will be rounded as the wave propagates over a certain distance. A shock or N-wave can be created by an aircraft in super-sonic flight.

The presence of gas or vapor in water can drastically reduce the speed of sound. As pointed out in Ref. [132] the speed of sound is about 1430 m/s in pure water and about 340 m/s in air. In an air-water mixture the speed of sound can be reduced to 20 m/s. The speed of sound in a liquid depends on the amount of gas in the liquid, pressure, temperature, and frequency and for small bubbles also on the radius of the

Fig. 11.1 Formation of an N-wave



bubbles as shown by Kieffer in Ref. [132]. For any laboratory experiment in water it should be ensured that gas bubbles have vanished before tests are started. This process could take a few days. In seawater, the speed of sound varies with small temperature fluctuations as $c = c_0 + 317(T - 273)$.

The equation governing pure longitudinal waves in infinite solids is on the same form as the equation for waves in fluids. Both are compression waves. In the first case, the displacement due to longitudinal waves in a solid is given by a scalar potential as defined in Sect. 4.1. This follows a traditional definition in solid mechanics. For waves in fluids, the particle velocity vector is obtained from a velocity potential as given in Eq. (11.8). This approach could also have been used in Sect. 4.1. It is only a matter of convenience which of the two definitions is used.

11.2 Energy and Intensity

The kinetic energy contained in a volume V of a fluid is given as

$$\mathcal{T} = \int \frac{\rho_0}{2} |\mathbf{v}|^2 dV = \int \frac{\rho_0}{2} |\mathbf{grad}\Phi|^2 dV \tag{11.20}$$

Potential energy is stored in a fluid when the fluid is compressed. The potential energy \mathcal{U} stored in the gas volume is equal to the work carried out to compress the gas of volume V to a volume $V - \Delta V$. During compression, the pressure inside the volume increases from p_0 to $p_0 + p$. The work performed or the stored potential energy is $\Delta\mathcal{U} = p\Delta V$, or in integral form

$$\mathcal{U} = - \int p dV$$

The sign is changed since the pressure p is positive and the integration is performed from a larger to a smaller volume. Considering the expression (11.10), which in the limit, can be written as $dV/dp = -V \cdot \kappa_T$, the potential energy stored in a volume V of a fluid with the overpressure p with respect to the ambient pressure is

$$\mathcal{U} = - \int p dV = \int p \kappa_T V dp = \kappa_T p^2 V / 2 \tag{11.21}$$

The compressibility κ_T is from Eq. (11.18) obtained as $\kappa_T = 1/(\rho_0 c^2)$. The potential energy per unit volume is thus

$$\mathcal{U}_V = \frac{\mathcal{U}}{V} = \frac{p^2}{2\rho_0 c^2} = \frac{\rho_0}{2c^2} \left(\frac{\partial \Phi}{\partial t} \right)^2 \quad (11.22)$$

The intensity, or rather the intensity vector, resulting from a wave motion in the fluid is defined as

$$\mathbf{I} = p \cdot \mathbf{v} \quad (11.23)$$

where p is the pressure and \mathbf{v} the particle velocity vector in the fluid.

Using complex notations and assuming a time dependence $\exp(i\omega t)$ the time averages of kinetic and potential energies per unit volume and the time average of the intensity in the fluid are given by

$$\begin{aligned} \bar{\mathcal{T}}_v &= \frac{\rho_0}{4} |\mathbf{v}|^2 = \frac{\rho_0}{4} |\mathbf{grad} \Phi|^2; & \bar{\mathcal{U}}_v &= \frac{|p|^2}{4\rho_0 c^2} = \frac{\rho_0}{4c^2} \left| \frac{\partial \Phi}{\partial t} \right|^2 = \frac{\omega^2 \rho_0 |\Phi|^2}{4c^2} \\ \bar{\mathbf{I}} &= \text{Re} \left(\frac{p \cdot \mathbf{v}^*}{2} \right) = -\text{Re} [i\omega \rho_0 \Phi (\mathbf{grad} \Phi)^*] \end{aligned} \quad (11.24)$$

In the last definition above, the intensity vector is set to equal the real part of the expression $p \cdot \mathbf{v}^*/2$. This part is referred to as the active intensity. The imaginary part of the intensity vector is the reactive intensity. Sound intensity in general and measurement procedures are discussed extensively in a number of papers by Finn Jacobsen, see, for example, Ref. [133]. The subject is also treated in a book by Fahy Ref. [134].

11.3 Losses

The wave equation as presented in Sect. 11.1 was derived assuming that the losses in the fluid could be neglected. In general, the losses in, for example, air are small. However, when sound propagates over large distances in infinite or semi-infinite space or in a flow through narrow openings or close to boundaries, the losses can no longer be neglected. In infinite space, the losses are due to a number of mechanisms in the fluid itself. In air the losses are caused by viscosity, heat conduction, diffusion of oxygen and nitrogen molecules, heat radiation, and molecular losses. The effect of viscosity in the equation of motion in a fluid leading up to the Navier-Stokes equation is discussed in for example Refs. [23, 135]. By maintaining higher order terms in the equation of conservation of momentum the Lighthill equation [136] is obtained as discussed in, for example, Refs. [137, 138]. In the Lighthill equation a source term, due to nonlinear effects, is added to the simple wave equation (11.18). See Problem 11.3. However, the simple wave equation (11.19) is sufficiently accurate for the applications discussed in this text.

In general, when sound propagates over long distances the molecular losses dominate. The molecules in a gas vibrate as coupled simple mass-spring systems with dissipative springs. The losses are consequently frequency dependent. The losses also depend on the type of molecules present in the gas. For losses in air, the humidity or number of water molecules per volume of the gas is an important parameter. In addition to humidity, the losses are functions of temperature, atmospheric pressure, and frequency.

The losses, if small, can be included in the wave equation by letting the compressibility be a complex quantity. This is in accordance with the introduction in Sect. 3.2 of a complex modulus of elasticity or for that matter a complex spring constant as in Sect. 1.6. Following this basic idea, the bulk modulus K of a fluid can be written as $K = K_0(1 + i\delta)$ where K_0 is a real quantity and δ the loss factor in the fluid. The compressibility κ or rather κ_T is for $\delta \ll 1$

$$\kappa = 1/K = 1/[K_0(1 + i\delta)]$$

For small losses the speed of sound in the fluid is obtained from Eq. (11.18) as

$$\begin{aligned} c &= \sqrt{1/(\kappa\rho_0)} = \sqrt{K/\rho_0} = \sqrt{K_0(1 + i\delta)/\rho_0} \\ &\approx \sqrt{K_0/\rho_0}(1 + i\delta/2) = c_0(1 + i\delta/2) \end{aligned} \quad (11.25)$$

The corresponding wavenumber k for waves propagating in the fluid is thus

$$k = \omega/c = \omega/[c_0(1 + i\delta/2)] \approx \omega/c_0(1 - i\delta/2) = k_0(1 - i\delta/2) \quad (11.26)$$

The velocity potential defining a plane wave propagating in the direction of the positive x -axis in a coordinate system, is assuming a time dependence $\exp(i\omega t)$, given by

$$\Phi = A \cdot e^{i(\omega t - kx)} = A \cdot e^{i(\omega t - k_0x) - k_0x\delta/2}$$

where A is the amplitude of the wave. The corresponding time averaged intensity is obtained from Eq. (11.24) as

$$\bar{I}_x = \frac{\rho_0\omega^2}{2c_0} |\Phi|^2 e^{-k_0x\delta}$$

The intensity is consequently being attenuated as the wave propagates in the fluid. The attenuation α in dB per 100m due to atmospheric attenuation is

$$\alpha = 100 \cdot k_0 \cdot \delta \cdot 10 \log e \approx 8.03 \cdot f \cdot \delta \quad (11.27)$$

where f is the frequency (Hz) and δ the loss factor. The attenuation parameter α as function of temperature and humidity is presented in Figs. 11.2 and 11.3 for the frequencies 1 and 2.5 kHz, respectively. For each frequency, α is shown as function

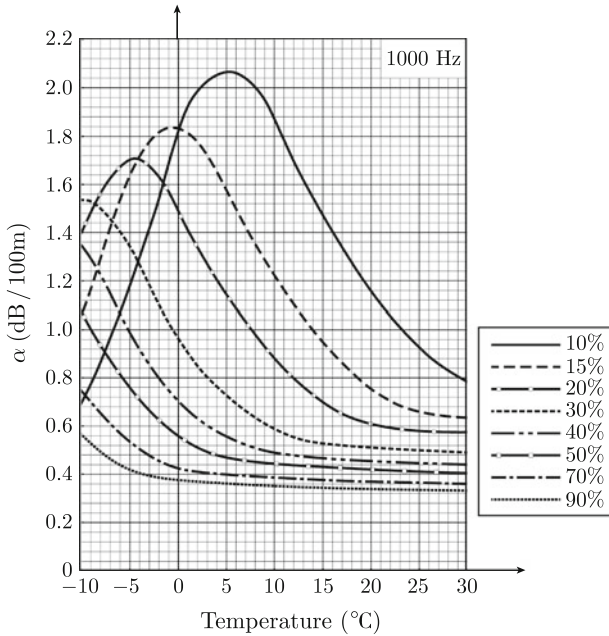


Fig. 11.2 Attenuation parameter α (dB per 100m) as function of humidity and temperature at 1 kHz. From Ref. [139]

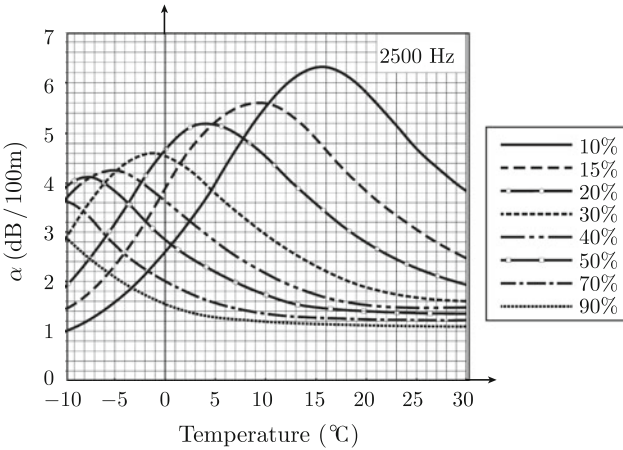


Fig. 11.3 Attenuation parameter α (dB per 100m) as function of humidity and temperature at 2.5 kHz. From Ref. [139]

of humidity and temperature. The results are from Ref. [139]. In this reference, sound propagation in the atmosphere is discussed in detail.

Attenuation of sound waves in the atmosphere is discussed in for example Ref. [140]. Sound absorption in air is tabulated in Ref. [141].

11.4 Basic Solutions to Wave Equation

There are three basic solutions to the wave equation (11.19) discussed in this section. The first solution describes the propagation of a plane wave, which has the same direction of propagation everywhere in space. The wavefronts are perpendicular to the direction of propagation. The second solution describes the field induced by a pulsating sphere assuming spherical symmetry. As the diameter of such a source is approaching zero the limiting case is a so-called ideal pointsource. The last example discussed in this section describes the field radiated by the breathing mode of an infinite cylinder.

In a Cartesian coordinate system, a plane propagating wave with time dependence $\exp(i\omega t)$ is defined by means of a velocity potential Φ as

$$\Phi(x, y, z, t) = A \cdot \exp[i(\omega t - k_x x - k_y y - k_z z)] = A \cdot \exp[i(\omega t - \mathbf{k}\mathbf{r})] \quad (11.28)$$

The velocity potential must satisfy the wave equation (11.19). Consequently,

$$k_x^2 + k_y^2 + k_z^2 = k^2 = (\omega/c)^2$$

The direction of propagation of the wave is defined by its intensity vector. According to Eqs. (11.8) and (11.9) the pressure and particle velocity due to the wave motion are

$$p = -i\omega\rho_0 A \cdot \exp[i(\omega t - \mathbf{k}\mathbf{r})]; \quad \mathbf{v} = -i\mathbf{k} \cdot A \cdot \exp[i(\omega t - \mathbf{k}\mathbf{r})] \quad (11.29)$$

From Eq. (11.24) the time average of the intensity vector is obtained as

$$\bar{\mathbf{I}} = \omega\rho_0 \mathbf{k} \cdot |A|^2 / 2 \quad (11.30)$$

Consequently, the wavenumber vector $\mathbf{k} = (k_x, k_y, k_z)$ determines the direction of propagation. For a plane wave traveling in the direction shown in Fig. 11.4 the components of the wavenumber vector are

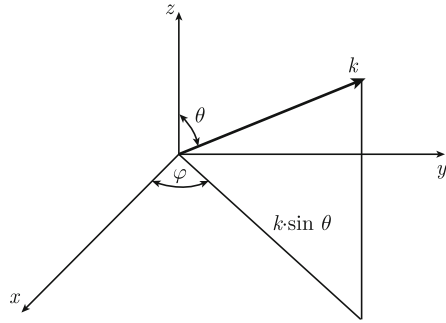
$$k_x = k \cdot \sin \theta \cdot \cos \varphi; \quad k_y = k \cdot \sin \theta \cdot \sin \varphi; \quad k_z = k \cdot \cos \theta \quad (11.31)$$

For a plane wave the ratio between pressure and particle velocity, in the direction of propagation, is equal to $\omega\rho_0/k = \rho_0 c$. This quantity is referred to as the wave impedance. For a plane wave propagating along the x -axis, the intensity in the direction of propagation, can be expressed as function of pressure or particle velocity as

$$\bar{I}_x = |\bar{p}|^2 / (\rho_0 c) = |\bar{v}|^2 \cdot (\rho_0 c)$$

For a plane wave traveling along the positive x -axis in a fluid not at rest but moving along the x -axis with velocity u_x the wavenumber is reduced to $k_+ = k(1 - u_x/c)$. It is assumed that $u_x \ll c$. For a wave travelling in the opposite direction the wavenumber

Fig. 11.4 Wave propagating in three-dimensional space. Definition of space angel



is $k_- = k(1 + u_x/c)$. The result is discussed in Problem 11.1. The ratio between the velocity of the fluid and the speed of sound is often referred to as the Mach number. This quantity can be somewhat deceptive. If, for example, an aircraft is said to fly at Mach 0.8, its relative speed cannot be determined if not the speed of sound is known. As previously discussed, the speed of sound depends on air temperature, which in turn depends on the altitude of the flight path.

There is an interesting example illustrating the consequences of the wavenumber being dependent on the flow velocity. The air cavity of a car tyre has certain natural frequencies. For a standard tyre, the first few natural frequencies are 224, 447, and 671 Hz. At these frequencies, the tyre is acoustically stiff since the losses inside the tyre are very small. The tyre vibrations induced by the contact between tyre and road surface are readily transmitted to the car body at these frequencies. The result is that pure tone noise is radiated into the car at the natural frequencies of the tyre cavity. However, when the car is moving the air inside the tyre is rotating. The acoustic waves induced at the contact point between tyre and road travels at different speeds, the wave traveling in the rotational direction of the wheel being the fastest. Due to the rotation of the wheel, there is a frequency split of the natural frequencies of the cavity. The frequency split is proportional to velocity of the car. At, for example, 60 km/h the frequency split is of the order 9 Hz for a standard tyre. The phenomenon is discussed in Ref. [142] and in Problem 11.4 at the end of this chapter. In the report Ref. [142] it is also demonstrated how to effectively reduce this type of noise.

A sound source with spherical symmetry, like a simple pulsating sphere, will generate a motion and thus a sound field in a loss free fluid. The resulting velocity potential, assuming spherical symmetry, should satisfy the wave equation in spherical coordinates

$$\frac{\partial^2 \Phi}{\partial r^2} + \frac{2}{r} \frac{\partial \Phi}{\partial r} - \frac{1}{c^2} \frac{\partial^2 \Phi}{\partial t^2} = 0 \quad (11.32)$$

By considering the product $r\Phi$ as a function this equation can be rearranged as

$$\frac{\partial^2 (r\Phi)}{\partial r^2} - \frac{1}{c^2} \frac{\partial^2 (r\Phi)}{\partial t^2} = 0 \quad (11.33)$$

Solutions to this type of wave equation were discussed in Sect. 3.4. The general solution to the Eq. (11.33) is

$$\Phi(r, t) = f(t - r/c)/r + g(t + r/c)/r \quad (11.34)$$

where f and g are two arbitrary functions. The first part of the velocity potential describes a wave propagating away from a source located at the origin. The second part describes a wave converging on the origin. For a source in unbounded space, there will be no converging field. Sommerfeld, in Ref. [143], formulated the radiation condition, which must be satisfied for waves to exist in free space. The velocity potential induced in an unbounded medium must satisfy the condition

$$\lim_{r \rightarrow \infty} \left\{ r \left[\frac{\partial \Phi}{\partial r} + \frac{1}{c} \frac{\partial \Phi}{\partial t} \right] \right\} = 0 \quad (11.35)$$

The expression $g(t + r/c)/r$, which is part of the general solution (11.34) does not satisfy the Sommerfeld condition. In an unbounded medium, the velocity potential induced by a pulsating sphere is completely described by an outgoing wave $f(t - r/c)/r$ where r is the distance to the source as long as (11.35) is satisfied.

For a source like a pulsating sphere, the particle velocity in the fluid at the surface of the source must be the same as the surface velocity of the sphere. For a sphere of radius r_0 and with a surface velocity $u_0 \cdot \exp(i\omega t)$ the boundary condition is

$$\frac{\partial \Phi}{\partial r} = \frac{1}{r} \frac{\partial f(t - r/c)}{\partial r} - \frac{f(t - r/c)}{r^2} = u_0 \cdot \exp(i\omega t) \quad \text{for } r = r_0 \quad (11.36)$$

Considering that the time dependence of the surface velocity of the sphere is $\exp(i\omega t)$ and the general solution for an outgoing wave, the velocity potential in the fluid is on the form

$$\Phi(r, t) = \frac{A}{r} \cdot \exp[i(\omega t - kr)]$$

where $k = \omega/c$ is the wavenumber in the fluid. The boundary condition (11.36) yields

$$A = -\frac{u_0 \cdot r_0^2 \cdot \exp(ikr_0)}{1 + ikr_0}$$

The pressure $p = -\rho_0 \partial \Phi / \partial t$ and particle velocity $v_r = \partial \Phi / \partial r$ in the radial direction are for $r \geq r_0$ obtained as

$$\begin{aligned} v_r(r, t) &= \frac{u_0 r_0^2 (1 + ikr)}{r^2 (1 + ikr_0)} \cdot \exp\{i[\omega t - k(r - r_0)]\} \\ p(r, t) &= \frac{i\omega \rho_0 u_0 r_0^2}{r(1 + ikr_0)} \cdot \exp\{i[\omega t - k(r - r_0)]\} \end{aligned} \quad (11.37)$$

The ratio between pressure and particle velocity is from these expressions obtained as

$$\frac{p}{v_r} = \rho_0 c \cdot \frac{\exp(i\varphi)}{\sqrt{1 + [c/(\omega r)]^2}}; \quad \varphi = \arctan[c/(\omega r)] \quad (11.38)$$

The pressure and velocity are not in phase. The ratio p/v_r for a spherical wave is less than $\rho_0 c$, which is the wave impedance for a plane wave. However, at large distances from the source the wave impedance for a spherical wave approaches that for a plane wave. At the same time, the phase difference between pressure and velocity tends to zero as the distance r to the source is increased.

In order to characterize the acoustical source strength, it is convenient to introduce the volume velocity U of the source as

$$U(t) = U_0 \cdot \exp(i\omega t) = 4\pi r_0^2 u_0 \cdot \exp(i\omega t) \quad (11.39)$$

The volume velocity defines the rate of flow away from the surface of the sphere. The particle velocity and pressure can be expressed as functions of the volume velocity by combining the results (11.37) and (11.39). Thus

$$\begin{aligned} v_r(r, t) &= \frac{U_0(1 + ikr)}{4\pi r^2(1 + ikr_0)} \cdot \exp\{i[\omega t - k(r - r_0)]\} \\ p(r, t) &= \frac{i\omega\rho_0 U_0}{4\pi r(1 + ikr_0)} \cdot \exp\{i[\omega t - k(r - r_0)]\} \end{aligned} \quad (11.40)$$

The time average of the intensity I_r and the time average of the total power Π radiated by the source are

$$\begin{aligned} \bar{I}_r &= \text{Re}(p \cdot v_r^*)/2 = \frac{\omega^2 \rho_0 |U_0|^2}{32c\pi^2 r^2 [1 + (kr_0)^2]} \\ \bar{\Pi} &= 4\pi r^2 \bar{I}_r = \frac{\omega^2 \rho_0 |U_0|^2}{8c\pi [1 + (kr_0)^2]} \end{aligned} \quad (11.41)$$

For an ideal point source with a finite volume velocity $U(t) = U_0 \cdot \exp(i\omega t)$ the Helmholtz number kr_0 is set to equal zero. The resulting velocity potential for the ideal point source is given by

$$\Phi(r, t) = \frac{U_0}{4\pi r} \cdot \exp[i(\omega t - kr)] \quad (11.42)$$

Equation (11.42) can be presented in a more general way. Suppose that the surface of a sphere, radius r_0 , is pulsating with a surface velocity $u(t)$. The rate of flow of air away from the sphere is in every direction $Q(t) = 4\pi r_0^2 u(t)$. The velocity potential outside the sphere is according to (11.34) and (11.35) given by $\Phi = A \cdot f(t - r/c)/r$.

On the boundary of the sphere, the particle velocity in the fluid is the same as the surface velocity of sphere. The boundary condition (11.36) gives for $kr_0 \ll 1$

$$\Phi(r, t) = -\frac{Q_0(t - r/c)}{4\pi r}; \quad p(r, t) = -\rho_0 \frac{\partial \Phi}{\partial t} = \frac{\rho_0 Q_0'(t - r/c)}{4\pi r} \quad (11.43)$$

For a source with the volume velocity $Q_0 \cdot \exp(i\omega t)$ at $r = 0$ the resulting velocity potential and pressure are

$$\Phi(r, t) = -\frac{Q_0 \cdot \exp[i(\omega t - kr)]}{4\pi r}; \quad p(r, t) = \frac{i\omega\rho_0 Q_0 \cdot \exp[i(\omega t - kr)]}{4\pi r} \quad (11.44)$$

Sound radiation from cylinders is also of interest. For an infinite cylinder with a surface velocity everywhere equal to $v_0 \cdot \exp(i\omega t)$ the resulting velocity potential must have a cylindrical symmetry and be a function of the distance r or the radial distance from the center line of the cylinder. For a velocity, potential given by $\Phi(r, t) = \Phi_0(r) \cdot \exp(i\omega t)$ the function Φ_0 should satisfy the Helmholtz equation

$$\frac{d^2\Phi_0}{dr^2} + \frac{1}{r} \frac{d\Phi_0}{dr} + k^2\Phi_0 = 0 \quad (11.45)$$

where $k = \omega/c$ is the wavenumber in the fluid. The general solution to Eq. (11.45) was discussed in Sect. 5.3. It was found that the solution is

$$\Phi_0(r) = C \cdot H_0^{(2)}(kr) \quad (11.46)$$

where $H_0^{(2)}(kr)$ is the Hankel function of second order and C a constant to be determined by the boundary condition. The asymptotic form of the solution as r approaches infinity is

$$H_0^{(2)}(kr) \rightarrow \sqrt{\frac{2}{\pi kr}} \cdot \exp[-(kr - \pi/4)] \quad (11.47)$$

For $kr \rightarrow 0$ the Hankel function approaches

$$H_0^{(2)}(kr) \rightarrow \frac{2i}{\pi} \cdot \ln(kr) \quad (11.48)$$

Assuming a velocity $u(t) = u_0 \cdot \exp(i\omega t)$ on the surface of the cylinder with radius r_0 the boundary condition is

$$\left[\frac{d\Phi_0}{dr} \right]_{r=r_0} = u_0 \quad (11.49)$$

For $kr_0 \ll 1$ the velocity potential for $r \geq r_0$ is obtained from Eqs. (11.46) through (11.49) as

$$\Phi(r, t) = -\frac{i u_0 \pi r_0}{2} \cdot H_0^{(2)}(kr) \cdot \exp(i\omega t) = -\frac{i U_l}{4} H_0^{(2)}(kr) \cdot \exp(i\omega t) \quad (11.50)$$

where U_l is the volume velocity per unit length of the cylinder. If kr_0 is not small the parameter C in Eq. (11.46) is obtained from the boundary condition (11.49) as $C = u_0 / \{k[H_0^{(2)}(kr_0)]'\}$. The sound intensity in the fluid can be expressed as function of the volume velocity per unit length U_l or the acoustical power $\bar{\Pi}_l$ radiated per length of the cylinder. The results are

$$\bar{I}_r = \frac{\omega^2 \rho_0}{16\pi r c} |U_l|^2 = \frac{\bar{\Pi}_l}{2\pi r} \quad (11.51)$$

The sound intensity level is decreasing by 3 dB per doubling of distance from the center of cylinder. The sound intensity level induced by an ideal point source is decaying by 6 dB per doubling of distance from the source. The decay rate of the sound pressure level is determined by the Hankel function $H_0^{(2)}(kr)$ and is thus not only a function of distance but also of the wavenumber or frequency. For a pure cylindrical wave and for $kr > 1$ the magnitude of pressure squared decays as approximately $1/r$. For $kr < 1$ the decay rate is slightly less.

11.5 Green's Function

In previous Sect. 1.3, 6.2 and 7.3, the forced excitation of first a simple 1-DOF systems and then of beams were derived using Green's function. A similar procedure can be used to find a solution to an inhomogeneous wave equation or rather to determine the acoustic field induced by a source. Assume that a source function is given by $f(\mathbf{r}) \cdot \exp(i\omega t)$ where $\mathbf{r} = (x, y, z)$. The resulting velocity potential induced by the source is $\Phi(\mathbf{r}, t) = \Phi_0(\mathbf{r}) \cdot \exp(i\omega t)$. The potential Φ_0 should satisfy the inhomogeneous equation

$$\nabla^2 \Phi_0 + k^2 \Phi_0 = -f(\mathbf{r}) \quad (11.52)$$

Let the function $g(\mathbf{r}|\mathbf{r}_0)$ be the Green's function in an unbounded medium. The function should be the solution to

$$\nabla^2 g + k^2 g = -\delta(\mathbf{r} - \mathbf{r}_0) \quad (11.53)$$

where $\delta(\mathbf{r} - \mathbf{r}_0)$ is a three-dimensional Dirac function. This Dirac function satisfies

$$\int_{V_0} dV \delta(\mathbf{r} - \mathbf{r}_0) = 1; \quad \int_{V_0} dV \delta(\mathbf{r} - \mathbf{r}_0) f(\mathbf{r}) = f(\mathbf{r}_0) \quad (11.54)$$

The volume V_0 should include the point $\mathbf{r}_0 = (x_0, y_0, z_0)$. The general solution to Eq. (11.53) is

$$g(\mathbf{r}|\mathbf{r}_0) = A \frac{e^{-ikr}}{r}; \quad r = |\mathbf{r} - \mathbf{r}_0|$$

The amplitude A is as yet undetermined. This result inserted in (11.53) and integrated over a small volume including \mathbf{r}_0 gives

$$\int_0^\varepsilon 4\pi r^2 \nabla^2 g dr + \int_0^\varepsilon 4\pi r^2 k^2 g dr = -1 \tag{11.55}$$

The second integral approaches zero as ε tends to zero. The first integral is, using the Gauss theorem, rewritten as

$$\int dV \nabla^2 g = \int dS \mathbf{n} \nabla g = 4\pi \varepsilon^2 A e^{-ik\varepsilon} \left(-\frac{1}{\varepsilon^2} - \frac{ik}{\varepsilon} \right) \rightarrow -4\pi A \quad \text{as } \varepsilon \rightarrow 0 \tag{11.56}$$

The parameter A is obtained from (11.55) and (11.56) as $A = 1/(4\pi)$. Consequently, the Green's function in unbounded space is

$$g(\mathbf{r}|\mathbf{r}_0) = \frac{e^{-ikr}}{4\pi r}; \quad r = |\mathbf{r} - \mathbf{r}_0| = \left[(x - x_0)^2 + (y - y_0)^2 + (z - z_0)^2 \right]^{1/2} \tag{11.57}$$

The expression (11.52) is now multiplied by g and Eq. (11.53) by Φ_0 and the results subtracted resulting in

$$g \nabla^2 \Phi_0 - \Phi_0 \nabla^2 g = -g(\mathbf{r}|\mathbf{r}_0) \cdot f(\mathbf{r}) + \Phi_0(\mathbf{r}) \delta(\mathbf{r} - \mathbf{r}_0)$$

An integration with respect to the volume V enclosing \mathbf{r}_0 gives

$$\int dV [g \nabla^2 \Phi_0 - \Phi_0 \nabla^2 g] = - \int dV g(\mathbf{r}|\mathbf{r}_0) f(\mathbf{r}) + \Phi_0(\mathbf{r}_0) \tag{11.58}$$

The expression inside the first bracket is rearranged as

$$g \nabla^2 \Phi_0 - \Phi_0 \nabla^2 g = \text{div}(g \cdot \mathbf{grad} \Phi_0) - \text{div}(\Phi_0 \cdot \mathbf{grad} g)$$

Using the Gauss theorem, the first volume integral is transformed into a surface integral as

$$\begin{aligned} \int dV [g \nabla^2 \Phi_0 - \Phi_0 \nabla^2 g] &= \int n dS [g \cdot \mathbf{grad} \Phi_0 - \Phi_0 \mathbf{grad} g] \\ &= 4\pi r^2 \left(g \frac{\partial \Phi_0}{\partial r} - \Phi_0 \frac{\partial g}{\partial r} \right) \end{aligned} \tag{11.59}$$

According to Somerfield's criterion, the expression (11.58) must tend to zero as r approaches infinity. The expression (11.58) is consequently reduced to

$$-\int dV g(\mathbf{r}|\mathbf{r}_0) f(\mathbf{r}) + \Phi_0(\mathbf{r}_0) = 0$$

By replacing \mathbf{r} by \mathbf{r}_0 and \mathbf{r}_0 by \mathbf{r} and considering that $g(\mathbf{r}|\mathbf{r}_0) = g(\mathbf{r}_0|\mathbf{r})$ the solution to Eq. (11.52) is finally written

$$\Phi_0(\mathbf{r}) = \int dV_0 g(\mathbf{r}|\mathbf{r}_0) f(\mathbf{r}_0) = \frac{1}{4\pi} \int_{V_0} \frac{e^{-ikr}}{r} f(\mathbf{r}_0) dV_0; \quad r = |\mathbf{r} - \mathbf{r}_0| \quad (11.60)$$

The result can be formulated in a more general way for a source function given by $f(\mathbf{r}_0, t)$. The resulting velocity potential is

$$\Phi(\mathbf{r}, t) = \frac{1}{4\pi} \int_{V_0} \frac{1}{r} f(\mathbf{r}_0, t - r/c) dV_0; \quad r = |\mathbf{r} - \mathbf{r}_0| \quad (11.61)$$

For $f(\mathbf{r}, t) = -Q(t)\delta(\mathbf{r})$ the resulting velocity potential is obtained from (11.60) as

$$\Phi(r, t) = -\frac{Q(t - r/c)}{4\pi r}; \quad r = |\mathbf{r} - \mathbf{r}_0| \quad (11.62)$$

Comparing Eq. (11.62) to the result of Eq. (11.43) it follows that $Q(t)$ is the volume velocity of a point source located at \mathbf{r}_0 . In summary, if a point source with the volume velocity $Q_0 \cdot \exp(i\omega t)$ is located at $\mathbf{r} = \mathbf{r}_0$ the velocity potential $\Phi(r, t) = \Phi_0(r) \cdot \exp(i\omega t)$ is the solution to

$$\nabla^2 \Phi_0 + k^2 \Phi_0 = Q_0 \delta(\mathbf{r} - \mathbf{r}_0) \quad (11.63)$$

Velocity potential, pressure, particle velocity, time average of radial intensity, and time average of the acoustic output power of the source are

$$\begin{aligned} \Phi(r, t) &= -\frac{Q_0}{4\pi r} \cdot \exp[i(\omega t - kr)]; \quad r = |\mathbf{r} - \mathbf{r}_0| \\ p(r, t) &= -\rho_0 \frac{\partial \Phi}{\partial t} = \frac{i\omega \rho_0 Q_0}{4\pi r} \cdot \exp[i(\omega t - kr)] \\ v_r(r, t) &= \frac{\partial \Phi}{\partial r} = \frac{ikQ_0}{4\pi r} \cdot \left(1 + \frac{1}{ikr}\right) \exp[i(\omega t - kr)] \\ \bar{\Pi} &= \frac{\omega^2 \rho_0 |Q_0|^2}{8\pi c}; \quad \bar{I}_r = \frac{\omega^2 \rho_0 |Q_0|^2}{32\pi^2 cr^2} = \frac{\bar{\Pi}}{4\pi r^2}; \quad |\bar{p}|^2 = \frac{\rho_0 c \bar{\Pi}}{4\pi r^2} \end{aligned} \quad (11.64)$$

11.6 Dipole and Other Multipole Sources

The basic wave equation was derived while making a number of approximations and not including a number of source terms. If a mass flow is injected in a fluid, spherical symmetry, the rate of flow will induce a velocity fluctuation and thus, a velocity potential in the fluid. The source, if small enough, can be described as an ideal point source or a monopole. A force acting on the fluid, for example, a small object moving back and forth, could induce an acoustic field equivalent to that created by two ideal point sources operating in opposite phase. More complicated sources, for example, caused by a jet flow, could to a certain extent be described as a combination of monopoles, pair of dipoles, or so-called quadruples. For more details, see, for example, Refs. [23, 135–138]. See also Problem 11.3.

The field from a dipole can be derived based on the configuration shown in Fig. 11.5. A point source is located at $\mathbf{r}_1 = (d/2, 0, 0)$. The field induced by this point source is $Qg(\mathbf{r}|\mathbf{r}_1)$ where $g(\mathbf{r}|\mathbf{r}_1)$ is given by Eq. (11.57) and Q is the source strength. The other source, located at $\mathbf{r}_2 = (-d/2, 0, 0)$ and operating at opposite phase to the first one, induces the field $-Qg(\mathbf{r}|\mathbf{r}_2)$. The total field is

$$\Phi_0(\mathbf{r}) = Q [g(\mathbf{r}|\mathbf{r}_1) - g(\mathbf{r}|\mathbf{r}_2)] \tag{11.65}$$

For the distance d between the sources being small the Green’s function can be expanded in a Taylor series. Including only terms of the first order of magnitude the result is

$$\Phi_0 = Q(\mathbf{r}_1 - \mathbf{r}_2)\mathbf{grad}[g(\mathbf{r}|0)]$$

Defining the dipole source as $\mathbf{D} = Q(\mathbf{r}_1 - \mathbf{r}_2)$ the result is

$$\Phi_0(\mathbf{r}) = -\frac{ike^{-ikr}}{4\pi r^2} \mathbf{r} \cdot \mathbf{D} \cdot \left(1 + \frac{1}{ikr}\right) \tag{11.66}$$

Fig. 11.5 A dipole source

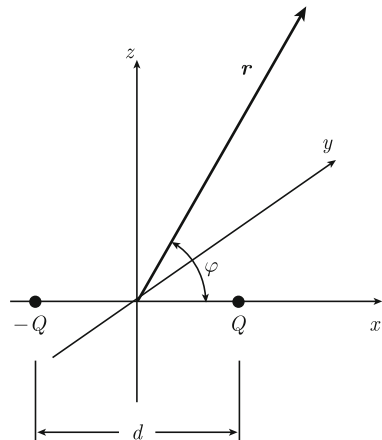
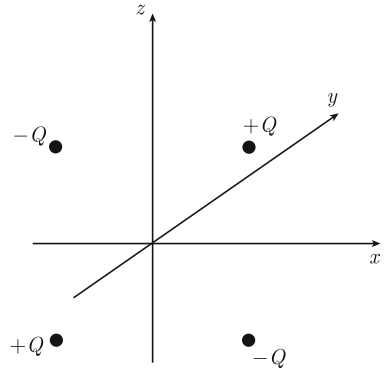


Fig. 11.6 Quadruple source



For the configuration shown in Fig. 11.5 the result is for $rk \gg 1$

$$\Phi_0(\mathbf{r}) = -|\mathbf{D}| \frac{ike^{-ikr}}{4\pi r} \cos \varphi; \quad p(r) = -|\mathbf{D}| \frac{\omega^2 \rho_0 e^{-ikr}}{4\pi r c} \cos \varphi \quad (11.67)$$

The absolute pressure has a maximum along the axis of the dipole and a minimum perpendicular to the dipole axis where the pressure is zero. The time average of the total power radiated by a dipole is

$$\bar{\Pi} = \frac{\rho_0 c D^2 k^4}{24\pi} \quad (11.68)$$

The intensity and the power of a dipole are discussed in Problem 11.5.

There can also be more complex source configurations as, for example, induced by a jet. These source elements have the configuration of assemblages of two dipoles. One such source, called a quadruple, is shown in Fig. 11.6. Positive sources $+Q$ are located at $(d/2, d/2, 0)$ and $(-d/2, -d/2, 0)$ and negative sources $-Q$ at $(d/2, -d/2, 0)$, and $(-d/2, d/2, 0)$. Following the same procedure as before the resulting velocity potential for this particular configuration is

$$\Phi_0(\mathbf{r}) = d |\mathbf{D}| \left[\frac{\partial^2}{\partial x_0 \partial y_0} g(\mathbf{r}|\mathbf{r}_0) \right]_{r_0=0} \quad (11.69)$$

The corresponding pressure is for $kr \gg 1$

$$p(\mathbf{r}) = \frac{d |\mathbf{D}| \rho_0 \omega^2 x y e^{-ikr}}{4\pi r^3 c} \quad (11.70)$$

This type of quadruple is denoted Q_{xy} referring to the derivatives of the Green's function. Other possible combinations are Q_{xz} , Q_{yz} , Q_{xx} , Q_{yy} and Q_{zz} . However, a combination of Q_{xx} , Q_{yy} and Q_{zz} of equal strength produces a monopole. According to definition $Q_{xy} = Q_{yx}$ etc.

Of these simple sources, the monopole is by far the most efficient radiator followed by the dipole and then the quadruple. There can be combinations of higher order, octupole, and so on. However, these sources are of less practical importance than the three basic ones since the intensity induced by these sources of higher order is low. Quadruple sources are discussed in Problem 11.3.

11.7 Additional Sources and Solutions

An acoustic field is not only induced by a mass flow, jet flow, turbulence, and heat injection but also by the motion of structures like a membrane of a loudspeaker, a vibrating plate, etc. It is, therefore, of interest to describe the acoustic field induced by a vibrating surface on structures of simple geometries like spheres, cylinders and plates. In this section, only the radiation from spheres, and cylinders will be discussed. The interaction between plates and fluids are discussed in Chaps. 12 and 13.

Starting with a radiating sphere. Solutions in spherical coordinates to the Helmholtz equation can be formulated in a more general way as compared to the results discussed in Sect. 11.4. To start with, consider sound fields, which can depend not only on the distance from a source but also on the azimuth angle θ shown in Fig. 11.4. For a velocity potential $\Phi_0(r, \theta) \cdot \exp(i\omega t)$, the function $\Phi_0(r, \theta)$ should satisfy the Helmholtz equation

$$\frac{1}{r^2} \cdot \frac{\partial}{\partial r} \left(r^2 \frac{\partial \Phi_0}{\partial r} \right) + \frac{1}{r^2 \sin \theta} \cdot \frac{\partial}{\partial \theta} \left(\sin \theta \cdot \frac{\partial \Phi_0}{\partial \theta} \right) + k^2 \Phi_0 = 0 \quad (11.71)$$

Let the function $\Phi_0(r, \theta)$ be defined as $\Phi_0(r, \theta) = R(r)P(\cos \theta)$. There is an infinite number of solutions satisfying the Helmholtz equation (11.71). The solutions can be written as a combination of spherical Hankel functions and Legendre functions. The general solution to Eq. (11.71) is

$$\Phi_0(r, \theta) = \sum_m \left(A_m P_m(\cos \theta) h_m^{(1)}(kr) + B_m P_m(\cos \theta) h_m^{(2)}(kr) \right) \quad (11.72)$$

In this solution $h_m^{(1)}(kr)$ is the spherical Hankel function of the first kind and $h_m^{(2)}(kr)$ of the second kind. The spherical Hankel functions or in fact $R(r)$ should satisfy the differential equation

$$\frac{d^2 R}{dr^2} + \frac{2}{r} \frac{dR}{dr} + \left[k^2 - \frac{m(m+1)}{r^2} \right] \cdot R = 0$$

The function $h_m^{(2)}(kr)$ represents outgoing waves whereas $h_m^{(1)}(kr)$ corresponds to waves converging on the source. In an infinite medium only outgoing waves can exist in agreement with the Sommerfeld radiation condition. Including only outgoing waves reduces Eq. (11.72) to

$$\Phi_0(r, \theta) = \sum_m B_m P_m(\cos \theta) h_m^{(2)}(kr) \quad (11.73)$$

The functions $P_m(\cos \theta)$ of the solution (11.72) are the Legendre functions. A Legendre function $P_m(z)$ satisfies the differential equation

$$(1 - z^2) \frac{d^2 P_m}{dz^2} - 2z \frac{dP_m}{dz} + m(m + 1)P_m = 0 \quad (11.74)$$

The solutions can be written as

$$P_m(z) = \frac{1}{2^m m!} \cdot \frac{d^m}{dz^m} (z^2 - 1)^m$$

The Legendre functions are finite in the interval $-1 \leq z \leq 1$. The functions P_m are orthogonal as

$$\int_{-1}^1 P_m(z) P_n(z) dz = \frac{2}{2m + 1} \cdot \delta_{mn}$$

where δ_{mn} is the Kronecker delta. Any continuous function $f(z)$ can be expanded in a series of Legendre functions in the interval $-1 \leq z \leq 1$ as

$$f(z) = \sum_m C_m P_m(z)$$

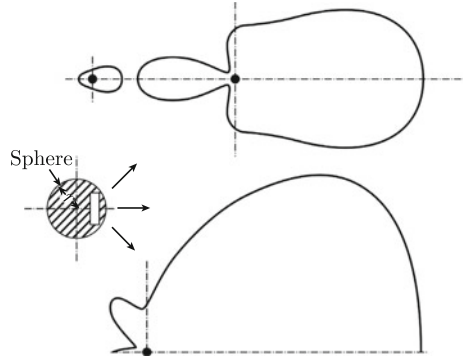
The coefficients C_m are according to the orthogonality condition obtained as

$$C_m = \frac{2m + 1}{2} \int_{-1}^1 P_m(z) f(z) dz$$

The acoustic field induced by a small piston mounted in a sphere is discussed in Problem 11.6. The directivity of the acoustic intensity is shown in Fig. 11.7. In the very low frequency region, kr_0 small, the acoustic field is almost omnidirectional. For increasing frequencies, kr_0 increasing, the intensity in the forward direction is increasing and developing into a distinct forward lobe. In the backward direction, the intensity is decreasing as kr_0 is increased.

In the general case, the velocity potential can be a function of the angle φ as well as the azimuth angle θ and the distance r . The inclusion of the azimuth angle makes any solution rather complex. However, the procedure to solve that kind of problem is indicated below. Detailed procedures can be found in, for example, Refs. [23, 69, 131]. The spherical coordinate system is identified in Fig. 11.4. A velocity potential $\Phi_0(r, \theta, \varphi) \cdot \exp(i\omega t)$ should satisfy the wave equation (11.19) and Φ_0 the Helmholtz equation in spherical coordinates

Fig. 11.7 Radiation from a small vibrating piston mounted in a sphere for kr_0 equal to 1, 2, and 3, starting from upper left hand corner. From Ref. [23]



$$\frac{1}{r^2} \cdot \frac{\partial}{\partial r} \left(r^2 \frac{\partial \Phi_0}{\partial r} \right) + \frac{1}{r^2 \sin \theta} \cdot \frac{\partial}{\partial \theta} \left(\sin \theta \cdot \frac{\partial \Phi_0}{\partial \theta} \right) + \frac{1}{r^2 (\sin \theta)^2} \cdot \frac{\partial^2 \Phi_0}{\partial \varphi^2} + k^2 \Phi_0 = 0 \tag{11.75}$$

It can be shown that the velocity potential can be written as $\Phi_0(r, \theta, \varphi) = R(r) \cdot G(\theta) \cdot H(\varphi)$.

For (11.75) to be satisfied these separate functions must also satisfy the following differential equations

$$\begin{aligned} \frac{\partial^2 H}{\partial \varphi^2} + n^2 H &= 0; & \frac{1}{\sin \theta} \cdot \frac{\partial}{\partial \theta} \left(\sin \theta \cdot \frac{\partial G}{\partial \theta} \right) + \frac{n^2}{(\sin \theta)^2} \cdot G + m(m + 1) &= 0 \\ \frac{1}{r^2} \cdot \frac{\partial}{\partial r} \left(r^2 \frac{\partial R}{\partial r} \right) + \left[k^2 - \frac{m(m + 1)}{r^2} \right] R &= 0 \end{aligned} \tag{11.76}$$

The general solution is, outgoing waves only

$$\begin{aligned} \Phi_0(r, \theta, \varphi) &= \sum_{mn} h_m^{(2)}(kr) \cdot G_{mn}(\theta) \cdot H_n(\varphi) \\ G_{mn}(\theta) &= C_{mn} P_m^n(\cos \theta) + D_{mn} Q_m^n(\cos \theta) \\ H_n(\varphi) &= \cos(n\varphi) + W_n \sin(n\varphi) \end{aligned} \tag{11.77}$$

The spherical Hankel function of the second kind is denoted $h_m^{(2)}(kr)$. P_m^n and Q_m^n are the associated Legendre functions—see, for example, the Refs. [5, 23, 69, 131]. The associated Legendre function $P_m^n(z)$ are defined as

$$P_m^n(z) = (1 - z^2)^{n/2} \cdot \left(\frac{d}{dz} \right)^n P_m(z)$$

where $P_m(z)$ is the Legendre function of order m . The functions $P_m^n(z)$ satisfy the associated Legendre differential equation

$$(1 - z^2) \frac{d^2 P_m^n}{dz^2} - 2z \frac{dP_m^n}{dz} + \left[m(m+1) - \frac{n^2}{1-z^2} \right] P_m^n = 0$$

The associated Legendre functions are orthogonal as

$$\int_{-1}^1 P_m^n(z) P_k^n(z) dz = \frac{(m+n)!}{(m-n)!} \cdot \frac{2}{2m+1} \cdot \delta_{mk}$$

The second solution to Legendre's equation is $Q_m^n(z)$. This solution is given as

$$Q_m^n = -P_m^n(z) \int_{\infty}^z \frac{d\zeta}{(\zeta^2 - 1)[P_m^n(\zeta)]^2}$$

The result (11.72) is just a special case of the complete solution. Equation (11.72) is obtained by setting $n = 0$ in the general solution (11.77).

In cylindrical coordinates the velocity potential is $\Phi_0(r, \varphi, z) \cdot \exp(i\omega t)$. The function Φ_0 should satisfy the Helmholtz equation

$$\frac{1}{r} \cdot \frac{\partial}{\partial r} \left[r \frac{\partial \Phi_0}{\partial r} \right] + \frac{1}{r^2} \cdot \frac{\partial^2 \Phi_0}{\partial \varphi^2} + \frac{\partial^2 \Phi_0}{\partial z^2} + k^2 \Phi_0 = 0 \quad (11.78)$$

The solution is for outgoing waves only

$$\begin{aligned} \Phi_0(r, \varphi, z) &= \sum H_m^{(2)}(r\sqrt{k^2 - k_z^2}) F_m(\varphi) Z_m(z); \\ F_m(\varphi) &= A_m \cdot \cos(m\varphi) + B_m \sin(m\varphi) \\ Z_m(z) &= C_m \cdot \cos(k_z z) + \cdot \sin(k_z z) \end{aligned} \quad (11.79)$$

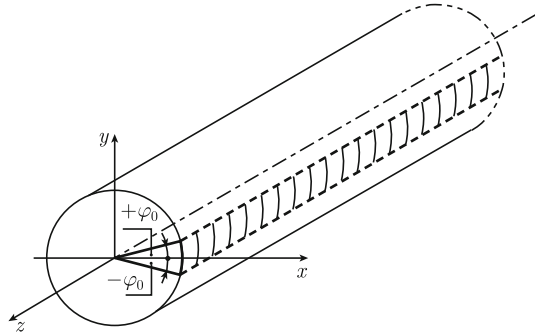
The parameters A_m , B_m , and C_m are determined from the boundary conditions.

Some characteristics of sound fields induced by vibrating cylinders can be illustrated by a simple example. Consider, an infinite cylinder as shown in Fig. 11.8. The cylinder has the radius r_0 . Part of the surface of the cylinder is vibrating with a velocity u defined as

$$u(\varphi, t) = u_0 \cdot \exp(i\omega t) \quad \text{for} \quad -\varphi_0 \leq \varphi \leq \varphi_0 \quad \text{otherwise zero}$$

The cylinder is assumed to radiate into an infinite fluid. Consequently, only outgoing waves as described by the Hankel function of the second kind can satisfy the general solution (11.79). The function defining the surface velocity is symmetric with respect to $\varphi = 0$. The surface velocity and the velocity potential in the fluid can, therefore, be expanded by means of cosine terms only. The velocity potential in the fluid is a function of r , φ , and t only and is written as

Fig. 11.8 An infinite cylinder, part of which is vibrating



$$\Phi(r, \varphi, t) = \exp(i\omega t) \cdot \sum_n A_n \cdot H_n^{(2)}(kr) \cdot \cos(n\varphi) \tag{11.80}$$

The particle velocity in the fluid at the surface of the cylinder must equal the surface velocity of the cylinder. Thus

$$\left[\frac{\partial \Phi}{\partial r} \right]_{r=r_0} = u_0 \exp(i\omega t) \quad \text{for } -\varphi_0 \leq \varphi \leq \varphi_0 \quad \text{otherwise zero} \tag{11.81}$$

The surface velocity of the cylinder can also be expanded in a cosine series. The result is

$$u(\varphi, t) = u_0 \cdot \exp(i\omega t) \left[\frac{\varphi_0}{\pi} + \sum_{n=1}^{\infty} \frac{2\varphi_0}{n\pi} \sin(n\varphi_0) \cos(n\varphi) \right] \tag{11.82}$$

The Eqs. (11.80) through (11.82) give the solution to the problem. Details are given in Problem 11.7. The velocity potential in the fluid induced by the infinite vibrating cylinder is obtained as

$$\Phi(r, \varphi, t) = \frac{u_0 \cdot \exp(i\omega t)}{\pi k} \left[\frac{\varphi_0 H_0^{(2)}(kr)}{[H_0^{(2)}(kr_0)]'} + \sum_{n=1}^{\infty} \frac{H_n^{(2)}(kr)}{[H_n^{(2)}(kr_0)]'} \frac{2\varphi_0}{n\pi} \sin(n\varphi_0) \cos(n\varphi) \right] \tag{11.83}$$

The sound pressure in the fluid is $p = -\rho_0 \partial \Phi / \partial t$ and the corresponding sound pressure level is $L_p = 10 \log[|p|^2 / (2p_{\text{ref}}^2)]$. Some results are shown in Fig. 11.9. The radius of the infinite cylinder is 2.5 m. The cylinder is submerged in water, $\rho_0 c = 1.45 \cdot 10^6 \text{ kg}/(\text{m}^2 \text{ s})$. The velocity of the cylinder is proportional to $\exp(i\omega t)$ within a sector defined by the angle $\varphi_0 = 5^\circ$. The variation of the sound pressure level at a distance of 7.5 m from the center of the cylinder is shown in Fig. 11.9. The relative sound pressure level as function of the angle φ is given for four frequencies

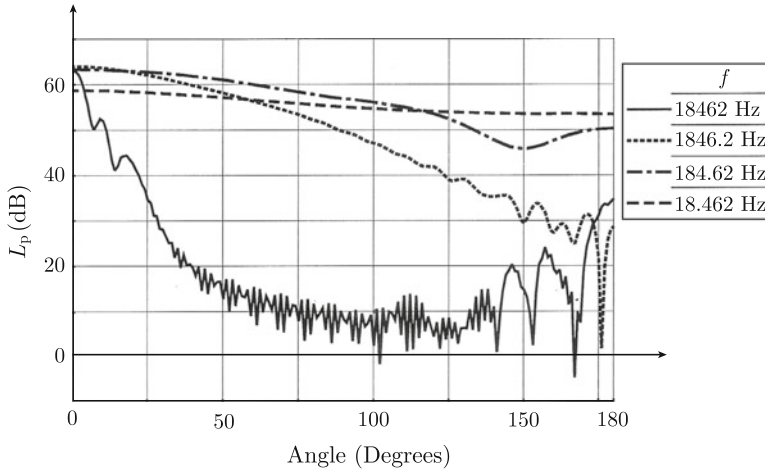


Fig. 11.9 Radiation from a strip along an infinite cylinder. $r = 7.5$ m, $r_0 = 2.5$ m

18, 184, 1846, and 18462 Hz corresponding to the Helmholtz numbers kr_0 equal to 0.2, 2, 20, and 200. For $kr_0 = 0.2$ the sound pressure level varies slowly as function of the angle φ . For larger Helmholtz numbers the fluctuations with respect to the angle become more pronounced. For kr_0 very large, the directivity pattern is very distinct. The highest sound pressure level is directly in front of the radiating surface, i.e., for $\varphi = 0$. For $\varphi = 13^\circ$ the sound pressure level has already decreased by 20 dB. The sound pressure level varies rapidly as the angle is changed. At the offside of the cylinder, i.e., as the angle approaches $\varphi = 180^\circ$, the sound pressure level increases again up to a maximum at $\varphi = 180^\circ$. A similar pattern but not as distinct is obtained for $kr_0 = 20$. The maximum or tail at the offside of the cylinder with respect to the source is well pronounced except for small Helmholtz numbers. The directivity pattern is becoming smoother as the Helmholtz number decreases. In the very low frequency region the sound pressure level tends to be independent of the angle.

The directivity pattern of the source is not only a function of the angle φ and the Helmholtz number but also of the distance r to the source or rather the product kr . This is illustrated in Fig. 11.10. The source is again the vibrating strip on an infinite cylinder as described in the previous case. The sound pressure levels shown in the figure are predicted at 7.5 and 75 m from the center of the cylinder. In front of the vibrating area, i.e., for $\varphi = 0$, the sound pressure level is decreased by 12 dB as the distance from the center is increased from 7.5 to 75 m. The distance from the surface of the cylinder is changed from 5 to 72.5 m. For a pure cylindrical attenuation this equivalent to 12 dB. The level difference varies for increasing angles. At the offside of the cylinder, the sound pressure level at 75 m, can at certain positions, even be higher than the level at 7.5 m from the center. The examples illustrate that the sound pressure at a certain point outside a source cannot be predicted based on a limited number of measurements if not the source is completely omnidirectional in two or

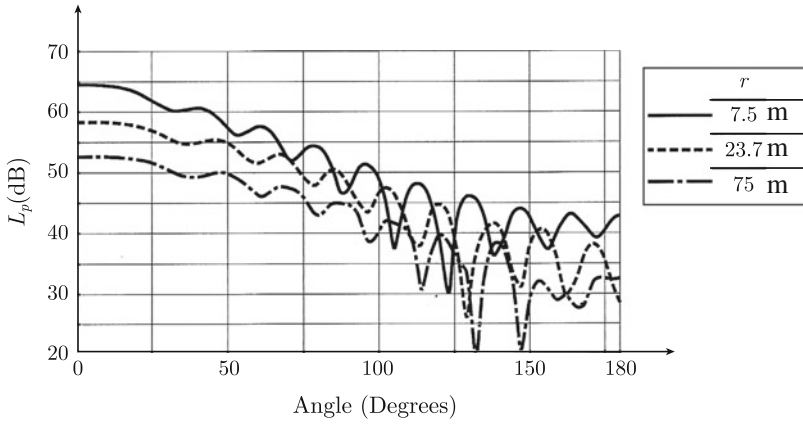


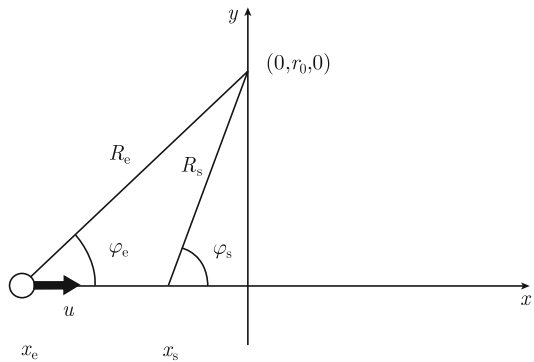
Fig. 11.10 Radiation from a strip along an infinite cylinder. $kr_0 = 20$

three dimensions or else if not the directivity pattern of the source is completely determined. Radiation from cylinders and sound radiation ratios are also discussed in Sect. 12.11.

11.8 Moving Monopole Sources

Acoustic fields induced by stationary sources were discussed in the previous sections. When a source is moving certain additional effects have to be considered. Some of these effects can be demonstrated by considering a simple monopole traveling with constant velocity u along a straight line. Figure 11.11 illustrates a source moving past a listener. The source is traveling along the x -axis. The x -coordinate of the source is $x_s = ut$. Thus, at $t = 0$ the source is at $x = 0$ and the distance r_0 from the

Fig. 11.11 A source moving along a straight path at constant speed passed a listener



observation point at $(0, r_0, 0)$. At time $t = t_e$, the source at $(ut_e, 0, 0)$ emits a signal which reaches the listener at $t = t_e + R_e/c$ where R_e is the distance between the source and listener as shown in Fig. 11.11.

When the signal reaches the listener the source has moved to a position $(x_s, 0, 0)$ at a distance R_s from the listener. The coordinate x_s is $x_s = u(t_e + R_e/c) = ut_e + MR_e$, where $M = u/c$ is the Mach number. Based on the geometry shown in Fig. 11.11 it is found that

$$R_e^2 = x_e^2 + r_0^2 = u^2(t - R_e/c)^2 + r_0^2 \quad (11.84)$$

The distance R_e is obtained from Eq. (11.84) as

$$R_e = -\frac{utM}{1-M^2} \pm \frac{\sqrt{(ut)^2 + r_0^2(1-M^2)}}{1-M^2} \quad (11.85)$$

For $M < 1$ there is only one solution whereas for $M > 1$ there are two. For subsonic motion, $M < 1$, the solution is

$$R_e = -\frac{utM}{1-M^2} + \frac{\sqrt{(ut)^2 + r_0^2(1-M^2)}}{1-M^2} = \frac{-utM + R_1}{1-M^2};$$

$$R_1 = \sqrt{(ut)^2 + r_0^2(1-M^2)} \quad (11.86)$$

The other solution for $M < 1$ gives a negative distance R_e . From Fig. 11.11, $-ut_e = u(-t + R_e/c) = R_e \cdot \cos \varphi_e$. Thus,

$$-ut = R_e(\cos \varphi_e - M) \quad (11.87)$$

Also from Fig. 11.11, $r_0 = R_e \cdot \sin \varphi$. Consequently, the distance R_1 is obtained as

$$R_1 = R_e \left[(\cos \varphi - M)^2 + (1 - \cos^2 \varphi) (1 - M^2) \right]^{1/2} = R_e(1 - M \cos \varphi) \quad (11.88)$$

The differential equation determining the velocity potential induced by point source moving along the x -axis at a velocity u as shown in Fig. 11.11 is

$$\nabla^2 \Phi - \frac{1}{c^2} \frac{\partial^2 \Phi}{\partial t^2} = -Q(t) \delta(x - ut) \delta(y) \delta(z) \quad (11.89)$$

The equation can be solved by introducing two transformations. The first, the so-called Lorentz transformation, is given as

$$x_1 = \gamma(x - ut); \quad y_1 = y; \quad z_1 = z; \quad t_1 = \gamma(t - ux/c^2); \quad \gamma = (1 - M^2)^{-1/2} \quad (11.90)$$

Thus, as discussed in Problem 11.17, $\nabla_1^2 \Phi - \frac{1}{c^2} \frac{\partial^2 \Phi}{\partial t_1^2} = \nabla^2 \Phi - \frac{1}{c^2} \frac{\partial^2 \Phi}{\partial t^2}$. See also, for example, Refs. [58, 131]. Since $\delta(y_1/\gamma) = \gamma \delta(y_1)$ the initial differential equation is, using the transforms (11.90), reduced to

$$\nabla_1^2 \Phi - \frac{1}{c^2} \frac{\partial^2 \Phi}{\partial t_1^2} = -\gamma Q[\gamma(t_1 + x_1 u/c^2)] \delta(x_1) \delta(y_1) \delta(z_1) \quad (11.91)$$

Yet another transformation reduces this differential to a standard equation governing the acoustic field from a stationary source. This second transform is given as

$$t_2 = \gamma t_1; \quad x_2 = \gamma x_1; \quad y_2 = \gamma y_1; \quad z_2 = \gamma z_1 \quad (11.92)$$

Since $\delta(\gamma y_1) = \delta(y_1)/\gamma$ the Eq. (11.91) is reduced to

$$\nabla_2^2 \Phi - \frac{1}{c^2} \frac{\partial^2 \Phi}{\partial t_2^2} = -\gamma^2 Q(t_2 + x_2 u/c^2) \delta(x_2) \delta(y_2) \delta(z_2)$$

The right-hand side of the equation can be simplified since the Dirac function $\delta(x_2)$ ensures that x_2 is equal to zero in the first expression. Consequently, the equation governing the acoustic field induced by a monopole traveling along a straight line at a constant speed is given by

$$\nabla_2^2 \Phi - \frac{1}{c^2} \frac{\partial^2 \Phi}{\partial t_2^2} = -\gamma^2 Q(t_2) \delta(x_2) \delta(y_2) \delta(z_2) \quad (11.93)$$

According to Eq. (11.43) the solution to the equation is

$$\Phi(r_2, t_2) = \gamma^2 \frac{Q(\tau)}{4\pi r_2}; \quad \tau = t_2 - r_2/c \quad (11.94)$$

Transformations back to the initial coordinates give

$$\Phi(r_2, t_2) = \gamma^2 \frac{Q(\tau)}{4\pi r_2}; \quad \tau = t_2 - r_2/c$$

$$\begin{aligned} \tau = t_2 - \frac{r_2}{c} &= \gamma t_1 - \gamma \frac{r_1}{c} = t - \frac{u(x - ut)}{c^2 - u^2} - \frac{\gamma}{c} \sqrt{\gamma^2(x - ut)^2 + r_0^2} \\ &= t - \frac{M(x - ut) - \sqrt{(x - ut)^2 + (1 - M^2)r_0^2}}{c(1 - M^2)} = t - \frac{R_e}{c} \end{aligned}$$

$$r_2 = \gamma^2 \left[(x - ut)^2 + (1 - M^2)(y^2 + z^2) \right]^{1/2} \quad (11.95)$$

For the listener located at $\mathbf{r}_0 = (0, r_0, 0)$ this expression is reduced to

$$\begin{aligned}\tau &= t - \frac{-Mut - \sqrt{(ut)^2 + (1 - M^2)r_0^2}}{c(1 - M^2)} = t - \frac{R_e}{c}; \\ R_e &= \frac{-Mut - \sqrt{(ut)^2 + (1 - M^2)r_0^2}}{(1 - M^2)} \\ r_2 &= \gamma^2 \left[(ut)^2 + (1 - M^2)r_0^2 \right]^{1/2}\end{aligned}\quad (11.96)$$

However, according to Eq. (11.87), $-ut = R_e(\cos \varphi_e - M)$ and in addition $r_0 = R_e \sin \varphi_e$ which gives $r_2 = \gamma^2 R_e(1 - M \cos \varphi_e)$. The parameter R_e represents the distance between the listener and the source at the time t_e when the signal was emitted as shown in Fig. 11.11.

The resulting velocity potential is

$$\Phi = \frac{Q(t - R_e/c)}{4\pi R_e(1 - M \cos \varphi_e)} \quad (11.97)$$

The sound pressure at $\mathbf{r}_0 = (0, r_0, 0)$ is

$$p = -\rho_0 \frac{\partial \Phi}{\partial t} = -\rho_0 \frac{Q'(t - R_e/c) \left(1 - \frac{1}{c} \frac{dR_e}{dt}\right)}{4\pi R_e(1 - M \cos \varphi_e)} + \rho_0 \frac{Q(t - R_e/c)}{4\pi r_2^2} \frac{dr_2}{dt} \quad (11.98)$$

Equation (11.96) gives

$$\begin{aligned}\frac{1}{c} \frac{dR_e}{dt} &= -\frac{1}{1 - M^2} \left[M^2 + \frac{M(x - ut)}{R_1} \right] \\ &= -\frac{M}{1 - M^2} \left[M + \frac{R_e(\cos \varphi_e - M)}{R_e(1 - M \cos \varphi_e)} \right] = -\frac{M \cos \varphi_e}{1 - M \cos \varphi_e} \\ \frac{dr_2}{dt} &= \frac{\gamma^2 u^2 t}{r_2} = -\frac{\gamma^2 u(\cos \varphi_e - M)}{(1 - M \cos \varphi_e)}\end{aligned}\quad (11.99)$$

The relationship $-ut = R_e(\cos \varphi_e - M)$ has been used. Hence,

$$p = \frac{\rho_0 Q'(t - R_e/c)}{4\pi R_e(1 - M \cos \varphi_e)^2} + \frac{\rho_0 Q(t - R_e/c) M c (\cos \varphi_e - M)}{4\pi R_e^2 (1 - M \cos \varphi_e)^3} \quad (11.100)$$

At large distances from the source the first term dominates. If the velocity of the source is not constant but a function of time an extra term must be added to the result (11.100). For this particular case the resulting pressure is

$$p = \frac{\rho_0 Q'(t - R_e/c)}{4\pi R_e(1 - M \cos \varphi_e)^2} + \frac{\rho_0 Q(t - R_e/c)Mc(\cos \varphi_e - M)}{4\pi R_e^2(1 - M \cos \varphi_e)^3} + \frac{\rho_0 Q(t - R_e/c)\dot{M}}{4\pi R_e(1 - M \cos \varphi_e)^3}$$

The first and dominating term of the result (11.100) can also be given as a function of the actual coordinates for the source at the time t the listener perceives the noise emitted by the source when at the distance R_e from the listener. Using the parameters R_s and φ_s defined in Fig. 11.11 the first part of Eq.(11.100) is written

$$p(0, r_0, 0, t) = \frac{\rho_0 Q \left[t - \frac{R_s(M \cos \varphi_s + \sqrt{1 - M^2 \sin^2 \varphi_s})}{c\sqrt{1 - M^2}} \right]}{4\pi R_s \sqrt{1 - M^2 \sin^2 \varphi_s}}$$

If the source has the time dependence $\exp(i\omega_0 t)$ the phase φ of the pressure given in Eq. (11.100) is

$$\varphi = \omega_0(t - R_e/c) \quad (11.101)$$

The angular frequency ω perceived by a listener at $\mathbf{r} = (0, r_0, 0)$ is then

$$\omega = \frac{d\varphi}{dt} = \omega_0 \left(1 - \frac{1}{c} \frac{dR_e}{dt} \right) = \frac{\omega_0}{1 - M \cos \varphi_e} \quad (11.102)$$

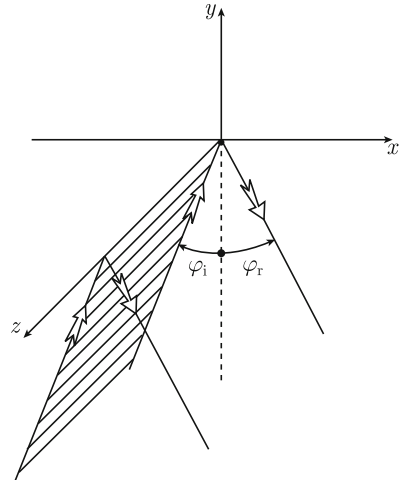
This is the Doppler formula. The result (11.99) has been used to derive Eq. (11.102). As the source approaches the listener from afar the perceived frequency is $f = f_0/(1 - M)$. When the source has passed the perceived frequency is decreased and is approaching $f = f_0/(1 + M)$. Also the pressure varies if a source is approaching or departing from a listener. At the same distance from a listener the noise from an approaching source is higher than for departing source as given by Eq. (11.100).

Acoustic fields induced by moving sources are also discussed in for example Refs. [23, 69, 137, 138].

11.9 Reflection from a Plane Surface

A sound wave incident on a surface is partly reflected and partly absorbed by the surface. The reflected field depends on the acoustic properties of the surface or its acoustic impedance, angle of incidence of the wave, and the frequency. A reflecting surface is often said to be either locally reacting or having an extended reaction. In the first case, the response at one point of the surface due to an incident wave is completely independent of the reaction or motion of any other part of the surface. Each small section of the surface is responding to the incident wave as if each infinitesimal surface element were supported by a separate spring uncoupled to any

Fig. 11.12 Incident and reflected plane waves. The wave is reflected in the x - z -plane



other part of the structure. For a surface with an extended reaction, the response of one part of the surface depends on the motion of any adjoining part.

The acoustic properties of a locally reacting surface is defined by its acoustic impedance Z . The impedance can be complex and a function of frequency and angle of incidence of the incoming wave. The acoustic impedance of the surface is equal to the ratio between the acoustic pressure on the surface and the particle velocity normal to the surface. For a plane wave incident on a reflecting surface, part of the sound field is reflected in the surface as illustrated in Fig. 11.12. The plane-reflecting surface is oriented in the x - z -plane as shown in the figure. The amplitude of the incident wave is set to equal unity, and that of the reflected wave to R . The velocity potentials Φ_i and Φ_r defining the incident and reflected fields are

$$\begin{aligned} \Phi_i(x, y, t) &= \exp [i(\omega t - xk \sin \varphi_i - yk \cos \varphi_i)] \\ \Phi_r(x, y, t) &= R \cdot \exp [i(\omega t - xk \sin \varphi_r + yk \cos \varphi_r)] \end{aligned} \tag{11.103}$$

The pressure p and the particle velocity normal to the surface are

$$p(x, y, t) = -\rho_0 \frac{\partial(\Phi_i + \Phi_r)}{\partial t}; \quad v_y(x, y, t) = \frac{\partial(\Phi_i + \Phi_r)}{\partial y} \quad \text{for } y = 0$$

The ratio p/v_y must be equal to the impedance Z anywhere on the surface or rather for any x . For this condition to be satisfied the angles φ_i and φ_r must be equal. Consequently, the ratio \hat{p}/\hat{v}_y is for $y = 0$ obtained as

$$\left[\frac{\hat{p}}{\hat{v}_y} \right]_{y=0} = Z = \frac{\rho_0 c (1 + R)}{\cos \varphi_i (1 - R)} \tag{11.104}$$

The relative amplitude R of the reflected wave is from this expression obtained as

$$R = \frac{Z \cdot \cos \varphi_i - \rho_0 c}{Z \cdot \cos \varphi_i + \rho_0 c} \tag{11.105}$$

The reflection coefficient ρ_s is equal to the ratio between the intensity I_r of the reflected wave and the intensity I_i of the incident wave or

$$I_r/I_i = |R|^2 = \rho_s \tag{11.106}$$

The intensity not reflected is absorbed by the surface. The absorption coefficient α is defined as the ratio between the absorbed intensity I_a and the incident intensity I_i . Thus

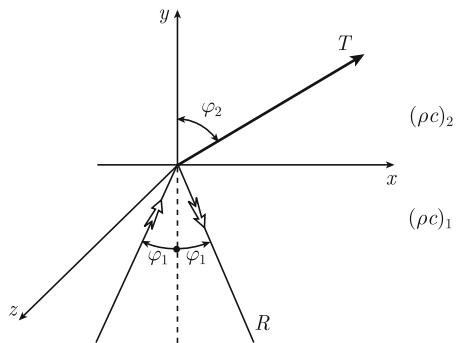
$$I_a = \alpha I_i = I_i - I_r; \quad \alpha = 1 - \rho_s \tag{11.107}$$

For $|Z| \gg \rho_0 c$ the relative amplitude R of the reflected wave tends to unity. The incident wave is almost completely reflected and the incident and reflected waves are in phase. For the other extreme case, $|Z| \ll \rho_0 c$ the incident wave is again almost completely reflected. However, the incident and reflected waves are 180° out of phase. For Z completely imaginary the reflection coefficient ρ_s is equal to unity. Part of the incident intensity is always absorbed if the real part of the surface impedance is different from zero.

A plane separating two fluids like a water surface separating a calm sea and air gives one example of a surface with an extended impedance. A plate surrounded by fluids is another example. In the first case, the problem can be illustrated as shown in Fig. 11.13.

Two fluids are separated by the plane $y = 0$. For $y < 0$ the wave impedance for the fluid is $(\rho_0 c)_1$. The corresponding wavenumber is $k_1 = \omega/c_1$. For $y > 0$ the wave impedance and wavenumber are $(\rho_0 c)_2$ and $k_2 = \omega/c_2$ respectively. The amplitude of the plane incident wave is unity. The angle of incidence is φ_1 . In order to satisfy any boundary condition for $y = 0$ the angle of the plane reflected wave must be equal to the angle φ_1 of the incident wave. The amplitude of the reflected

Fig. 11.13 Two fluids are separated by the x - z -plane. A plane wave is incident on the plane. Part of the incident wave is reflected and part is transmitted



wave is R . The transmitted wave has the amplitude T . The angle between the plane transmitted wave and the normal to the surface is φ_2 . The velocity potentials Φ_1 and Φ_2 in the two fluids are

$$\begin{aligned}\Phi_1(x, y, t) &= \exp[i(\omega t - k_1 x \sin \varphi_1)] \cdot [\exp(-ik_1 y \cos \varphi_1) + R \cdot \exp(ik_1 y \cos \varphi_1)] \\ \Phi_2(x, y, t) &= T \cdot \exp[i(\omega t - k_2 x \sin \varphi_2)] \cdot [\exp(-ik_2 y \cos \varphi_2)]\end{aligned}\quad (11.108)$$

At the surface, i.e., for $y = 0$, the pressure in fluid 1 must be equal to the pressure in fluid 2. Further, the particle velocities normal to the joint boundary must be equal in both fluids. Viscosity in the fluids is neglected. Therefore, there are no requirements to the tangential velocities. Consequently, the boundary conditions are

$$-\rho_{01} \frac{\partial \Phi_1}{\partial t} = -\rho_{02} \frac{\partial \Phi_2}{\partial t}; \quad \frac{\partial \Phi_1}{\partial y} = \frac{\partial \Phi_2}{\partial y} \quad \text{for } y = 0 \quad (11.109)$$

For these boundary conditions to be satisfied for any x , the x -dependent exponents must always be equal. Consequently, the angles φ_1 and φ_2 must be related as

$$k_1 \sin \varphi_1 = k_2 \sin \varphi_2$$

The basic expressions (11.108) and the boundary conditions (11.109) yield

$$R = \frac{Z_2 \cos \varphi_1 - Z_1 \cos \varphi_2}{Z_2 \cos \varphi_1 + Z_1 \cos \varphi_2}; \quad T = \frac{2\rho_{01}c_2 \cos \varphi_1}{Z_2 \cos \varphi_1 + Z_1 \cos \varphi_2} \quad (11.110)$$

From Eq. (11.109) $\cos \varphi_2$ is obtained as

$$\cos \varphi_2 = \sqrt{1 - \left(\sin \varphi_1 \cdot \frac{c_2}{c_1} \right)^2}$$

This expression is imaginary if $c_2 > c_1$ and $\varphi_1 > \arcsin(c_1/c_2)$. In this case, the absolute value of the amplitude of the reflected wave is equal to unity. Thus, no intensity is transmitted. In fluid 2, the waves are propagating along the x -axis. The amplitude of the waves decays for increasing distances to the plane separating the fluids. The velocity potential in fluid 2 is for this particular case given by

$$\Phi_2(x, y, t) = \exp[i(\omega t - k_1 x \sin \varphi_1)] \cdot \exp[-y(k_1^2 \sin^2 \varphi_1 - k_2^2)^{1/2}] \quad (11.111)$$

The two possibilities are illustrated in Fig. 11.14. Compare also the discussion in Sect. 5.8 regarding the transmission of bending waves across a junction between two flat plates of different thicknesses.

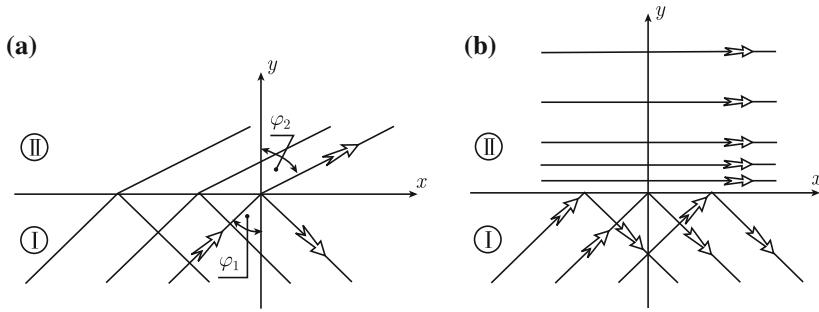


Fig. 11.14 Reflected and transmitted waves, ($c_2 > c_1$). In **a** a wave is transmitted, in **b** total reflection of incident intensity

For $Z_2 \gg Z_1$ the amplitude R of the reflected wave is almost equal to unity. For $R = 1$ the particle velocity normal to the surface of the plane separating the fluids is zero. In practice, this is almost the case when airborne sound is reflected in a calm water surface. For this case the ratio $Z_2/Z_1 \approx 3.5 \cdot 10^3$. For the inverse case, water-borne sound reflected in the water surface facing air, or when $Z_2 \ll Z_1$, the amplitude R of the reflected wave is approximately equal to -1 . The result is that the incident intensity is almost completely reflected back into the water. The reflected wave is 180° out of phase with the incident wave. The pressure at the surface is, therefore, almost equal to zero.

The sound field generated by a source over a completely reflecting surface for which R is either $+1$ or -1 can be described by means of real and imaginary sources. The procedure can be demonstrated by first considering a simple point source in free space. The velocity potential for this case is, as shown in Eq.(11.42), equal to $\Phi(r, t) = U_0 \cdot \exp[i(kr - \omega t)] / (4\pi r)$ where r is the distance from the source to some observation point. The source is moved to a point $(0, y_0, 0)$ above a totally reflecting plane oriented in the x - z -plane. The surface has an infinite acoustic impedance. The particle velocity v_y normal to the surface is thus equal to zero at the boundary. The same particle velocity, $v_y = 0$ for $y = 0$, is achieved in free space by two identical sources located at the points $(0, y_0, 0)$ and $(0, -y_0, 0)$. Compare the discussion on dipoles in Sect. 11.6. The velocity potential resulting from these two sources in a point (x, y, z) is

$$\Phi(x, y, z, t) = U_0 \cdot \exp(i\omega t) \left[\frac{e^{-ikr_1}}{4\pi r_1} + \frac{e^{-ikr_2}}{4\pi r_2} \right]$$

$$r_1 = [x^2 + (y - y_0)^2 + z^2]^{1/2}; \quad r_2 = [x^2 + (y + y_0)^2 + z^2]^{1/2} \quad (11.112)$$

The y -component of the particle velocity is

$$\begin{aligned} v_y(x, y, z, t) &= \frac{\partial \Phi}{\partial y} \\ &= -U_0 \cdot \exp(i\omega t) \left[\frac{e^{-ikr_1}}{4\pi r_1} \left(ik + \frac{1}{r_1} \right) (y - y_0) \right. \\ &\quad \left. + \frac{e^{-ikr_2}}{4\pi r_2} \left(ik + \frac{1}{r_2} \right) (y + y_0) \right] \end{aligned}$$

On the surface, $y = 0$, $r_1 = r_2$ and the particle velocity normal to the surface is zero, $v_y = 0$, for any y . The conclusion is that a field from a point source at $(0, y_0, 0)$ above a plane and totally reflecting surface, $R = 1$ at $y = 0$ is equivalent to the field in free space generated by two identical sources, one at the point of the real source $(0, y_0, 0)$ and the other one at its image point at $(0, -y_0, 0)$. For $y < 0$ the sound field is zero.

In a similar way, the field generated by a point source above a pressure release surface, with $R = -1$, is

$$\Phi(x, y, z, t) = U_0 \cdot \exp(i\omega t) \left[\frac{e^{-ikr_1}}{4\pi r_1} - \frac{e^{-ikr_2}}{4\pi r_2} \right] \quad (11.113)$$

As before the volume velocity of the point source is U_0 . The distances r_1 and r_2 are defined in Eq. (11.112). The pressure $p = -\rho_0 \partial \Phi / \partial t$ is zero for $y = 0$, i.e., everywhere on the surface. The field from a point source above an acoustically soft surface, $R = -1$, is equivalent to the field in an unbounded medium from the point source and its negative image source.

In general, the field incident on a surface is not a simple plane wave but rather a spherical wave. The field from a point source above a plane surface with the reflection coefficient R can according to Ref. [144] be written as

$$\Phi(x, y, z, t) = U_0 \cdot \exp(i\omega t) \left\{ \frac{e^{-ikr_1}}{4\pi r_1} + \frac{e^{-ikr_2}}{4\pi r_2} [R + (1 - R)\mathcal{F}] \right\} \quad (11.114)$$

The function \mathcal{F} depends on r_1 , r_2 , k , Z_1 , Z_2 and the angle of incidence as discussed in Ref. [144]. For grazing incidence, $\varphi_i \approx \pi/2$, or for r_2 approaching infinity, the function \mathcal{F} is approximately equal to zero. Thus, at large distances from a source and close to the ground the surface appears to be totally reflecting for $Z_2 \gg Z_1$.

The interference effects between the direct and reflected sound from a source above a plane can be considerable. Reflection effects complicate outdoor acoustic measurements. A rather typical test situation is illustrated in Fig. 11.15. A sound source is located fairly close to the ground, which is assumed to be acoustically hard. The height of the source above the ground is h_s . The sound pressure from the source is recorded at a point h_r above the ground and at the horizontal distance x from the source. It is assumed that $x \gg h_r$ and h_s . The reflecting plane is replaced by an

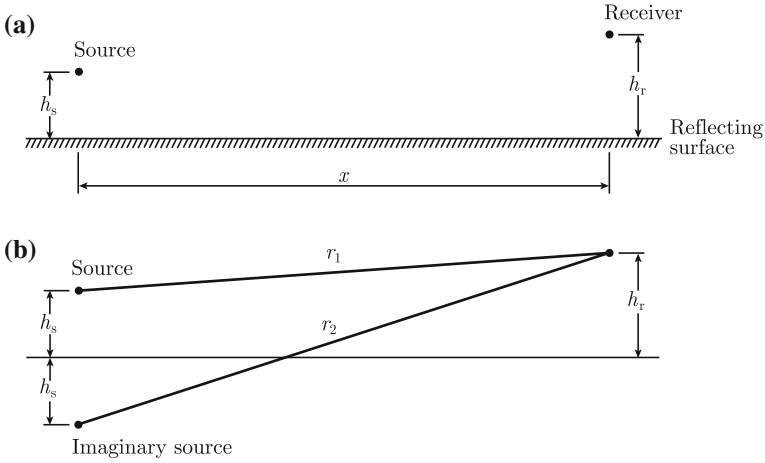


Fig. 11.15 A source above a totally reflecting plane. The acoustic field above the surface is equivalent to a field induced by a real and an imaginary source having the same power

imaginary source as shown in Fig. 11.15. The distances r_1 and r_2 from the real and imaginary sources are

$$r_1 = [x^2 + (h_r - h_s)^2]^{1/2} \approx x + \frac{(h_r - h_s)^2}{2x}$$

$$r_2 = [x^2 + (h_r + h_s)^2]^{1/2} \approx x + \frac{(h_r + h_s)^2}{2x} \tag{11.115}$$

The approximate results are valid as long as the heights are small compared to the distance x between source and receiver. The distances r_2 can be written as

$$r_2 = r_1 + 2\Delta r; \quad \Delta r = h_s h_r / x \tag{11.116}$$

The resulting velocity potential representing the direct and reflected fields is

$$\Phi(x, y, z, t) = \frac{U_0}{4\pi r_1} \cdot \exp[i(\omega t - kr_1)] \left[1 + \frac{r_1}{r_2} \exp(2ik\Delta r) \right] \tag{11.117}$$

The ratio r_1/r_2 is almost equal to unity for Δr small. However, the product $k\Delta r$ is not necessarily small. Thus for $\Delta r \rightarrow 0$ the velocity potential tends to

$$\Phi = \frac{U_0}{4\pi r_1} \cdot \exp[i(\omega t - kr_1 + k\Delta r)] \cdot 2 \cos(k\Delta r) \tag{11.118}$$

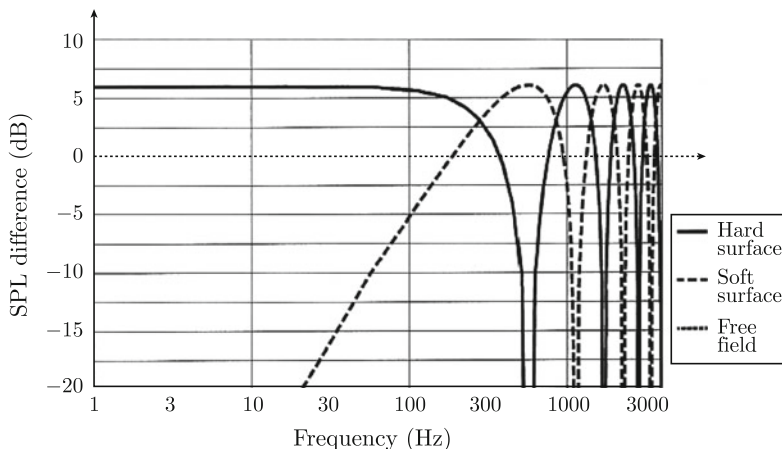


Fig. 11.16 Sound pressure level from a point source above a surface for which $R = 1$ (solid line) and $R = -1$ (dashed line) compared to the corresponding sound pressure level under free field conditions (dotted line). $h_s = 1.5\text{ m}$, $h_r = 1.5\text{ m}$, $x = 10\text{ m}$

The time average of the pressure squared is

$$|\bar{p}|^2 = |\bar{p}_0|^2 4 \cos^2(k\Delta r); \quad |\bar{p}_0|^2 = \left| \frac{\bar{U}_0}{4\pi r_1} \right|^2 \tag{11.119}$$

The time average of the pressure squared for free field conditions is given by $|\bar{p}_0|^2$. The sound pressure level L_r for the source above the reflecting plane as compared to the sound pressure level L_0 in free field and at the same distance from the source is shown in Fig. 11.16 as function of frequency. In the example $h_s = h_r = 1\text{ m}$ and $x = 20\text{ m}$. The level difference is $L_r - L_0 = 10 \log(|\bar{p}|^2 / |\bar{p}_0|^2)$. Minima are obtained for the frequencies $f_n = xc(1 + 2n)/(4h_r h_s)$ where n is an integer and c the speed of sound in the fluid.

For a ground, which is not acoustically hard the frequency corresponding to the first minimum is primarily determined by the ground impedance rather than by the geometry. The expression (11.114) can be used to estimate the sound pressure above ground. For $\Delta r \ll 1$ the function \mathcal{F} in Eq. (11.114) is approximately equal to zero. In practice, a surface is not completely reflecting. Consequently, energy is lost when sound propagates over ground. The losses depend on ground impedance, frequency, and geometry. In general, ground attenuation dominates over air absorption in the low frequency region. One example is presented in Fig. 11.17. At large distances r from a source close to the ground, the sound pressure tends to decrease as $1/r^2$. For free field conditions spherical attenuation corresponds to a decay $1/r$. Generalized and simplified models for the prediction of ground attenuation are for example presented in Ref. [140].

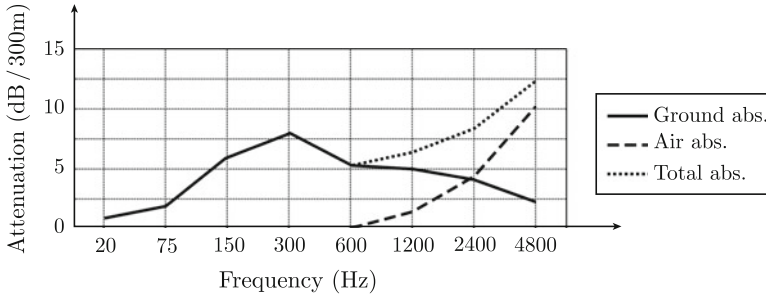


Fig. 11.17 Attenuation due air absorption (*dashed curve*) and ground absorption (*solid line*). Total attenuation given by *dotted line*

Measurements of underwater noise are influenced by reflections in the water surface, which is acoustically soft with $R \approx -1$. The field induced by a source close to an acoustically soft surface can be derived in a similar way as discussed above in connection with reflections in a hard surface. Thus, consider a source at the depth h_s below a water surface. The resulting pressure is measured at the horizontal distance x from the source and at the depth h_r . The pressure as compared to free field conditions is, using the same definitions as before

$$|\bar{p}|^2 = |\bar{p}_0|^2 4 \sin^2(k\Delta r); \quad |\bar{p}_0|^2 = \left| \frac{\bar{U}_0}{4\pi r_1} \right|^2 \quad (11.120)$$

The sound pressure level difference $L_r - L_0$ is also shown in Fig. 11.16. For this particular case the level difference has minima for the frequencies $f_n = xc_n / (2h_r h_s)$.

11.10 Reflection from a Water Surface

Underwater measurements for determining the acoustical radiation from a submerged plate element or source can be particularly difficult. This is due to reflections in the water surface. Furthermore, the water surface is seldom or never completely smooth. The reflected waves from the surface cause cancelation of the direct field from a source in the low frequency region. In practice, some of these problems are encountered when underwater noise radiated from ships is to be determined. Very often there are special requirements to underwater noise for various types of research, navy and fishing vessels and even cruise liners. The surface effects can change the radiation pattern from a single structure considerably as compared to free field conditions. The radiation into free field from a ship-like structure like a cylinder was discussed in Sect. 11.7. The sound pressure level induced by the breathing mode of the infinite cylinder is obtained from Eq. (11.50). If the same cylinder is semi-submerged the surface velocity, due to reflection effects and as seen from the water, will be

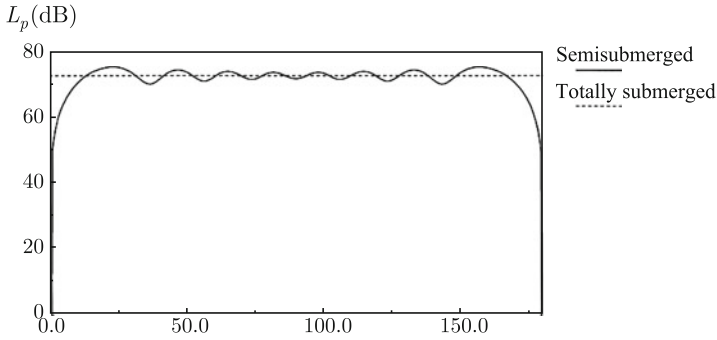


Fig. 11.18 Radiation from an infinite cylinder with uniform surface velocity. The sound pressure levels for the semi-submerged (solid line) and totally submerged (dashed line) cases are shown. The angle between the watersurface and the line of observation varies between 0 and 180°

$$\begin{aligned}
 u(\varphi, t) &= -u_0 \cdot \exp(i\omega t) & \text{for } 0 \leq \varphi \leq \pi \\
 u(\varphi, t) &= u_0 \cdot \exp(i\omega t) & \text{for } \pi < \varphi < 2\pi
 \end{aligned}
 \tag{11.121}$$

The resulting velocity potential in the water is obtained from Eq. (11.83) as

$$\Phi(r, \varphi, t) = -\frac{2u_0 \cdot \exp(i\omega t)}{\pi k} \left[\sum_{m=1}^{\infty} \frac{H_m^{(2)}(kr)}{m[H_m^{(2)}(kr_0)]'} [1 - \cos(m\pi)] \sin(m\varphi) \right]
 \tag{11.122}$$

The details of solving the problem are left for Problem 11.9. The variation of the sound pressure level as function of the angle φ is given in Fig. 11.18. The diameter of the cylinder is 2.5 m. The sound pressure level is calculated at a distance of 7.5 m from the center of the cylinder at $f = 1846$ Hz, $kr_0 = 20$. For φ equal to 0° and 180° the sound pressure is zero. From approximately 20° to 160°, the sound pressure level oscillates around the level obtained for the totally submerged cylinder. When recording underwater sound from an object, measurement positions close to the water surface should be avoided.

Yet another example is illustrated in Fig. 11.19. A cylinder is again semi-submerged in water. Part of the surface of the cylinder is vibrating with a velocity $u_0 \exp(i\omega t)$ for $-\varphi_0 \leq \varphi \leq 0$. Considering the image effects the pressure in the water can be calculated as if the cylinder is in an unbounded medium. The velocity $u(\varphi, t)$ of the surface of the cylinder as seen from the water is

$$\begin{aligned}
 u(\varphi, t) &= -u_0 \cdot \exp(i\omega t) & \text{for } 0 \leq \varphi \leq \varphi_0 \\
 u(\varphi, t) &= u_0 \cdot \exp(i\omega t) & \text{for } -\varphi_0 < \varphi < 0 \quad \text{otherwise zero}
 \end{aligned}
 \tag{11.123}$$

Following the procedure outlined in Sect. 11.7 and discussed in Problem 11.10 the velocity potential in the water is

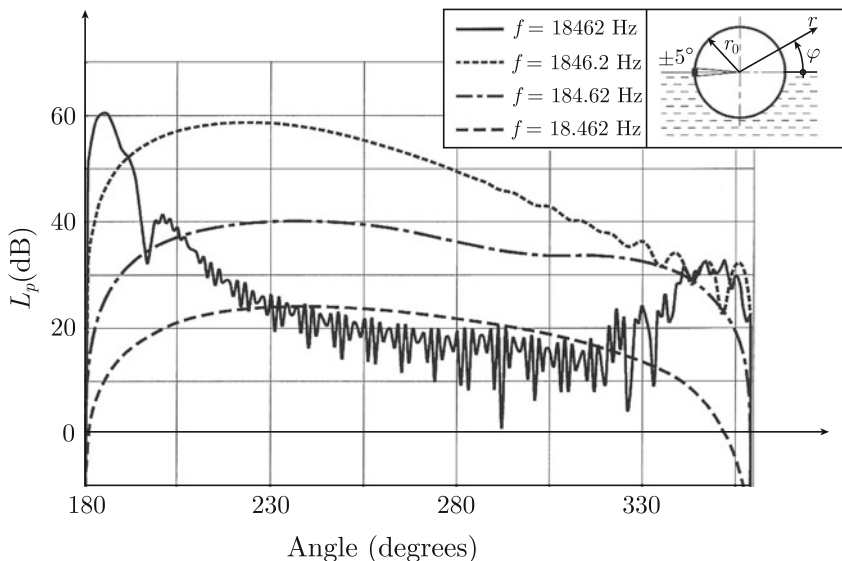


Fig. 11.19 Radiation from a strip on an infinite cylinder semi- submerged in water, $r = 7.5$ m, $r_0 = 2.5$ m

$$\Phi(r, \varphi, t) = -\frac{2u_0 \cdot \exp(i\omega t)}{\pi k} \left[\sum_{m=1}^{\infty} \frac{H_m^{(2)}(kr)}{m[H_m^{(2)}(kr_0)]'} [1 - \cos(m\varphi_0)] \sin(m\varphi) \right] \tag{11.124}$$

The resulting sound pressure level in the water is shown in Fig. 11.19. The result is compared to the radiation from a cylinder in an unbounded medium, water, discussed in Sect. 11.7, Fig. 11.9 for which $u(\varphi, t) = u_0 \cdot \exp(i\omega t)$ and $-\varphi_0 < \varphi < \varphi_0$. In both examples φ_0 is set to equal 5° . Again it is found that the sound pressure is zero at the watersurface, in this case for $\varphi = 180^\circ$ and $\varphi = 360^\circ$. The directivity pattern is much more pronounced for high rather than for low frequencies. In the high frequency region the sound pressure shows a distinct interference pattern. The sound pressure is for high frequencies increasing slightly at the back side of the cylinder before dropping off close to the water surface.

11.11 Influence of Temperature and Velocity Gradients

The propagation of sound in fluids is influenced by temperature and flow and to an even larger extent by temperature and velocity gradients and turbulence. In addition, the sound absorption in air depends on humidity. The speed of sound in water has a strong dependence on the air contents in the water in the form of bubbles. When sound propagates in a fluid with varying temperature and flow velocity the sound rays tend to bend. For sound propagating over ground, wind gradients can be very

strong close to the ground. Typical wind profiles $v(z)$ and gradients $\partial v/\partial z$ vary with the height z above the ground as

$$v(z) = V_0 \ln \left(\frac{z + z_0}{z_0} \right); \quad \frac{\partial v}{\partial z} = \frac{V_0}{z + z_0} \tag{11.125}$$

The parameters V_0 and z_0 depend the character of the ground surface. V_0 is also a function of the average wind speed. In addition, there is turbulence, which means that the wind velocity varies as function of time and space. In general, turbulence caused by normal wind speeds exhibits low frequency variations, typically below 20 Hz. Close to the ground variations due to turbulence are most dominant parallel to the ground. Higher up, $z > 25$ m, the variations are more or less the same in all directions resulting in isotropic turbulence. Basic theories on turbulence and sound propagation in turbulent media are for example discussed in Refs. [145, 146].

Temperature gradients above ground are often inversely proportional to the height z over the ground. In the most simple case, sound propagating in air with constant wind and temperature gradients, the curvature of the sound rays is constant. The example is illustrated in Fig. 11.20. At the height z above the ground the total velocity, speed of sound and vector wind velocity, is $c + v \cos \varphi$. The angle between the wind direction and the direction of sound propagation is φ . At the height $z + \Delta z$, the total

Fig. 11.20 Curvature of an acoustic ray propagating in a fluid having velocity and temperature gradients, $\varphi = 0$

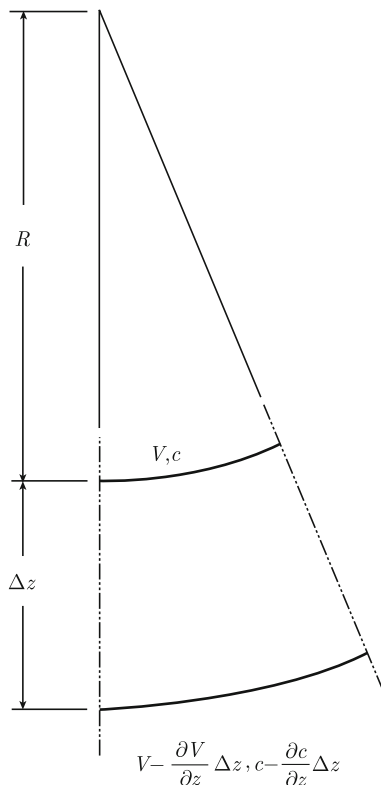
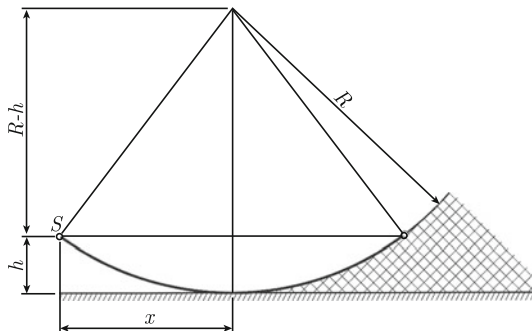


Fig. 11.21 Rays bending upwards creating a shadow zone



velocity is $c + v \cos \varphi + \Delta z(\partial c/\partial z + \cos \varphi \cdot \partial v/\partial z)$. The radius of curvature R_c is from Fig. 11.20 obtained as

$$R_c = -\frac{v \cdot \cos \varphi + c}{\frac{\partial v}{\partial z} \cos \varphi + \frac{\partial c}{\partial z}} \approx -\frac{c}{\frac{\partial v}{\partial z} \cos \varphi + \frac{\partial c}{\partial z}} \tag{11.126}$$

For moderate winds $v \ll c$. Since c is proportional to the square root of the absolute temperature T it follows that $\partial c/\partial z = (c/2T)\partial T/\partial z$. For $(\partial c/\partial z + \cos \varphi \cdot \partial v/\partial z) < 0$ the radius R is positive. The rays bend upwards as shown in Fig. 11.21. For $(\partial c/\partial z + \cos \varphi \cdot \partial v/\partial z) > 0$ the rays bend downwards from a source. The ray patterns in the down and upwind directions are different since the radius of curvature varies with the angle φ . When the rays are bent upwards, a shadow zone is formed as shown in Fig. 11.21. Within this zone there is no direct sound from the source. The sound pressure level is reduced drastically when a measurement position is moved from the direct field into the shadow zone. Within the shadow zone the sound pressure level decays rapidly as the distance from the source is increased. Measurements within the shadow zone should be avoided. The bending of acoustic rays due to temperature gradients is shown in Fig. 11.22.

In the atmosphere as well as in the ocean there can be layers separated by strong flow and temperature gradients. Sound waves can propagate within these layers over long distances. For this type of sound waves, the geometrical attenuation is no longer spherical.

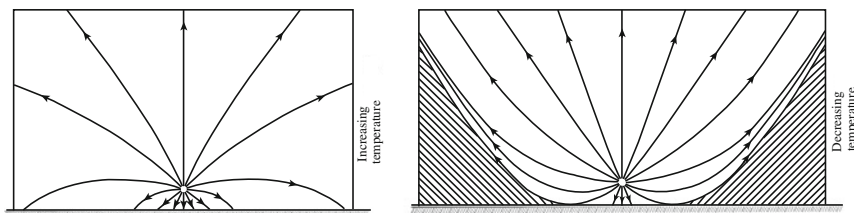


Fig. 11.22 Bending of acoustic rays due to temperature gradients. In the left figure temperature is increasing with height over ground. In the right figure temperature is decreasing with height

11.12 Acoustic Fields in Closed Rooms

In any type of enclosed space, there are certain losses, which will influence the acoustic field in the room. These losses are due to the fluid in the room and to a certain absorption of energy of the enclosing structures. The losses in the fluid, for example, air, depend on room temperature, air humidity, and frequency. Even in a room with acoustically hard walls, for example concrete with a very smooth surface, part of the acoustic energy in the room is absorbed due to an infinite number of reflections in the walls. The total loss factor due to the losses in the fluid or air and due to the absorption of the walls are denoted δ . In general, the losses due to the sound absorption of the walls are much higher than the losses in the fluid. A similar approach was adopted to describe losses in structures, interior, and at boundaries, as discussed in Sect. 5.12.

In a room with acoustically hard walls, the particle velocity in the fluid perpendicular to the wall must be equal to zero. For a room with the geometry shown in Fig. 11.23 the particle velocity v_x in the x -direction must be on the form $v_x \propto \sin(l\pi x/L_x)$, i.e. $v_x = 0$ for $x = 0$ and $x = L_x$ for l being an integer. A corresponding argument holds for v_y and v_z . The particle velocity vector is defined as $\mathbf{v} = \mathbf{grad}\Phi$ where Φ is the velocity potential in the room. Consequently, to satisfy the boundary conditions, the velocity potential in the room must be on the form

$$\Phi(x, y, z, t) = \sum_{l,m,n} F_{lmn}(t) \cdot \cos\left(\frac{l\pi x}{L_x}\right) \cos\left(\frac{m\pi y}{L_y}\right) \cos\left(\frac{n\pi z}{L_z}\right) \quad (11.127)$$

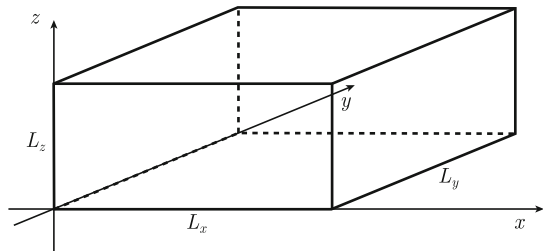
The summation is made over all possible combinations of the integers l , m and n . $F_{lmn}(t)$ is some function of time satisfying some initial conditions.

The Eq. (11.127) can also be written as

$$\Phi(x, y, z, t) = \sum_{l,m,n} F_{lmn}(t) \cdot \varphi_{lmn}(x, y, z) \quad (11.128)$$

where φ_{lmn} are the eigenfunctions satisfying the boundary conditions. Thus for a parallelepiped room with the dimensions L_x , L_y and L_z as shown in Fig. 11.23 and with acoustically hard walls the eigenfunctions are

Fig. 11.23 A room and its dimensions



$$\varphi_{lmn}(x, y, z) = \cos\left(\frac{l\pi x}{L_x}\right) \cos\left(\frac{m\pi y}{L_y}\right) \cos\left(\frac{n\pi z}{L_z}\right) \quad (11.129)$$

The eigenfunctions satisfy the equation

$$\nabla^2 \varphi_{lmn} = k_{lmn}^2 \varphi_{lmn}; \quad k_{lmn}^2 = \left(\frac{l\pi}{L_x}\right)^2 + \left(\frac{m\pi}{L_y}\right)^2 + \left(\frac{n\pi}{L_z}\right)^2 \quad (11.130)$$

The eigenfunctions are orthogonal satisfying

$$\iiint_V \varphi_{lmn} \varphi_{qrs} dV = \langle \varphi_{lmn} | \varphi_{qrs} \rangle = L_x L_y L_z \varepsilon_l \varepsilon_m \varepsilon_n \delta_{lq} \delta_{mr} \delta_{ns} / 8, \\ \varepsilon_l = 2 \text{ for } l = 0, \quad \varepsilon_l = 1 \text{ for } l > 0 \text{ etc.} \quad (11.131)$$

The velocity potential must also satisfy the wave equation. For the source free case the wave equation is, including losses as discussed in Sects. 11.1 and 11.2.

$$\nabla^2 \Phi - \frac{1}{c^2} \frac{\partial^2 \Phi}{\partial t^2} = 0; \quad c^2 = c_0^2 (1 + i\delta)$$

The total loss factor is δ .

In accordance with the discussion in Chap. 1 the function $F_{lmn}(t)$, introduced in Eq. (11.127) must satisfy

$$\frac{d^2 F_{lmn}}{dt^2} + \omega_{lmn}^2 (1 + i\delta) F_{lmn} = 0 \\ \omega_{lmn}^2 = c_0^2 \cdot k_{lmn}^2 = c_0^2 \left[\left(\frac{l\pi}{L_x}\right)^2 + \left(\frac{m\pi}{L_y}\right)^2 + \left(\frac{n\pi}{L_z}\right)^2 \right] \quad (11.132)$$

The solution to Eq. (11.132) is

$$F_{lmn}(t) = \exp(-\delta \omega_{lmn} t / 2) [A_{lmn} \cos(\omega_{lmn} t) + B_{lmn} \sin(\omega_{lmn} t)] \quad (11.133)$$

where the amplitudes A_{lmn} and B_{lmn} are determined by the initial conditions. The mode (l, m, n) is oscillating at the natural frequency f_{lmn} with

$$f_{lmn} = \frac{\omega_{lmn}}{2\pi} = \frac{c_0}{2} \left[\left(\frac{l}{L_x}\right)^2 + \left(\frac{m}{L_y}\right)^2 + \left(\frac{n}{L_z}\right)^2 \right]^{1/2} \quad (11.134)$$

The time average over one oscillation of the pressure squared is decaying as

$$|\bar{p}|^2 \propto \exp(-\omega_{lmn} \delta t) \quad (11.135)$$

The reverberation time T_r , i.e., the time for the sound pressure level in the room to decrease 60 dB, is, as discussed in Chap. 1 given by

$$T_r = \frac{2.2}{f\delta} \quad (11.136)$$

The number of natural frequencies in the frequency range below the frequency f is given by

$$N = \frac{4\pi f^3 V}{3c^3} + \frac{\pi f^2 S_{\text{tot}}}{4c^2} + \frac{f L_{\text{tot}}}{8c} \quad (11.137)$$

where V is the volume of the room, S_{tot} the total wall area and L_{tot} the sum of the lengths of all the edges of the room. In the high frequency region the first term dominates. From (11.137) the modal density \mathcal{N}_f and the spacing Δf between two natural frequencies are for high frequencies obtained as (see Problem 11.11)

$$\mathcal{N}_f = \frac{\Delta N}{\Delta f} = \frac{4\pi f^2 V}{c^3}; \quad \Delta f = \frac{c^3}{4\pi f^2 V} \quad (11.138)$$

The distance between two natural frequencies decreases rapidly as the frequency is increasing. In the high frequency range there is a large number of modes which results in a near diffuse acoustic field in the room. In the low frequency range there are just a few modes and the field is far from diffuse. In Table 11.2, the first few natural frequencies for a rectangular room are listed as functions of the integers l , m and n . The dimensions of the room are $L_x = 5$ m, $L_y = 2.5$ m, and $L_z = 10/3$ m. In the table the angle of incidence γ_x at the wall $x = 0$ is given. The angle is obtained as $\cos \gamma_x = k_x/k$. The center frequency f_0 for each 1/3 octave band is also listed in the table.

The sound pressure $p = -\rho_0 \partial \Phi / \partial t$ in the room for some of the first few modes is

$$l = 2; \quad m = 0; \quad n = 0; \quad p \propto \cos(2\pi x/L_x)$$

$$l = 1; \quad m = 1; \quad n = 0; \quad p \propto \cos(\pi x/L_x) \cos(\pi y/L_y)$$

$$l = 2; \quad m = 1; \quad n = 0; \quad p \propto \cos(2\pi x/L_x) \cos(\pi y/L_y) L = 2$$

Sound pressure contour plots in the room are shown in Fig. 11.24. The absolute value of the sound pressure is shown in the plot. Note that the absolute value of the sound pressure in the corners of the room always has a maximum. Within a frequency band, the resulting sound pressure is the sum of the pressure for all the modes within the band. In the low frequency region, the sound pressure can vary considerably between various positions in the room. In particular, this is true when the losses in the room are small.

For forced excitation, a source with the volume velocity $Q_0 \cdot \exp(i\omega t)$, located at (x_0, y_0, z_0) inside the room, the resulting velocity potential $\Phi_0(x, y, z) \cdot \exp(i\omega t)$

Table 11.2 Modes in a room, $L_x = 5\text{ m}$, $L_y = 2.5\text{ m}$ and $L_z = 10/3\text{ m}$

l	m	n	γ_x (°)	f_{lmn} (Hz)	f_0 (Hz)
1	0	0	0	34	31.5
0	0	1	90	51	50
1	0	1	56	62	63
0	1	0	90	68	
2	0	0	0	68	
1	1	0	64	82	80
0	1	1	90	85	
2	0	1	37	85	
1	1	1	68	92	100
2	1	0	45	97	
3	0	0	0	102	
0	0	2	90	102	
1	0	2	72	107	
2	1	1	51	109	
3	0	1	26	113	125
2	0	2	56	122	
3	1	0	34	122	
0	1	2	90	122	
1	1	2	74	128	
0	2	0	90	136	
4	0	0	0	136	

should satisfy $\nabla^2 \Phi_0 + k^2 \Phi_0 = Q\delta(\mathbf{r} - \mathbf{r}_0)$. The Dirac function is not defined if \mathbf{r}_0 is on the boundary, i.e., $0 < x_0 < L_x$. Compare Problem 11.13. By multiplying the wave by φ_{lmn} and integrating over the volume of the room the result is

$$\Phi_0 = \sum_{l,m,n} \frac{8Q_0 \varphi_{lmn}(\mathbf{r}) \varphi_{lmn}(\mathbf{r}_0)}{V \varepsilon_l \varepsilon_m \varepsilon_n (k^2 - k_{lmn}^2)} \tag{11.139}$$

The pressure is from Eq. (11.9) obtained as

$$p = -\rho_0 \frac{\partial \Phi}{\partial t} = -i\omega \rho_0 \Phi_0 \exp(i\omega t)$$

The Fourier transform of the pressure can according to the discussion in Sect. 2.2 be written as

$$\hat{p} = -i\omega \rho_0 \Phi_0 \tag{11.140}$$

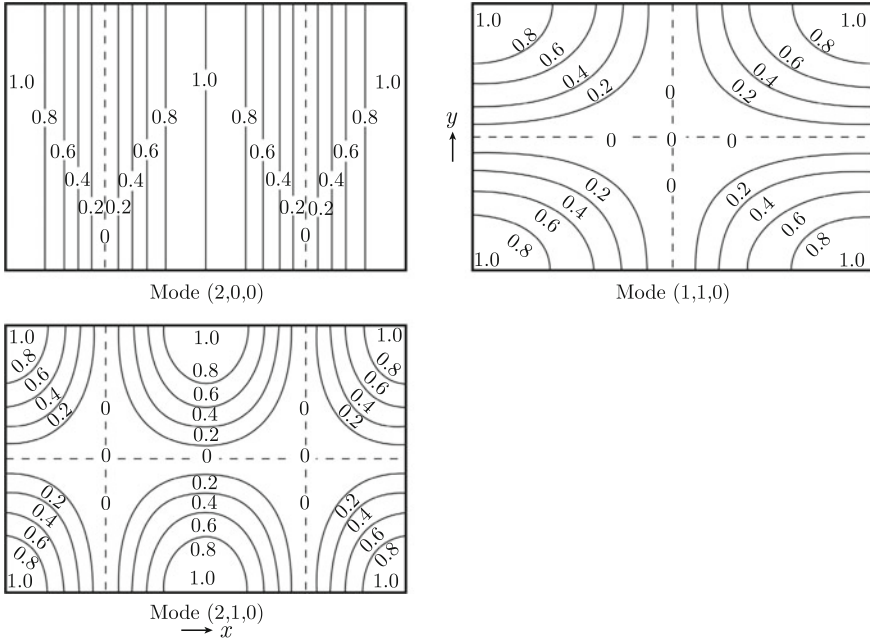


Fig. 11.24 Variation of the absolute value of the sound pressure in a room for the modes (2, 0, 0), (1, 1, 0), and (2, 1, 0). From Ref. [48]

The space average of square of the FT of the pressure is

$$\begin{aligned}
 \langle |\hat{p}|^2 \rangle &= \omega^2 \rho_0^2 \frac{1}{V} \int_V dV |\Phi_0|^2 = \frac{\omega^2 \rho_0^2}{V^2} \sum_{l,m,n} \frac{8 |Q_0|^2 \varphi_{lmn}^2(\mathbf{r}_0)}{\varepsilon_l \varepsilon_m \varepsilon_n |k^2 - k_{lmn}^2|^2} \\
 &= \frac{f^2 \rho_0^2}{V^2 \pi^2} \sum_{l,m,n} \frac{2c^4 |Q_0|^2 \varphi_{lmn}^2(\mathbf{r}_0)}{\varepsilon_l \varepsilon_m \varepsilon_n [(f^2 - f_{lmn}^2)^2 + (\delta f_{lmn}^2)^2]} \\
 &= \sum_{l,m,n} \langle |\hat{p}_{lmn}|^2 \rangle \tag{11.141}
 \end{aligned}$$

The space average of the pressure squared is a rapidly varying function of frequency. The frequency average of $\langle |\hat{p}|^2 \rangle$ of the mode (l, m, n) is

$$\langle |\bar{\hat{p}}_{lmn}|^2 \rangle = \frac{1}{\Delta f} \int df \langle |\hat{p}_{lmn}|^2 \rangle; \quad \Delta f = \frac{c^3}{4\pi f^2 V}$$

The distance in the frequency domain between two modes is Δf as given by (11.138). So eventually the space and frequency average of the square of the FT of the pressure is as discussed in Problem 11.14 obtained as

$$\langle |\bar{p}_{lmn}|^2 \rangle = \frac{4c\rho_0^2 f_{lmn} |Q_0|^2 \varphi_{lmn}^2(\mathbf{r}_0)}{V\delta}$$

It is assumed that the frequency f_{lmn} is sufficiently high to set ε_l , ε_m and ε_n to equal one. For a source mounted inside the room the average of $\varphi_{lmn}^2(\mathbf{r}_0)$ is $1/8$ with respect to the parameters l , m , and n . Statistically, the space and frequency average of the squared of the FT of the pressure can by replacing f_{lmn} by f be written as

$$\langle |\bar{p}_{lmn}|^2 \rangle = \frac{c\rho_0^2 f |Q_0|^2}{2V\delta} \quad (11.142)$$

The frequency and space average of $|\bar{p}|^2$ within a frequency band Δf is

$$\langle |\bar{p}|^2 \rangle_{\Delta f} = \sum_{lmn} \langle |\bar{p}_{lmn}|^2 \rangle$$

The summation is made over all modes $N_{\Delta f}$ for which $f - \Delta f/2 < f_{lmn} < f + \Delta f/2$ or for $N_{\Delta f} = \Delta f \cdot \mathcal{N}_f$ where \mathcal{N}_f is the modal density in the room. Thus,

$$\langle |\bar{p}|^2 \rangle_{\Delta f} = \Delta f \cdot \frac{2\pi f^3 \rho_0 |Q_0|^2}{c^2 \delta} \quad (11.143)$$

The results are only valid as long as there are a sufficient number of modes in the room as discussed in next section.

11.13 Geometrical Acoustics

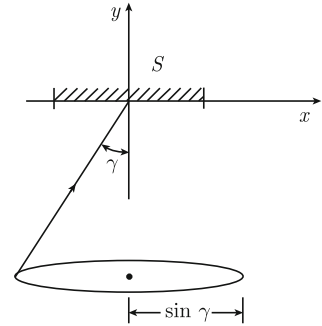
The acoustic field in a large room fitted with diffusers can in the high frequency region be assumed diffuse. In a diffuse acoustic field the sound intensity in any direction is the same. This is the basis for geometrical acoustics.

Based on the assumption that a sound field is diffuse, a number of simple relationships concerning acoustic energy, intensity can be derived. Consider, a flat surface with the area S located on a wall defined by the coordinate $y = 0$ as shown in Fig. 11.25. A plane acoustic wave propagating in the x - y -plane is defined by its velocity potential as

$$\Phi(x, y, z, t) = A \cdot \exp[i(\omega t - kx \sin \gamma - ky \cos \gamma)] \quad (11.144)$$

where k is the wavenumber and γ the angle of incidence. The amplitude A is for a diffuse field independent of the angle of incidence. The time average of the acoustic power incident on the surface S is

Fig. 11.25 A wave incident on a surface



$$\bar{\Pi} = \bar{I}_y S = \frac{S}{2} \operatorname{Re} \left[\int_0^{\pi/2} p v_y^* \cdot 2\pi \sin \gamma d\gamma \right] \quad (11.145)$$

The pressure is defined as $p = -\rho_0 \partial \Phi / \partial t$ and the particle velocity normal to the wall as $v_y = \partial \Phi / \partial y$. Thus, the total incident intensity on the wall is thus

$$\bar{I}_y = \frac{1}{2} \operatorname{Re} \left[|A|^2 \int_0^{\pi/2} \omega \rho_0 k \cdot 2\pi \sin \gamma \cos \gamma d\gamma \right] = \pi |A|^2 \omega \rho_0 k / 2 \quad (11.146)$$

The time average of the pressure squared in the room is

$$|\bar{p}|^2 = \frac{1}{2} \int_0^{\pi} \rho_0^2 \left| \frac{\partial \Phi}{\partial t} \right|^2 2\pi \sin \gamma d\gamma = 2\pi (\rho_0 \omega)^2 |A|^2 \quad (11.147)$$

The time averages of the kinetic and potential energies per unit volume are obtained from (11.24) as

$$\bar{E}_V = \bar{T}_V + \bar{U}_V = \frac{1}{2} \int_0^{\pi} \left[\frac{\rho_0}{2c^2} \left| \frac{\partial \Phi}{\partial t} \right|^2 + \frac{\rho_0}{2} |\mathbf{grad} \Phi|^2 \right] 2\pi \sin \gamma d\gamma = 2\pi |A|^2 \omega^2 \rho_0 / c^2 \quad (11.148)$$

The Eqs. (11.146) through (11.148) give

$$\bar{I}_y = \frac{c \bar{E}_V}{4} = \frac{|\bar{p}|^2}{4\rho_0 c} \quad (11.149)$$

Now assume that a sound source with the acoustic power $\Pi(t)$ is located in the room. Let the room be large enough for the sound field to be considered as diffuse. The power dissipated in room is the sum of the lost power Π_f in fluid and the power Π_a absorbed by the walls. The power lost in the fluid is

$$\Pi_f = \omega \delta_a \bar{E}_V V \quad (11.150)$$

where δ_a is the loss factor in the fluid, \mathcal{E}_V the acoustic energy per volume and V the volume of the room. The power absorbed by the walls is

$$\Pi_a = I_n A \quad (11.151)$$

where I_n is the component of the intensity perpendicular to the wall. The intensity components parallel to the wall are assumed not to contribute to the absorbed power. A is the equivalent absorption area of the wall which also can be written as

$$A = \int dS \alpha(x, y, z) \quad \text{or} \quad A = \sum_i \alpha_i S_i$$

where α_i is the sound absorption coefficient of the surface element i . The energy balance in the room requires that

$$V \frac{\partial \mathcal{E}_V}{\partial t} + I_n A + \omega \delta_a \mathcal{E}_V V = \Pi$$

However, as shown in Eq. (11.149), $I_n = c\mathcal{E}_V/4$. Thus,

$$V \frac{\partial \mathcal{E}_V}{\partial t} + c\mathcal{E}_V A/4 + \omega \delta_a \mathcal{E}_V V = \Pi \quad (11.152)$$

The solution to (11.152) is

$$\mathcal{E}_V = \frac{1}{V} e^{-\lambda t} \int_{-\infty}^t e^{\lambda \tau} \Pi(\tau) d\tau; \quad \lambda = \frac{cA}{4V} + \omega \delta_a \quad (11.153)$$

If the field is stationary, i.e. $\partial \mathcal{E}_V / \partial t = 0$, the energy in the room is from (11.152) given by

$$\bar{\mathcal{E}}_V = \frac{\bar{\Pi}}{V[Ac/(4V) + \omega \delta_a]}; \quad |\bar{p}|^2 = \frac{4\rho_0 c \bar{\Pi}}{A + 4V\omega \delta_a/c} \quad (11.154)$$

In general, the losses in the fluid are small as compared to the losses of the walls. If this is the case

$$|\bar{p}|^2 = \frac{4\rho_0 c \bar{\Pi}}{A}; \quad \bar{\mathcal{E}}_V = \frac{4\bar{\Pi}}{Ac} = \frac{|\bar{p}|^2}{\rho_0 c^2}; \quad \bar{I}_n = \frac{|\bar{p}|^2}{4\rho_0 c} = \frac{\bar{\Pi}}{A} \quad (11.155)$$

If the acoustic power Π in room is turned on at $t = -t_0$ and turned off at $t = 0$ the energy and thus the pressure squared in the room will decay as

$$|\bar{p}|^2 = |\bar{p}_0|^2 \cdot e^{-\lambda t} = |\bar{p}_0|^2 \cdot \exp[-tAc/(4V)] \quad (11.156)$$

The reverberation time T_r is as before defined as the time after the sound source is turned off for the sound pressure level to decrease by 60 dB or the time for the acoustic energy or $|\bar{p}|^2$ to decay by a factor 10^{-6} . Thus from Eq. (11.156)

$$10^{-6} = \exp \left[-T_r \left(\frac{cA}{4V} + \omega\delta_a \right) \right]$$

For $\omega\delta_a \ll cA/(4V)$ the reverberation time is

$$T_r = \frac{24 \ln 10}{Ac/V[1 + 4\omega\delta_a/(Ac)]} \approx \frac{0.16 \cdot V}{A} \quad (11.157)$$

The reverberation time is in seconds, the volume in m^3 and the equivalent absorption area in m^2 . Equation (11.157) is often referred to as Sabine's formula. Later Eyring in Ref. [147] formulated an improved version of the expression giving the reverberation time. Eyring's formula reads

$$T_r = \frac{0.16 \cdot V}{-S \cdot \ln(1 - \bar{\alpha})} \quad (11.158)$$

The average sound absorption coefficient of the structures in the room is given by $\bar{\alpha}$. If the absorption is small $\ln(1 - \bar{\alpha}) \approx -\bar{\alpha}$ and the result (11.158) is approximately equal to (11.157). However, for most problems discussed in this text the accuracy given by the last part of the expression (11.157) is sufficient. Reverberation time curves were discussed in Sect. 2.9. Compare also Fig. 2.11. The average slope of the upper part of the decay curve should determine the reverberation time.

The decay of an acoustic field was first, Eq. (11.135), expressed as function of the loss factor δ and later, Eq. (11.156), by means of the equivalent absorption area A of the room. The two expressions must be identical. Thus,

$$\delta = \frac{Ac}{4\omega V} \quad (11.159)$$

This result inserted in Eq. (11.143) gives

$$\langle |\bar{p}|^2 \rangle = \frac{4\pi\rho_0^2 f^2 |Q_0|^2}{A} \quad (11.160)$$

For a source located inside the room this expression is reduced to

$$\langle |\bar{p}|^2 \rangle = \frac{4\rho_0 c |\hat{\Pi}|}{A} \quad (11.161)$$

The sound pressure in the reverberant field in a room depends on the sound absorption or equivalent absorption area A in the room as shown in Eq. (11.155). Thus if the acoustic power of a source is known, the equivalent absorption in the room can

be calculated by measuring the resulting average sound pressure level. Thus, let an acoustic source have the acoustic power Π . The resulting sound pressure in the reverberant field in the room is given in Eq. (11.155). If the sound power level of the source is L_Π in dB re 10^{-12} W and the average sound pressure level in the room is L_p in dB re $2 \cdot 10^{-5}$ Pa the equivalent absorption area A in m^2 is obtained as

$$10 \cdot \log A = L_\Pi - L_p + 6$$

The expression (11.157) can be used for determining the sound absorption coefficient of a material. A so-called reverberation room is used for the measurements. According to the ISO norms there are certain requirements to the minimum volume of the room as well as to the reverberation time of the room. The volume of the reverberation room should be at least 200 m^3 for measurements above 100 Hz. The area S of the test sample should exceed 10 m^2 . The test sample should be rectangular and should not be closer to any wall than 1 m. The reverberation time T_1 with an empty room is measured first. The test sample is thereafter mounted in the room and the new reverberation time T_2 is measured. The average absorption coefficient of the test sample is obtained as

$$\alpha = \frac{A_2 - A_1}{S} = \frac{0.16 \cdot V}{S} \left(\frac{1}{T_2} - \frac{1}{T_1} \right) \quad (11.162)$$

Theoretically, the absorption coefficient could vary between zero and unity. However, due to certain edge effects for finite samples and an approximate theory, the measurement technique outlined above and following the existing ISO requirements can result in a measured sound absorption coefficient, which exceeds unity. Various types of sound absorbers are discussed in for example Refs. [148, 149].

Geometrical acoustics require that an acoustic field in a room is reasonably diffuse. Schröder in Refs. [150, 151] defined a lower frequency limit f_s for a so-called diffuse field as

$$f_s = 2000 \sqrt{T_r / V} \quad (11.163)$$

Here T_r is in seconds and V in m^3 giving the frequency in Hz. The Schröder frequency is also discussed in Ref. [148].

11.14 Near and Reverberant Acoustic Fields in a Room

In Sect. 11.13, it was assumed that the acoustic field in the room was reverberant and diffuse. This condition cannot be satisfied if there is an acoustic source in the room. Close to the source, there is an acoustic near field dominating over the reverberant field. The resulting field in the room can be described by means of a simple model. Thus, assume that an omnidirectional source with the acoustic power Π is located in the room. In the direct acoustic field of the source the intensity I_r in the direction away from the source is given by

$$I_r = \frac{\Pi}{4\pi r^2} \quad (11.164)$$

where r is the radial distance from the source. The resulting pressure p_d from the omnidirectional source far from any reflecting surfaces is according to (11.64) obtained as

$$|\bar{p}_d|^2 = \frac{\rho_0 c \bar{\Pi}}{4\pi r^2}$$

However, if the source is mounted on a surface the resulting field in the room and close to the source will not only be determined by the source itself but also by its image source. For a source in free space the space angle as seen from the source is 4π . For the same source mounted on a hard surface the space angle is reduced to 2π and the intensity is doubled. For a source mounted at a junction between two surfaces the space angle is reduced to π and the intensity in near field of the source increased by a factor 4. Finally, the space for a source in a corner is $\pi/2$. The intensity is thus increased by a factor 8. Thus, the average of the pressure squared in the near field of a source is

$$|\bar{p}_d|^2 = \frac{\rho_0 c \bar{\Pi} \mathcal{P}}{4\pi r^2} \quad (11.165)$$

$\mathcal{P} = 8$ source in a corner

$\mathcal{P} = 4$ source in junction between two surfaces

$\mathcal{P} = 2$ sources mounted close to a flat surface

$\mathcal{P} = 1$ source mounted inside the room far from any reflecting surface

The output power of the source is assumed independent of its position. The average of the square of the sound pressure in the reverberant field is

$$|\bar{p}_r|^2 = \frac{4\rho_0 c \bar{\Pi}}{A} \quad (11.166)$$

The sources, the real causing the direct field and the imaginary or reflecting sources inducing the reverberant field, are assumed to be uncorrelated, the total pressure p_{tot} is thus

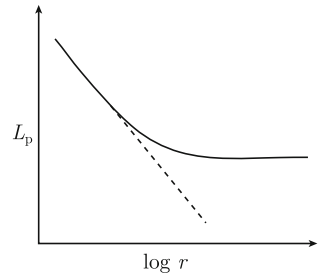
$$|\bar{p}_{\text{tot}}|^2 = |\bar{p}_r|^2 + |\bar{p}_d|^2 = \rho_0 c \bar{\Pi} \left[\frac{\mathcal{P}}{4\pi r^2} + \frac{4}{A} \right] \quad (11.167)$$

For $r < \sqrt{16\pi/(AP)}$ the first term inside the bracket of the expression (11.167) dominates, in this region the near field dominates, whereas further away from the source, the reverberant field determines the sound pressure in the room. The sound pressure level L_p in the room is from (11.167) obtained as

$$L_p = 10 \log \left[\frac{\rho_0 c \bar{\Pi}}{p_{\text{ref}}^2} \right] + 10 \log \left[\frac{\mathcal{P}}{4\pi r^2} + \frac{4}{A} \right] \quad (11.168)$$

The result is illustrated in Fig. 11.26.

Fig. 11.26 Near and reverberant fields in a room



11.15 Measurement of the Sound Transmission Loss of a Wall

A structure or wall mounted between a noise source and a listener can effectively reduce the noise exposure of the listener. The sound transmitted through a wall is determined by its sound reduction index R . The sound transmission loss or sound reduction index R (dB) is defined as $R = 10 \log(1/\tau)$ where τ is the sound transmission coefficient of the structure. The sound reduction index of a structure mounted between two rooms can be measured according to some well-established procedures.

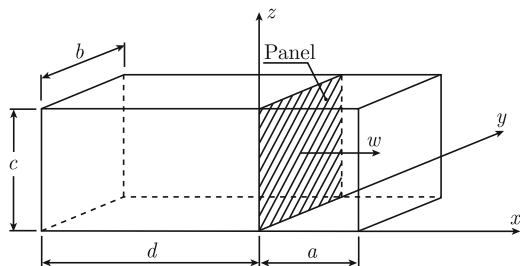
Consider, a wall mounted between two rooms as shown in Fig. 11.27. The area of the wall is S . A sound source with the power Π is located in room 1. The equivalent sound absorption area in room 1 is equal to A_1 . The intensity I_{in} in Room 1 incident on the wall is from Eq. (11.155) given by

$$\bar{I}_{in} = \frac{|\bar{p}_1|^2}{4\rho_0 c} \tag{11.169}$$

The sound pressure in Room 1 is p_1 . The sound transmission coefficient for the wall is given by τ . The acoustic power Π_{tr} transmitted from the wall is

$$\bar{\Pi}_{tr} = \bar{I}_{in} S \tau = \frac{|\bar{p}_1|^2 S \tau}{4\rho_0 c} \tag{11.170}$$

Fig. 11.27 Wall between two rooms



Assuming that the resulting field in Room 2 is diffuse and that the equivalent absorption area in the room is A_2 the sound pressure in the room is obtained as

$$|\bar{p}_2|^2 = \frac{4\rho_0 c \bar{\Pi}_{tr}}{A_2} = \frac{4\rho_0 c \tau S \bar{\Pi}}{A_2 A_1} = |\bar{p}_1|^2 \tau S / A_2 \quad (11.171)$$

The definition $R = 10 \log(1/\tau)$ in combination with Eq. (11.171) gives

$$L_{p1} - L_{p2} = R + 10 \log(A_2/S) \quad (11.172)$$

where L_{p1} and L_{p2} are the sound pressure levels in Room 1 and Room 2, respectively.

The sound pressure level L_{p2} (dB re $2 \cdot 10^{-5}$ Pa) in Room 2 can also be expressed as function of the acoustic power level L_{Π} (dB re 10^{-12} W) of the source in Room 1. The result is obtained as

$$L_{p2} = L_{\Pi} - R - 10 \log(A_1 A_2 / S) + 6 \quad (11.173)$$

In order to reduce the noise level in a room adjoining a space with a certain source the result shows the following possibilities:

1. Reduction of the source strength L_{Π} ;
2. An increase of the sound absorption in the source room;
3. An increase of the sound absorption in the receiving room;
4. An increase of the sound reduction index of the wall separating the rooms.

The sound reduction index of a structure separating two rooms can be determined in different ways as described in relevant ISO standards. The traditional way is first to determine the equivalent sound absorption in Room 2 by means of reverberation time measurements. An acoustic source is thereafter located in Room 1. The sound pressure levels in the two rooms are determined and R calculated from (11.172). Alternatively, the sound intensity I_2 radiated by the wall into Room 2 is measured. The sound intensity I_1 incident on the wall in Room 1, the source room, is determined from the expression (11.169) to give $\bar{I}_1 = |\bar{p}_1|^2 / (4\rho_0 c)$. The resulting sound reduction index is for normal room temperature given by

$$R = 10 \log \left| \bar{I}_1 / \bar{I}_2 \right| = L_{p1} - L_{I2} - 6 \text{ (dB)} \quad (11.174)$$

for L_{p1} in dB re $2 \cdot 10^{-5}$ Pa and the intensity level of the sound radiated into Room 2 is given by L_{I2} in dB re 10^{-12} W/m².

The measurement procedures and requirements to laboratory facilities are described in various ISO documents. In general the sound reduction index is determined in 1/3 octave bands starting with the 100 Hz band and ending with the 3150 Hz band. The measurement is based on the assumption that the acoustic fields in the rooms are diffuse. In particular, in the low frequency region this assumption is not readily satisfied as previously discussed. However, all measurement procedures

should at least satisfy the existing ISO requirements. Measurements of sound reduction indices are discussed in Sect. 13.8.

A structure separating two rooms could consist of many different elements. For example, the separating structure could be a wall with a door or a wall with a window. If the sound reduction index R_i and area S_i of each element are known the effective sound reduction index R_0 of the entire structure can be estimated. The sound transmission coefficient τ_i for structure i is defined as $\tau_i = 10^{-R_i/10}$. The total transmission from the structure is

$$\bar{\Pi}_{\text{tot}} = \bar{I}_{\text{in}} \sum_i \tau_i S_i = \bar{I}_{\text{in}} \sum_i 10^{-R_i/10} S_i = \bar{I}_{\text{in}} \tau_{\text{tot}} S_0 = \bar{I}_{\text{in}} 10^{-R_0/10} S_0$$

The parameter S_0 is the total area of the structure and R_0 the effective sound transmission loss of the entire structure. Thus,

$$R_0 = 10 \log \left[\frac{\sum_i S_i}{\sum_i S_i 10^{-R_i/10}} \right] \quad (11.175)$$

The effect of a small opening in a structure can be devastating as demonstrated in Problem 11.15.

Problems

11.1 A fluid is moving with the velocity $\mathbf{u} = (u_x, 0, 0)$. A plane wave is propagating along the positive x -axis. Determine, the wavenumber for this wave. The same thing for a wave propagating in the opposite direction.

11.2 A straight duct has a constant cross section and the length L . At one end of the duct, $x = 0$, a piston is moving with the velocity $u_0 \exp(i\omega t)$. The opposite wall has the acoustic impedance Z . Determine the acoustic field inside the duct. Consider only plane waves propagating along the x -axis.

11.3 Derive the wave equation using the exact expressions (11.3) and (11.6). Show that the secondary terms form a source term of the quadruple type.

11.4 Determine the natural frequencies inside a tyre which is rotating with a velocity U .

The dimensions of a standard tyre are inner radius $r_0 = 0.21$ m, outer radius $R_0 = 0.275$ m, width $z_0 = 0.205$ m.

11.5 Determine the intensity from the dipole shown in Fig. 11.5.

11.6 Determine the acoustic field induced by a vibrating sector on a sphere. The velocity on the sphere is

$$u(\theta, t) = u_0 \exp(i\omega t) \quad \text{for } 0 \leq \theta \leq \theta_0 \ll 1$$

Coordinates defined in Sect. 11.7

11.7 An infinite cylinder has the radius r_0 . Part of the surface of the cylinder is vibrating with a velocity u defined as (Fig. 11.8) $u(\varphi, t) = u_0 \cdot \exp(i\omega t)$ for $-\varphi_0 \leq \varphi \leq \varphi_0$ otherwise zero. Determine the acoustic field in the fluid outside the cylinder.

11.8 A point source is mounted above a hard surface. The resulting sound pressure level is measured away from the source and above the ground, see Fig. 11.14. Determine in a frequency band the sound pressure level difference between the measured sound pressure level and the level representative for free field conditions.

11.9 An infinite cylinder is semi submerged in water. The surface velocity is $u(\varphi, t) = u_0 \cdot \exp(i\omega t)$. Determine the velocity potential in the water.

11.10 A cylinder is semi submerged in water. Part of the surface of the cylinder is vibrating with a velocity $u_0 \exp(i\omega t)$ for $-\varphi_0 \leq \varphi \leq \varphi_0$. Determine the velocity potential in the water.

11.11 Determine the modal density in a room with the volume V .

11.12 A source is travelling at a velocity v . The position of the source is given by \mathbf{r} the vector from an observer to the source. The vector velocity of the source is \mathbf{v} . Determine the frequency shift due to the motion of the source as experienced by the observer.

11.13 Consider two ducts. The first one, length L , has one source $Q = Q_0 \exp(i\omega t)$ at $x = x_0$. Both ends of the duct are acoustically hard. In the second duct, length $2L$, there are two sources one at $x = x_0$ and the other at $x = -x_0$. The strength of each source is the same as in the previous case. Determine the space average of the pressure squared for both cases. The cross sections of the ducts are the same.

11.14 Determine the frequency average of $\langle |\hat{p}_{lmn}|^2 \rangle$ defined in Eq. (11.141).

11.15 A door is mounted in a wall between two rooms. The area of the wall is 6 m^2 and of the door 2 m^2 . Below the door is an airgap. The area of the opening is $2 \times 10^{-2} \text{ m}^2$. In a particular frequency band the sound reduction index of the wall is 40 dB and of the door 30 dB. Assume that the sound transmission coefficient through the air gap is 1. Determine the effective sound reduction index for the entire construction in this particular frequency band. Determine also the sound reduction index after closing the gap.

11.16 An acoustic source with the power Π is turned on at $t = 0$ and turned off at $t = t_0$. Determine how the sound pressure varies in the room, volume V , and equivalent absorption area A .

11.17 Show that $\nabla_1^2 \Phi - \frac{1}{c^2} \frac{\partial^2 \Phi}{\partial t_1^2} = \nabla^2 \Phi - \frac{1}{c^2} \frac{\partial^2 \Phi}{\partial t^2}$ when the coordinates in the two systems are defined as $x_1 = \gamma(x - ut)$, $y_1 = y$, $z_1 = z$, $t_1 = \gamma(t - ux/c^2)$ and $\gamma = c/\sqrt{c^2 - u^2}$. Compare Sect. 11.8.

Chapter 12

Fluid Structure Interaction and Radiation of Sound

Vibrating structures radiate noise. In fact, most sources of sound and noise, from loudspeakers to engines and vehicles, are really due to vibrating structures. A typical noise reducing measure is therefore to limit the transmission of structure-borne sound from vibrating sources to large structures. The second step is to reduce the vibration levels and radiation properties of the structure.

The acoustical coupling effects between structures and fluids are discussed in this chapter. The sound radiation characteristics of simple plates are described by means of the sound radiation ratio.

A fluid load on a structure influences its vibration level and its natural frequencies. In particular, this is the case for lightweight structures enclosing an air volume. Examples of these structures are, for example, car and aircraft bodies. A structure exposed to a heavy fluid-like water has an effective or apparent mass much greater than the same plate vibrating in air. The loading on a plate from a heavy fluid has a marked influence on the dynamic performance of the structure. For ship constructions, the water loading on hull plates can have a very significant effect.

12.1 Radiation and Fluid Loading of Infinite Plates

In Sects. 11.4 through 11.7 acoustic fields generated by pulsating spheres and cylinders were discussed. It was shown that structural vibrations induce a motion in a surrounding fluid. The resulting particle velocity in the fluid creates a wave motion and thus a pressure field in the fluid. This pressure or reacting load from the fluid will influence the motion of the structure. The field in the fluid and the motion of the plate are coupled.

The wave field induced in a fluid by a vibrating plate, or in this case an infinite plane plate, can be derived based on some simple assumptions. Let a plate be oriented in the x - y -plane as shown in Fig. 12.1. The mass per unit area of the plate is μ and its bending stiffness is D . A plane bending wave is forced to propagate along the positive x -axis. The displacement in the z -direction of the plate is w . The corresponding lateral

The additional solution, $k_z = -\sqrt{k^2 - \kappa_x^2}$, corresponds to waves propagating toward the plate. Since no waves are reflected back from infinite space, this solution is excluded. The wave number k_z is, neglecting losses in fluid and plate, real for $k \geq \kappa_x$, otherwise imaginary.

The pressure squared and the intensity induced in the fluid by one side of the vibrating plate is for $z > 0$

$$\begin{aligned}\bar{I}_z &= \frac{1}{2} \operatorname{Re}(p \cdot v_z^*) = \frac{1}{2} \operatorname{Re} \left[-\rho_0 \frac{\partial \Phi_+}{\partial t} \left(\frac{\partial \Phi_+}{\partial z} \right)^* \right] = \frac{\omega \rho_0 |v_0|^2}{2} \operatorname{Re} \left(\frac{1}{k_z} \right) \\ |\bar{p}|^2 &= \frac{1}{2} \left| \rho_0 \frac{\partial \Phi_+}{\partial t} \right|^2 = \frac{(\omega \rho_0)^2 |\Phi_+|^2}{2}\end{aligned}\quad (12.5)$$

For $\kappa_x > k$ the z -component k_z of the wave number in the fluid is imaginary. The intensity \bar{I}_z , as defined in Eq. (12.5), is consequently zero and there is no propagating wave traveling away from the plate for $\kappa_x > k$. Considering that the time average of the plate velocity squared is equal to $|v_0|^2/2$ or $|\bar{v}|^2 = |v_0|^2/2$ it follows that for $z > 0$

$$\begin{aligned}\bar{I}_z &= 0; \quad |\bar{p}|^2 = (\rho_0 c)^2 |\bar{v}|^2 \cdot \frac{\exp[-2z\sqrt{\kappa_x^2 - k^2}]}{|1 - (\kappa_x/k)^2|} \quad \text{for } \kappa_x > k \\ \bar{I}_z &= \rho_0 c |\bar{v}|^2 \cdot \frac{1}{\sqrt{1 - (\kappa_x/k)^2}}; \\ |\bar{p}|^2 &= (\rho_0 c)^2 |\bar{v}|^2 \cdot \frac{1}{|1 - (\kappa_x/k)^2|} \quad \text{for } \kappa_x < k\end{aligned}\quad (12.6)$$

The vibrating plate always generates a pressure in the fluid. For $\kappa_x > k$ the generated wave propagates along the plate. The pressure amplitude decays exponentially with increasing distance from the plate as illustrated in Fig. 11.14. For $\kappa_x < k$, a propagating wave travels away from the plate. The direction of propagation is φ as shown in Fig. 12.1. The angle φ is given by

$$\cos \varphi = k_z/k = \sqrt{1 - (\kappa_x/k)^2}\quad (12.7)$$

For k_z real and k approaching κ_x the intensity of the radiated acoustic power tends to be very high or in theory infinite. This implies that in order to maintain the lateral velocity at $v_z = v_0 \cdot \exp[i(\omega t - \kappa_x x)]$ an increasing power input to the plate is required as k tends to κ_x . For $k = \kappa_x$ the plate has infinite losses due to the radiated power and the motion of the plate cannot be maintained.

For a plate in vacuo, the wave number for bending waves is $\kappa = (\mu\omega^2/D)^{1/4}$ as discussed in Chap. 8. However, the load of a fluid will influence the motion of the

plate and thus also the wave number. For a plate in flexure in a fluid, the displacement w must satisfy the wave equation (8.20)

$$\nabla^2(\nabla^2 w) + \frac{\mu}{D} \cdot \frac{\partial^2 w}{\partial t^2} = -\frac{p}{D} \quad (12.8)$$

The pressure p from the fluid on the plate is acting in the opposite direction to the motion w of the plate; therefore, a minus sign. In the expression (8.20), the force f per unit area is driving the plate. The reacting pressure p is equal to the difference between the pressure p_+ on the top side of the plate and the pressure p_- at the other side of the plate. Thus

$$p = p_+ - p_- = -\rho_0 \left[\frac{\partial \Phi_+}{\partial t} - \frac{\partial \Phi_-}{\partial t} \right]_{z=0} \quad (12.9)$$

For a bending wave propagating along the x -axis with a velocity $v_z = v_0 \cdot \exp[i(\omega t - \kappa_x x)]$ the wave Eq.(12.9) can, after being derivated with respect to t , be written as

$$\nabla^2(\nabla^2 v_z) + \frac{\mu}{D} \cdot \frac{\partial^2 v_z}{\partial t^2} = -\frac{\rho_0}{D} \left[\frac{\partial^2 \Phi_+}{\partial t^2} - \frac{\partial^2 \Phi_-}{\partial t^2} \right]_{z=0} \quad (12.10)$$

The expressions for v_z , Φ_+ and Φ_- , Eqs.(12.1), (12.2), and (12.4) inserted in Eq.(12.10) give

$$v_z \cdot [\kappa_x^4 - \kappa^4 - 2i\rho_0\omega^2/(Dk_z)] = 0 \quad (12.11)$$

For nontrivial solutions and following the definition of $k_z = \sqrt{k^2 - \kappa_x^2}$, Eq.(12.4), it follows that κ_x must satisfy the equation

$$\kappa_x^4 = \kappa^4 + \frac{2\omega^2\rho_0}{D\sqrt{\kappa_x^2 - k^2}}$$

For a fluid load on only one side of the plate, the corresponding expression is

$$\kappa_x^4 = \kappa^4 + \frac{\omega^2\rho_0}{D\sqrt{\kappa_x^2 - k^2}} = \kappa^4 \left[1 + \frac{\rho_0}{\mu\sqrt{\kappa_x^2 - k^2}} \right] \quad (12.12)$$

Numerical methods must be used to solve the Eq.(12.12). Iteration can be used to find some of the basic solutions to Eq.(12.12) by first setting κ_x equal to κ on the right-hand side of the equation to calculate a new κ_x and so forth. The case for which κ_x tends to k is discussed in Problem 12.1. However, approximate solutions can be obtained for certain cases, for example, if the second term inside the bracket of Eq.(12.12) is small as compared to unity. For $\kappa_x \gg k$ one set of solutions is obtained as

$$\kappa_x = \pm \kappa \left[1 + \frac{\rho_0}{\mu \sqrt{\kappa_x^2 - k^2}} \right]^{1/4} \approx \pm \kappa \left[1 + \frac{\rho_0}{4\mu \sqrt{\kappa_x^2 - k^2}} \right] \approx \pm \kappa \left[1 + \frac{\rho_0}{4\mu \kappa_x} \right] \quad (12.13)$$

Another set of solutions is

$$\kappa_x \approx \pm i \kappa \left[1 - \frac{i \rho_0}{4\mu \kappa_x} \right] \quad (12.14)$$

The high frequency solutions $\kappa_x \approx k$ are discussed in Problem 12.1. However, for this solution $\kappa_x > k$ which according to Eq. (12.4) means that the wave number k_z for the outgoing wave is imaginary. Consequently, this wave type does not radiate any sound from the plate. It is only the first pair of solutions (12.13) representing waves traveling along the plate, which are of importance for the acoustic power radiated from the plate. The positive wave number represents a wave propagating along the positive x -axis. The last pair of solutions (12.14) corresponds to evanescent waves.

The fluid loading increases the wave number for the traveling waves. The fluid loading does not influence the bending stiffness of the plate. The increased wave number is attributed to the added mass $\Delta\mu$ caused by the fluid loading. In the low frequency region, part of the fluid moves with the plate thus increasing its apparent mass. For a plate with a fluid on both sides, the apparent mass μ_{tot} of the plate is for free plate vibrations obtained by setting $\kappa_x = (\mu_{\text{tot}}\omega^2/D)^{1/4}$ in Eq. (12.13). The result is

$$\mu_{\text{tot}} = \mu + \Delta\mu \approx \mu + 2\rho_0/\kappa \quad \text{for } \kappa \gg k \quad \text{and} \quad \mu \gg 2\rho_0/\kappa \quad (12.15)$$

For a plate vibrating in air the added mass effect can be neglected except for very light and stiff panels like lightweight sandwich or honeycomb panels. This is discussed in Chap. 14. For a plate vibrating in air the wave number κ_x can be set to equal κ , the wave number for the plate vibrating in vacuo, as long as $2\rho_0/(\kappa\mu) \ll 1$. The wave number for flexural waves propagating in a plate is $\kappa = (\mu\omega^2/D)^{1/4}$ as shown in (3.117). In the low frequency range $\kappa > k$, the added mass $\Delta\mu$ due to fluid loading is $2\rho_0/\kappa$. The added mass effect is consequently decreasing for increasing frequencies. For a plate submerged in water, the fluid loading effect can be considerable as shown in Fig. 12.2. The figure shows the wave number, flexural waves, for a 4 mm steel plate with a water load on one side and the wave number for the same plate vibrating in vacuo. In the high frequency region, the wave number κ_x is larger than but approaching k as discussed in Problem 12.1. This particular wave does not radiate acoustical power since k_z is imaginary. The amplitude of the pressure in the fluid induced by this wave type is decaying weakly with increasing distance from the plate. The added mass effect, corresponding to this wave number, is substantial in the high frequency region. This type of wave is, therefore, not readily excited in the very high frequency region.

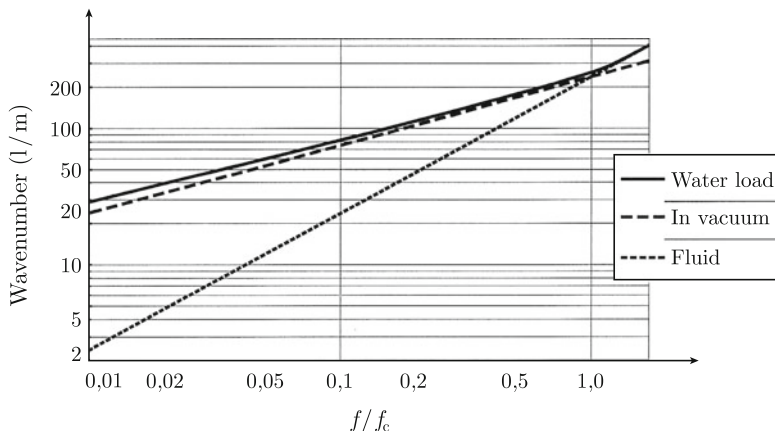


Fig. 12.2 wave numbers for flexural waves traveling along a 4 mm infinite steel plate in vacuum and with a water load on one side. The wave number in water is also shown. For $f > f_c$ one solution is given by Eq. (12.16)

The weight per area of the 4 mm steel plate is 30 kg/m^2 . The added mass due to the water load on one side is 96 kg/m^2 at 100 Hz and 32 kg/m^2 at 1 kHz . For plates with a mass per unit area of more than 10 kg/m^2 the fluid loading in air can be neglected.

In the high frequency region or for $k > \text{Re}\kappa_x$ one set of solutions to Eq. (12.12) can be written as

$$\kappa_x = \pm \kappa(1 - i\eta_r/4) \quad (12.16)$$

where η_r is equivalent to a loss factor for bending waves as defined in Sect. 5.6. For $\eta_r \ll 1$ and $k > \text{Re}\kappa$ Eq. (12.16) inserted in Eq. (12.12) gives

$$\eta_r \approx \frac{\rho_0}{\mu\sqrt{k^2 - \kappa^2}} \quad (12.17)$$

The loss factor or rather the losses are due to the acoustic power radiated from one side of the plate. In addition, $\kappa_x = \pm i\kappa(1 - i\eta_r)$ are also solutions to Eq. (12.12) in the high frequency region. These solutions represent evanescent waves. It can be concluded that for free vibrations of an infinite plate in a fluid, the load induced by the fluid increases the apparent mass of the plate in the low frequency region or for $\kappa_x > k$. For $k > \text{Re}\kappa$ the plate radiates acoustic power resulting in an energy flow from the panel. This energy loss is included in the loss factor η_r . For $k > \text{Re}\kappa$ there is no mass load on the plate. The frequency for which $k = \kappa$, or rather $k = \text{Re}\kappa$, is called the critical frequency f_c . For a homogeneous single-leaf panel, thickness h , density ρ_p , Young's modulus E , and Poisson's ratio ν , the critical frequency f_c for which $k = \omega/c = \text{Re}\kappa = \kappa_0$ is

$$f_c = \frac{c^2}{2\pi} \left(\frac{\mu}{D_0} \right)^{1/2} = \frac{c^2}{2\pi h} \left[\frac{12\rho_p(1 - \nu^2)}{E_0} \right]^{1/2} \quad (12.18)$$

The speed of sound in the fluid is c . The critical frequency is inversely proportional to the thickness of the plate. For a 4 mm steel plate, the critical frequency is 2890 Hz in air. For the same plate in water f_c it is 53 kHz. The wave number for flexural waves, plate in vacuo, can be written as $\kappa = (2\pi/c)\sqrt{f \cdot f_c}$. Neglecting the fluid loading in the expressions (12.6) the ratio $(\kappa_x/k)^2$ is equal to f_c/f . Considering this, the intensity \bar{I}_z induced by a vibrating and weakly loaded infinite plate can be written as

$$\bar{I}_z = \rho_0 c |\bar{v}|^2 \bar{\sigma}_r$$

$$\bar{\sigma}_r = 0 \quad \text{for } f < f_c; \quad \bar{\sigma}_r = \frac{1}{\sqrt{1 - f_c/f}} \quad \text{for } f > f_c \quad (12.19)$$

The function $\bar{\sigma}_r$ is the sound radiation ratio or sound radiation efficiency of the plate. A completely stiff and infinite piston vibrating with the velocity v radiates the intensity $\bar{I}_z = \rho_0 c |\bar{v}|^2$. The function $\bar{\sigma}_r$ defines the radiation efficiency of a flexible plate as compared to an infinite and rigid piston vibrating with the same rms velocity as the plate.

In summary, the wave number for flexural waves traveling along a homogeneous plate with a fluid loading on one side can be approximated by the expressions

$$\kappa_x \approx \kappa \left[1 + \frac{\rho_0}{4\mu\kappa} \right] \quad \text{for } \kappa > k \text{ or } f < f_c;$$

$$\kappa_x = \kappa(1 - i\eta_r) \quad \text{for } \kappa < k \text{ or } f > f_c; \quad \eta_r \approx \frac{\rho_0}{\mu\sqrt{k^2 - \kappa^2}}$$

For a panel having a fluid loading on both sides, the terms containing ρ_0 should be multiplied by a factor 2.

12.2 Radiation—General Formulation

The sound pressure in a fluid induced by a source region and a vibrating structure can be derived by means of the so-called Kirchhoff–Helmholtz integral equation. The basis for the equation is the by now familiar Green's function. However, Green's function is not readily derived except for vibrating structures with simple geometries. One such case is an infinite flat plate shown in Fig. 12.1. On the upper side of the plate, i.e., for $z > 0$ there is a fluid, which is unbounded in the upper half plane. The density and speed of sound in the fluid are ρ_0 and c , respectively. A source region is located in the fluid and defined by its FT $f(\mathbf{r})$. The pressure in the fluid or rather its FT should satisfy the equation

$$\nabla^2 p + k^2 p = -f(\mathbf{r}) \quad (12.20)$$

The wave number in the fluid is k . Let the Green's function $G(\mathbf{r}|\mathbf{r}_0)$ be the solution to the equation

$$\nabla^2 G + k^2 G = -\delta(\mathbf{r} - \mathbf{r}_0) \quad (12.21)$$

Equation (12.20) is multiplied by the Green's function $G(\mathbf{r}|\mathbf{r}_0)$ and Eq. (12.21) by $p(\mathbf{r})$. The resulting two expressions are subtracted resulting in

$$p\nabla^2 G - G\nabla^2 p = -\delta(\mathbf{r} - \mathbf{r}_0)p(\mathbf{r}) + f(\mathbf{r})G(\mathbf{r}|\mathbf{r}_0) \quad (12.22)$$

This expression is rewritten as

$$\text{div}[p \cdot \mathbf{grad}G - G \cdot \mathbf{grad}p] = -\delta(\mathbf{r} - \mathbf{r}_0)p(\mathbf{r}) + f(\mathbf{r})G(\mathbf{r}|\mathbf{r}_0) \quad (12.23)$$

An integration over the entire volume V of the upper half plane is thereafter carried out. The resulting integral on the left-hand side of Eq. (12.23) can be simplified using the Gauss theorem, i.e., the identity

$$\int \text{div} \mathbf{a} dV = \int \mathbf{n} \cdot \mathbf{a} dS$$

The unit vector \mathbf{n} is normal to the surface S over which the integration is carried out. The unit vector \mathbf{n} is pointing out from the surface. The integration of the expression (12.23) yields

$$\int dS \mathbf{n} [p \cdot \mathbf{grad}G - G \cdot \mathbf{grad}p] = - \int dV \delta(\mathbf{r} - \mathbf{r}_0)p(\mathbf{r}) + \int dV f(\mathbf{r})G(\mathbf{r}|\mathbf{r}_0) \quad (12.24)$$

For a time dependence $\exp(i\omega t)$ the particle vector velocity in the fluid is obtained from Eq. (11.7) as

$$\mathbf{v} = i \mathbf{grad} p / (\omega \rho_0) \quad (12.25)$$

Following the definition of a Dirac function, the first part of the integral on the right-hand side of Eq. (12.24) is quite simply equal to $-p(\mathbf{r}_0)$. Consequently, Eq. (12.24) is reduced to

$$p(\mathbf{r}_0) = - \int dS \mathbf{n} [p \cdot \mathbf{grad}G + i\omega \rho_0 \mathbf{v} \cdot G] + \int dV f(\mathbf{r})G(\mathbf{r}|\mathbf{r}_0)$$

Since $G(\mathbf{r}|\mathbf{r}_0) = G(\mathbf{r}_0|\mathbf{r})$ the vectors \mathbf{r} and \mathbf{r}_0 can be interchanged. Thus

$$p(\mathbf{r}) = - \int dS_0 \mathbf{n} [p \cdot \mathbf{grad}G + i\omega \rho_0 \mathbf{v} \cdot G] + \int dV_0 f(\mathbf{r}_0)G(\mathbf{r}|\mathbf{r}_0) \quad (12.26)$$

The expression (12.26) is referred to as the Kirchhoff–Helmholtz or quite simply the Helmholtz integral equation. As the integral equation stands, the pressure on the plate, the velocity of the plate as well as the function G must be known in order to

calculate the pressure p at a point \mathbf{r} in the fluid. However, the general expression (12.26) is simplified considerably if a function G can be found satisfying the basic differential equation (12.21) as well as the boundary condition $\mathbf{n} \cdot \mathbf{grad}G = 0$ on the surface of the plate. A solution satisfying these conditions is discussed in the next section.

12.3 Green's Function—Rigid Plane Boundary

The Green's function satisfying Eq. (12.21) and the boundary condition $\mathbf{n} \cdot \mathbf{grad}G = 0$ on the surface of a flat plate is written

$$G(\mathbf{r}|\mathbf{r}_0) = g_1(\mathbf{r}|\mathbf{r}_0) + g_2(\mathbf{r}|\mathbf{r}_0)$$

where g_1 is the particular solution and g_2 is the complementary solution to Eq. (12.21). The function g_2 should be chosen so that the boundary condition $\mathbf{n} \cdot \mathbf{grad}G = 0$ is satisfied on the surface of the plate.

In order to find the required solutions let a point source be located at $\mathbf{r}_0 = (x_0, y_0, z_0)$ above a totally reflecting and flat plate oriented in the x - y -plane. The particular solution must be equal to a spherical wave propagating away from the ideal point source. Omitting the time dependence $\exp(i\omega t)$, g_1 is given by Eq. (11.57) as

$$g_1(\mathbf{r}|\mathbf{r}_0) = \frac{e^{-ikr_1}}{4\pi r_1}; \quad r_1 = |\mathbf{r} - \mathbf{r}_0| = \left[(x - x_0)^2 + (y - y_0)^2 + (z - z_0)^2 \right]^{1/2} \quad (12.27)$$

The complementary solution g_2 should satisfy the basic homogenous equation and also be such that on the boundary

$$\mathbf{n} \cdot \mathbf{grad}G = \mathbf{n} \cdot \mathbf{grad}(g_1 + g_2) = 0 \quad (12.28)$$

This means, since $\mathbf{n} = (0, 0, -1)$ on the surface of the plate, that

$$\frac{\partial}{\partial z}(g_1 + g_2) = 0$$

The following argument can be used to find g_2 . For a source above a completely reflecting plane, the field above the plate at $z = 0$ is due to the real source at (x_0, y_0, z_0) and an imaginary source at $\mathbf{r}'_0 = (x_0, y_0, -z_0)$ as discussed in Sect. 11.9. This means that g_2 above the plate at $z = 0$ is of the form

$$g_2(\mathbf{r}|\mathbf{r}_0) = \frac{e^{-ikr_2}}{4\pi r_2}; \quad r_2 = |\mathbf{r} - \mathbf{r}'_0| = \left[(x - x_0)^2 + (y - y_0)^2 + (z + z_0)^2 \right]^{1/2} \quad (12.29)$$

The function r_2 is equal to the distance between the observation point (x, y, z) and the location of the imaginary source at $(x_0, y_0, -z_0)$. The function g_2 satisfies the basic homogenous differential equation for $z \geq 0$. Further

$$\frac{\partial}{\partial z}(g_1 + g_2) = -\frac{e^{-ikr_1}}{4\pi r_1^2} \left(ik + \frac{1}{r_1} \right) (z - z_0) - \frac{e^{-ikr_2}}{4\pi r_2^2} \left(ik + \frac{1}{r_2} \right) (z + z_0)$$

At the boundary $z = 0$, r_1 is equal to r_2 which gives

$$\frac{\partial}{\partial z}(g_1 + g_2) = 0 \quad \text{for } z = 0$$

Consequently, the Green's function for a rigid boundary at $z = 0$ is equal to the sum of g_1 and g_2 or

$$G(\mathbf{r}|\mathbf{r}_0) = \frac{e^{-ikr_1}}{4\pi r_1} + \frac{e^{-ikr_2}}{4\pi r_2}$$

$$\begin{aligned} r_1 &= \left[(x - x_0)^2 + (y - y_0)^2 + (z - z_0)^2 \right]^{1/2}; \\ r_2 &= \left[(x - x_0)^2 + (y - y_0)^2 + (z + z_0)^2 \right]^{1/2} \end{aligned} \quad (12.30)$$

For $z > 0$, Green's function (12.30) is the solution to the equation

$$\nabla^2 G + k^2 G = -\delta(\mathbf{r} - \mathbf{r}_1) - \delta(\mathbf{r} - \mathbf{r}_2); \quad \mathbf{r}_1 = (x_0, y_0, z_0); \quad \mathbf{r}_2 = (x_0, y_0, -z_0) \quad (12.31)$$

This means that the field induced by a point source above a completely reflecting plate is equivalent to the field resulting from two identical point sources located symmetrically with respect to the plane $z = 0$ in the absence of the plate. The analogy is shown in Fig. 11.15.

Returning to the basic integral equation (12.24), the surface integration should be carried out across the x - y -plane and over a semi-sphere above the plane closing the surface. At large distances r from a source region the functions p and G are of the form $\exp(-ikr)/r$. The contribution to the surface integral, left-hand side of Eq. (12.24), over the half sphere approaches zero as the radius r goes to infinity. This is the Sommerfeld radiation condition. The total integral is thus determined by the contribution of the surface integral over the plate only. On the surface of the plate, i.e., for $z = 0$, the function G is equal to

$$G(x, y, 0|x_0, y_0, z_0) = \frac{e^{-ikr}}{2\pi r} \quad r = \left[(x - x_0)^2 + (y - y_0)^2 + z_0^2 \right]^{1/2} \quad (12.32)$$

The Green's function can also be written as

$$G(x, y, z|x_0, y_0, 0) = \frac{e^{-ikr}}{2\pi r} \quad r = \left[(x - x_0)^2 + (y - y_0)^2 + z^2 \right]^{1/2}$$

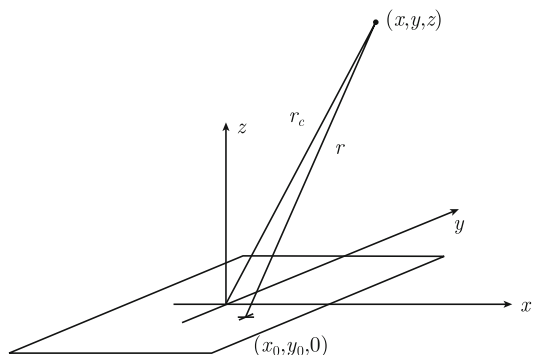
If part of the plate, area S , is given a velocity $v(x, y)$ with the time dependence $\exp(i\omega t)$ the resulting pressure in the fluid above the plate in the absence of any sources in the fluid, $f(\mathbf{r}) = 0$, is according to Eq. (12.26) and for $\mathbf{n} = (0, 0, -1)$ equal to

$$\begin{aligned} p(\mathbf{r}) &= \iint_{S_0} i\omega\rho_0 v(x_0, y_0) G(x, y, z|x_0, y_0, 0) dx_0 dy_0 \\ &= \iint_{S_0} i\omega\rho_0 v(x_0, y_0) \frac{e^{-ikr}}{2\pi r} dx_0 dy_0 \\ r &= \left[(x - x_0)^2 + (y - y_0)^2 + z^2 \right]^{1/2} \end{aligned} \quad (12.33)$$

This special case of the general Helmholtz integral equation determines the pressure p in a fluid induced by a flat, vibrating, and infinite plate.

If only a small part of the infinite plate is allowed to vibrate the expression (12.33) can be simplified if the pressure is only to be calculated at points at large distances from the center of the vibrating area. The problem is illustrated in Fig. 12.3. The distance r from one such observation point to any point on the vibrating surface is as a first approximation equal to the distance r_c to the center of the plate. However, the phase of the function $\exp(-ikr)$ can, since the product kr is not necessarily small, be a rapidly varying function as x_0 and y_0 are traversing the vibrating surface of the plate. Since r in the denominator in Eq. (12.33) is approximately constant, this factor can be placed outside the integral. The result or the so-called Rayleigh formula is thus equal to

Fig. 12.3 Radiation from a vibrating area in the x - y -plane. The observation point is far from the radiating area



$$p(\mathbf{r}) = \frac{1}{2\pi r_c} \iint_{S_0} i\omega\rho_0 v(x_0, y_0) e^{-ikr} dx_0 dy_0; \quad r_c \gg 1$$

$$r_c = [x^2 + y^2 + z^2]^{1/2}; \quad r = [(x - x_0)^2 + (y - y_0)^2 + z^2]^{1/2} \quad (12.34)$$

The usefulness of this expression is demonstrated in subsequent sections.

12.4 Spatial Fourier Transforms—Several Variables

For many problems and in particular for problems concerning the coupling between structures and fluids, Fourier transforms with respect to space coordinates are extremely useful. Spatial FT were introduced in Sect. 5.4. The spatial FT $\tilde{u}(k_x, k_y)$ of a function $u(x, y)$ which is defined for all x and y is according to Eq. (5.61) given as

$$\tilde{u}(k_x, k_y) = \int_{-\infty}^{\infty} \int_{-\infty}^{\infty} u(x, y) \cdot e^{-i(k_x x + k_y y)} dx dy$$

The inverse transform is

$$u(x, y) = \frac{1}{(2\pi)^2} \int_{-\infty}^{\infty} \int_{-\infty}^{\infty} \tilde{u}(k_x, k_y) \cdot e^{i(k_x x + k_y y)} dk_x dk_y$$

As an example, consider a finite rectangular plate oriented in the x - y -plane with the corners at $(L_x/2, L_y/2)$, $(-L_x/2, L_y/2)$, $(-L_x/2, -L_y/2)$, and $(L_x/2, -L_y/2)$. Let the velocity of the plate be given by $v(x, y) \cdot \exp(i\omega t)$. The spatial FT of the velocity is \tilde{v} . The time and space average of the velocity squared over the plate area is

$$\langle |\tilde{v}|^2 \rangle = \frac{1}{2L_x L_y} \iint_S |v|^2 dx dy = \frac{1}{2L_x L_y} \iint_S v v^* dx dy \quad (12.35)$$

The factor 2 in the denominator is due to the time dependence $\exp(i\omega t)$ as discussed in Chap. 2. Introducing the spatial FT of v and the corresponding transform for v^* in Eq. (12.35) the result reads

$$\langle |\tilde{v}|^2 \rangle = \frac{1}{2L_x L_y} \iint_S dx dy \frac{1}{(2\pi)^4} \int_{-\infty}^{\infty} \int_{-\infty}^{\infty} \tilde{v}(k_x, k_y) \cdot e^{i(k_x x + k_y y)} dk_x dk_y \int_{-\infty}^{\infty} \int_{-\infty}^{\infty} \tilde{v}^*(\xi, \eta) \cdot e^{-i(\xi x + \eta y)} d\xi d\eta$$

Without loss of generality, the order of integration can be changed. Starting with the integration over the x and y coordinates, the integral is rewritten as

$$\langle |\bar{v}|^2 \rangle = \frac{1}{2L_x L_y (2\pi)^4} \int_{-\infty}^{\infty} \int_{-\infty}^{\infty} \tilde{v}(k_x, k_y) \cdot dk_x dk_y \int_{-\infty}^{\infty} \int_{-\infty}^{\infty} \tilde{v}^*(\xi, \eta) d\xi d\eta \int \int_S dx dy \exp[ix(k_x - \xi) + iy(k_y - \eta)] \quad (12.36)$$

The integral over x and y is according to the definition of the two-dimensional Dirac function equal to

$$\int \int_S dx dy \exp[ix(k_x - \xi) + iy(k_y - \eta)] = (2\pi)^2 \delta(\xi - k_x) \delta(\eta - k_y)$$

This expression inserted in (12.36) yields

$$\langle |\bar{v}|^2 \rangle = \frac{1}{2L_x L_y (2\pi)^2} \int_{-\infty}^{\infty} \int_{-\infty}^{\infty} |\tilde{v}(k_x, k_y)|^2 dk_x dk_y \quad (12.37)$$

In a similar way, the average power radiated from the surface can be derived as a function of the spatial Fourier transforms \tilde{p} and \tilde{v} of the pressure on the plate and the velocity of the plate. The resulting integral is equal to

$$\langle |\bar{\Pi}| \rangle = \frac{1}{2(2\pi)^2} Re \int_{-\infty}^{\infty} \int_{-\infty}^{\infty} \tilde{p}(k_x, k_y) \tilde{v}^*(k_x, k_y) dk_x dk_y \quad (12.38)$$

If, in three dimensions, the Fourier transforms of $f(\mathbf{r})$ is $\tilde{f}(\mathbf{k})$ and if $f(\mathbf{r})$ is continuous and if the function and its derivatives approach zero as r goes to infinity then the spatial Fourier transforms of $\nabla^2 f$ and $\nabla^2(\nabla^2 f)$ can also be obtained.

Consider the integral

$$J = \int_{-\infty}^{\infty} \nabla^2 f(\mathbf{r}) \cdot \exp(-i\mathbf{k}\mathbf{r}) d^3r$$

By means of partial integration the result is, considering the boundary conditions

$$\begin{aligned} J &= \int_{-\infty}^{\infty} f(\mathbf{r}) \cdot \nabla^2 [\exp(-i\mathbf{k}\mathbf{r})] d^3r \\ &= - \int_{-\infty}^{\infty} f(\mathbf{r}) \cdot (k_x^2 + k_y^2 + k_z^2) [\exp(-i\mathbf{k}\mathbf{r})] d^3r \\ &= -(k_x^2 + k_y^2 + k_z^2) \int_{-\infty}^{\infty} f(\mathbf{r}) \cdot [\exp(-i\mathbf{k}\mathbf{r})] d^3r = -(k_x^2 + k_y^2 + k_z^2) \tilde{f}(\mathbf{k}) \end{aligned}$$

This means that the Fourier transform of $\nabla^2 f$ in three dimensions is

$$\text{FT} \nabla^2 f(\mathbf{r}) = -(k_x^2 + k_y^2 + k_z^2) \tilde{f}(\mathbf{k}) \quad (12.39)$$

In a similar way

$$\text{FT}\nabla^2[\nabla^2 f(\mathbf{r})] = (k_x^2 + k_y^2 + k_z^2)^2 \tilde{f}(\mathbf{k}) \quad (12.40)$$

In two dimensions, the result reads

$$\text{FT}\nabla^2 f(x, y) = -(k_x^2 + k_y^2) \tilde{f}(k_x, k_y) \quad (12.41)$$

It was demonstrated in Sect. 12.3 that the Green's function defined in Eq. (12.31) is, for $z > 0$, the solution to the equation

$$\begin{aligned} \nabla^2 G + k^2 G &= -\delta(\mathbf{r} - \mathbf{r}_1) - \delta(\mathbf{r} - \mathbf{r}_2) \\ \mathbf{r}_1 &= (x_0, y_0, z_0); \quad \mathbf{r}_2 = (x_0, y_0, -z_0) \end{aligned} \quad (12.42)$$

The three-dimensional Fourier transform \tilde{G} of $G(\mathbf{r}|\mathbf{r}_0)$ satisfying (12.42) is obtained using the results (12.39). Define the function G and its Fourier transform as

$$\begin{aligned} G(\mathbf{r}|\mathbf{r}_0) &= \frac{1}{(2\pi)^3} \int_{-\infty}^{\infty} \tilde{G}(\mathbf{k}) \exp(i\mathbf{k}\mathbf{r}_0) d^3k \\ \tilde{G}(\mathbf{k}) &= \int_{-\infty}^{\infty} G(\mathbf{r}|\mathbf{r}_0) \exp(-i\mathbf{k}\mathbf{r}_0) d^3r_0 \end{aligned}$$

The function \tilde{G} is obtained by multiplying Eq. (12.42) by $\exp(-i\mathbf{k}\mathbf{r}_0)$. Integration over space is thereafter carried out. The result is

$$\tilde{G}[k^2 - (k_x^2 + k_y^2 + k_z^2)] = -\exp[-i(k_x x + k_y y + k_z z)] + \exp[-i(k_x x + k_y y - k_z z)]$$

Thus

$$\tilde{G} = 2 \cos(k_z z) \cdot \frac{\exp[-i(k_x x + k_y y)]}{k_x^2 + k_y^2 + k_z^2 - k^2} \quad (12.43)$$

In order to calculate the pressure in a fluid induced by a vibrating flat plate the Green's function on the surface of the plate must be known as displayed by the Eqs. (12.32) and (12.33). At the boundary, i.e., for $z = 0$, the function G is

$$\begin{aligned} G(x, y, 0|x_0, y_0, z_0) &= \frac{1}{(2\pi)^2} \int_{-\infty}^{\infty} \int_{-\infty}^{\infty} \exp[ik_x(x_0 - x) + ik_y(y_0 - y)] dk_x dk_y \\ &\quad \times \int_{-\infty}^{\infty} \frac{2 \exp(ik_z z_0)}{k_x^2 + k_y^2 + k_z^2 - k^2} dk_z \end{aligned} \quad (12.44)$$

The last integral can be evaluated by means of contour integration in the upper half of the complex plane. The integrand has one pole in the upper half plane. This pole is equal to

$$k_z = i\sqrt{k_x^2 + k_y^2 - k^2}$$

A contour integration follows a path C , a semicircle in the upper half of the complex plane closed by the real axis of k_z . The result is

$$\begin{aligned} \oint_C \frac{2 \exp(ik_z z_0)}{k_x^2 + k_y^2 + k_z^2 - k^2} dk_z &= \int_{-\infty}^{\infty} \frac{2 \exp(ik_z z_0)}{k_x^2 + k_y^2 + k_z^2 - k^2} dk_z \\ &= \frac{2\pi \exp(-z_0 \sqrt{k_x^2 + k_y^2 - k^2})}{\sqrt{k_x^2 + k_y^2 - k^2}} \end{aligned}$$

Combining this result and the original expression (12.44) for G gives

$$\begin{aligned} G(x, y, 0|x_0, y_0, z_0) &= \frac{1}{(2\pi)^2} \int_{-\infty}^{\infty} \int_{-\infty}^{\infty} dk_x dk_y \\ &\quad \times \frac{\exp[ik_x(x_0 - x) + ik_y(y_0 - y) - z_0 \sqrt{k_x^2 + k_y^2 - k^2}]}{\sqrt{k_x^2 + k_y^2 - k^2}} \end{aligned} \quad (12.45)$$

This formulation of Green's function will be used in the next section to determine the radiation from an infinite point-excited plate.

12.5 Radiation from Infinite Point-Excited Plates

This problem might seem to be very academic. However, for fairly large plates with high loss factors the effects of the boundary conditions on the radiation pattern can be small with respect to the total radiation from the plate. In particular, this is the case for large plates in heavy fluids like water. It has been shown that hull sections of a submarine in fact radiate in a similar way as point- or line-excited infinite fluid-loaded plates.

Again, consider an infinite and flat plate oriented in the x - y -plane. On the upper side of the plate, for $z > 0$, there is a fluid with density ρ_0 and speed of sound c . The fluid is, except for the plate, unbounded. A point force $F \cdot \exp(i\omega t)$ is exciting the plate at the origin, $x = y = 0$. The direction of the force is perpendicular to the plate. A pressure $p \cdot \exp(i\omega t)$ is induced by the fluid due to the motion of the plate. The resulting velocity of the plate is $v(x, y) \cdot \exp(i\omega t)$. Omitting the time-dependent function the equation of motion for the plate is

$$\nabla^2(\nabla^2 v) - \kappa^4 v = i\omega F \delta(x)\delta(y)/D - i\omega p/D \quad (12.46)$$

The wavenumber for flexural waves on the plate in vacuo is κ . The bending stiffness of the plate is D . The force and velocity are defined positive in the same direction. The pressure p induced by the fluid on the plate is counter acting its motion. The velocity of the plate can be expressed as a Fourier integral. Thus

$$v(x, y) = \frac{1}{(2\pi)^2} \int_{-\infty}^{\infty} \int_{-\infty}^{\infty} \tilde{v}(\xi, \eta) \exp[i(x\xi + y\eta)] d\xi d\eta$$

$$\tilde{v}(\xi, \eta) = \int_{-\infty}^{\infty} \int_{-\infty}^{\infty} v(x, y) \exp[-i(x\xi + y\eta)] dx dy \quad (12.47)$$

The FT of $\nabla^2(\nabla^2 v)$ is according to (12.40) equal to

$$\text{FT} \nabla^2(\nabla^2 v) = (\xi^2 + \eta^2)^2 \tilde{v}(\xi, \eta) \quad (12.48)$$

The FT of the first expression on the right-hand side of Eq. (12.46) is quite simply equal to $i\omega F/D$. This follows directly from the definition of the Dirac function. The pressure reacting on the plate at $(x, y, 0)$ is from Eqs. (12.32) to (12.33) given by

$$p(x, y, 0) = \int_{-\infty}^{\infty} \int_{-\infty}^{\infty} i\omega \rho_0 v(x_0, y_0) G(x, y, 0|x_0, y_0, 0) dx_0 dy_0 \quad (12.49)$$

In Eq. (12.49) the Fourier transforms of the plate velocity and the Green's function, Eq. (12.45), are introduced as

$$v(x_0, y_0) = \int_{-\infty}^{\infty} \int_{-\infty}^{\infty} \tilde{v}(\xi, \eta) \exp[i(x_0\xi + y_0\eta)] d\xi d\eta$$

$$G(x, y, 0|x_0, y_0, 0) = \frac{1}{(2\pi)^2} \int_{-\infty}^{\infty} \int_{-\infty}^{\infty} dk_x dk_y \frac{\exp[ik_x(x_0 - x) + ik_y(y_0 - y)]}{\sqrt{k_x^2 + k_y^2 - k^2}}$$

These transforms are inserted in (12.49). The order of integration is changed giving

$$p(x, y) = \frac{i\omega \rho_0}{(2\pi)^4} \int_{-\infty}^{\infty} \int_{-\infty}^{\infty} \tilde{v}(\xi, \eta) d\xi d\eta \int_{-\infty}^{\infty} \int_{-\infty}^{\infty} \frac{\exp(-ik_x x - ik_y y)}{\sqrt{k_x^2 + k_y^2 - k^2}} dk_x dk_y$$

$$\times \int_{-\infty}^{\infty} \int_{-\infty}^{\infty} \exp[ix_0(k_x - \xi) + iy_0(k_y - \eta)] dx_0 dy_0 \quad (12.50)$$

The last integral is based on the definition of the FT of a two-dimensional Dirac function equal to

$$\int_{-\infty}^{\infty} \int_{-\infty}^{\infty} \exp[ix_0(k_x - \xi) + iy_0(k_y - \eta)] dx_0 dy_0 = (2\pi)^2 \delta(\xi - k_x) \delta(\eta - k_y)$$

This result in combination with (12.50) yields

$$p(x, y) = \frac{i\omega\rho_0}{(2\pi)^2} \int_{-\infty}^{\infty} \int_{-\infty}^{\infty} \tilde{v}(\xi, \eta) \frac{\exp[i(\xi x + \eta y)]}{\sqrt{\xi^2 + \eta^2 - k^2}} d\xi d\eta \quad (12.51)$$

The spatial FT of p consequently compares the general definition (12.47) of Fourier transforms

$$\tilde{p}(\xi, \eta) = \omega\rho_0\tilde{v}(\xi, \eta)/\lambda; \quad \lambda = \sqrt{k^2 - \xi^2 - \eta^2} \quad (12.52)$$

In the basic Eq. (12.46), each term is replaced by its spatial Fourier transform. The result is

$$\begin{aligned} \tilde{v}[(\xi^2 + \eta^2)^2 - \kappa^4] &= \frac{i\omega F}{D} - \frac{i\omega^2\rho_0\tilde{v}}{D\lambda} \\ \tilde{v} &= \frac{i\omega F}{D[(\xi^2 + \eta^2)^2 - \kappa^4 + i\omega^2\rho_0/(D\lambda)]} \end{aligned} \quad (12.53)$$

The time average of the total power Π radiated by the plate is

$$\bar{\Pi} = \frac{1}{2} \text{Re} \iint p v^* dx dy = \frac{1}{2} \text{Re} \iint \tilde{p} \tilde{v}^* d\xi d\eta = \frac{1}{2} \text{Re} \iint |\tilde{v}|^2 \frac{\omega\rho_0}{(2\pi)^2\lambda} d\xi d\eta \quad (12.54)$$

The integrand is only real as long as $\xi^2 + \eta^2 \leq k^2$. If it is assumed that $F = 0$ for frequencies larger than f_1 and $f_1 \ll f_c$ where f_c is the critical frequency defined in (12.18), then $k < \kappa$. Based on these assumptions an approximate expression for \tilde{v} in the frequency range $f \ll f_c$ is

$$\tilde{v} = \frac{-i\omega F}{D[\kappa^4 - i\omega^2\rho_0/(D\lambda)]}$$

This expression inserted in Eq. (12.54) gives the time average of the radiated power as

$$\bar{\Pi} = \frac{1}{8\pi^2} \text{Re} \iint \frac{\omega^3\rho_0|F|^2}{D^2\lambda[\kappa^8 + \omega^4\rho_0^2/(D\lambda)^2]} d\xi d\eta \quad (12.55)$$

The integration is carried out for $k^2 \geq \xi^2 + \eta^2 \geq 0$. Outside this region λ is complex and no power is radiated. It is convenient to change to cylindrical coordinates as

$$\begin{aligned} \zeta^2 &= \xi^2 + \eta^2; \quad \lambda = \sqrt{k^2 - \zeta^2} \\ d\xi d\eta/\lambda &\rightarrow 2\pi\zeta d\zeta/\lambda \rightarrow -2\pi d\lambda \end{aligned}$$

The wave number κ for the plate is given by $\kappa^4 = \mu\omega^2/D$ where μ is the mass per unit area of the plate. Considering these substitutions and after changing the integration limits, the expression (12.55) is simplified to

$$\bar{\Pi} = \frac{\rho_0 |F|^2}{4\pi\omega\mu^2} \int_0^k \frac{\lambda^2}{\lambda^2 + (\rho_0/\mu)^2} d\lambda = \frac{\rho_0 |F|^2}{4\pi\omega\mu^2} \left[k - \frac{\rho_0}{\mu} \arctan\left(\frac{k\mu}{\rho_0}\right) \right]$$

For a heavy fluid loading on the plate, i.e., for $k\mu/\rho_0 \ll 1$ the arctan term can be expanded in a Taylor series. Substituting $\arctan(z)$ by $z - z^3/3$ in the result above, the time average of the radiated power from the point-excited infinite plate is given as

$$\bar{\Pi} = \frac{|F|^2 k^3}{12\pi\omega\rho_0} = \frac{|F|^2 k^2}{12\pi c\rho_0} = \frac{|\bar{F}|^2 k^2}{6\pi c\rho_0} \quad (12.56)$$

This is indeed a remarkable result. The radiated acoustical power is not a function of the material parameters of the plate but only of properties of the fluid and the frequency. The same result is obtained if the plate is exchanged by a membrane as shown by Morse and Ingard, [23]. The result (12.56) was first derived by Maidanik and Kerwin using a different approach as presented in Ref. [152]. It should be noted that F in Eqs. (12.46) and (12.56) is the amplitude of the force and not the rms value of the force as used in Ref. [152]. This distinction is not made in some references. This can cause some confusion.

For an infinite plate with a fluid on both sides the density ρ_0 is replaced by $2\rho_0$. The area of the radiating plate and the vibration resistance are both doubled. This means that the total radiated power is the same for plates with fluid loading on one or two sides.

For a light fluid loading, i.e., for $k\mu/\rho_0 \gg 1$ and for $k \ll \kappa$ or $f \ll f_c$ the second term inside the bracket in the denominator of the integral (12.55) can be neglected. The radiated power is thus equal to

$$\bar{\Pi} = \frac{\rho_0 |F|^2}{4\pi\mu^2 c} = \frac{\rho_0 |\bar{F}|^2}{2\pi\mu^2 c} \quad (12.57)$$

In the high frequency region, for $k \gg \kappa$ or $f \gg f_c$ the corresponding result for the lightly loaded plate is

$$\bar{\Pi} = \frac{|F|^2}{16\sqrt{\mu D}} = \frac{|\bar{F}|^2}{8\sqrt{\mu D}} \quad (12.58)$$

It is assumed that the internal losses of the plate are negligible. This means that all the power fed into the plate is lost as radiated acoustic power from the plate. The expression (12.58) is readily derived by considering the point mobility for an infinite plate as discussed in Sect. 8.4. The implication of the results (12.57) and (12.58) above are discussed in Sect. 12.8.

12.6 Mobilities of Fluid-Loaded Infinite Plates

The point mobility of a structure is an important parameter. As discussed in Sect. 2.8 and elsewhere, the power spectral density G_{Π} of the acoustic power induced in a structure by a force having the power spectral density G_{FF} is $G_{\Pi} = G_{FF} \text{Re}Y$ where Y is the point mobility of the structure. Clearly, one way to reduce the input power to a structure is, if possible, to change its point mobility. It is therefore essential to model the mobility functions of various types of structures. In previous discussions, the mobilities have been derived without considering the effects of fluid loading. In most cases, this is a valid approximation. However, for a structure exposed to a heavy fluid loading the mobility would differ as compared to that valid for the same structure in vacuo. Real structures are obviously finite. However, the response of or the energy flow to a finite structure can very often be estimated by considering the coupling between the corresponding infinite structures. This was already discussed in Sect. 8.5.

For an infinite structure, as before oriented in the x - y -plane and with a fluid load on one side as described in Sect. 12.5, the plate velocity v at the excitation point is from Eq. (12.53) given as

$$\hat{v} = \frac{i\omega\hat{F}}{(2\pi)^2 D} \int_{-\infty}^{\infty} \int_{-\infty}^{\infty} \frac{d\xi d\eta}{(\xi^2 + \eta^2)^2 - \kappa^4 + i\rho_0\kappa^4/(\mu\lambda)}$$

The plate has certain losses. These losses are included in the standard way by writing $\kappa^4 = \kappa_0^4(1 - i\eta_p)$ where η_p is the loss factor of the plate. By changing to cylindrical coordinates as previously demonstrated and by including the loss factor η_p the result is

$$\hat{v} = \frac{i\omega\hat{F}}{(2\pi)D} \int_0^{\infty} \frac{\zeta d\zeta}{\zeta^4 - \kappa^4 + i\eta_p\kappa^4 + i\rho_0\kappa^4/(\mu\lambda)}; \quad \lambda = \sqrt{k^2 - \zeta^2} \quad (12.59)$$

If the fluid loading can be neglected the velocity v is given by

$$\hat{v} = \frac{i\omega\hat{F}}{(2\pi)D} \int_0^{\infty} \frac{\zeta d\zeta}{\zeta^4 - \kappa^4 + i\eta_p\kappa^4}$$

This integral was discussed in Sect. 8.5. For an infinite plate with negligible fluid loading the point impedance is obtained from (8.77) as

$$Y_{\infty} = \frac{1}{8\sqrt{\mu D}}$$

For a plate exposed to a heavy fluid, the last term in the denominator of Eq. (12.59) cannot be neglected. The parameter λ is a function of ζ which makes a straightforward integration impossible. Crighton [153–155] has published a large number of papers on the effect a fluid load has on a plate. When a fluid is very heavy like water, certain

simplifications can be made when solving Eq. (12.59) as suggested by Crighton. As a starting point, a parameter Q is defined as

$$Q = \left(\rho_0 \kappa^4 / \mu \right)^{1/5} \quad (12.60)$$

For a fluid with a high density, $\rho_0 / \mu \gg \kappa$ and $Q \gg \kappa$. Considering these assumptions the basic expression (12.59) is reduced to

$$\hat{v} = \frac{i\omega \hat{F}}{(2\pi)D} \int_0^\infty \frac{\zeta d\zeta}{\zeta^4 + iQ^5/\lambda} = \frac{i\omega \hat{F}}{(2\pi)D} \int_0^\infty \frac{(\zeta^4 \lambda^2 - i\lambda Q^5)\zeta d\zeta}{\zeta^8 \lambda^2 + Q^{10}}$$

For simplicity, the integral is written as

$$\hat{v} = \frac{i\omega \hat{F}}{(2\pi)D} (J_1 + J_2)$$

$$J_1 = \int_0^\infty \frac{\zeta^4 \lambda^2 \zeta d\zeta}{\zeta^8 \lambda^2 + Q^{10}}; \quad J_2 = \int_0^\infty \frac{-i\lambda Q^5 \zeta d\zeta}{\zeta^8 \lambda^2 + Q^{10}} \quad (12.61)$$

The integrand has poles for $\zeta^8 \lambda^2 + Q^{10} = 0$. However, $Q \gg k$ which according to (12.59) implies that $\zeta^8 \lambda^2 = \zeta^8 (k^2 - \zeta^2) \approx -\zeta^{10}$. The poles ζ_n are consequently

$$\zeta_n \approx Q \cdot e^{-i\pi n/5} \quad \text{for } n = 0, 1, \dots, 9, \quad (12.62)$$

At any of these poles $\lambda^2 = k^2 - \zeta^2 \approx -\zeta^2$ and according to (12.59), $\lambda = -i(\zeta^2 - k^2)^{1/2} \approx -i\zeta$. For a time dependence $\exp(i\omega t)$ the pressure in the fluid is of the form

$$p(r, t) \propto \oint \tilde{\Phi}(\zeta) \zeta \exp[i(\omega t - r\zeta)] d\zeta$$

A contour integration of this integral can only include poles with negative arguments for the integral to be finite. The same is the case for Eq. (12.61). For $|\zeta_n| \gg k$ the expressions J_1 and J_2 of the integral (12.61) can be approximated as

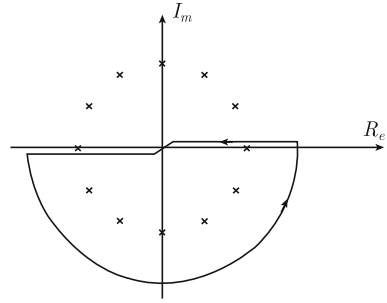
$$J_1 = \int_0^\infty \frac{\zeta^4 \lambda^2 \zeta d\zeta}{\zeta^8 \lambda^2 + Q^{10}} \approx \int_0^\infty \frac{\zeta^7 d\zeta}{\zeta^{10} - Q^{10}};$$

$$J_2 = \int_0^\infty \frac{-i\lambda Q^5 \zeta d\zeta}{\zeta^8 \lambda^2 + Q^{10}} \approx \frac{1}{2} \int_{-\infty}^\infty \frac{Q^5 \zeta^2 d\zeta}{\zeta^{10} - Q^{10}} \quad (12.63)$$

The integral J_2 is solved by means of integration along the path shown in Fig. 12.4. Thus

$$J_2 = -\frac{1}{2} \oint_C \frac{Q^5 \zeta^2 d\zeta}{\zeta^{10} - Q^{10}} = -i\pi \sum_{n=0}^4 \frac{\zeta_n^2 Q^5}{10\zeta_n^9} = -\frac{i\pi}{10Q^2} \sum_{n=0}^4 e^{7in\pi/5} \quad (12.64)$$

Fig. 12.4 Integration path for solving Eq. (12.61)



The other integral J_1 includes an odd function and can therefore not directly be extended to minus infinity. The standard procedure for this type of problem is to multiply the integrand by $\ln \zeta$. Thereafter, the contour integration is carried out. Thus, consider the integral

$$J_3 = \oint \frac{\ln \zeta \cdot \zeta^7 d\zeta}{\zeta^{10} - Q^{10}}$$

The argument for ζ along the positive axis is 0 and along the negative axis $-i\pi$ for the contour is shown in Fig.12.4. Thus

$$J_3 = 0 - i\pi \int \frac{\zeta^7 d\zeta}{\zeta^{10} - Q^{10}} - \int_0^\infty \frac{\ln |\zeta| \cdot \zeta^7 d\zeta}{\zeta^{10} - Q^{10}} - \int_{-\infty}^0 \frac{\ln |\zeta| \cdot \zeta^7 d\zeta}{\zeta^{10} - Q^{10}}$$

$$J_1 = -J_3/(i\pi) = -2 \sum_{n=0}^4 \frac{\zeta_n^7 \ln |\zeta_n|}{10\zeta_n^9} = -\frac{2}{10Q^2} \sum_{n=0}^4 \frac{-in\pi}{5} \cdot e^{2in\pi/5}$$

The total integral J is thus equal to

$$J = J_1 + J_2 = -\frac{i\pi}{10Q^2} \sum_{n=0}^4 \left(e^{7i\pi n/5} - \frac{2n}{5} \cdot e^{2i\pi n/5} \right) = \frac{2i\pi}{10Q^2} [1 - i \tan(\pi/10)] \tag{12.65}$$

For frequencies well below the critical frequency, the point mobility of heavily fluid-loaded plates is obtained from (12.61) to (12.65) as

$$Y_\infty = \left(\frac{\omega}{D^3 \rho_0^2} \right)^{1/5} [1 - i \tan(\pi/10)]/10 \tag{12.66}$$

The point mobility for a plate clearly depends on the type of fluid loading on the plate. This is discussed further in next section.

12.7 Discussion of Results—Infinite Fluid-Loaded Plates

Maidanik and Kerwin [152] have derived the acoustical power radiated by a fluid-loaded plate. The plate is either considered to be excited by a point force, line force, or a point moment. In Sect. 12.6 the first case is discussed, the other results can be derived in a similar way. The corresponding mobilities have been investigated by Crighton. Some of the main results by Crighton are presented in [153]. The procedure used by Crighton to determine the point mobility of a plate exposed to a heavy fluid loading is for the “low frequency” case outlined in Sect. 12.6. Crighton has shown that the low frequency approximation gives satisfactory results as long as $k/\kappa < 1/10$, where k is the wave number in the fluid and κ the wave number for flexural waves propagating along the plate in vacuo.

For infinite plates excited by a point or line force the results can be summarized as

1. Infinite plate excited by a point force F

Light fluid loading

Radiated power

$$\bar{\Pi} = \frac{\rho_0 |\bar{F}|^2}{2\pi c \mu^2} \quad (12.67)$$

Point mobility

$$Y_\infty = \frac{1}{8\sqrt{\mu D}} \quad (12.68)$$

Heavy fluid loading

Radiated power

$$\bar{\Pi} = \frac{k^2 |\bar{F}|^2}{6\pi c \rho_0} \quad (12.69)$$

Point mobility

$$Y_\infty = \frac{1}{10} \left(\frac{\omega}{D^3 \rho_0^2} \right)^{1/5} [1 - i \tan(\pi/10)] \quad (12.70)$$

2. Infinite plate excited by a line force F_l

Light fluid loading

Radiated power per unit length

$$\bar{\Pi}_l = \frac{\pi \rho_0 |\bar{F}_l|^2}{4\omega \mu^2} \quad (12.71)$$

Mobility per unit length

$$Y_{l\infty} = \left(\frac{1}{\omega^2 D \mu^3} \right)^{1/4} \frac{1+i}{4} \quad (12.72)$$

Heavy fluid loading

Radiated power per unit length

$$\bar{\Pi} = \frac{\pi \omega |\bar{F}_l|^2}{8 \rho_0 c^2} \quad (12.73)$$

Mobility per unit length

$$Y_{l\infty} = \frac{1}{5} \left(\frac{1}{\omega D^2 \rho_0^3} \right)^{1/5} [1 + i \tan(\pi/10)] \quad (12.74)$$

For a point-excited infinite plate with a heavy fluid loading the time average of the power fed into the plate is

$$\bar{\Pi}_{in} = |\bar{F}|^2 \operatorname{Re} Y_{l\infty} = \frac{|\bar{F}|^2}{10} \left(\frac{\omega}{D^3 \rho_0^2} \right)^{1/5}$$

The acoustical power radiated out from the plate is

$$\bar{\Pi}_{rad} = \frac{\rho_0 |\bar{F}|^2}{2\pi c \mu^2}$$

The ratio $\bar{\Pi}_{rad}/\bar{\Pi}_{in}$ is less than unity in the low frequency region. For high frequencies well above the critical frequency, $\bar{\Pi}_{rad} = \bar{\Pi}_{in}$ if the losses in the plate itself are neglected. In the low frequency region, an additional wave type is propagating parallel to the plate and away from the excitation point. As previously pointed out, the amplitude of this type of wave is decreasing exponentially with the distance from the plate. No power is radiated perpendicular away from the plate due to this field. However, the wave propagating parallel to the plate carries power away from the excitation point. The intensity vector of the wave is pointing away from the excitation point and is parallel to the plate. The total power $\bar{\Pi}_{surface}$ radiated by these waves clinging to the plate is, for a loss-free plate,

$$\bar{\Pi}_{surface} = \bar{\Pi}_{in} - \bar{\Pi}_{rad}$$

Numerical calculations of the response of finite plates show that the displacement of the plate is large at the excitation point and rapidly decaying with increasing distance from the excitation point. The dominating part of the radiated power is caused

by the plate displacement very close to the excitation point. For this reason the radiated power from sufficiently large fluid-loaded plates can, as a first approximation, be estimated as if the plates were infinite.

The vibrational field of a finite plate consists of a near field and a reverberant field. The effect of the fluid loading on the reverberant field can be calculated as discussed in Sect. 12.1. The additional mass per unit area due to the fluid loading is

$$\mu_{\text{add}} \approx \rho_0 / \kappa_x$$

where κ_x is the wave number for flexural waves traveling along a fluid-loaded plate. For a point force exciting a fluid-loaded plate it can be shown that at the excitation point the apparent mass of the plate is considerably higher than the corresponding added mass felt by a reverberant field. See Problem 12.7.

12.8 Radiation from Finite Baffled Plates

A real structure is finite. Consequently, it is of great importance to determine the radiation from finite plates and the influence on the radiation of the area, geometry, and the boundary conditions of the plate. In principle, a plate can be baffled or unbaffled. The baffle is a structure in which a plate can be mounted. The baffle is typically assumed to be completely stiff and consequently nonradiating. Two vibrating plates are shown in Fig. 12.5. One is mounted in an infinite baffle and the other without. In the last case, the two acoustic fields generated below and above the plate can interfere. This interference reduces the acoustic radiation efficiency of the plate. In the other case, there is no coupling effect or negative interference between the upper and lower acoustic fields. Consequently, the baffled plate is a more efficient acoustic radiator than the unbaffled plate. In the very low frequency range, close to the first natural frequency of the plate, the baffled plate radiates like a monopole and the unbaffled plate like a dipole.

In order to illustrate the radiation from a baffled plate consider a rectangular and simply supported plate mounted in an infinite and rigid baffle oriented in the x - y -plane. In the region, $z > 0$ there is a fluid with the density ρ_0 and speed of sound c and wave number k . The reverse side of the plate is unloaded. The plate has the dimensions L_x and L_y . The center of the plate is at the origin of the coordinate system as shown in Fig. 12.6.



Fig. 12.5 Radiation from a baffled and an unbaffled plate. First vibrational mode

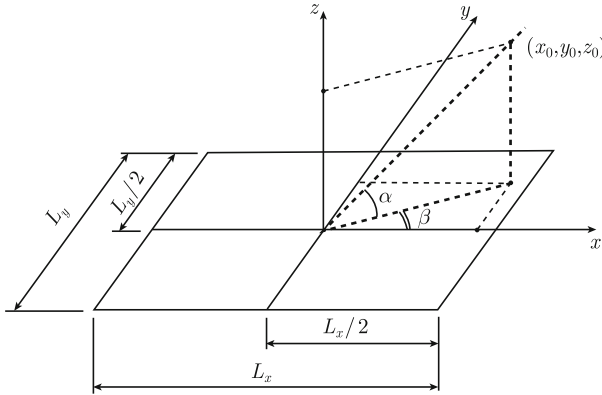


Fig. 12.6 A radiating simply supported plate

At a large distance from the plate the pressure p in an observation point (x, y, z) is, neglecting a time dependence $\exp(i\omega t)$, according to Eq. (12.34) given by

$$p(\mathbf{r}) = \frac{1}{2\pi r_c} \iint_{S_0} i\omega\rho_0 v(x_0, y_0) e^{-ikr} dx_0 dy_0; \quad r_c \gg 1$$

$$r_c = [x^2 + y^2 + z^2]^{1/2}; \quad r = [(x - x_0)^2 + (y - y_0)^2 + z^2]^{1/2}$$

It is assumed that the distance from the plate to the observation point is much larger than the plate dimensions, i.e., $r_c \gg |x_0|$ and $|y_0|$. Thus, the distance r between a point $(x_0, y_0, 0)$ on the plate and the observation point (x, y, z) is written as

$$r = \left(r_c^2 - 2xx_0 + x_0^2 - 2yy_0 + y_0^2 \right)^{1/2} \approx r_c - \frac{xx_0}{r_c} - \frac{yy_0}{r_c} \quad (12.75)$$

An approximate expression for the pressure in the fluid is obtained by inserting (12.75) in the preceding expression. The result is

$$p(\mathbf{r}) = \frac{e^{-ikr_c}}{2\pi r_c} \iint_{S_0} i\omega\rho_0 v(x_0, y_0) \exp(-ikxx_0/r_c - ikyy_0/r_c) dx_0 dy_0 \quad (12.76)$$

The velocity is defined for $-L_x/2 < x < L_x/2$ and $-L_y/2 < y < L_y/2$. The velocity is equal to zero elsewhere on the plane defined by $z = 0$. The eigenfunction for the simply supported rectangular plate is

$$g_{mn}(x, y) = \sin \left[\frac{m\pi(x + L_x/2)}{L_x} \right] \cdot \sin \left[\frac{n\pi(y + L_y/2)}{L_y} \right] \quad (12.77)$$

The lateral velocity of the rectangular and simply supported plate is for mode (m, n) given by

$$v(x, y, t) = v_{mn} \cdot \exp(i\omega t) \cdot g_{mn}(x, y)$$

The resulting pressure $p(\mathbf{r})$ at the observation point \mathbf{r} induced by the vibrational mode (m, n) of the plate is according to Eqs. (12.76) and (12.77) equal to

$$p_{mn}(\mathbf{r}) = \frac{e^{-ikr_c}}{2\pi r_c} i\omega\rho_0 v_{mn} H_x H_y$$

$$H_x = \int_{-L_x/2}^{L_x/2} \sin\left[\frac{m\pi(x_0 + L_x/2)}{L_x}\right] \exp(-ikx x_0/r_c) dx_0$$

$$H_y = \int_{-L_y/2}^{L_y/2} \sin\left[\frac{n\pi(y_0 + L_y/2)}{L_y}\right] \exp(-iky y_0/r_c) dy_0 \quad (12.78)$$

The functions H_x and H_y are solved by partial integration. The results are

$$H_x = \frac{(m\pi/L_x)\{\exp[ikxL_x/(2r_c)] - \cos(m\pi)\exp[-ikxL_x/(2r_c)]\}}{(m\pi/L_x)^2 - (kx/r_c)^2}$$

$$H_y = \frac{(n\pi/L_y)\{\exp[ikyL_y/(2r_c)] - \cos(n\pi)\exp[-ikyL_y/(2r_c)]\}}{(n\pi/L_y)^2 - (ky/r_c)^2} \quad (12.79)$$

The time average of the absolute value of the pressure squared at the point \mathbf{r} is from Eqs. (12.78) to (12.79) given by

$$|\bar{p}_{mn}|^2 = \left(\frac{\omega\rho_0}{2\pi r_c}\right)^2 \frac{|v_{mn}|^2}{2} G_x G_y$$

$$G_x = 2 \frac{(m\pi/L_x)^2 [1 - \cos(m\pi)\cos(kxL_x/r_c)]}{[(m\pi/L_x)^2 - (kx/r_c)^2]^2}$$

$$G_y = 2 \frac{(n\pi/L_y)^2 [1 - \cos(n\pi)\cos(kyL_y/r_c)]}{[(n\pi/L_y)^2 - (ky/r_c)^2]^2} \quad (12.80)$$

The rms pressure along the z-axis, i.e., for $x = y = 0$ is quite simply given by (12.80) as

$$|\bar{p}_{mn}|^2 = \left(\frac{\omega\rho_0}{\pi r_c}\right)^2 \frac{|v_{mn}|^2}{2} \frac{[1 - \cos(m\pi)]}{(m\pi/L_x)^2} \times \frac{[1 - \cos(n\pi)]}{(n\pi/L_y)^2} \quad (12.81)$$

For m or n even, the pressure is zero along the normal through the center of the plate. The reason is that one-half of the plate is moving in opposite phase as compared to the other part. The total field along the center line is consequently zero. If for the modes (1, 1) and (1, 3) the modal velocity v_{mn} has the same amplitude, the ratio $|\bar{p}_{11}/\bar{p}_{13}|^2$ is equal to 9. The radiation pattern for mode (1, 3) is schematically shown in Fig.12.7.

The plate is radiating as if it consisted of six sources, four in phase and two in antiphase. The four central sources extinguish each other. Only the two sources along the edges contribute to the field along the center axis. Along this axis, it seems as if only 1/3 of the plate is radiating. The pressure squared is inversely proportional to the area squared. Consequently, the ratio $|\bar{p}_{11}/\bar{p}_{13}|^2$ is equal to 9. In the low frequency region, only a few vibrational modes are excited. In this case, the acoustic power radiated by the plate is the result of the motion of the edges or corners of the plate. When the boundary conditions of the plate are changed from simply supported to clamped the uncanceled radiation area is increased suggesting that a clamped plate radiates more acoustic power assuming the velocity being the same. See Problem 12.6.

At a large distance from the plate the intensity in the radial direction as seen from the center of the plate is $\bar{I} = |\bar{p}|^2 / (\rho_0 c)$. The total radiated power induced by the vibrational mode (m, n) is thus

$$\bar{\Pi} = \int_S \bar{I} dS = \frac{L_x L_y}{\rho_0 c} \int_0^{2\pi} d\beta \int_0^{\pi/2} d\alpha \cos \alpha |\bar{p}|^2 r_c^2 \tag{12.82}$$

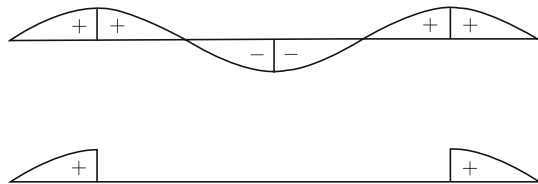
The area integration is made over a semi-sphere with the radius r_c . The radiated power from the plate induced by the mode (m, n) can also be written as

$$\bar{\Pi} = \rho_0 c \langle |\bar{v}|^2 \rangle \sigma_{mn} L_x L_y = \rho_0 c \left| v_{mn}^2 \right| (\sigma_r)_{mn} L_x L_y / 8 \tag{12.83}$$

The time and space average of the square of the plate velocity is given by $\langle |\bar{v}|^2 \rangle = |v_{mn}|^2 / 8$. The sound radiation ratio for mode (m, n) is denoted as $(\sigma_r)_{mn}$. The square of the modal pressure $|\bar{p}_{mn}|^2$ is given by Eq.(12.80). Thus, the Eqs.(12.80)–(12.83) give the radiation ratio $(\sigma_r)_{mn}$ as

$$(\sigma_r)_{mn} = \frac{k^2}{\pi^2} \int_0^{2\pi} d\beta \int_0^{\pi/2} G_x G_y \cos \alpha d\alpha \tag{12.84}$$

Fig. 12.7 Radiation pattern for mode (3,1) along the x -axis of a simply supported plate. The lower illustration shows the effect of cancelation of central radiators



In the low frequency region or rather if kL_x and $kL_y \ll 1$ the cosine terms in Eq. (12.80) that are functions of these products can be expanded in Taylor series as

$$\cos(kxL_x/r_c) \approx 1 - \frac{1}{2} \left(\frac{kxL_x}{r_c} \right)^2$$

The coordinates x and y are defined by means of the angles α and β . Thus

$$x = r_c \cos \alpha \cos \beta; \quad y = r_c \cos \alpha \sin \beta;$$

The denominators of G_x and G_y in Eq. (12.80) are in the low frequency region, i.e., for kL_x and $kL_y \ll 1$, approximated by $(m\pi/L_x)^4$ and $(n\pi/L_y)^4$, respectively. Thus

$$G_x \approx \frac{2[1 - \cos(m\pi)][1 - (kL_x \cos \alpha \cos \beta)^2/2]}{(m\pi/L_x)^2};$$

$$G_y \approx \frac{2[1 - \cos(n\pi)][1 - (kL_y \cos \alpha \sin \beta)^2/2]}{(n\pi/L_y)^2}$$

The approximate expressions giving G_x and G_y inserted in the expression (12.84) yield σ_{mn} . As demonstrated by Wallace [157] the result is for kL_x and $kL_y \ll 1$

(i) m and n odd

$$\sigma_{mn} = \frac{32k^2 L_x L_y}{m^2 n^2 \pi^5} \left\{ 1 - \frac{k^2 L_x L_y}{12} \left[\left(1 - \frac{8}{(m\pi)^2} \right) \frac{L_x}{L_y} + \left(1 - \frac{8}{(n\pi)^2} \right) \frac{L_y}{L_x} \right] \right\} \quad (12.85)$$

(ii) m odd n even

$$\sigma_{mn} = \frac{8k^4 L_x L_y^3}{3m^2 n^2 \pi^5} \left\{ 1 - \frac{k^2 L_x L_y}{20} \left[\left(1 - \frac{8}{(m\pi)^2} \right) \frac{L_x}{L_y} + \left(1 - \frac{24}{(n\pi)^2} \right) \frac{L_y}{L_x} \right] \right\} \quad (12.86)$$

For n odd and m even exchange m and n and L_x and L_y .

(iii) m and n even

$$\sigma_{mn} = \frac{2(k^2 L_x L_y)^3}{15m^2 n^2 \pi^5} \left\{ 1 - \frac{5k^2 L_x L_y}{64} \left[\left(1 - \frac{24}{(m\pi)^2} \right) \frac{L_x}{L_y} + \left(1 - \frac{24}{(n\pi)^2} \right) \frac{L_y}{L_x} \right] \right\} \quad (12.87)$$

It is evident that the odd–odd modes are the most efficient radiators. However, the requirement kL_x and $kL_y \ll 1$ limits the applicability of the formulas given in Eqs. (12.85)–(12.87).

A more general and useful presentation of the results are obtained by normalizing the wave number k with respect to the wave number κ for flexural waves propagating on the plate. Thus for

$$\kappa = [(m\pi/L_x)^2 + (n\pi/L_y)^2]^{1/2}; \quad \gamma = k/\kappa \quad (12.88)$$

the modal radiation ratios are written as

(i) m and n odd

$$\sigma_{mn} = \frac{32k^2 L_x L_y}{mn\pi^3} \left(\frac{nL_x}{mL_y} + \frac{mL_y}{nL_x} \right) \times \gamma^2 \left\{ 1 - \left[\left(1 - \frac{8}{(m\pi)^2} \right) \frac{L_x}{L_y} + \left(1 - \frac{8}{(n\pi)^2} \right) \frac{L_y}{L_x} \right] \right\} \quad (12.89)$$

(ii) m odd n even

$$\sigma_{mn} = \frac{8L_y}{3\pi L_x} \left(\frac{nL_x}{mL_y} + \frac{mL_y}{nL_x} \right)^2 \times \gamma^4 \left\{ 1 - \left[\left(1 - \frac{8}{(m\pi)^2} \right) \frac{L_x}{L_y} + \left(1 - \frac{24}{(n\pi)^2} \right) \frac{L_y}{L_x} \right] \right\} \times \left(\frac{nL_x}{mL_y} + \frac{mL_y}{nL_x} \right) \frac{mn\pi}{20} \gamma^2 \left. \right\} \quad (12.90)$$

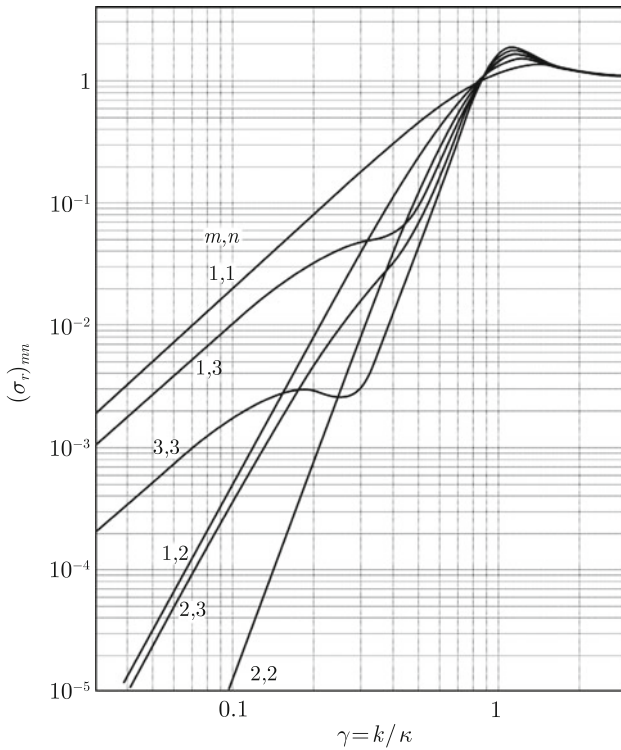


Fig. 12.8 Radiation ratios for the first few modes of a simply supported rectangular plate. From Ref. [157]

For n odd and m even exchange m and n and L_x and L_y .

(iii) m and n even

$$\begin{aligned} \sigma_{mn} = & \frac{2mn\pi}{15} \left(\frac{nL_x}{mL_y} + \frac{mL_y}{nL_x} \right)^3 \\ & \times \gamma^6 \left\{ 1 - \left[\left(1 - \frac{24}{(m\pi)^2} \right) \frac{L_x}{L_y} + \left(1 - \frac{24}{(n\pi)^2} \right) \frac{L_y}{L_x} \right] \right. \\ & \left. \times \left(\frac{nL_x}{mL_y} + \frac{mL_y}{nL_x} \right) \frac{5mn\pi}{64} \gamma^2 \right\} \end{aligned} \quad (12.91)$$

It is stated by Wallace that the expressions given in Eqs. (12.89)–(12.91) are only valid as long as $\gamma^2 \ll 1$.

The radiation ratios for the first modes of a simply supported rectangular plate are shown in Fig. 12.8. The radiation ratios are given as function of $\gamma = k/\kappa$. In the low frequency region, it is evident that the odd–odd modes are more efficient radiators than the even–even modes. However, as $\gamma \rightarrow 1$ this difference is decreasing.

12.9 Radiation Ratios—Finite Baffled Plates

In Sect. 12.1 it was demonstrated that no sound is radiated from a vibrating and infinite flat plate for frequencies below the critical frequency. The results of the previous section reveal that a finite vibrating plate radiates sound even in the low frequency range below the critical frequency of the plate. Although the results discussed in the previous section are approximate and only valid in the low frequency range it is clearly demonstrated how the various type of panel modes influence the acoustic power radiated by the plate. However, in most cases it is not convenient or practically possible to calculate the radiation ratio and the power radiated by each mode. The radiation ratio should preferably be averaged over all possible modes within a frequency band. Maidanik was the first to formulate expressions giving in Ref. [158] radiation ratios averaged over the dominating modes. Maidanik started off defining the acoustic radiation from a simply supported, homogeneous, and vibrating rectangular plate. It was assumed that the velocity of each plate mode was the same. Further, the acoustic coupling between each plate mode and any acoustic mode in the fluid was equal. Although the end result is very compact and simple to use the derivations leading up to the final results are not always readily understood. Later Leppington et al. [159] treated the same problem and using the same basic equations and assumptions but according to the authors, a more stringent approach was followed as compared to the procedures presented in some previous papers. Still the results obtained by Maidanik and Leppington are identical except for frequencies very close to the critical frequency. However, in both cases the results are based on rather long and complicated derivations.

The basis for both methods is the same. A homogeneous plate is oriented in the x - y -plane, $z = 0$. The coordinates of the corners are at $(0, 0)$, $(L_x, 0)$, (L_x, L_y) , and $(0, L_y)$. According to Eq. (12.33) the pressure $p(x, y)$ on the surface of the plate is induced by the vibrating plate and is written as

$$p(x, y) = \int_0^{L_x} \int_0^{L_y} i\omega\rho_0 v(x_0, y_0) \frac{e^{-iks}}{2\pi s} dx_0 dy_0 \quad (12.92)$$

where $v(x_0, y_0)$ is the plate velocity and s is the distance between a vibrating point at the plate defined by the coordinates (x_0, y_0) and an observation point (x, y) on the same plate. Consequently, $s = \sqrt{(x - x_0)^2 + (y - y_0)^2}$. The time average of the acoustic power radiated from one side of the plate is

$$\bar{\Pi} = \frac{1}{2} \text{Re} \int_0^{L_x} \int_0^{L_y} p(x, y) \cdot v^*(x, y) dx dy \quad (12.93)$$

Equations (12.92) and (12.93) give

$$\begin{aligned} \bar{\Pi} &= \frac{1}{2} \text{Re} \int_0^{L_x} \int_0^{L_y} v^*(x, y) dx dy \int_0^{L_x} \int_0^{L_y} i\omega\rho_0 v(x_0, y_0) \frac{\cos(ks) - i \sin(ks)}{2\pi s} dx_0 dy_0 \\ &= \frac{\omega\rho_0}{4\pi} \int_0^{L_x} \int_0^{L_y} v^*(x, y) dx dy \int_0^{L_x} \int_0^{L_y} \omega\rho_0 v(x_0, y_0) \frac{\sin(ks)}{2\pi s} dx_0 dy_0 \end{aligned} \quad (12.94)$$

For a simply supported plate with the corners at $(0, 0)$, $(L_x, 0)$, (L_x, L_y) , and $(0, L_y)$ the eigenfunctions of the plate are

$$\varphi_{mn}(x, y) = \sin(m\pi x/L_x) \cdot \sin(n\pi y/L_y)$$

The velocity for this particular mode is $v(x, y) = v_{mn} \cdot \varphi_{mn}(x, y)$ omitting the time dependence $\exp(i\omega t)$. The time and space average of the velocity squared is

$$\langle |\bar{v}|^2 \rangle = \frac{1}{2} \iint_S v^2(x, y) dx dy = \frac{v_{mn}^2}{8} \quad (12.95)$$

The radiation ratio for the plate is according to Eq. (12.19) obtained as

$$\sigma_r = \frac{\bar{I}_z}{\langle |\bar{v}|^2 \rangle \rho_0 c} = \frac{\bar{\Pi}}{\langle |\bar{v}|^2 \rangle S \rho_0 c}$$

Consequently, the radiation ratio for mode (m, n) is obtained as

$$\sigma_{mn} = \frac{8\omega k}{4\pi c L_x L_y} \int_0^{L_x} \int_0^{L_y} \varphi_{mn}(x, y) dx dy \int_0^{L_x} \int_0^{L_y} \varphi_{mn}(x_0, y_0) \frac{\sin(ks)}{2\pi s} dx_0 dy_0 \quad (12.96)$$

This expression can be somewhat simplified by making the transformation $x_0 = x + \xi$ and $y_0 = y + \eta$ and $s = \sqrt{\xi^2 + \eta^2}$. Considering the definition of the eigenvectors, the expression (12.96) is reduced to

$$\sigma_{mn} = \frac{2k^2}{\pi L_x L_y} \int_0^{L_x} \int_0^{L_y} [(L_x - \xi) \cos(m\pi\xi/L_x) + L_x/(m\pi) \sin(m\pi\xi/L_x)] \\ \times [(L_y - \eta) \cos(n\pi\eta/L_y) + L_y/(n\pi) \sin(n\pi\eta/L_y)] \frac{\sin(ks)}{ks} d\xi d\eta \quad (12.97)$$

The next step is to change to cylindrical coordinates. The result (12.97) seems deceptively simple. However, a certain effort is required to solve the integral as demonstrated in Ref. [159].

The radiation ratio given in Eq. (12.97) is in principle valid for the plate mode (m, n) . The numerically calculated radiation ratios for some modes are shown in Fig. 12.9. It is shown that for small wavenumbers k , the odd-odd modes radiate more than the even-even modes. For higher frequencies but still below the critical

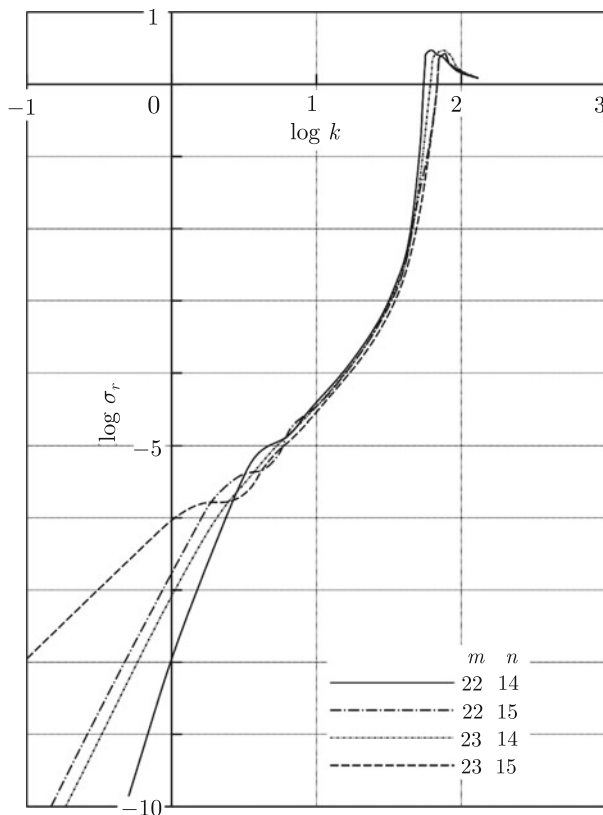


Fig. 12.9 Radiation ratios for some higher plate modes. From Ref. [159]

frequency, the difference between the radiation ratios for odd–odd and even–even modes is very small. In the previous example, Fig. 12.8, the differences between the odd–odd and even–even for low mode numbers were shown to be much bigger than shown in Fig. 12.9.

One basic assumption made by Maidanik and Leppington is that the velocity of every mode is the same. This assumption makes it possible to formulate an average of the radiation ratio for all the possible modes within a frequency band. The wavenumber in the x -direction for the bending waves is $\kappa_x = m\pi/L_x$. In the y -direction the wavenumber is $\kappa_y = n\pi/L_y$. However, the total wavenumber κ for the flexural waves is given by $\kappa^2 = \kappa_x^2 + \kappa_y^2$. Assuming that m and n can vary continuously over all positive values the following substitutions can be made: $m\pi/L_x = \kappa \cos \phi$ and $n\pi/L_y = \kappa \sin \phi$. These expressions inserted in (12.97) give $\sigma(\phi)$. The average radiation ratio taken over all possible angles is

$$\bar{\sigma}_r = \frac{2}{\pi} \int_0^{\pi/2} \sigma(\phi) d\phi$$

The final result as given by Leppington is with $q = \sqrt{f_c/f}$

$$\bar{\sigma}_r = \frac{L_x + L_y}{\pi q k L_x L_y \sqrt{q^2 - 1}} \left[\ln \left(\frac{q + 1}{q - 1} \right) + \frac{2q}{q^2 - 1} \right] \quad \text{for } q > 1 \text{ or } f < f_c \quad (12.98)$$

where f is the frequency and f_c the critical frequency defined in Eq. (12.18).

At the critical frequency, Leppington gives the result as

$$\bar{\sigma}_r \approx \left(\frac{1}{2} - 0.15 \frac{L_{\min}}{L_{\max}} \right) \sqrt{k L_{\min}} \quad \text{for } q = 1, f = f_c \quad (12.99)$$

where L_{\min} is the lesser and L_{\max} the greater of L_x, L_y .

For frequencies above the critical frequency the result is the same as for an infinite panel, or

$$\bar{\sigma}_r = \frac{1}{\sqrt{1 - f_c/f}} \quad \text{for } q < 1 \text{ or } f/f_c > 1 \quad (12.100)$$

For frequencies below the first natural frequency f_{11} of the plate, $\bar{\sigma}_r$ is given by Maidanik [158] as

$$\bar{\sigma}_r \approx \frac{32L_x L_y k^2}{\pi^5} \approx \frac{L_x L_y k^2}{\pi^2} = \frac{4L_x L_y f^2}{c^2} \quad \text{for } f < f_{11}$$

The radiation ratios given by (12.98) and (12.100) can, however, never be greater than the radiation ratio at the critical frequency. The expression (12.98) requires as pointed out by Leppington that $kL_{\min}(q - 1) \gg 1$. The expression (12.98) is similar to that given by Maidanik. However, for $f < f_c/2$ Maidanik has added a term g_1 . In Ref. [159] it is argued that this term g_1 is negligible and probably not correct.

In conclusion, the main difference between the models derived by Leppington and Maidanik is the expression (12.99) giving the radiation ratio at the critical frequency. The result (12.99) being the more accurate. Some predicted radiation ratios are shown in Fig. 12.10.

In the low frequency region $f \ll f_c$ the result (12.98) is given by

$$\bar{\sigma}_r \approx \frac{2(L_x + L_y)c\sqrt{f}}{\pi^2 L_x L_y \sqrt{f_c^3}} \quad (12.101)$$

The radiation ratio depends on the area and the ratio between the two sides of the plate. The result (12.98) indicates that a plate has a constant area while changing the ratio between the lengths of the sides and the minimum radiation ratio is obtained for a quadratic plate. The sound radiation ratio is also changed by the addition of stiffeners. It can be assumed that the velocity of the stiffeners if stiff enough can be neglected as compared to the velocity of the plates. As an example, consider a rectangular plate with the dimensions L_x and L_y . Two stiffeners are mounted to the plate dividing the plate into four equal sections, each having the sides $L_x/2$ and $L_y/2$. In the first case, the radiation ratio of the entire plate without stiffeners is, according to Eq. (12.98), proportional to $(L_x + L_y)/(L_x L_y)$. In the second case, the lengths of the sides are decreased by a factor 2 and the radiation ratio is proportional to $2(L_x + L_y)/(L_x L_y)$. Consequently, in the low frequency region, the effective radiation ratio is doubled by the addition of the two stiffeners.

The boundary conditions are also of importance. The radiation ratio is increased as the boundary conditions of the plate are constrained. Thus, a clamped plate has a higher radiation ratio than a simply supported plate of the same dimensions. The radiation ratio for corner and edge modes is increased by a factor 2 as simply sup-

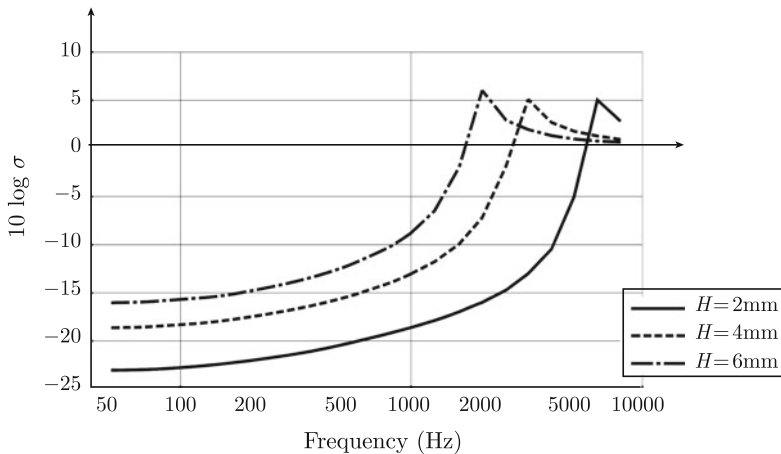


Fig. 12.10 Radiation ratios for steel plate thicknesses 2, 4, and 6 mm. $L_x = 1.4$ m and $L_y = 0.8$ m

ported boundary conditions are changed to clamped. However, the edge and corner modes become less significant for increasing frequencies as f tends to f_c . If the sound radiation ratio is written $X \cdot \bar{\sigma}_r$ where $\bar{\sigma}_r$ is given by (12.98)–(12.100) then the parameter X is equal to unity for a simply supported plate. For a clamped plate $X \approx 2$ for $f < f_c/3$ and $X \approx 2 - 3f_c/2(f - f_c/3)$ for $f_c > f > f_c/3$. For $f > f_c$ $X = 1$.

The radiation ratio also depends on how the plate is excited. The results (12.98)–(12.100) were derived assuming the vibrational field of the plate to be reverberant. In the low frequency region, the wave number for the plate vibrations were determined by the properties of the plate. However, when a plate is excited by an acoustic field the nonresonant wave pattern of the plate is forced by the acoustic field. The radiation ratio for a plate excited by an acoustic field is much higher than for a freely vibrating plate for frequencies below the critical frequency. This is discussed in Chap. 13.

The losses of a plate can also influence its radiation ratio below the critical frequency as discussed by Liu et al. [294]. It is demonstrated in [294] that if the loss factor of a finite plate is increased from 0.05 to 0.10 the corresponding radiation ratio could increase by 4 to 6 dB. The results imply that a damping treatment may effectively reduce the response of a plate while it has less effect on the acoustic power radiated by the structure.

12.10 Radiation from Point-Excited Plates

In a room with a sound source, the total acoustic field can be separated into a reverberant and a near field as discussed in Sect. 11.14. A somewhat similar approach is sometimes adopted to describe the radiation from finite plates excited by a point force. For estimating the radiated power from the plate, it is assumed that the radiation from the near field close to the force is approximately equal to the power radiated by the plate if it were infinite. The radiation from an infinite point-excited plate is for $f \ll f_c$ given by Eq. (12.57) as

$$\bar{\Pi}_\infty = \frac{\rho_0 |\bar{F}|^2}{2\pi\mu^2c} \quad \text{or} \quad \langle G_{\Pi_\infty} \rangle = \frac{\rho_0 \langle G_{FF} \rangle}{2\pi\mu^2c}$$

The acoustical power Π radiated by the reverberant plate vibrations is equal to

$$\bar{\Pi}_{\text{rev}} = \rho_0 c \langle |\bar{v}|^2 \rangle S \bar{\sigma}_r \quad (12.102)$$

In this expression S is the area of the plate, $\bar{\sigma}_r$ the radiation efficiency given in Eqs. (12.98) through (12.100). The product $(\rho_0 c)$ is the characteristic wave impedance for the fluid surrounding the plate. For air $\rho_0 c$ is equal to 415 kg/(m²s) at room temperature and normal pressure. The corresponding number for water is 1.45×10^6 kg/(m²s). Consequently, the spectral density of the total radiated acoustic

power is, including both direct and reverberant fields,

$$\begin{aligned}\bar{\Pi}_{\text{tot}} &= \bar{\Pi}_{\infty} + \bar{\Pi}_{\text{rev}} = |\bar{F}|^2 \left[\frac{\rho_0 c \bar{\sigma}_r}{8\omega\eta\mu\sqrt{D\mu}} + \frac{\rho_0}{2\pi\mu^2 c} \right] \\ &= |\bar{F}|^2 \frac{\rho_0}{2\pi\mu^2 c} \left[1 + \frac{\pi\bar{\sigma}_r \cdot f_c}{4\eta f} \right]\end{aligned}\quad (12.103)$$

The first term inside the bracket dominates as long as $\pi\bar{\sigma}_r f_c/(4\eta f) < 1$. If this is the case, the radiated acoustical power from the point-excited plate is only reduced insignificantly if the losses of the plate are increased. If a damping layer is added to the plate, the extra damping will have no effect for this particular case. The only effect on the radiation is that the mass of the structure is increased. The radiated power is inversely proportional to the mass squared of the plate. By using the approximate expression for the radiation ratio (12.101) the first term of Eq. (12.103) dominates, or rather $\pi\bar{\sigma}_r f_c/(4\eta f) < 1$, as long as $f < f_{\text{rev}}$ where

$$f_{\text{rev}} = \frac{1}{f_c} \left[\frac{c(L_x + L_y)}{4\pi\eta L_x L_y} \right]^2 \quad (12.104)$$

For $f > f_{\text{rev}}$ the sound radiation is not decreased by increasing the damping for a point-excited plate. For example, a 1 mm Al plate has a critical frequency of 12 kHz. The loss factor could be of the order 4% if the plate is connected to other structures. For $L_x = L_y = 1$ m, the parameter f_{rev} is approximately 150 Hz. Thus in a frequency range 150 to say 4000 Hz any additional damping will have no appreciable effect on acoustic power radiated by the point-excited plate.

For a lightly damped plate, the second term of (12.103) dominates and the acoustical power Π radiated by a plate is given by Eq. (12.102). In order to limit the radiated power from a plate there are some obvious possibilities namely to reduce the plate velocity and/or the radiation efficiency. The plate velocity can be changed by changing the plate dimensions. However, this will also affect the radiation efficiency. Therefore, the combined effect must be considered.

As an example, assume that a point force F with the power spectral density G_{FF} is exciting a uniform and rectangular plate. The power input to the structure is

$$G_{\Pi} = G_{FF} \text{Re}Y$$

where Y is the point mobility of the plate at the excitation point. Within a frequency band Δf which includes a large number of natural frequencies of the plate, the frequency average of the real part of the point mobility is equal to the point mobility of an infinite plate as discussed in Sect. 8.5. Thus, for white noise excitation within the frequency band Δf the average of the power spectral density can be written as

$$\langle G_{\Pi} \rangle_{\Delta f} = \langle G_{FF} \rangle_{\Delta f} \text{Re}Y_{\infty} \quad (12.105)$$

The power spectral density of the plate velocity can from (8.54) be written as

$$G_{vv} = G_{\Pi}/(\mu\omega\eta S) \tag{12.106}$$

where μ is the mass per unit area of the plate and η its loss factor. The expressions (12.105) and (12.106) give

$$\langle G_{\Pi} \rangle_{\Delta f} = \langle G_{FF} \rangle_{\Delta f} \frac{\rho_0 c}{\mu\omega\eta} \text{Re} Y_{\infty} \tag{12.107}$$

The power spectral density of the radiated acoustical power can also be written as

$$\langle G_{\Pi} \rangle_{\Delta f} = \langle G_{vv} \rangle_{\Delta f} \rho_0 c S \bar{\sigma}_r \tag{12.108}$$

The frequency average of the power spectral density of the radiated power is from (12.107) and (12.68) equal to

$$\langle G_{\Pi} \rangle_{\Delta f} = \langle G_{FF} \rangle_{\Delta f} \frac{\rho_0 c \bar{\sigma}_r}{8\omega\eta\sqrt{D}\mu} \tag{12.109}$$

For white noise excitation G_{FF} is constant. The plate velocity is decreased if the bending stiffness is increased. However, the radiation efficiency is also increased as the plate stiffness is increased as shown in Fig. 12.10. The acoustical power radiated by a simply supported plate is shown in Fig. 12.11. The spectral density of the radiated power is calculated from Eq. (12.109). The radiation efficiency is obtained from Eqs. (12.98) through (12.100). The dimensions of the steel plate are $L_x = 1.4$ m and $L_y = 0.8$ m. The radiated power is calculated for three plate thicknesses namely 2, 4, and 6 mm. The power spectral density of the force is the same for the three cases.

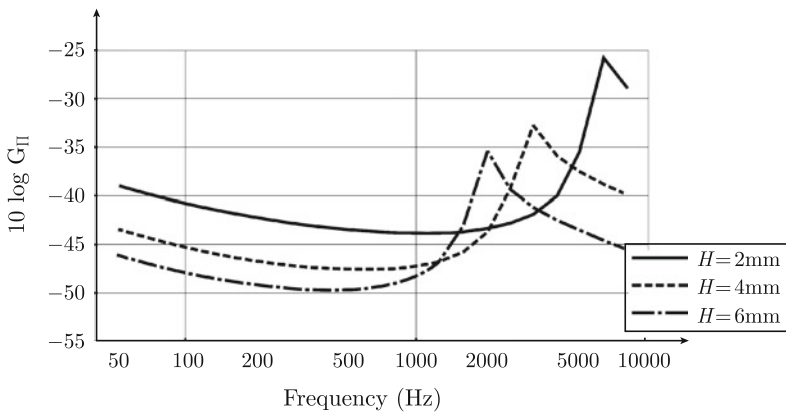


Fig. 12.11 Radiated power from steel plate thicknesses 2, 4 and 6 mm. $L_x = 1.4$ m and $L_y = 0.8$ m. White noise excitation

Well below the critical frequency, it is advantageous to increase the plate thickness in order to reduce the radiated acoustical power. Close to and at the critical frequency the plate is radiating readily. In this region the plate, which has a critical frequency closest to the frequency of the driving force, is radiating most efficiently. In the very high frequency range above the critical frequency, the radiation efficiency is approximately equal to unity. In this region, the radiated power is decreased if the bending stiffness of the plate is increased.

The sound radiation from structures having a fairly simple geometrical surface can be estimated by replacing the radiating surface by a number of simple sources inside the surface. The location and strength of the sources are determined so as to give an approximately correct surface velocity of the source. The sound pressure outside the structure is approximated by the fields of all the sources. The technique is summarized in Ref. [169]. The radiation from complicated structures must be determined by means of numerical methods. One such technique, the Boundary Element Method, is described in, for example, Refs. [170, 171].

12.11 Sound Radiation Ratios—Cylinders

The sound radiation from cylinders was discussed in Sect. 11.7. It was found that if the velocity distribution around the circumference of a cylinder is known then the velocity potential in the adjoining fluid is given by the expression (11.78). If it is assumed that the surface velocity of the cylinder is the same for every section of the cylinder the velocity potential is given by Eq. (11.79) as

$$\Phi(r, \varphi, t) = \exp(i\omega t) \cdot \sum_n A_n H_n^{(2)}(kr) \cdot \cos(n\varphi) \quad (12.110)$$

The pressure p_n induced by mode n is

$$p_n(r, \varphi, t) = -i\omega\rho_0 \exp(i\omega t) \cdot A_n H_n^{(2)}(kr) \cdot \cos(n\varphi) \quad (12.111)$$

The acoustic power radiated per unit length of the cylinder into the fluid is

$$\begin{aligned} (\bar{\Pi}_n)_l &= \int_0^{2\pi} \frac{|p_n|^2}{2(\rho_0 c)} r d\varphi = (\omega\rho_0)^2 \int_0^{2\pi} |A_n|^2 \left| H_n^{(2)}(kr) \right|^2 \frac{r \cdot \cos^2(n\varphi)}{2(\rho_0 c)} d\varphi \\ &= \frac{\pi(\omega\rho_0)^2 |A_n|^2 r \left| H_n^{(2)}(kr) \right|^2}{2(\rho_0 c)} \cdot \varepsilon_n \\ \varepsilon_n &= 2 \text{ for } n = 0; \quad \varepsilon_n = 1 \text{ for } n > 0 \end{aligned} \quad (12.112)$$

For $kr \gg 1$ the Hankel function tends to

$$H_n^{(2)}(kr) \rightarrow \sqrt{\frac{2}{\pi kr}} \cdot e^{-i(kr - n\pi/2 - \pi/4)}$$

This asymptotic value inserted in (12.112) gives

$$(\bar{\Pi}_n)_l = \frac{(\omega\rho_0)^2 |A_n|^2}{k(\rho_0 c)} \cdot \varepsilon_n \quad (12.113)$$

The velocity on the surface of the cylinder is obtained from Eq. (12.110) as

$$v(r_0, \varphi, t) = \exp(i\omega t) \left[\frac{\partial}{\partial r} \sum_n A_n H_n^{(2)}(kr) \cdot \cos(n\varphi) \right]_{r=r_0}$$

The velocity for mode n is

$$v_n(r_0, \varphi, t) = \exp(i\omega t) A_n \cos(n\varphi) k \left[H_n^{(2)}(z) \right]'_{z=kr_0}$$

The time and space average of the velocity squared is

$$\langle |\bar{v}_n|^2 \rangle = \frac{1}{2} \cdot \frac{1}{2\pi} \int_0^{2\pi} |v_n|^2 d\varphi = \frac{|A_n|^2 k^2}{4} \left| \left[H_n^{(2)}(z) \right]'_{z=kr_0} \right|^2 \cdot \varepsilon_n \quad (12.114)$$

Introducing the radiation ratio σ_n per unit length of the cylinder, the acoustic power radiated by mode n per unit length of the cylinder can be written as

$$(\bar{\Pi}_n)_l = \rho_0 c (2\pi r_0) \langle |\bar{v}_n|^2 \rangle \sigma_n \quad (12.115)$$

The Eqs. (12.113) through (12.115) give

$$\sigma_n = \frac{2}{\pi k r_0 \left\{ \left[H_n^{(2)}(z) \right]'_{z=kr_0} \right\}^2} \quad (12.116)$$

The radiation ratio σ_n is shown in Fig. 12.12 for $n = 0, 1, 2$. The corresponding vibrational modes are shown in Fig. 12.13. Again, as for a plate, it is found that the radiation ratio is increasing with frequency up to a maximum and thereafter leveling out to unity in the high frequency region.

For $kr_0 \ll 1$ the radiation ratios can be approximated as

$$\sigma_0 = \frac{\pi}{2} (kr_0); \quad \sigma_n = \frac{4\pi}{(n!)^2} \left(\frac{kr_0}{2} \right)^{2n+1} \quad \text{for } n > 0$$

The result is derived in Problem 12.5.

Fig. 12.12 Radiation ratios for the first three modes of a cylinder

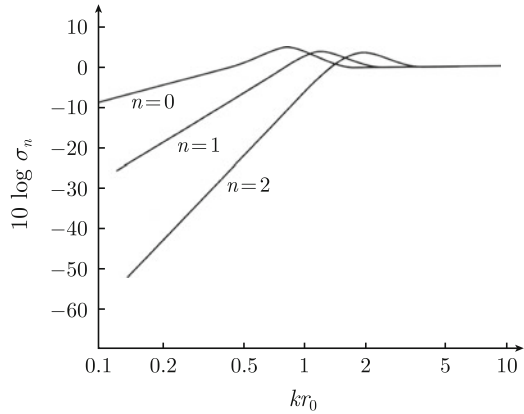
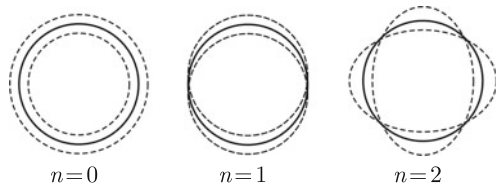


Fig. 12.13 First three vibrational modes for a cross section of a cylinder



12.12 Losses Due to Radiation

The acoustical power radiated from a panel will contribute to its losses. The power lost by radiation from the panel is

$$\bar{\Pi}_{\text{rad}} = 2\rho_0 c \langle |\bar{v}|^2 \rangle S \bar{\sigma}_r \tag{12.117}$$

It is assumed that both sides of the panel are radiating into the same type of fluid. The power lost due to radiation can also be written as

$$\bar{\Pi}_{\text{rad}} = \omega \eta_{\text{rad}} \bar{E} = \omega \eta_{\text{rad}} \langle |\bar{v}|^2 \rangle \mu S \tag{12.118}$$

where η_{rad} is the loss factor resulting from the radiation. The two expressions (12.117) and (12.118) give

$$\eta_{\text{rad}} = \frac{2\rho_0 c \bar{\sigma}_r}{\omega \mu} \tag{12.119}$$

In general, this quantity is very small except for very light structures with a high radiation ratio. In the low frequency region, the radiation ratio for a panel can be approximated by the expression (12.101). This expression inserted in (12.119) gives for $f \ll f_c$

$$\eta_{\text{rad}} = \frac{\rho_0 c^2 (L_x + L_y)}{\pi^3 L_x L_y \mu \sqrt{f_c^3} f} \tag{12.120}$$

For a 1 m×1 m Al plate, thickness 1 mm, the loss factor in the low frequency region is obtained from (12.119) as

$$\eta_{\text{rad}} \approx 2.5 \times 10^{-3} / \sqrt{f}$$

For this type of plate, the radiation losses are negligible as compared to losses at the boundaries as discussed in Sect. 5.12. However, for frequencies at and around the critical frequency of the plate or when $\bar{\sigma}_r$ is large, the losses due to radiation can be significant. This is considered in next chapter in connection with the derivation of the sound transmission loss of panels at frequencies close to or at the critical frequency.

The Statistical Energy Analysis method, SEA, is frequently used to predict the energy transfer between various components assembled within a complex structure, for example, a car. The use of SEA requires that the interior loss factors are known for each component. Nijman has presented measurements of loss factors for a cast iron oil sump and a cast iron cylinder block in Ref. [160]. For both structures, which are very stiff, the sound radiation ratio is of the order unity within the most important frequency range. Further, the interior loss factor for cast iron is very low, of the order 10^{-4} . It was therefore not clear if the measured loss factors were determined by radiation or interior losses. To resolve this problem, the loss factors were first measured with the components in air and afterward the same measurements were repeated with the structure submerged in helium. The ratio between $\rho_0 c$ for air and helium is of the order 2.4. The speed of sound in He is almost three times as high as in air. The critical frequency, Eq. (12.18), for a structure in He is almost ten times as high as for the same structure in air. Therefore, the radiation ratio is much smaller for a structure submerged in He than in air. The radiation losses in He are therefore much smaller than the corresponding losses in air. For the oil sump, the average loss factor measured in the frequency range 380–1200 Hz was 1.9×10^{-3} in air and 3.2×10^{-4} in He. For the cylinder block, the average loss factor in the frequency range 1050–2400 Hz was 1.6×10^{-3} in air and 1.2×10^{-3} in He. The results of the measurements indicated that the total losses of the structure when measured in air were mainly determined by radiation losses. However, the losses measured with the structure in helium were representative of the inner losses of the structure. After the components were mounted in a complete car, the loss factors of the components were found to be of the order 3×10^{-2} . The material or inner loss factor was estimated to be less than 2×10^{-3} . The loss factor due to radiation was given as 2×10^{-3} . Thus, as discussed in Sect. 5.12, the total loss factor of a component mounted to a built-up structure is mainly determined by transmission losses, i.e., by energy flow from the component to adjoining structures.

In Sect. 12.1 the wave number for flexural waves traveling on a fluid-loaded plate, one side, was given as

$$\kappa_x = \kappa \left[1 + \frac{\rho_0}{4\mu\sqrt{\kappa_x^2 - k^2}} \right]$$

For a plate with a fluid loading on both sides and for $k > \kappa$ the wave number is approximately given by

$$\begin{aligned}\kappa_x &= \kappa \left[1 - \frac{i\rho_0}{2\mu\sqrt{k^2 - \kappa_x^2}} \right] = \kappa \left[1 - \frac{i\rho_0 c}{2\mu\omega\sqrt{1 - f_c/f}} \right] \\ &= \kappa \left[1 - \frac{i\rho_0 c \bar{\sigma}_r}{2\mu\omega} \right] \quad \text{for } f > f_c\end{aligned}$$

The wave number can according to Eq. (5.28) also be written as $\kappa = \kappa_0(1 - i\eta/4)$, where η is the loss factor. Comparing the two expressions, the loss factor due to radiation is written as

$$\eta_r = \frac{2\rho_0 c \bar{\sigma}_r}{\mu\omega} \quad (12.121)$$

This loss factor is in agreement with η_{rad} as given in Eq. (12.119).

12.13 Radiation from Fluid-Loaded Finite Plates

The generation of underwater noise can be of main concern for certain types of vessels, for example, research and navy ships. Two of the major problems to be considered for these cases are the effect of the fluid loading on plates and the reflections in the water surface. Andresen has in Ref. [161] compared various prediction models to laboratory and field measurements of sound radiated from water-loaded plates. The predictions are based on a number of available theoretical models like Refs. [158, 159, 162, 172]. In some of the experiments reported by Andresen in Ref. [161], rectangular plates were mounted to a stiff wooden box. The natural frequencies of the plates mounted to the box were first measured in air. The measurements were repeated with the box semisubmerged in water leaving one side of the plate exposed to water and the other to air as shown in Fig. 12.14.

A modal analysis of the vibration pattern of the plate in air indicated that the boundary conditions of the plate could be described as clamped. The natural frequencies of the clamped plate were predicted as discussed in Sect. 8.6. For the same plate with a water load on one side, the total mass μ_{tot} of plate plus water load is calculated based on Eq. (12.12). The wave number κ_x for the water-loaded plate is written as

$$\kappa_x = \left(\frac{\mu_{\text{tot}}\omega^2}{D} \right)^{1/4} = \left(\frac{\mu_{\text{tot}}}{\mu} \right)^{1/4} \left(\frac{\mu\omega^2}{D} \right)^{1/4} = \kappa \cdot \left(\frac{\mu_{\text{tot}}}{\mu} \right)^{1/4} \quad (12.122)$$

where μ is the mass per unit area of the plate itself and κ the wave number in vacuo. Consequently,

$$\mu_{\text{tot}} = \mu \cdot \left(\frac{\kappa_x}{\kappa} \right)^4 \quad (12.123)$$

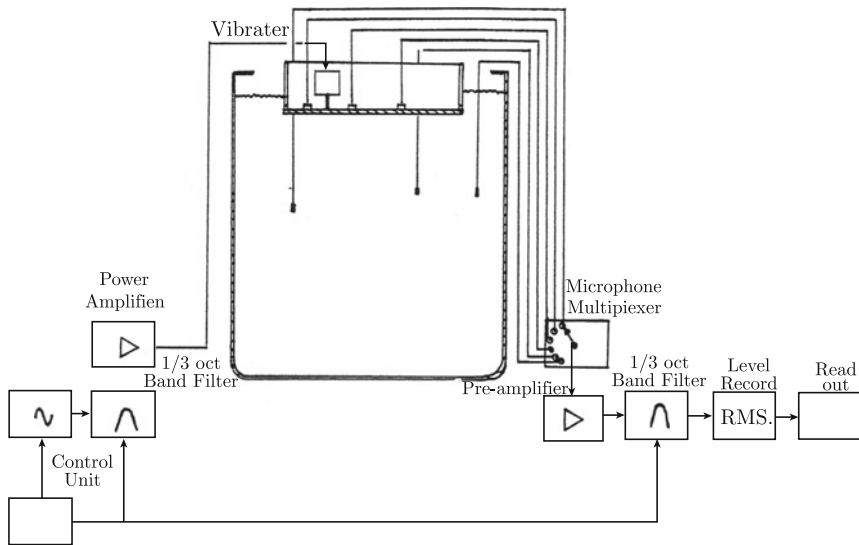


Fig. 12.14 Schematic drawing of plate mounted in box-like structure and semisubmerged in a water tank

The wave number κ_x for the water-loaded (one side) plate is obtained from

$$\begin{aligned} \kappa_x^4 &= \kappa^4 \left[1 + \frac{\rho_0}{\mu \sqrt{\kappa_x^2 - k^2}} \right] \quad \text{for } \kappa_x > \kappa_{11}; \\ \kappa_x^4 &= \kappa^4 \left[1 + \frac{\rho_0}{\mu \sqrt{\kappa_{11}^2 - k^2}} \right] \quad \text{for } \kappa_x \leq \kappa_{11} \end{aligned} \quad (12.124)$$

The wave number κ_{11} corresponds to the first natural frequency of the water-loaded plate. The natural frequencies of the plate are predicted from Eq. (8.87) by setting the mass per unit area in the denominator equal to μ_{tot} as given by Eqs. (12.123) and (12.124). Some comparisons between predicted and measured natural frequencies for an Al plate with and without a water load are shown in Table 12.1.

The results show that a water load on a plate decreases the natural frequencies quite significantly. Further, the results also show that the measured natural frequencies can exceed the predicted values. Whenever the Rayleigh–Ritz method is used for predicting natural frequencies, the predicted value is expected to be larger than the measured. However, as shown in Table 12.1 this is not always the case for the water-loaded plate. Obviously, measurements are always sensitive to errors, etc. In addition, the total mass per unit area of the water-loaded plate was calculated as if the plate were infinite. Thus, the total mass is slightly overestimated resulting in a too low predicted natural frequency. Further, the edges of the plate are not perfectly clamped.

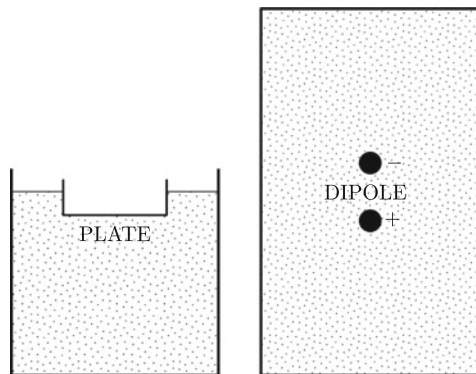
Table 12.1 Eigenfrequencies for a clamped 4 mm thick and 1.34 m by 0.74 m Al plate

Mode (m)	n	Water load on one side		No water load	
		f_{mn} (Hz) predicted	f_{mn} (Hz) measured	f_{mn} (Hz) predicted	f_{mn} (Hz) measured
1	1	11.2	14.2	45.3	45.0
2	1	19.5	16.6	62.2	61.9
3	1	26.9	28.6	91.8	90.1
1	2	35.7	35.3	116.2	107.1
2	2	41.9	41.8	132.2	126.6
4	1	42.8	43.9	133.4	130.5

The loss factors for plates with and without a water load were also registered by Andresen in Ref. [161]. It was found that the measured loss factors for a plate mounted in a box, Fig. 12.14, were considerably higher with a water load than without. However, measurements on ships reported by Nilsson [163] and Plunt [164] indicate that loss factors of hull plates are more or less the same independent of a water load.

Measurements of noise radiated from plates were carried out in two different ways as reported in [161]. First, the usual box with a plate was semisubmerged in a large water-filled cylindrical tank. The plate was excited by a point force or rather a shaker as shown in Fig. 12.14. The average sound pressure in the water was measured by a number of hydrophones. The reverberation time in the tank was recorded and the acoustical power radiated into the water was determined. The volume of the tank limited the measurements to frequencies above 500 Hz. Due to the reflections in the water surface the source must be considered as a dipole, compare Fig. 12.15. Twice the depth of the plate determines the distance between the two sources of the dipole. The radiation from the plate is determined as if the dipole is located in a tank with a volume twice the real tank as indicated in Fig. 12.15. The main power radiated

Fig. 12.15 Box plus plate in water tank and equivalent acoustic system



by the plate is due to the displacement at and very close to the excitation point. It is therefore concluded in Ref. [161] that the finite plate radiates approximately the same acoustic power as an infinite plate. The power radiated by an infinite plate with water on one side is according to (12.69)

$$\bar{\Pi} = \frac{k^2 |\bar{F}|^2}{6\pi c \rho_0} \quad (12.125)$$

The ratio between the power radiated by a dipole and a monopole is according to Eqs. (11.64) and (11.68) equal to

$$\frac{\bar{\Pi}_d}{\bar{\Pi}_m} = \frac{\omega^2 l^2}{3c^2} \quad (12.126)$$

The distance between the two sources of the dipole is l . The power of the two sources, though of different phase, is the same as the monopole. The power radiated by the dipole is obtained from (12.120) to (12.121) as

$$\bar{\Pi}_d = \frac{\omega^2 l^2}{3c^2} \bar{\Pi}_m = \frac{2h^2 k^4 |\bar{F}|^2}{9\pi c \rho_0} \quad (12.127)$$

where $h = l/2$ is the distance between the water surface and the plate element. The input power to the plate is according to Eq. (12.70) given by

$$\bar{\Pi}_{\text{in}} = |\bar{F}|^2 \text{Re} Y_\infty = |\bar{F}|^2 \frac{1}{10} \left(\frac{\omega}{D^3 \rho_0^2} \right)^{1/5} \quad (12.128)$$

In Ref. [161] it is assumed that most of the input power due to white noise excitation is dissipated as losses in the plate and that the velocity field of the plate is reverberant. The time and space average of the velocity is obtained from (8.72), i.e.,

$$\bar{\Pi}_{\text{in}} = \omega \eta \mu_{\text{tot}} \langle |\bar{v}|^2 \rangle S \quad (12.129)$$

Here η is the total loss factor of the submerged plate and μ_{tot} the total mass of the fluid-loaded plate. The area of the plate is denoted S . The Eqs. (12.128) and (12.129) give

$$\langle |\bar{v}|^2 \rangle = \frac{|\bar{F}|^2}{10\omega\eta\mu_{\text{tot}}S} \left(\frac{\omega}{D^3 \rho_0^2} \right)^{1/5} \quad (12.130)$$

From Eq. (12.127) it is found that

$$|\bar{F}|^2 = \frac{9\pi\rho_0c}{2h^2k^4} \bar{\Pi}_{\text{rad}}$$

This expression in combination with (12.130) and the definition $\bar{\Pi}_{\text{rad}} = \langle |\bar{v}|^2 \rangle S \rho_0 c \sigma_r$ give

$$\bar{\sigma}_r = \left(\frac{D^3 \rho_0^2}{\omega} \right)^{1/5} \frac{20h^2 k^4 \omega \eta \mu_{\text{tot}}}{9\pi(\rho_0 c)^2} \quad (12.131)$$

The power radiated by the plate into the water was experimentally determined in two different ways. First, with the plate and box semisubmerged in a water tank by measuring the average sound pressure in the water and the reverberation time in the tank. The radiated power is obtained from (11.161) as

$$\bar{\Pi}_{\text{rad}} = \frac{|\bar{p}|^2 A}{4\rho_0 c}; \quad A = \frac{0.16 \cdot 2V}{T} \quad (12.132)$$

The equivalent absorption area in the tank is A and the reverberation time T . Note that the actual volume V of the water is multiplied by a factor 2 to account for the reflections at the water surface, compare Fig.12.15. The velocity of the panel was measured by means of accelerometers. When intensity measurements are used, the radiated power is given by $\bar{\Pi}_{\text{rad}} = L_x L_y \langle I \rangle$. The velocity of the plate is measured as before. The radiation ratio is obtained from the measurements as

$$\bar{\sigma}_r = \frac{\bar{\Pi}_{\text{rad}}}{\rho_0 c L_x L_y \langle |\bar{v}|^2 \rangle}$$

The radiation ratio given in Eq. (12.131) is averaged over frequency. The result is valid for a point-excited plate exposed to a heavy fluid loading. The results derived by Leppington and summarized in Eqs. (12.98)–(12.100) are also averaged over frequency. For a point-excited plate the modal contributions can vary significantly resulting in that the radiation ratio varies considerably with respect to the averaged result given by Eqs. (12.98)–(12.100). An alternative way to determine the radiation in a frequency band is proposed by Andresen and given as

$$\bar{\sigma}_r = \frac{\sum_{m,n} \sigma_{mn} \langle |\bar{v}_{mn}|^2 \rangle}{\sum_{m,n} \langle |\bar{v}_{mn}|^2 \rangle} \quad (12.133)$$

where v_{mn} is the modal velocity of the plate. The summation is made over all m and n within each frequency band. Assuming equipartition of energy Eq. (12.133) is much simplified since $\langle |\bar{v}_{mn}|^2 \rangle$ is constant and independent on mode number. For a large number of modes in each band the radiation ratios tend to the results given by Leppington. The modal radiation ratios σ_{mn} derived by Wallace are given in Eqs. (12.89)–(12.91). These results are only valid in the low frequency region or as long as $\gamma^2 \ll 1$. Davies has in Ref. [172] presented modal radiation ratios which are valid for higher frequencies. Davies discusses sound radiation from water-loaded plates in Ref. [173]. The models by Davies and Wallace agree well in the

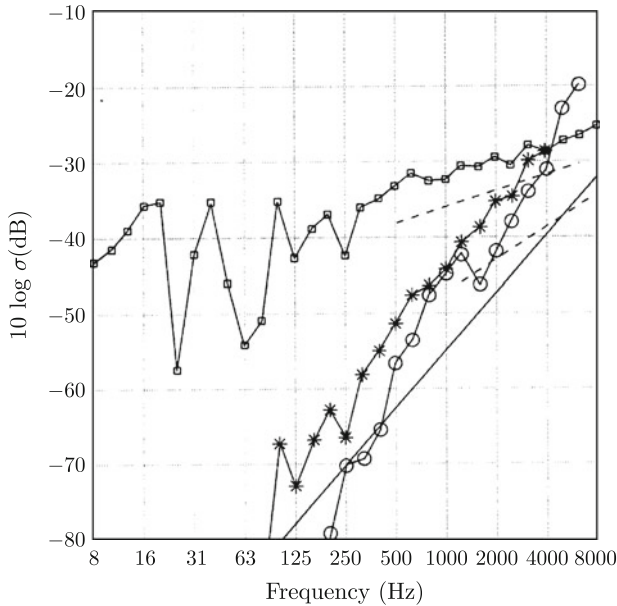
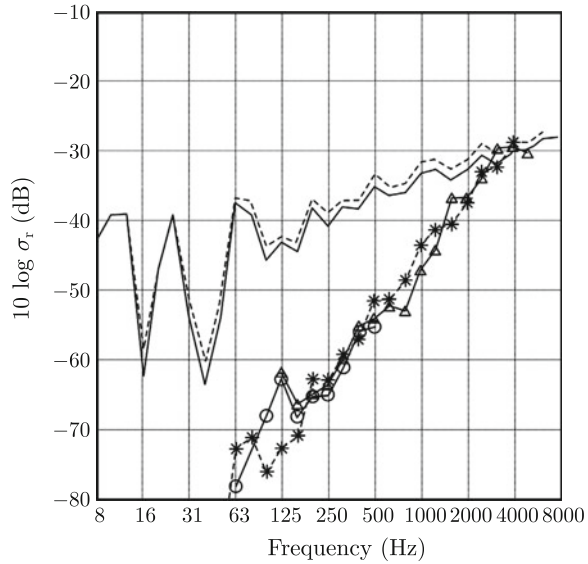


Fig. 12.16 Predicted and measured radiation ratios from a 4 mm thick Al plate with dimensions 0.76 m by 1.36 m. Radiated acoustic power measured in tank. \circ - \circ measurement; —Eq. (12.133); -* — Eq. (12.133) corrected for surface reflections; *bottom straight line* Eq. (12.131). From Ref. [161]

low frequency region. A comparison from Ref. [161] between a predicted and measured radiation ratio is shown in Fig. 12.16. The upper curve is predicted according to Eq. (12.133) using the modal radiation ratios proposed by Davies. The result is thereafter corrected according to Eq. (12.126) to account for reflection effects in the water surface. The solid straight line in Fig. 12.16 is derived from Eq. (12.131). The approximate formula (12.131) gives rather satisfactory results.

Additional measurements are reported in Ref. [161]. Experiments on the plate-box structure were also carried out in a deep, secluded bay. The sound intensity radiated by point-excited plates was measured by means of two different intensity hydrophone probes. Again, the surface effects had to be considered. Once more, the plate was approximated as an acoustic dipole. In this case, this approximation is not as readily explained as in the previous case. However, the agreement between predicted and measured results is fairly convincing. One example is shown in Fig. 12.17. The radiation ratio is for a 4 mm thick aluminum plate, length 1.364 m and width 0.764 m and with water on one side. The depth of the plate is 0.05 m. The plate is mounted to the box shown in Fig. 12.14. The predicted results are derived from Eq. (12.133) using Davies modal radiation ratios shown by the two top curves. The predicted result is thereafter corrected for surface effects and compared to the measurements with two different intensity probes. The agreement between measured and predicted radiation ratios is good. The predicted and corrected results vary smoothly with frequency

Fig. 12.17 Predicted and measured radiation ratios from a 4 mm thick Al plate with dimensions 0.76 m by 1.36 m. Radiated acoustic power measured by two different intensity probes with and without surface correction. — * — predicted from Eq. (12.97) and corrected for surface reflections. The two upper predicted *upper curves* are not corrected for surface effects. From Ref. [161]



indicating that the averaged radiation ratios given in Eq. (12.98) could have been used.

Junger and Feit [165] have compared various radiation mechanisms for water-loaded plates. For a point-excited plate with a fluid loading on one side the radiation from the bending near field is dominating over the radiation from the resonant modes if the loss factor η of the plate satisfies the inequality

$$\eta > \frac{8\rho_0\sqrt{1+\beta^{-2}}}{k\kappa^2\mu L_x L_y} \left[1 + \beta \left(\frac{f_c}{f} - 1 \right)^{-1/2} \right]^{-3/2} ; \quad \beta = \frac{\rho_0 c}{\mu \omega} \quad (12.134)$$

The critical frequency f_c is defined in Eq. (12.18). The result implies that adding damping does not reduce the sound radiation from a point-excited plate if the loss factor already exceeds the value given by Eq. (12.134). Compare the discussion in Sect. 12.10 and Eq. (12.104).

Hull plates on a ship are not always excited by some point forces. In fact, any engine or mechanical device should never be mounted directly to a hull plate to avoid excessive radiation into the water or in fact to the accommodation spaces. The hull plates are typically excited by bending moments along its edges as discussed in Chaps. 15 and 16. The radiated noise from a hull plate is caused by modal radiation and not a small area excited by a point force. Andresen [161] makes certain assumptions about the character of the radiation. It is assumed that the vibration fields of hull plates are basically uncorrelated for frequencies above the first natural frequency of the plate. For typical ship constructions the first natural frequencies of hull plates are between 80 and 160 Hz. The plates radiate as if they were mounted in

an infinite baffle. The velocity of a plate element is much higher than the velocity of the frames limiting the plate. The radiation ratio for such a hull plate can in the low frequency region be calculated from (12.133) using the modal radiation ratios given in Eqs. (12.89)–(12.91) by assuming $\gamma = k/\kappa_x$. The wave number κ_x for the water-loaded plate is given by Eq. (12.12). In the high frequency region, the radiation ratios are given by Eq. (12.98) where the radiation ratio for $f < f_c$ is given as function of the parameter q . For a fluid-loaded plate, water load on one side, the parameter q is written as

$$q = \frac{\kappa_x}{k} \quad (12.135)$$

where κ_x is the wave number for flexural waves propagating along a fluid-loaded plate. The wave number κ_x is the solution to Eq. (12.12).

Again, reflections in the water surface must be considered. The location of the plate with respect to the water surface must be observed. However, the reflections in the water surface depend on the sea waves. The absolute value of the reflection coefficient is decreasing with increasing wave height. The reflection coefficient also depends on the angle of incidence and frequency. The absolute value of the coefficient decreases with increasing frequencies. Compare Sect. 11.8. Andresen estimated reflection coefficients at the water surface as suggested in Refs. [166, 167]. The reflection coefficient R is written on the form $R = -\exp(Cf \cos \varphi)^2$ where C is a parameter depending on the height of the surface waves, f is the frequency, and φ the angle between the normal to the water surface and the incident wave as defined in Fig. 11.14. Reflection coefficients of the order -0.5 for sea waves with a height of 0.4 m could be expected for an angle of incidence of 45° and at 500 Hz. Measurements and predictions of sound radiated from hull plates show good agreement as reported in Ref. [161].

In Sect. 11.10 the sound radiation from semisubmerged vibrating cylinders were discussed. In Fig. 11.18, it was shown that the sound pressure level in the water within a large angular segment was almost independent of reflections in the water surface. Figure 11.19 illustrates yet another case of the effect of reflections in a water surface.

In Chap. 4, a so-called “thin” plate was defined. It was argued that a plate could be considered as thin as long as the wave number for flexural waves propagating along the plate did not differ by more than 10% of the correct value. In a similar way, it could be argued that the fluid loading of a plate could be neglected if the fluid loading is increasing the wave number by less than 10%. The wave number for a plate with a fluid loading on one side is given by Eq. (12.13). The expression is valid in the low frequency region or for $\kappa \gg k$. For a plate with a fluid loading on both sides the wave number is approximately given by

$$\kappa_x \approx \kappa \left[1 + \frac{\rho_0}{2\mu\kappa_x} \right] \approx \kappa \left[1 + \frac{\rho_0}{2\mu\kappa} \right] \quad (12.136)$$

For the error neglecting the last term inside the bracket to be less than 10%, if the fluid is air, it follows that the condition for neglecting the term is

$$\mu\kappa > 6 \quad (12.137)$$

For a steel or aluminum plate thicker than 1 mm the air loading can be neglected in the entire acoustic frequency range. Whenever the fluid loading can be neglected the response of a structure to external forces can be calculated as if the structure were vibrating in vacuum or quite simply uncoupled to the surrounding fluid. The sound radiated from the structure can thereafter be calculated as function of velocity level of the element itself.

If the condition (12.137) is not satisfied, the coupled problem should be solved. This means that the acoustic field depends on the vibrational field of the structure, which in turn depends on the reaction of the acoustic field. In general, the coupled problem is much more complicated than the uncoupled problem. However, certain approximations can often be made to simplify the handling of coupled problems. In the case of ships or any structures exposed to a water load it can be assumed that the total mass of a structure submerged in water is equal to its actual mass plus the additional mass due to the water load. The total mass μ_{tot} is calculated from Eqs. (12.123) to (12.124). Consequently, the total mass of a water-loaded plate is frequency dependent. This simplified procedure to include the fluid loading has been used successfully for the prediction of the propagation of structure-borne sound in ship structures as discussed in Refs. [163, 168]. In the low frequency region, the technique has been verified by FEM calculations.

Problems

12.1 Find the solution κ_x to Eq. (12.12) as $\kappa_x \rightarrow k$.

12.2 Determine the sound pressure in a fluid induced by a plane flexural wave traveling along an infinite flat plate. The velocity of the plate perpendicular to the surface is $v(x_0, y_0, t) = v_0 \exp[i(\omega t - \kappa x_0)]$. The plate is oriented in the $x_0 - y_0$ -plane. Use Eq. (12.33) and the Green's function (12.45).

12.3 The area of rectangular plate is S_0 . The ratio between the lengths of the sides is ξ . Determine the sound radiation ratio as function of ξ .

12.4 Determine the mass load on a rectangular plate, sides L_x and L_y , at the first natural frequency of the plate. Fluid loading on one side only.

12.5 Determine the sound radiation ratio σ_m for a cylindrical shell as $kr_0 \rightarrow 0$, r_0 is the radius of the cylinder and k the wave number in the fluid.

12.6 The power radiated by the edge mode of a plate is proportional to the square of the uncancelled area of the edge mode. Calculate the square of the uncancelled area for a simply supported beam mode and in the same way the uncancelled area for a clamped beam mode. Consider only odd modes.

12.7 Show that for a point force exciting a fluid-loaded plate that at the excitation point the apparent mass of the plate is much higher than the corresponding added weight due to fluid loading for the reverberant field.

Chapter 13

Sound Transmission Loss of Panels

In general, the noise level inside a building or structure is determined by the transmission of air-borne sound from external and internal acoustic sources and by structure-borne sound induced by some mechanical sources. For example in a train, the interior noise is due to air-borne noise created by the contact between the rolling wheel and the rail. The air-borne noise is transmitted to the interior through floor, wall, and window constructions. The structure-borne sound is mainly induced by the contact forces between wheel and rail. These forces excite structural vibrations. The structure-borne sound is transmitted through wheel and bogie to the car body construction, which in turn radiates noise into the interior. For high-speed trains, the flow-induced noise is of great importance. For the design of any noise control measures, the sound transmission properties of structures must be well understood whenever air-borne sound is a dominating factor.

In the field of building acoustics, a large number of important papers on sound transmission through structures were published after the Second World War during the building boom in Europe. Cremer, Ref. [174], published the most important paper of all. Many of the prediction models derived were adjusted to the type of materials and constructions then being used for buildings. Many of these constructions were heavy and large. Today lightweight and stiff materials are used in many types of vehicles and even in buildings. There is nowadays a tendency to test only fairly small samples of these materials. This is often due to the cost of producing the material. The testing of small samples requires an understanding of the importance of boundary conditions and geometrical parameters. For a large heavy concrete or brick wall, these effects can be insignificant. In the vehicle industry and in particular in the aircraft industry, the acoustic properties of lightweight structures are vital. An improvement of the sound transmission loss of an aircraft structure by just a few dB could be of great importance. Consequently, it must be understood when comparing different measurement results if an observed improvement is due to an improvement of the structure itself or to some changes of the mounting conditions.

In this chapter, the sound transmission loss of single leaf structures is discussed. The effects of boundary conditions and panel and room dimensions are considered. The somewhat lengthy discussion on these effects is summarized in Sect. 13.9.

Measured and predicted results are compared in Sect. 13.8. The response of structures excited by an acoustic field and the resulting sound radiation ratios are also considered. The sound transmission through ribbed panels and double wall structures is reported in Sect. 13.10. Flanking transmission is discussed in Sect. 13.11. The sound transmission through composite panels and curved panels is discussed in Chap. 14. Flow-induced noise is reported in Chap. 15.

13.1 Sound Transmission Through Infinite Flat Panels

A sound wave, which is incident on a plate, sets the plate in motion. The vibrating plate induces pressure waves in the fluid on both sides of the plate. Part of the incident intensity is reflected from the plate and part is transmitted from the opposite side of the plate. The problem is illustrated in Fig. 13.1.

Figure 13.1 shows an infinite plate oriented in the x - y -plane. The fluid is the same on both sides of the plate. The mass per unit area of the plate is μ and its bending stiffness D . The lateral displacement w of the plate must satisfy Eq. (8.20) or

$$\nabla^2(\nabla^2 w) + \frac{\mu}{D} \frac{\partial^2 w}{\partial t^2} = \frac{p(x, y, t)}{D} \quad (13.1)$$

where p is the pressure driving or exciting the plate. The pressure or the force per unit area of the plate and the displacement are defined positive along the positive z -axis.

Assume that a plane wave with the amplitude A is incident on the plate. The angle of incidence is φ as shown in Fig. 13.1. The velocity potential for this incident wave is $\Phi_i = A \cdot \exp[i(\omega t - kx \sin \varphi - kz \cos \varphi)]$ where k is the wavenumber in the fluid and A the amplitude of the incident wave. The reflected wave has the amplitude $R \cdot A$. The reflection angle must be equal to the incident angle for the boundary conditions to be satisfied for any x . The reflected wave is given by the velocity potential $\Phi_r = R \cdot A \cdot \exp[i(\omega t - kx \sin \varphi + kz \cos \varphi)]$. The transmitted

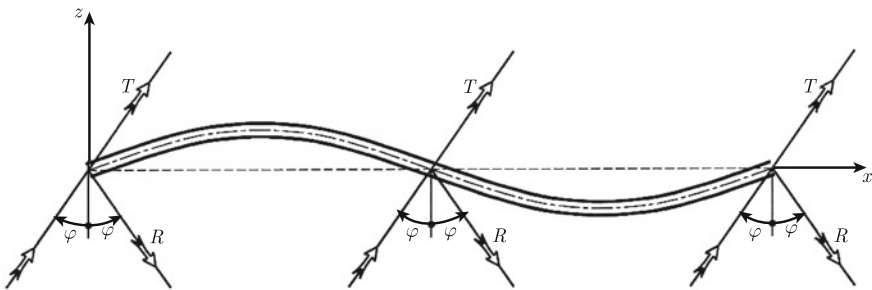


Fig. 13.1 Incident, reflected and transmitted waves and resulting motion of plate

wave, amplitude $T \cdot A$, must propagate in the same direction as the incident wave to satisfy the boundary conditions. Thus $\Phi_t = T \cdot A \cdot \exp[i(\omega t - kx \sin \varphi - kz \cos \varphi)]$. No energy is reflected back to the plate from any outer boundaries. The velocity potentials below and above the plate are

$$\begin{aligned}\Phi_- &= A \cdot \{\exp[i(\omega t - kx \sin \varphi - kz \cos \varphi)] \\ &\quad + R \cdot \exp[i(\omega t - kx \sin \varphi + kz \cos \varphi)]\}; \quad z < 0 \\ \Phi_+ &= A \cdot T \exp[i(\omega t - kx \sin \varphi - kz \cos \varphi)]; \quad z > 0\end{aligned}\quad (13.2)$$

The pressure acting on the plate in the direction of the positive z -axis is

$$p = p_- - p_+ = -\rho_0 \left(\frac{\partial \Phi_-}{\partial t} - \frac{\partial \Phi_+}{\partial t} \right)_{z=0} \quad (13.3)$$

The velocity normal to the plate induced by the pressure is written $v_z = v_0 \exp[i(\omega t - \kappa_x x)]$. For any boundary condition on the surface of the plate to be satisfied, the parameter κ_x must be equal to $k \sin \varphi$. The plate velocity is consequently

$$v_z = v_0 \exp[i(\omega t - kx \sin \varphi)] \quad (13.4)$$

Equation (13.1) is derivated with respect to time and after using Eq. (13.3) the result is

$$\nabla^2(\nabla^2 v_z) + \frac{\mu}{D} \frac{\partial^2 v_z}{\partial t^2} = -\frac{\rho_0}{D} \left(\frac{\partial^2 \Phi_-}{\partial t^2} - \frac{\partial^2 \Phi_+}{\partial t^2} \right)_{z=0} \quad (13.5)$$

The particle velocity in the fluid and normal to the plate must be equal to the panel velocity v_z on either side of the panel. Thus,

$$\left(\frac{\partial \Phi_+}{\partial z} \right)_{z=0} = \left(\frac{\partial \Phi_-}{\partial z} \right)_{z=0} = v_z \quad (13.6)$$

There are two boundary conditions (13.6) and one wave equation (13.5) to be satisfied. The unknown parameters R , T and v_z can be determined from these equations. The boundary conditions (13.6) yield

$$R = 1 - T; \quad v_0 = -ik \cdot \cos \varphi \cdot T \cdot A \quad (13.7)$$

Equations (13.2) and (13.4) inserted in the wave equation (13.5) give

$$-ik \cos \varphi \cdot T \cdot [(k \sin \varphi)^4 - \kappa^4] = 2\rho_0 \omega^2 (1 - T)/D; \quad \kappa^4 = \mu \omega^2 / D \quad (13.8)$$

From these equations the ratio T between the amplitudes of the transmitted and incident waves is obtained as

$$T = \left[1 - \frac{ikD \cdot \cos \varphi}{2\rho_0\omega^2} \{ (k \cdot \sin \varphi)^4 - \kappa^4 \} \right]^{-1} \quad (13.9)$$

The plate has losses. These are included in the usual way by defining the bending stiffness D as $D = D_0(1 + i\eta)$ and the wave number for flexural waves as $\kappa^4 = \mu\omega^2/D$. The critical frequency f_c is defined in Eq. (12.18) as

$$f_c = \frac{c^2}{2\pi} \left(\frac{\mu}{D_0} \right)^{1/2}$$

Following this definition of the critical frequency, other useful relationships are

$$\kappa_0 = \frac{2\pi}{c} \sqrt{f \cdot f_c}; \quad \frac{k}{\kappa_0} = \sqrt{\frac{f}{f_c}} \quad (13.10)$$

The definitions of D , D_0 and f_c inserted in (13.9) give

$$T = \left\{ 1 + \frac{\mu\omega}{2\rho_0c} \cdot \cos \varphi \left(\frac{f}{f_c} \right)^2 \cdot (\sin \varphi)^4 \cdot \eta - \frac{i\mu\omega}{2\rho_0c} \cdot \cos \varphi \cdot \left[\left(\frac{f}{f_c} \right)^2 \cdot (\sin \varphi)^4 - 1 \right] \right\}^{-1} \quad (13.11)$$

The sound transmission coefficient $\tau(\varphi)$ is defined as the ratio between the intensity I_t of the transmitted wave and the intensity I_i of the incident wave at the angle φ or

$$\tau(\varphi) = \frac{I_t(\varphi)}{I_i(\varphi)} = |T(\varphi)|^2 \quad (13.12)$$

The last part of the equation, $\tau(\varphi) = |T(\varphi)|^2$, is only valid as long as the fluid is the same on both sides of the infinite panel.

The velocity potential of the incident wave was defined as $\Phi_i = A \cdot \exp[i(\omega t - kx \sin \varphi - kz \cos \varphi)]$. The time average of the intensity of the plane wave traveling toward the plate is $\bar{I}_0 = (1/2)\text{Re}(p \cdot v^*) = \omega\rho_0k |A|^2/2$. The intensity \bar{I}_z of the wave incident on the plate is

$$\bar{I}_z = (1/2)\text{Re}(p \cdot v_z^*) = \omega\rho_0k |A|^2 \cdot \cos \varphi/2 = \bar{I}_0 \cdot \cos \varphi \quad (13.13)$$

where, as before, φ is the angle of incidence of the wave as shown in Fig. 13.1. For an ideally diffuse field, the intensity of the acoustic field is the same in every direction, i.e., \bar{I}_0 is constant. The average of the intensity incident on the plate, considering all angles of incidence or integrated over a half sphere, and divided by the total space angle 4π is

$$\langle \bar{I}_i \rangle = \frac{1}{4\pi} \int_0^{\pi/2} (\bar{I}_0 \cos \varphi) 2\pi \sin \varphi d\varphi = \bar{I}_0/4 \quad (13.14)$$

Compare Sect. 11.13. The time average of the transmitted intensity is

$$\langle \bar{I}_t \rangle = \frac{1}{4\pi} \int_0^{\pi/2} [\bar{I}_0 \cdot \tau(\varphi) \cdot \cos \varphi] \cdot 2\pi \sin \varphi d\varphi \quad (13.15)$$

The transmission coefficient τ_d obtained for a diffuse incident field is defined as

$$\tau_d = \frac{\langle \bar{I}_t \rangle}{\langle \bar{I}_i \rangle} = 2 \int_0^{\pi/2} \tau(\varphi) \sin \varphi \cdot \cos \varphi d\varphi \quad (13.16)$$

The transmission coefficient $\tau(\varphi)$ is obtained from Eqs. (13.11) and (13.12) as

$$\begin{aligned} \tau(\varphi) = & \left\{ \left[1 + \frac{\mu\omega}{2\rho_0c} \cdot \cos \varphi \left(\frac{f}{f_c} \right)^2 \cdot (\sin \varphi)^4 \cdot \eta \right]^2 \right. \\ & \left. + \left[\frac{\mu\omega}{2\rho_0c} \cdot \cos \varphi \cdot \left[\left(\frac{f}{f_c} \right)^2 \cdot (\sin \varphi)^4 - 1 \right] \right]^2 \right\}^{-1} \end{aligned} \quad (13.17)$$

The character of the transmission coefficient depends on the ratio between the frequency f of the incident wave and the critical frequency f_c . Two simple expressions defining the sound transmission through a simple homogeneous single leaf plate can be derived as discussed below in the frequency ranges $f \ll f_c$ and $f > f_c$.

Case 1. $f \ll f_c$

In the low frequency region $(f/f_c)^2 \ll 1$ and the transmission coefficient $\tau(\varphi)$, Eq. (13.17), is reduced to

$$\tau(\varphi) \approx \left\{ 1 + \left(\frac{\mu\omega}{2\rho_0c} \cdot \cos \varphi \right)^2 \right\}^{-1} \quad (13.18)$$

The transmission coefficient for a diffuse incident field is thus

$$\begin{aligned} \tau_d &= 2 \int_0^{\pi/2} \frac{\cos \varphi \cdot \sin \varphi d\varphi}{1 + [\mu\omega/(2\rho_0c)]^2 (\cos \varphi)^2} = \int_0^1 \frac{d\xi}{1 + [\mu\omega/(2\rho_0c)]^2 \xi} \\ &= \ln \left[1 + \left(\frac{\mu\omega}{2\rho_0c} \right)^2 \right] / \left(\frac{\mu\omega}{2\rho_0c} \right)^2 \end{aligned} \quad (13.19)$$

In the low frequency region $\tau_d \rightarrow 1$ as $\mu\omega/(\rho_0c) \rightarrow 0$. In fact $0 < \tau_d < 1$ in the entire frequency range. The sound reduction index or sound transmission loss R_d for a diffuse incident field is defined as

$$R_d = 10 \log(1/\tau_d) \quad (13.20)$$

For this particular case the sound reduction index is obtained from Eq. (13.19) as

$$R_d = 20 \log \left(\frac{\mu\omega}{2\rho_0c} \right) - 10 \log \left\{ \ln \left[1 + \left(\frac{\mu\omega}{2\rho_0c} \right)^2 \right] \right\} \quad (13.21)$$

The last part of this expression is a slowly varying function of frequency. For $\mu\omega/(2\rho_0c) = 10$, this part of the expression is 6.6. For $\mu\omega/(2\rho_0c) = 20$, the value is 7.8.

In the first case R_d is $R_d \approx 20 \log \mu + 20 \log f - 49$ dB for $f \ll f_c$ and μ expressed in kg/m^2 . However, results predicted from this formula are claimed to be somewhat too low as compared to measurements. It is therefore practice to express the sound reduction index as

$$R_d \approx 20 \log \mu + 20 \log f - 47 \text{ dB for } f \ll f_c \quad (13.22)$$

To justify this result it has been suggested, [175], that the expression (13.19) should be integrated over the angles of incidence from 0 to 78° rather than between 0 and 90° . There is no physical justification for changing the limit for the angle of incidence. However, measured sound transmission losses also depend on the geometries of facilities used for the tests. This is discussed in Sect. 13.8. Since $0 < \tau_d < 1$ it follows that $R_d > 0$ indicating that the expression (13.22) can not be extended to the low frequency range.

In the low frequency region, the mass per unit area of the panel is the only plate parameter determining the sound reduction index as given by (13.22). A doubling of mass or frequency adds 6 dB to the sound reduction index.

the sound transmission loss $R(0) = -10 \log[\tau(0)]$ for normal incidence on the plate is according to Eqs. (13.18) and (13.22) about 5 dB higher than for the transmission loss due to a diffuse incident field or $R(0) \approx R_d + 5$ dB.

Case 2. $f > f_c$

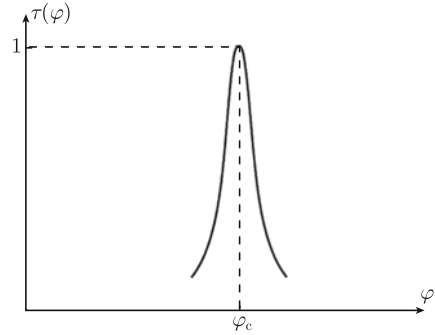
Returning to Eq. (13.17), it is found that in the high frequency region the transmission coefficient strongly depends on the angle of incidence. For a plate with small losses, the transmission coefficient has a very sharp maximum when the angle of incidence φ satisfies the expression $(f/f_c)^2 \sin^4 \varphi = 1$. This is illustrated in Fig. 13.2.

The sound transmission through the plate is almost completely determined by the acoustic transparency of the plate at this particular angle, which is often referred to as the coincidence angle φ_c where

$$\sin \varphi_c = \sqrt{f_c/f} \quad (13.23)$$

At this angle of incidence, the trace of the wavenumber in the fluid on the panel is equal to the wave number of flexural waves propagating along the plate. The magnitude of the transmission coefficient at this angle is almost equal to unity for a plate with small losses. For a hypothetic loss free plate, $\tau = 1$ for $\varphi = \varphi_c$. The

Fig. 13.2 Sound transmission coefficient as function of angle of incidence for $f > f_c$



sound transmission coefficient drops rapidly as φ is increased or decreased with respect to φ_c . The transmission coefficient τ_d for diffuse incidence can, as suggested by Cremer [174], be estimated by determining the sound transmission through the plate for angles close to the angle of coincidence. For this reason, the angle of incidence is defined through

$$\sin \varphi = (1 + \xi) \cdot \sin \varphi_c = (1 + \xi)\sqrt{f_c/f}; \quad |\xi| \ll 1 \quad (13.24)$$

Combining Eqs. (13.17) and (13.24) and neglecting second-order terms like $\eta\xi$ and ξ^2 , etc., Eq. (13.17) is reduced to

$$\tau(\varphi) = \left\{ \left[1 + \frac{\mu\omega}{2\rho_0c} \cdot \cos \varphi_c \cdot \eta \right]^2 + \left[\frac{\mu\omega}{2\rho_0c} \cdot \cos \varphi_c \cdot 4\xi \right]^2 \right\}^{-1} \quad (13.25)$$

For high frequencies $\mu\omega\eta \cos \varphi_c / (2\rho_0c) \gg 1$ for $\cos \varphi_c > 0$. Thus,

$$\tau(\varphi) \approx \frac{(2\rho_0c)^2}{(\mu\omega)^2(\eta^2 + 16\xi^2) \cos^2 \varphi_c} \quad (13.26)$$

The transmission coefficient for diffuse incidence is from Eq. (13.26) obtained as

$$\tau_d \approx \frac{2}{[\mu\omega/(2\rho_0c)]^2(\cos \varphi_c)^2} \int_0^{\pi/2} \frac{\cos \varphi \cdot \sin \varphi d\varphi}{\eta^2 + 16\xi^2} \quad (13.27)$$

The angle φ is a function of ξ as defined in Eq. (13.24). Thus $2 \sin \varphi \cos \varphi d\varphi = d(\sin \varphi)^2 = 2 \sin^2 \varphi_c \cdot d\xi$. The integration is carried out for $-\xi_0 \leq \xi \leq \xi_0$, i.e., for angles close to φ_c . The expression (13.27) is reduced to

$$\tau_d \approx \frac{2(\sin \varphi_c)^2}{[\mu\omega/(2\rho_0c)]^2(\cos \varphi_c)^2} \int_{-\xi_0}^{\xi_0} \frac{d\xi}{\eta^2 + 16\xi^2} = \left[\frac{2\rho_0c \cdot \sin \varphi_c}{\mu\omega \cdot \cos \varphi_c} \right]^2 \frac{\arctan(4\xi_0/\eta)}{\eta} \quad (13.28)$$

For small losses or for $\eta \ll 4\xi_0$, $\arctan(4\xi_0/\eta) \approx \pi/2$. According to Eq. (13.23) $\sin^2 \varphi_c = f_c/f$. Thus, $\cos^2 \varphi_c = 1 - f_c/f$. The transmission coefficient for diffuse incidence can for $f > f_c$ finally be written as

$$\tau_d \approx \left[\frac{2\rho_0 c}{\mu\omega} \right]^2 \cdot \frac{\pi}{2\eta} \cdot \frac{f_c/f}{1 - f_c/f} \tag{13.29}$$

The corresponding sound reduction index, Eq. (13.20), for a diffuse incident field is

$$R_d = 20 \log \mu + 30 \log f - 10 \log f_c + 10 \log \eta + 10 \log(1 - f_c/f) - 45 \text{ dB} \tag{13.30}$$

The mass per unit area of the plate, μ , is given in kg/m^2 and f and f_c in Hz. The term $10 \log(1 - f_c/f)$ is often neglected for $f \gg f_c$ reducing (13.30) to

$$R_d = 20 \log \mu + 30 \log f - 10 \log f_c + 10 \log \eta - 45 \text{ dB for } f \gg f_c \tag{13.31}$$

The sound reduction index (13.31) depends on the mass of the plate as well as its stiffness and loss factor. The reduction index appears to increase by 9 dB per doubling of frequency. However, the approximate sound reduction index given by (13.31) cannot exceed the value given by Eqs. (13.19) and (13.20) as long as $\eta < 1$. This is revealed by a simple parameter study using the numerical result of Eqs. (13.16) and (13.17). See Fig. 13.3.

The loss factor for a simple panel is typically decreasing with increasing frequency. The total losses should also include those due to radiation as given by Eq. (12.121). The critical frequency is proportional to $\sqrt{\mu/D_0}$. An increased bending stiffness but constant mass increases the reduction index for $f > f_c$. If the mass is increased, so is the critical frequency. In theory, a doubling of the thickness and the mass of a plate

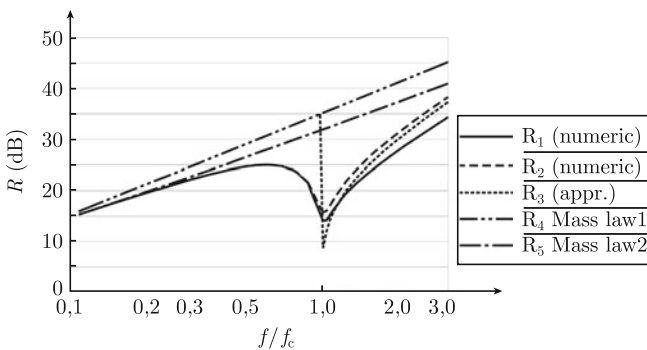


Fig. 13.3 Sound transmission loss of a 5 cm thick chipboard panel, $f_c = 720 \text{ Hz}$, $\mu = 22 \text{ kg/m}^2$. R_1 Eqs. (13.16), (13.17) and (13.20) with $\eta = 0.01$; R_2 Eqs. (13.19) and (13.20) with $\eta = 0.03$; R_3 Eq. (13.22) for $f < f_c$, Eq. (13.30) for $f > f_c$, $\eta = 0.03$; R_4 Eq. (13.22); R_5 Eq. (13.21)

will improve the sound reduction index by 9 dB for $f > f_c$ since both the mass and bending stiffness are changed. Compare Problem 13.2.

The predicted sound reduction index for 5 cm thick chipboard panel is shown in Fig. 13.3 as function of f/f_c . The mass per unit area is 22 kg/m^2 and the critical frequency is 720 Hz for the panel. The sound reduction indices R_1 and R_2 are obtained by means of numerical integration of Eq. (13.16) with $\tau(\varphi)$ defined by (13.17). The sound reduction index is calculated for two different loss factors. For R_1 the loss factor η is set to equal 0.01 and for R_2 the loss factor is increased to 0.03. The sound reduction index R_3 is predicted from the simplified expression (13.22) for $f \ll f_c$ and Eq. (13.31) with $\eta = 0.03$ for $f \gg f_c$. The asymptotes R_4 and R_5 are obtained from Eqs. (13.22) and (13.21). The level of these curves is only determined by the mass of the plate or the so-called mass law. The simplified result R_4 over-estimates the sound reduction index. In theory the mass law, as defined by Eq. (13.21) and shown in Fig. 13.3 as R_5 represents the upper achievable limit for the reduction index for the chipboard panel for any loss factor and frequency. However, the sound reduction index for finite plates can exceed the reduction index predicted by the mass law. This is discussed in Sects. 13.7 and 13.8.

The sound reduction index R_2 starts to deviate from the mass law R_5 at $f \approx f_c/3$. The deviation is maintained up to the critical frequency. For higher frequencies, the sound reduction index steadily increases. The loss factor is only of importance for frequencies higher than approximately $0.8 \cdot f_c$ for large panels. A significant improvement of the sound reduction index by increasing the losses is for large panels only obtained for frequencies above the critical frequency. For small panel elements, the loss factor can be of significance also in the low frequency region as discussed in Sects. 13.6 and 13.9. For finite plates mounted between closed spaces or rooms, the boundary conditions of the plate as well plate and room geometries can influence the sound reduction index as discussed in Sect. 13.6.

13.2 Plate Velocity Induced by an Acoustic Field

The response of plates excited by dynamic forces was discussed in Chap. 8 and later in Chap. 12. The input power to a plate was found to be partly dissipated in the plate, radiated as sound or transmitted to adjoining structures. The power injected in a plate by an acoustic field is also distributed in a similar way. Figure 13.1 shows the response of an infinite plate which is excited by an incident plane acoustic wave, amplitude A . The angle of incidence is φ and the time average of the incident intensity of the plane wave is \bar{I}_0 . The resulting velocity v_0 normal to the surface of the plate is in Eq. (13.7) given as $v_0 = -ik \cdot \cos \varphi \cdot T \cdot A$. The parameter T is defined in Eq. (13.11). The time average of the velocity squared of the plate averaged over all angles of incidence is following the discussions leading up to Eqs. (13.14) and (13.15) given by

$$\langle |\bar{v}_0|^2 \rangle = \frac{1}{2} \cdot \frac{1}{4\pi} \int_0^{\pi/2} 2\pi k^2 (\cos \varphi)^2 \sin \varphi \cdot |AT|^2 d\varphi \quad (13.32)$$

The total intensity incident on the structure is given by Eq. (13.15) as $\langle \bar{I}_i \rangle = \bar{I}_0/4$. If the acoustic field exciting the plate is completely diffuse and if the average pressure squared in the field is $|\bar{p}|^2$ the resulting average intensity on the plate is $\langle \bar{I}_i \rangle = |\bar{p}|^2/(4\rho_0c)$ as shown in Sect. 11.13. The ratio between the velocity squared of the plate and the incident intensity is, considering Eqs. (13.32) and (13.12) and the definition of the incident power given by

$$\frac{\langle |\bar{v}_0|^2 \rangle}{\langle \bar{I}_i \rangle} = \frac{2}{\rho_0c} \int_0^{\pi/2} (\cos \varphi)^2 \sin \varphi \cdot \tau(\varphi) d\varphi \quad (13.33)$$

The intensity radiated from the vibrating plate or the intensity transmitted through the plate is given by (13.12). This intensity can also be described by introducing a sound radiation ratio σ_a for the plate resulting from the acoustic excitation of the plate. In analogy with the discussion in Sect. 12.1, Eq. (12.19), the parameter $\bar{\sigma}_a$ is defined as

$$\bar{\sigma}_a = \frac{\langle \bar{I}_t \rangle}{\rho_0c \langle |\bar{v}_0|^2 \rangle} \quad (13.34)$$

The transmitted intensity can according to Eqs. (13.14) through (13.16) be written as $\langle \bar{I}_t \rangle = \tau_d \cdot \langle \bar{I}_i \rangle$. This expression in combination with Eqs. (13.33) and (13.34) gives

$$\bar{\sigma}_a = \frac{\tau_d}{2 \int_0^{\pi/2} \cos^2 \varphi \cdot \sin \varphi \cdot \tau(\varphi) d\varphi} = \frac{\tau_d}{W} \quad (13.35)$$

Considering that the incident intensity is $\langle \bar{I}_i \rangle = \langle |\bar{p}|^2 \rangle / (4\rho_0c)$ it follows from (13.33) that

$$\frac{\langle |\bar{v}_0|^2 \rangle (\rho_0c)^2}{\langle |\bar{p}|^2 \rangle} = \frac{1}{2} \int_0^{\pi/2} \cos^2 \varphi \cdot \sin \varphi \cdot \tau(\varphi) d\varphi \quad (13.36)$$

In the previous section, simple expressions for the sound reduction index of an infinite plate were derived in the high and low frequency regions. A similar approach can be followed to find the radiation ratio $\bar{\sigma}_a$ for a plate.

Case 1 $f \ll f_c$

The velocity squared of the plate excited by a diffuse incident field is given by Eq. (13.32). The transmission coefficient for $f \ll f_c$ is presented in Eq. (13.18). Thus, the parameter W in Eq. (13.35) is given as

$$W = \int_0^{\pi/2} \frac{2(\cos \varphi)^2 \sin \varphi}{1 + [\mu\omega \cos \varphi / (2\rho_0c)]^2} d\varphi = \int_0^1 \frac{2\xi^2 d\xi}{1 + [\mu\omega / (2\rho_0c)]^2 \xi^2} \quad (13.37)$$

The result is for $f \ll f_c$

$$W = \frac{2}{X^2} \left(1 - \frac{\arctan X}{X} \right); \quad X = \frac{\mu\omega}{2\rho_0c} \quad (13.38)$$

For $f \ll f_c$ the transmission coefficient τ_d is given by Eq. (13.19). Consequently, the radiation ratio is reduced to

$$\bar{\sigma}_a = \frac{\ln(1 + X^2)}{2 \cdot (1 - \arctan X/X)}; \quad X = \frac{\mu\omega}{2\rho_0c} \quad (13.39)$$

In the very low frequency range $X \ll 1$ and $\ln(1 + X^2) \approx X^2$ and $(1 - \arctan X/X) \approx X^2/3$. Thus

$$\lim_{f \rightarrow 0} \bar{\sigma}_a = 1.5 \quad (13.40)$$

The radiation ratio $\bar{\sigma}_a$ is weakly increasing with increasing frequency. See Problem 13.1. The radiation from a plate resulting from a free wave propagating along the plate gives a sound radiation equal to zero for $f < f_c$ as discussed in Sect. 12.1. For an infinite plate excited by an acoustic field a certain vibration pattern is forced on the plate. This vibration pattern is well coupled to the acoustic field on the opposite side of the plate as long as the fluid is the same on both sides of the plate. This results in a radiation ratio larger than zero. The radiation ratio of an infinite plate depends on how the plate is excited. The same is true for finite plates as discussed in Sect. 13.9. The radiation ratio $\bar{\sigma}_a$ is much lower for finite plates than for infinite plates.

It can be shown that for $f \ll f_c$ the response of the plate is approximately given by

$$10 \log \left| \frac{(\rho_0c)^2 \langle |\bar{v}_0|^2 \rangle}{\langle |\bar{p}_1|^2 \rangle} \right| \approx -9 - R \text{ dB}$$

where $\langle |\bar{p}_1|^2 \rangle$ is the frequency and space average of the pressure squared in the source room and R the sound transmission loss of the plate for $f \ll f_c$.

Case 2 $f > f_c$

In the high frequency region, the sound transmission coefficient $\tau(\varphi)$ is given by Eq. (13.25). The radiation ratio is defined in Eq. (13.35). The transmission coefficient is large for $\varphi \approx \varphi_c$. Again, the expansion (13.24) is used to determine the function W introduced in Eq. (13.35).

$$\begin{aligned} W &= \int_0^{\pi/2} 2 \cos^2 \varphi \cdot \sin \varphi \cdot \tau(\varphi) d\varphi \approx \int_0^{\pi/2} 2 (\sin \varphi_c)^2 \cos \varphi_c \tau(\xi) d\xi \\ &= \cos \varphi_c \cdot \int_0^{\pi/2} 2 (\sin \varphi_c)^2 \tau(\xi) d\xi = \cos \varphi_c \cdot \tau_d \end{aligned} \quad (13.41)$$

As before $\sin \varphi_c = \sqrt{f_c/f}$ and $\cos \varphi_c = \sqrt{1 - f_c/f}$. Equations (13.35) and (13.41) give

$$\bar{\sigma}_a = \frac{1}{\cos \varphi_c} = \frac{1}{\sqrt{1 - f_c/f}} \quad \text{for } f > f_c \quad (13.42)$$

This is the same result as derived in Sect. 12.1 for free waves propagating along the plate. For resonant transmission through the plate, the wave number for the waves induced by the acoustic field will be same as for free waves. Consequently $\bar{\sigma}_a = \bar{\sigma}_r$ for $f > f_c$.

The response of the plate is given by Eq. (13.36). Thus

$$\begin{aligned} \frac{\langle |\bar{v}_0|^2 \rangle (\rho_0 c)^2}{\langle |\bar{p}_1|^2 \rangle} &= \frac{1}{2} \int_0^{\pi/2} \cos^2 \varphi \cdot \sin \varphi \cdot \tau(\varphi) d\varphi = \frac{\cos \varphi_c}{4} 2 \int_0^{\pi/2} \cos \varphi \cdot \sin \varphi \cdot \tau(\varphi) d\varphi \\ &= \frac{\cos \varphi_c \cdot \tau_d}{4} = \frac{\tau_d}{4\sqrt{1 - f_c/f}} \end{aligned} \quad (13.43)$$

The response of the plate is obtained from

$$10 \log \left| \frac{(\rho_0 c)^2 \langle |\bar{v}_0|^2 \rangle}{\langle |\bar{p}_1|^2 \rangle} \right| \approx -6 - R \text{ dB}$$

where again $\langle |\bar{p}_1|^2 \rangle$ is the frequency and space average of the pressure squared in the source room and R the sound transmission loss of the plate for $f > f_c$.

13.3 Sound Transmission Between Rooms Separated by a Single Leaf Panel

The sound transmission through an infinite wall or rather an infinite single leaf plate was discussed in Sect. 13.1. The sound pressure level difference between two rooms separated by a single wall with a sound source in one of the rooms is given by (11.172) as

$$L_{p1} - L_{p2} = R + 10 \log(A_2/S)$$

The sound transmission loss or sound reduction index of the wall is defined by R. The area of the wall is S and the equivalent sound absorption area in the receiving room is A_2 . Based on measurement results, the sound reduction index of a simple wall is known to depend on panel dimensions, the mounting or boundary conditions of the panel and a number of material parameters of the wall. It has also been observed that different shapes of the measurement rooms and test openings in laboratories can lead to quite different measured sound reduction indices for a specific structure. However, in practice little or nothing is really done to compensate for these effects. Thus, measurement results from different laboratories do not always show satisfactory agreement as discussed in Sect. 13.8. It is therefore not always possible to determine to what extent the observed discrepancies between measurements are due to differences of material parameters or due to variations of mounting or laboratory design.

In order to describe the effect of boundary conditions, etc., the acoustic fields in the two rooms plus the vibration field of the wall and the coupling between these

fields must be described. Some models have been presented by Sewell [176, 177], Crocker and Price [178], Josse and Lamure [179], and Nilsson [180]. Some of these models are somewhat cumbersome. Still it is here considered useful to demonstrate and discuss the basic principles of the model described in Ref. [180]. The results are summarized in Sect. 13.9. Measurements compared to predictions are presented in Sect. 13.8.

To start with, let a rectangular single leaf panel separate two rooms. The configurations of the rooms are shown in Fig. 13.4. An acoustic source is located in Room 1, the left room in Fig. 13.4.

The dimensions of the plate and the two rooms are L_y and L_z along the y and z axes. The left room is the source room and extends from $x = -d$ to $x = 0$ in the coordinate system shown in Fig. 13.4. The receiving room extends from $x = 0$ to $x = a$. The acoustic field in Room 1, the source room, excites the wall which in turn radiates acoustic power into the two rooms. It is assumed that the outer walls of the rooms are acoustically hard so that the particle velocity in the fluid normal to the outer walls is equal to zero everywhere. The particle velocity in the x -direction at $x = 0$ should equal the velocity of the wall separating the rooms. The wall and the rooms have losses. Initially, it is assumed that the boundary conditions of the wall can be described as stiff and sliding as illustrated in Fig. 8.2. This assumption will ensure that the eigenfunctions in the rooms along the y - z -axes are the same as for the plate. These eigenfunctions are

$$\varphi_{mn}(y, z) = \cos\left(\frac{m\pi y}{L_y}\right) \cos\left(\frac{n\pi z}{L_z}\right) \tag{13.44}$$

The velocity of the wall can be written as

$$v(y, z, t) = \sum_{mn} v_{mn} \cdot \varphi_{mn}(y, z) \cdot \exp(i\omega t) \tag{13.45}$$

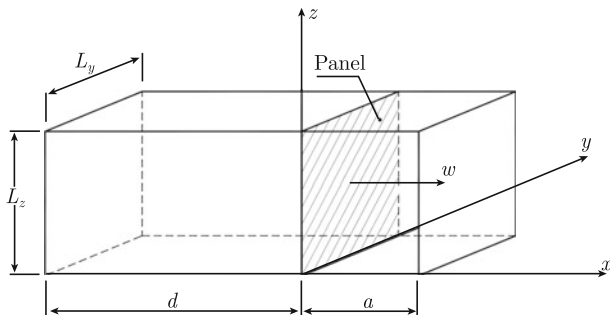


Fig. 13.4 Two rooms separated by a wall. A sound source is located in the left room

The velocity potential induced in Room 2, the receiving room, by the vibrating wall is

$$\Phi_2 = \sum_{mn} A_{mn} \cos[\lambda_{mn}(x - a)] \varphi_{mn}(y, z) \exp(i\omega t) \quad (13.46)$$

The expression satisfies the boundary conditions that the particle velocities normal to all outer walls are zero. The velocity potential must satisfy the wave equation $\nabla^2 \Phi + k^2 \Phi = 0$. Thus

$$\lambda_{mn} = (k^2 - k_{mn}^2)^{1/2} = [k^2 - (m\pi/L_y)^2 - (n\pi/L_z)^2]^{1/2} \quad (13.47)$$

The parameter λ_{mn} is complex since the wave number is $k = k_0(1 - i\delta_2/2)$ to account for the losses δ_2 in the room

At $x = 0$ the boundary condition is

$$\partial \Phi_2 / \partial x = v \quad (13.48)$$

The Eqs. (13.45), (13.46) and (13.48) give

$$A_{mn} = \frac{v_{mn}}{\lambda_{mn} \sin(\lambda_{mn} a)} \quad (13.49)$$

Consequently the velocity potential in the receiving room, defined by $0 \leq x \leq a$, is

$$\Phi_2 = \sum_{mn} \frac{v_{mn} \cos[\lambda_{mn}(x - a)] \varphi_{mn}(y, z) \exp(i\omega t)}{\lambda_{mn} \sin(\lambda_{mn} a)} \quad (13.50)$$

In the source room, the velocity potential is written as the sum of a field Φ_{Π} induced by the acoustic source in the room and a field Φ_w induced by the vibrating wall. In the first case, it is assumed that the particle velocities normal to all walls are equal to zero. With a source mounted in a corner of the room, the resulting field in Room 1 is according to Eq. (11.139)

$$\Phi_{\Pi} = \sum_{lmn} \frac{P \cdot \cos(l\pi x/d) \cdot \varphi_{mn}(y, z) \cdot \exp(i\omega t)}{\varepsilon_l \varepsilon_m \varepsilon_n (k^2 - k_{lmn}^2)} \quad (13.51)$$

where P is a function of the acoustical power of the source and $\varepsilon_l = 2$ for $l = 0$ and $\varepsilon_l = 1$ for $l > 0$ etc. However, the lower modes are of no great importance for the derivation of the sound transmission loss, which makes it possible to leave out the indices ε_l etc. The field Φ_w should satisfy the boundary conditions $\partial \Phi_w / \partial x = 0$ for $x = -d$ and $\partial \Phi_w / \partial x = v$ at $x = 0$. Consequently, the velocity potential induced by the vibrating wall is written

$$\Phi_w = \sum_{mn} - \frac{v_{mn} \cos[\lambda_{mn}(x + d)] \varphi_{mn}(y, z) \exp(i\omega t)}{\lambda_{mn} \sin(\lambda_{mn} d)} \quad (13.52)$$

Thus, the total velocity potential in the source room is

$$\Phi_1 = \Phi_{\Pi} + \Phi_w \quad (13.53)$$

The differential equation governing the vibration of the plate is

$$\nabla^2(\nabla^2 v) - \kappa^4 v = \frac{(\dot{p}_1 - \dot{p}_2)_{x=0}}{D} = \frac{\rho_0 \omega^2}{D} [\Phi_1 - \Phi_2]_{x=0} \quad (13.54)$$

where $\kappa^4 = \mu \omega^2 / D$ and $D = D_0(1 + i\eta)$. The Eqs. (13.46), (13.51) and (13.52) inserted in (13.54) give

$$\begin{aligned} & [k_{mn}^4 - \kappa^4] v_{mn} \\ &= -\frac{\rho_0 \omega^2}{D} v_{mn} \left[\frac{\cos(\lambda_{mn} d)}{\lambda_{mn} \sin(\lambda_{mn} d)} + \frac{\cos(\lambda_{mn} a)}{\lambda_{mn} \sin(\lambda_{mn} a)} \right] - \frac{\rho_0 \omega^2}{D} \sum_l \frac{P}{k_{lmn}^2 - k^2} \end{aligned} \quad (13.55)$$

The summation on the right hand side can be made as discussed in Problem 13.3 giving

$$\sum_l \frac{1}{k^2 - k_{lmn}^2} = \frac{d}{2\lambda_{mn} \tan(\lambda_{mn} d)} \quad (13.56)$$

The Eqs. (13.55) and (13.56) give

$$\begin{aligned} & v_{mn} \left[k_{mn}^4 - \kappa^4 + \frac{\rho_0 \omega^2}{D} \left(\frac{1}{\lambda_{mn} \tan(\lambda_{mn} d)} + \frac{1}{\lambda_{mn} \tan(\lambda_{mn} a)} \right) \right] \\ &= \frac{\rho_0 \omega^2 d P}{2D \lambda_{mn} \tan(\lambda_{mn} d)} \end{aligned} \quad (13.57)$$

The terms $1/[\lambda_{mn} \tan(\lambda_{mn} d)]$ are large whenever $\text{Re}(\lambda_{mn} d) \approx n\pi$ or rather at frequencies coinciding with any of the natural frequencies of the source room. At any of these frequencies, the reaction of the acoustic field in the room will decrease the mobility of the wall. Compare Problem 13.4. The reacting field in the source room is increasing the added mass of the wall due to the fluid loading. However, for a light fluid like air the added mass effect is small and can in fact be neglected if the rooms are comparatively large. See also Sect. 12.1. Neglecting the secondary terms describing the effect of the fluid loading on the wall, i.e., the parenthesis inside the bracket on the left hand side of Eq. (13.57), this expression is reduced to

$$v_{mn} = \frac{dP}{2Z_{mn} \lambda_{mn} \tan(\lambda_{mn} d)}; \quad Z_{mn} = \frac{D}{\rho_0 \omega^2} (k_{mn}^4 - \kappa^4) \quad (13.58)$$

The function λ_{mn} is complex, which means that the velocity v_{mn} is finite at any frequency coinciding with a natural frequency in the room.

The pressure in the fluid is $p = -i\omega\rho_0\Phi$. Assuming that the direct field from the acoustic source in the room dominates over the secondary field induced by the vibrating wall the velocity potential Φ_1 in Room 1 can be set to equal Φ_{Π} . The space average of the pressure squared in room 1 is

$$\langle |p_1^2| \rangle = \frac{(\rho_0\omega)^2}{V} \int_v dV |\Phi_1|^2 = \frac{(\rho_0\omega)^2}{8} \sum_{lmn} \frac{|P|^2}{|k_{lmn}^2 - k^2|^2} \quad (13.59)$$

The frequency or wave number average of the pressure squared is

$$\begin{aligned} \langle |\bar{p}_1^2| \rangle &= \frac{(\rho_0\omega)^2}{8} \sum_{lmn} \frac{1}{\Delta k} \int_{k-\Delta k/2}^{k+\Delta k/2} dk \frac{|P|^2}{|k_{lmn}^2 - k^2|^2} \\ &= \frac{(\rho_0\omega)^2}{8} \frac{\Delta N}{\Delta k} \int_{k-\Delta k/2}^{k+\Delta k/2} dk \frac{|P|^2}{|k_{lmn}^2 - k^2|^2} \end{aligned} \quad (13.60)$$

The number of modes within the wavenumber domain $k - \Delta k/2$ and $k + \Delta k/2$ is given by ΔN . The number of modes in room of volume V_1 is for wave numbers less than k given by $N = k^3 V_1 / (6\pi^2)$. See Eqs. (11.137) and (11.138). Consequently

$$\frac{\Delta N}{\Delta k} = \frac{k^2 V_1}{2\pi^2} \quad (13.61)$$

To account for the losses in Room 1 the wavenumber for the fluid is according to standard practice written $k(1 - i\delta_1/2)$, where δ_1 is the loss factor. Following the procedure outlined in Sect. 11.12, the space and wavenumber average of the pressure squared in Room 1 is

$$\langle |\bar{p}_1^2| \rangle = \frac{|\rho_0\omega P|^2 V_1}{32\pi\delta_1 k} \quad (13.62)$$

From Eq. (13.50) the space average of the pressure squared in Room 2 is given as

$$\begin{aligned} \langle |p_2|^2 \rangle &= \frac{(\rho_0\omega)^2}{V_2} \int dV |\Phi_2|^2 = \sum_{mn} \frac{(\omega\rho_0)^2 |v_{mn}|^2}{4[\lambda_{mn} \sin(\lambda_{mn}a)]^2} \int_0^a \frac{\cos^2[\lambda_{mn}(x-a)]}{a} dx \\ &= \sum_{mn} \frac{(\omega\rho_0)^2 |v_{mn}|^2}{8 \cdot [\lambda_{mn} \sin(\lambda_{mn}a)]^2} \left[\frac{\sin(2\lambda_{mn}a)}{2\lambda_{mn}a} + 1 \right] \end{aligned} \quad (13.63)$$

This expression is also written

$$\langle |p_2|^2 \rangle = \sum_{mn} \frac{(\omega\rho_0)^2 |v_{mn}|^2}{8} Y_{mn}(a);$$

$$Y_{mn}(a) = \frac{1}{[\lambda_{mn} \sin(\lambda_{mn}a)]^2} \left[\frac{\sin(2\lambda_{mn}a)}{2\lambda_{mn}a} + 1 \right] \quad (13.64)$$

For unequal rooms $|v_{mn}|^2$ and $Y_{mn}(a)$ have maxima at different frequencies. The wavenumber averages of the functions can therefore be made separately. The wavenumber average of $\langle |p_2|^2 \rangle$ can therefore be written as

$$\langle |\bar{p}_2|^2 \rangle = \sum_{mn} \frac{(\omega\rho_0)^2 |\bar{v}_{mn}|^2}{8} \bar{Y}_{mn}(a) \quad (13.65)$$

The frequency average of $Y_{mn}(a)$ is given by $\bar{Y}_{mn}(a)$. The function $Y_{mn}(a)$ is large when $\lambda_{mn}a \approx n\pi$ or when $k_0 = k_{0a}(1 + \xi)$ for ξ small and

$$k_{0a} = \left[k_{mn}^2 + \left(\frac{N\pi}{a} \right)^2 \right]^{1/2} \quad (13.66)$$

Considering that $k = k_0(1 - i\delta_2/2) = k_{0a}(1 + \xi)(1 - i\delta_2/2) \approx k_{0a}(1 + \xi - i\delta_2/2)$ where δ_2 represents the losses in Room 2 then for small ξ and δ_2 the function $Y_{mn}(a)$ is expanded as

$$|Y_{mn}(a)| = \frac{1}{(ak_{0a}^2)^2(\xi^2 + \delta_2^2/4)} \quad (13.67)$$

Compare Problem 13.5. The wavenumber average of this function is

$$|\bar{Y}_{mn}(a)| = \frac{1}{\Delta k} \int \frac{dk_0}{(ak_{0a}^2)^2(\xi^2 + \delta_2^2/4)} = \frac{1}{\Delta k} \cdot \frac{1}{a^2 k_{0a}^3} \int \frac{d\xi}{(\xi^2 + \delta_2^2/4)}$$

From Eq. (13.66) $\Delta k_{0a} = \Delta N(N\pi/a)(\pi/a)/k_{0a}$. For $\Delta N = 1$ and $(N\pi/a) = (k_0^2 - k_{mn}^2)^{1/2} = k_0 \cos \varphi$ where φ is the angle between the outgoing wave and the normal to the plate. The wavenumber spacing Δk is obtained for $\Delta N = 1$ as

$$\Delta k_{0a} = (N\pi/a)(\pi/a)/k_{0a} = \pi \cos \varphi/a \quad (13.68)$$

Consequently

$$|\bar{Y}_{mn}(a)| = \frac{2}{ak_{0a}^3 \delta_2 \cos \varphi} \quad (13.69)$$

The velocity of the plate is given by Eq. (13.58). The velocity components v_{mn} are large whenever $\tan(\lambda_{mn}d)$ is small or whenever $\text{Re}\lambda_{mn}d \approx n\pi$ or at any of the natural frequencies of the source room. The function $\lambda_{mn} \tan(\lambda_{mn}d)$ can in a similar way as $Y_{mn}(a)$ be expanded with respect to a wavenumber k_{0d} corresponding to one of the natural frequencies in Room 1. Thus, write $k = k_{0d}(1 + \xi - i\delta_1/2)$ where $k_{0d} = [k_{mn}^2 + (N\pi/d)^2]^{1/2}$. The losses in Room 1 are given by δ_1 . Based on these assumptions the modal velocity of the panel is

$$v_{mn} = \frac{P}{2[Z_{mn}k_{0d}^2(\xi - i\delta_1/2)]} \quad (13.70)$$

The wavenumber average of v_{mn}^2 is for $\Delta k = \pi \cos \varphi / d$

$$|\bar{v}_{mn}|^2 = \frac{|P|^2}{4|Z_{mn}k_{0d}^2|^2 \Delta k} \int_{k-\Delta k/2}^{k+\Delta k/2} \frac{k_x d\xi}{\xi^2 + \delta_1^2/4} = \frac{|P|^2 d}{2 \cos \varphi |Z_{mn}^2| k_{0d}^3 \delta_1} \quad (13.71)$$

Setting $k = k_{0d}$ and using (13.62) the result is written

$$|\bar{v}_{mn}|^2 = \langle |\bar{p}_1|^2 \rangle \frac{16\pi}{L_y L_z \cos \varphi (\rho_0 \omega)^2 |Z_{mn}^2| k^2} \quad (13.72)$$

The pressure p_2 in Room 2 is given by the expression (13.65) as a sum of the product between $|\bar{v}_{mn}|^2$ and $\bar{Y}_{mn}(a)$. For sound transmission between two unequal rooms these two functions have maxima at different wavenumbers. The summation (13.65) can therefore be approximated by the expression

$$\langle |\bar{p}_2|^2 \rangle = [\bar{Y}_{mn}(a)]_{\text{av}} \sum_{mn} \frac{(\omega \rho_0)^2 |\bar{v}_{mn}|^2}{8} \quad (13.73)$$

The function $[\bar{Y}_{mn}(a)]_{\text{av}}$ is defined as the modal average of $\bar{Y}_{mn}(a)$ or as

$$[\bar{Y}_{mn}(a)]_{\text{av}} = \sum_{mn} \bar{Y}_{mn}(a) / N_{\text{tot}} \quad (13.74)$$

where N_{tot} is the total number of modes projected on the wall for all wavenumbers less than k . The wavenumber k_{mn} projected on the wall is $k_{mn} = k \sin \varphi$. For a certain angle φ , the total number of modes N projected on the plate is

$$N = L_y L_z k_{mn}^2 / (4\pi) = L_y L_z k^2 \sin^2 \varphi / (4\pi) \quad (13.75)$$

Thus the number of modes ΔN within a section $\Delta \varphi$ of the angle of incidence is

$$\Delta N = L_y L_z k^2 \sin \varphi \cos \varphi \Delta \varphi / (2\pi) \quad (13.76)$$

$$\sum |\bar{Y}_{mn}(a)| = \int_0^{\pi/2} \frac{L_y L_z k^2 \sin \varphi \cos \varphi d\varphi}{\pi a k_{0N}^3 \delta_2 \cos \varphi} = \frac{L_y L_z k^2}{\pi a k_{0N}^3 \delta_2} = \frac{V_1}{\pi a^2 k \delta_2} \quad (13.77)$$

The number of modes projected on the plate for wavenumbers less than k is obtained from Eq. (13.76) as

$$N_{\text{tot}} = \frac{1}{2\pi} \int_0^{\pi/2} L_y L_z k^2 \sin \varphi \cos \varphi d\varphi = \frac{L_y L_z k^2}{4\pi} \quad (13.78)$$

Following the definition (13.74) and the result (11.159), $\delta k = A/4V$, the function $[\bar{Y}_{mn}(a)]_{\text{av}}$ is obtained as

$$[\bar{Y}_{mn}(a)]_{\text{av}} = \frac{4V_2}{a^2 k^3 \delta_2 L_y L_z} = \frac{4}{ak^3 \delta_2} = \frac{16S}{k^2 A_2} \quad (13.79)$$

The equivalent absorption area in Room 2 is A_2 and the area of the wall is $S = L_y L_z$ and the volume of the room is $V_2 = Sd$. For sufficiently high frequencies or rather for sufficiently many modes in the rooms the summation in Eq. (13.73) can using (13.76) be transformed into an integral as

$$\sum_{mn} Q_{mn} \rightarrow \frac{L_y L_z k^2}{2\pi} \int_0^{\pi/2} Q(\varphi) \sin \varphi \cos \varphi d\varphi \quad (13.80)$$

Finally the expressions (13.71), (13.74), (13.79) and (13.80) give

$$\langle |\bar{p}_2|^2 \rangle = \langle |\bar{p}_1|^2 \rangle \frac{16S}{A_2 k^2} \int_0^{\pi/2} \frac{\sin \varphi d\varphi}{|Z(\varphi)|^2} \quad (13.81)$$

The function Z_{mn} is given in Eq. (13.58). By setting $D = D_0(1 + i\eta)$, $\kappa^4 = \mu\omega^2/D$ and $\kappa_0^4/k^4 = (f/f_c)^2$, $k_{mn} = k \sin \varphi$ the new function $Z(\varphi)$ is

$$|Z|^2 = \left(\frac{\mu}{\rho_0}\right)^2 \left\{ \left[\left(\frac{f}{f_c}\right)^2 \sin^4 \varphi - 1 \right]^2 + \left[\eta \left(\frac{f}{f_c}\right)^2 \sin^4 \varphi \right]^2 \right\} \quad (13.82)$$

Together with Eq. (13.81) the pressure in Room 2 is finally obtained as

$$\langle |\bar{p}_2|^2 \rangle = \langle |\bar{p}_1|^2 \rangle \frac{16S(\rho_0 c)^2}{A_2 (\mu\omega)^2} \int_0^{\pi/2} \frac{\sin \varphi d\varphi}{\left[\left(\frac{f}{f_c}\right)^2 \sin^4 \varphi - 1 \right]^2 + \left[\eta \left(\frac{f}{f_c}\right)^2 \sin^4 \varphi \right]^2} \quad (13.83)$$

For $f \ll f_c$, $|Z|^2 \approx (\mu/\rho_0)^2$ and

$$\langle |\bar{p}_2|^2 \rangle = \langle |\bar{p}_1|^2 \rangle \frac{16S(\rho_0 c)^2}{A_2 (\mu\omega)^2}$$

For μ expressed in kg/m^2 and f in Hz the difference between the sound pressure level L_{p1} in Room 1 and the sound pressure level L_{p2} in Room 2 is written

$$L_{p1} - L_{p2} = 20 \log \mu + 20 \log f - 48 + 10 \log (A_2/S) \text{ dB} \quad (13.84)$$

For $f > f_c$ and following the procedure outlined in Sect. 13.1 the result is

$$\begin{aligned} \langle |\bar{p}_2|^2 \rangle &= \langle |\bar{p}_1|^2 \rangle \frac{4\pi S(\rho_0 c)^2 f_c}{A_2 \eta (\mu \omega)^2 f \sqrt{1 - f_c/f}} \\ L_{p1} - L_{p2} &= 20 \log \mu + 30 \log f - 10 \log f_c + 10 \log \eta \\ &\quad + 5 \log(1 - f_c/f) - 47 + 10 \log(A_2/S) \end{aligned} \quad (13.85)$$

Considering the definition (11.172), the sound transmission loss is written as

$$R = 20 \log \mu + 20 \log f - 48 \text{ for } f \ll f_c \quad (13.86)$$

$$R = 20 \log \mu + 30 \log f - 10 \log f_c + 10 \log \eta + 5 \log(1 - f_c/f) - 47 \text{ for } f > f_c \quad (13.87)$$

As discussed in Sect. 13.1, the sound reduction index R always satisfies $R > 0$. Further the sound reduction index given by (13.87) cannot exceed the value given by (13.86) at any frequency.

The expression (13.84) was derived assuming that the secondary field in Room 1 could be neglected. This is not the case when the sound reduction index is small. Not neglecting the secondary terms in Eq. (13.57) would ensure that $R > 0$ as the frequency tends to zero. The radiation losses, defined in Eq. (12.119) should be included in the total loss factor given by η in Eq. (13.87). For $f > f_c$ the radiation losses are

$$\eta_{\text{rad}} = \frac{2\rho_0 c}{\omega \mu \sqrt{1 - f_c/f}}$$

rendering R finite as $f \rightarrow f_c$.

13.4 Sound Transmission Between Equal Rooms

The acoustical coupling between the rooms shown in Fig. 13.4 is changed if the dimensions of the rooms are made identical. In this particular case, it means that $a = d$ in Fig. 13.4. By setting $a = d$ in Eq. (13.57) the modal velocity v_{mn} is obtained as

$$v_{mn} = \frac{aP}{2Z_{mn}\lambda_{mn}\tan(\lambda_{mn}a)} = \frac{P}{2Z_{mn}k_{0a}^2(\xi - i\delta_1/2)} \quad (13.88)$$

The pressure squared in Room 2 is given by Eq. (13.64). For unequal rooms the functions $|v_{mn}|$ and Y_{mn} could be averaged separately with respect to the wavenumber. For equal rooms, the functions have maxima for the same wavenumber and must therefore be averaged together. By inserting Eqs. (13.88) and (13.67) in (13.64), the pressure squared in Room 2 is written as

$$\langle |p_2|^2 \rangle = \frac{(\omega\rho_0)^2 |P|^2}{32a^2k^8} \sum_{mn} \frac{1}{|Z_{mn}|^2 (\xi^2 + \delta_1^2/4)(\xi^2 + \delta_2^2/4)} \quad (13.89)$$

The wavenumber average of (13.89) is given by

$$\langle |\bar{p}_2|^2 \rangle = \frac{1}{\Delta k} \int \langle |p_2|^2 \rangle k d\xi; \quad \Delta k = \pi \cos \varphi/a$$

Thus,

$$\langle |\bar{p}_2|^2 \rangle = \sum_{mn} \frac{(\omega\rho_0)^2 |P|^2}{32\pi \cos \varphi a k^7 |Z_{mn}|^2} \cdot \Gamma; \quad \Gamma = \oint \frac{d\xi}{(\xi^2 + \delta_1^2/4)(\xi^2 + \delta_2^2/4)} \quad (13.90)$$

The integration is made along a contour of a half-circle in the upper part of the complex plane. The procedure is discussed in Problem 13.6. The function Γ is obtained as

$$\Gamma = \frac{8\pi}{\delta_1 \delta_2 (\delta_1 + \delta_2)} \quad (13.91)$$

For sufficiently many modes in the rooms, the summation of (13.90) is made into an integration as given by Eq. (13.80). Thus

$$\langle |\bar{p}_2|^2 \rangle = \int_0^{\pi/2} \frac{(\omega\rho_0)^2 |P|^2 S \sin \varphi d\varphi}{8\pi a k^5 |Z(\varphi)|^2 \delta_1 \delta_2 (\delta_1 + \delta_2)} \quad (13.92)$$

The pressure squared in Room 1 is defined in Eq. (13.62). The loss factor δ_1 in Room 1 is as before given by $\delta_1 k = A_1/4V$ where A_1 is the equivalent absorption area in Room 1. The Eqs. (13.62) and (13.92) give

$$\langle |\bar{p}_2|^2 \rangle = \langle |\bar{p}_1|^2 \rangle \frac{64S^2}{A_2(A_1 + A_2)} \int_0^{\pi/2} \frac{\sin \varphi d\varphi}{k^2 |Z(\varphi)|^2} \quad (13.93)$$

A comparison with the results (13.84) through (13.87) gives the sound pressure level difference between two equal rooms as

$$L_{p1} - L_{p2} = R + 10 \log(A_2/S) + 10 \log[(A_1 + A_2)/(4S)] \quad (13.94)$$

A_1 and A_2 are the equivalent absorption areas in Room 1 and Room 2 respectively. The sound reduction index R is given in Eq. (13.86) for $f \ll f_c$ and in Eq. (13.87) for $f > f_c$. The result given by Eq. (13.94) is valid even when the rooms are slightly different. It can be shown that if the rooms have the same shape but slightly different volumes V and $V + \Delta V$ the result (13.94) is valid as long as

$$\frac{\delta_1 + \delta_2}{2} > \frac{2\Delta V}{3V} \text{ or } \Delta V < c(A_1 + A_2)/(16\omega) \quad (13.95)$$

This condition is more readily satisfied in the low frequency region. Whenever the transmission rooms are equal, the sound pressure level difference between the rooms, a sound source in one room, depends on the losses in both rooms. Experimentally, the sound reduction index of a wall is, as discussed in Sect. 11.15, Eq. (11.172), determined through $R = L_{p1} - L_{p2} - 10 \log(A_2/S)$. A comparison with Eq. (13.94) gives a difference between reduction indices measured between equal and unequal rooms as

$$R_{\text{equal}} - R_{\text{unequal}} = 10 \log[(A_1 + A_2)/(4S)] \quad (13.96)$$

13.5 Sound Transmission Between Irregular Rooms

In Sects. 13.3 and 13.4, the sound pressure level difference between two rooms were discussed. One of the rooms having a sound source and the rooms being separated by a simple wall. In the first case, Fig. 13.5a, the height and width of the adjoining rooms were the same whereas the lengths of the rooms were different. In the second example, Fig. 13.5b, the two rooms were identical. The sound pressure level difference between the rooms was found to be different in the two cases. A third type of room configuration can also be considered, Fig. 13.5c. The two rooms are completely irregular and the cross-sectional modes in the rooms and of the wall are uncoupled. It can be shown that the sound pressure level difference between the rooms, one having a sound source, is given by the expression (11.172) where R is given by Eqs. (13.21) and (13.30). This result is obtained by considering that in Eq. (13.57) λ_{mn} is complex since $k = k_0(1 - i\delta/2)$. Thus $\tan(\lambda_{mn}a)$ and $\tan(\lambda_{mn}d)$ tend to $1/i$ as the lengths of the rooms, a and d , approaches infinity. Further, averages and summations over the modes in the source room, receiving room and the panel can be made separately as the modes are uncoupled. Compare Problem 13.12.

Thus, in summary, the sound pressure level difference ΔL_p between two rooms, one having a sound source, is given by

(i) Configuration of rooms according to Fig. 13.5a

$$\Delta L_p = R + 10 \log(A_2/S)$$

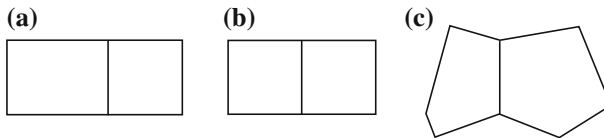


Fig. 13.5 Three configurations of rooms separated by a simple panel. **a** Width and height of rooms and panel are identical; **b** Width and height of rooms and panel and lengths of rooms are identical; **c** The rooms are completely irregular

where R is defined in (13.83) or approximately given by (13.86) and (13.87). The equivalent sound absorption area in the receiving room is given by A_2 . The area of the panel separating the rooms is S .

(ii) Configuration of rooms according to Fig. 13.5b

$$\Delta L_p = R + 10 \log(A_2/S) + 10 \log[(A_1 + A_2)/(4S)]$$

where R is defined in (13.83) or approximately given by (13.86) and (13.87). The equivalent sound absorption area in the receiving room is given by A_2 and in the source room A_1

(iii) Configuration of rooms according to Fig. 13.5c

$$\Delta L_p = R + 10 \log(A_2/S)$$

where R is defined in (13.16) and (13.17) or approximately given by (13.22) and (13.30). The equivalent sound absorption area in the receiving room is given by A_2 .

However, as discussed in the next few sections the boundary conditions and the dimensions of the panel can also influence the sound transmission loss of a panel.

13.6 Effect of Boundary Conditions of Plate on Sound Transmission Loss

The sound transmission through a panel separating two rooms was discussed in Sect. 13.3. The transmission can be said to be due to a non-resonant process in the very low frequency region. The transmission loss is mainly determined by the simple mass law. For increasing frequencies, the transmission due to resonant phenomena starts to be of importance finally to dominate completely for frequencies above the critical frequency f_c . The sound transmission loss of a panel often starts to deviate from the simple mass law for frequencies $f > f_c/2$. The resonant transmission or rather the resonant response of a plate is in the high frequency region more or less independent of the boundary conditions. The response and the transmission are for high frequencies determined by material parameters of panel and the modal density for bending waves on the plate. In this frequency region, the modal density is independent of boundary conditions as shown in Sect. 8.5. See Problem 13.7. In Chap. 12, it was concluded that the sound radiation ratio of a plate is independent of boundary conditions for $f > f_c$ whereas in the low frequency region the radiation ratio is higher for a clamped than for a simply supported plate. It is also concluded that the sound radiation ratio for a plate for $f < f_c$ depends on the dimensions of the plate. In the high frequency range, this is no longer the case. In a similar way, it can be shown that the resonant sound transmission through a panel is, as a first approximation, independent of boundary conditions and length and width of plate.

In this section, a discussion is included on the influence of boundary conditions on the non-resonant sound transmission through a plate. The influence of panel and room dimensions is discussed in Sect. 13.7.

The sound transmission loss of a panel mounted between two rooms was discussed in Sect. 13.3. A sound source was operating in one room. The sound pressure in the receiving room was found to be a function of the plate velocity or rather its modal amplitudes v_{mn} as given in Eq. (13.63). These modal parameters were derived for the special case that the panel satisfied the boundary conditions for a sliding edge illustrated in Fig. 8.2. The eigenfunctions for the plate and the cross modes in the room were consequently the same, see Eq. (13.44). In the low frequency region, non-resonant transmission, the plate velocity is a function of the differential equation

$$\nabla^2(\nabla^2 v) - \kappa^4 v = \sum_{mn} Q_{mn} \cdot \varphi_{mn}(y, z) \quad (13.97)$$

where for a diffuse field in the source room the parameter Q_{mn} is independent of the mode numbers m and n . If in Eq. (13.55) the secondary acoustic fields are neglected the source terms Q_{mn} are found to be of approximately the same amplitude for $\kappa \gg k \geq k_{mn}$. Following the discussion in Sect. 13.5 the frequency average of the product $Q_{mn} \cdot Q_{rs}$ of the modal amplitudes is equal to $|\bar{Q}|^2 \delta_{mr} \delta_{ns}$. One possible way to find a solution to Eq. (13.97) for a panel with clamped boundaries would be to use approximate eigenfunctions for the plate. These could be a combination of beam functions describing the flexural vibrations of clamped beams as discussed in Sect. 8.6. The amplitudes of the resulting modes could thereafter be obtained using Galerkin's method, Sect. 9.9. However, a different approach is to be followed here. The technique is described in Ref. [180]. It is assumed that if the problem is treated in one dimension the extra contribution or perturbation due to a changed boundary condition could be calculated directly. The result for the two dimensional case is obtained by super-imposing two one-dimensional and perpendicular wave motions. A similar one-dimensional approach has previously been used by Nikiforov in Ref. [181] to model the sound radiation from finite plates with different boundary conditions. The use of a one-dimensional model can also be justified by considering the radiation from a finite plate discussed in Sect. 12.9. It was demonstrated that the dominant part of the acoustic energy radiated by a vibrating finite plate was caused by the edge modes.

The wave equation for a plate excited by a diffuse field is given by Eq. (13.97). In one dimension, the y -direction, this would correspond to

$$\frac{\partial^4 v}{\partial y^4} - \kappa^4 v = \sum_m Q_m \cdot \varphi_m(y); \quad 0 \leq y \leq L_y \quad (13.98)$$

In order to save space the discussion is confined to symmetric fields or m even. However, the complete solution, including both symmetric and asymmetric fields, gives the same result. Thus for the symmetric case, $v(y) = v(L_y - y)$, the eigenfunctions

φ_m are $\varphi_m(y) = \cos(2m\pi y/L_y)$. The total solution to Eq. (13.98) is the sum of the particular and the complementary solutions. The particular solution to the inhomogeneous equation (13.98) is

$$v_1 = \sum_m v_{1m} \varphi_m(y); \quad v_{1m} = \frac{Q_m}{k_m^4 - \kappa^4}; \quad k_m = 2m\pi/L_y \quad (13.99)$$

For frequencies far below the critical frequency, $k \ll \kappa$ and consequently $k_m \ll \kappa$ for the modes exciting the structure. Thus,

$$v_{1m} \approx -\frac{Q_m}{\kappa^4} \quad (13.100)$$

The complementary and symmetric solution to the homogeneous problem is on the form

$$v_2 = B_1 \cos \kappa(y - L_y/2) + B_2 \cosh \kappa(y - L_y/2)$$

For a structure clamped at the ends $y = 0$ and $y = L_y$ the total solution $v = v_1 + v_2$ should satisfy the boundary conditions

$$v = \frac{dv}{dy} = 0 \text{ for } y = 0 \text{ and } y = L_y$$

The second boundary condition requires that $\partial v_2/\partial y = 0$ for $y = 0$. Thus,

$$v_2 = U \left[\frac{\cos \kappa(y - L_y/2)}{\sin(\kappa L_y/2)} + \frac{\cosh \kappa(y - L_y/2)}{\sinh(\kappa L_y/2)} \right]$$

The function U is determined from the boundary condition $v = v_1 + v_2 = 0$ for $y = 0$. Consequently,

$$U = -\frac{1}{\cot(\kappa L_y/2) + \coth(\kappa L_y/2)} \sum_{m=0}^M \frac{Q_m}{\kappa^4}$$

The summation is made for all positive m up to M . The limit M is equal to the number of modes of the pressure in the frequency range up to f . Thus $2M\pi/L_y = k$ where k is the wavenumber in the fluid, speed of sound c . Consequently, $M \approx fL_y/c$. For $\kappa L_y > 1$, $\coth(\kappa L_y/2) \approx 1$ and the function U is reduced to

$$U \approx -\frac{1}{\cot(\kappa L_y/2) + 1} \sum_{m=0}^M \frac{Q_m}{\kappa^4} \quad (13.101)$$

The complementary function can also be expanded along the eigenfunctions $\varphi_m(y) = \cos(2m\pi y/L_y)$. The result is

$$v_2(y) = \frac{8\kappa^3 U}{L_y} \left[\sum_m \frac{\varphi_m(y)}{\kappa^4 - k_m^4} \right] \approx \frac{8\kappa^3 U}{L_y} \left[\sum_m \frac{\varphi_m(y)}{\kappa^4} \right] \quad f \ll f_c$$

For non-resonant transmission, $\kappa \gg k_m$ this expression is reduced to

$$v_2 = \sum_m v_{2m} \varphi_m = \frac{8U}{\kappa L_y} \sum_m \varphi_m; \quad v_{2m} = \frac{8U}{\kappa L_y} \quad (13.102)$$

The amplitude of U is large when $\text{Re}(\kappa L_y/2) = 3\pi/4 + N\pi = \alpha_0$ where N is an integer. Following the definition of the wavenumber, the parameter α_0 is also equal to

$$\alpha_0 = \frac{\pi L_y \sqrt{f \cdot f_c}}{c} \quad (13.103)$$

where c is the speed of sound of the fluid in the rooms, i.e., typically air. Let now the frequency dependent function $\kappa L_y/2$ be expanded around α_0 as

$$\frac{\kappa L_y}{2} = \frac{\alpha_0(1 + \xi)}{(1 + i\eta)^{1/4}} \approx \alpha_0(1 + \xi - i\eta/4)$$

Using this result, the function U , Eq. (13.101), is for $\kappa L_y/2 \approx \alpha_0$ obtained as

$$U \approx -\frac{1}{2\alpha_0(\xi - i\eta/4)} \cdot \sum_{m=0}^M \frac{Q_m}{\kappa^4} \quad (13.104)$$

In the low frequency region or for non-resonant transmission, and excitation by a diffuse field the parameters Q_m are assumed to have the same absolute value. Further, the frequency average of a product $Q_m \cdot Q_n$ can be set to equal $|Q|^2 \cdot \delta_{mn}$. Compare the result (13.58) for the two dimensional case.

The response of a clamped one-dimensional structure excited by a diffuse pressure field is

$$v = \sum_m v_m \varphi_m = v_1 + v_2 = \sum_m (v_{1m} + v_{2m}) \varphi_m;$$

The amplitudes of the modes are given by Eqs. (13.100) and (13.102).

The power radiated from the one-dimensional structure is proportional to the frequency average of $|v_{1m} + v_{2m}|^2$. Thus

$$\bar{v}_m^2 = \frac{1}{\Delta f} \int_{f-\Delta f/2}^{f+\Delta f/2} |v_{1m}^2 + 2v_{1m}v_{2m} + v_{2m}^2| df$$

The frequency average of the cross term is equal to zero. Considering that the definition (13.102) the frequency average is obtained as

$$\bar{v}_m^2 = \bar{v}_{1m}^2 + \frac{1}{\Delta f} \int_{f-\Delta f/2}^{f+\Delta f/2} |U^2| df \quad (13.105)$$

The function $|U|^2$ has a maximum for $\kappa L_y/2 = \alpha_0$. Maxima occur with a frequency π . The symmetric interval including one maximum is $\alpha_0 - \pi/2 < \kappa L_y/2 < \alpha_0 + \pi/2$. Considering the expansion of κ the interval is also equal to $\xi_1 = -\pi/(2\alpha_0) < \xi < \pi/(2\alpha_0) = \xi_2$. The integral of Eq. (13.105) can therefore be written as

$$\frac{1}{\Delta f} \int_{f-\Delta f/2}^{f+\Delta f/2} |U^2| df = \frac{1}{\pi\alpha_0} \int_{\xi_1}^{\xi_2} \frac{d\xi}{4\alpha_0^2(\xi^2 + \eta^2/16)} \left| \sum_{m=0}^M \frac{Q_m}{\kappa^4} \right|^2 \approx \frac{M}{\alpha_0^3 \eta} \frac{|Q_m|^2}{\kappa^8}$$

The number M of modes is $M \approx f L_y/c$. The quantity \bar{v}_{1m}^2 is given in Eq. (13.100). Consequently,

$$\bar{v}_m^2 = \bar{v}_{1m}^2 \left[1 + \frac{64}{\pi L_y^2 \eta \kappa^2} \sqrt{\frac{f}{f_c}} \right] = \bar{v}_{1m}^2 \left[1 + \frac{16c^2}{\pi^3 L_y^2 \eta f^{1/2} f_c^{3/2}} \right] \quad (13.106)$$

Thus, by constraining the boundary condition the frequency average of the modal velocity squared of the panel and the radiated acoustical power are increased. For a sliding edge, the panel movement can adjust to the pressure field exciting the structure. The pressure field and the panel motion are for that case described by means of the same eigenfunctions. This increases the inertia of the structure and thus its apparent mass. The edge effect is decreased as the dimension L_y is increased or when the frequency is increased or the critical frequency is decreased. The sound radiation ratio discussed in Sect. 12.9 showed a similar behavior.

Super-imposing two perpendicular wave motions writes the modal energy of a rectangular panel

$$\bar{v}_{mn}^2 = \bar{v}_{0mn}^2 \left[1 + \frac{32}{\pi \eta \kappa^2} \sqrt{\frac{f}{f_c}} \left(\frac{1}{L_y^2} + \frac{1}{L_z^2} \right) \right] = \bar{v}_{0mn}^2 \Lambda \quad (13.107)$$

The total perturbation is due to one half of the contributions from each of the two directions.

A similar approach can be followed to describe the effect of changing the boundary conditions of a rectangular plate with sliding edges to simply supported edges. See also Problem 13.8. The result is

$$\bar{v}_{mn}^2 = \bar{v}_{0mn}^2 \left[1 + \frac{8}{\pi \eta \kappa^2} \sqrt{\frac{f}{f_c}} \left(\frac{1}{L_y^2} + \frac{1}{L_z^2} \right) \right] = \bar{v}_{0mn}^2 \Lambda \quad (13.108)$$

By writing $\kappa = 2\pi\sqrt{f \cdot f_c}/c$, where c is the speed of sound of the fluid, the expression for Λ is for air at room temperature reduced to

$$\Lambda(S) = 1 + \frac{3 \cdot 10^4}{4\eta \cdot f^{1/2} \cdot f_c^{3/2}} \left(\frac{1}{L_y^2} + \frac{1}{L_z^2} \right)$$

The panel dimensions L_x and L_y are in m and the frequencies in Hz. The panel area S is defined as $S = L_y \cdot L_z$. The resulting pressure squared in the receiving room due to the non-resonant transmission through the plate is

$$\langle \bar{p}_2^2 \rangle = \bar{p}_0^2 \Lambda$$

where \bar{p}_0^2 is the resulting pressure induced by a plate with sliding edges. Let the contribution from the resonant transmission be $\bar{p}_0^2 G$. The resonant transmission and thus also the function G is independent of the boundary conditions of the plate. Following the discussion in Sect. 13.3 and Eq. (13.83) the function G is written

$$G = \int_0^{\pi/2} \frac{\sin \varphi d\varphi}{\left[\left(\frac{f}{f_c} \right)^2 \sin^4 \varphi - 1 \right]^2 + \left[\eta \left(\frac{f}{f_c} \right)^2 \sin^4 \varphi \right]^2} - 1 \quad (13.109)$$

It is apparent that the function G tends to zero as the frequency f decreases. As the frequency increases and gets close to the critical frequency f_c , the function G grows rapidly. The approximate result at $f = f_c$ is $G \approx \pi/(4\eta^{3/2})$. The function G is given in Appendix A, Table A.1 for some typical loss factors.

The sound transmission loss R of a rectangular and homogeneous single leaf panel mounted between two rooms as shown in Fig. 13.4 and discussed in Sect. 13.3 can be written as

1. $f < f_c$

$$R = 20 \log \mu + 20 \log f - 10 \log[\Lambda(S) + G] - 48 \text{ dB}$$

Sliding edges $\Lambda(S) = 1$

Simply supported edges $\Lambda(S) = 1 + \frac{3 \cdot 10^4}{4\eta \cdot f^{1/2} \cdot f_c^{3/2}} \left(\frac{1}{l_y^2} + \frac{1}{l_z^2} \right)$

Clamped edges $\Lambda(S) = 1 + \frac{3 \cdot 10^4}{\eta \cdot f^{1/2} \cdot f_c^{3/2}} \left(\frac{1}{l_y^2} + \frac{1}{l_z^2} \right) \quad (13.110)$

The plate dimensions, expressed in m, are l_y and l_z . In this particular case $l_y = L_y$ and $l_z = L_z$ where L_y and L_z are the cross dimensions of the rooms.

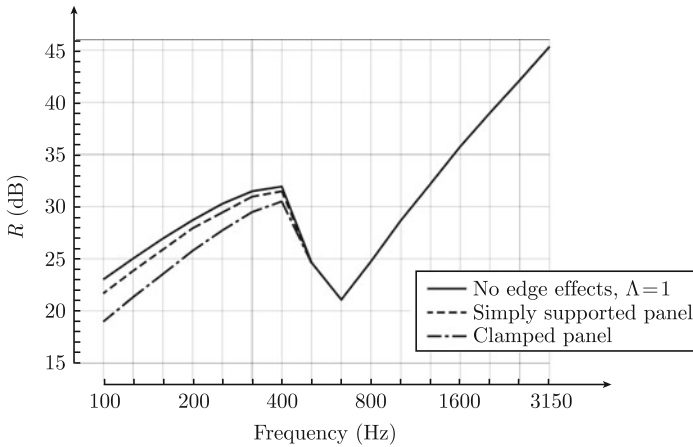


Fig. 13.6 Predicted sound transmission loss of a lightweight concrete wall. $\mu = 41 \text{ kg/m}^2$, $f_c = 570 \text{ Hz}$, $\eta = 2.5 \%$, $L_y = 4.5 \text{ m}$ and $L_z = 2.8 \text{ m}$

2. $f > f_c$

$$R = 20 \log \mu + 30 \log f - 10 \log f_c + 10 \log \eta + 5 \log(1 - f_c/f) - 47 \text{ dB} \quad (13.111)$$

The mass μ per unit area is in kg/m^2 . The frequencies are in Hz. The results for $f < f_c$ clearly shows that as the boundary conditions are constrained the sound transmission loss of the structure is decreased. By constraining the boundary conditions, the inertia of the panel and thus its apparent mass is decreased. The effect of the boundary conditions is most pronounced for small and stiff panels. For very large panels, the boundary effects are negligible. The loss factor of panels is discussed in Sect. 13.9.

The predicted sound transmission loss for a lightweight concrete wall is shown in Fig. 13.6 for three different boundary conditions. The parameters for the wall are $\mu = 41 \text{ kg/m}^2$, $f_c = 570 \text{ Hz}$, $\eta = 2.5 \%$, $L_y = 4.5 \text{ m}$ and $L_z = 2.8 \text{ m}$. The sound reduction index is calculated in 1/3 OB.

13.7 Effect of a Baffle on Sound Transmission Loss

The pressure squared in the receiving room was in Sect. 13.6 assumed to be proportional to $|\bar{v}_{mn}^2|$ where $v_{mn} = \langle v | \varphi_{mn} \rangle$. In Eq. (13.108) the square of the expansion coefficients were written as

$$|\bar{v}_{mn}^2| = \Lambda(S) |\bar{v}_{0mn}^2|$$

The parameter $\Lambda(S)$ is determined by the boundary conditions and the dimensions of the plate. The expansion coefficients v_{0mn} are the expansion coefficients of the panel velocity v_1 , Eq. (13.99), which is the particular solution to Eq. (13.98). The velocity v_1 has the same mode shape as the cross mode in the room. Thus

$$v_{0mn} = \langle v_1 | \varphi_{mn} \rangle \tag{13.112}$$

The motion v_1 is in the low frequency region or rather for the non-resonant contribution given by

$$v_1 = - \sum_{qr} \frac{Q_{qr}}{\kappa^4} \cdot \varphi_{qr} \tag{13.113}$$

where φ_{qr} is defined in Eq. (13.44). For frequencies well below coincidence the source coefficients are defined for $0 \leq q \leq M$ and $0 \leq r \leq N$ where

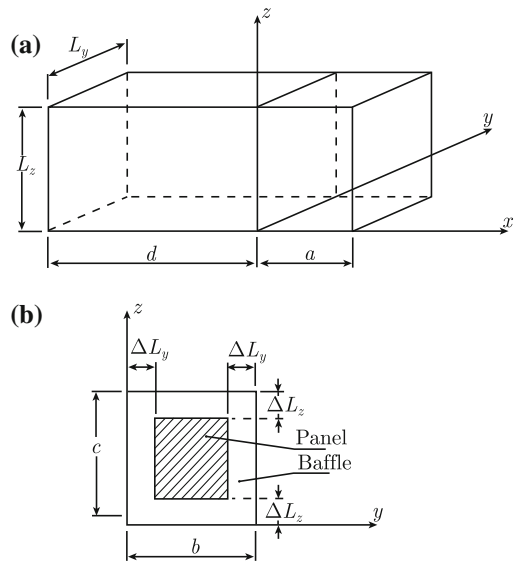
$$\left(\frac{M\pi}{L_y} \right)^2 + \left(\frac{N\pi}{L_z} \right)^2 = k^2$$

where k is the wave number in the fluid.

For a panel in baffle as shown in Fig. 13.7, the panel velocity is defined for $\Delta L_y \leq y \leq L_y - \Delta L_y$ and $\Delta L_z \leq z \leq L_z - \Delta L_z$. The parameters v_{0mn} are obtained from (13.112) and (13.113) as

$$v_{0mn} = \langle v_1 | \varphi_{mn} \rangle_S = - \sum_{qr} \frac{Q_{qr}}{\kappa^4} \cdot \langle \varphi_{qr} | \varphi_{mn} \rangle_S \tag{13.114}$$

Fig. 13.7 A panel mounted in a baffle between two rooms



The subscript S indicates that the integration of the eigenfunctions should be carried over the panel surface, i.e., for $\Delta L_y \leq y \leq L_y - \Delta L_y$ and $\Delta L_z \leq z \leq L_z - \Delta L_z$. Assuming again that the parameters Q_{rs} are uncorrelated and having the same absolute value $|Q|$ it follows from Eq. (13.114) that

$$|\bar{v}_{0mn}|^2 = \left| \frac{Q}{\kappa^4} \right|^2 \sum_{qr} |\langle \varphi_{qr} | \varphi_{mn} \rangle_S|^2 \quad (13.115)$$

Assuming the natural frequencies in the receiving room and the natural frequencies of the panel to be uncorrelated then the room and panel response can be averaged separately over frequency. Thus, the average pressure squared in the receiving room is proportional to the sum of the square of the coefficients v_{mn} . This means that if all parameters except the panel area are kept constant then according to the Eqs. (13.65) and (13.115), the resulting space and frequency average of the pressure squared is proportional to a function

$$H(S) = \Lambda(S) \cdot \sum_{mn}^{MN} \sum_{qr}^{MN} |\langle \varphi_{qr} | \varphi_{mn} \rangle_S|^2 \quad (13.116)$$

Keeping the room dimensions constant and decreasing the panel area by mounting the panel in a baffle the frequency and space average of the pressure squared in the receiving room is change from $\langle |\bar{p}_2|^2 \rangle_0$ to $\langle |\bar{p}_2|^2 \rangle$ where

$$\langle |\bar{p}_2|^2 \rangle = \langle |\bar{p}_2|^2 \rangle_0 \cdot \frac{H(S)}{H(S_0)} \quad (13.117)$$

The area of panel plus baffle is S_0 and the area of the panel is $S \leq S_0$.

Introducing the parameters D and E as

$$D = \frac{\pi(L_y - 2\Delta L_y)}{L_y} = \frac{\pi l_y}{L_y}; \quad E = \frac{\pi(L_z - 2\Delta L_z)}{L_z} = \frac{\pi l_z}{L_z}$$

and after some effort, see Ref. [180], the function $H(S)$ is written as

$$H(S) = \Lambda(S) \cdot \left(\frac{S}{S_0} \right)^2 \cdot (1 + M_1)(1 + N_1) [1 + Z(MD)] \cdot [1 + Z(NE)] \quad (13.118)$$

where

$$M = \frac{\sqrt{\pi} L_y f}{c}; \quad M_1 = \text{Integer}(M); \quad M_2 = \text{Integer}(M/2)$$

$$M_3 = \text{Integer}(M - 2); \quad M_4 = \text{Integer}\left(\frac{M - m}{2}\right); \quad \xi_m = (-1)^m \quad (13.119)$$

The function $Z(MD)$ is given by

$$Z(MD) = \frac{1}{1 + M_1} \left\{ \sum_{m=1}^{M_1} \left[\left(\frac{\sin(mD)}{mD} \right)^2 + 2\xi_m \frac{\sin(mD)}{mD} \right] + 4 \sum_{m=1}^{M_2} \left(\frac{\sin(mD)}{mD} \right)^2 \right\} \\ + \frac{2}{1 + M_1} \left\{ \sum_{m=1}^{M_3} \sum_{l=1}^{M_4} \left[\xi_m \frac{\sin[(m+l)D]}{(m+l)D} + \frac{\sin(lD)}{lD} \right]^2 \right\} \quad (13.120)$$

The function $Z(NE)$ is defined in a similar way with $N = \sqrt{\pi}L_z f/c$, $N_1 = \text{Integer}(N)$, etc. The expression is readily solved numerically. However, for the sake of simplicity some results are tabulated in Appendix A, Table A.2. In the table, the expression $Z(MD)$ is given as function of the product $f \cdot L_y$ for various values of $X = (L_y - 2\Delta L_y)/L_y = l_y/L_y$.

The sound pressure level difference between two rooms is partly determined by the ratio $H(S)/H(S_0)$ where the function $H(S)$ is defined in Eq. (13.118). For the case the panel is mounted without a baffle the parameters $D = E = \pi$ resulting in $Z(MD) = 0$ and $Z(NE) = 0$. Consequently $H(S_0) = \Lambda(S_0)(1 + M_1)(1 + N_1)$. The corresponding expression $H(S)$ is for $0 \leq S \leq S_0$ given by

$$H(S) = \Lambda(S)(1 + M_1)(1 + N_1)[1 + Z(MD)][1 + Z(NE)] \cdot S^2/S_0^2$$

For non-resonant transmission the ratio between the radiated acoustic power from a panel with the area $S < S_0$ and a panel with the area S_0 is

$$\frac{H(S)}{H(S_0)} = \frac{\Lambda(S)}{\Lambda(S_0)} \left(\frac{S}{S_0} \right) \Gamma(S); \quad \Gamma(S) = \left(\frac{S}{S_0} \right) \cdot [1 + Z(MD)] \cdot [1 + Z(NE)] \\ S_0 = L_y \cdot L_z; \quad S = l_y \cdot l_z \quad (13.121)$$

The corresponding result for resonant transmission is $H(S)/H(S_0) = S/S_0$. Thus in the high frequency range, $f > f_c$, the acoustic power is just proportional to the area of the radiating panel.

A number of limiting values for the various functions are discussed in [180]. For small baffles $\Delta L_y/L_y < 1/10$ and $\Delta L_z/L_z < 1/10$ the functions $Z(MD)$ and $Z(NE)$ are rather small for low frequencies. In the high frequency region and for very large baffles the functions $Z(MD)$ and $Z(NE)$ are small or in fact negligible. This means the sound transmission loss of a panel mounted without a baffle is almost the same as the sound reduction index for the same panel when mounted in a very large baffle. See Table A.2 in Appendix A. The parameter $H(S)$ can be shown to vary as $1 \geq \Gamma(S) \geq S/(4S_0)$.

The sound transmission loss for a panel can now be written as

$$\begin{aligned}
 R &= 20 \log \mu + 20 \log f - 10 \log[\Gamma \cdot \Lambda(S) + G] - 48 \text{ dB for } f < f_c \\
 R &= 20 \log \mu + 30 \log f - 10 \log f_c + 10 \log \eta \\
 &\quad + 5 \log(1 - f_c/f) - 47 \text{ dB for } f > f_c
 \end{aligned}
 \tag{13.122}$$

The functions $\Gamma(S)$, $\Lambda(S)$ and G are defined in Eqs. (13.121), (13.110) and (13.109) respectively.

In Fig. 13.8, the predicted sound reduction index for a clamped gypsum-board is shown as function of the panel area. The dimensions $L_y = 5.45 \text{ m}$ and $L_z = 3.5 \text{ m}$ are kept constant. The material parameters for the panel are $\mu = 10.1 \text{ kg/m}^2$, $f_c = 2350 \text{ Hz}$. The loss factor of the panel is shown in the graph. Comparisons with measurements are discussed in Sect. 13.8.

The sound pressure level in a room has always maxima close to walls and corners. In the low frequency domain there are only a few modes in the room. Consequently, the high sound pressure area close to a wall can be quite distinct. Consider for example the (1, 1, 1) mode for which the pressure on the plate shown in Fig. 13.7 is proportional to $\cos(\pi y/L_y) \cdot \cos(\pi z/L_z)$. By mounting a panel in a baffle the high sound pressure levels close to the adjoining walls do not excite the panel at all.

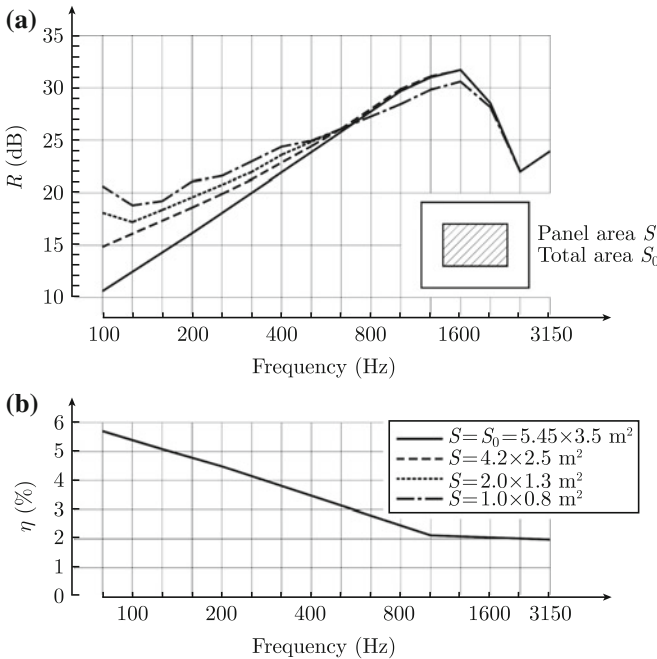


Fig. 13.8 Predicted sound transmission loss of a clamped gypsum-board panel; $\mu = 10.1 \text{ kg/m}^2$, $f_c = 2350 \text{ Hz}$, $S_0 = 5.45 \times 3.5 \text{ m}^2$, loss factor shown in graph (b)

The apparent sound transmission loss therefore seems to be higher than for the same panel without a baffle. However, as the frequency is increased the number of modes exciting the plate is also increased and the baffle effect is decreased.

The results discussed in Sects. 13.1 through 13.7 show that the sound transmission loss of a single leaf panel depends on a number of material parameters like mass per unit area, stiffness, loss factor, boundary conditions, and dimensions and in addition also the respective geometries of the transmission rooms. In the literature, it is agreed that the sound reduction index of a panel is independent of boundary conditions and baffle effects for frequencies above the critical frequency. Below coincidence there are a number of models (Refs. [176–178, 180]) describing the effects of boundary conditions and panel dimensions on the sound transmission loss. In principal, the end results are rather similar. The sound transmission loss is decreased as the boundary conditions of the plate are constrained and also the sound transmission loss is decreased in the low frequency region as the plate dimensions are decreased for a plate mounted in an infinite baffle. In the low frequency range, a finite baffle increases the sound transmission loss.

In the low frequency region, the results given in [179] agree very well with the results of Eq. (13.122). The effect of the boundary conditions was in Sect. 13.6 as well as in Refs. [176, 177] found to decrease as the frequency is increasing toward the critical frequency. These findings are confirmed by measurements. It is shown in Fig. 13.8 that a baffle can increase the apparent sound transmission loss of a panel. The importance of a baffle on the sound transmission loss of a panel has also been reported in Refs. [176, 177].

13.8 Measurement Results

The boundary conditions clamped and simply supported are naturally difficult or impossible to reproduce for a panel mounted in a standard sound transmission laboratory. However, Fig. 13.9 shows the measured sound transmission losses for a panel first firmly and then resiliently mounted in a test opening of a transmission laboratory. Only the boundary conditions are different for the two measurements. The mass of the chipboard panel was 22 kg/m^2 and its critical frequency 720 Hz. The measurement procedure and mounting conditions are described in Refs. [180, 182]. Diffusers were mounted in both transmission rooms during all measurements. The results indicate, as predicted by Eq. (13.110), that the sound transmission loss for the panel is increased below coincidence as the boundary conditions are changed from firm to elastic mounting. The difference is decreasing as the frequency is approaching the critical frequency. Above coincidence the sound transmission loss is more or less independent of boundary conditions.

A resilient mounting can also have positive effects on the sound reduction index even in the high frequency region. For example, comparing the reduction index for a glass plate firmly mounted or resiliently mounted to a frame, the sound reduction index for the resiliently mounted plate is found to be higher than the result for the

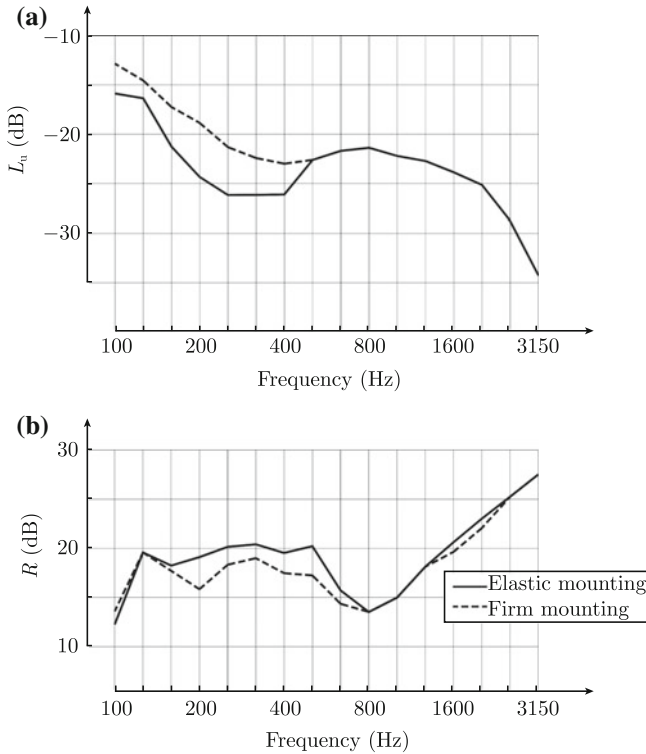


Fig. 13.9 Measured sound transmission loss and velocity level of a chip board panel; $\mu = 22 \text{ kg/m}^2$, $f_c = 720 \text{ Hz}$

clamped panel. Below the critical frequency, the result is a consequence of the relaxed boundary condition as discussed in Sect. 13.6. The resilient mounting if achieved by means of a rubber lining is likely to increase the losses of the panel and thus also the sound transmission loss above the critical frequency.

The effect of a baffle is shown in Fig. 13.10. A lightweight concrete wall, $\mu = 41 \text{ kg/m}^2$, $f_c = 570 \text{ Hz}$, is firmly mounted in a frame as shown in Fig. 13.10 (A). Thereafter the frame is hidden by wedges made of chipboard resulting in a configuration denoted Lab. B. The loss factors of the panel was measured in 1/3 OB giving $\eta = 2.5\%$ for $f < 315 \text{ Hz}$, $\eta = 1.9\%$ for $f = 315 \text{ Hz}$ and $\eta = 1.7\%$ for $f > 315 \text{ Hz}$. Predicted and measured results agree fairly well and show that the sound transmission loss of the panel is increased due to the baffle for frequencies below the critical frequency. There is no significant difference between the two cases in the high frequency region.

The predicted sound transmission loss for a panel with varying area was shown in Fig. 13.8. Measurements were carried out on a clamped gypsum panel mounted without a baffle between two transmission rooms. The baffle surrounding the panel was gradually made larger and the panel area smaller without otherwise changing

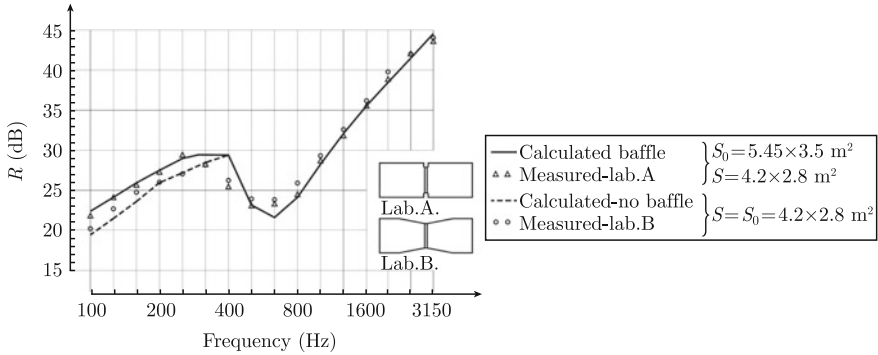


Fig. 13.10 Measured and predicted sound transmission losses for a baffled and unbaffle firmly mounted plate of lightweight concrete; $\mu = 41 \text{ kg/m}^2$, $f_c = 570 \text{ Hz}$, $\eta = 2.5\%$ for $f < 315 \text{ Hz}$, $\eta = 1.9\%$ for $f = 315 \text{ Hz}$ and $\eta = 1.7\%$ for $f > 315 \text{ Hz}$

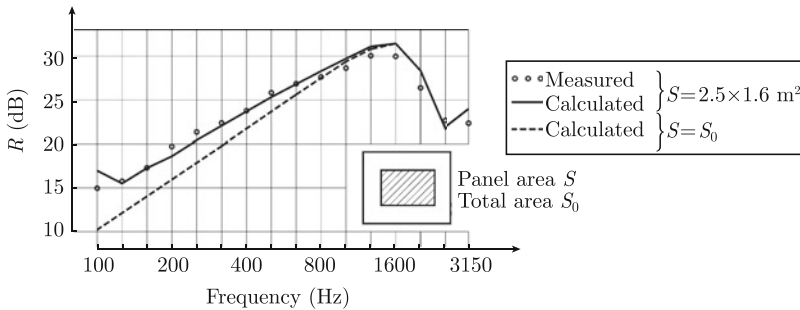


Fig. 13.11 Predicted sound transmission loss for a clamped gypsum-board panel; $\mu = 10.1 \text{ kg/m}^2$, $f_c = 2350 \text{ Hz}$, $S_0 = 5.45 \times 3.5 \text{ m}^2$, loss factor shown in Fig. 13.8b)

the mounting, room or panel parameters. Predicted and measured results are shown in Figs. 13.11 and 13.12.

A so-called niche can also have an effect on the measured sound transmission loss of a structure. Three configurations have been tested. In the first case, a wall was mounted in a frame with a baffle. A niche around the panel was thereafter mounted on one side of the panel and the measurements were repeated. An additional niche was thereafter mounted on the other side of the wall. The results shown in Fig. 13.13 show that a niche tends to increase the sound transmission loss of a panel in the low frequency region. In particular, an asymmetric niche can increase the transmission loss significantly. Similar results were obtained by Gösele [183].

All the effects discussed, geometry of rooms, baffle, and niche effects and boundary conditions can in a very critical way influence the measured sound transmission loss of a structure as revealed in a round robin test reported in Ref. [180, 182]. A certain number of single leaf partitions were tested in six laboratories all satisfying the existing ISO recommendations. Schematic drawings of the laboratories are shown

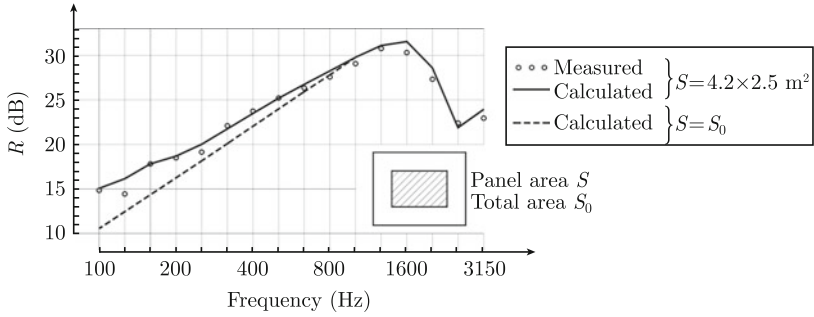


Fig. 13.12 Predicted sound transmission loss for a clamped gypsum-board panel; $\mu = 10.1 \text{ kg/m}^2$, $f_c = 2350 \text{ Hz}$, $S_0 = 5.45 \times 3.5 \text{ m}^2$, loss factor shown in Fig. 13.8b)

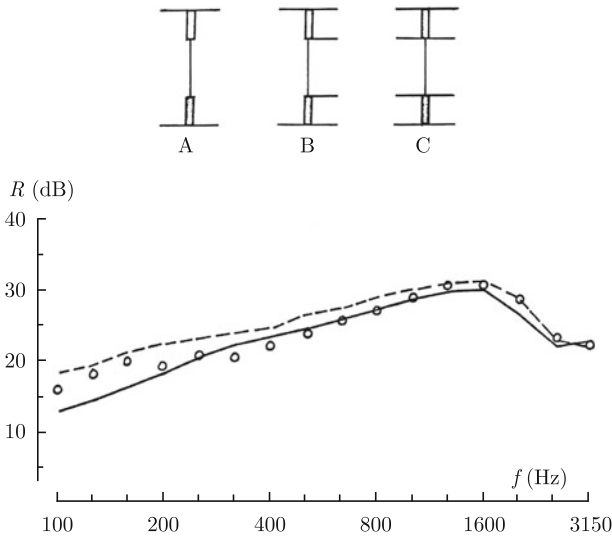


Fig. 13.13 Measurements of sound transmission loss of a panel mounted with **a** no niche —; **b** a niche on one side ---; **c** niches on both sides ○○○

in Fig. 13.14. The same structures were used for all measurements. The mounting procedures of the structures were described in detail. Materials and linings for the mounting of the panels in each laboratory were also identical. The number of microphone positions used during the measurements was much higher than prescribed in the existing ISO recommendations.

The results of one set of measurements are shown in Fig. 13.15. The spread of the results is quite discouraging. However, it is noted that the measured sound transmission loss in Lab 1B is the lowest. In this laboratory there no baffles and no niches. The highest sound transmission loss is measured in Lab. 3. In this laboratory, there is a very deep niche and in addition a substantial frame around the test specimen. In other cases,

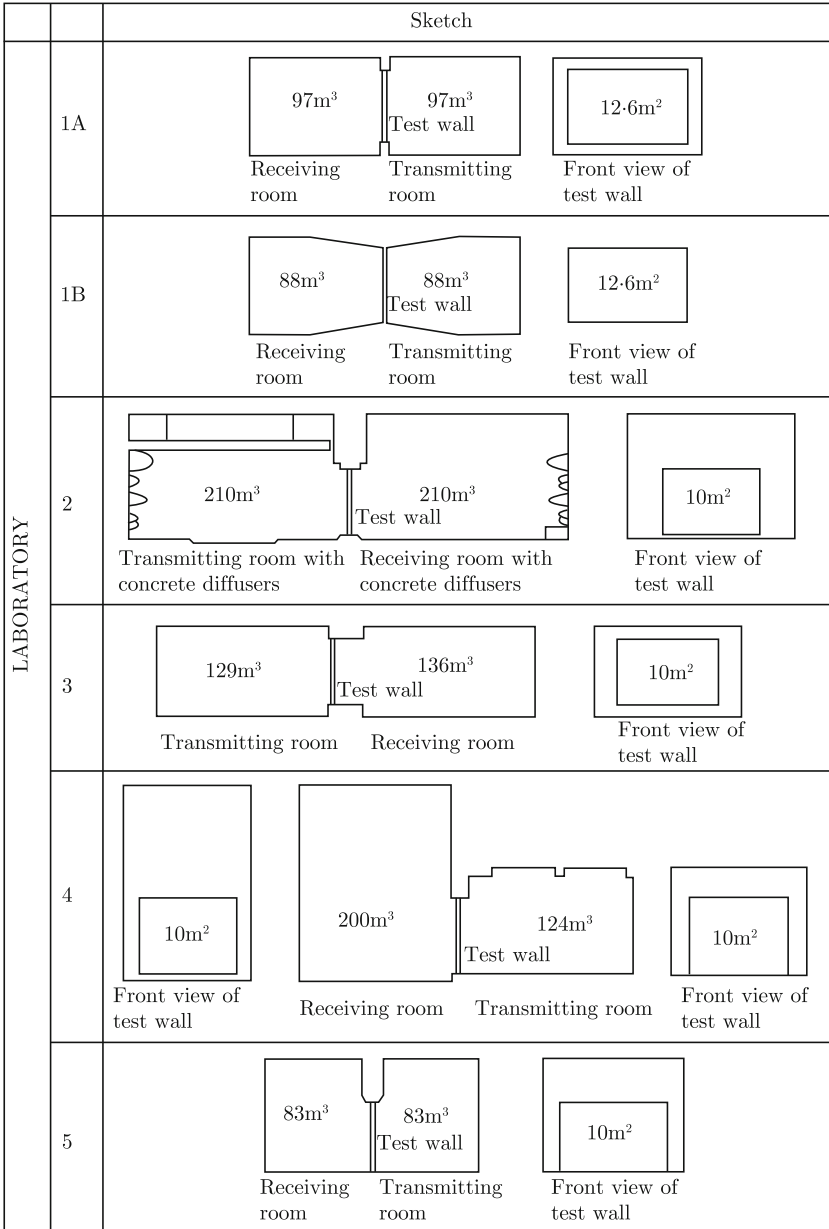


Fig. 13.14 Schematic drawings of the laboratories participating in round robin test

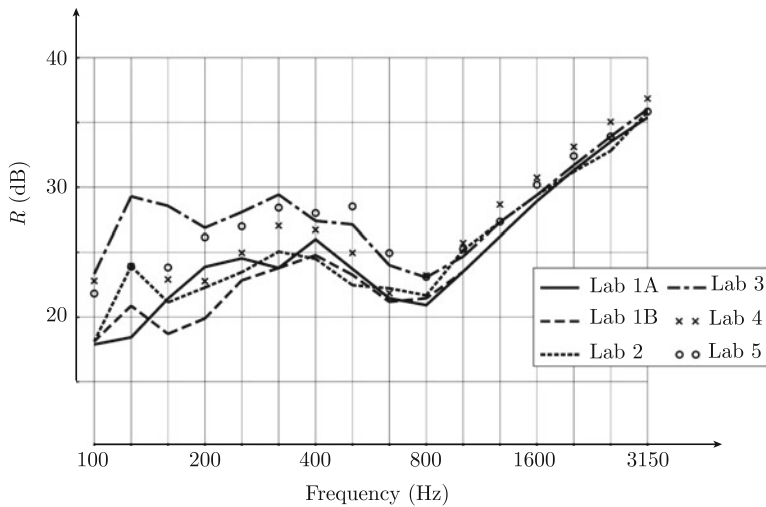


Fig. 13.15 Measured sound transmission loss for a firmly mounted chipboard panel; $\mu = 22 \text{ kg/m}^2$, $f_c = 720 \text{ Hz}$

frames or niches of varying degree do influence and in fact increase the measured sound reduction index with respect to the results obtained in Lab 1B having no niches or baffles. In all cases, there were sound diffusers in the measurements rooms to avoid coupling effects between equal rooms discussed in Sect. 13.4. The results shown in Fig. 13.15 also indicate that the differences between the measured results decrease as the frequency is increasing and approaching the critical frequency. For $f > f_c$ the discrepancies between the results are small. All this is in agreement with the results presented in Sects. 13.6 and 13.7.

13.9 Loss Factors and Summary

A general observation comparing any measured and predicted sound transmission losses is that predicted sound transmission losses at and around the critical frequency are underestimated. This problem has been investigated by Feng in Ref. [184]. Typically, a loss factor of a plate is measured in situ by means of reverberation time measurements. The losses are determined in 1/3 OB. In general, transmission losses to adjoining structures and internal losses determine the total losses. However, for frequencies close to the critical frequency the radiation losses can be significant. Vibration modes having a high loss factor due to radiation are attenuated rapidly. The vibration modes having a low loss factor will therefore determine the reverberation time in the frequency bands close to the critical frequency. The loss factor due to radiation from two sides of a structure is according to Eq. (12.119) given as

$\eta_r = 2\rho_0 c \bar{\sigma}_r / (\mu\omega)$ where $\bar{\sigma}_r$ is the sound radiation ratio for the structure and given in Eqs. (12.98) through (12.100) for flat rectangular plates. It is suggested in [184] that the loss factor for a panel should be written

$$\eta = \eta_{\text{measured}} + 2\rho_0 c \bar{\sigma}_r / (\mu\omega)$$

It could be argued that for the radiation ratio $\bar{\sigma}_a$ rather than $\bar{\sigma}_r$ should be used. However, for frequencies close to the critical frequency $\bar{\sigma}_r$ and $\bar{\sigma}_a$ are rather similar. The sound radiation ratio induced by an acoustic field is given by $\bar{\sigma}_a$ and is discussed for an infinite plate in Sects. 13.2 and 13.9 for a finite plate. See also Sect. 16.7.

The sound transmission loss R for a single leaf and rectangular plate, dimensions l_y and l_z , mounted between two rooms, width L_y and height L_z , can be written as:

1. $f < f_c$

$$R = 20 \log \mu + 20 \log f - 10 \log[\Gamma \cdot \Lambda(S) + G] - 48 \text{ dB}$$

Sliding clamped edges, Fig. 8.2

$$\Lambda = 1$$

Simply supported edges

$$\Lambda = 1 + \frac{3 \cdot 10^4}{4\eta \cdot f^{1/2} \cdot f_c^{3/2}} \left(\frac{1}{l_y^2} + \frac{1}{l_z^2} \right)$$

Clamped edges

$$\Lambda = 1 + \frac{3 \cdot 10^4}{\eta \cdot f^{1/2} \cdot f_c^{3/2}} \left(\frac{1}{l_y^2} + \frac{1}{l_z^2} \right)$$

Baffle effects, see Table A.2, Appendix A

$$\Gamma(S) = [1 + Z(MD)][1 + Z(NE)]; \quad D = \frac{\pi l_y}{L_y}; \quad E = \frac{\pi l_z}{L_z}$$

Resonant transmission function, see Table A.1, Appendix A

$$G = \int_0^{\pi/2} \frac{\sin \varphi d\varphi}{\left[\left(\frac{f}{f_c} \right)^2 \sin^4 \varphi - 1 \right]^2 + \left[\eta \left(\frac{f}{f_c} \right)^2 \sin^4 \varphi \right]^2} - 1$$

2. $f > f_c$

$$R = 20 \log \mu + 30 \log f - 10 \log f_c + 10 \log \eta + 5 \log(1 - f_c/f) - 47 \text{ dB} \quad (13.123)$$

Loss factor, all frequencies $\eta = \eta_{\text{measured}} + 2\rho_0 c \bar{\sigma}_r / (\mu\omega)$

Radiation ratio $\bar{\sigma}_r$ given by Eqs. (12.98)–(12.100).

The sound transmission loss close to and at the critical frequency should be determined by the maximum value of R for $f < f_c$ and $f > f_c$ as f tends to f_c . Measurement results reveal that predicted sound transmission losses close to the critical frequency typically are too low. One reason for this is that the bending stiffness of a real plate varies across the structure due to material imperfections, variation

of thickness or due to some slight curvature of the plate. The critical frequency is a function of the bending stiffness. If for example the bending stiffness is assumed to vary by a certain percentage, the resulting sound transmission loss of the structure can be derived as an average of these variations.

The response or rather average velocity squared of a plate excited by an acoustic field is discussed in Ref. [180]. Results are given for different boundary conditions of the plate. The effects of baffles are also discussed in [180]. The frequency and space average of the plate velocity is given by the quantity

$$L_{v/p} = 10 \log \left[\frac{(\rho_0 c)^2 \langle \bar{v}^2 \rangle}{\langle \bar{p}_1^2 \rangle} \right] \quad (13.124)$$

where $\langle \bar{p}_1^2 \rangle$ is the frequency and space average of the pressure squared in the source room. According to Ref. [180] the quantity $L_{v/p}$ is for an unbaffled rectangular panel given by

1. $f < f_c$

$$L_{v/p} = 39 - 20 \log \mu - 20 \log f - 10 \log [T + G] \text{ dB}$$

Sliding clamped edges, Fig. 8.2

$$T = 1$$

Simply supported edges

$$T = 1 + \frac{50}{\eta \cdot f^{1/2} \cdot f_c^{1/2}} \left(\frac{1}{l_y} + \frac{1}{l_z} \right)$$

Clamped edges

$$T = 1 + \frac{100}{\eta \cdot f^{1/2} \cdot f_c^{1/2}} \left(\frac{1}{l_y} + \frac{1}{l_z} \right)$$

2. $f > f_c$

$$L_{v/p} = 41 - 20 \log \mu - 30 \log f + 10 \log f_c - 10 \log \eta \quad (13.125)$$

Compare Fig. 13.9a. The sound radiation ratio for a rectangular plate without a baffle is obtained from (13.124) and (13.125) as

$$\bar{\sigma}_a = \frac{2(\Lambda + G)}{T + G} \text{ for } f < f_c$$

$$\bar{\sigma}_a = \frac{1}{\sqrt{1 - f_c/f}} \text{ for } f > f_c \quad (13.126)$$

The velocity level of a plate mounted in a baffle is given in Appendix B. Predicted results are shown in Fig. 13.16.

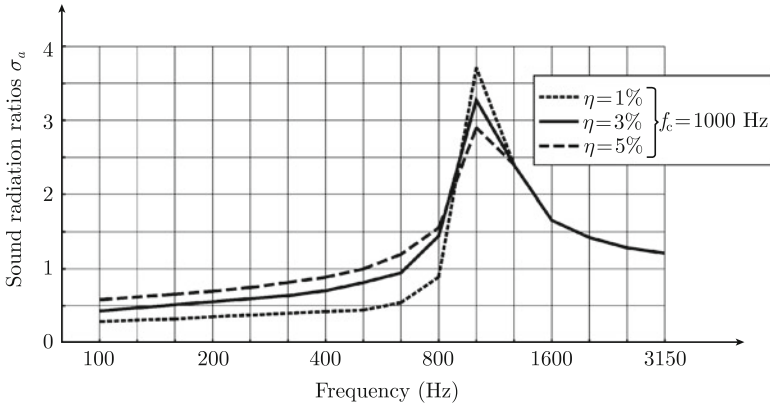


Fig. 13.16 Predicted sound radiation ratio σ_a for a clamped and unbaffled panel, $L_y = 4.5$ m, $L_z = 2.8$ m. The panel is excited by an acoustic field

13.10 Sound Transmission Through Complex Structures

Frames or beams often stiffen partitions in vehicles. These stiffeners influence the sound transmission through the structure. This is illustrated in Fig. 13.17 from Ref. [185]. The sound transmission loss is first measured for a simple 4 mm Al-plate. The

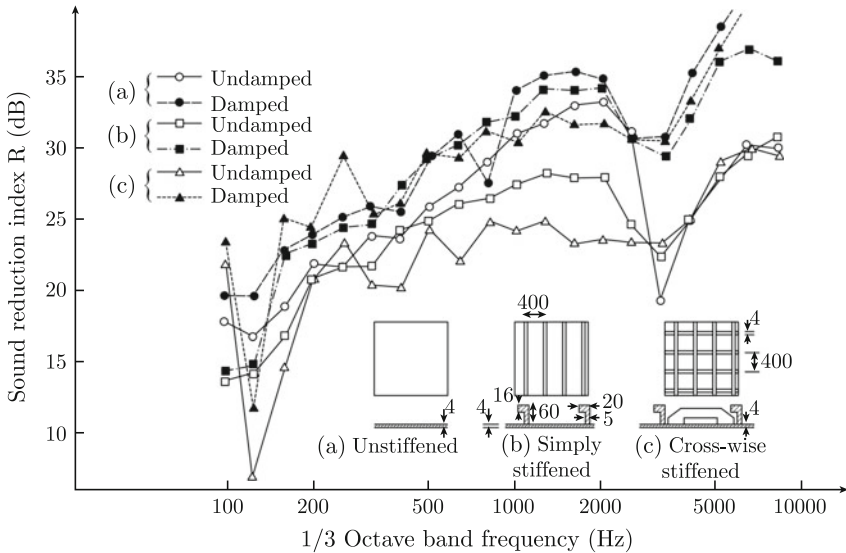


Fig. 13.17 Measured sound transmission loss of unribbed and ribbed, damped and undamped 4 mm Al plates. From Ref. [185]

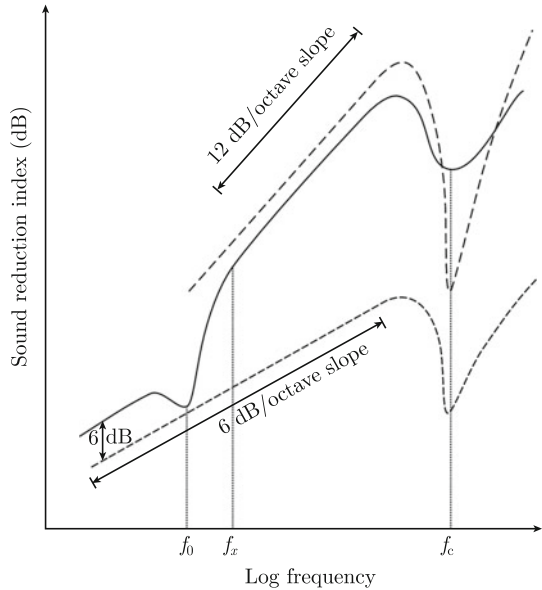
plate is thereafter stiffened by vertical ribs and finally also by horizontal ribs. For the undamped plate, it is found that the transmission loss is decreased as the panel is stiffened. In the low frequency region, the transmission loss for the stiffened plate has distinct minima just above 100 Hz. These dips correspond to the first natural frequency of the sub-element between the stiffeners. Well above this first natural frequency, the transmission loss is mainly determined by the various sub-elements. The transverse motion along the ribs is comparatively small. Compare the discussion in Sect. 8.7. The plate elements are more or less clamped along the ribs. These boundary conditions will reduce the inertia of the plate and thus also its apparent mass and consequently also the sound transmission of the structure. Returning to the Sect. 13.9 and the sound transmission loss, Eq. (13.123) it is found that the parameter Λ is increased as the dimensions of the sub-element are decreased and also when the boundary conditions of the element is constrained. As Λ increases, the sound transmission loss of the structure decreases. As damping is added to the structure the parameter Λ is decreased and thus the transmission loss increased. If the sub-element is surrounded by other elements or if the entire ribbed construction is mounted in a large frame or baffle the parameter Γ in Eq. (13.123) is close to unity. The effect of the added damping is most pronounced at the first natural frequency of the sub-elements. The resonant transmission is also decreased as the damping is increased. The parameter G in (13.123) is decreased as the losses are increased. Consequently, the added damping will increase the sound transmission loss in the entire frequency range. The loss factor for an Al-plate is in general very low. Therefore, the added damping can have a positive effect even in the low frequency region. However, for a large structure with a rather high loss factor the effect of added damping is insignificant for $f < f_c/2$.

The sound transmission loss of a single leaf panel is in principle only increased by 6 dB due to the doubling of the mass of the panel for $f < f_c$. This type of increase of the sound transmission loss is often unacceptable due to weight constraints. The use of double structures is an alternative to drastically increase the sound transmission loss while keeping the weight low. A double structure is quite simply two single leaf panels separated by an air filled cavity or a cavity with some sound absorbing material. An example of the first is an ordinary window with double-glazing. The vibration of a double structure was discussed in Sect. 7.9 and illustrated in Fig. 7.14. When a coupled double structure is excited on one side, the coupled structures move almost in phase in the low frequency region. As the frequency is increased the structures start moving in antiphase and having a large amplitude close to and at the double resonance f_0 . Well above this frequency, the velocity level difference between the coupled plates is increasing as approximately $40 \log(f/f_0)$ up to certain limit determined by the added sound transmission loss achieved by the two panels separated by a cavity with a certain sound absorption. The resulting sound transmission loss of a double structure is schematically shown in Fig. 13.18.

In the low frequency range, $f < f_0$ the double structure vibrates as a single structure with the mass equal to the total mass of the two partitions. Thus

$$R_I = 20 \log(\mu_1 + \mu_2) + 20 \log f - 49 \text{ dB for } f < f_0 \quad (13.127)$$

Fig. 13.18 Schematic drawing of the sound transmission loss of a double leaf construction



In the frequency region $f_x > f > f_0$ the transmission loss increases by an added $40 \log(f/f_0)$. Thus

$$R_{II} = 20 \log(\mu_1 + \mu_2) + 20 \log f + 40 \log(f/f_0) - 49 \text{ dB for } f_x > f > f_0 \tag{13.128}$$

In the very high frequency range $f > f_x$ the total transmission is the sum of the transmission for each panel plus a correction for absorption in the cavity. The result is

$$R_{III} = R_1 + R_2 + 6 \text{ dB for } f > f_x \tag{13.129}$$

The correction term of 6 dB is often explained by claiming that the sound absorption between the plates make the sound field in the cavity non-diffuse. The absorbent rather effectively attenuates the modes propagating parallel to the plates. Hence, the acoustical intensity incident on the second plate has close to normal incidence. The sound transmission for normal incidence is about 5 dB higher than the transmission loss for diffuse incidence.

The frequency f_x is the solution to $R_{II}(f_x) = R_{III}(f_x)$. Compare Problem 13.9. Assuming the cavity between the plates being filled with a gas, density ρ_0 and speed of sound c , the double wall resonance f_0 is

$$f_0 = \frac{1}{2\pi} \left[\frac{\rho_0 c^2 (\mu_1 + \mu_2)}{d \mu_1 \mu_2} \right]^{1/2} \tag{13.130}$$

where d is the distance between the two plate elements. Compare Problem 13.10. The effect of increasing the absorption inside the cavity between the plates has been investigated by Sharp [186]. Some measurement results are shown in Fig. 13.19.

It is evident that an addition of sound absorbing material inside the cavity drastically increases the sound transmission loss of the structure. The improvement due to the doubling of the thickness of the sound absorbing material is less dramatic. If, however, the entire cavity is filled with sound absorbing material the apparent stiffness of the entrapped air and sound absorbing material could be increased. This would also increase the double wall resonance and thus also reduce the sound transmission loss of the entire structure for $f_0 \leq f \leq f_x$.

It is often necessary to stiffen lightweight double wall constructions. Strength and stability of the structure is achieved by mounting studs between the plates of the double structure. Clearly, these connections will reduce the acoustic efficiency of a double wall construction. There will be an acoustic energy flow between the plates through the studs. The total transmission loss will depend on the distance between studs and type of studs used. Some measurement results are shown in Fig. 13.20. The measurements reported by Northwood [187] reveal that by changing a wooden stud to a more flexible metal stud the sound transmission loss is increased considerable. Again, as in Fig. 13.19, it is also demonstrated that the sound transmission of a double structure is improved by adding some sound absorbing material between the plates.

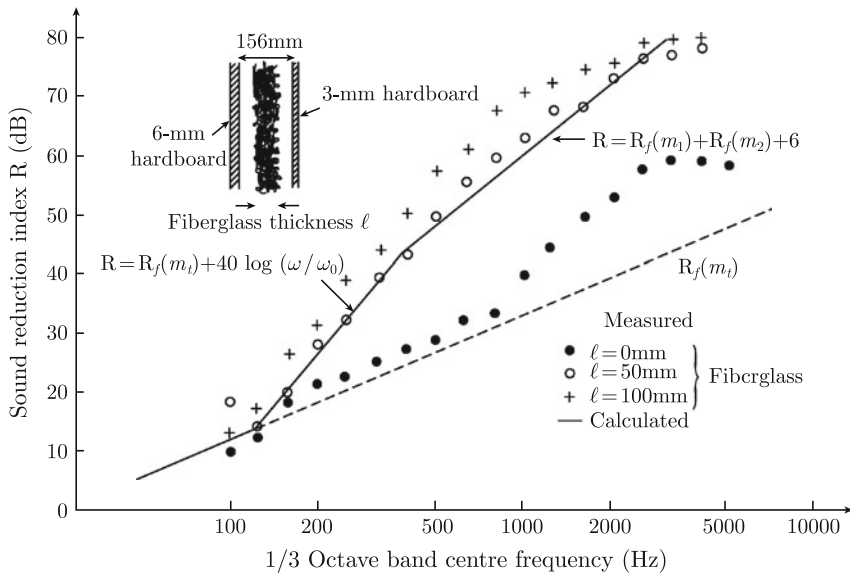


Fig. 13.19 Sound transmission loss of a double wall construction as function of sound absorption material in cavity. From Ref. [186]

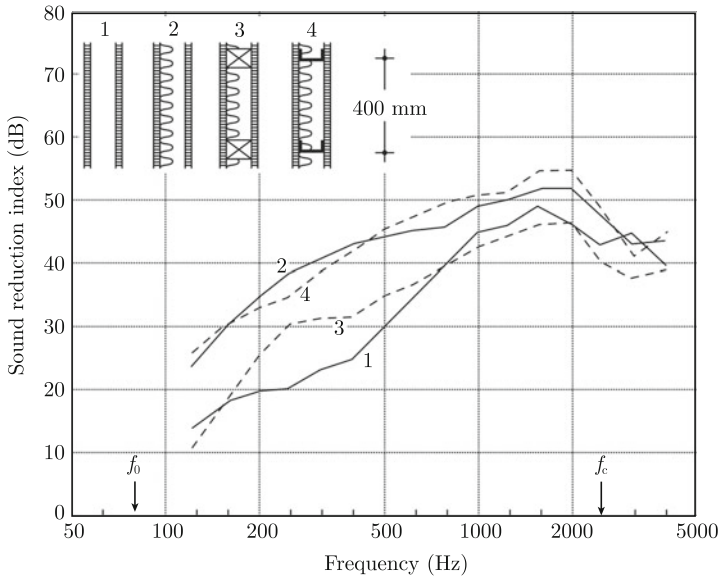


Fig. 13.20 Influence of added sound absorption and studs on the sound transmission loss of a double wall construction. 1 Two 13 mm plasterboard panels with a spacing of 106 mm; 2 Sound absorbing material added to cavity; 3 Wooden studs connecting plates; 4 Metal studs connecting plates. From Ref. [187]

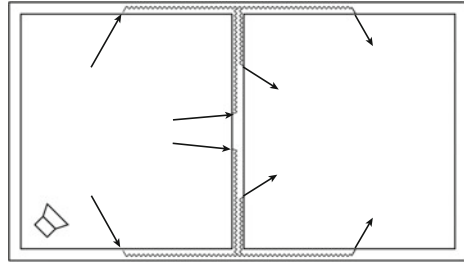
Models for estimating the effects on the transmission loss of various types of couplings between the panels of a double wall structure have been formulated by Sharp [186]. The sound transmission loss of double structures is extensively discussed in for example Refs. [149, 188, 189].

13.11 Flanking Transmission

The procedures for the measurement of the sound transmission loss of structures are described in a number of ISO standards, Refs. [190–192]. Comparing laboratory and field measurements made for the same type of structure there is a tendency that laboratory measurements give a slightly better result than field measurements. One reason for this is the so-called flanking transmission as illustrated in Fig. 13.21.

An acoustic source in a room not only excites the wall to an adjoining room but also floor, ceiling and other walls in the source room. The vibration energy of these structures is transmitted to the structures enclosing the receiving room. The sound pressure level is thus determined not only by the sound directly transmitted through the separating wall but also from acoustic power radiated by the other structures into the room. A typical sound transmission laboratory is built in such a way as to reduce

Fig. 13.21 Direct and flanking transmission between two adjoining rooms



the flanking transmission to a minimum. Consequently, field measurements tend to give a lower sound transmission for a structure as compared to laboratory measurements. Kihlman has discussed and estimated the effects of flanking transmission in Ref. [193]. Flanking transmission is also discussed at the end of Sect. 16.6.

13.12 Sound Transmission Through Fluid Loaded Plates

In certain cases, it is of interest to estimate the sound transmission through a plate or the response of a structure having a fluid loading on one side. For example, large electric transformers are often submerged in a heavy fluid and enclosed in a steel container. The vibrating transformer emits noise in the fluid and the noise excites the surrounding panels, which in turn radiate noise to the environment. It is readily demonstrated, see Problem 13.11, that the transmission through this type of enclosure is mainly determined by the impedance differences between the entrapped heavy fluid and the outside air. Consequently, an increase of the thickness of the enclosing structure would only marginally decrease the sound intensity transmitted from the enclosure.

For designing noise reducing measures in large buildings or constructions it is of importance to determine if a noise problem is caused by air-borne or structure-borne sound as discussed in Sect. 13.1. For example on a ship, one of the main noise problems is due to the main engines. The engines, when in operation, induce an energy flow of structure-borne sound through the engine foundation to hull plates and from there to the accommodation spaces. The engines also induce a very high sound pressure level in the engine room. This acoustic field excites the hull structure. The hull structure is typically exposed to a water load. The vibration level of hull plates exposed to a one sided water load can be calculated from the results given in Sect. 13.2. The mass of the structure should be corrected for the fluid loading as described in Sect. 12.1. In a similar way, the transmission of sound through hull platings into the water can be determined. However, structure-borne sound induced by air-borne sound is generally of less importance than structure-borne sound induced by mechanical forces. So for example in a catamaran, model shown in Fig. 10.24, the sound pressure level in the engine room is of the order 115 dB(A) during normal

cruising conditions. The passenger compartments are located directly above the engine room. Still, the noise in this space is exclusively determined by structure-borne sound induced by the vibrating main engines.

A propeller is also a major noise source on ships. The acoustic power induced in the water loaded hull plates above a cavitating propeller is discussed in Ref. [163].

Problems

13.1 Calculate the radiation ratio $\bar{\sigma}_a$ for an infinite plate, $\mu = 22 \text{ kg/m}^2$ and $f_c = 720 \text{ Hz}$, in the frequency range up to 500 Hz .

13.2 Determine how the sound transmission loss for a single leaf panel is changed if the thickness of the homogeneous plate is changed from h_1 to h_2 . Consider the frequency intervals $f \ll f_c$ and $f > f_c$.

13.3 Show that

$$\sum_l \frac{1}{k^2 - k_{lmn}^2} = \frac{d}{2\lambda_{mn} \tan(\lambda_{mn}d)}$$

For notations, see Sect. 13.3.

13.4 A stiff plate is mounted as shown in Fig. 13.22. Determine the mobility of the plate as function of the distance d between plate and bottom structure. The mass per unit area of the infinitely stiff plate is μ and its area S . The fluid in the cavity is air.

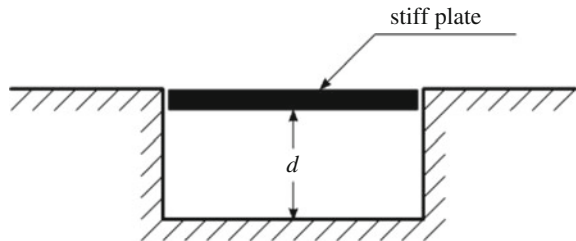
13.5 Show that

$$Y_{mn}(a) = \frac{1}{[\lambda_{mn} \sin(\lambda_{mn}a)]^2} \left[\frac{\sin(2\lambda_{mn}a)}{2\lambda_{mn}a} + 1 \right]$$

can close to a maximum be expanded as

$$|Y_{mn}(a)| = \frac{1}{(ak_{0a}^2)^2(\xi^2 + \delta_a^2/4)}$$

Fig. 13.22 Stiff plate coupled to cavity



13.6 Solve

$$\Gamma = \oint \frac{d\xi}{(\xi^2 + \delta_1^2/4)(\xi^2 + \delta_2^2/4)}$$

Make the integration along a semi-circle in the upper half plane of the complex plane.

13.7 Show that the sound transmission loss is independent of boundary conditions for $f > f_c$.

13.8 Follow the one-dimensional procedure for the clamped plate to indicate the solution for a simply supported plate.

13.9 Determine the sound transmission loss of a double construction consisting of two panels with a cavity between them. Assume that the acoustic field between the plates is diffuse.

13.10 Determine the double wall resonance frequency given in Eq. (13.130).

13.11 Determine the sound transmission loss of a structure with a water load on one side. Consider only normal incidence.

13.12 Show that the sound transmission loss for a panel between two rooms tends to the sound transmission loss of an infinite panel as the dimensions of the rooms becomes infinite.

Chapter 14

Waveguides

A waveguide is a system, which by means of its boundaries contains and directs the flow of energy in a construction. One such system is a structural waveguide typical of a ship construction. Aircraft and certain train constructions are also built up of frames and plates. Parallel frames mounted to plate elements guide the propagation of waves in a direction of the frames. A sandwich or honeycomb plate forms another type of waveguide. The laminates coupled to a core contain the energy flow in the structure. A third type of a waveguide system is a cylinder.

In this chapter, the discussion starts with structural waveguides. The coupling between a number of finite structural waveguides is investigated. Methods for reducing the energy flow in these waveguides are considered. Predictions and measurements of the distribution of energy in structures similar to ship, train and aircraft constructions are compared.

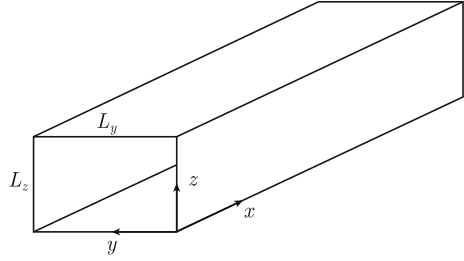
Sandwich structures were first investigated in Sect. 4.7. The basic equations governing the vibration of sandwich and honeycomb structures were derived in Sect. 9.3 using Hamilton's principle. In this chapter, it is shown that how some of the basic dynamic properties of sandwich and honeycomb structures can be determined by means of some simple tests. In addition, the response due to external excitation of sandwich beams and plates is explored. In this discussion, the sound transmission loss of sandwich plates is included.

In the final part of this chapter, the basic principles of the propagation of structure-borne sound in cylinders are described. As part of this section, the sound transmission loss of shell elements typical of aircraft structures is studied. Predicted and measured sound transmission losses are compared for stiffened and unstiffened shell elements with and without overpressure on one side of the panel.

14.1 Introduction

Some characteristics of a waveguide can be illustrated by considering an infinite and straight duct shown in Fig. 14.1. The cross section of the duct is rectangular with the dimensions L_y and L_z . The walls of the duct are assumed to be infinitely stiff. The

Fig. 14.1 An acoustic waveguide



particle velocities in the fluid inside the duct are therefore equal to zero normal to the duct walls. An acoustic wave is induced to propagate along the infinite duct in the direction of the positive x -axis.

The velocity potential describing the acoustic field inside the infinite duct is of the form

$$\begin{aligned}\Phi(x, y, z, t) &= \sum_{mn} A_{mn} \exp[i(\omega t - \lambda_{mn}x)] \cdot \varphi_{mn}(y, z) \\ \varphi_{mn}(y, z) &= \cos(m\pi y/L_y) \cdot \cos(n\pi z/L_z)\end{aligned}\quad (14.1)$$

Since the duct is assumed infinite, there is no reflected field. The velocity potential must satisfy the wave equation (11.19). Thus,

$$\lambda_{mn} = \left[k^2 - (m\pi/L_y)^2 - (n\pi/L_z)^2 \right]^{1/2} = \left[k^2 - k_{mn}^2 \right]^{1/2} \quad (14.2)$$

The parameter λ_{mn} is only real if $k \geq k_{mn} = [(m\pi/L_y)^2 + (n\pi/L_z)^2]^{1/2}$. For λ_{mn} real, a wave can propagate along the positive x -axis of the duct. For $k_{mn} > k$, λ_{mn} is imaginary giving an evanescent and thus an attenuated wave.

The time average of the energy flow in the duct is written as

$$\bar{\Pi}_x = \int dS \frac{1}{2} \operatorname{Re}(p \cdot v^*) = \int dS \frac{1}{2} \operatorname{Re} \left[-\rho \frac{\partial \Phi}{\partial t} \left(\frac{\partial \Phi}{\partial x} \right)^* \right]$$

The integration is carried out over the cross-sectional area S of the duct. Inserting the expressions (14.1) and (14.2) in this equation the result is

$$\bar{\Pi}_x = \sum_{mn} \omega \rho |A_{mn}|^2 \operatorname{Re}(\lambda_{mn}) L_y L_z / 8 \quad (14.3)$$

There is no energy flow for modes for which $k_{mn} \geq k$ since for this case $\operatorname{Re}(\lambda_{mn}) = 0$. If say, the energy flow in a duct has to be described in the frequency range up to f_0 only modes for which $(2\pi/c) [(m\pi/L_y)^2 + (n\pi/L_z)^2]^{1/2} = f_{mn} \leq f_0$ have to be

considered. All other modes are represented by evanescent waves carrying no energy assuming a loss-free fluid.

The frequency f_{mn} at which the mode (m, n) starts propagating is often referred to as the cut-on frequency of the waveguide. For a duct with a rectangular cross section, the largest dimension of the cross section of the duct determines the cut-on frequency. For a duct with a circular cross section with radius a , the cut-on frequencies f_n for the first five modes are $f_n = c\beta_n/(2\pi a)$ where c is the speed of sound in the fluid. The parameter β_n is equal to 1.841, 3.054, 3.832, 4.201, and 5.318 for $n = 1-5$. Compare Problem 14.1.

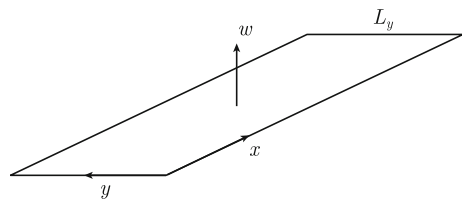
The coupling between various types of acoustic waveguides with and without flow has been discussed extensively by Bodén and Åbom. The main results are summarized in Ref. [194]. See also [138]. The acoustic waveguide model is also an essential part of any design of exhaust and muffler systems for cars, ships, and other vehicles.

14.2 Structural Waveguides

Many large constructions are built up by a combination of plates and frames. Parallel frames are supporting plate constructions. Typical examples of this type of construction are ships, aircraft, and to a certain extent train carriages. The parallel frames as discussed in, for example, [42] mainly contain the energy flow in such constructions. The frames constitute a waveguide. The energy flow in the plate element between the frames is in general completely dominating over the flow in the frames. A conventional ship is an interesting example of a waveguide system. The main sources of structure-borne sound are mounted in the hull of the ship. The structure-borne sound induced by main engines, etc. is traveling between the vertical frames to the upper decks of the ship. On any of the upper decks, it is readily possible, just by listening, to identify the positions of the main sources with respect to any frame. Similar observations can be made for other large constructions, which are built up of plates and frames. It is therefore of importance to investigate the energy flow and its possible reduction in structural waveguides.

A simple structural waveguide is shown in Fig. 14.2. A plate element, width L_y , is limited by two parallel boundaries. The plate element has the bending stiffness D and the mass per unit area μ . As discussed in Sect. 8.3 the lateral displacement w of

Fig. 14.2 A structural waveguide



the plate can only be described in a simple analytical way if the boundary conditions along the edges $y = 0$ and $y = L_y$ are assumed to be simply supported. Sliding edges as illustrated in Fig. 8.2 is a possible but an unrealistic option for a real construction. Following the discussion in Sect. 8.3, Eqs. (8.47) through (8.49), the displacement of a plate element having two parallel sides simply supported can be written as

$$w(x, y, t) = e^{i\omega t} \cdot \sum_{n=1}^{\infty} \varphi_n(y) \cdot X_n(x)$$

$$\varphi_n(y) = \sin(k_n y); \quad k_n = n\pi/L_y; \quad n = 1, 2, 3 \dots \quad (14.4)$$

The boundary conditions $w = 0$ and $\partial^2 w / \partial y^2 = 0$ along the edges $y = 0$ and $y = L_y$ are satisfied. The displacement w must also satisfy the wave equation for flexural waves. Thus, by setting the external force F equal to zero in Eq. (8.51) the wave equation reads

$$\frac{d^4 X_n}{dx^4} - 2k_n^2 \frac{d^2 X_n}{dx^2} + k_n^4 X_n - \kappa^4 X_n = 0 \quad (14.5)$$

where as usual $\kappa = (\mu\omega^2/D)^{1/4}$ is the wavenumber for flexural waves propagating in the plate. According to standard procedure, it is assumed that X_n can be written in the form of $A_n \exp(\lambda_n x)$, with λ_n satisfying the equation

$$\lambda_n^4 - 2k_n^2 \lambda_n^2 + k_n^4 - \kappa^4 = 0$$

The four resulting solutions to this equation are

$$\lambda_{n1} = i\sqrt{\kappa^2 - k_n^2} = i\kappa_1; \quad \lambda_{n2} = -i\sqrt{\kappa^2 - k_n^2} = -i\kappa_1$$

$$\lambda_{n3} = \sqrt{\kappa^2 + k_n^2} = \kappa_2; \quad \lambda_{n4} = -\sqrt{\kappa^2 + k_n^2} = -\kappa_2 \quad (14.6)$$

For $\kappa > k_n$ the solution λ_{n1} represents a wave propagating along the negative x -axis, λ_{n2} a wave propagating along the positive x -axis, λ_{n3} an evanescent wave decaying for increasing negative values of x , and finally, λ_{n4} an evanescent wave decaying for increasing positive values of x .

Assuming that the semi-infinite waveguide shown in Fig. 14.2 is excited at $x = 0$, two waves are induced in the structure corresponding to the solutions λ_{n2} and λ_{n4} . No waves are reflected toward the excitation point. The displacement of the plate element within the waveguide is consequently

$$w(x, y, t) = e^{i\omega t} \sum_{n=1}^{\infty} \varphi_n(y) \cdot (A_n \cdot e^{-i\kappa_1 x} + B_n \cdot e^{-\kappa_2 x}) \quad (14.7)$$

The amplitudes A_n and B_n are determined by the boundary conditions. The parameter κ_1 is only real as long as $\kappa > k_n$. For $\kappa < k_n$ no waves can propagate in the plate if the plate is assumed to be loss free.

The energy flow in plates due to flexure is discussed in Sect. 3.11, and formulated in Eq. (3.138). Using complex notations, the time average of the energy flow $\bar{\Pi}'_x$ along the x -axis is per unit width of the plate given by

$$\bar{\Pi}'_x = -\frac{1}{2} \operatorname{Re} \left[D \left\{ \frac{\partial^2 w}{\partial x^2} \left(\frac{\partial^2 w}{\partial x \partial t} \right)^* - \frac{\partial^3 w}{\partial x^3} \left(\frac{\partial w}{\partial t} \right)^* \right\} \right] \quad (14.8)$$

The total energy flow in the plate is

$$\bar{\Pi}_x = \int_0^{L_y} \bar{\Pi}'_x dy \quad (14.9)$$

The expressions (14.7) and (14.8) inserted in (14.9) yield

$$\bar{\Pi}_x = \frac{1}{2} \operatorname{Re} \left[L_y \omega D \sum_{n=1}^{\infty} |A_n|^2 \kappa_1^3 \right] = \frac{1}{2} \operatorname{Re} \left[L_y \omega D \sum_{n=1}^{\infty} |A_n|^2 (\kappa^2 - k_n^2)^{3/2} \right] \quad (14.10)$$

Thus, only the propagating waves contribute to the energy flow. For $\kappa < k_1$ there is no energy flow. For simply supported edges, the cut-on frequency f_{co1} is obtained when $\kappa = k_1$, i.e., $f_{co1} = \pi / (2L_y^2) \sqrt{D_0 / \mu}$. The cut-on frequency for the cross mode n is

$$f_{con} = \frac{\pi n^2}{2L_y^2} \sqrt{\frac{D_0}{\mu}} \quad (14.11)$$

For the type of acoustic waveguide discussed in Sect. 14.1 there can be an energy flow in the low frequency region below the first cut-on frequency. This corresponds to a plane wave traveling along the waveguide. For a loss-free structural waveguide there can be no energy flow in the low frequency region below the first cut-on frequency. For a more or less symmetric excitation of a structural waveguide the cross modes for which n is odd will dominate. For this particular case, the first and the third and higher odd cross modes will determine the energy flow in the plate. If, for example, the waveguide shown in Fig. 14.2 is excited by a constant bending moment $M \exp(i\omega t)$ at $x = 0$ across the plate element the resulting energy flow $\bar{\Pi}_{xn}$ for the cross mode n is, as shown in Problem 14.2, given by

$$\bar{\Pi}_{xn} = \frac{1}{2} \operatorname{Re} \left\{ \frac{4\omega M^2 [\kappa^2 - (n\pi/L_y)^2]^{3/2}}{n^2 \pi^2 D \kappa^4 L_y} \right\} \text{ for } n \text{ odd, otherwise zero} \quad (14.12)$$

Clearly, the energy flow corresponding to the first cross mode is completely dominating over the higher modes even for frequencies above the third cut-on frequency. The energy flow in waveguides is also discussed in [196].

For the plate element, the boundaries parallel to the x -axis are assumed to be clamped, a complete solution of the plate displacement cannot readily be derived. An approximate solution can be formulated by representing the shape of the cross mode by a simple sine function with an eigenvalue within 0.4% of the correct value. The first cross mode can be described as

$$\varphi_1(y) = \sin\left(\frac{3\pi y}{2L_y} - \frac{\pi}{4}\right) \text{ for } L_y/6 \leq y \leq 5L_y/6 \text{ otherwise zero} \quad (14.13)$$

Approximate expressions for the second and higher cross modes are

$$\varphi_n(y) = \sin\left[\frac{(2n+1)\pi y}{2L_y} - \frac{\pi}{4}\right] \text{ for } \frac{L_y}{2(2n+1)} \leq y \leq \frac{L_y(4n+1)}{2(2n+1)} \quad (14.14)$$

However, these approximate eigenfunctions are not orthogonal. The displacement of the plate element can therefore not be expanded along these approximate functions $\varphi_n(y)$.

14.3 Coupled Structural Waveguides

Large constructions are often built up by plates and frames as previously discussed. At a junction between two adjoining plate elements, energy from one element is transferred to the next element by a bending moment. This bending moment induces an angular displacement around the junction. The total bending moment around the junction must be zero. Further, the angular displacement of one element should equal the angular displacement of the adjoining element. During the rotation of the elements around the junction it is assumed that the angle between the elements is maintained or in fact being constant. These assumptions are the same as those discussed in Sect. 5.9 in connection with the derivation of the transmission of flexural waves across junctions. In Sect. 5.9, it was also argued that the lateral motion of the junctions could be neglected. This assumption was found to be relevant even for coupled plate elements freely suspended in space. However, in real constructions plate elements and junctions are coupled to supporting structures. Consequently, the lateral motion of any real junction is very much restricted. Thus, neglecting the lateral motion of a junction between two plate elements leads to that longitudinal waves induced by flexural waves can be disregarded. This assumption is discussed further in Chap. 16. The coupling between finite waveguides is also discussed in Refs. [56, 197, 198].

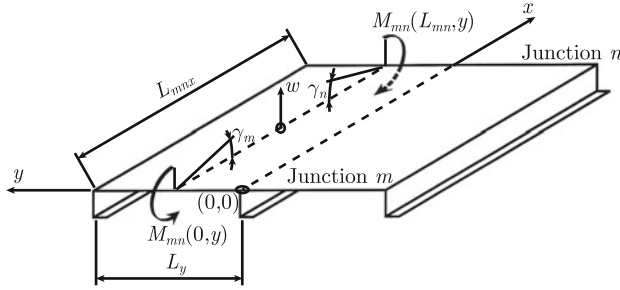


Fig. 14.3 Structural waveguide element between two junctions m and n and limited in the y -direction by two frames

A structural waveguide element is illustrated in Fig. 14.3. The finite waveguide connects two junctions denoted as m and n . The length of the element is L_{mnx} and its width is L_y . The bending stiffness of the plate is $D = Eh^3/[12(1 - \nu^2)]$ and its mass per unit area is μ . The corresponding wavenumber for flexural waves is $\kappa = (\mu\omega^2/D)^{1/4}$. The angular displacement along the junction m is γ_m and at the junction n equal to γ_n . The displacement of the plate element is zero along the boundaries. The cross modes are given by $\varphi_n(y)$. For simply supported boundaries along the frames the cross modes are given by Eq. (14.4) and for clamped boundaries by (14.13) and (14.14). The displacement w of the plate is written as

$$w(x, y, t) = \exp(i\omega t) \sum_n \varphi_n(y) X_n(x) \tag{14.15}$$

As given by Eq. (14.5) the function X_n should for free vibrations and simply supported boundaries along the frames satisfy the differential equation

$$\frac{d^4 X_n}{dx^4} - 2k_n^2 \frac{d^2 X_n}{dx^2} + k_n^4 X_n - \kappa^4 X_n = 0$$

The general solution to this equation is

$$X_n = C_{1n} \sin(\kappa_2 x) + C_{2n} \cos(\kappa_2 x) + C_{3n} \sinh(\kappa_1 x) + C_{4n} \cosh(\kappa_1 x) \\ \kappa_1 = \sqrt{\kappa^2 + k_n^2}; \quad \kappa_2 = \sqrt{\kappa^2 - k_n^2} \tag{14.16}$$

The boundary conditions at the two ends of the waveguide are $X_n(0) = X_n(L_{mnx}) = 0$ and $dX_n/dx = \gamma_m$ for $x = 0$ and $dX_n/dx = \gamma_n$ for $x = L_{mnx}$. Introducing the parameters α_1, α_2 and χ as $\alpha_1 = \kappa_1 L_{mnx}$, $\alpha_2 = \kappa_2 L_{mnx}$, and $\chi = \kappa_1/\kappa_2$, the amplitudes C_{1n} , etc. of Eq. (14.16) are obtained as

$$\begin{aligned}
C_{1n} &= \frac{\gamma_m [\chi(1 - \cos \alpha_2 \cosh \alpha_1) - \sinh \alpha_1 \sin \alpha_2] - \gamma_n \chi (\cosh \alpha_1 - \cos \alpha_2)}{\kappa_2 [2\chi(1 - \cos \alpha_2 \cosh \alpha_1) - \sinh \alpha_1 \sin \alpha_2 (1 - \chi^2)]} \\
C_{2n} &= \frac{\gamma_m [\chi(\sin \alpha_2 \cosh \alpha_1) - \cos \alpha_2 \sinh \alpha_1] - \gamma_n [\chi \sin \alpha_2 - \sinh \alpha_1]}{\kappa_2 [2\chi(1 - \cos \alpha_2 \cosh \alpha_1) - \sinh \alpha_1 \sin \alpha_2 (1 - \chi^2)]} \\
C_{3n} &= \frac{\gamma_m}{\chi \kappa_2} - \frac{C_{1n}}{\chi}; \quad C_{4n} = -C_{2n}
\end{aligned} \tag{14.17}$$

These expressions can be somewhat simplified since

$$\alpha_1 = L_{xmn} \sqrt{\kappa^2 + (\pi/L_y)^2} \geq \pi L_{xmn}/L_y.$$

For $L_{mnx} > L_y$, α_1 is large enough to ensure that $\sinh \alpha_1 \approx \cosh \alpha_1 \gg 1$. Consequently, the expression (14.17) is reduced to

$$\begin{aligned}
C_{1n} &= \frac{\gamma_m [\chi \cos \alpha_2 + \sin \alpha_2] + \gamma_n \chi}{\kappa_2 [2\chi \cos \alpha_2 + \sin \alpha_2 (1 - \chi^2)]} \\
C_{2n} &= \frac{\gamma_m [\cos \alpha_2 - \chi \sin \alpha_2] - \gamma_n}{\kappa_2 [2\chi \cos \alpha_2 + \sin \alpha_2 (1 - \chi^2)]} \\
C_{3n} &= C_{2n}; \quad C_{4n} = -C_{2n}
\end{aligned} \tag{14.18}$$

The resulting bending moment around the junction m is

$$M_{mn}(0) = \sum_j M_{jmn}(0) \varphi_j(y) = -D_{mn} \sum_j w_j''(0) \varphi_j(y) \tag{14.19}$$

The bending stiffness of the element is now denoted as D_{mn} . For $j = 1$, i.e., for the first cross mode the parameter M_{1mn} can be written as

$$\begin{aligned}
M_{1mn} &= X_{mn} \gamma_m - Y_{mn} \gamma_n \\
X_{mn} &= D_{mn} \kappa_{mn}^2 \frac{\kappa_2 \cos \alpha_2 - \kappa_1 \sin \alpha_2}{\kappa_1 \kappa_2 \cos \alpha_2 - k_1^2 \sin \alpha_2}; \\
Y_{mn} &= D_{mn} \kappa_{mn}^2 \frac{\kappa_2}{\kappa_1 \kappa_2 \cos \alpha_2 - k_1^2 \sin \alpha_2} \\
\kappa_{mn} &= \left[\frac{\mu_{mn} \omega^2}{D_{mn}} \right]^{1/4}; \\
\kappa_1 &= \left[\kappa_{mn}^2 (1 - i\eta/2) + k_1^2 \right]^{1/2}; \quad \kappa_2 = \left[\kappa_{mn}^2 (1 - i\eta/2) - k_1^2 \right]^{1/2}; \\
k_1 &= \frac{\pi}{L_y}; \quad \alpha_2 = \kappa_2 L_{xmn}
\end{aligned} \tag{14.20}$$

The bending moment $M_{1mn}(L_{xmn})$ at the other end of the plate element is found to be

$$M_{1mn}(L_{xmn}) = Y_{mn}\gamma_m - X_{mn}\gamma_n \tag{14.21}$$

The frequency and space average of the velocity squared of the element is

$$\langle |\bar{v}|^2 \rangle = \frac{1}{2L_{xmn}L_y\Delta f} \int_0^{L_{xmn}} dx \int_0^{L_y} dy \int_f^{f+\Delta f} df \omega^2 |w|^2$$

After a certain effort it is found that the average velocity squared corresponding to the first cross mode is

$$\langle |\bar{v}_1|^2 \rangle = \frac{\omega^2 |\kappa_2| (|\gamma_{1m}|^2 + |\gamma_{1n}|^2)}{6\eta L_{xmn} \kappa^4} \text{ for } \kappa > k_1 \tag{14.22}$$

The angular displacements γ_{1m} and γ_{1n} represent the displacement for the first cross mode following that $\gamma_m = \sum_i \gamma_{im} \varphi_i(y)$. The frequency average of the product $\gamma_m \gamma_n$ has been set to equal zero.

A system of equations relating the rotation at each junction and the resulting bending moments can now be formulated. Consider the junction shown in Fig. 14.4. It is assumed that there is no translatory motion at any junction. The energy transfer from one element to the adjoining is caused by a bending moment at the junction. During rotation the angle between the plate elements is constant, i.e., each element is rotated

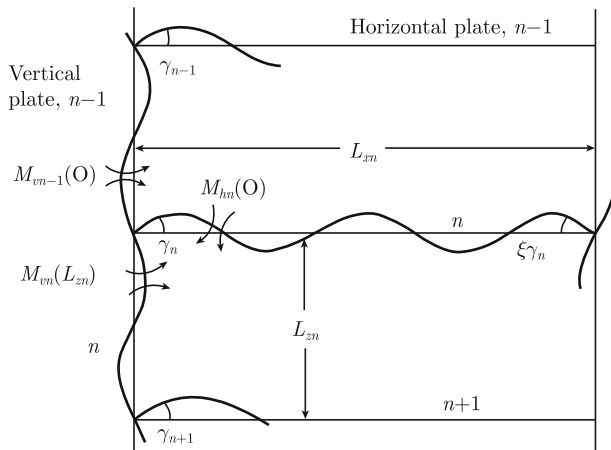
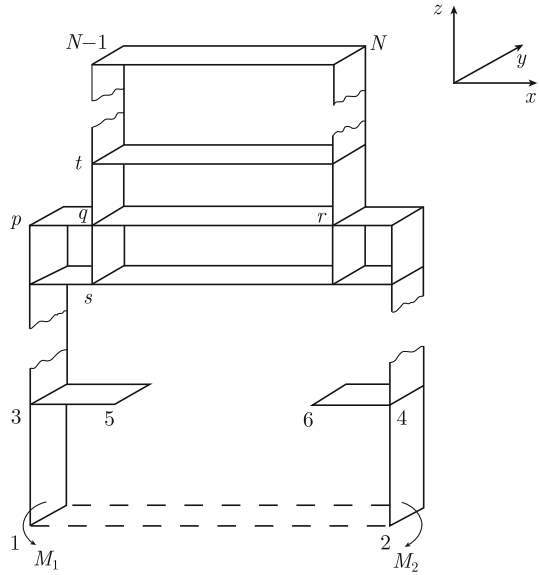


Fig. 14.4 Resulting bending moments and angular displacement at a junction n of a structural network

Fig. 14.5 A system of coupled waveguides



the angle γ_n around the junction n . The sum of the bending moments around a junction must equal zero. Thus, using the notations in Fig. 14.4, $M_{vn-1}(0) + M_{hn}(0) = M_{vn}(L_{zn})$.

Consider now the model shown in Fig. 14.5. The junctions in a vertical plane of a built-up structure are numbered from 1 to N . The width L_y of the model is determined by the distance between the parallel frames. The length of a plate element between the junctions m and n is given by L_{mnx} . Assume that the energy flow to the structure is induced by bending moments M_1 and M_2 at the junctions 1 and 2 as shown in Fig. 14.5. The angular displacement of the first cross mode at junction m is γ_m . Only the first propagating mode is considered, since according to Eq. (14.12) this mode is completely dominating for symmetric excitation of a waveguide structure.

Based on the assumptions made above, the resulting system of equations relating the rotations at the various junctions can be written in matrix form as

$$[A] \{\gamma\} = \{M\} \tag{14.23}$$

where

$$\{\gamma\} = \begin{Bmatrix} \gamma_1 \\ \gamma_2 \\ \dots \\ \dots \\ \dots \\ \gamma_N \end{Bmatrix}; \quad \{M\} = \begin{Bmatrix} M_1 \\ M_2 \\ \dots \\ \dots \\ \dots \\ M_N \end{Bmatrix} \tag{14.24}$$

The elements M_m are equal to zero except at those junctions where the structure is excited. For the configuration shown in Fig. 14.5, $M_m = 0$ for $m > 2$.

The elements A_{mn} in the $N \times N$ matrix $[A]$ are defined as

$$A_{mm} = \sum_{n=1, n \neq m}^N X_{mn}; \quad A_{mn} = -Y_{mn} \text{ for } m \neq n \quad (14.25)$$

The functions X_{mn} and Y_{mn} are equal to zero if there is no plate element between the junctions m and n . For the configuration shown in Fig. 14.5 the elements of the matrix $[A]$ are

$$\begin{aligned} A_{11} &= X_{13}; \quad A_{13} = -Y_{13}; \quad A_{1n} = 0 \text{ for } n \neq 1, 3 \\ A_{qq} &= X_{qp} + X_{qr} + X_{qs} + X_{qt} \\ A_{qn} &= -Y_{qn} \text{ for } n = p, r, s, t; \quad A_{qn} = 0 \text{ for } n \neq p, q, r, s, t \text{ etc.} \end{aligned}$$

The matrix $[A]$ is symmetric, i.e., $A_{mn} = A_{nm}$.

The frequency and space average of the velocity squared of the element between the junctions m and n is given by Eq. (14.22). In most practical cases, only the velocity level difference between various plate elements is of interest. Thus, assuming a symmetric excitation of the structure, the bending moments M_1 and M_2 can be set to be equal to unity.

The velocity of a plate element is a rapidly varying function of frequency. The total kinetic energy of an element for a certain frequency band must therefore be solved by means of numerical integration within this band.

Considering that the dominating energy flow is determined by the first cross mode for a frame distance L_y the eigenfunction corresponding to clamped boundaries along frames is given by Eq. (14.13) and for simply supported boundaries by Eq. (14.4).

If the technique described above is used in the frequency range below the first natural frequency of the plate element, the resulting attenuation between two adjoining plate elements becomes far too high compared with measured results. One reason for this is that the clamped boundary conditions along the frames no longer are applicable in the low frequency range. The boundary conditions for the plates along the frames clearly depend on the relative stiffness between the frames and the plates. The moment impedance for a plate is obviously different for frequencies below and above the first natural frequency of the plate. This will naturally influence the apparent boundary conditions of the plate. Further, measurements indicate that for frequencies decreasing below the first natural frequency of the plate the shape of the cross mode is determined by simply supported rather than clamped boundary conditions. For these reasons an approach different from the one discussed above is used to determine the coupling between plate elements in the low frequency region. The method is based on the Galerkin variational method discussed in Sect. 9.9. The result is presented in Ref. [198]. Compare also Sect. 16.2.

In the low frequency range, a more simple technique can also be applied. In the low frequency range or rather for frequencies below the cut-on frequency, the frames and the plate element between the frames tend to vibrate with the same amplitude. A plate and the adjoining frames can therefore be modeled as a beam with a certain bending stiffness and mass per unit area. The built-up structure, Fig. 14.5, can for this case be modeled as a grillage of beams. For this particular case, the parameters X_{mn} and Y_{mn} are discussed in Problem 14.3 obtained as

$$\begin{aligned} M_{1mn} &= X_{mn}\gamma_m - Y_{mn}\gamma_n; & M_{1mn}(L_{xmn}) &= Y_{mn}\gamma_m - X_{mn}\gamma_n \\ X_{mn} &= D_{mn} \frac{\kappa_{mn} \cos \alpha - \kappa_{mn} \sin \alpha}{\cos \alpha}; & Y_{mn} &= D_{mn} \frac{\kappa_{mn}}{\cos \alpha} \\ \kappa_{mn} &= \left[\frac{\mu_{mn} \omega^2}{D_{mn}} \right]^{1/4}; & \alpha &= \kappa_{mn}(1 - i\eta/4)L_{xmn} \end{aligned} \quad (14.26)$$

The space average of the velocity squared is

$$\langle |v|^2 \rangle \approx \frac{\omega^2 (|\gamma_m|^2 + |\gamma_n|^2)}{2\kappa^2 \cos^2 \alpha} \quad (14.27)$$

The velocity squared is again a rapidly varying function of frequency. A frequency average of the quantity must be calculated numerically. This is in analogy with the discussion on the coupling of beams discussed in Sect. 7.6.

14.4 Measurements and Predictions

A number of model and full-scale measurements have been carried out to verify the waveguide model discussed in the previous section. A simple beam-plate structure was used by Haettel [200] to measure and predict energy flow in some simple waveguide systems. The structure was also used for the investigation of various means to reduce the energy flow in the structure. The basic structure is shown in Fig. 14.6. During measurements, the entire structure was resiliently suspended.

The parallel frames or beams supporting the plates on both sides are 15 mm high with a thickness of 2 mm. The dimensions of the plate elements are given in Table 14.1. All elements are made of steel.

At the junctions the plate elements were coupled in three different ways:

- (i) The plates were line welded along the entire junction;
- (ii) The plates were spot welded along the junction;
- (iii) Open coupling, the plate elements were connected and held in place by the frames only.

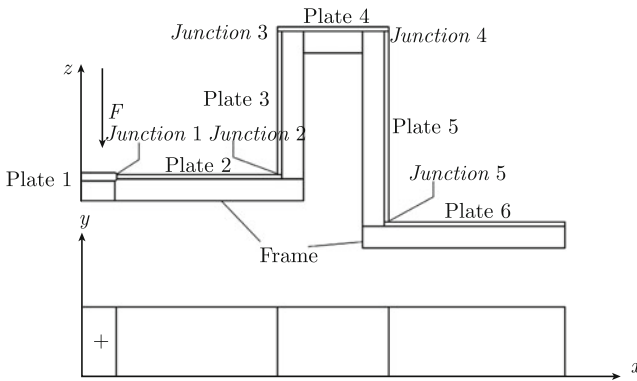


Fig. 14.6 Basic waveguide structure. From Ref. [200]

Table 14.1 Dimensions of plate elements

Plate	1	2	3	4	5	6
L_x (m)	0.3	0.7	1.0	0.8	1.2	0.9
L_y (m)	0.3	0.3	0.3	0.3	0.3	0.3
Thickness (m)	0.01	0.003	0.003	0.003	0.003	0.003

The plate element 1 was excited by an electrodynamic shaker and the velocity levels of the various plate elements were measured. Figure 14.7 shows the measured velocity level difference $\Delta L_{2,6}$ between the elements 2 and 6 for the three different couplings between the plate elements. The result shows that changing the coupling from line welded to open the velocity level difference $\Delta L_{2,6}$ is increased by more than 10 dB in a very wide frequency range. A substantial reduction is also obtained by changing the coupling from line welded to spot welded. Compare also the discussion on structural couplings discussed in Sect. 5.13. The measurements confirm the assumption that the dominating energy flow is in the plate elements and not in the frames.

The effect of damping layers on the energy flow in the model structure was also tested. Measurements were carried out with and without damping layers on the elements 3 and 5 of the model shown in Fig. 14.6. The measured velocity level difference $\Delta L_{2,5}$ between the elements 2 and 5 and the velocity level difference $\Delta L_{2,6}$ are shown in Figs. 14.8 and 14.9, respectively.

The velocity level of element 2 was the same in both cases. Figure 14.8 shows that a damping layer mounted on element 5 decreases the velocity level of this element by almost 10 dB in a wide frequency range. The velocity level of the adjoining element 6 is also decreased but to a much lesser extent than element 5 as shown in Fig. 14.9.

The excitation point of plate 1 of Fig. 14.6 was also varied from a center position to positions more close to one of the stiffeners. It was found that the transfer mobilities between excitation point and any position on any of the other plates increased as the

Fig. 14.7 Velocity level difference $\Delta L_{2,6}$ between the elements 2 and 6 of the model shown in Fig. 14.6 for three different plate couplings. From Ref. [200]

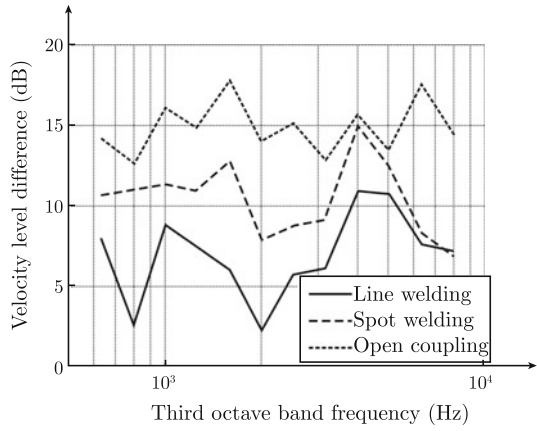


Fig. 14.8 Velocity level difference $\Delta L_{2,5}$ between the elements 2 and 5. With and without damping layers on the elements 3 and 5. From Ref. [200]

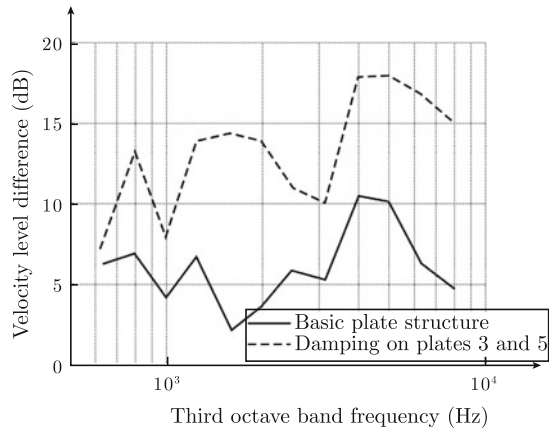


Fig. 14.9 Velocity level difference $\Delta L_{2,6}$ between the elements 2 and 6. With and without damping layers on the elements 3 and 5. From Ref. [200]

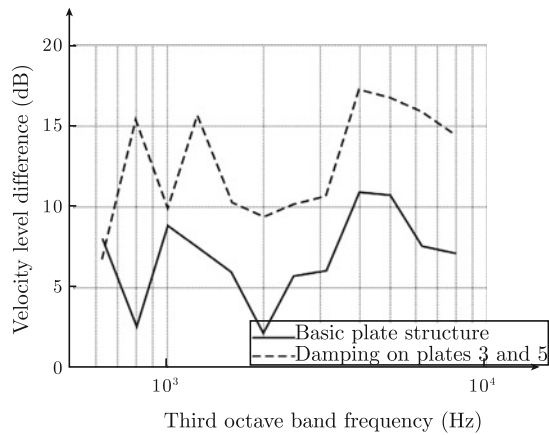


Fig. 14.10 Predicted and measured velocity level difference $\Delta L_{2,3}$ between elements 2 and 3 of model Fig. 14.6. From Ref. [200]

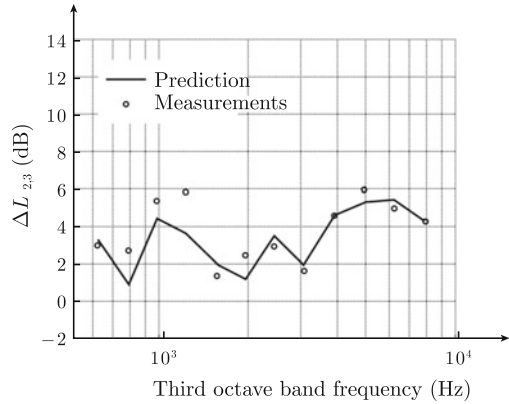
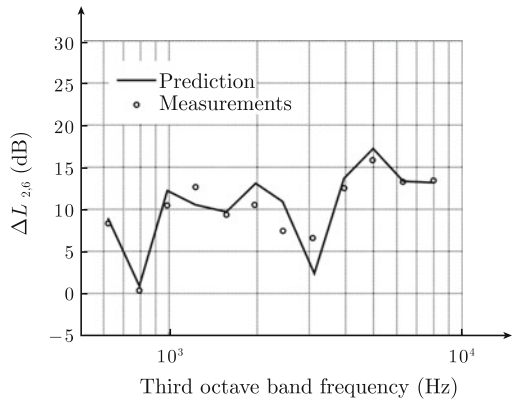


Fig. 14.11 Predicted and measured velocity level difference $\Delta L_{2,6}$ between elements 2 and 6 of model Fig. 14.6. From Ref. [200]



excitation was changed from a stiff point to a weak point. This is in accordance with the discussion in Sect. 10.12, see Figs. 10.26 and 10.27.

Some additional tests were carried out with a slightly modified waveguide structure. The plate element 1 was cut off in the structure shown in Fig. 14.6. The loss factors of the remaining elements were measured and were approximated by the expression $\eta = [0.07 + 0.21 \times \exp(-1.7 \times 10^{-3} \times f)]$ where f is the frequency. Predicted and measured velocity level differences are shown in Figs. 14.10 and 14.11. The measured velocity level differences are fairly well predicted by the waveguide model. In the predictions only flexural waves are considered. Any translatory motion of the joints is neglected.

Predicted and measured results were also compared for the structure with one damping layer on plate element 4. The loss factor of the plate with the damping layer was measured and found to be 6% for $f \leq 1000$ Hz and 1.1% for higher frequencies. Predicted and measured velocity levels are shown in Figs. 14.12 and 14.13.

Again, the agreement between predicted and measured results is satisfactory. By comparing the results shown in Figs. 14.11 and 14.13, it is found that the velocity

Fig. 14.12 Predicted and measured velocity level difference $\Delta L_{2,4}$ between elements 2 and 4 of model Fig. 14.6. Damping layer on element 4. From Ref. [200]

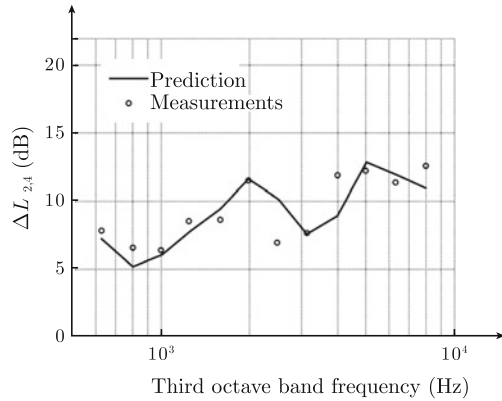
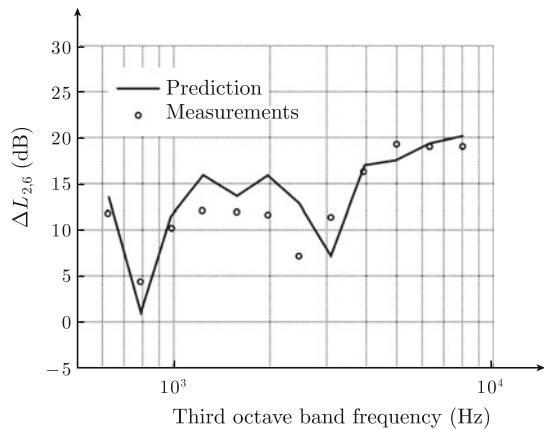


Fig. 14.13 Predicted and measured velocity level difference $\Delta L_{2,6}$ between elements 2 and 6 of model Fig. 14.6. Damping layer on element 4. From Ref. [200]



level difference $\Delta L_{2,6}$ between elements 2 and 6 are almost the same with and without a damping layer on element 4. The damping layer decreased the velocity level of the element 4 by approximately 5 dB in a wide frequency range. Despite this, the velocity level of element 6 is only changed moderately by the addition of damping on plate 4. This indicates that a damping layer applied in the transmission path between source and receiving elements is not very effective.

The effectiveness of damping layers applied to a built-up structure has been discussed in a number of papers. Damping layers can be applied either at the foundation of a source, at the receiving end, or at the propagation path between source and receiver. An example of the first method is reported in Ref. [201]. The structure-borne sound induced by a small pump on a ship was reduced by the application of damping layers on the steel structure around the pump. The resulting noise reduction in an adjoining cabin was reduced by 10 dB by the reduction of the structure-borne sound induced by the pump. However, for large sources like Diesel engines the foundation is quite heavy and naturally well damped. For this particular case, the addition of

damping layers on the engine foundation is of minor importance. Compare the discussion in Sect. 10.12. The application of damping layers at the receiving end, on the steel deck, and on steel bulkheads facing a cabin, can also be effective as reported in Ref. [202]. In the case investigated, constrained viscoelastic layers partially covered the steel structures. The noise reduction achieved in the cabin was of the order 4–5 dB.

Van Tol [203] has performed model tests with damping layers. When only part of the transmission path between source and receiver was clad with viscoelastic materials, the resulting noise reduction at the receiving end was minor. The noise reduction was increased considerably when the treated area was extended all the way between source and receiver.

Full-scale experiments are reported by Buiten [204] and Turner [205]. In the first investigation, layers of a viscoelastic material were applied to two decks and the intermediate hull section on a Rhine cruiser. The total area covered was 400 m². The auxiliary engines and a number of cabins were situated on the lower of the two decks. The treated area was not extended all the way up to the engines and cabins. The resulting noise reduction in the cabins on the same deck as the auxiliary engines was estimated to be less than 1 dB. The results repudiate the idea that added damping anywhere in a structure “absorbs” energy and thus decreases noise levels.

A discussion on the apparent inefficiency of damping layers on stiffened steel structures is presented in Ref. [206]. It is argued that the low damping which is often observed is due to the waveguide characteristics of the structure. In the report, it is also concluded that the incorporation of dissipative elements in frames which are part of a waveguide does not seem to be useful.

Some of the damping effects summarized above and predictions of the flow of structure-borne sound using the waveguide technique were investigated using a scale model shown in Fig. 14.14. The results reported in Refs. [197, 198] suggest that the main power flow in a ship structure is caused by flexural waves propagating in the plate elements. It should thus be possible to test the theoretical model discussed in [197] and presented in Sect. 14.3 by means of measurements on a structure, the width of which is equal to the distance between two frames and where the frames are acting as boundaries. Measurements on sections of ships were pioneered by Odegaard-Jensen [207], and Ohlrich [116].

The basic model used for the test is shown in Fig. 14.14. The thickness of the steel plates is 0.6 mm for the elements 4–11 and 1 mm for the elements 1–3. The dimensions of the frames on elements 1–3 are 60 × 15 × 1 mm and for the frames of elements 4–11 6 × 5 × 0.6 mm. The other dimensions are indicated in Fig. 14.14. The upper part of the structure could correspond to a super structure on a ship and the lower part to the hull section and the main deck. The structure is not really made to scale with respect to a real ship structure. However, the scaling factor is roughly 1:20. The structure is excited at position 1 shown in Fig. 14.14. The force on the structure is acting primarily in the vertical direction. The transmission of structure-borne sound from the main deck, plate 3, to the superstructure, elements 4–11, is determined for the following configurations:

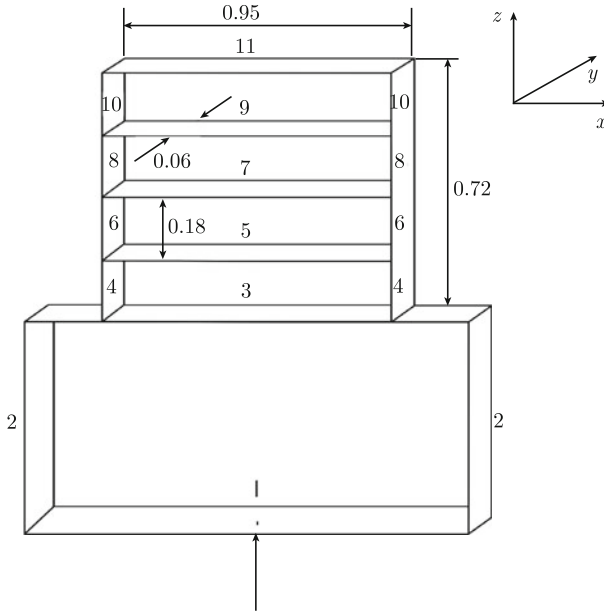


Fig. 14.14 Basic ship model

- (i) bare steel model, Fig. 14.14;
- (ii) damping layers on plates 4 and 6;
- (iii) damping layers on plates 5 and 7;
- (iv) damping layers on the center third part of plates 5 and 7;
- (v) damping layers on the main deck, plate 5, plus on plates between elements 2 and 4;
- (vi) the superstructure, elements 4–11, resiliently mounted on main deck, see Fig. 14.15;
- (vii) the plate elements 3 and 4 connected only via the frames, see Fig. 14.16.

The velocity levels of the various plate elements were measured while the structure was excited at the position 1 shown in Fig. 14.14. The velocity level differences between the plate elements 4–11 in the superstructure and the main deck, plate 3, were determined. The average loss factor of the elements was measured. For the plates in the superstructure, elements 4–11, the loss factor was 8×10^{-4} up to and including the 1.6 kHz third octave band and decreased with increasing frequency to 5×10^{-4} at 50 kHz. Since the scaling factor is 1:20, a frequency f in model scale corresponds approximately to a frequency $f/20$ in full scale. The lowest cut-on frequency for the plates clamped along the frames is of the order 0.9 kHz for the elements in the superstructure. The excitation is symmetric with respect to the frames. It can therefore be expected that the odd cross modes determine the energy flow. Following the result (14.12) only the energy flow due to the first cross mode is considered in the

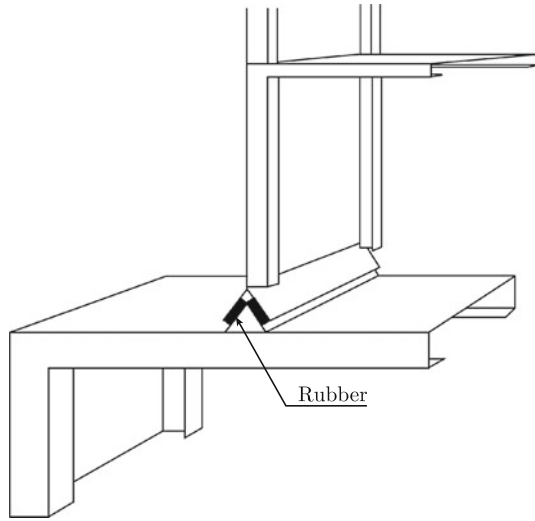


Fig. 14.15 Elastic mounts supporting superstructure

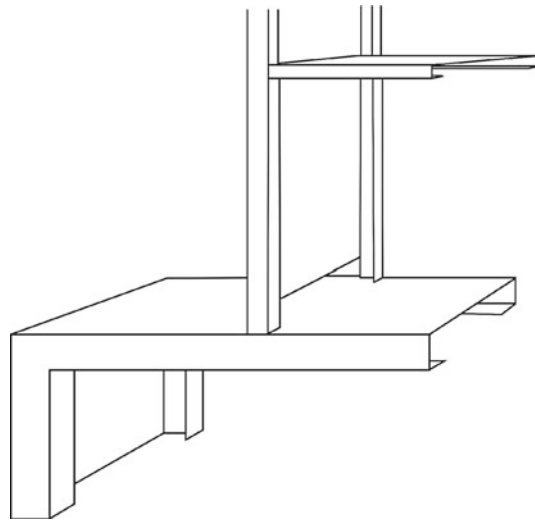


Fig. 14.16 Coupling between the elements 3 and 5

predictions. The higher modes were found to be much less dominant. Comparisons between measured and predicted results are shown in Figs. 14.17 and 14.18.

As shown in Figs. 14.17 and 14.18 the agreement between predicted and measured results is satisfactory for most practical purposes. It is interesting to note that $\Delta L_{3,9} - \Delta L_{3,11} = L_{11} - L_9$ is positive in most of the frequency range. Thus, the velocity

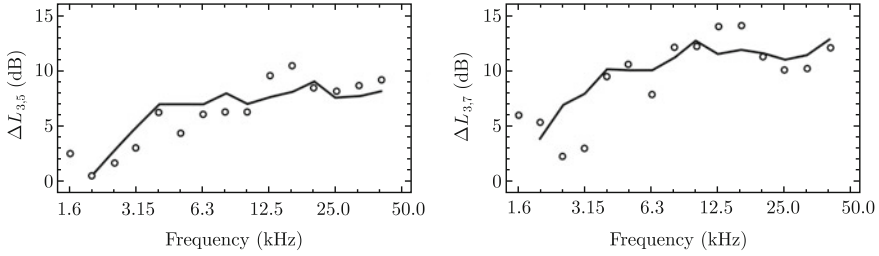


Fig. 14.17 Measured $\circ - \circ$ and predicted—velocity level differences $\Delta L_{3,5}$ (left) and $\Delta L_{3,7}$ (right)

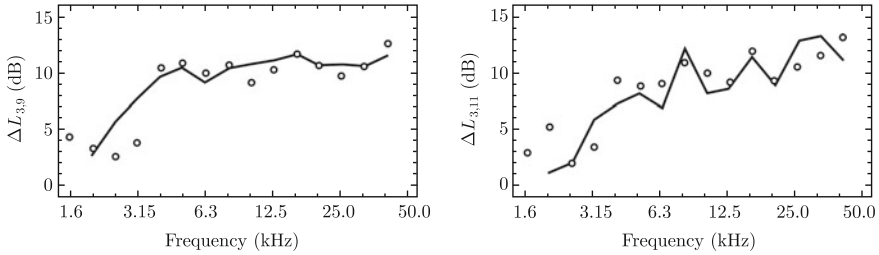
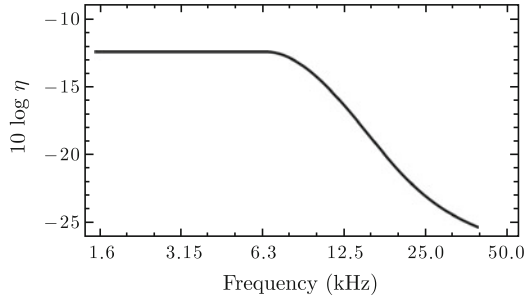


Fig. 14.18 Measured $\circ - \circ$ and predicted—velocity level differences $\Delta L_{3,9}$ (left) and $\Delta L_{3,11}$ (right)

Fig. 14.19 Measured loss factor of plate element with a damping layer



level of the top deck is higher than for the deck below. This is generally also the case for full-scale structures as discussed in Chap. 16.

Some of the damping effects summarized above were investigated through measurements on the models 2–5. The damping layers used consisted of viscoelastic self-adhesive material. The weight per unit area was 1.6 kg/m^2 . The loss factor for plate and damping layer was measured. The average result for a damped element is shown in Fig. 14.19. Predicted and measured velocity level differences between plate 3 and the plates 5, 7, 9, and 11 are compared for the models 2 and 3 in Figs. 14.20 and 14.21. The predictions are all based on the simple waveguide model presented above. The plate elements were assumed to be clamped along the frames. In the calculations the added mass of the damping layer is considered. The stiffness of the layer is neglected.

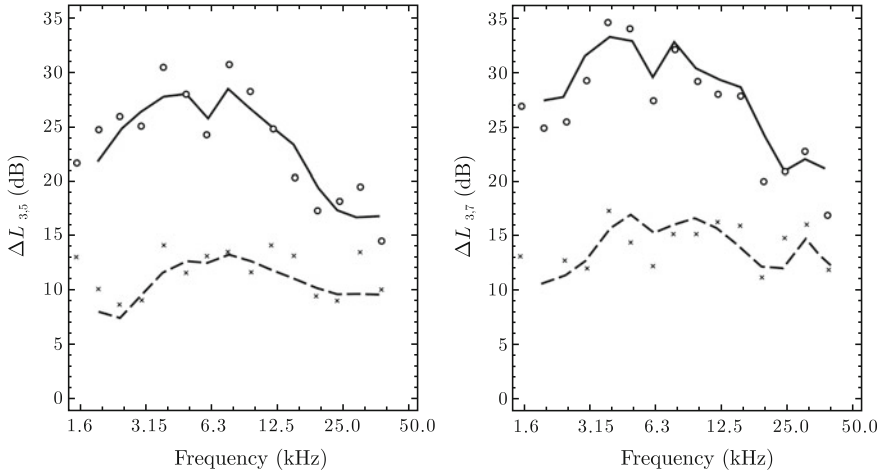


Fig. 14.20 Measured and predicted velocity level differences: $\circ - \circ$ measured model 3; $—$ predicted model 3; $\times \times$ measured model 2; $- - -$ predicted model 2. The velocity level difference $\Delta L_{3,5}$ is shown in left graph and $\Delta L_{3,7}$ in the right graph

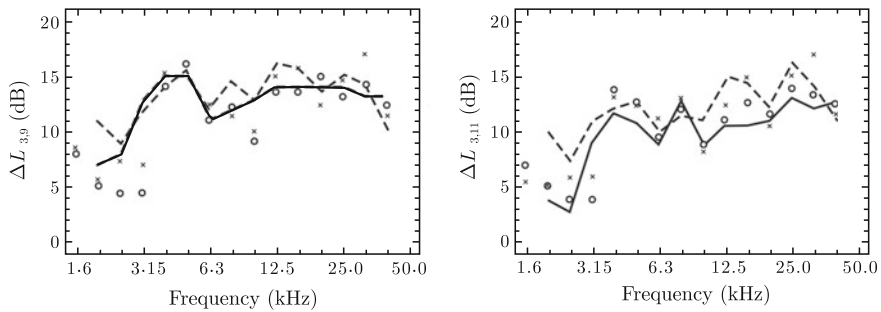
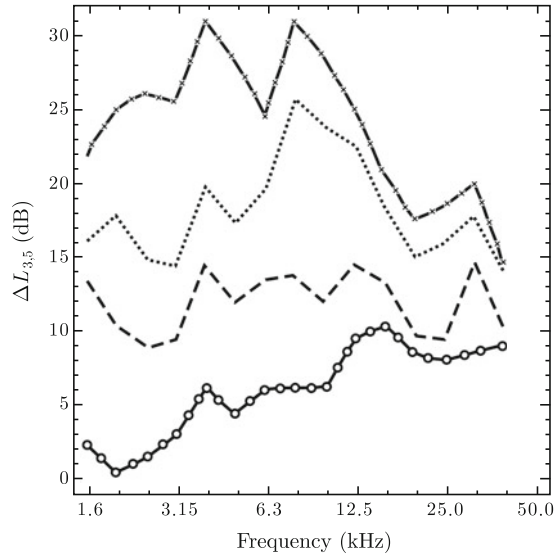


Fig. 14.21 Measured and predicted velocity level differences: $\circ - \circ$ measured model 3; $—$ predicted model 3; $\times \times$ measured model 2; $- - -$ predicted model 2. The velocity level difference $\Delta L_{3,9}$ is shown in left graph and $\Delta L_{3,11}$ in the right graph

The results for model 2 and 3 indicate that the velocity level of a deck is decreased more effectively if the damping layer is applied directly to the deck itself rather than to the vertical plate sections below the deck. The velocity levels of the two top decks, elements 9 and 11, are more or less independent of where on the lower plate elements the damping layers are applied. In fact, the velocity level of the top plate, element 11, is approximately equal for the models 1–5 if the input power to the structure is kept constant.

The damping layers on the elements 4 and 6 on model 2 decrease the energy flow due to flexural waves more effectively than the flow caused by longitudinal waves. It could therefore be expected that the velocity levels of the decks on model 2 were determined by longitudinal waves. However, the agreement between measured and

Fig. 14.22 Measured velocity level differences between elements 3 and 5:
 ○ — ○ — ○ model 1; ---- model 2; -x-x-x model 3;
 model 4



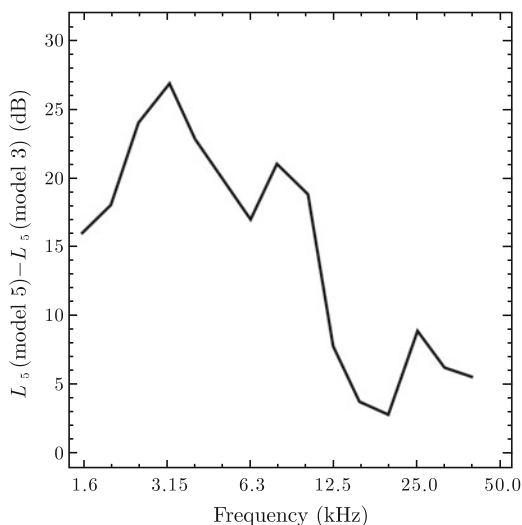
predicted levels using the waveguide model, flexural waves only, indicate that the role of the longitudinal waves is comparatively insignificant in these model tests. The full-scale measurements reported in Refs. [197, 198] confirm that the power flow in typical waveguide structures is mainly determined by flexural waves.

In Fig. 14.22 the measured velocity level differences $\Delta L_{3,5}$ are compared for models 1–4. For models 2 and 4 the total area clad with damping layers is the same. Method 4 is however more effective. The velocity level of a deck is not just a simple function of the total losses. A reduction of the clad area to one third of the total area of deck 5 increases the velocity level by 10 dB in the low frequency range as shown in Fig. 14.22, and this should be compared with the results for models 3 and 4. In the high frequency range, the difference is considerably smaller.

Damping layers applied to a transmission path between a source and receiver perform poorly. The reason is that the transmission from one element to another is due to forced rather than resonant transmission. A damping layer on a plate is only effective at frequencies at or close to some natural frequency of the plate. Compare the discussion in Sect. 6.4, see also Fig. 6.5. For a plate, having the same natural frequency as an adjoining plate the effect of a damping layer on the energy flow between the plates would be significant. However, in a finite structure like the one shown in Fig. 14.14 even equal plates do not necessarily have coinciding natural frequencies. The natural frequency of an element not only depends on its material parameters and geometry but also on its coupling to adjoining structures and on its position in a built-up structure. Thus, no elements in Fig. 14.14 are dynamically identical.

The measured velocity levels of deck 5 for model 3, damping on two decks in superstructure, and model 5, damping on main deck or plate 3, are compared

Fig. 14.23 Comparison between the measured velocity levels of plate 5 for models 5 and 3. The input power to the structure was the same in both cases

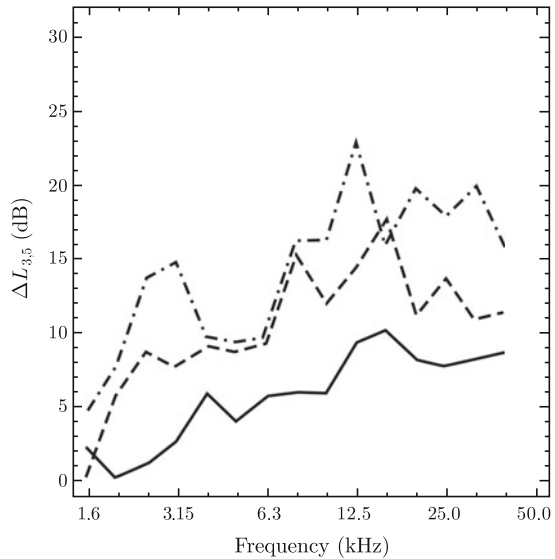


in Fig. 14.23. The result confirms the general conclusion that if the velocity of an element is to be decreased the best result is obtained if the damping layer is applied to the element itself.

The noise transmission to a superstructure is reduced if the entire construction is resiliently mounted. The concept has been used for ships with deadweight up to 30,000 tons. The simple natural frequency for the mass–spring system is in full scale of the order 5–10 Hz. Full-scale measurements indicate that a resilient mounting can reduce noise levels in a superstructure of the order 10 dB. Model 6, Fig. 14.15 is not directly comparable to a real ship structure. The reason is that on a ship there is an additional deck directly above the resilient mounts. The configuration shown in Fig. 14.15 was chosen to make all models comparable. The first natural frequency for the mass–spring system is of the order 140 Hz corresponding to 7 Hz in full scale. For model 6, the elastically mounted superstructure, the measured velocity level differences between plate elements 3 and 9 are shown in Fig. 14.24. For comparison, the corresponding results for the original configuration, model 1, are included. The reduction of the velocity levels due to the elastic mounts is of the same order as observed for full-scale measurements. An apparent advantage of elastic mounts as compared to damping layers is that the velocity levels of all structures beyond the mounts are reduced whereas a damping layer primarily reduces the velocity level of the structure to which the layer is applied.

The waveguide model is based on the assumption that the main energy flow is due to flexural waves propagating in plate elements between parallel frames. This assumption has been verified by means of full-scale measurements. Based on this assumption it could be expected that the energy flow between two waveguide elements could be reduced if the coupling between the plate elements is disconnected. Figure 14.16 shows an example of this type of coupling. The vertical plate element 4 was connected to the main deck via the frames only. All other junctions were

Fig. 14.24 Measured velocity level difference between elements 3 and 5 — model 1; --- model 6; ---- model 7



unchanged. The measured velocity level difference between the elements 3 and 5 is shown in Fig. 14.24. The corresponding results for model 1, the basic design, and for model 6, the resiliently mounted structure, are also shown in the graph. On the average the velocity level difference $\Delta L_{3,5}$ is increased by 5 dB by decoupling the plate elements 3 and 4 as shown in Fig. 14.16. This indicates that the energy flow in a plate element is of the order 5 dB higher than in the energy flow in the coupled frames.

The results of the model-scale measurement show that with a certain degree of accuracy the energy flow in coupled waveguide systems like a ship can be predicted from a simple waveguide model in which only flexural waves are included. The additional attenuation due to damping layers can also be estimated based on the same type of model. Damping layers on a part of a structure tend to decrease the velocity level of only that part of the structure that is damped. The velocity level of adjoining elements is reduced to a much lesser extent. If the boundary conditions between a superstructure and the hull are changed the energy flow to the superstructure can be reduced considerably. A resilient mounting could give a reduction of 10 dB and a decoupling of plate elements 5 dB.

Some general conclusions:

- (i) Damping layers applied to a transmission path between source and receiver is in general ineffective with respect to the energy flow transmitted to the receiving plate element.
- (ii) Damping of elements at receiving end most effective for reducing the energy of these elements.
- (iii) Relaxation of coupling between elements decreases energy flow to all elements beyond the coupling.

- (iv) Simple waveguide models predict well the energy flow in waveguide structures with and without damping layers.

The points (i)–(iii) apply to any type of built-up structure.

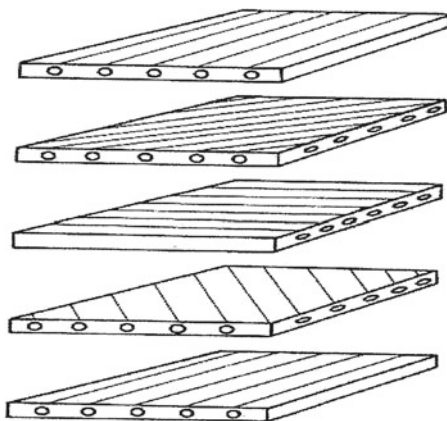
Full-scale measurements and predictions are discussed further in Chap. 16. See also Refs. [196, 208].

14.5 Composite, Sandwich, and Honeycomb Plates

For many applications the use of lightweight structures is of great importance. This has always been the case for the aircraft industry. The shipbuilding, car, truck, and train industries have now followed suit. To meet a growing demand a variety of different types of sandwich panels have been developed during the last few decades. A sandwich panel is a structure with a fairly thick lightweight core with thin laminates bonded to each side of either a foam or a honeycomb core. A sandwich plate combines low weight with high strength. However, for certain types of sandwich plates the acoustic properties can be very poor. The absence of acoustic qualities can severely restrict the use of sandwich elements. Some dynamic properties of sandwich elements have already been discussed in Sects. 4.7 through 4.11. In these sections, the general wave equation was used to describe the displacement in the thick core of a sandwich structure. In Sect. 9.3 the bending of a sandwich structure was derived based on Hamilton's principle. The results from Sect. 9.3 in this chapter are used to determine the response of finite sandwich beams and plates.

The laminates of a sandwich structure can often consist of 3–20 layers of fibers oriented in different directions to give anisotropic dynamic properties. One example is shown in Fig. 14.25. This type of very strong and lightweight structure can also be used on its own, i.e., without the backing of a core and an additional laminate. Again, this type of composite structure is nowadays frequently used by the aircraft industry.

Fig. 14.25 Construction of a laminate



The laminates of a sandwich structure could also be thin metal sheets. In the building industry the “laminates” could even be made of lightweight concrete. A number of textbooks, papers on applications, measurements and theories on laminated plates, and sandwich structures have been published. The Refs. [32, 40, 41, 79–81, 209–213] are just a few examples. The first model describing the flexural vibrations of slender beams was developed independently by Euler and Bernoulli in the mid-eighteenth century. They both assumed that the deflection of a beam is due to only pure bending. Later Lord Rayleigh [90] and Timoshenko [214] considered shear and rotational effects to describe the lateral displacement of beams which were not necessarily slender. However, these models are not sufficient for describing the lateral motion of sandwich or honeycomb beams. In the Bernoulli–Euler theory it is assumed that the shear modulus of the beam is infinite. The theory is therefore only applicable as long as the wavelength of the flexural waves is much larger than the dimensions of the cross section of the beam. The Timoshenko theory predicts that in the high frequency region the lateral deformation of a beam is governed by the effects of shear and rotation. For a three-layered sandwich beam the lateral displacement is governed by the bending of the laminates. Thus, although the Timoshenko theory can be used for higher frequencies than the basic Bernoulli–Euler theory, even this theory fails for increasing frequencies or in fact in the frequency range of greatest importance for typical sandwich constructions.

Research on the flexural displacement of sandwich beams has intensified during the last few decades. So, for example, Kerwin [215] analyzed the damping of flexural waves in composites with viscoelastic layers. Mead and Markus [216] introduced a sixth-order theory neglecting rotational inertia. They investigated the response of a sandwich beam subjected to “damped normal loadings” and presented orthogonality relations for describing the displacement of the beam. Mead presented in Ref. [217] a short review of some different theories on sandwich beams and also presented a new model taking into account the effects of inertia and shear deformation in the laminates resulting in sixth- and eighth-order differential equations describing the lateral motion of symmetric as well as asymmetric sandwich beams. Boundary conditions were not discussed. In Ref. [80] even a 10th-order differential equation is briefly discussed. However, it is concluded in [80] that in most practical cases and in a frequency range up to 5 kHz a sixth-order differential equation should be sufficient to describe the displacement of a typical sandwich beam. In Ref. [40] an “exact” model is presented which describes the lateral displacement of sandwich beams with a thick core and thin laminates. The basic model was discussed in Sects. 4.9–4.11. The model was investigated further in [41]. It was found that the wavenumbers necessary for describing the displacement of the beam could only be determined by using rather sophisticated numerical methods for solving ill-conditioned and huge systems of equations. In addition boundary conditions for finite beams were not readily defined. However, the model allows a detailed mapping of the displacement of core and laminates. One result from Ref. [41] is shown in Fig. 14.26. The figure represents deformation due to bending at 3.5 kHz of a standard sandwich beam.

A simple model based on Hamilton’s principle was introduced in Ref. [79] to describe the lateral displacement of sandwich and honeycomb beams. The result was

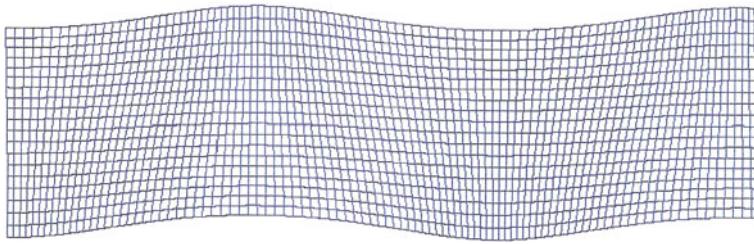
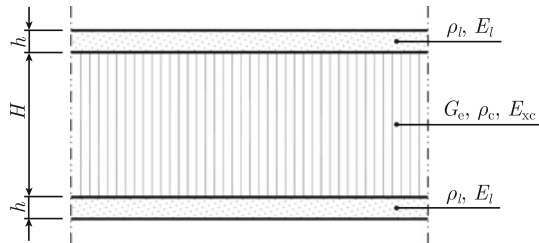


Fig. 14.26 Deformation of the cross section of a sandwich beam. From Ref. [41]

Fig. 14.27 Sandwich structure made up of laminates and core

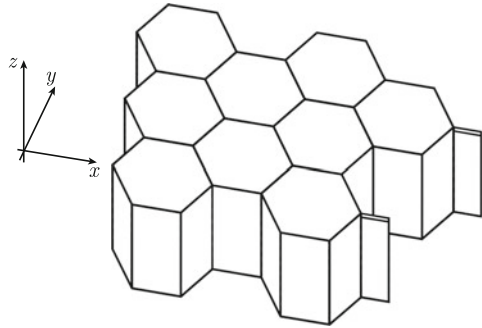


a sixth-order differential equation governing the lateral displacement of symmetric beams as demonstrated in Sect. 9.3. Boundary conditions are included. The model agrees well with results derived from the “exact” model [40] and with measured results. Vibration of asymmetric sandwich structures are discussed in for example Ref. [81]. Models resulting in eighth-order differential equations do not significantly improve the accuracy of predictions of the response and vibration of standard sandwich elements. However, the computational efforts are multiplied.

The geometry of the type of sandwich element considered here is shown in Fig. 14.27. In general, a sandwich construction is symmetric with respect to the center line. The thickness of the lightweight core is typically of the order 5–75 mm whereas the thickness of the laminates could vary between 0.5 and 8 mm. The E -modulus for a laminate is high and much higher than the corresponding modulus for the core. A laminate can be treated as thin as long as the wavelength for pure bending waves in the structure is larger than six times the thickness of the laminate. For the lateral motion or the bending of the entire sandwich construction, it is assumed that the displacement of a laminate is determined by flexural and longitudinal waves.

The displacement of the laminates can therefore be described by means of longitudinal waves in the plane of the plate or beam and by simple flexural waves (Euler beam or Kirchhoff plate theory). For a sandwich element with an isotropic foam core the displacement within the core can be described by means of the general wave equation as discussed in Ref. [40] and summarized in Sect. 4.9. In general, both the in-phase and antiphase motion of the laminates must be considered for foam cores. However, for typical honeycomb cores, Fig. 14.28, the stiffness of the core material in the direction perpendicular to the laminates is sufficiently high to allow only the in-phase motion of the laminates except in the very high frequency range.

Fig. 14.28 Ideal honeycomb structure



The dynamical properties of a composite beam or plate depend on the geometry of the structure as well as on the material properties of core and laminates. The method of bonding laminates to core can also influence the dynamic properties of sandwich constructions. For example, a bonding substance can increase the spacing between the laminates. As compared to metal laminates the properties of a composite laminate depend on the build up of the structure, the number of plies and their orientation, the type of resin used, etc. Figure 14.25 shows a fiber construction of a laminate.

In order to determine dynamic properties like bending stiffness of a laminate the material and geometrical properties of the plies or layers must be well known. This is not always the case. Besides, existing tools for predicting properties of composite structures are not always sufficiently accurate. The area weight is readily controlled whereas the E -modulus of a structure is far much more complicated to determine. The E -modulus of a small sample of a laminate can, for example, be determined by means of the ISO procedure 6721, Part 5. For the prediction of the response of a composite structure due to some external dynamic force the bending stiffness of the structure should be known. The thickness of a metal plate used, for example, in the car, aircraft, or ship industries shows very small variations from its nominal thickness. In addition the E -modulus, Poisson's ratio, and density of a metal structure are known with good precision helping to improve the accuracy of any type of FEM calculation. The opposite seems to be the case for composite laminates. Due to local variations of a laminate, E -modulus and thickness can vary considerably with location. It can therefore be very misleading to determine the bending stiffness of a laminate based on measurements on small samples. The average bending stiffness of a beam representing part of a plate can be measured in a simple but yet sufficiently accurate way. The beam investigated is suspended by strings to simulate free-free boundary conditions as discussed in Sect. 14.9. The beam is excited by an impact hammer and its response measured by means of a laser. Based on the recorded frequency response function the first few natural frequencies are determined. The bending stiffness of a thin laminate can be considered as frequency independent up to fairly high frequencies. For a beam with a length of approximately 1.2 m, the first ten bending modes and natural frequencies can often be identified. The average bending stiffness of a beam can therefore be determined fairly accurately based on these measurements.



Fig. 14.29 Aluminum foam core

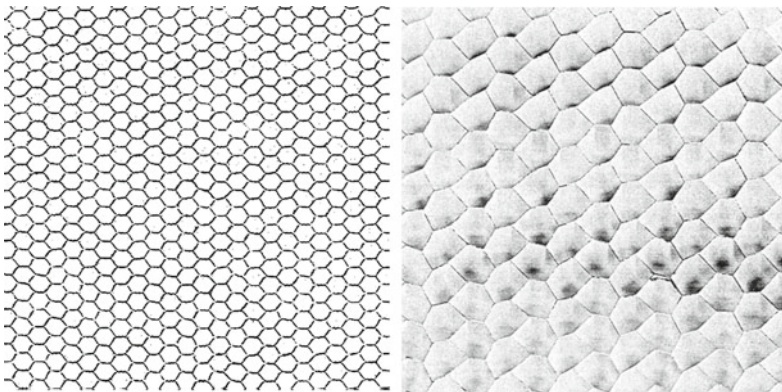


Fig. 14.30 Geometries of a Nomex and an aluminum honeycomb core

The bending stiffness was in this way measured for eight beams cut out of four composite test panels, consisting of 14–16 plies, which were carefully manufactured to be used for various types of tests. The average bending stiffness of the beams could be determined within $\pm 4\%$, assuming a 95% confidence interval. The deviation between the bending stiffness measured on beams and on small samples of the same structure could however vary by as much as $\pm 30\%$!

The properties of core materials can also vary considerably. Plastic foams can often be considered as being isotropic and homogeneous. Other types of foams, for example, aluminum foam, can show large geometrical variations as indicated in Fig. 14.29. The geometries of one Nomex and one aluminum honeycomb core are shown in Fig. 14.30. It is evident that the corresponding dynamic properties of such core structures must be based on some space average. Means of estimating the dynamic properties are discussed in Sect. 14.9.

14.6 Flexural Vibrations of Honeycomb/Sandwich Beams

The normal deflection of a sandwich panel is primarily caused by bending but also by shear and rotation in the core as discussed in Sect. 9.3. The total lateral displacement w of a sandwich beam is a result of the angular displacement due to bending of the core as defined by β and the angular displacement γ due to shear in the core as $\partial w/\partial x = \gamma + \beta$ for a beam oriented along x -axis of a coordinate system. The differential equations governing w , β , and γ can be determined using Hamilton’s principle as shown in Sect. 9.3. In deriving the equations governing the lateral displacement of the structure shown in Fig. 14.31 the symmetry is assumed. The identical laminates have a Young’s modulus E_l , bending stiffness D_2 , density ρ_l , and thickness h . The effective shear stiffness of the core is G_c , its Young’s modulus E_c , its equivalent density ρ_c , and its thickness H . The parameter G_c is for a thick core not necessarily equal to the shear stiffness G as suggested by Timoshenko [218]. The core itself is assumed to have a very low stiffness E_{cx} in the x -direction. In the y -direction, the core is assumed to be sufficiently stiff to ensure that the laminates move in phase within the frequency range of interest. The static bending stiffness of the beam, width b , is

$$D'_1 = b[E_{cx}H^3/12 + E_l(H^2h/2 + Hh^2 + 2h^3/3)]$$

In general $E_l \gg E_{cx}$. The bending stiffness of one laminate is $D'_2 = bE_lh^3/12$. The mass moment of inertia is defined as $I'_w = b[\rho_cH^3/12 + \rho_l(H^2h/2 + Hh^2 + 2h^3/3)]$ while the mass per unit length is $m' = \mu b = b(2h\rho_l + H\rho_c)$. The cross-sectional area of the core is $S = b \cdot H$.

As demonstrated in Sect. 9.3 it is found that the displacement w and the angular displacement β caused by an external force F' per unit length of the beam must satisfy the differential equations

$$- G_c S \left\{ \frac{\partial^2 w}{\partial x^2} - \frac{\partial \beta}{\partial x} \right\} + 2D'_2 \left\{ \frac{\partial^4 w}{\partial x^4} - \frac{\partial^3 \beta}{\partial x^3} \right\} + m' \frac{\partial^2 w}{\partial t^2} - F' = 0 \quad (14.28)$$

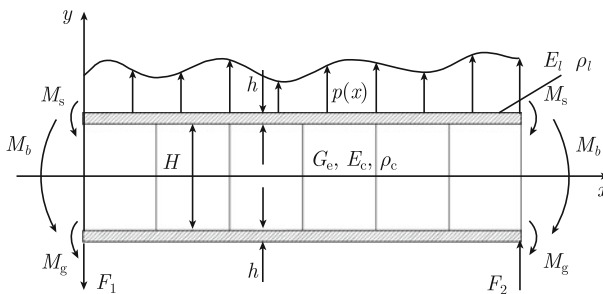


Fig. 14.31 Excitation of beam and resulting forces and moments. For a symmetric beam $M_g = M_s$

$$-G_c S \left\{ \frac{\partial w}{\partial x} - \beta \right\} - D'_1 \frac{\partial^2 \beta}{\partial x^2} + 2D'_2 \left\{ \frac{\partial^3 w}{\partial x^3} - \frac{\partial^2 \beta}{\partial x^2} \right\} + I'_\omega \frac{\partial^2 \beta}{\partial t^2} = 0 \quad (14.29)$$

Eliminating β the equation governing w is obtained as

$$\begin{aligned} -2D'_1 D'_2 \frac{\partial^6 w}{\partial x^6} + 2D'_2 I_\omega \frac{\partial^6 w}{\partial x^4 \partial t^2} + G_c S D'_1 \frac{\partial^4 w}{\partial x^4} - [(D'_1 + 2D'_2)m' + G_c S I'_\omega] \frac{\partial^4 w}{\partial x^2 \partial t^2} \\ + G_c S m' \frac{\partial^2 w}{\partial t^2} + m' I_\omega \frac{\partial^4 w}{\partial t^4} = G_c S F' - (D'_1 + 2D'_2) \frac{\partial^2 F'}{\partial x^2} + I'_\omega \frac{\partial^2 F'}{\partial t^2} \end{aligned} \quad (14.30)$$

Eliminating w instead gives the corresponding equation for β as given by Eq. (9.41). For no external force on the structure, $F' = 0$, w , and β satisfy the same differential equation.

The boundary conditions to be satisfied are also obtained from the variational expression as shown in Sect. 9.3. The boundary conditions are:

$$F = G_c S \left\{ \frac{\partial w}{\partial x} - \beta \right\} - 2D'_2 \left\{ \frac{\partial^3 w}{\partial x^3} - \frac{\partial^2 \beta}{\partial x^2} \right\} \text{ or } w = 0 \quad (14.31)$$

$$M - 2M_s = -D'_1 \frac{\partial \beta}{\partial x} + 2D'_2 \left\{ \frac{\partial^2 w}{\partial x^2} - \frac{\partial \beta}{\partial x} \right\} \text{ or } \beta = 0 \quad (14.32)$$

$$M_s = -D'_2 \left\{ \frac{\partial^2 w}{\partial x^2} - \frac{\partial \beta}{\partial x} \right\} \text{ or } \frac{\partial w}{\partial x} = 0 \quad (14.33)$$

For a simply supported edge both M and M_s are zero. The conditions for some simple boundary conditions are again summarized in Table 14.2. The boundary conditions were derived in Sect. 9.3.

The corresponding expressions for asymmetric sandwich panels are, for example, presented in [80].

Table 14.2 Boundary conditions for a sandwich beam

End condition			
Simply supported	$w = 0$	$\partial \beta / \partial x = 0$	$\partial^2 w / \partial x^2 = 0$
Clamped	$w = 0$	$\beta = 0$	$\partial w / \partial x = 0$
Free	$\partial \beta / \partial x = 0$	$\partial^2 w / \partial x^2 = 0$	$D'_1 \partial^2 \beta / \partial x^2 - I'_\omega \partial^2 \beta / \partial t^2 = 0$

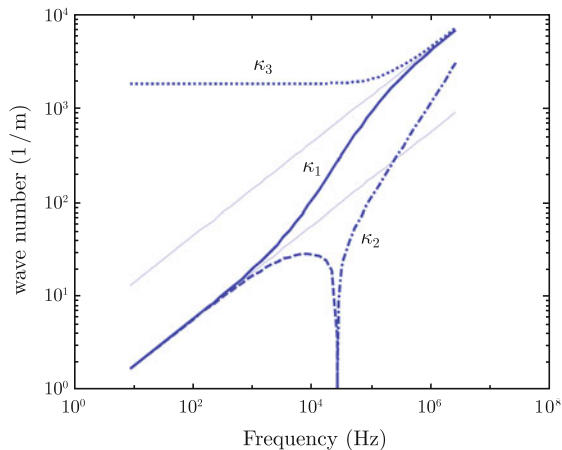
14.7 Wavenumbers, Sandwich/Honeycomb Beams

The dispersion relation, giving the wavenumber as function of frequency and material parameters, is for flexural vibration of a honeycomb beam obtained by setting $w = W \cdot \exp[i(\omega t - k_x x)]$ in the wave equation (14.30) and by assuming the external forces to be zero. The possible wavenumbers k_x must satisfy the equation

$$2D'_1 D'_2 k_x^6 - 2D'_2 I_\omega k_x^4 \omega^2 - [m'(D'_1 + 2D'_2) + I'_\omega G_c S] k_x^2 \omega^2 + G_c S [D'_1 k_x^4 - m' \omega^2] + m' I'_\omega \omega^4 = 0 \tag{14.34}$$

There are six solutions to Eq. (14.34). These solutions are written $k_x = \pm \kappa_1, \pm i \kappa_2, \pm i \kappa_3$ where κ_1 and κ_3 are real whereas κ_2 shifts from being real in the low frequency region to being imaginary for high frequencies. For one particular structure, the wavenumbers or rather their absolute values are shown in Fig. 14.32. The parallel lines in the figure define the upper and lower asymptotes of the wavenumbers describing propagating waves. The bottom line represents the wavenumber for flexural waves propagating in a slender or Euler beam as given by Eq. (3.78). The upper asymptote gives the wavenumber for flexural waves propagating in one of the laminates. The wavenumber for the first propagating mode is given by κ_1 . The second propagating wave is given by κ_2 . This wave is developing from an evanescent wave and could be described as a rotational wave. When wavenumbers are calculated from the approximate expressions derived based on Hamilton’s principle as discussed in Sect. 9.3 only two wavenumbers for propagating waves are obtained. However, if the more exact technique described in Sect. 4.9 is used, the result is an infinite number of wavenumbers. Compare Fig. 4.12 showing the wavenumbers for the first three propagating waves. For most practical problems, the results based on the sixth-order differential equation (14.30) are sufficient to describe the displacement of a sandwich plate.

Fig. 14.32 Wavenumbers for flexural motion of a sandwich beam. From Ref. [79]



The dotted and dashed lines in Fig. 14.32 correspond to purely imaginary roots of Eq. (14.34) and represent near-field solutions or evanescent waves. The wavenumber κ_2 is equal to zero for $f = f_p$ where

$$f_p = \frac{1}{2\pi} \left(\frac{G_c S}{I'_\omega} \right)^{1/2} = \frac{1}{2\pi} \left(\frac{G_c H}{I_\omega} \right)^{1/2} \quad (14.35)$$

For frequencies below f_p the wavenumbers $k_x = \pm i\kappa_2$ are imaginary defining evanescent waves. For $f > f_p$ the solution $k_x = \pm i\kappa_2$ is real representing a rotating and propagating wave. The frequency f_p is decreased as the moment of inertia is increased.

In summary, the limiting values for the wavenumbers are

$$\begin{aligned} \lim |\kappa_1| = \lim |\kappa_2| &= \left(\frac{m'\omega^2}{D'_1} \right)^{1/4} \quad \text{as } f \rightarrow 0; \quad \lim |\kappa_3| = \left(\frac{G_c S}{2D'_2} \right)^{1/2} \quad \text{as } f \rightarrow 0; \\ \lim |\kappa_1| = \lim |\kappa_3| &= \left(\frac{m'\omega^2}{2D'_2} \right)^{1/4} \quad \text{as } f \rightarrow \infty; \quad \lim |\kappa_2| = \left(\frac{I'_\omega \omega^2}{D'_1} \right)^{1/2} \quad \text{as } f \rightarrow \infty \end{aligned} \quad (14.36)$$

Throughout the discussion, it has been assumed that the laminates move in phase. In general, this assumption is valid for sandwich elements with honeycomb cores, which have a high stiffness in the direction perpendicular to the laminates. For sandwich elements with foam cores, the antiphase motion of the laminates should be considered for frequencies close to and above the double-wall resonance f_d where $f_d \approx \sqrt{E_{cy}/(2H\mu)}/(\pi)$. The E -modulus of core in a direction perpendicular to the laminates is denoted as E_{cy} .

The wavenumbers derived using Hamilton's principle agree very well with "exact" solutions discussed in Sect. 4.9 and in Ref. [40]. The "exact" solution yields an infinite number of wavenumbers. However, only the first few are really essential for describing the vibration of a sandwich structure. Further, the boundary conditions obtained from using Hamilton's principle can readily be used to describe the vibration of sandwich structures with simple geometries. The formulation of boundary conditions using the "exact" solution requires very cumbersome numerical methods as discussed in Ref. [41]. Solutions based on Hamilton's principle should be preferred to "exact" solutions as discussed in Refs. [78–82].

14.8 Displacement

For a finite honeycomb beam oriented along the x -axis the displacement w must satisfy the differential equation (14.30). For no external force, $F' = 0$, the angular displacement β should also satisfy the same differential equation. The displacement w must be defined as a function of the wavenumbers κ_1 , κ_2 , and κ_3 . Consequently

$$w = (A_1 \sin \kappa_1 x + A_2 \cos \kappa_1 x + A_3 e^{-\kappa_2 x} + A_4 e^{\kappa_2(x-L)} + A_5 e^{-\kappa_3 x} + A_6 e^{\kappa_3(x-L)}) e^{i\omega t} \quad (14.37)$$

where the boundary conditions and the external forces determine the amplitudes A_1 to A_6 . The angular displacement can be expressed in a similar way as w . Thus,

$$\beta = (B_1 \sin \kappa_1 x + B_2 \cos \kappa_1 x + B_3 e^{-\kappa_2 x} + B_4 e^{\kappa_2(x-L)} + B_5 e^{-\kappa_3 x} + B_6 e^{\kappa_3(x-L)}) e^{i\omega t} \quad (14.38)$$

where κ_1 , κ_2 , and κ_3 are solutions to equation (14.34). In order to completely describe the displacement w and β for a beam, the parameters A_i and B_i need to be determined. However, the parameters A_i and B_i are not independent of each other. By inserting the definitions (14.37) and (14.38) in Eq. (14.29) the result is a function of $\sin \kappa_1 x$, $\cos \kappa_1 x$, etc. The resulting expression should be valid for any x . Thus it follows that the amplitudes of the functions $\sin \kappa_1 x$, $\cos \kappa_1 x$, etc. must equal zero. Consequently, the amplitudes B_i can be determined as functions of the amplitudes A_j . The result, using the abbreviations $D'_i = D'_1 + 2D'_2$ and $\Omega = G_c S - \omega^2 I'_\omega$, is

$$\begin{aligned} B_1 &= -A_2 \frac{2D'_2 \kappa_1^3 + G_c S \kappa_1}{D'_1 \kappa_1^2 + \Omega} = A_2 X_2; & B_2 &= A_1 \frac{2D'_2 \kappa_1^3 + G_c S \kappa_1}{D'_1 \kappa_1^2 + \Omega} = A_1 X_1 \\ B_3 &= -A_3 \frac{2D'_2 \kappa_2^3 - G_c S \kappa_2}{D'_1 \kappa_2^2 - \Omega} = A_3 X_3; & B_4 &= A_4 \frac{2D'_2 \kappa_2^3 - G_c S \kappa_2}{D'_1 \kappa_2^2 - \Omega} = A_4 X_4 \\ B_5 &= -A_5 \frac{2D'_2 \kappa_3^3 - G_c S \kappa_3}{D'_1 \kappa_3^2 - \Omega} = A_5 X_5; & B_6 &= A_6 \frac{2D'_2 \kappa_3^3 - G_c S \kappa_3}{D'_1 \kappa_3^2 - \Omega} = A_6 X_6 \end{aligned} \quad (14.39)$$

From these results it follows that $X_1 = -X_2$, $X_3 = -X_4$, and $X_5 = -X_6$. For a finite beam there are three boundary conditions at each end to be satisfied. These boundary conditions are sufficient for determining the relative amplitudes A_2/A_1 , etc. as well as the eigenfrequencies for the beam.

The procedure of defining the eigenfrequencies and their corresponding modes of vibrations for a finite beam is demonstrated by considering a clamped beam. The boundary conditions for a beam clamped at both ends are according to Table 14.2 given as $w = 0$, $\beta = 0$, and $\partial w / \partial x = 0$ for $x = 0$ and $x = L$. The displacement w is given in Eq. (14.37). The angular displacement β satisfies the same differential equation as w for free vibrations of the beam, i.e., for $F' = 0$ in Eq. (14.30). The six boundary conditions in combination with the Eq. (14.39) give a system of equations, which can be written in matrix form as

$$\begin{bmatrix}
 0 & 1 & 1 & e^{-\kappa_2 L} & 1 & e^{-\kappa_3 L} \\
 \sin \kappa_1 L & \cos \kappa_1 L & e^{-\kappa_2 L} & 1 & e^{-\kappa_3 L} & 1 \\
 X_1 & 0 & X_3 & X_4 e^{-\kappa_2 L} & X_5 & X_6 e^{-\kappa_3 L} \\
 X_1 \cos \kappa_1 L & X_2 \sin \kappa_1 L & X_3 e^{-\kappa_2 L} & X_4 & X_5 e^{-\kappa_3 L} & X_6 \\
 \kappa_1 & 0 & -\kappa_2 & \kappa_2 e^{-\kappa_2 L} & -\kappa_3 & \kappa_3 e^{-\kappa_3 L} \\
 \kappa_1 \cos \kappa_1 L & -\kappa_1 \sin \kappa_1 L & -\kappa_2 e^{-\kappa_2 L} & \kappa_2 & -\kappa_3 e^{-\kappa_3 L} & \kappa_3
 \end{bmatrix}
 \times
 \begin{bmatrix}
 A_1 \\
 A_2 \\
 A_3 \\
 A_4 \\
 A_5 \\
 A_6
 \end{bmatrix}
 = 0 \tag{14.40}$$

The first line is obtained for $w = 0$ at $x = 0$ and the second at $x = L$. The third and fourth are for $\beta = 0$ first at $x = 0$ and then at $x = L$. The last two lines are obtained when $\partial w / \partial x = 0$ for $x = 0$ and $x = L$ respectively. The eigenfrequencies are obtained as solutions to the determinant of the matrix being zero. For each solution or eigenfrequency the relative ratio of the amplitudes is derived from Eq. (14.40) by setting $A_1 = 1$. The amplitudes B_i are thereafter obtained from Eq. (14.39). A corresponding matrix for a beam with free ends is discussed in Problem 14.5. A more general expression valid also for mixed boundary conditions for beams is presented in Ref. [80].

Simple analytical expressions giving the natural frequencies of simply supported beams of length L can be derived by setting $w = A \sin(n\pi x/L)$ and $\beta = B \cos(n\pi x/L)$. The details are left for Problem 14.6. For this particular case the natural frequencies f_n are, neglecting I_ω , given by

$$f_n = \frac{n^2 \pi}{2L^2} \left\{ \frac{D'_1 [2D'_2 \pi^2 n^2 + G_c S L^2]}{m' [(D'_1 + 2D'_2) \pi^2 n^2 + G_c S L^2]} \right\}^{1/2} \tag{14.41}$$

The same result is obtained using the proper matrix equation for simply supported ends as discussed above. For a simple Euler beam, the shear modulus is assumed to be infinite. For this case, the natural frequency of the simply supported sandwich beam is reduced to $f_n = n^2 \pi \sqrt{(D'_1/m')/(2L^2)}$ as given by Eq. (7.12).

By using the method outlined above, the first eight natural frequencies for a lightweight and thin honeycomb beam are predicted for three different boundary conditions. The resulting natural frequencies are listed in Table 14.3. For comparison, the corresponding natural frequencies using the Euler beam theory are also given in Table 14.3. For the Euler beam, the bending stiffness is set to equal the bending stiffness D_1 of the honeycomb beam in the low frequency range.

The natural frequencies predicted from the Euler beam theory are always higher than the corresponding natural frequencies derived as described above. The deviations between the results derived from the two models tend to increase for increasing

Table 14.3 Predicted natural frequencies for a honeycomb beam $L = 1.2$ m; $\mu = 6.14$ kg/m²; $H = 10$ mm; $h = 1$ mm; $G_c = 45 \times 10^6$ Pa; $E_l = 70 \times 10^9$ Pa; $E_c = 0.13 \times 10^9$ Pa

Natural frequency (Hz)	Free ends		Clamped ends		Simply supported ends	
	Euler	Sandw.	Euler	Sandw.	Euler	Sandw.
f_1	71	68	71	61	31	30
f_2	196	168	196	144	125	110
f_3	383	289	383	246	282	217
f_4	634	416	634	357	501	336
f_5	947	544	947	474	783	458
f_6	1323	671	1323	592	1128	582
f_7	1762	796	1762	712	1535	705
f_8	2263	921	2263	832	2005	827

frequencies. For the Euler beam, the natural frequencies for clamped and free boundaries are the same. This is not the case using the model for a sandwich beam. For a clamped beam shear is induced at the boundaries thus rendering the beam more flexible as compared to a beam with free edges. The natural frequencies for a clamped beam are consequently lower than the corresponding natural frequencies for the same beam with free edges. If the length of the beam or the shear stiffness of the core was increased the differences between the natural frequencies for a sandwich beam having free or clamped ends would decrease. See also Fig. 14.33.

The apparent bending stiffness of a sandwich beam is defined as the bending stiffness of a Bernoulli–Euler beam having the same natural frequencies as the sandwich beam. The apparent bending stiffness is thus frequency dependent. The apparent bending stiffness also depends on the boundary conditions of the sandwich beam as shown in [80]. The apparent bending stiffness per unit width of a beam is for three different boundary conditions shown in Fig. 14.33. Each symbol indicates a predicted natural frequency for the beam for each specific boundary condition. In addition, the bending stiffness obtained from κ_1 as discussed in Sect. 14.7 is also illustrated in the figure. The graph shows that the apparent bending stiffness decreases as the boundary conditions are constrained. The influence of the boundary conditions on the apparent bending stiffness would decrease if the length of the beam or the shear stiffness of its core is increased. The influence of the boundary conditions is also reduced as the frequency is increased. The bending stiffness derived from κ_1 is almost identical to the apparent bending stiffness of a simply supported beam.

Plotting the displacement of the honeycomb beam at any of the natural frequencies shows the influence of shear and bending. The displacement w and the angular displacement β and γ are shown in Fig. 14.34 for a clamped beam at the eigenfrequency f_8 . The shear has maxima at the two ends of the clamped panel. Shear and rotational angles are large when the displacement of the beam is small as shown in Fig. 14.34.

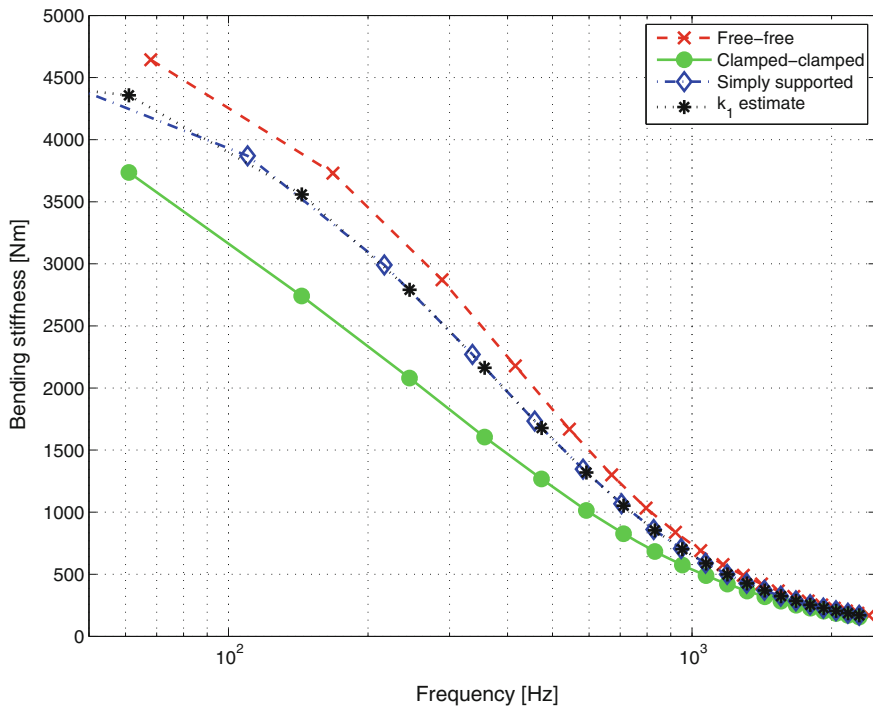


Fig. 14.33 Apparent bending stiffness as function of boundary conditions and frequency for a sandwich beam

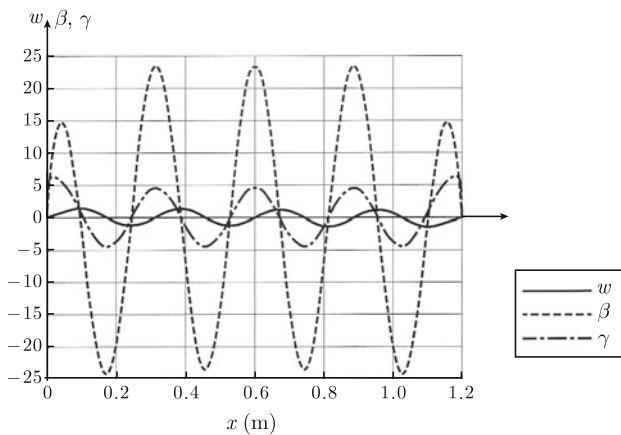


Fig. 14.34 Relative displacement, bending, and shear of a beam along its x -axis at 1054 Hz. Material parameters are given in Table 14.3

For a vibrating lightweight and stiff structure the fluid loading of the surrounding air has a certain effect in the low frequency range. This is demonstrated in Ref. [79]. The natural frequencies of a 1.2 m long sandwich beam, weight per area 2.6 kg/m^2 , were measured with the beam suspended in a vacuum chamber. The first natural frequency of the beam was 32 Hz with fluid loading and 37 Hz in vacuo. This corresponds a weight increase of approximately 40% due to the fluid loading. The effect of the fluid loading is decreasing for increasing frequencies as discussed in Sect. 12.1.

14.9 Dynamic Properties of Sandwich Beams

In the previous section, the wave equation governing the displacement of a honeycomb beam was derived. Based on this differential equation the wavenumbers, eigenfrequencies, and modes of vibration can be determined for different boundary conditions. For the response of a beam to be calculated all the material parameters of the beam must be known. The dynamic properties of a composite beam are not always well defined as previously discussed. In addition, the elements of the assembled structure perform differently when bonded together as compared to when vibrating separately. However, the main dynamic properties of a composite beam can be determined from measurements of the first few eigenfrequencies of the structure when freely suspended.

Returning to Eq. (14.34) the wavenumber $k_x = \kappa_1$ for the first propagating wave can be written as $k_x^4 = \omega^2 m' / D'_x$ where D'_x is the apparent bending stiffness of the structure. Consequently D'_x can, as a first approximation, be defined as the bending stiffness of a simple homogeneous beam, which at a certain frequency has the same dynamic properties as the honeycomb structure. By inserting the definition of k_x in the expression (14.34) an equation in D'_x is obtained. The resulting expression can generally be simplified whenever $D'_1 \gg D'_2$ and $\omega^2 I'_\omega \ll G_c S$. For the structures discussed here, these assumptions hold for frequencies below 4 kHz as shown in Ref. [219]. The apparent bending stiffness D'_x is, considering these approximations, obtained as the solution to the equation

$$\left(\frac{G_c S}{\sqrt{m' \omega}} \right) \left[\frac{D_x'^{3/2}}{D_1'} - D_x'^{1/2} \right] + D'_x - 2D'_2 = 0 \quad (14.42)$$

In the low frequency range, or as $\omega \rightarrow 0$, the first part of the equation dominates why $D'_x \rightarrow D'_1$. The bending stiffness is consequently determined by pure bending of the beam. In the high frequency range, when $\omega \rightarrow \infty$, then $D'_x \rightarrow 2D'_2$. For high frequencies, the laminates are assumed to move in phase. In this frequency range, the bending stiffness for the entire beam is equal to the sum of the bending stiffness of the laminates. This agrees with the results discussed in the previous sections.

For a beam with boundary conditions well defined, the bending stiffness can be determined by means of simple measurements. The apparent bending stiffness D'_{xn} for mode n having the eigenfrequency f_n is for a beam with free ends, length L and mass per unit area μ , given by

$$D'_{xn} = 4\pi^2 f_n^2 m' L^4 / \alpha_n^4; \quad \alpha_n = 4.73, 7.85, 11.00, 14.14 \text{ for } n=1, 2, 3, 4 \text{ resp.}, \\ \text{for } n \geq 5 \quad \alpha_n = n\pi + \pi/2$$

The bending stiffness of a composite beam is strongly frequency dependent as given by Eq. (14.42). Equation (14.42) is written in a more general way as

$$\frac{A}{f} D_x'^{3/2} - \frac{B}{f} D_x'^{1/2} + D'_x - C = 0 \quad (14.43)$$

where

$$A = \frac{G_c S}{\sqrt{m'} 2\pi D'_1}; \quad B = \frac{G_c S}{\sqrt{m'} 2\pi}; \quad C = 2D'_2 \quad (14.44)$$

For nonmetallic materials, Young's modulus could exhibit a slight frequency dependency as discussed in, for example, Ref. [211] and demonstrated in Refs. [18, 20]. However, within the frequency range of interest, here up to 4 kHz, the parameters D'_1 , D'_2 , and G_c in Eq. (14.44) are assumed to be constant for the structures investigated. Using the measured data, the parameters A , B , and C can be determined by means of the least square method. The quantity Q_1 is defined by

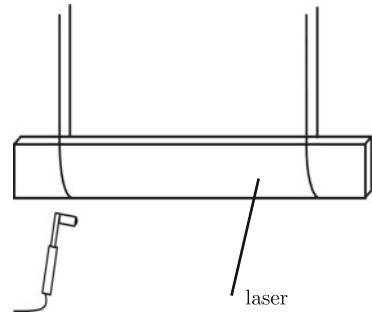
$$Q_1 = \sum_i \left(\frac{A}{f_i} D_{xi}'^{3/2} - \frac{B}{f_i} D_{xi}'^{1/2} + D'_{xi} - C \right)^2 \quad (14.45)$$

where D'_{xi} is the measured bending stiffness at the frequency f_i for mode i . The parameters A , B , and C are chosen to give the minimum of Q_1 . The shear modulus G_c and the bending stiffnesses D'_1 and D'_2 can be determined, once the parameters A , B , and C are calculated from Eq. (14.43).

The method to determine the dynamic parameters of a beam based on the expression (14.45) can be somewhat improved. By using Eq. (14.45) to determine the parameters A , B , and C of Eq. (14.43) the low frequency measurements will dominate. The parameter A , which depends on the static bending stiffness D'_1 is therefore determined from (14.45) by solving the system of equations resulting from setting $\partial Q_1 / \partial A = \partial Q_1 / \partial B = \partial Q_1 / \partial C = 0$. If instead the quantity

$$Q_2 = \sum_i \left(A D_{xi}'^{3/2} - B D_{xi}'^{1/2} + f_i D'_{xi} - f_i C \right)^2 \quad (14.46)$$

Fig. 14.35 Suspension of beam to simulate free–free boundary conditions. An impedance hammer is used for excitation and laser for recording the response of the beam



is minimized the high frequency response of the beam will dominate. The parameter A obtained from Eq. (14.45) is inserted in Eq. (14.46) and the parameter C is determined from a system of equations by setting $\partial Q_2/\partial B = \partial Q_2/\partial C = 0$. In the mid-frequency region the variational expression is written as

$$Q_3 = \sum_i \left(\frac{A}{\sqrt{f_i}} D_{xi}^{\prime 3/2} - \frac{B}{\sqrt{f_i}} D_{xi}^{\prime 1/2} + \sqrt{f_i} D_{xi}' - \sqrt{f_i} C \right)^2 \quad (14.47)$$

The parameters A and C are known and B is the solution to $\partial Q_3/\partial B = 0$.

Measurements reported in Refs. [79, 219] were performed on beams with different boundary conditions to verify the theories outlined above. The survey included beams with honeycomb as well as foam cores. The beams investigated had also different types of laminates. In order to determine the apparent bending stiffness of a beam, the beam was suspended by strings to simulate free–free boundary conditions as shown in Fig. 14.35.

An accelerometer was mounted on the beam. Alternatively, a laser measured the velocity for lightweight structures. An impedance hammer was used to excite the beam. The resulting FRF was recorded and the natural frequencies of the free–free beam were recorded. For the sandwich beams tested, the first ten modes and natural frequencies could at least be identified. In every case the length of each beam was approximately 1.2 m. The measurement technique was first tested on a beam with well-defined bending stiffness. The repeatability of the measurements was found to be satisfactory. Measurements of the velocity on both laminates were recorded to verify that the laminates were moving in phase in the frequency range of interest. The details are discussed in Ref. [219].

Since honeycomb plates are predominantly anisotropic, measurements should be performed on beams representing the two main in-plane directions of the plate. The vibration measurements should preferably be made with a laser vibrometer to achieve noncontact measurements. The natural frequencies are determined from the measured frequency response function. Based on the frequency response function the loss factor can also be determined. The effect of the boundary conditions on the apparent bending stiffness has also been investigated. Measurements were made on

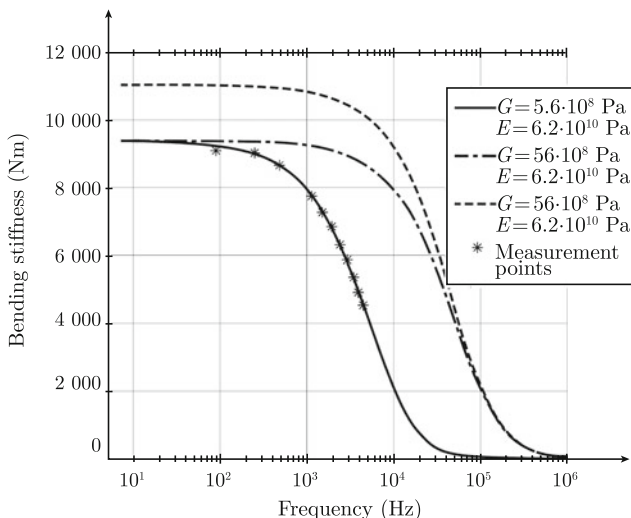


Fig. 14.36 Predicted bending stiffness of a honeycomb beam

a beam with both ends free and with one end free and the other firmly mounted to simulate a clamped boundary. For each natural frequency f_n the corresponding apparent bending stiffness D_{xn} is determined in Ref. [219]. At least three sets of data, f_n and D'_{xn} , determine the shear modulus G_c and the bending stiffnesses D'_1 and D'_2 .

The apparent frequency-dependent bending stiffness $D_x = D'_x/b$ per unit width for one type of honeycomb beam is shown in Fig. 14.36. The predicted bending stiffness or rather the value D_x giving the best fit to the measured results, the solid line, is determined from the first 12 natural frequencies of the freely suspended beam. For comparison, the effect of increasing the shear modulus by a factor 10 is also indicated in the figure. In addition, the figure shows the effect of increasing the E -modulus of the laminates from 6.2×10^{10} Pa to 8×10^{10} Pa.

Losses can be included in the prediction models by allowing shear and E -modulus to be complex or by defining the modulus as $E_n = E_{0n}(1 + i\eta_n)$, etc. in Eq. (14.34). The resulting wavenumber for propagating waves is then obtained as $\kappa_1 = \kappa_{10}(1 - i\eta_{tot}/4)$ where η_{tot} is the total loss factor of the structure as discussed in Sect. 5.6. A comparison between predicted and measured losses is shown in Fig. 5.15.

14.10 Bending Stiffness of Sandwich Plates

It is not always convenient or possible to cut beams from a plate for determining the bending stiffness of a structure. An alternative method is to measure the point mobility of the plate. Based on this type of measurement the apparent bending stiffness of the plate can be estimated.

The point mobility of a rectangular plate, sides L_x and L_y , can, according to Eq. (8.73), be written as

$$Y(x_j, y_j) = \sum_{mn} \frac{4i\omega\varphi_{mn}^2(x_j, y_j)}{(2\pi)^2 m_p (f_{mn}^2 - f^2 + i\eta f_{mn}^2)}$$

The mass m_p of plate is $\mu \cdot L_x \cdot L_y$, where μ mass per unit area of plate. The natural frequencies of the plate are denoted as f_{mn} . The frequency is given by f . The angular frequency is $\omega = 2\pi f$ where f is the frequency. The loss factor of the plate is η . The eigenfunctions satisfying the boundary conditions of the plate are $\varphi_{mn}(x, y)$. For a simply supported plate with the corners at $(0, 0)$, $(0, L_y)$, (L_x, L_y) , and $(L_x, 0)$ the eigenfunctions are $\varphi_{mn}(x, y) = \sin(m\pi x/L_x) \sin(n\pi y/L_y)$. The mobility is determined at a point with the coordinates (x_j, y_j) .

Since $\frac{1}{N} \sum_{j=1}^N \varphi_{mn}^2(x_j, y_j) \approx \frac{1}{4}$ for $m > 0$ and $n > 0$ the space average $\langle Y \rangle$ of the mobility measured in N points is

$$\langle Y \rangle = \frac{1}{N} \sum_{j=1}^N Y \approx \sum_{mn} \frac{if}{(2\pi)m_p (f_{mn}^2 - f^2 + i\eta f_{mn}^2)}$$

For a freely suspended plate m and n can equal zero. For either m or n zero $\frac{1}{N} \sum_{j=1}^N \varphi_{mn}^2(x_j, y_j) \approx \frac{1}{2}$. The real part of $\langle Y \rangle$ is for $m > 0$ and $n > 0$

$$\text{Re}\langle Y \rangle = \sum_{mn} \frac{\eta f f_{mn}^2}{2\pi m_p [(f_{mn}^2 - f^2)^2 + (\eta f_{mn}^2)^2]} \quad (14.48)$$

The frequency average of $\text{Re}\langle Y \rangle$ is

$$\text{Re}\langle \bar{Y} \rangle = \frac{1}{\Delta f} \int_{f_{mn}-\Delta f/2}^{f_{mn}+\Delta f/2} df \text{Re}\langle Y \rangle$$

where Δf is frequency distance between two natural frequencies of the plate. For sufficiently high frequencies Δf is independent of the boundary conditions of the plate and as given in Eq. (8.19) equal to $\Delta f = 2\sqrt{D/\mu}/S$. Consequently, the frequency average of Eq. (14.48) gives

$$\text{Re}\langle \bar{Y} \rangle = \frac{\eta\sqrt{\mu}}{4\sqrt{D}\pi\mu} \frac{\pi}{2\eta} = \frac{1}{8\sqrt{D}\mu} \quad (14.49)$$

Thus

$$D = \frac{1}{64\mu[\text{Re}\langle\bar{Y}\rangle]^2} \quad (14.50)$$

The frequency average requires that there is a sufficient number of modes N within a frequency band Δf . The number of modes within a band Δf is based on Eqs. (8.83) and (14.50) approximately given by Eq. (8.83) as

$$N \approx 4\mu S \Delta f \text{Re}\langle\bar{Y}\rangle$$

Sandwich and honeycomb panels are often lightweight. A small added mass can change the mobility of the plate considerably. This is a problem encountered when the mobility of a plate is measured by a force transducer and an accelerometer. If the mass of the transducer mounted to the plate is Δm the measured mobility Y_m is given by $Y_m/(1 + i\omega Y \Delta m)$ where Y is the point mobility of the structure and Y_m the measured point mobility. Thus

$$\text{Re}Y_m = \frac{Y}{1 + (\omega Y \Delta m)^2}$$

For the error in Y to be less than 10% based on this type of measurement it is required that $\omega Y \Delta m < 0.3$. The mobility technique is only useful in a certain frequency band. The lower frequency limit is determined by the number of modes in a frequency band. The number of modes per band should preferably exceed four. The high frequency limit is determined by the requirement $f < 0.3/(2\pi \Delta m Y)$. The bending stiffness D_n measured in frequency band n should satisfy the expression introduced in Sect. 14.9 or

$$\frac{A}{f_n} D_n^{3/2} - \frac{B}{f_n} D_n^{1/2} + D_n - C = 0 \quad (14.51)$$

The parameters A , B , and C are determined as discussed in Sect. 14.9.

14.11 Response of Sandwich Beams

The forced response of a sandwich beam can be calculated based on Eqs. (9.35)–(9.41). An alternative approach is first to calculate the so-called apparent bending stiffness of the beam and thereafter use the Bernoulli–Euler equations assuming the bending stiffness to be frequency dependent and equal to the apparent bending stiffness.

Predicted and measured transfer accelerances for a beam with free ends are compared in Fig. 14.37. The results were predicted in Ref. [80] using the full sixth-order

Fig. 14.37 Predicted and measured transfer accelerances of a sandwich beam with free edges. The full model corresponds to Eq. (14.30). The response assuming a Bernoulli–Euler model using a frequency-dependent bending stiffness is denoted by B-E. From Ref. [80]

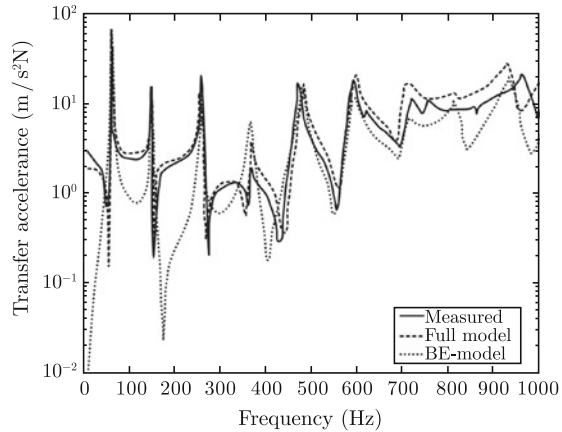
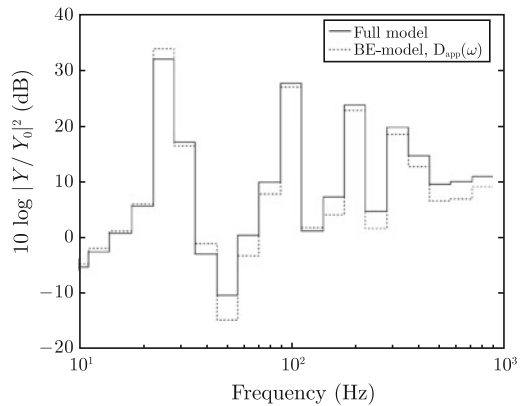


Fig. 14.38 Predicted mobility levels in third octave bands. From Ref. [80]



differential equation (14.30) for sandwich beams. The result is given by the dashed line in Fig. 14.37. The dotted line represents the predicted transfer accelerance using the Bernoulli–Euler equation with a frequency-dependent apparent stiffness. The solid line represents measured results. The transfer accelerance is well predicted close to the natural frequencies even by using the simple B-E, Bernoulli–Euler, model with a frequency-dependent bending stiffness.

Calculating the mobility levels in third octave bands gives a satisfactory agreement between the results from the sandwich model and the B-E model with a frequency-dependent bending stiffness. This is demonstrated in Fig. 14.38.

The forced response of a structure can, when predicted in third octave bands, be estimated fairly accurately by using the apparent bending stiffness of the structure in combination with the Bernoulli–Euler theory for beams or the Kirchhoff theory for plates. These results imply that expressions defining sound transmission loss and radiation ratios for homogeneous single-leaf panels with constant bending stiffness

can be used for sandwich panels by allowing the bending stiffness to be frequency dependent.

It can be shown that the point mobility of an infinite sandwich beam is given by

$$Y_{\text{sandbeam}} = \frac{\omega}{2D'_1\kappa_1\kappa_2\kappa_3} \left[\frac{\kappa_2\kappa_3(Y_3 - Y_2) + i\kappa_1\kappa_3(Y_1 - Y_3) - i\kappa_1\kappa_2(Y_1 - Y_2)}{\kappa_1^2 Y_1(Y_3 - Y_2) - \kappa_2^2 Y_2(Y_1 - Y_3) + \kappa_3^2(Y_1 - Y_2)} \right]$$

where

$$Y_1 = \frac{2D'_2\kappa_1^2 + G_c S}{(D'_1 + 2D'_2)\kappa_1^2 + G_c S}; \quad Y_2 = \frac{2D'_2\kappa_2^2 - G_c S}{(D'_1 + 2D'_2)\kappa_2^2 - G_c S};$$

$$Y_3 = \frac{2D'_2\kappa_3^2 - G_c S}{(D'_1 + 2D'_2)\kappa_3^2 - G_c S}$$

The details are left for Problem 14.7.

The response of a simply supported sandwich beam can be expressed as a sum over the appropriate eigenfunctions in analogy with derivation of the response of an Euler beam demonstrated in Sect. 7.4. Assuming the beam to be extended from $x = 0$ to $x = L$, the displacement w can be expanded along the eigenfunctions $\varphi_n = \sin(n\pi x/L)$. The angular displacement β due to pure bending of the beam is consequently expanded along the functions $g_m = \cos(n\pi x/L)$. The displacements w and β should satisfy Eqs. (14.28) and (14.29). Let a force $F \cdot \exp(i\omega t)$ excite the beam at $x = x_1$. Neglecting the moment of inertia, the response of the beam is obtained as

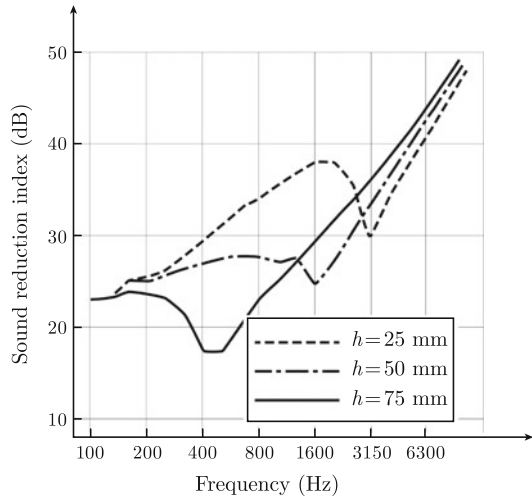
$$w(x, t) = \frac{2F \cdot e^{i\omega t}}{Lm'} \sum_{n=1}^{\infty} \frac{\sin(n\pi x/L) \sin(n\pi x_1/L)}{(2\pi)^2 [f_n^2(1 + i\eta) - f^2]} \quad (14.52)$$

The mass per unit length of the beam is m' . The loss factor is η . The natural frequencies f_n are given by Eq. (14.41). The details are left for Problem 14.6.

The sound transmission loss for single-leaf panels was discussed in Chap. 13. The sound transmission loss R was derived as function of the material parameters of the panel and its boundary condition and the geometries of panel as well as the baffle in which the panel is mounted. The expressions presented in Chap. 13 can, after some modifications, also be used to predict the sound transmission loss of sandwich plates. The sound transmission loss of a single-leaf panel depends on the bending stiffness of the plate and a number of other parameters. The critical frequency f_c defined in Eq. (12.18) is a function of the bending stiffness of the plate. For a thin homogeneous single-leaf panel the critical frequency is a constant and equal to frequency for which the trace matching between flexural waves on the plate and waves in the surrounding medium coincides. For a sandwich panel, a parameter f'_c is introduced as

$$f'_c = \frac{c^2}{2\pi} \sqrt{\frac{\mu}{D(f)}} \quad (14.53)$$

Fig. 14.39 Predicted sound transmission loss for three sandwich plates with different core thickness h . Core material and laminates identical for all plates



where $D(f)$ is the frequency-dependent bending stiffness of the plate and μ its mass per unit area. If the bending stiffness $D'(f)$ is measured for a beam, width b , then $D(f) \approx D'(f)/b$. For $D(f)$ constant $f'_c = f_c$. By replacing f_c by f'_c in all the expressions giving the sound transmission loss of a single-leaf panel in Chap. 13, the sound transmission loss of a sandwich/honeycomb panel with a frequency-dependent bending stiffness could be estimated. The procedure is analogous to calculating the response in 1/3 OB of a sandwich beam using the Bernoulli–Euler equations and a frequency-dependent bending stiffness.

Figure 14.39 shows predicted sound transmission losses for three plates with different core thicknesses. The laminates are identical for the plates. The weight is almost the same for the three plates. The core thickness has a very significant effect on the sound transmission loss.

The sound transmission losses of the sandwich plates were predicted according to Eq. (13.122). The wavenumber, flexural waves, for the panel having the 50 mm core is almost equal to the wavenumber in air in a very wide frequency range from 300 to 1600 Hz. The sound reduction index of the panel is consequently rather poor in this frequency range.

The sound transmission losses of a laminate and a sandwich element were measured and predicted. The result is shown in Fig. 14.40. The panels were mounted in a baffle between the transmission rooms. It is interesting to note that in the mid-frequency region the sound transmission loss for just one laminate is higher than the transmission loss of the entire structure consisting of two laminates and a core.

Radiation ratios calculated according to Leppington Ref. [159] using a frequency-dependent bending stiffness also show good agreement with measurements.

Once the bending stiffness and the parameters A , B , and C , Eq. (14.44), have been determined for a beam element of a sandwich plate various parameter studies with respect to the sound transmission loss of the structure can be carried out as

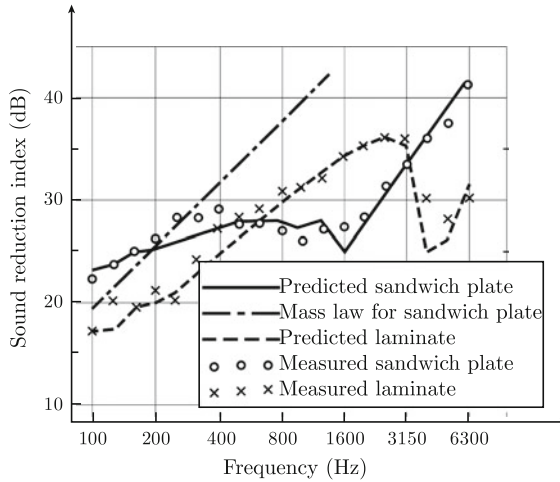


Fig. 14.40 Measured and predicted sound transmission losses for sandwich plate and one of the laminates which is part of the sandwich structure

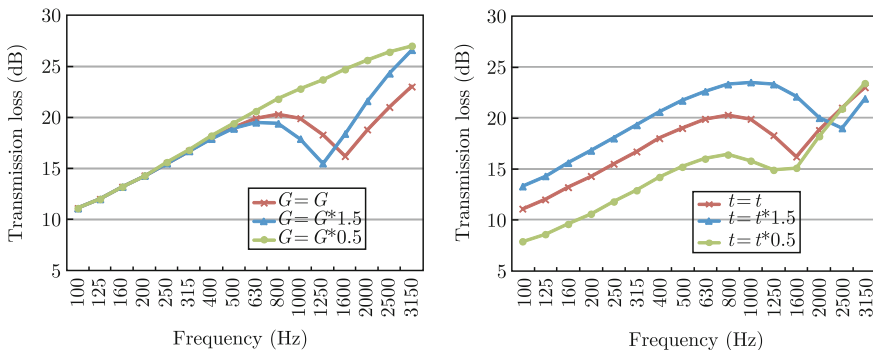


Fig. 14.41 Predicted sound transmission loss for an aluminum honeycomb panel. The results to the *left* illustrate the effect of changing the shear modulus by $\pm 50\%$. The results to the *right* give the sound transmission loss as the thickness of the laminates are varied by $\pm 50\%$

discussed in Ref. [220]. If, for example, the shear modulus of the core is changed the constants A and B of Eq. (14.44) are also changed. Using the new constants the resulting bending stiffness is predicted from Eq. (14.40). The sound transmission loss is thereafter calculated as previously described. Two examples are shown in Fig. 14.41. The basic structure was an aluminum honeycomb panel with an area weight of 6.2 kg/m^2 . In the first example, the shear stiffness of the core is varied by $\pm 50\%$ while all other parameters are kept constant. The sound transmission losses are predicted for infinite plates. In the second example, the thickness of the laminates is varied by $\pm 50\%$. The effect of changing the core thickness is already demonstrated in Fig. 14.39. The sound transmission loss of a sandwich panel can

obviously be changed considerably by varying some of the main parameters of the plate.

There is a tendency to determine the acoustic properties of composite structures based on measurements on fairly small samples, typically with an area of 1 m^2 . The reason is often stated to be the cost of manufacturing the sample. However, the area of a sample is of importance when measuring and predicting the sound transmission loss and sound radiation ratio of a panel as discussed in Chap. 13.

14.12 Energy Flow in Sandwich Beams

A plane flexural wave propagating in a thin plate, thickness h and width b , can be described by means of the Euler–Bernoulli differential equation. For the wave propagating along an x -axis in the plane of the plate the lateral displacement of the beam is defined as

$$w(x, t) = A \cdot \exp[i(\omega t - \kappa x)]; \quad \kappa = \left[\frac{\omega^2 m'}{D'_0} \right]^{1/4}; \quad D'_0 = \frac{Ebh^3}{12} \quad (14.54)$$

The resulting time average of the energy flow in the x -direction is according to Eq. (3.91) equal to

$$\bar{\Pi}_x = \omega \kappa^3 D'_0 |A|^2 \quad (14.55)$$

In a sandwich plate, the displacement is not only due to pure bending but also to shear in the core. Thus, if the displacement w_l of a laminate and its rotational angle β are described as

$$w_l(x, t) = A \cdot \exp[i(\omega t - \kappa_1 x)]; \quad \beta(x, t) = B \cdot \exp[i(\omega t - \kappa_1 x)] \quad (14.56)$$

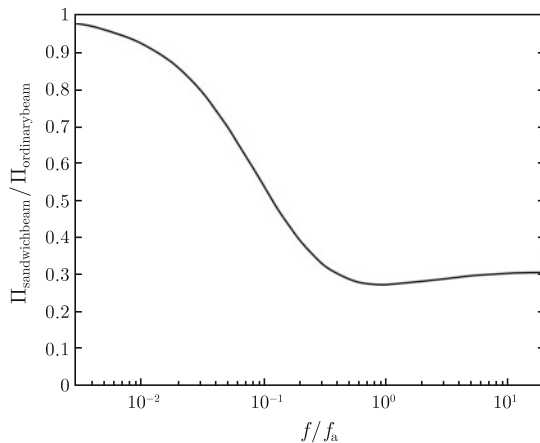
where κ_1 is the wavenumber for the propagating wave in the plate. Equation (14.56) should satisfy Eq. (14.29) giving the ratio between the amplitudes A and B as

$$B = -iA\kappa_1 Y_1; \quad Y_1 = \frac{2D_2\kappa_1^2 + GH}{\kappa_1^2(D_1 + 2D_2) + GH - I\omega^2} \quad (14.57)$$

The mass moment of inertia per unit width of plate is defined as $I_\omega = \rho_c H^3/12 + \rho_l(H^2h/2 + Hh^2 + 2h^3/3)$. Note that $D_1 \approx D'_1/b$, etc. The time average of the energy flow per unit width of the sandwich plate is

$$\bar{\Pi}_x = \frac{1}{2} \text{Re} \left\{ -F \cdot \dot{w}^* + M \cdot \left(\frac{\partial \beta}{\partial t} \right)^* + 2M_s \cdot \left(\frac{\partial \gamma}{\partial t} \right)^* \right\} \quad (14.58)$$

Fig. 14.42 Energy flow in sandwich beam as compared to a slender beam both having the same weight and bending stiffness in the low frequency region. Amplitude the same in both cases. From [81]



In Eq. (14.58) F is the force defined in Eq. (14.31). The bending moment M is due to pure bending of the entire beam and the bending moment M_s in the laminates is caused by shear in the core are defined in Eqs. (14.32) and (14.33).

Neglecting I_w the resulting energy flow in the beam is

$$\bar{\Pi}_x = \frac{|A|^2}{2} \cdot \omega \kappa^3 \left\{ D_1 Y_1 (1 + Y_1) + 2D_2 (1 - Y_1)^2 \right\} \quad (14.59)$$

In the low frequency region as $f \rightarrow 0$ the energy flow approaches $\bar{\Pi}_x = \omega \kappa^3 D_1 |A|^2$ which is the energy flow in a simple Bernoulli–Euler beam, bending stiffness $D_0 = D_1$ due to a flexural wave defined as $w(x, t) = A \cdot \exp[i(\omega t - \kappa x)]$. In the high frequency region, the energy flow is $\bar{\Pi} = 2\omega \kappa^3 D_2 |A|^2$ or twice the energy flow in one laminate with the bending stiffness D_2 and the wavenumber κ describing flexural waves. Figure 14.42 shows the ratio $\bar{\Pi}_x / \bar{\Pi}$ between the energy flow in a sandwich beam and the energy flow in a Bernoulli–Euler beam. The amplitude A of the displacement is the same in both cases. In the low frequency the ratio approaches unity and in the high frequency region $[2D_2 / (D_1 + 2D_2)]^{1/4}$.

The frequency in Fig. 14.42 has been normalized with respect to f_a . This frequency f_a indicates the upper limit for the applicability of the Timoshenko theory to sandwich beam vibrations as discussed in [81]. The frequency f_a is defined as

$$f_a = \frac{G_c H}{2\pi \sqrt{2\mu D_2}}$$

The time average of the energy flow $\bar{\Pi}_x$ in a beam can be written as $\bar{\Pi}_x = c_{gs} \bar{E}_{total}$ where c_{gs} is the group velocity and \bar{E}_{total} the time average of the total energy per unit length of the structure. Compare Sect. 3.7. For a sandwich beam, the time average of the total energy per unit length is obtained from Eqs. (9.26) through (9.31) as

$$\bar{E}_{\text{total}} = \frac{1}{4} \left[D_1' \left| \frac{\partial \beta}{\partial x} \right|^2 + SG_c |\gamma|^2 + 2D_2' \left| \frac{\partial \gamma}{\partial x} \right|^2 + m' \left| \frac{\partial w}{\partial t} \right|^2 + I_\omega' \left| \frac{\partial \beta}{\partial t} \right|^2 \right]$$

The energy flow is given by Eq. (14.57). Thus, neglecting the moment of inertia, the group velocity is

$$c_{\text{gs}} = \frac{\kappa_1 [6D_1 D_2 \kappa_1^4 + 2G_c H D_1 \kappa_1^2 - \mu \omega^2 (D_1 + 2D_2)]}{\mu \omega [\kappa_1^2 (D_1 + 2D_2) + G_c H]} \tag{14.60}$$

14.13 Energy Flow Across Pinned Joints

The shear effects in the core of sandwich beams influence the vibroacoustic coupling between beam elements. The difference between the coupling effects across a junction connecting two sandwich or two Euler–Bernoulli beams can be illustrated by means of an elementary case. Consider two identical and semi-infinite beams joined together by a pinned joint allowing rotation but no translatory motion of the joint. The structure is illustrated in Fig. 14.43. The joint coincides with the center line of the beam. Assume that a “bending” wave is propagating in beam *a* toward the junction. Part of the incident energy is reflected at and part is transmitted across the junction. Assuming a time dependence $\exp(i\omega t)$ the lateral displacement w_a of beam *a* reads

$$w_a = \exp(-i\kappa_1 x) + A_1 \cdot \exp(i\kappa_1 x) + A_2 \cdot \exp(\kappa_2 x) + A_3 \cdot \exp(\kappa_3 x) \tag{14.61}$$

where A_1 is the amplitude of the reflected propagating wave and A_2 and A_3 are the amplitudes of the evanescent waves induced in beam *a* at the junction. The displacement w_a is caused by shear and bending.

The pure bending displacement β_a is defined as

$$\begin{aligned} \beta_a = & (-i\kappa_1) \cdot Y_1 \cdot \exp(-i\kappa_1 x) + A_1 \cdot (i\kappa_1) \cdot Y_1 \cdot \exp(i\kappa_1 x) \\ & + A_2 \cdot \kappa_2 \cdot Y_2 \cdot \exp(\kappa_2 x) + A_3 \cdot \kappa_3 \cdot Y_3 \cdot \exp(\kappa_3 x) \end{aligned} \tag{14.62}$$

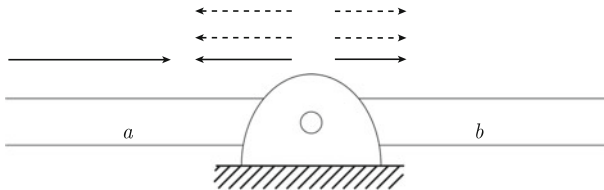


Fig. 14.43 Two semi-infinite beams coupled across a pinned joint

The expressions w_a and β_a must satisfy Eq. (14.29). As a result, the parameters Y_i are obtained as

$$Y_1 = \frac{2D_2\kappa_1^2 + G_cH}{\kappa_1^2(D_1 + 2D_2) + G_cH - I_\omega\omega^2}; \quad Y_2 = \frac{2D_2\kappa_2^2 - G_cH}{\kappa_2^2(D_1 + 2D_2) - GH + I_\omega\omega^2};$$

$$Y_3 = \frac{2D_2\kappa_3^2 - G_cH}{\kappa_3^2(D_1 + 2D_2) - G_cH + I_\omega\omega^2} \quad (14.63)$$

The displacement w_b and the corresponding field β_b in beam b are written

$$w_b = B_1 \cdot \exp(-i\kappa_1x) + B_2 \cdot \exp(-\kappa_2x) + B_3 \cdot \exp(-\kappa_3x)$$

$$\beta_b = (-i\kappa_1) \cdot B_1 \cdot Y_1 \cdot \exp(-i\kappa_1x) - B_2 \cdot \kappa_2 \cdot Y_2 \cdot \exp(-\kappa_2x)$$

$$- B_3 \cdot \kappa_3 \cdot Y_3 \cdot \exp(-\kappa_3x) \quad (14.64)$$

The amplitude of the transmitted wave is B_1 . The boundary conditions at $x = 0$ are

$$w_a = 0; \quad w_b = 0; \quad \frac{\partial w_a}{\partial x} = \frac{\partial w_b}{\partial x}; \quad \beta_a = \beta_b; \quad M_a = M_b; \quad (M_s)_a = (M_s)_b \quad (14.65)$$

The third condition means that the rotational angle of both beams is the same. The fourth condition ensures that the angle due to pure bending is the same for the beams. The third and fourth conditions also give $\gamma_a = \gamma_b$. Based on the six boundary conditions the six amplitudes A_1, B_1 , etc. are solved. The amplitude B_1 of the transmitted propagating wave is

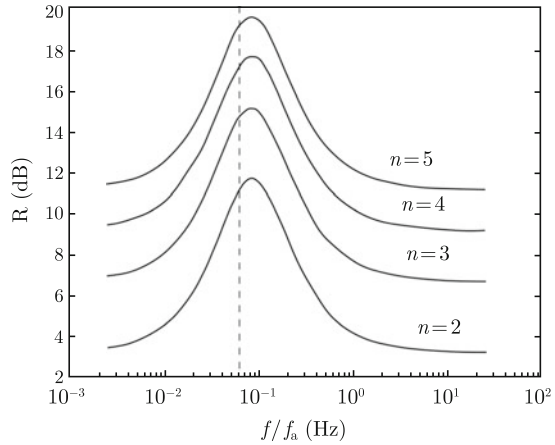
$$B_1 = \frac{i[\kappa_1(\kappa_2 - \kappa_3)Y_1 - \kappa_1\kappa_2Y_2 + \kappa_1\kappa_3]}{i(\kappa_1\kappa_2 - \kappa_1\kappa_3)Y_1 + (\kappa_2\kappa_3 - i\kappa_1\kappa_2)Y_2 + (i\kappa_1\kappa_3 - \kappa_2\kappa_3)Y_3} \quad (14.66)$$

The transmission loss R across the junction is defined as

$$R = 10 \cdot \log \frac{1}{|B_1|^2} \quad (14.67)$$

The transmission loss across the junction is shown in Fig. 14.44. The transmission loss is plotted as function of the ratio f/f_a where f_a is defined in Sect. 14.12. The transmission loss is approaching 3 dB for decreasing frequencies and then increasing to a maximum and then again decreases to approach 3 dB in the very high frequency range. In the low frequency region, the beam is vibrating as a simple Euler beam and consequently the transmission is equal to 3 dB as discussed in Sect. 5.9. In the high frequency region, the transmission is determined by the coupling between the laminates. The transmission loss across a junction between two thin laminates is 3 dB, Sect. 5.9. The transmission loss predicted based on the sixth-order differential equation approaches the right asymptotes for both high and low frequencies.

Fig. 14.44 Predicted transmission loss across a pinned junction. The number of beams connected at the junction is given by n . From Ref. [81]



This simple example also shows that the concept of equivalent stiffness for a beam cannot be applied for the calculation of coupling effects between sandwich elements. Even assuming a frequency-dependent bending stiffness in combination with the Euler theory for the two beams shown in Fig. 14.41 the resulting transmission loss would be 3 dB as long as the beams are identical.

In Ref. [81] it is demonstrated that the transmission loss R_n of a junction between n identical sandwich beams is written as

$$R_n = R + 20 \log(n/2) \tag{14.68}$$

where R is given by Eq. (14.61). In Sect. 5.9 the transmission loss between two of n equal Euler beams was found to be $R_n = 10 \log(n^2/2) = R + 20 \log(n/2)$ for $R = 3$ dB.

14.14 Wave Propagation on Infinite Cylinders

The noise inside an aircraft in-flight is to a large extent determined by turbulent boundary layers. The turbulent boundary layers induce vibrations of the fuselage. The vibrating plate elements of the structure radiate noise into the cabin. In addition, air-borne noise from engines transmitted through the fuselage contributes to the interior noise level. A fuselage can to a certain degree be modeled as a circular cylinder. The plates between stringers and frames are equivalent to shell elements. The curvature of the shell influences the vibration pattern of the structure. Pipes filled with a moving fluid constitute another important class of noise radiators, which can be modeled as circular cylinders.

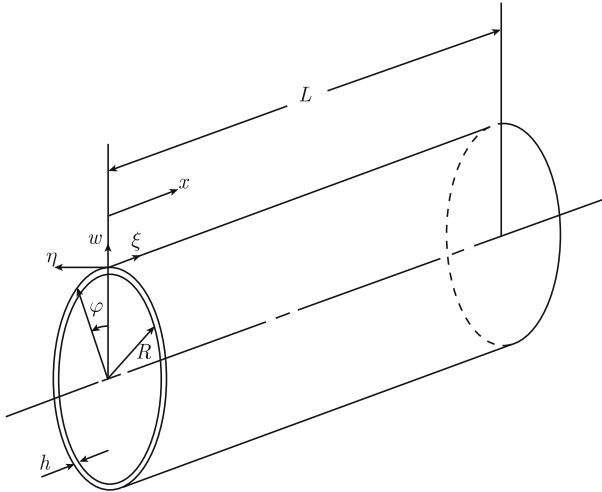


Fig. 14.45 Coordinates and displacement of a cylindrical shell

Infinite cylinders can be considered as folded structural wave guides having cut-off frequencies for various types of propagating waves. This is in analogy with waves propagating in structural waveguides and sandwich and honeycomb structures.

The differential equations governing the propagation of waves on cylinders were derived in Sect. 9.7. The displacements w , ξ , and η of a cylindrical shell are shown in Fig. 14.45.

By setting F_1 , F_2 , and F_3 equal to zero in the expressions (9.90) the three equations governing the displacement of a cylindrical shell are obtained as

$$\begin{aligned} \frac{\partial^2 \xi}{\partial x^2} + \frac{1 - \nu}{2R^2} \frac{\partial^2 \xi}{\partial \varphi^2} - \frac{1 - \nu^2}{Eh} \mu \ddot{\xi} + \frac{1 + \nu}{2R} \frac{\partial^2 \eta}{\partial x \partial \varphi} + \frac{\nu}{R} \frac{\partial w}{\partial x} &= 0 \\ \frac{1 + \nu}{2R} \frac{\partial^2 \xi}{\partial x \partial \varphi} + \frac{1 - \nu}{2} \frac{\partial^2 \eta}{\partial x^2} + \frac{1}{R^2} \frac{\partial^2 \eta}{\partial \varphi^2} - \frac{1 - \nu^2}{Eh} \mu \ddot{\eta} + \frac{1}{R^2} \frac{\partial w}{\partial \varphi} &= 0 \quad (14.69) \\ \frac{\nu}{R} \frac{\partial \xi}{\partial x} + \frac{1}{R^2} \frac{\partial \eta}{\partial \varphi} + \frac{w}{R^2} + \frac{h^2}{12} \left(\frac{\partial^4 w}{\partial x^4} + \frac{1}{R^4} \frac{\partial^4 w}{\partial \varphi^4} + \frac{2}{R^2} \frac{\partial^4 w}{\partial x^2 \partial \varphi^2} \right) \\ + \frac{\mu(1 - \nu^2)}{Eh} \ddot{w} &= \frac{p(1 - \nu^2)}{Eh} \end{aligned}$$

For a wave propagating along the positive x -axis and assuming w to be symmetric around $\varphi = 0$ the displacement can be written as

$$w(x, \varphi, t) = \sum_n A_n \cos(n\varphi) \cdot \exp[i(\omega t - \lambda_n x)] \quad (14.70)$$

The in-plane displacement must propagate in a similar manner to satisfy any boundary conditions. The displacements ξ and η must satisfy the three expressions of (14.69). Consequently, ξ and η are written as

$$\xi(x, \varphi, t) = \sum_n i B_n \cos(n\varphi) \cdot \exp[i(\omega t - \lambda_n x)] \quad (14.71)$$

$$\eta(x, \varphi, t) = \sum_n C_n \sin(n\varphi) \cdot \exp[i(\omega t - \lambda_n x)] \quad (14.72)$$

The amplitude B_n is multiplied by i to avoid complex numbers in the equations resulting from inserting Eqs. (14.70)–(14.72) in (14.69). For free vibrations, $p = 0$ in the last expression of Eq. (14.69). Equations (14.70)–(14.72) inserted in (14.69) yield a system of equations written as

$$[Q] \cdot \begin{Bmatrix} A_n \\ B_n \\ C_n \end{Bmatrix} = \begin{Bmatrix} 0 \\ 0 \\ 0 \end{Bmatrix} \quad (14.73)$$

The elements of the symmetric matrix $[Q]$ are

$$\begin{aligned} Q_{11} &= \frac{1}{R^2} + \frac{h^2}{12} \left(\lambda_n^4 + \frac{n^4}{R^4} + \frac{2n^2 \lambda_n^2}{R^2} \right) - \frac{\mu \omega^2 (1 - \nu^2)}{Eh}; & Q_{12} &= \frac{\nu \lambda_n}{R}; \\ Q_{13} &= \frac{n}{R^2}; & Q_{21} &= \frac{\nu \lambda_n}{R} = Q_{12}; & Q_{22} &= \lambda_n^2 + \frac{(1 - \nu)n^2}{2R^2} - \frac{\omega^2 \mu (1 - \nu^2)}{Eh}; \\ Q_{23} &= \frac{n \lambda_n (1 + \nu)}{2R}; & Q_{31} &= \frac{n}{R^2} = Q_{13}; & Q_{32} &= \frac{n(1 + \nu) \lambda_n}{2R} = Q_{23}; \\ Q_{33} &= \frac{n^2}{R^2} + \frac{(1 - \nu^2) \lambda_n^2}{2} - \frac{(1 - \nu^2) \mu \omega^2}{Eh} \end{aligned} \quad (14.74)$$

The wavenumbers for waves propagating in the cylinder can be derived using the nondimensional frequency parameter Ω defined as

$$\Omega = R\omega \sqrt{\frac{\rho(1 - \nu^2)}{E}} = \frac{R\omega}{c_l} \quad (14.75)$$

The phase velocity of longitudinal waves propagating in a thin plate is given by c_l . The wavenumber λ_n for free waves propagating in an infinite cylinder is the solution to $\text{Det}[Q] = 0$. Thus, according to Ref. [87]

$$\begin{aligned}
\Omega^6 - K_2\Omega^4 + K_1\Omega^2 - K_0 &= 0 \\
K_2 &= 1 + \frac{(3-\nu)}{2} \left[n^2 + \lambda_n^2 R^2 \right] + \frac{h^2}{12R^2} \left[n^2 + \lambda_n^2 R^2 \right]^2 \\
K_1 &= \frac{1-\nu}{2} \left[(3+2\nu)\lambda_n^2 R^2 + n^2 + (n^2 + \lambda_n^2 R^2)^2 \right] + \frac{(3-\nu)}{(1-\nu)} \frac{h^2}{12R^2} \left(n^2 + \lambda_n^2 R^2 \right)^3 \\
K_0 &= \frac{(1-\nu)}{2} \left[(1-\nu^2)\lambda_n^4 R^4 + \frac{h^2}{12R^2} \left(n^2 + \lambda_n^2 R^2 \right)^4 \right] \tag{14.76}
\end{aligned}$$

For any given frequency and integer n there are eight solutions of λ_n or rather four pairs of solutions. Each pair represents waves traveling in both the positive and negative directions. For λ_n^2 negative, the solution λ_n is imaginary representing an evanescent wave. There is at least one pair of evanescent waves for each frequency.

The cut-on frequencies for various wave types are obtained by setting $\lambda_n = 0$ in the equations given $\text{Det}[Q] = 0$. Since for $\lambda_n = 0$ the matrix elements Q_{12} , Q_{21} , Q_{23} , and Q_{32} are equal to zero, the determinant of $[Q]$ is given by

$$Q_{22}[Q_{11} \cdot Q_{33} - Q_{13}^2] = 0 \tag{14.77}$$

The first cut-on angular frequency is the solution to $Q_{22} = 0$, i.e.,

$$\omega_n^2 = \frac{n^2 E_0}{2\rho(1+\nu)R^2} = \frac{n^2 G_0}{\rho R^2} = \frac{n^2 c_t^2}{R^2}; \quad f_n = \frac{c_t n}{2\pi R} \tag{14.78}$$

where c_t is the phase velocity of transverse or torsional waves propagating in a cylindrical shell. The circumference of the circular cylinder is a multiple of the wavelength λ_t of the transverse or torsional waves. Thus, $n \cdot \lambda_t = 2\pi R$.

Other solutions giving $\lambda_n = 0$ are obtained from the second part of Eq. (14.77), i.e., from $[Q_{11} \cdot Q_{33} - Q_{13}^2] = 0$. Using the definition of Ω this expression is written as

$$\Omega^4 - \Omega^2 \left[(1+n^2) + \frac{h^2 n^4}{12R^2} \right] + \frac{h^2 n^6}{12R^2} = 0 \tag{14.79}$$

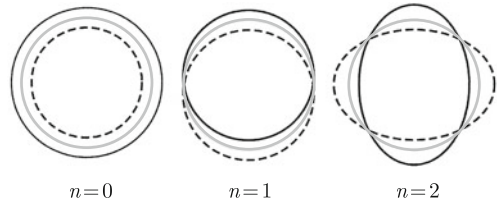
Thus, for $h^2/(12R^2) \ll 1$

$$\Omega^2 \approx 1 + n^2 + \frac{h^2 n^4}{12R^2(1+n^2)} \approx 1 + n^2$$

The cut-on angular frequencies are

$$\omega_n \approx \frac{c_l}{R} \sqrt{1+n^2} \tag{14.80}$$

Fig. 14.46 Cross section displacement of a cylindrical shell for some different n or vibrational modes



For $n = 0$ the resulting cut-on frequency is $f_0 = c_l/(2\pi R)$. This is the so-called ring frequency. At this frequency a longitudinal wave is propagating in the shell and perpendicular to the axis of the cylinder. This wave motion will cause the shell to expand and contract in a breathing mode. See Fig. 14.46. This type of motion of the shell is in general readily excited. This mode is an effective radiator of sound. Consequently, the sound transmission loss of a circular cylinder has a minimum at the ring frequency as discussed in Sect. 14.16 and subsequent sections in this chapter. For large integers n the result (14.80) is approximately given by $\omega_n \approx n \cdot c_l/R$. In analogy with the previous result this is also written as $n \cdot \lambda_l = 2\pi R$ where λ_l is the wavelength of longitudinal waves propagating on the cylinder.

Another solution to Eq. (14.79) is for $h^2/(12R^2) \ll 1$ given by

$$\omega_n = \left[\frac{E_0 h^3}{12R^4 \mu (1 - \nu^2)} \right]^{1/2} \left(\frac{n^6}{1 + n^2} \right)^{1/2} = \frac{1}{R^2} \left(\frac{D_0}{\mu} \right)^{1/2} \left(\frac{n^6}{1 + n^2} \right)^{1/2} \quad (14.81)$$

where D is the bending stiffness of a flat plate of thickness h and a Young's modulus E . Equation (14.81) can also be written as $(R\kappa)^2 = [n^6/(1 + n^2)]^{1/2}$ where κ is the wavenumber for flexural waves propagating in a flat plate with the same properties as the shell. For n large $R\kappa \approx n$ or $n \cdot \lambda_f \approx 2\pi R$ where λ_f is the wavelength of flexural waves propagating in the structure. The expression (14.81) gives the cut-on angular frequencies for flexural waves propagating in the shell.

In the high frequency region, there are eight solutions λ_n to Eq. (14.76). As discussed in Problem 14.8 these solutions are $\pm k_l, \pm k_t, \pm \kappa,$ and $\pm i\kappa$ where $k_l, k_t,$ and κ represent wavenumbers for longitudinal, torsional, and flexural waves, respectively.

The mode associated with each wavenumber can be classified as flexural, longitudinal, or torsional. The relative amplitudes corresponding to a specific $n,$ wavenumber, and frequency can be determined by setting $A_n = 1$ in Eq. (14.73) and thereafter by solving B_n and $C_n.$

For $n = 0$ there are two waves propagating along the positive x -axis in the low frequency region. One is a longitudinal wave with the wavenumber $k_l = \omega \sqrt{\rho/E}$ and the other a torsional wave with the wavenumber $k_t = \omega \sqrt{\rho/G}$. The longitudinal wave is transformed into a flexural wave for increasing frequencies. The other solutions λ_n to Eq. (14.76) are imaginary in the low frequency region and represent evanescent waves. For $n = 1$ the cylinder is vibrating like an infinite beam in the low frequency region with a wavenumber of $\lambda_1 = [m'\omega^2/D']^{1/4} = [2\pi\rho\omega^2(1 - \nu^2)/(ER^2)]^{1/4}$ where $D' = EhR^3/(1 - \nu^2)$ is the bending stiffness of a thin circular cylinder and

$m' = 2\pi R h \rho$ its mass per unit length. For $n \geq 2$ there are three types of propagating waves—longitudinal, torsional, and flexural—at frequencies above their respective cut-on frequencies.

The resulting displacement w or rather its real part is shown in Fig. 14.46 for n equal to 0, 1, and 2.

For $n = 0$ the displacement w of the shell is, at the cut-on frequency for longitudinal waves, determined by the so-called breathing mode of the cylinder. This frequency is referred to as the ring frequency of the cylinder. At this frequency longitudinal waves can propagate in the shell perpendicular to the axis of the cylinder. For $n = 1$ the cylinder is vibrating like a beam, the upper and lower parts of the cylinder are moving in phase.

In certain cases, the basic equation (14.76) can be simplified as suggested by Rayleigh [221] and Love [222, 223]. For $h^2/(12R^2) \ll 1$, Eq. (14.76) is reduced to

$$\begin{aligned} \frac{\partial^2 \xi}{\partial x^2} + \frac{1-\nu}{2R^2} \frac{\partial^2 \xi}{\partial \varphi^2} - \frac{1-\nu^2}{Eh} \mu \ddot{\xi} + \frac{1+\nu}{2R} \frac{\partial^2 \eta}{\partial x \partial \varphi} + \frac{\nu}{R} \frac{\partial w}{\partial x} &= 0 \\ \frac{1+\nu}{2R} \frac{\partial^2 \xi}{\partial x \partial \varphi} + \frac{1-\nu}{2} \frac{\partial^2 \eta}{\partial x^2} + \frac{1}{R^2} \frac{\partial^2 \eta}{\partial \varphi^2} - \frac{1-\nu^2}{Eh} \mu \ddot{\eta} + \frac{1}{R^2} \frac{\partial w}{\partial \varphi} &= 0 \\ \frac{\nu}{R} \frac{\partial \xi}{\partial x} + \frac{1}{R^2} \frac{\partial \eta}{\partial \varphi} + \frac{w}{R^2} + \frac{\mu(1-\nu^2)}{Eh} \ddot{w} &= \frac{p(1-\nu^2)}{Eh} \end{aligned} \quad (14.82)$$

The approximation implies that the bending stiffness of the shell is negligible at every point. The shell is reduced to a membrane without stiffness. The expressions (14.82) are often referred to as the membrane equations.

Another simplification is obtained by assuming plain strain in the cylinder. This is equivalent to assuming no displacement of the shell in the direction of the axis of the cylinder and that the displacements do not depend on the location along the length of the cylinder. The case of plane strain requires $w = w(\varphi)$, $\xi = 0$ and $\eta = \eta(\varphi)$. Thus, assuming plane strain, the expressions (14.69) are reduced to

$$\begin{aligned} \frac{1}{R^2} \frac{\partial^2 \eta}{\partial \varphi^2} - \frac{1-\nu^2}{Eh} \mu \ddot{\eta} + \frac{1}{R^2} \frac{\partial w}{\partial \varphi} &= 0 \\ \frac{1}{R^2} \frac{\partial \eta}{\partial \varphi} + \frac{w}{R^2} + \frac{h^2}{12R^2} \cdot \frac{1}{R^2} \frac{\partial^4 w}{\partial \varphi^4} + \frac{\mu(1-\nu^2)}{Eh} \ddot{w} &= \frac{p(1-\nu^2)}{Eh} \end{aligned} \quad (14.83)$$

Yet another very useful approximation is obtained by neglecting the inertia terms of the in-plane motion of the shell. This is equivalent to setting $\mu = 0$ in the first two equations of the expression (14.69). This simplification permits the uncoupling of the three differential equations. It is found that the resulting equations give

$$\frac{h^2}{12R^2} \nabla_k^8 w + (1-\nu^2) R^4 \frac{\partial^4 w}{\partial x^4} + \frac{\mu(1-\nu^2) R^2}{Eh} \nabla_k^4 \frac{\partial^2 w}{\partial t^2} = 0 \quad (14.84)$$

The operator ∇_k^2 is defined as

$$\nabla_k^2 = R^2 \frac{\partial^2}{\partial x^2} + \frac{\partial^2}{\partial \varphi^2} \tag{14.85}$$

The displacements ξ and η should satisfy the expressions

$$\nabla_k^4 \xi = \nu R^3 \frac{\partial^3 w}{\partial x^3} - R \frac{\partial^3 w}{\partial x \partial \varphi^2}; \quad \nabla_k^4 \eta = -R^2(2 + \nu) \frac{\partial^3 w}{\partial x^2 \partial \varphi} - R^3 \frac{\partial^3 w}{\partial x^3} \tag{14.86}$$

The results (14.84) and (14.86) are often referred to as the Donnell–Musthahari–Vlasov equations and will be used in Sect. 14.15 for the prediction of the sound transmission loss of a section of a cylindrical shell.

The wavenumbers derived for $n = 0$ and $n = 1$ using any of the approximate models (14.82) through (14.84) give rather large errors as compared to the exact results. For example, a plane longitudinal wave can always propagate along the axis of a cylinder. However, due to the approximations made when deriving Eq. (14.82), this plane longitudinal wave can only satisfy Eq. (14.82) for the radius being infinite. However, according to Ref. [87], the simplified models yield acceptable results for $n \geq 2$.

14.15 Vibration of Open Circular Cylindrical Shells

An open circular cylindrical shell is shown in Fig. 14.47. For $\varphi_0 \ll 2\pi$ the shell is considered shallow. For shallow shells, it can be assumed that terms containing transverse shearing forces are negligibly small compared to other terms.

The boundary conditions for this type of element are $T_x = M_x = 0$ and $w = \eta = 0$ for $x = 0$ and $x = L$ where T_x is the shear force and M_x the bending moment. In

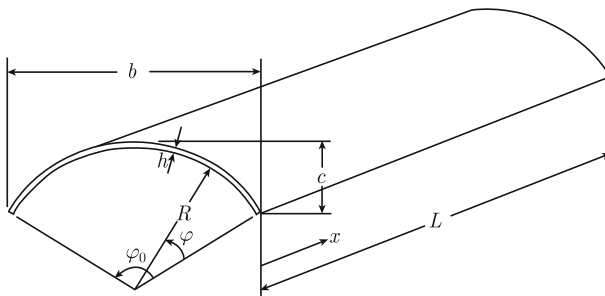


Fig. 14.47 An open circular cylindrical shell

addition $T_\varphi = M_\varphi = 0$ and $w = \xi = 0$ for $\varphi = 0$ and $\varphi = \varphi_0$. The boundary conditions are satisfied by

$$\begin{aligned} w(x, \varphi, t) &= \sum_{mn} A_{mn} \sin(mx\pi/L) \sin(n\pi\varphi/\varphi_0) \exp(i\omega_{mn}t) \\ \xi(x, \varphi, t) &= \sum_{mn} B_{mn} \cos(mx\pi/L) \sin(n\pi\varphi/\varphi_0) \exp(i\omega_{mn}t) \\ \eta(x, \varphi, t) &= \sum_{mn} C_{mn} \sin(mx\pi/L) \cos(n\pi\varphi/\varphi_0) \exp(i\omega_{mn}t) \end{aligned} \quad (14.87)$$

The natural angular frequencies ω_{mn} are derived from Eq. (14.77) by replacing λ_n by $m\pi/L$ and n by $n\pi/\varphi_0$ and by defining Ω as $R\omega_{mn}/c_l$.

If, however, the simplified equation of motion given by (14.84) is used in combination with the expression for w in Eq. (14.87) the natural angular frequencies are obtained as solutions to

$$\begin{aligned} \frac{h^2}{12R^2(1-\nu^2)} \left[R^2 \left(\frac{m\pi}{L} \right)^2 + \left(\frac{n\pi}{\varphi_0} \right)^2 \right]^4 + R^4 \left(\frac{m\pi}{L} \right)^4 \\ = \frac{\mu\omega_{mn}^2 R^2}{E_0 h} \left[R^2 \left(\frac{m\pi}{L} \right)^2 + \left(\frac{n\pi}{\varphi_0} \right)^2 \right]^2 \end{aligned}$$

The natural angular frequencies are

$$\omega_{mn}^2 = \frac{D_0}{\mu} \left[\left(\frac{m\pi}{L} \right)^2 + \left(\frac{n\pi}{R\varphi_0} \right)^2 \right]^2 + \frac{E_0 \left(\frac{m\pi}{L} \right)^4}{\rho R^2 \left[\left(\frac{m\pi}{L} \right)^2 + \left(\frac{n\pi}{R\varphi_0} \right)^2 \right]^2} \quad (14.88)$$

As R tends to infinity the natural angular frequencies approach the angular natural frequencies of a rectangular simply supported plate with sides L and $R\varphi_0$ and mass per unit area μ and bending stiffness D .

The response w of a segment of a circular cylinder excited by an internal pressure $p = p_0 \exp(i\omega t)$ where p_0 is independent of x and φ can be found by using the Donnell–Musthahari–Vlasov approach neglecting the inertia terms of the in-plane motion of the shell. This is discussed in Ref. [87]. Thus, by setting $\mu = 0$ in the first two equations of the expression (14.69) and by defining the displacement of the shell through Eq. (14.87), the amplitude A_{mn} is obtained as

$$A_{mn} = \frac{4\langle p|h_{mn} \rangle}{\mu L \varphi_0 (\omega_{mn}^2 - \omega^2 - i\eta_{mn}\omega_{mn}^2)}; \quad \langle p|h_{mn} \rangle = \int_0^{\varphi_0} d\varphi \int_0^L dx h_{mn} p \quad (14.89)$$

The loss factor for mode (m, n) is denoted as η_{mn} . The orthogonal eigenfunctions h_{mn} are defined as

$$h_{mn}(x, \varphi) = \sin(mx\pi/L) \sin(n\pi\varphi/\varphi_0) \quad (14.90)$$

The angular natural frequencies of the shell segment are ω_{mn}^2 as given by Eq. (14.88). The orientation of the coordinate system is shown in Fig. 14.47.

14.16 Sound Transmission Loss of Shallow Shell Segments

The sound transmission loss of a segment of circular cylinder has, for example, been discussed by Liu Ref. [224]. It is assumed in Ref. [224] that the radius R of the cylinder is large and that the thickness h of the structure is small. It is also assumed that the displacement of the structure can be approximated by means of the Donnell–Musthtari–Vlasov equations (14.85) and (14.86). However, the starting point in Ref. [224] is a simply supported flat, rectangular, and homogeneous plate with the dimensions L_x and L_y , the bending stiffness D , and mass per unit area μ . The differential equation governing the displacement w of the plate in flexure is

$$\nabla^2(\nabla^2 w) - \kappa^4 w = p/D$$

where the pressure on the plate is given by p . A time dependence $\exp(i\omega t)$ is assumed. The resulting displacement is written as

$$\begin{aligned} w(x, y) &= \sum_{mn} \frac{4\langle p|g_{mn}\rangle g_{mn}(x, y)}{L_x L_y \mu [\omega_{mn}^2 (1 + i\eta_{mn}) - \omega^2]} \\ &= \sum_{mn} \frac{4p_{mn} g_{mn}(x, y)}{L_x L_y \mu [\omega_{mn}^2 (1 + i\eta_{mn}) - \omega^2]} = \sum_{mn} w_{mn} g_{mn} \end{aligned} \quad (14.91)$$

Assuming the panel to be flat, rectangular, and simply supported having its corners located at $(L_x/2, L_y/2)$, $(L_x/2, -L_y/2)$, $(-L_x/2, -L_y/2)$, and $(-L_x/2, L_y/2)$ the eigenfunctions g_{mn} satisfying the differential equation and the boundary conditions are

$$g_{mn}(x, y) = \sin \left[\frac{m\pi(x + L_x/2)}{L_x} \right] \cdot \sin \left[\frac{n\pi(y + L_y/2)}{L_y} \right] \quad (14.92)$$

The time average of the acoustical power radiated by mode (m, n) is according to Sect. 12.9 given by

$$\bar{\Pi}_{mn} = \frac{\rho_0 c (\sigma_r)_{mn}}{2} \iint dx dy \omega^2 |w_{mn}|^2 = \frac{2\rho_0 c \omega^2 (\sigma_r)_{mn} |p_{mn}|^2}{L_x L_y \mu^2 [(\omega_{mn}^2 - \omega^2)^2 + (\eta_{mn} \omega_{mn}^2)^2]} \quad (14.93)$$

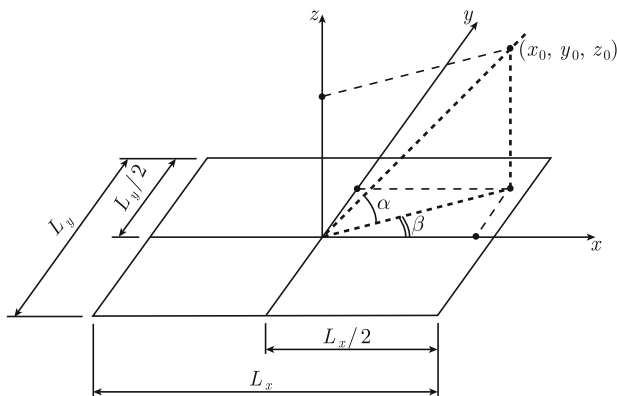


Fig. 14.48 Geometry of a wave incident on a plate

The radiation ratios $(\sigma_r)_{mn}$ are given in expression (12.97). In the low frequency region, the radiation ratio $(\sigma_r)_{mn}$ can be approximated as given by Wallace, Eqs. (12.89)–(12.91). The pressure incident on the plate is written as $p = p_0 \cdot \exp[i(\omega t - \mathbf{k} \cdot \mathbf{r})]$. On the surface of the plate the pressure is doubled and given by

$$p = 2p_0 \exp[i(\omega t - k_x x - k_y y)] = 2p_0 \exp[i(\omega t - kx \cos \alpha \cos \beta - ky \cos \alpha \sin \beta)] \tag{14.94}$$

The result is obtained by setting $k_x = k \cos \alpha \cos \beta$ and $k_y = k \cos \alpha \sin \beta$. The angles are defined in Fig. 14.48.

The quantity $p_{mn} = \langle p | g_{mn} \rangle$ in Eq. (14.93) is

$$\begin{aligned} p_{mn} &= 2p_0 \int_{-L_x/2}^{L_x/2} dx \int_{-L_y/2}^{L_y/2} dy g_{mn} \\ &\quad \times \exp(-ikx \cos \alpha \cos \beta -iky \cos \alpha \sin \beta) = 2p_0 H_x H_y \\ H_x &= \int_{-L_x/2}^{L_x/2} \sin \left[\frac{m\pi(x + L_x/2)}{L_x} \right] \exp(-ikx \cos \alpha \cos \beta) dx \\ H_y &= \int_{-L_y/2}^{L_y/2} \sin \left[\frac{n\pi(y + L_y/2)}{L_y} \right] \exp(-iky \cos \alpha \sin \beta) dy \end{aligned} \tag{14.95}$$

The functions H_x and H_y are solved by partial integration as shown in Sect. 12.8. Following the discussion in Sect. 12.8, Eq. (12.76), the function $|p_{mn}|^2$ in Eq. (14.95) is written as

$$|p_{mn}|^2 = 4p_0^2 G_x G_y \tag{14.96}$$

For a diffuse incident field

$$|p_{mn}|_d^2 = 4p_0^2 \int_0^{2\pi} d\beta \int_0^{\pi/2} G_x G_y \cos \alpha d\alpha \quad (14.97)$$

This integral was discussed in Sect. 12.8. Using the result (12.84), Eq. (14.97) is written as

$$|p_{mn}|_d^2 = \frac{4\pi^2 p_0^2 \sigma_{mn}}{k^2} \quad (14.98)$$

This expression inserted in Eq. (14.93) yields

$$\bar{\Pi}_{mn} = \frac{8\rho_0 c \omega^2 \pi^2 \sigma_{mn}^2 p_0^2}{k^2 \mu^2 [(\omega_{mn}^2 - \omega^2)^2 + (\eta_{mn} \omega_{mn}^2)^2]}$$

The total radiated power is

$$\bar{\Pi}_{\text{rad}} = \sum_{mn} \bar{\Pi}_{mn} = \sum_{mn} \frac{8\rho_0 c \omega^2 \pi^2 \sigma_{mn}^2 p_0^2}{k^2 \mu^2 [(\omega_{mn}^2 - \omega^2)^2 + (\eta_{mn} \omega_{mn}^2)^2]} \quad (14.99)$$

The incident power is

$$\bar{\Pi}_{\text{in}} = \frac{p_0^2 L_x L_y}{2\rho_0 c} \int_0^{2\pi} d\beta \int_0^{\pi/2} d\alpha \sin \alpha \cos \alpha = \frac{\pi L_x L_y p_0^2}{2\rho_0 c} \quad (14.100)$$

The sound transmission coefficient τ_d for a diffuse incident field is

$$\tau_d = \sum_{mn} \frac{16\pi \rho_0^2 c^4 \sigma_{mn}^2}{\mu^2 L_x L_y [(\omega_{mn}^2 - \omega^2)^2 + (\eta_{mn} \omega_{mn}^2)^2]} \quad (14.101)$$

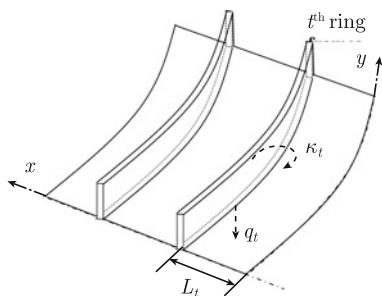
The loss factor, including radiation losses, is

$$\eta_{mn} = \eta + 2 \frac{\omega \rho_0 c (\sigma_r)_{mn}}{\mu \omega_{mn}^2} \quad (14.102)$$

Now returning to the discussion on the sound transmission through an open shallow circular shell. For a shallow shell, the sound radiation ratios are approximately equal to the radiation ratios for a flat plate of the same material and thickness having the same dimensions and boundary conditions as the shell, Ref. [88]. Thus, the sound transmission coefficient τ_d for the shell and the corresponding sound transmission loss R, assuming a diffuse incident field, are written as

$$\tau_d = \sum_{mn} \frac{16\pi \rho_0^2 c^4 (\sigma_r)_{mn}^2}{\mu^2 L R \varphi_0 [(\omega_{mn}^2 - \omega^2)^2 + (\eta_{mn} \omega_{mn}^2)^2]}; \quad R = 10 \log(1/\tau_d) \quad (14.103)$$

Fig. 14.49 A curved, rectangular panel with circumferential stiffeners



The natural angular frequencies ω_{mn} are given by the expression (14.88). The sound radiation ratios $(\sigma_r)_{mn}$ are obtained from Eq. (12.97) by setting $L_x = L$ and $L_y = R\varphi_0$. Compare Problem 14.9.

The effect of stringers and ring frames on the transmission coefficient can also be included as discussed in Ref. [224]. A stiffened shell is shown in Fig. 14.49. The distance between the boundary and ring frame number t is denoted as L_t . The radial force on the shell caused by a vibrating frame is q_t per unit length of the frame. The corresponding forcing bending moment per unit length of the stringer is κ_t .

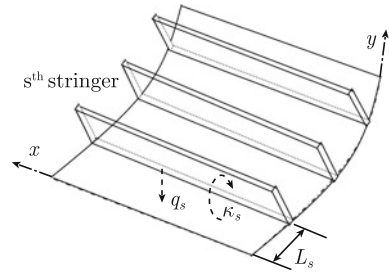
The total pressure p_{tot} on the shell due the incident pressure field and the reaction of the stringer can be written as

$$p_{\text{tot}} = p - \sum_{t=1}^T q_t \delta(x - L_t) - \sum_{t=1}^T \kappa_t \delta'(x - L_t) \quad (14.104)$$

The total number of frames supporting the plate element is T . The resulting modal pressure $\langle p_{\text{tot}} | g_{mn} \rangle$ acting on the plate is

$$\begin{aligned} (p_{\text{tot}})_{mn} &= p_{mn} - Q_{mn} - M_{mn} \\ Q_{mn} &= \sum_{t=1}^T \int_0^{\varphi_0} d\varphi \sin\left(\frac{n\pi\varphi}{\varphi_0}\right) \int_0^L dx q_t \sin\left(\frac{m\pi x}{L}\right) \delta(x - L_t) \\ &= \sum_{t=1}^T \int_0^{\varphi_0} d\varphi q_t \sin\left(\frac{m\pi L_t}{L}\right) \sin\left(\frac{n\pi\varphi}{\varphi_0}\right) \\ M_{mn} &= \sum_{t=1}^T \int_0^{\varphi_0} d\varphi \sin\left(\frac{n\pi\varphi}{\varphi_0}\right) \int_0^L dx \kappa_t \sin\left(\frac{m\pi x}{L}\right) \delta'(x - L_t) \\ &= - \sum_{t=1}^T \int_0^{\varphi_0} d\varphi \kappa_t \left(\frac{L}{m\pi}\right) \cos\left(\frac{m\pi L_t}{L}\right) \sin\left(\frac{n\pi\varphi}{\varphi_0}\right) \end{aligned} \quad (14.105)$$

Fig. 14.50 A stiffened curved plate



The modal pressure p_{mn} is as before given by Eq. (14.98). The equations determining the forces q_t and torsional moment κ_t per unit length of rib frame are according to Refs. [88, 226] given by

$$q_t = \frac{D_r}{R^4} \left(\frac{\partial^4 w_t}{\partial \varphi^4} + 2 \frac{\partial^2 w_t}{\partial \varphi^2} + w_t \right) - m'_r \omega^2 w_t \tag{14.106}$$

The displacement along the frame t is given by $w_t = w(L_t, \varphi)$. The corresponding equation defining κ_t is

$$\kappa_t = \frac{T_r}{R^2} \frac{\partial^2 \theta_t}{\partial \varphi^2} - \frac{E_t I_\varphi}{R^2} \theta_r + \rho_t I_\rho \omega^2 \theta_r; \quad \theta_t = \left[\frac{\partial w}{\partial x} \right]_{x=L_t} \tag{14.107}$$

The torsional stiffness of the frame t is T_r , its bending stiffness D_r , mass per unit length m'_r . The warping stiffness of the frame is I_φ and its moment of inertia I_ρ . The modulus of elasticity is E_t . The bending stiffness of the frame is D_t and its mass per unit length m'_r .

The effect of stringers on a shell can be formulated in a similar way as described in Ref. [224]. A shell stiffened by stringers is shown in Fig. 14.50. The distance between the boundary and stringer number s is denoted as L_s . The radial force on the shell caused by the stringer is q_s per unit length of the stringer. The corresponding bending moment per unit length of stringer is κ_s . The total pressure p_{tot} on the shell due the incident pressure field and the reaction of the stringer can be written as

$$p_{tot} = p - \sum_{s=1}^S q_s \delta(R\varphi - L_s) - \sum_{s=1}^S \kappa_s \delta'(R\varphi - L_s) \tag{14.108}$$

The total number of stringers on the element is S . The resulting modal pressure $\langle p_{tot} | g_{mn} \rangle$ is

$$\begin{aligned}
(p_{\text{tot}})_{mn} &= p_{mn} - Q_{mn} - M_{mn} \\
Q_{mn} &= \sum_{s=1}^S \int_0^L dx \sin\left(\frac{m\pi x}{L}\right) \int_0^{\varphi_0} d\varphi q_s \sin\left(\frac{n\pi\varphi}{\varphi_0}\right) \delta(R\varphi - L_s) \\
&= \sum_{s=1}^S \int_0^L dx \sin\left(\frac{m\pi x}{L}\right) \frac{q_s}{R} \sin\left(\frac{n\pi L_s}{R\varphi_0}\right) \\
M_{mn} &= \sum_{s=1}^S \int_0^L dx \sin\left(\frac{m\pi x}{L}\right) \int_0^{\varphi_0} d\varphi \kappa_s \sin\left(\frac{n\pi\varphi}{\varphi_0}\right) \delta'(R\varphi - L_s) \\
&= - \sum_{s=1}^S \int_0^L dx \sin\left(\frac{m\pi x}{L}\right) \frac{\kappa_s}{\varphi_0 R^2} \cos\left(\frac{n\pi L_s}{R\varphi_0}\right)
\end{aligned} \tag{14.109}$$

The parameters q_s and κ_s are in Ref. [224] given as

$$q_s = D_s \frac{\partial^4 w_s}{\partial x^4} - \mu\omega^2 w_s; \quad \kappa_s = T_s \frac{\partial^2 \theta_s}{\partial x^2} - EI_w \frac{\partial^4 \theta_s}{\partial x^4} + \rho_s I_p \omega^2 \theta_s$$

where D_s and T_s are the bending and torsional stiffness of the beam or stiffener. I_w is the warping constant of the stiffener and I_p its polar moment of inertia. The combined effect of stringers and frames is discussed in Ref. [224].

14.17 Comparison Between Measured and Predicted TL

Measurements on various shallow plate elements are reported by Liu et al. in Refs. [224, 225]. In these papers, predictions of the sound transmission loss of shallow elements were compared to measurements carried out at the Marcus Wallenberg Laboratory for Sound and Vibration Research (MWL), KTH, Sweden. The purpose of the measurements was to verify the various models discussed in Sect. 14.16. In particular, the influence on the sound transmission loss of plate curvature, frames, and overpressure was investigated. The test samples were mounted in between a reverberation room and an anechoic room as shown in Fig. 14.51. The reverberation room (6.21 m × 7.86 m × 5.05 m) was used as the source room. Diffusers were mounted in the source room. The sound pressure level in the room was measured by means of a rotating microphone. The anechoic room (7 m × 5.95 m × 5.8 m, cutoff frequency 80 Hz) is used as the receiving room and the average sound intensity level over the surface of the sample was measured using a scanning method. The sound transmission losses of the panels were measured according to the ISO standard 15186-1:2000 Ref. [227] using the intensity method. The repeatability of the measurements was within 0.5 dB in the frequency range 100–5000 Hz. The intensity sound reduction index or the sound transmission loss R is calculated according to the standard as

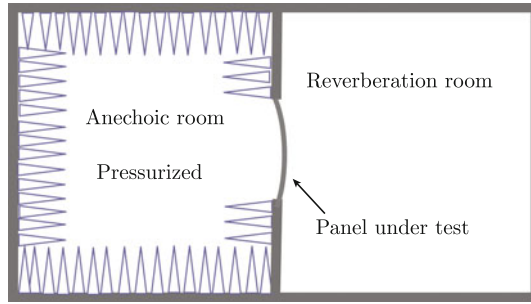


Fig. 14.51 Test arrangement for sound transmission loss measurements

Table 14.4 Description of panels

Panel	Material	Radius (m)	Size (m ²)	Skin area density (kg/m ²)	Young's modulus (N/m ²)	Stiffener	Loss factor
A	Al.	∞	0.87 × 0.87	2.7	6.85 × 10 ¹⁰	No	0.01
B	Al.	4	0.87 × 0.91	2.7	6.85 × 10 ¹⁰	No	
C	Al.	1	0.87 × 0.95	2.7	6.85 × 10 ¹⁰	No	
D	Composite	∞	0.535 × 1.25	4.0	3.25 × 10 ¹⁰	No	0.15
E	Composite	∞	0.535 × 1.25	4.9	3.25 × 10 ¹⁰	Yes	See
F	Al.	2	1.67 × 2.2	5.4	6.85 × 10 ¹⁰	Yes	Table 14.4
G	Composite	2	1.67 × 2.2	5.4	3.25 × 10 ¹⁰ × 10 ¹⁰	Yes	

$$R = L_{ps} - L_{Ir} - 6 \text{ dB} \tag{14.110}$$

where L_{ps} , dB (re 2×10^{-5} Pa), is the averaged sound pressure level in the source room and L_{Ir} , dB (re 10^{-12} W/m²), the averaged sound intensity level radiated from the panel into the receiving room. The area over which the intensity was measured was equal to the area of the test panel.

Seven panels, data shown in Table 14.4, were used for the measurements. Panels A, B, and C were made of aluminum plates of the same thickness. The panels had different curvatures. Panel D was a small composite aircraft panel without stringers. Panel E was the same as D but stiffened with densely arranged stringers. In addition Panel E is heavily damped. The structure is shown in Fig. 14.52. Panels F and G are large aircraft structures. Panel F is made of aluminum whereas Panel G is a composite structure of the same weight and having the same geometry as Panel F. Panels F and G are stiffened with stringers, ring frames, and heavily damped on the concave side of the structure, Fig. 14.53. The panel area, 40% of the total, without stringers are designed for the allocation of windows. Therefore, two areas, stringer area and window area, may be classified for Panels F and G. The thicknesses of the panels vary between the window and stringer areas. In all predictions, an effective



Fig. 14.52 Mounting of panel E. *Left picture* as seen from the reverberation room, *right picture* seen from the anechoic room



Fig. 14.53 Mounting of Panel F. *Left picture* as seen from the reverberation room, *right picture* from the anechoic room

Table 14.5 Loss factors for panels E, F, and G

Frequency (Hz)	100	125	160	200	250	315	400	500	630	800	$\geq 1k$
Panel E	0.13	0.11	0.06	0.07	0.063	0.043	0.024	0.021	0.02	0.02	0.015*
Panel F	0.11	0.07	0.05	0.04	0.04	0.04	0.03	0.03	0.02	0.02	0.015*
Panel G	0.12	0.12	0.07	0.06	0.06	0.04	0.03	0.03	0.02	0.02	0.015*

* The loss factors below 1 kHz are measured and above 1 kHz are estimated

thickness of 2 mm is used for Panel F and 3.3 mm for Panel G. The measured loss factors for the mounted panels are listed in Table 14.5. The panels are clamped at the edges. More information on the stiffeners is given in Ref. [224].

The influence of the curvature on the sound transmission loss of a shallow plate element is illustrated in Fig. 14.54. The figure shows the measured sound transmission loss for the plates A, B, and C. The plates are made of the same material and have the same thickness. Plate A is flat, the radius of plate B is 4 m, and of plate C

Fig. 14.54 Measured sound transmission loss for panels with different curvature: — Panel A, flat; - - - Panel B, $R = 4$ m; —●— Panel C, $R = 1$ m

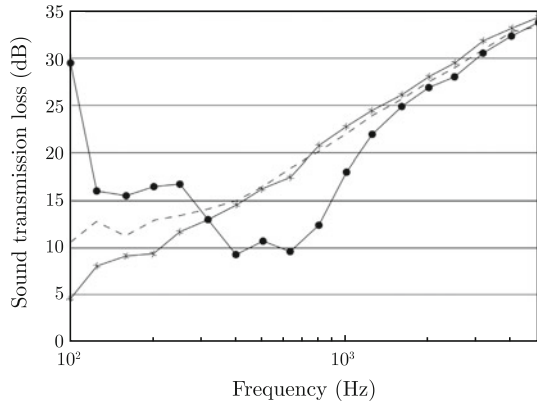
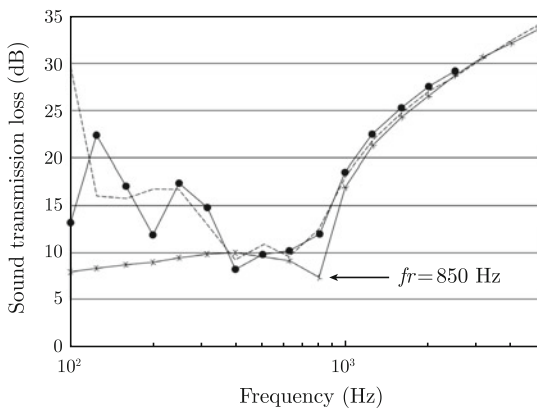


Fig. 14.55 Measured and predicted sound transmission loss for Panel C: - - - Measurement; —●— predicted, clamped; —*— predicted, infinite model



is 1m. The first natural frequency of a curved plate is increased as the radius of the plate is reduced. According to Eq. (14.88) the first natural frequency for plate A is 6 Hz assuming simply supported boundary conditions. For plate B and C the corresponding natural frequencies are 105 and 436 Hz respectively. The measured sound transmission loss for Panel B has a minimum at around 100 Hz and for Panel C somewhere around 400–600 Hz. In the high frequency region, m and n large, the first part of Eq. (14.88) determines the natural frequencies of the curved plate. Consequently, the natural frequencies for curved and flat plates are almost the same, which also leads to similar sound transmission losses. In the low frequency region, the sound transmission loss of a curved plate element is higher than for the corresponding flat plate.

For Panel C predicted and measured sound transmission losses are compared in Fig. 14.55. The infinite model corresponds to an infinitely long circular Al cylinder with a plate thickness of 1 mm, [228]. The ring frequency $f_r = c_l / (2\pi R)$ for the full cylinder is 850 Hz. The predicted results indicate that predictions based on an infinite model give fairly accurate results for frequencies above twice the ring frequency.

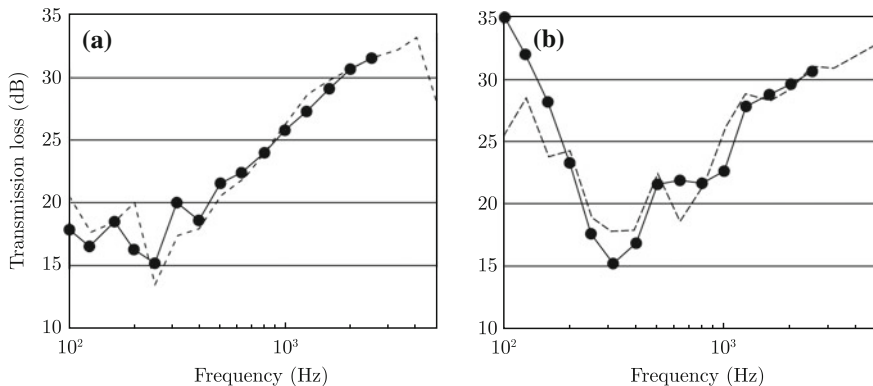


Fig. 14.56 Comparison between predicted and measured sound transmission loss of **a** Panel D without stiffeners and **b** Panel E with stiffeners. ---- predicted; —●— measured

The influence of stiffeners on the sound transmission loss of a flat panel is shown in Fig. 14.56. The figure on the left-hand side (a), shows the measured and predicted sound transmission loss of a flat panel (D in Table 14.4) without any stiffeners. The sound transmission loss for the same panel (E in Table 14.4) with stiffeners is shown on the right-hand side (b) of the figure. The results indicate that the stiffeners improve the sound transmission loss at low frequencies. At high frequencies, the stiffeners decrease the sound transmission loss. In the high frequency region, each subpanel vibrates more or less independently of other elements. The radiation ratios are therefore increased resulting in a lower transmission loss as predicted by Eq. (14.103). Compare also Fig. 13.17 and the discussion in Sect. 13.10.

Measured and predicted sound transmission losses for two large and curved aircraft panels are shown in Figs. 14.57, 14.58, 14.59 and 14.60. The data for these panels, F and G, are given in Tables 14.4 and 14.5. Panel F, the Al structure, is shown in Fig. 14.53. The configuration of Panel G, the composite structure, is the same as for Panel F. The ring frequency, assuming a full circular section, is 420 Hz for Panel

Fig. 14.57 Measured and predicted sound transmission loss for Panel F. — measurement; ----predicted., skin + ring frames; —●— predicted, skin + axial stringers

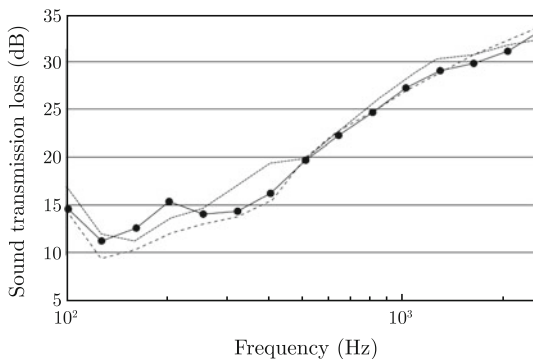


Fig. 14.58 Measured and predicted sound transmission loss for Panel G. — measurement; ---predicted., skin + ring frames; ●— predicted, skin + axial stringers

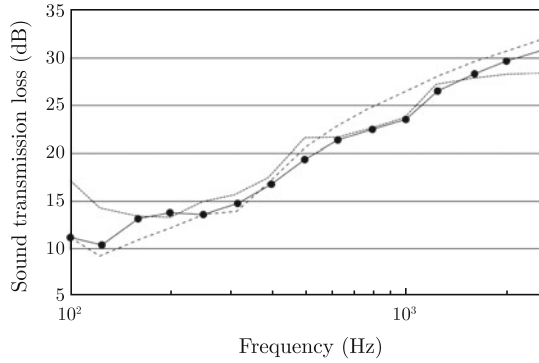


Fig. 14.59 Measured sound transmission loss for Panels F and G. ●— Panel F; *— Panel G

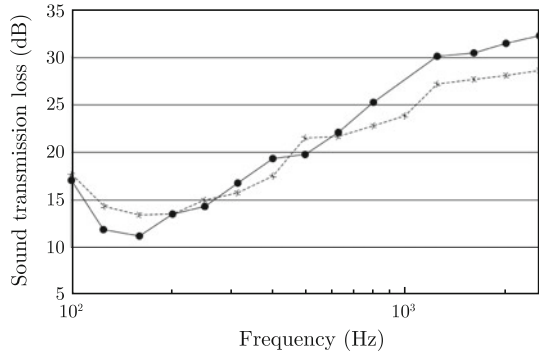
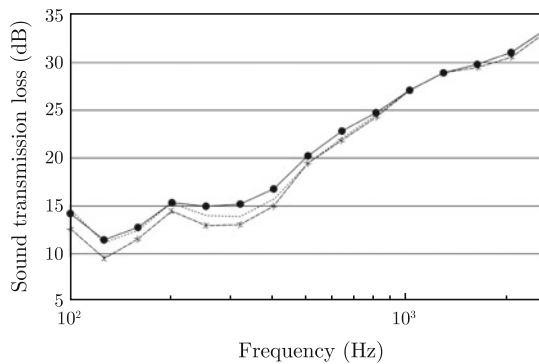


Fig. 14.60 Predicted sound transmission loss for Panel F for three different loss factors; ●— skin loss factor 10%; --- skin loss factor same as Table 14.4; *— skin loss factor is 1%. The stringer loss factor is 1.5%, $f_r \approx 420$ Hz



F and 410Hz for Panel G. The critical frequency of the skin is 5700Hz for Panel F and 3700Hz for Panel G. Measurements are compared to predicted results based on three different models. The first is valid for a curved plate without stringers or frames, the second is applicable for a curved plate with ring frames, and the third is used for a curved plate with stringers. Predictions for a curved plate with both stringers and frames give approximately the same result as for a curved plate with

stringers. However, the computational time, including both stringers and frames, is very long.

The results indicate that the ring frames have very little effect on the sound transmission loss below 400 Hz and no apparent effect at frequencies above 630 Hz. Unlike the ring frames, the axial stiffeners slightly improve the sound transmission loss below 400 Hz. For the Al structure, Panel G, the stringers have no effect in the high frequency region. However, for the composite panel, the sound transmission loss is slightly reduced due to the stringers. For large curved aircraft panels, the ring frames have little influence on the sound transmission loss in the frequency range of interest. Compared with the ring frames, the stringers may have a significant influence on the sound transmission loss of a structure. The stringers will slightly improve the sound transmission loss of a curved panel around the ring frequency, but it may result in a potential deterioration of the sound transmission loss above the ring frequency.

The results shown in Figs. 14.57 and 14.58 indicate that the agreement between measured and predicted results using the skin/stringer model is fairly good. Comparing the Al (F) and the composite (G) panel in Fig. 14.59, it is found that the Al structure has the higher sound transmission loss despite the fact that the mass per unit area of the skin of the panels is the same.

The influence of the loss factor of the skin on the sound transmission loss is illustrated in Fig. 14.60. The numerical results reveal that an increase of the skin loss factor from 1 to 10% increases sound transmission loss by about 1 to 2 dB below 500 Hz. In this frequency range, the sound transmission is dominated by resonant transmission of the subpanels.

During in-flight operations of an aircraft, there is a pressure difference between the cabin and the outside atmosphere. The pressure difference or rather the overpressure in the cabin will induce a tension in the fuselage. The tension in the plate elements will increase the natural frequencies of the structures. Compare Sect. 8.14. For a shell element exposed to tension T'_x and T'_y in the x - and y -directions the natural angular frequencies are approximately given by

$$\omega_{mn}^2 = \frac{D_0}{\mu} \cdot \left\{ \left[\left(\frac{m\pi}{L_x} \right)^2 + \left(\frac{n\pi}{L_y} \right)^2 \right]^2 + \frac{12}{(hR_y)^2 [1 + (nL_x/mL_y)^2]^2} + \left[\frac{T'_x}{D_0} \left(\frac{m\pi}{L_x} \right)^2 + \frac{T'_y}{D_0} \left(\frac{n\pi}{L_y} \right)^2 \right] \right\} \quad (14.111)$$

For $T'_x = T'_y = 0$ Eq. (14.111) is reduced to Eq. (14.88). For a finite circular cylinder with an inside overpressure Δp the tensions T'_x and T'_y are discussed in Problem 14.10 approximated by $T'_x = \Delta p R_y / 2$ and $T'_y = \Delta p R_x$. Consequently, the response and sound transmission loss of the elements will also change. The sound transmission loss is calculated by inserting Eq. (14.111) in the expression (14.103). The effect of an overpressure on the sound transmission loss of an aircraft structure was investigated in Ref. [225]. The panel was again mounted as illustrated in Fig. 14.51. The overpressure

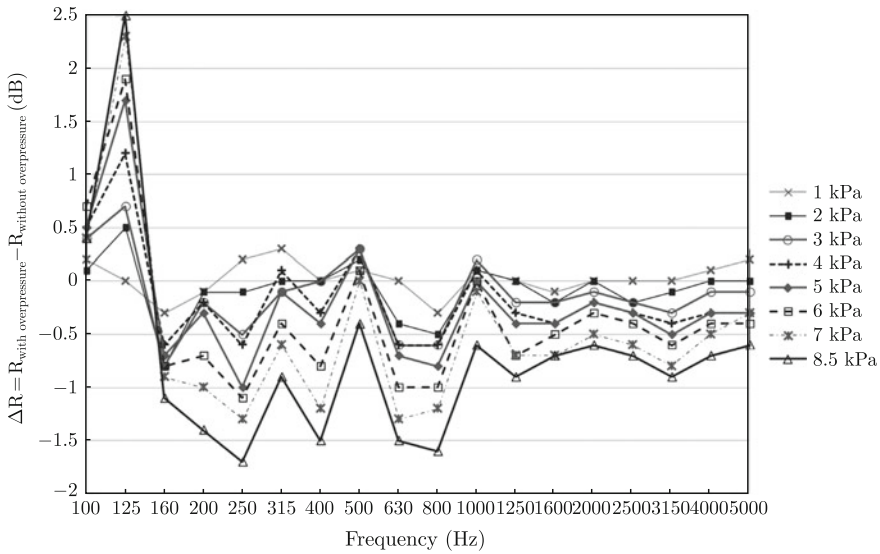


Fig. 14.61 Measured TL difference $\Delta R = R(\text{with overpressure}) - R(\text{no overpressure})$ for different overpressures on one side of the panel

in the anechoic room could be increased stepwise up to 8500 Pa. The effect ΔR defined as $\Delta R = R_{\text{with overpressure}} - R_{\text{without overpressure}}$ was measured (Fig. 14.61).

When the anechoic room was pressurized, the air density inside the anechoic room is increased to $\rho_{\Delta P}$, with the relation to ρ_0 as

$$\rho_{\Delta P} = \frac{\Delta P + P_{\text{atm}}}{P_{\text{atm}}} \rho_0$$

where ρ_0 is the air density without overpressure, ΔP is the overpressure, P_{atm} is the ambient atmospheric pressure.

Predicted results obtained by changing the natural frequencies of the plate due to the added tension and considering the change of the air density in the receiving room agreed well with measurements as discussed by Liu in Ref. [225]. At frequencies higher than the ring frequency both predicted and measured results reveal that an overpressure tends to reduce the sound transmission loss at the rate of 0.5 dB per 10 kPa. Approximately 80% of this reduction is due to a mismatch caused by the different air densities on each side of the panel and by 20% due to the added tension. At low frequencies, below the ring frequency, ΔR is mainly determined by the shift of the natural frequencies of the plate element caused by the in-plane tension, which in turn is a result of the overpressure. The tension in the plates depends also on the arrangements of stringers and frames. See also the discussion in Sect. 15.6 on the excitation of shell elements by turbulent boundary layers.

Problems

14.1 Determine the first five cut-on frequencies for an acoustic cylindrical waveguide.

14.2 A structural waveguide, Fig. 14.2, is excited by a bending moment $M \exp(i\omega t)$ at $x = 0$. The bending moment is constant along the y -axis. Determine the energy flow in the waveguide. The plate element is simply supported along the lines $y = 0$ and $y = L_y$. Assume the waveguide to be semi-infinite.

14.3 Assume that the elements in Fig. 14.5 are beam elements. Determine the coupling elements in the matrix $[A]$ of Eq. (14.23) for this particular case.

14.4 Use Eq. (14.34) to prove the results given in Eq. (14.36).

14.5 Determine the matrix giving the natural frequencies of a sandwich beam with free ends.

14.6 Determine the response of a simply supported sandwich beam, length L , mass per unit length m' , and bending stiffness D' . The beam is extended along the x -axis of a coordinate system from $x = 0$ to $x = L$. The beam is excited by a force $F \exp(i\omega t)$ at x_1 where $0 < x_1 < L$.

14.7 Determine the point mobility of an infinite sandwich beam.

14.8 Determine the high frequency limits for the wavenumbers for waves propagating on a circular cylinder.

14.9 Use Eq. (14.100) to predict the sound transmission loss of a curved panel for $f > f_c$ and well above the ring frequency.

14.10 Show that in a finite circular cylinder with an inside over pressure Δp the tensions T'_x and T'_y are approximated by $T'_x = \Delta p R_y / 2$ and $T'_y = \Delta p R_y$.

Chapter 15

Random Excitation of Structures

The excitation of some simple continuous systems like beams and plates was discussed in Chaps. 6 through 8. In the majority of those examples, the excitation of the structure was a point force or a pressure distribution across the surface of the structure. The response due to harmonic as well as white noise or random excitation was discussed. The response of a structure due to a random distribution of forces across a plate was discussed briefly in Sects. 7.4 and 8.2.

In this chapter, a more general approach is presented for the prediction of the response of structures exposed to certain random distributions of forces. One important example is a structure subjected to random excitation, uncorrelated in space and time, often referred to as “rain on the roof” excitation. Another important problem is flow-induced vibrations of plate structures. Examples of this type of phenomenon are aerodynamic excitation of fast moving aircraft, trains, and cars as well as fast vessels or ships moving through water. Another example is the excitation of duct walls due to a flow inside the duct.

In the first section of this chapter, some basic mathematical tools are introduced as outlined by Newland in Ref. [11]. This section is an extension of Chap. 2. However, not only time but also space dependent signals are considered. Thereafter follows some examples, first on rain on the roof excitation of plates followed by a basic example of flow-induced vibrations. Although prediction procedures are somewhat cumbersome, the examples discussed can be useful for parameter studies on the influence of plate geometry, stiffness, etc., on the power induced in a plate due to a turbulent flow. For rain on the roof excitation, the resulting energy of the plate can be formulated in a very compact way.

15.1 Introduction

In Chap. 2 the auto- and cross-correlation functions were introduced for time-dependent functions. For a stationary time-dependent signal $u(t)$ the autocorrelation function $R_{uu}(\tau)$ was in Eq. (2.19) defined as

$$R_{uu}(\tau) = E[u(t)u(t + \tau)] = \lim_{T \rightarrow \infty} \frac{1}{T} \int_{-T/2}^{T/2} u(t)u(t + \tau) dt \quad (15.1)$$

where $E[u(t)u(t + \tau)]$ represents the ensemble average of the product of the signal at time t and the signal at a later time $t + \tau$. The corresponding power spectral density $S_{uu}(\omega)$ is according to Eq. (2.34) defined as the temporal Fourier transform of $R_{uu}(\tau)$ as

$$S_{uu}(\omega) = \int_{-\infty}^{\infty} R_{uu}(\tau) \exp(-i\omega\tau) d\tau \quad (15.2)$$

The inverse FT of this expression gives

$$R_{uu}(\tau) = \frac{1}{2\pi} \int_{-\infty}^{\infty} S_{uu}(\omega) \exp(i\omega\tau) d\omega \quad (15.3)$$

A signal can depend not only on time but also on its spatial coordinates. For a spatially stationary signal $u(x)$ the spatial autocorrelation function between the signal at the coordinate x and the signal at $x + \xi$ is defined as

$$R_{uu}(\xi) = E[u(x)u(x + \xi)] = \lim_{X \rightarrow \infty} \frac{1}{X} \int_{-X/2}^{X/2} u(x)u(x + \xi) dx \quad (15.4)$$

The spatial spectral density $\tilde{S}_{uu}(k)$ is defined as

$$\tilde{S}_{uu}(k) = \int_{-\infty}^{\infty} R_{uu}(\xi) \exp(-ik\xi) d\xi \quad (15.5)$$

The inverse spatial FT of the spatial spectral density gives

$$R_{uu}(\xi) = \frac{1}{2\pi} \int_{-\infty}^{\infty} \tilde{S}_{uu}(k) \exp(ik\xi) dk \quad (15.6)$$

In analogy with the discussion in Sect. 2.3, it follows that a signal $u(x)$ defined as $u(x) = A \sin(k_0 x)$ has the spatial autocorrelation function $R_{uu}(\xi) = A^2/[2 \cdot \cos(k_0 \xi)]$. For a stationary and random signal $u(x)$ the corresponding spatial autocorrelation function is $R_{uu}(\xi) = a \cdot \delta(\xi)$ where a is a positive nonzero constant. The parameter a is equal to the spatial spectral density $\tilde{S}_{uu}(k)$, compare Eq. (2.39). While a temporal FT is a transform from the time domain to the frequency domain, a spatial FT is a transform from the space to the wavenumber domain.

In general a signal not only depends on time t but also on the coordinates x and y of the observation point. The autocorrelation function of a signal $u(x, y, t)$ is defined as the ensemble average of the product of the signal u at the coordinates (x, y, t) and the signal at the coordinates $(x + \xi_x, y + \xi_y, t + \tau)$. For a signal u , stationary in two-dimensional space and time, the ensemble average depends only on the separation

ξ_x and ξ_y in space and τ in time. Thus, the autocorrelation function R_{uu} is defined as

$$R_{uu}(\xi_x, \xi_y, \tau) = E[u(x, y, t)u(x + \xi_x, y + \xi_y, t + \tau)] \quad (15.7)$$

The three-dimensional spectral density $\tilde{S}(k_x, k_y, \omega)$ is given by

$$\begin{aligned} \tilde{S}_{uu}(k_x, k_y, \omega) &= \int_{-\infty}^{\infty} d\xi_x \int_{-\infty}^{\infty} d\xi_y \int_{-\infty}^{\infty} d\tau \cdot R_{uu}(\xi_x, \xi_y, \tau) \\ &\quad \cdot \exp[-i(k_x \xi_x + k_y \xi_y + \omega \tau)] \\ &= \int_{-\infty}^{\infty} d\xi_x \int_{-\infty}^{\infty} d\xi_y S_{uu}(\xi_x, \xi_y, \omega) \cdot \exp[-i(k_x \xi_x + k_y \xi_y)] \end{aligned} \quad (15.8)$$

The cross-power spectral density between the two signals observed at positions separated by the vector $\mathbf{r} = (\xi_x, \xi_y)$ is defined by $S_{uu}(\xi_x, \xi_y, \omega)$ as

$$S_{uu}(\xi_x, \xi_y, \omega) = \int_{-\infty}^{\infty} d\tau \cdot R_{uu}(\xi_x, \xi_y, \tau) \cdot \exp(-i\omega\tau) \quad (15.9)$$

The function $\tilde{S}_{uu}(k_x, k_y, \omega)$ of Eq. (15.8) is the spatial FT of $S_{uu}(\xi_x, \xi_y, \omega)$. Consequently,

$$S_{uu}(\xi_x, \xi_y, \omega) = \frac{1}{(2\pi)^2} \int_{-\infty}^{\infty} dk_x \int_{-\infty}^{\infty} dk_y \tilde{S}_{uu}(k_x, k_y, \omega) \cdot \exp[i(k_x \xi_x + k_y \xi_y)] \quad (15.10)$$

Thus, for a homogeneous and stationary random process $u(\mathbf{r}, t)$ with a spectral density $\tilde{S}(\mathbf{k}, \omega)$, the cross-power spectral density $S(\xi_x, \xi_y, \omega)$ between any two points separated by the vector (ξ_x, ξ_y) can be derived as given by Eq. (15.10).

The inverse three-dimensional FT of the first part of Eq. (15.8) reads

$$\begin{aligned} R_{uu}(\xi_x, \xi_y, \tau) &= \frac{1}{(2\pi)^3} \int_{-\infty}^{\infty} dk_x \int_{-\infty}^{\infty} dk_y \int_{-\infty}^{\infty} d\omega \cdot \tilde{S}_{uu}(k_x, k_y, \omega) \\ &\quad \cdot \exp[i(k_x \xi_x + k_y \xi_y + \omega \tau)] \end{aligned} \quad (15.11)$$

Introducing the wavenumber vector $\mathbf{k} = (k_x, k_y)$ and the two-dimensional space vector $\mathbf{r} = (x, y)$ the transforms (15.8) and (15.10) can be written in a more compact form as

$$\tilde{S}_{uu}(\mathbf{k}, \omega) = \int_{-\infty}^{\infty} d^2\mathbf{r} \int_{-\infty}^{\infty} d\tau \cdot R_{uu}(\mathbf{r}, \tau) \cdot \exp[-i(\mathbf{k} \cdot \mathbf{r} + \omega \tau)] \quad (15.12)$$

$$R_{uu}(\mathbf{r}, \tau) = \frac{1}{(2\pi)^3} \int_{-\infty}^{\infty} d^2\mathbf{k} \int_{-\infty}^{\infty} d\omega \cdot \tilde{S}_{uu}(\mathbf{k}, \omega) \cdot \exp[i(\mathbf{k} \cdot \mathbf{r} + \omega \tau)] \quad (15.13)$$

The time and two-dimensional space averages of the signal $u(x, y, t)$ with the power spectral density $\tilde{S}_{uu}(\mathbf{k}, \omega)$ is from Eqs. (15.7) and (15.13) obtained as

$$\begin{aligned} \langle \bar{u}^2 \rangle &= E[u(x, y, t)u(x, y, t)] = R_{uu}(0, 0, 0) \\ &= \frac{1}{(2\pi)^3} \int_{-\infty}^{\infty} d^2\mathbf{k} \int_{-\infty}^{\infty} d\omega \cdot \tilde{S}_{uu}(\mathbf{k}, \omega) \end{aligned} \quad (15.14)$$

In a three-dimensional coordinate system with $\mathbf{r} = (\xi_x, \xi_y, \xi_z)$ and $\mathbf{k} = (k_x, k_y, k_z)$ the power spectral density $\tilde{S}_{uu}(\mathbf{k}, \omega)$ and the corresponding correlation function $R_{uu}(\mathbf{r}, \tau)$ read

$$\begin{aligned} \tilde{S}_{uu}(k_x, k_y, k_z, \omega) &= \tilde{S}_{uu}(\mathbf{k}, \omega) \\ &= \int_{-\infty}^{\infty} d^3\mathbf{r} \int_{-\infty}^{\infty} d\tau \cdot R_{uu}(\mathbf{r}, \tau) \cdot \exp[-i(\mathbf{k} \cdot \mathbf{r} + \omega\tau)] \\ &= \int_{-\infty}^{\infty} d\xi_x \int_{-\infty}^{\infty} d\xi_y \int_{-\infty}^{\infty} d\xi_z \int_{-\infty}^{\infty} d\tau \cdot R_{uu}(\xi_x, \xi_y, \xi_z, \tau) \\ &\quad \cdot \exp[-i(k_x\xi_x + k_y\xi_y + k_z\xi_z + \omega\tau)] \end{aligned} \quad (15.15)$$

$$\begin{aligned} R_{uu}(\xi_x, \xi_y, \xi_z, \tau) &= R_{uu}(\mathbf{r}, \tau) \\ &= \frac{1}{(2\pi)^4} \int_{-\infty}^{\infty} d^3\mathbf{k} \int_{-\infty}^{\infty} d\omega \cdot \tilde{S}_{uu}(\mathbf{k}, \omega) \cdot \exp[i(\mathbf{k} \cdot \mathbf{r} + \omega\tau)] \\ &= \frac{1}{(2\pi)^4} \int_{-\infty}^{\infty} dk_x \int_{-\infty}^{\infty} dk_y \int_{-\infty}^{\infty} dk_z \int_{-\infty}^{\infty} d\omega \cdot \tilde{S}_{uu}(k_x, k_y, k_z, \omega) \\ &\quad \cdot \exp[i(k_x\xi_x + k_y\xi_y + k_z\xi_z + \omega\tau)] \end{aligned} \quad (15.16)$$

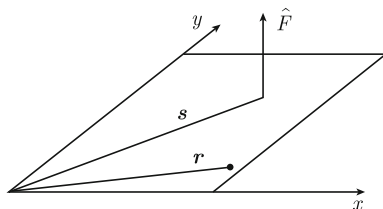
15.2 Excitation of Plates

As a starting point, consider a continuous linear system, in this case, a thin homogeneous flat plate. The plate is oriented in the x - y -plane of a Cartesian coordinate system. The plate is excited by a force perpendicular to the plate at a point defined by the position vector \mathbf{s} as illustrated in Fig. 15.1.

The temporal FT of the force exciting the plate at the coordinates \mathbf{s} is $\hat{F}(\mathbf{s}, \omega)$. The temporal FT of the response of the plate at a point defined by the space vector \mathbf{r} is $\hat{w}(\mathbf{r}, \omega)$. The frequency response function defining the steady state harmonic response $\hat{w}(\mathbf{r}, \omega)$ at \mathbf{r} due to the force $\hat{F}(\mathbf{s}, \omega)$ at \mathbf{s} is denoted $H(\mathbf{r}, \mathbf{s}, \omega)$. Thus

$$\hat{w}(\mathbf{r}, \omega) = \hat{F}(\mathbf{s}, \omega) \cdot H(\mathbf{r}, \mathbf{s}, \omega) \quad (15.17)$$

Fig. 15.1 Plate excited by a point force at s . The response is observed at r



The power spectral density $S_{ww}(\mathbf{r}, \omega)$ of the response is from Eq. (2.33) obtained as

$$\begin{aligned}
 S_{ww}(\mathbf{r}, \omega) &= \lim_{T \rightarrow \infty} \frac{1}{T} \hat{w}^* \hat{w} = \lim_{T \rightarrow \infty} \frac{1}{T} H(\mathbf{r}, \mathbf{s}, \omega) H^*(\mathbf{r}, \mathbf{s}, \omega) \hat{F}(\mathbf{s}, \omega) \hat{F}^*(\mathbf{s}, \omega) \\
 &= S_{FF}(\mathbf{s}, \omega) H(\mathbf{r}, \mathbf{s}, \omega) H^*(\mathbf{r}, \mathbf{s}, \omega)
 \end{aligned}
 \tag{15.18}$$

The spectral density of the force is according to Sect. 2.4 defined as

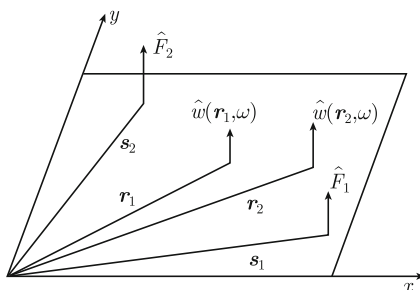
$$S_{FF}(\mathbf{s}, \omega) = \lim_{T \rightarrow \infty} \frac{1}{T} \hat{F}(\mathbf{s}, \omega) \hat{F}^*(\mathbf{s}, \omega)$$

For the case shown in Fig. 15.2, there are two separate forces exciting the plate at the points defined by the vectors \mathbf{s}_1 and \mathbf{s}_2 . The response functions $\hat{w}(\mathbf{r}_1, \omega)$ and $\hat{w}(\mathbf{r}_2, \omega)$ at the points \mathbf{r}_1 and \mathbf{r}_2 respectively are

$$\begin{aligned}
 \hat{w}(\mathbf{r}_1, \omega) &= \hat{F}(\mathbf{s}_1, \omega) \cdot H(\mathbf{r}_1, \mathbf{s}_1, \omega) + \hat{F}(\mathbf{s}_2, \omega) \cdot H(\mathbf{r}_1, \mathbf{s}_2, \omega) \\
 \hat{w}(\mathbf{r}_2, \omega) &= \hat{F}(\mathbf{s}_1, \omega) \cdot H(\mathbf{r}_2, \mathbf{s}_1, \omega) + \hat{F}(\mathbf{s}_2, \omega) \cdot H(\mathbf{r}_2, \mathbf{s}_2, \omega)
 \end{aligned}
 \tag{15.19}$$

Defining $H(\mathbf{r}_i, \mathbf{s}_j, \omega)$ as the frequency response function between the points \mathbf{r}_i and \mathbf{s}_j . For linear systems reciprocity holds, i.e., $H(\mathbf{r}_i, \mathbf{s}_j, \omega) = H(\mathbf{r}_j, \mathbf{s}_i, \omega)$. The cross-spectral density $S_{ww}(\mathbf{r}_1, \mathbf{r}_2, \omega)$ between the response $\hat{w}(\mathbf{r}_1, \omega)$ at \mathbf{r}_1 and the response $\hat{w}(\mathbf{r}_2, \omega)$ at \mathbf{r}_2 is

Fig. 15.2 Two-point forces, $\hat{F}(\mathbf{s}_1, \omega)$ and $\hat{F}(\mathbf{s}_2, \omega)$, at the positions \mathbf{s}_1 and \mathbf{s}_2 excite a plate. The response at the points \mathbf{r}_1 and \mathbf{r}_2 are $\hat{w}(\mathbf{r}_1, \omega)$ and $\hat{w}(\mathbf{r}_2, \omega)$, respectively



$$\begin{aligned}
S_{ww}(\mathbf{r}_1, \mathbf{r}_2, \omega) &= S_{FF}(\mathbf{s}_1, \mathbf{s}_1, \omega)H^*(\mathbf{r}_2, \mathbf{s}_1, \omega)H(\mathbf{r}_2, \mathbf{s}_1, \omega) \\
&\quad + S_{FF}(\mathbf{s}_1, \mathbf{s}_2, \omega)H^*(\mathbf{r}_1, \mathbf{s}_1, \omega)H(\mathbf{r}_2, \mathbf{s}_2, \omega) \\
&\quad + S_{FF}(\mathbf{s}_2, \mathbf{s}_1, \omega)H^*(\mathbf{r}_1, \mathbf{s}_2, \omega)H(\mathbf{r}_2, \mathbf{s}_1, \omega) \\
&\quad + S_{FF}(\mathbf{s}_2, \mathbf{s}_2, \omega)H^*(\mathbf{r}_1, \mathbf{s}_2, \omega)H(\mathbf{r}_2, \mathbf{s}_2, \omega) \quad (15.20)
\end{aligned}$$

where $S_{FF}(\mathbf{s}_i, \mathbf{s}_j, \omega)$ is the cross-power spectral density between the forces exciting the plate at the points defined by the position vectors \mathbf{s}_i and \mathbf{s}_j . The result is just an extension of Eq. (15.18). The cross-power spectral density $S_{ww}(\mathbf{r}_2, \mathbf{r}_1, \omega)$ is obtained by exchanging \mathbf{r}_1 and \mathbf{r}_2 in Eq. (15.20). Expressed in general terms the result is written

$$S_{ww}(\mathbf{r}_i, \mathbf{r}_j, \omega) = S_{ww}^*(\mathbf{r}_j, \mathbf{r}_i, \omega) \quad (15.21)$$

For N separate forces exciting the plate structure the cross-spectral density between the response $w(\mathbf{r}_1, t)$ at the position \mathbf{r}_1 and response $w(\mathbf{r}_2, t)$ at \mathbf{r}_2 is defined as

$$S_{ww}(\mathbf{r}_1, \mathbf{r}_2, \omega) = \sum_{i=1}^N \sum_{j=1}^N S_{FF}(\mathbf{s}_i, \mathbf{s}_j, \omega)H^*(\mathbf{r}_1, \mathbf{s}_i, \omega)H(\mathbf{r}_2, \mathbf{s}_j, \omega) \quad (15.22)$$

The result is a generalization of the expression (15.20). In the limiting case when the number of sources is approaching infinity the FT of a force at \mathbf{s}_i can be written

$$\hat{F}(\mathbf{s}_i, \omega) = \hat{p}(\mathbf{s}_i, \omega) \cdot \Delta \mathbf{s}_i \quad (15.23)$$

where $\hat{p}(\mathbf{s}_i, \omega)$ is the temporal FT of the pressure at the point \mathbf{s}_i on the plate and $\Delta \mathbf{s}_i$ the small area exposed to this pressure. The cross-spectral density between the pressure $p(\mathbf{s}_1, t)$ at the position \mathbf{s}_1 and the pressure $p(\mathbf{s}_2, t)$ at \mathbf{s}_2 is defined as $S_{pp}(\mathbf{s}_1, \mathbf{s}_2, \omega)$. In the limiting case as N , the number of sources, goes to infinity and the area $\Delta \mathbf{s}_i$ approaches zero, the result (15.22) is written in integral form as

$$S_{ww}(\mathbf{r}_1, \mathbf{r}_2, \omega) = \iint d^2 \mathbf{s}_1 d^2 \mathbf{s}_2 S_{pp}(\mathbf{s}_1, \mathbf{s}_2, \omega)H^*(\mathbf{r}_1, \mathbf{s}_1, \omega)H(\mathbf{r}_2, \mathbf{s}_2, \omega) \quad (15.24)$$

The symbols $d^2 \mathbf{s}_1$ and $d^2 \mathbf{s}_2$ represent surface integrals. The cross-power spectral density $S_{pp}(\mathbf{s}_1, \mathbf{s}_2, \omega)$ can following Eq. (15.8) also be written as

$$\begin{aligned}
S_{pp}(\mathbf{s}_1, \mathbf{s}_2, \omega) &= \frac{1}{(2\pi)^2} \int d^2 \mathbf{k} \cdot \tilde{S}_{pp}(\mathbf{k}, \omega) \exp[i\mathbf{k}(\mathbf{s}_2 - \mathbf{s}_1)] \\
&= \frac{1}{(2\pi)^2} \int dk_x \int dk_y \tilde{S}_{pp}(\mathbf{k}, \omega) \exp[i(k_x \xi_x + k_y \xi_y)] \quad (15.25)
\end{aligned}$$

The space vector between the observation points is $\mathbf{s}_2 - \mathbf{s}_1 = (\xi_x, \xi_y)$. The inverse transform of Eq. (15.25) is

$$\tilde{S}_{pp}(\mathbf{k}, \omega) = \int d\xi_x \int d\xi_y S_{pp}(\mathbf{s}_1, \mathbf{s}_2, \omega) \exp[-i(k_x \xi_x + k_y \xi_y)] \quad (15.26)$$

The results (15.24) and (15.25) give

$$S_{ww}(\mathbf{r}_1, \mathbf{r}_2, \omega) = \frac{1}{(2\pi)^2} \iint d^2s_1 d^2s_2 H^*(\mathbf{r}_1, \mathbf{s}_1, \omega) H(\mathbf{r}_2, \mathbf{s}_2, \omega) \times \int d^2\mathbf{k} \cdot S_{pp}(\mathbf{k}, \omega) \cdot \exp[i\mathbf{k}(\mathbf{s}_2 - \mathbf{s}_1)] \quad (15.27)$$

After changing the order of integration the result reads

$$S_{ww}(\mathbf{r}_1, \mathbf{r}_2, \omega) = \frac{1}{(2\pi)^2} \int d^2\mathbf{k} \cdot \tilde{S}_{pp}(\mathbf{k}, \omega) \int d^2s_1 H^*(\mathbf{r}_1, \mathbf{s}_1, \omega) \exp(-i\mathbf{k}\mathbf{s}_1) \times \int d^2s_2 H(\mathbf{r}_2, \mathbf{s}_2, \omega) \exp(i\mathbf{k}\mathbf{s}_2) \quad (15.28)$$

By introducing the function $G(\mathbf{r}, \mathbf{k}, \omega)$ as

$$G(\mathbf{r}, \mathbf{k}, \omega) = \int d\mathbf{s} H(\mathbf{r}, \mathbf{s}, \omega) \exp(i\mathbf{k}\mathbf{s}) \quad (15.29)$$

the power spectral density $S_{ww}(\mathbf{r}_1, \mathbf{r}_2, \omega)$ is written

$$S_{ww}(\mathbf{r}_1, \mathbf{r}_2, \omega) = \frac{1}{(2\pi)^2} \int d^2\mathbf{k} \cdot \tilde{S}_{pp}(\mathbf{k}, \omega) G^*(\mathbf{r}_1, \mathbf{k}, \omega) G(\mathbf{r}_2, \mathbf{k}, \omega) \quad (15.30)$$

The power spectral density with respect to the displacement of the plate is for $\mathbf{r}_1 = \mathbf{r}_2 = \mathbf{r}$

$$S_{ww}(\mathbf{r}, \omega) = \frac{1}{(2\pi)^2} \int d^2\mathbf{k} \cdot \tilde{S}_{pp}(\mathbf{k}, \omega) |G(\mathbf{r}, \mathbf{k}, \omega)|^2 \quad (15.31)$$

The corresponding power spectral density with respect to the velocity is following the result (2.53) given by

$$S_{vv}(\mathbf{r}, \omega) = \frac{1}{(2\pi)^2} \int d^2\mathbf{k} \cdot \omega^2 \tilde{S}_{pp}(\mathbf{k}, \omega) |G(\mathbf{r}, \mathbf{k}, \omega)|^2 \quad (15.32)$$

The function $S_{vv}(\mathbf{r}, \omega)$ is the autospectrum of the velocity at the point \mathbf{r} on the plate. The time and space average of the velocity squared across the surface of the plate is thus

$$\langle |\bar{v}|^2 \rangle = \frac{1}{2\pi A} \int_A d^2\mathbf{r} \int_{-\infty}^{\infty} d\omega S_{vv}(\mathbf{r}, \omega) \quad (15.33)$$

where A is the area of the plate.

15.3 Rain on the Roof Excitation of Plates

Consider a flat and homogeneous plate subjected to random excitation, uncorrelated in space and time, referred to as “rain on the roof excitation.” The plate is oriented in the x – y -plane. The direction of the forces acting on the plate is in the z -direction of the coordinate system as shown in Fig. 15.3. The plate is rectangular and simply supported along its edges.

The equation of motion for the plate in flexure is according to Eq. (8.20).

$$\nabla^2(\nabla^2 w) + \frac{\mu}{D} \frac{\partial^2 w}{\partial t^2} = \frac{p}{D} \quad (15.34)$$

As before the mass per unit area of the plate is μ and its bending stiffness of the plate is $D = D_0(1 + i\eta)$ where η is its loss factor. The pressure on the plate or force per unit area caused by the rain on the roof excitation is defined by $p = p(x, y, t)$. The excitation $p(x, y, t)$ is homogeneous, stationary, and uncorrelated in space and time. The spatial autocorrelation function as defined in Eq. (15.7) is independent of the coordinates x and y and t and depends only on the vector (ξ_x, ξ_y) between the observation points and on the time interval τ between the observations. For the correlation function to be uncorrelated in space and time it must be on the form

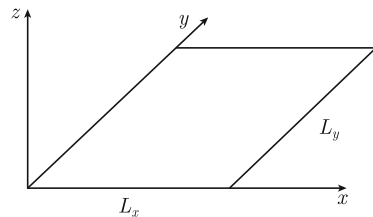
$$R_{pp}(\xi_x, \xi_y, \tau) = S_0 \cdot \delta(\xi_x) \cdot \delta(\xi_y) \cdot \delta(\tau) \quad (15.35)$$

where S_0 is a constant. The three-dimensional spectral density $\tilde{S}_{pp}(k_x, k_y, \omega)$ is obtained by inserting the definition (15.35) in Eq. (15.8). The result is

$$\tilde{S}_{pp}(k_x, k_y, \omega) = \tilde{S}_{pp}(\mathbf{k}, \omega) = S_0 \quad (15.36)$$

The cross-power spectral density between the pressure at the point $\mathbf{s}_1 = (s_{1x}, s_{1y})$ and the pressure at $\mathbf{s}_2 = (s_{2x}, s_{2y})$ where $\mathbf{s}_2 - \mathbf{s}_1 = (\xi_x, \xi_y)$ is according to Eqs. (15.25) and (15.36) given by

Fig. 15.3 A simply supported and rectangular plate



$$\begin{aligned}
S_{pp}(s_1, s_2, \omega) &= \frac{1}{(2\pi)^2} \int d^2\mathbf{k} \cdot \tilde{S}_{pp}(\mathbf{k}, \omega) \exp[i\mathbf{k}(s_2 - s_1)] \\
&= \frac{1}{(2\pi)^2} \int d^2\mathbf{k} \cdot S_0 \exp[i\mathbf{k}(s_2 - s_1)] \\
&= \frac{S_0}{(2\pi)^2} \int_{-\infty}^{\infty} dk_x \exp(ik_x \xi_x) \int_{-\infty}^{\infty} dk_y \exp(ik_y \xi_y) \quad (15.37)
\end{aligned}$$

According to Eq. (2.4) the solution to the last integral is

$$\int_{-\infty}^{\infty} dk_y \exp(ik_y \xi_y) = 2\pi \delta(\xi_y)$$

Thus, the cross-power spectral density S_{pp} of Eq. (15.37) is equal to

$$S_{pp}(s_1, s_2, \omega) = S_0 \delta(s_1 - s_2) = S_0 \delta(\xi_x) \delta(\xi_y) \quad (15.38)$$

Once the cross-power spectral density of the pressure is determined, the corresponding cross-power spectral density between the displacements at the coordinates \mathbf{r}_1 and \mathbf{r}_2 is obtained by inserting Eq. (15.36) in (15.28). Thus

$$\begin{aligned}
S_{ww}(\mathbf{r}_1, \mathbf{r}_2, \omega) &= \frac{1}{(2\pi)^2} \int d^2s_1 \int d^2s_2 H^*(\mathbf{r}_1, s_1, \omega) H(\mathbf{r}_2, s_2, \omega) \\
&\quad \times \int d^2\mathbf{k} \cdot S_0 \cdot \exp[i\mathbf{k}(s_2 - s_1)] \quad (15.39)
\end{aligned}$$

However, the last integral in the expression above is, based on Eq. (2.4), equal to

$$\int d^2\mathbf{k} \cdot S_0 \cdot \exp[i\mathbf{k}(s_2 - s_1)] = (2\pi)^2 \cdot S_0 \cdot \delta(s_1 - s_2)$$

This result inserted in the expression (15.39) gives

$$S_{ww}(\mathbf{r}_1, \mathbf{r}_2, \omega) = S_0 \int d^2s_1 H^*(\mathbf{r}_1, s_1, \omega) H(\mathbf{r}_2, s_1, \omega) \quad (15.40)$$

The corresponding cross-power spectral density between the velocities at the two points is

$$S_{vv}(\mathbf{r}_1, \mathbf{r}_2, \omega) = S_0 \int d^2s_1 \omega^2 H^*(\mathbf{r}_1, s_1, \omega) H(\mathbf{r}_2, s_1, \omega) \quad (15.41)$$

For a plate in flexure satisfying the differential equation (15.34) the response $w(\mathbf{r}, t)$ at position \mathbf{r} due to a point force $F_0 \cdot \exp(i\omega t)$ at \mathbf{s} is written as

$$w(\mathbf{r}, t) = F_0 \cdot H(\mathbf{r}, \mathbf{s}, \omega) \cdot \exp(i\omega t) \quad (15.42)$$

The frequency response function $H(\mathbf{r}, \mathbf{s}, \omega)$ is according to Eq.(8.21) the solution to

$$\nabla^2(\nabla^2 H) - \kappa^4 H = \delta(\mathbf{r} - \mathbf{s})/D \quad (15.43)$$

The wavenumber for flexural waves is κ and the bending stiffness of the plate is $D = D_0(1 + i\eta)$. The solution to the Eq.(15.43) is also equal to Green's function discussed in Sect. 8.2. The frequency response function $H(\mathbf{r}, \mathbf{s}, \omega)$ is according to Eq. (8.28) written

$$H(\mathbf{r}, \mathbf{s}, \omega) = \sum_{mn} \frac{\varphi_{mn}(\mathbf{r})\varphi_{mn}(\mathbf{s})}{N_{mn}D(\kappa_{mn}^4 - \kappa^4)} \quad (15.44)$$

The orthogonal eigenfunctions for the plate are given by φ_{mn} and the corresponding eigenvalues by κ_{mn} . The norm N_{mn} of the eigenvector φ_{mn} is $N_{mn} = \langle \varphi_{mn} | \varphi_{mn} \rangle$. For a simply supported rectangular and homogeneous plate oriented in a coordinate system as shown in Fig. 15.3 the eigenfunctions, norm, and eigenvalue are

$$\begin{aligned} \varphi_{mn}(x, y) &= \sin\left(\frac{m\pi x}{L_x}\right) \sin\left(\frac{n\pi y}{L_y}\right); N_{mn} = L_x L_y / 4; \\ \kappa_{mn}^2 &= \left(\frac{m\pi}{L_x}\right)^2 + \left(\frac{n\pi}{L_y}\right)^2 \end{aligned} \quad (15.45)$$

By writing $\kappa^4 = \mu\omega^2/D$ and $\kappa_{mn}^4 = \mu\omega_{mn}^2/D_0$ as in Eq. (8.32) the frequency response function is

$$\begin{aligned} H(\mathbf{r}_1, \mathbf{s}_1, \omega) &= \sum_{mn} W_{mn} \varphi_{mn}(\mathbf{r}_1) \varphi_{mn}(\mathbf{s}_1); \\ W_{mn} &= \frac{4}{L_x L_y \mu [\omega_{mn}^2 (1 + i\eta) - \omega^2]} \end{aligned} \quad (15.46)$$

The time average of the kinetic energy \mathcal{U} of the plate is

$$\bar{\mathcal{U}} = \int_A d^2\mathbf{r} \mu |\bar{v}(\mathbf{r}, t)|^2 / 2 = \iint_A dx dy \mu |\bar{v}(x, y, t)|^2 / 2 \quad (15.47)$$

where A is the area of the plate. The time average of the velocity squared is

$$|\bar{v}(\mathbf{r})|^2 = \frac{1}{2\pi} \int_{-\infty}^{\infty} d\omega \cdot S_{vv}(\mathbf{r}, \mathbf{r}, \omega) \quad (15.48)$$

Considering the orthogonality of the eigenfunctions, Eqs. (15.41), (15.44) through (15.48) give the autospectrum of the velocity at the position \mathbf{r} as

$$\begin{aligned}
 S_{vv}(\mathbf{r}, \mathbf{r}, \omega) &= \omega^2 S_0 \int d^2s \left[\sum_{mn} W_{mn}^* \varphi_{mn}(\mathbf{r}) \varphi_{mn}(s) \right] \left[\sum_{mn} W_{mn} \varphi_{mn}(\mathbf{r}) \varphi_{mn}(s) \right] \\
 &= \frac{\omega^2 S_0 L_x L_y}{4} \sum_{mn} |W_{mn}|^2 \varphi_{mn}^2(\mathbf{r})
 \end{aligned}$$

The time average of the kinetic energy is from Eqs. (15.47) and (15.48) obtained as

$$\begin{aligned}
 \bar{\mathcal{V}} &= \frac{S_0}{4\pi\mu} \sum_{mn} \int_{-\infty}^{\infty} \frac{d\omega \cdot \omega^2}{(\omega_{mn}^2 - \omega^2)^2 + (\eta\omega_{mn}^2)^2} = \sum_{mn} \frac{S_0}{4\mu\omega_{mn}\eta} = \sum_{mn} \bar{\mathcal{U}}_{mn} \\
 \bar{\mathcal{U}}_{mn} &= \frac{S_0}{4\mu\omega_{mn}\eta}
 \end{aligned} \tag{15.49}$$

Compare also Sect. 2.7. Equation (15.49) gives the kinetic energy of a plate subjected to random excitation, uncorrelated in space and time, i.e., for rain on the roof excitation. For viscous losses, the product $\omega_{mn}\eta$ is constant which means that the kinetic energy \mathcal{U}_{mn} for each mode is also constant and thus independent of frequency. For white noise excitation, the potential energy of a linear system is equal to its kinetic energy as discussed in Sect. 2.7. The time average of the total energy per mode $\bar{\mathcal{E}}_{mn}$ is thus also constant per mode for rain on the roof excitation of a plate having viscous losses. Consequently,

$$\bar{\mathcal{E}}_{mn} = \frac{S_0}{2\mu\omega_{mn}\eta} \tag{15.50}$$

In Sect. 8.2 the response of a plate excited by randomly distributed forces, each having a constant one-sided power spectral density G_{FF} , was given in Eq. (8.35). The corresponding modal energy was given in Eq. (8.39). The parameter S_0 in Eq. (15.50) is equal to the two-sided power spectral density of the pressure on the plate. Thus $2S_0 = G_{FF}/(L_x L_y)$. This expression in combination with Eq. (15.50) gives the result (8.39).

The results (15.49) and (15.50) hold for a flat plate of any shape with boundary conditions which do not allow energy flow across the edges of the plate. The vibration of such plates can be described by means of orthogonal eigenfunctions as discussed in Chap. 8. The edges of the plate can, for example, be simply supported, clamped, or free or satisfy any combination of these conditions. For such plates having viscous losses and being exposed to rain on the roof excitation the energy per mode is the same. This is referred to as equipartition of energy. The total energy within a frequency band Δf of a plate exposed to rain on the roof excitation is following the discussion in Sects. 7.4 and 8.6 given by

$$\bar{\mathcal{E}}_{\Delta f} = \mathcal{N}_f \cdot \Delta f \cdot \frac{S_0}{4\pi\mu f_{mn}\eta} \tag{15.51}$$

where \mathcal{N}_f is the modal density of the plate as defined in Eq. (8.18). In the high frequency region, the modal density tends to be independent of the boundary conditions of the plate. The modal density is approximately given by Eq. (8.18) as $\mathcal{N}_f = (L_x L_y / 2) \sqrt{\mu / D_0}$. Thus, the total energy of a flat plate of any shape having viscous losses and boundary conditions not allowing an energy flow across the boundaries can, within a frequency band Δf , in the high frequency range be calculated from Eq. (15.51) for sufficiently wide frequency bands assuming rain on the roof excitation. Compare Sect. 6.4. In practice S_0 in Eq. (15.51) can be assumed constant. However, in theory the energy would approach infinity as the frequency interval is increasing.

The time average of the input power Π_{mn} to mode (m, n) can be shown to be

$$\bar{\Pi}_{mn} = \omega \eta \bar{E}_{mn} = S_0 / (2\mu)$$

The details are for Problem 15.5.

15.4 Turbulent Boundary Layers

A turbulent boundary layer—TBL is developed in a fluid close to a structure at sufficiently high flow velocities. For an in-flight aircraft, the TBL, when developed, excites the fuselage and its plate structures. The structures enclosing the aircraft cabin radiates noise into the cabin. The acoustic power radiated due to this effect is proportional to the kinetic energy induced in the fuselage structure by the TBL. It is therefore essential to determine the relative importance of the TBL effect as compared to the acoustic energy induced in the fuselage structure by other sources like engines, propellers, ventilation systems, etc. A model describing the effect of a TBL or rather the acoustic energy induced in a fuselage as function of flight velocity, plate geometry, etc., could possibly be used to minimize the effect of the TBL by changing the design of the fuselage (Fig. 15.4).

The first parameter that determines the nature of turbulence in a boundary layer is the Reynolds number \mathcal{R} defined as $\mathcal{R} = U_\infty L / \nu_f$ where U_∞ is the velocity of the fluid well away from a structure, L is the distance of the origin of the boundary layer and ν_f the kinematic viscosity of the fluid in m^2/s . The viscosity of air depends on

Fig. 15.4 Flow across a plate in x - y -plane resulting in a turbulent boundary layer. The velocity profile of the flow is shown as function of the distance z from plate

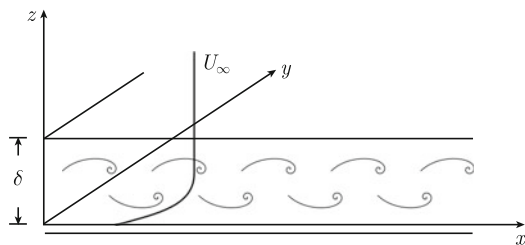


Table 15.1 Atmospheric data as function of altitude H over sea level

H (m)	T (°K)	P_{static} (atm)	ρ_0 (kg/m ³)	c (m/s)	ν_f (10 ⁻⁴ m ² /s)
0	288	1	1.25	340	0.146
1000	282	0.89	1.13	336	0.158
2000	275	0.78	1.03	333	0.171
3000	269	0.69	0.93	329	0.186
4000	262	0.61	0.83	325	0.203
5000	256	0.53	0.75	321	0.221
6000	249	0.47	0.67	316	0.242
7000	243	0.40	0.60	312	0.265
8000	236	0.35	0.53	308	0.291
9000	230	0.30	0.48	304	0.320
10000	223	0.26	0.42	299	0.353
12000	217	0.19	0.32	295	0.456
14000	217	0.14	0.23	295	0.626

1 atm = 1.01325×10^5 Pa at 15 °C

the ambient pressure and the temperature. Some values are listed in Table 15.1 for pressures and temperatures typical for some flight conditions. The tabled values are according to US standards.

As discussed by Blake [162] turbulence can build up spotwise for $\mathcal{R} \approx 2 \times 10^6$. For $\mathcal{R} \approx 10^7$ the turbulence is fully developed. The thickness of the boundary layer in a fluid having a turbulent flow close to a structure is given by δ and is defined as the distance from the wall at which the mean flow velocity is $0.99 \cdot U_\infty$ where U_∞ is the free velocity well away from the wall. The boundary layer thickness is according to Ref. [229] given as

$$\delta = 0.38 \cdot L \cdot \mathcal{R}^{-1/5} = 0.38 \cdot L \cdot \left(\frac{\rho U_\infty L}{\nu_f} \right)^{-1/5} \quad (15.52)$$

Within the boundary layer, eddies are formed due to shear effects in the fluid caused by the velocity profile. The principal boundary layer eddies are moving across the wall at the convection velocity U_c . Both experimental and numerical simulations indicate, according to Howe Ref. [230], that $0.5 \cdot U_\infty \leq U_c \leq 0.7 \cdot U_\infty$ with only a weak dependence on frequency.

The pressure p caused by a turbulent boundary layer at a point on a plate, oriented in the x - y -plane, not only depend on time t but also on the coordinates x and y of the observation point. The autocorrelation function of the pressure $p(x, y, t)$ on the plate is defined as the ensemble average of the pressure p at the coordinates (x, y, t) and the pressure at the coordinates $(x + \xi_x, y + \xi_y, t + \tau)$. For a pressure p , stationary in two-dimensional space and time, the ensemble average depends only on the separation ξ_x and ξ_y in space and τ in time as discussed by, for example, Newland Ref. [11]. The cross-power correlation function R_{pp} is following Eq. (15.53) defined as

$$R_{pp}(\xi_x, \xi_y, \tau) = E[p(x, y, t)p(x + \xi_x, y + \xi_y, t + \tau)] \quad (15.53)$$

The function $R_{pp}(\xi_x, \xi_y, \tau)$ is real. The cross-power spectral density between the two signals observed at two positions separated by the vector (ξ_x, ξ_y) is according to Eq. (15.9) defined by $S_{pp}(\xi_x, \xi_y, \omega)$ as

$$S_{pp}(\xi_x, \xi_y, \omega) = \int_{-\infty}^{\infty} d\tau \cdot R_{pp}(\xi_x, \xi_y, \tau) \cdot \exp(-i\omega\tau) \quad (15.54)$$

where ω is the angular frequency.

The resulting power spectral density of the velocity of the plate is determined by the function S_{pp} as well as the material and geometrical parameters of the plate element. Finally, the acoustic power radiated by the structure depends on the velocity of the structure as well as on the geometrical and material parameters of the structure.

There are a number of models describing the cross-power spectral density induced by a flow or turbulent boundary layer across a structure. Some of the most widely used models are attributed to Corcos [231, 232], Efimtsov [233], Chase [234, 235], Smolyakov and Tkachenko [236], and Ffowcs Williams [237]. Graham in Ref. [238] has discussed the merit of these various models. It is concluded in Ref. [238] that the Corcos model can give satisfactory results when used to predict the response of plate structures excited by turbulent boundary layers. The Efimtsov extension can underestimate the plate response. The shortcomings of the Corcos model are most evident in the high-frequency region. This is naturally a problem when predicting the absolute velocity level of a structure. This problem is much less important when the relative response of different structures are compared assuming all the structures being excited by the same pressure field.

15.5 TBL Models

The model proposed by Corcos has during the last few decades been widely used for many different types of problems. The model is applicable in the immediate neighborhood of the so-called convective ridge, Refs. [230, 231], or rather when $\omega\delta/U_\infty > 1$. In this expression δ is the thickness of the boundary layer defined in Eq. (15.5) and U_∞ the velocity of the flow well away from the structure. Compare Fig. 15.5 and the discussion in Sect. 15.6. In Fig. 15.5, k is the wavenumber in the fluid and U_c is the convection velocity and according to Howe [230], $0.5 \cdot U_\infty \leq U_c \leq 0.8 \cdot U_\infty$. The strongest pressure fluctuations exciting the wall occur within the convective ridge as indicated in Fig. 15.5.

As a starting point for the discussion, assume that the plate exposed to the turbulent flow is flat and rectangular. The results derived can thereafter be modified to include a curvature of the plate or for that matter also a doubly curvature. Thus, for simplicity, assume that the plate exposed to the turbulent boundary layer is flat, homogeneous, rectangular, and oriented in the x - y -plane of a Cartesian coordinate

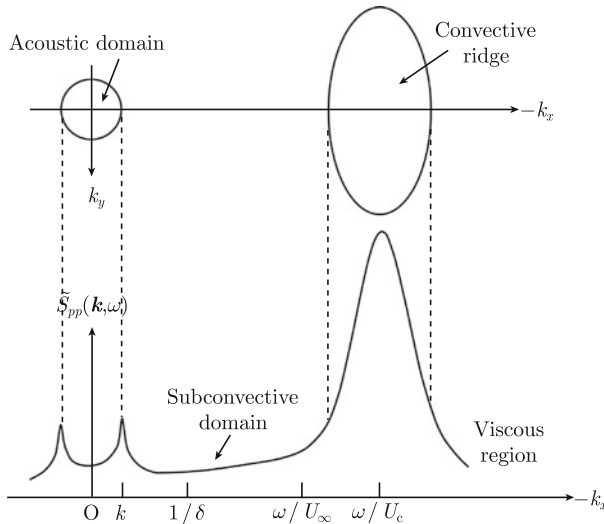


Fig. 15.5 Wall pressure spectrum induced by TBL. Note $-k_x$ on horizontal axis

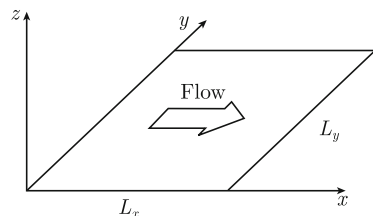
system as shown in Fig. 15.6. The coordinates for the corners of the rectangular plate are $(0, 0)$, (L_x, L_y) , $(0, L_y)$ and $(L_x, 0)$, where L_x is the width and L_y is the length of the plate. A turbulent flow across the plate in the direction of the x -axis is the seat of local pressure fluctuations. It is assumed that the field is statistically stationary and homogeneous.

Corcos assumes that the cross-power spectral density, defined in Eq. (15.22), between the pressures induced by TBL at two different positions separated by the vector (ξ_x, ξ_y) can be expressed as

$$S_{pp}(\xi_x, \xi_y, \omega) = \Phi_{pp}(\omega) \exp[-\gamma_1 |\omega \xi_x / U_c|] \exp[-\gamma_3 |\omega \xi_y / U_c|] \exp[-i\omega \xi_x / U_c] \tag{15.55}$$

The point autospectrum of the pressure is $\Phi_{pp}(\omega)$. The quantity $\omega \xi_x / U_c$ in the last part of Eq. (15.55) is equal to the phase shift between two signals the distance ξ_x apart along the x -axis in the coordinate system is shown in Fig. 15.6. The average convection or translation velocity is U_c . The sign in the last exponent depends on the definition of the Fourier transforms. This sign convention can be somewhat confusing

Fig. 15.6 Rectangular plate excited by a TBL. Flow in x -direction



when comparing results from various texts. The parameters γ_1 and γ_3 are determined from experimental data. Initially, Corcos assumed the parameters γ_1 and γ_3 to be constant. The magnitude of the dimensionless parameters has been estimated in a number of papers. Some examples are given in Table 15.2.

The parameters determined by Finnveden are found to give good results as compared to some in-flight measurements as discussed in Sect. 15.9.

The Efimtsov model assumes, as in the Corcos model, that the lateral and the longitudinal effects of the TBL can be separated. However, in the Efimtsov model the dependence of spatial correction on boundary layer thickness, δ , as well as spatial separation is taken into account. The Efimtsov model gives the cross-power spectral density of the pressure at two different positions separated by the vector (ξ_x, ξ_y) as

$$S_{pp}(\xi_x, \xi_y, \omega) = \Phi_{pp}(\omega) \exp[-|\xi_x/L'_x|] \exp[-|\xi_y/L'_y|] \exp[-i\omega\xi_x/U_c] \tag{15.56}$$

where L'_x and L'_y are the so-called correlation lengths in the x and y directions of the panel. Efimtsov, based on in-flight measurements, has estimated these correlation lengths. The parameters are in [233] given as

$$\begin{aligned} L'_x &= \delta \left[\left(\frac{0.1Sh}{U_c/U_\tau} \right)^2 + \frac{5300}{Sh^2 + 2235} \right]^{-1/2} ; \\ L'_y &= \delta \left[\left(\frac{0.77Sh}{U_c/U_\tau} \right)^2 + \frac{300300}{Sh^2 + 1648} \right]^{-1/2} \end{aligned} \tag{15.57}$$

where Sh is the Strouhal number and equal to $Sh = \omega\delta/U_\tau$ and U_τ the friction velocity which varies with the Reynolds number but is typically of the order $0.03U_\infty$ to $0.04U_\infty$. At high frequencies these expressions correspond to a Corcos model with $\gamma_1 = 0.1$ and $\gamma_3 = 0.77$. Since Efimtsov's results are derived from an extensive series of measurements on aircraft, over a Mach number range of 0.41–2.1, they have been taken in preference to Blake's recommendations [162] for the predictions presented in Sect. 15.8.

Table 15.2 Corcos parameters

	γ_1	γ_3
Willmarth [239]	0.12	0.70
Efimtsov [233]	0.10	0.77
Robert [240]	0.13	0.83
Blake [162]	0.12	0.70
Finnveden [241]	0.116	0.70

By comparing the Eqs. (15.55) and (15.56) it follows that the Corcos constants when extended as suggested by Efimtsov can be written as

$$\gamma_1 = \frac{U_c}{\omega L'_x} \text{ and } \gamma_3 = \frac{U_c}{\omega L'_y} \quad (15.58)$$

Chase's model is believed to describe the low-wavenumber domain better than Corcos's model. Chase's original model gave a reasonable, but not quite satisfactory, description of the measured cross-correction. Improvements of the model, or rather a modified Chase model, has been proposed by Finnveden [241]. Accordingly, the power spectral density of the TBL-induced pressure is written as

$$S_{pp}(\xi_x, \xi_y, \omega) = \Phi_{pp}(\omega)[A_M(\omega)f_M(\xi_x, \xi_y, \omega)\exp(-z_M - i\omega\xi_x/U_c) + A_T(\omega)f_T(\xi_x, \xi_y, \omega)\exp(-z_T - i\omega\xi_x/U_c)] \quad (15.59)$$

where

$$f_M(\xi_x, \xi_y, \omega) = 1 + z_M + \alpha_M^2 \mu_M^2 (1 - z_{M1}^2/z_M) + 2i\alpha_M \mu_M z_{M1},$$

$$f_T(\xi_x, \xi_y, \omega) = 1 + z_T + \alpha_T^2 \gamma_T^2 (1 - z_{T2}^2/z_T) + \alpha_T^2 \mu_T^2 (1 - z_{T1}^2/z_T) + 2i\alpha_T \mu_T z_{T1},$$

$$z_M = \sqrt{z_{M1}^2 + z_{M2}^2}, \quad z_T = \sqrt{z_{T1}^2 + z_{T2}^2}, \quad z_{M1} = \alpha_M \mu_M \omega \xi_x / U_c, \\ z_{T1} = \alpha_T \mu_T \omega \xi_x / U_c,$$

$$z_{M2} = \alpha_M \gamma_M \omega \xi_y / U_c, \quad z_{T2} = \alpha_T \gamma_T \omega \xi_x / U_c,$$

$$\alpha_M = \sqrt{1 + (b_M \omega \delta / U_c)^{-2}}, \quad \alpha_T = \sqrt{1 + (b_T \omega \delta / U_c)^{-2}}. \quad (15.60)$$

The relative magnitude $A_{M,T}$ is as proposed by Finnveden given as

$$A_M(\omega, U_c) = (1 - r)/(1 + \alpha_M^2 \mu_M^2), \quad A_T(\omega, U_c) = r/(1 + \alpha_T^2 \gamma_T^2 + \alpha_T^2 \mu_T^2) \quad (15.61)$$

with

$$r(\omega, U_c) = a_r - b_r \omega / \omega_0, \quad \omega_0 = 10^5, \quad 0 \leq r(\omega, U_c) \leq 1 \quad (15.62)$$

The modified Chase model is defined by Eqs. (15.60) through (15.62). For the Corcos and Efimtsov models, the lateral and longitudinal effects of the TBL can be separated. This assumption greatly simplifies numerical calculations as demonstrated in Sect. 15.6. This characterization does not apply to the Chase model.

Predicted results based on the three models are compared to in-flight measurements in Sect. 15.8.

Robert [240] estimated the autospectrum $\Phi_{pp}(\omega)$ given in Eq. (15.55) based on a number of measurements. The Robert model is given as

$$\frac{\Phi_{pp}(\omega)U_\infty}{q^2\delta^*} = \begin{cases} 2.14 \times 10^{-5} & \omega\delta^*/U_\infty \leq 0.25 \\ 7.56 \times 10^{-6} \times (\omega\delta^*/U_\infty)^{-3/4} & 0.25 < \omega\delta^*/U_\infty \leq 3.5 \\ 1.27 \times 10^{-4} \times (\omega\delta^*/U_\infty)^{-3} & 3.5 < \omega\delta^*/U_\infty \end{cases} \quad (15.63)$$

where the boundary layer displacement thickness is denoted as δ^* . This quantity is defined as

$$\delta^* = \int_0^\infty [1 - v(z)/U_\infty] dz$$

where $v(z)$ is the flow velocity. For practical purposes, it may be assumed that $\delta^* = \delta/8$. The dynamic pressure is given by $q = \rho_0 U_\infty^2/2$ with ρ_0 the density of the fluid. Compare Eq. (15.84).

15.6 Plate Response Due to TBL Excitation

The basic theory on the TBL excitation of plates is discussed in for example Refs. [162, 230, 242]. The response of plates excited TBL has, for example, also been discussed in Refs. [243–247] in addition to the Refs. [231–241]. As a starting point for the prediction of the response of a plate excited by TBL, consider a thin homogeneous, flat and rectangular plate that is simply supported along its edges. The plate is oriented in x - y -plane as shown in Fig. 15.6. The plate is excited by a TBL flow across the plate in the direction of the x -axis. Corcos and Efimtsov assume that the cross-power spectral density $S_{pp}(\xi_x, \xi_y, \omega)$ can be expressed in separable form as given by Eqs. (15.55) and (15.56), respectively, where $\Phi_{pp}(\omega)$ is the point autospectrum. The Robert model of the autospectrum is given by Eq. (15.63).

The velocity spectrum of a flat rectangular plate can now be determined as discussed in Sect. 15.2. The starting point is to determine the three-dimensional spectral density $\tilde{S}_{pp}(\mathbf{k}, \omega)$ of the pressure on the plate. Following the definition (15.9) $\tilde{S}_{pp}(\mathbf{k}, \omega)$ is given as

$$\begin{aligned} \tilde{S}_{pp}(k_x, k_y, \omega) &= \int_{-\infty}^{\infty} d\xi_x \int_{-\infty}^{\infty} d\xi_y \int_{-\infty}^{\infty} d\tau \cdot R_{pp}(\xi_x, \xi_y, \tau) \\ &\quad \times \exp[-i(k_x\xi_x + k_y\xi_y + \omega\tau)] \\ &= \int_{-\infty}^{\infty} d\xi_x \int_{-\infty}^{\infty} d\xi_y S_{pp}(\xi_x, \xi_y, \omega) \cdot \exp[-i(k_x\xi_x + k_y\xi_y)] \end{aligned}$$

From these expressions and since R_{pp} is real it follows that $\tilde{S}_{pp}(\mathbf{k}, \omega) = \tilde{S}_{pp}(-\mathbf{k}, -\omega)$. The definition above of $\tilde{S}_{pp}(\mathbf{k}, \omega)$ in combination with the expression (15.55) yield

$$\tilde{S}_{pp}(k_x, k_y, \omega) = 4 \cdot \frac{\Phi_{pp}(\omega) \cdot \frac{\omega\gamma_1}{U_c} \cdot \frac{\omega\gamma_3}{U_c}}{\left[\left(\frac{\omega\gamma_1}{U_c} \right)^2 + \left(\frac{\omega}{U_c} + k_x \right)^2 \right] \cdot \left[\left(\frac{\omega\gamma_3}{U_c} \right)^2 + k_y^2 \right]} \quad (15.64)$$

The power spectral density of the velocity is given in Eq. (15.32). The time and space average of the velocity squared of the panel is given in Eq. (15.33). The Eqs. (15.32) and (15.33) give

$$\langle |\bar{v}|^2 \rangle = \frac{1}{A(2\pi)^3} \int d^2\mathbf{r} \int d\omega \int d^2\mathbf{k} \cdot \omega^2 \tilde{S}_{pp}(\mathbf{k}, \omega) |G(\mathbf{r}, \mathbf{k}, \omega)|^2 \quad (15.65)$$

where A is the area of the plate. The function $G(\mathbf{r}, \mathbf{k}, \omega)$ is defined in Eq. (15.29) and following the result (15.46) equal to

$$\begin{aligned} G(\mathbf{r}, \mathbf{k}, \omega) &= \sum_{mn} \int d^2\mathbf{s} \cdot \exp(-i\mathbf{k}\mathbf{s}) \cdot W_{mn} \varphi_{mn}(\mathbf{r}) \varphi_{mn}(\mathbf{s}) \\ &= \sum_{mn} W_{mn} I_{mn}(\mathbf{k}) \varphi_{mn}(\mathbf{r}) \\ I_{mn}(\mathbf{k}) &= \int d^2\mathbf{s} \cdot \exp(-i\mathbf{k}\mathbf{s}) \cdot \varphi_{mn}(\mathbf{s}) \end{aligned} \quad (15.66)$$

For a simply supported plate shown in Fig. 15.6 the eigenfunctions are defined in Eq. (15.45). Consequently,

$$\begin{aligned} I_{mn} &= \int_0^{L_x} d\xi_x \cdot \sin\left(\frac{m\pi\xi_x}{L_x}\right) \exp(-ik_x\xi_x) \int_0^{L_y} d\xi_y \cdot \sin\left(\frac{n\pi\xi_y}{L_y}\right) \exp(-ik_y\xi_y) \\ &= \frac{(m\pi/L_x)(n\pi/L_y)[1 - \cos(m\pi) \exp(-ik_x L_x)] \cdot [1 - \cos(n\pi) \exp(-ik_y L_y)]}{[k_x^2 - (m\pi/L_x)^2] \cdot [k_y^2 - (n\pi/L_y)^2]} \end{aligned} \quad (15.67)$$

For a homogeneous plate, the time and space average of the velocity squared is from Eqs. (15.65) and (15.66) written as

$$\langle |\bar{v}|^2 \rangle = \frac{1}{(2\pi)^3 A} \int d\omega \cdot \omega^2 \int d^2\mathbf{k} \cdot \tilde{S}_{pp}(\mathbf{k}, \omega) \int d^2\mathbf{r} \left| \sum_{mn} W_{mn} \varphi_{mn}(\mathbf{r}) I_{mn} \right|^2$$

Considering the orthogonality of the eigenfunctions φ_{mn} this expression is reduced to

$$\langle |\bar{v}|^2 \rangle = \frac{1}{4(2\pi)^3} \sum_{mn} \int d\omega \cdot \omega^2 |W_{mn}|^2 \int d^2\mathbf{k} \cdot \tilde{S}_{pp}(\mathbf{k}, \omega) |I_{mn}|^2 \quad (15.68)$$

The main contributions to the last integral are obtained as $\tilde{S}_{pp}(\mathbf{k}, \omega)$ and $|I_{mn}|^2$ have maxima. Thus according to Eq. (15.64) $\tilde{S}_{pp}(\mathbf{k}, \omega)$ has a maximum for $k_x = -\omega/U_c$

and $k_y = 0$ within the so-called convective ridge. Since $\gamma_3/\gamma_1 \approx 6$ the function $\tilde{S}_{pp}(\mathbf{k}, \omega)$ at constant ω/U_c appears elliptical as shown in Fig. 15.5. The function $|I_{mn}|^2$ has according to Eq. (15.67) maxima for $k_x = m\pi/L_x$ and $k_y = n\pi/L_y$ or whenever $k_x^2 + k_y^2 = \kappa^2$ where κ is the wavenumber for flexural waves propagating on the plate. The wall pressure spectrum on a plate is shown in Fig. 15.5 at low Mach number and for $\omega\delta/U_\infty \gg 1$.

For the Corcos and Efimtsov models, the expression $\tilde{S}_{pp}(\mathbf{k}, \omega)|I_{mn}|^2$ can be written in separable form. The last double integral of Eq. (15.68) can therefore be defined as a product between two integrals. Thus

$$\iint d^2\mathbf{k} \cdot \tilde{S}_{pp}(\mathbf{k}, \omega) |I_{mn}|^2 = 4 \left[\frac{\omega\gamma_1}{U_c} \right] \cdot \left[\frac{\omega\gamma_3}{U_c} \right] \cdot \Phi_{pp}(\omega) \cdot \Lambda_m \cdot \Gamma_n \quad (15.69)$$

The expressions Λ_m and Γ_n are in integral form given as

$$\Lambda_m = 2 \left[\frac{m\pi}{L_x} \right]^2 \int_{-\infty}^{\infty} dk_x \cdot \frac{[1 - \cos(m\pi) \cos(k_x L_x)]}{\left[k_x^2 - \left(\frac{m\pi}{L_x} \right)^2 \right]^2 \left[\left(k_x + \frac{\omega}{U_c} \right)^2 + \left(\frac{\omega\gamma_1}{U_c} \right)^2 \right]} \quad (15.70)$$

$$\Gamma_n = 2 \left[\frac{n\pi}{L_y} \right]^2 \int_{-\infty}^{\infty} dk_y \cdot \frac{[1 - \cos(n\pi) \cos(k_y L_y)]}{\left[k_y^2 - \left(\frac{n\pi}{L_y} \right)^2 \right]^2 \left[k_y^2 + \left(\frac{\omega\gamma_3}{U_c} \right)^2 \right]} \quad (15.71)$$

The solutions to integrals (15.70) and (15.71) are as demonstrated in Problem 15.7 given by

$$\begin{aligned} \Lambda_m = & 2\pi \left(\frac{m\pi}{L_x} \right)^2 \left[\frac{L_x}{4(m\pi/L_x)^2 [(m\pi/L_x + \omega/U_c)^2 + (\omega\gamma_1/U_c)^2]} \right] \\ & + 2\pi \left(\frac{m\pi}{L_x} \right)^2 \left[\frac{L_x}{4(m\pi/L_x)^2 [(m\pi/L_x - \omega/U_c)^2 + (\omega\gamma_1/U_c)^2]} \right] \\ & + 2\pi \left(\frac{m\pi}{L_x} \right)^2 \left[\frac{1 - \cos m\pi \exp(-iL_x\omega/U_c - \omega\gamma_1 L_x/U_c)}{(2\omega\gamma_1/U_c)[(\omega/U_c - i\omega\gamma_1/U_c)^2 - (m\pi/L_x)^2]} \right] \\ & + 2\pi \left(\frac{m\pi}{L_x} \right)^2 \left[\frac{1 - \cos m\pi \exp(i\omega L_x/U_c - \omega\gamma_1 L_x/U_c)}{(2\omega\gamma_1/U_c)[(\omega/U_c + i\omega\gamma_1/U_c)^2 - (m\pi/L_x)^2]} \right] \end{aligned} \quad (15.72)$$

$$\begin{aligned} \Gamma_n = & 2\pi \left(\frac{n\pi}{L_y} \right)^2 \left[\frac{L_y}{2(n\pi/L_y)^2 [(n\pi/L_y)^2 + (\omega\gamma_3/U_c)^2]} \right] \\ & + 2\pi \left(\frac{n\pi}{L_y} \right)^2 \left[\frac{1 - \cos n\pi \exp(-\omega\gamma_3 L_y)}{(\omega\gamma_3/U_c)[(\omega\gamma_3/U_c)^2 + (n\pi/L_y)^2]} \right] \end{aligned} \quad (15.73)$$

It has been shown, for example, by Totaro and Guyader [246] that the expressions Λ_m and Γ_n can be simplified when the frequency f satisfies the inequality $f > U_c/L$ where L is the maximum of L_x and L_y . In this frequency range, the last two expressions inside the bracket of Eq. (15.72) and the last expression inside the bracket of Eq. (15.73) can be neglected.

The space and time average of the velocity squared can following Eq. (15.41) be written

$$\langle |\bar{v}|^2 \rangle = \frac{1}{2\pi} \int d\omega \langle S_{vv}(\mathbf{r}, \omega) \rangle = \frac{1}{2\pi} \int d\omega \frac{1}{A} \int d^2\mathbf{r} S_{vv}(\mathbf{r}, \omega) \quad (15.74)$$

The average across the plate of the power spectral density or autospectrum $\langle S_{vv}(\mathbf{r}, \omega) \rangle = S_{vv}(\omega)$ of the plate velocity is now following the results (15.68) through (15.73) written as

$$\begin{aligned} S_{vv}(\omega) &= \langle S_{vv}(\mathbf{r}, \omega) \rangle = \frac{1}{L_x L_y} \int d^2\mathbf{r} S_{vv}(\mathbf{r}, \omega) \\ &= \sum_{mn} \frac{1}{(2\pi)^2} \cdot \Phi_{pp}(\omega) \cdot \omega^2 |W_{mn}|^2 \cdot \frac{\omega\gamma_1}{U_c} \cdot \frac{\omega\gamma_3}{U_c} \cdot \Lambda_m(\omega) \cdot \Gamma_n(\omega) \end{aligned} \quad (15.75)$$

Once the parameters γ_1 and γ_3 are known, the power spectral density of the velocity can be calculated for a flat plate. However, the result (15.75) is only valid for the Corcos and Efimtsov models. The basis for the result is that the TBL model can be written in separable form. This is not the case for the Chase model.

In the frequency range above the first natural frequency of the plate, i.e., for $f > f_{11}$ the expression $|W_{mn}|^2$ is a rapidly varying function of frequency. Whenever the velocity level of or input power to a plate is to be estimated within a frequency band the function $|W_{mn}|^2$ can be replaced by its frequency average $|\bar{W}_{mn}|^2$ as suggested by Guyader et al. [246]. A similar approach was discussed in Chaps. 2 and 7. Thus, from Eq. (15.46)

$$\begin{aligned} |\bar{W}_{mn}|^2 &= \frac{1}{\Delta\omega} \int_{\omega_1}^{\omega_2} d\omega |W_{mn}|^2 \\ &= \frac{1}{\Delta\omega} \int_{\omega_1}^{\omega_2} d\omega \frac{16}{(L_x L_y \mu)^2 [(\omega_{mn}^2 - \omega^2)^2 + (\eta\omega_{mn}^2)^2]} \end{aligned} \quad (15.76)$$

where $\Delta\omega$ is the spacing of the angular frequency between two natural angular frequency of the plate. The integration limits are $\omega_1 = \omega_{mn} - \Delta\omega/2$ and $\omega_2 = \omega_{mn} + \Delta\omega/2$. Equation (8.19) gives $\Delta\omega$ as

$$\Delta\omega = \frac{4\pi}{L_x L_y} \sqrt{\frac{D_0}{\mu}}$$

For a lightly damped system, $\eta \ll 1$, the integration limits can be extended since the main contribution to the integral is in the close vicinity to ω_{mn} . Thus the limits ω_1 and ω_2 are set to equal zero and infinity respectively. Similar problems were discussed in Sects. 6.4, 7.4 and 8.5. From Eq. (2.61), it follows that the integral (15.76) is reduced to

$$|\bar{W}_{mn}|^2 = \frac{2}{\eta\mu^2 L_x L_y \omega_{mn}^3} \sqrt{\frac{\mu}{D_0}} \tag{15.77}$$

Considering this result the approximate auto-power spectral density of Eq. (15.75) is written

$$\bar{S}_{vv}(\omega) \approx \frac{1}{\Delta N} \sum_{mn} \frac{2}{\mu^2 \omega \eta L_x L_y} \cdot \sqrt{\frac{\mu}{D_0}} \cdot \Phi_{pp}(\omega) \cdot \frac{\omega \gamma_1}{U_c} \cdot \frac{\omega \gamma_3}{U_c} \cdot \Lambda_m(\omega) \cdot \Gamma_n(\omega) \tag{15.78}$$

For any ω the summation is made for all m and n satisfying the inequality

$$(\omega - \Delta\omega/2) \leq \sqrt{\frac{D_0}{\mu}} \left[\left(\frac{m\pi}{L_x} \right)^2 + \left(\frac{n\pi}{L_y} \right)^2 \right] \leq (\omega + \Delta\omega/2)$$

The number of modes ΔN within the band is obtained from Eq. (8.18) as

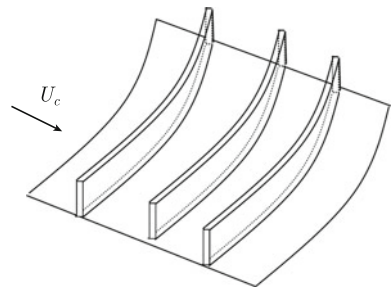
$$\Delta N = N_f \Delta\omega / (2\pi) = \frac{L_x L_y}{4\pi} \sqrt{\frac{\mu}{D_0}} \cdot \Delta\omega$$

The results (15.77) and (15.78) are only valid for flat plates which are not exposed to any in-plane tension.

For a curved plate shown in Fig. 15.7 the natural angular frequencies ω_{mn} are, according to Eq. (14.88), given by the expression

$$\omega_{mn}^2 = \frac{D_0}{\mu} \cdot \left\{ \left[\left(\frac{m\pi}{L_x} \right)^2 + \left(\frac{n\pi}{L_y} \right)^2 \right]^2 + \frac{12}{(hR_y)^2 [1 + (nL_x/mL_y)^2]^2} \right\} \tag{15.79}$$

Fig. 15.7 Curved plate exposed to TBL excitation. The flow U_c is in the x -direction, the frame distance is L_x , and the height of the plate along the frames is L_y



The curvature of the plate is along the y -axis. The dimensions of the plate are L_x and L_y and its thickness is h . The bending stiffness of the structure is D . The corresponding expression for a doubly curved panel is

$$\omega_{mn}^2 = \frac{D_0}{\mu} \cdot \left\{ \left[\left(\frac{m\pi}{L_x} \right)^2 + \left(\frac{n\pi}{L_y} \right)^2 \right]^2 + \frac{12}{(h)^2} \frac{\left[\frac{1}{R_y} \left(\frac{m\pi}{L_x} \right)^2 + \frac{1}{R_x} \left(\frac{n\pi}{L_y} \right)^2 \right]^2}{\left[\left(\frac{m\pi}{L_x} \right)^2 + \left(\frac{n\pi}{L_y} \right)^2 \right]^2} \right\}$$

For an aircraft in-flight, there is a difference Δp between the outside and inside pressures. For the tensions in the x and y -directions being T'_x and T'_y the natural angular frequencies are for $R_x \rightarrow \infty$ given by

$$\omega_{mn}^2 = \frac{D_0}{\mu} \cdot \left\{ \left[\left(\frac{m\pi}{L_x} \right)^2 + \left(\frac{n\pi}{L_y} \right)^2 \right]^2 + \frac{12}{(hR_y)^2 [1 + (nL_x/mL_y)^2]^2} + \left[\frac{T'_x}{D_0} \left(\frac{m\pi}{L_x} \right)^2 + \frac{T'_y}{D_0} \left(\frac{n\pi}{L_y} \right)^2 \right] \right\} \quad (15.80)$$

For a finite circular cylinder with an inside overpressure Δp the tensions T'_x and T'_y are as discussed in Sect. 14.17 and in Problem 14.10 approximated by $T'_x = \Delta p R_y / 2$ and $T'_y = \Delta p R_y$. However, it can be argued that in an aircraft the tension T'_x can be neglected since due to the frames and stringers of the fuselage a plate segment is exposed to a minimum of strain in the x -direction. In the high-frequency region, $(m\pi/L_x)^2 + (n\pi/L_y)^2 \gg 1$, the natural frequencies for curved plate segments, with and without in-plane tension, tend to the natural frequencies of a flat plate. In the high-frequency region, the autospectrum $S_{vv}(\omega)$ for a curved plate under tension tends to the autospectrum valid for a flat plate of the same dimensions exposed to no tension.

The space average of an autospectrum of the velocity of a plate segment under tension and with a curvature R_y as shown in Fig. 15.7 excited by a turbulent flow in the x -direction is given by Eq. (15.75). The natural angular frequencies ω_{mn} in Eq. (15.75) are given by Eq. (15.80).

The autospectrum, Eq. (15.78), of the plate velocity can be written as

$$S_{vv}(\omega) = \sum_{mn} [S_{vv}(\omega)]_{mn} \quad (15.81)$$

where $[S_{vv}(\omega)]_{mn}$ is the autospectrum of the velocity of the mode (m, n) . The summation over m and n as for Eq. (15.78). By comparing Eqs. (15.78) and (15.81) the modal autospectrum components $[S_{vv}(\omega)]_{mn}$ are obtained as

$$[S_{vv}(\omega)]_{mn} = \frac{1}{(2\pi)^2} \cdot \Phi_{pp}(\omega) \cdot \omega^2 |W_{mn}|^2 \cdot \frac{\omega\gamma_1}{U_c} \cdot \frac{\omega\gamma_3}{U_c} \cdot \Delta_m(\omega) \cdot \Gamma_n(\omega) \quad (15.82)$$

The power spectrum $[S_{\Pi}(\omega)]_{mn}$ of the acoustic power radiated by mode (m, n) is

$$[S_{\Pi}(\omega)]_{mn} = (\rho c) \cdot A \cdot (\sigma_r)_{mn} \cdot [S_{vv}(\omega)]_{mn} \quad (15.83)$$

where A is the area of the plate (ρc) the wave impedance of the fluid— ρ is its density and c the speed of sound in the fluid. The parameter $(\sigma_r)_{mn}$ is the sound radiation ratio for mode (m, n) defined in Eq. (12.97).

15.7 Measurements of TBL-Induced Vibrations

Finnveden et al. have reported laboratory measurements of wall pressure correlation and plate vibrations in Ref. [241]. The wind tunnel used for the experiments is shown in Fig. 15.8. A test panel was mounted in the stiff duct. The plate was excited by the TBL induced by a flow through the duct. A fan was used to build up an overpressure in an anechoic room. Due to the overpressure there was a flow through the duct. The capacity of the fan resulted in an airflow of $10 \text{ m}^3/\text{s}$ through the duct and a pressure drop of 10 kPa. The background noise level in the duct was below 25 dB during tests. As reported in Ref. [241], the basic Corcos and Chase models were modified to better

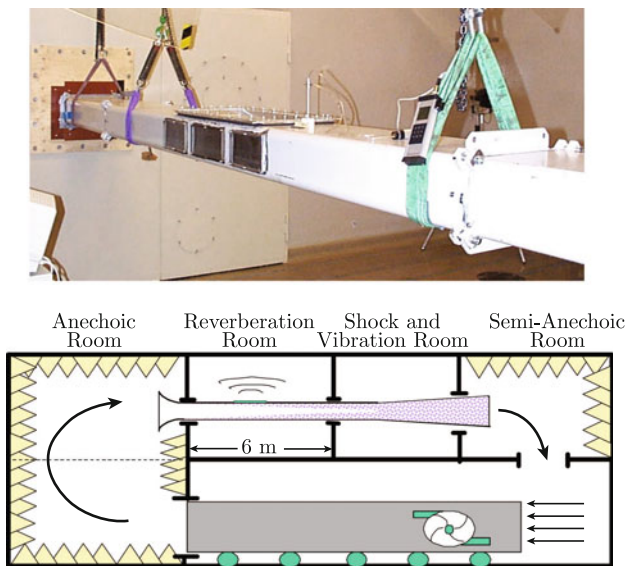


Fig. 15.8 Wind tunnel used for measurements of TBL at MWL, KTH from [241]

comply with measured results. In the Chase model, the relation between the terms describing the self-noise and the shear noise was made frequency and flow speed dependent.

An alternative to laboratory measurements is in-flight measurements. One example of in-flight measurements was first described in Ref. [247] and later in Ref. [248]. A small business aircraft of type Piaggio 180 was used for these in-flight measurements. The aircraft is shown in Fig. 15.9. The total length of the aircraft is 14.41 m, the wing span is 14.03 m, and the wing area 16 m². The aircraft is powered by two five-bladed propellers. Interior linings were removed for vibration measurements to be made directly on the fuselage. Loss factor measurements of the structures were made with engines and all equipment turned off and aircraft parked in hangar. During in-flight measurements, no auxiliary equipment was in operation. The noise induced by propulsion system was readily identified by its blade-passing frequencies. The velocity levels of the plate elements shown in Fig. 15.10 were measured at three different flight velocities. The dimensions of the plate elements are given in Table 15.3. The flight data are listed in Table 15.4.

During the test flights, 15 accelerometers were mounted on the inside of the fuselage on one side of the aircraft. The accelerometers were mounted in such a way with respect to the frames as to give a good average for each class of plates.

Accelerometers mounted on the plates 2, 7, 12, and 14 give an average of the velocities of the lower plates and accelerometers on the plates 1, 6, 10, and 13 of the upper plates. The accelerometers 3 and 8 were mounted at junctions of stringers just below the upper plates. In a similar way the accelerometers 5 and 9 were mounted to stiff points just above the lower panels.



Fig. 15.9 Piaggio 180 aircraft used for in-flight measurements

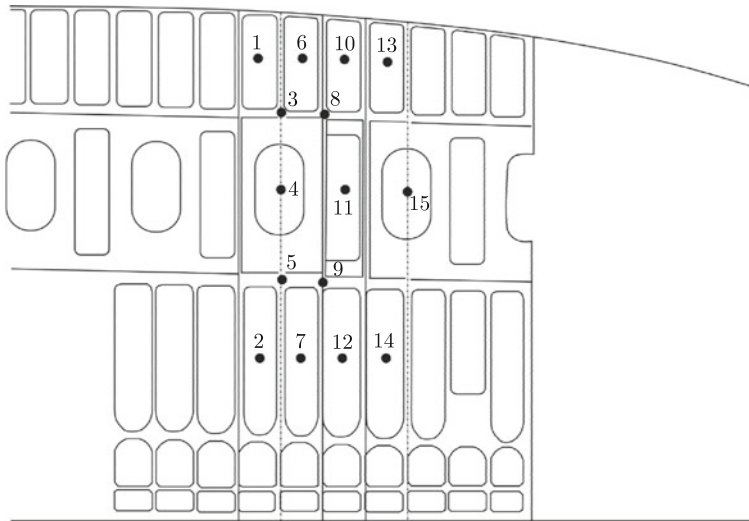


Fig. 15.10 Position of plate elements on fuselage. The elements 4 and 15 are windows. Numbers 3, 5, 8, and 9 represent connection points between stringers and frames

Table 15.3 Panel parameters

Panel width	L_x	0.206 m
Panel length	L_y	0.629 m
Panel thickness	h	1 mm
Loss factor	η	$10 \times f^{-0.8}$
Curvature of plate	R_y	0.96 m
E-modulus of plate	E	0.72 N/m ²
Density plate	ρ	2700 kg/m ³
Poisson's ratio	ν	0.3

Table 15.4 Flight data

Flight Test	Height (m)	Airspeed (m/s)	Mach number	Outside Temp. (°C)	Pressure (Pa)	Propeller rpm
1	9000	192	0.626	-40	22490	1986
2	9000	173	0.566	-40	24020	1980
3	9000	149	0.485	-40	25720	1978

The theory developed to describe the excitation of the plates was based on the assumption that the velocities of a plate element are much higher than the velocity of its boundaries. In Fig. 15.11 the average velocity level of the lower plates, numbered 2, 7, 12, and 14 in Fig. 15.10, are compared to the average velocity of the adjoining

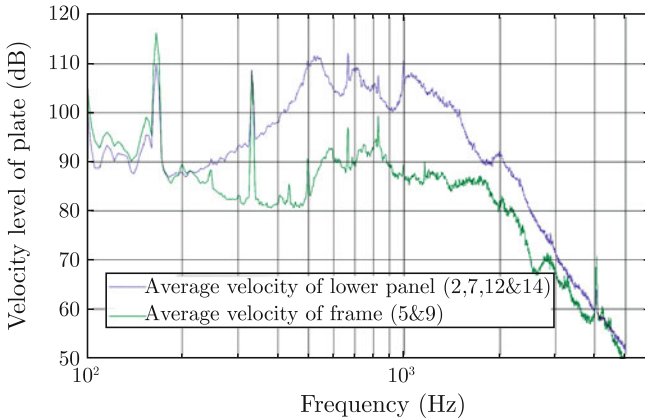


Fig. 15.11 Velocity level of plate, *top curve*, and velocity level of frame, *bottom curve*. Airspeed 173 m/s, test condition 2

frames, indicated by 5 and 9 in Fig. 15.10. The measurements clearly show that the plate velocity is much higher than the velocity of the stringers and frames in the frequency range 600–1250 Hz that determines the A-weighted internal noise level in this particular aircraft. In the frequency range of importance, the plate velocity is 10–20 dB higher than the velocity of the frames. Thus, the assumption concerning the relative velocities of plates and stringer/frames is well supported.

The flight data for the tests are given in Table 15.4, data on the geometries of the lower plate, positions 1, 6, 10, and 13 are given in Table 15.3. The location of the lower plates on the fuselage is shown in Fig. 15.10.

The curvature is along the length L_y of the plate. For a fully equipped aircraft the loss factor is $14 \times f^{-0.8}$. The loss factors are based on measurements on the P.180 aircraft parked on ground as described in Ref. [247]. During all in-flight tests conditions the turbulence was fully developed at the measurement positions. Compare the discussion in Sect. 15.4.

The density of the external air was set to 0.44 kg/m^3 . The interior pressurization was $0.97 \text{ atm} = 98940 \text{ Pa}$ and the static outside pressure 0.30 atm , $1 \text{ atm} = 1.013 \times 10^5 \text{ Pa}$. The pressure given in Table 15.4 is the pressure on the fuselage.

The measured velocity levels, lower plates, narrow-band analysis, are shown in Fig. 15.12 for the three different test conditions defined in Table 15.4. The corresponding result based on a 1/3 octave band analysis is shown in Fig. 15.13.

The plate response due to the propeller blade excitation is clearly shown in Fig. 15.12. The rpm of the five-bladed propeller was approximately 1980 corresponding to a frequency of 33 Hz. The fundamental tone 33 Hz and its harmonics 66 and 99 Hz are quite distinct in Fig. 15.12. The first blade passing frequency of the five-bladed propeller is 165 Hz with the harmonics 330, 495, 660 Hz and so on. The first few blade passing frequencies are also readily distinguished in Fig. 15.12.

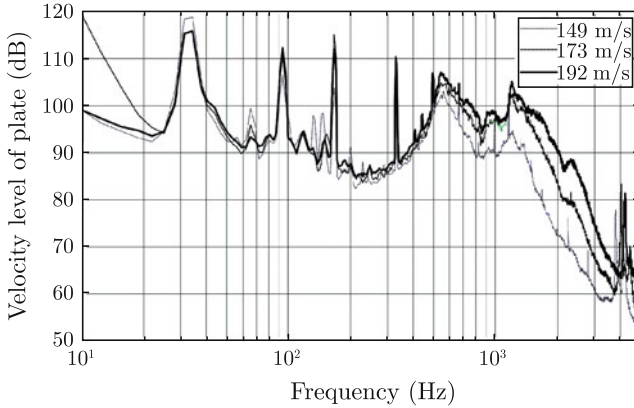


Fig. 15.12 Measured velocity levels of the *lower* plates. Narrow-band analysis

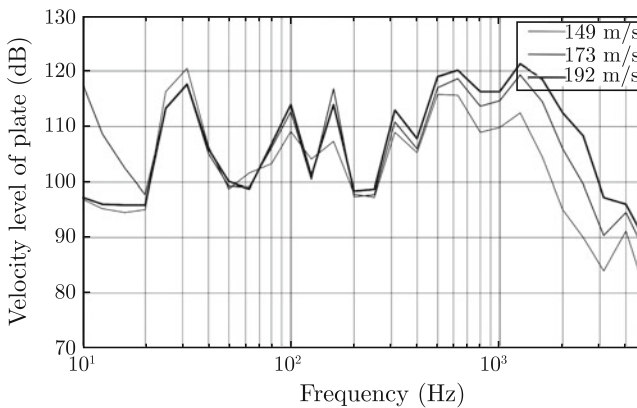


Fig. 15.13 Measured velocity levels of the *lower* plates. 1/3 OB analysis

15.8 Comparison Between Measured and Predicted Velocity Levels Induced by TBL

Measurements of velocity levels were compared to predictions based on the Corcos, Efimtsov, and modified Chase models. In the Corcos model, Eq. (15.55), the Finnveden parameters were used, i.e., $\gamma_1 = 0.116$ and $\gamma_3 = 0.7$. The Efimtsov parameters are defined in Eq. (15.57). The parameters used in the Chase model are given in Table 15.5. The parameters U_c and U_τ in Eqs. (15.56) and (15.57) are given by Graham [238] as $U_c = 0.7 \cdot U_\infty$ and $U_\tau = 0.03 \cdot U_\infty$. The boundary layer thickness is set to equal 0.06 m for all flight conditions.

A comprehensive study of measured in-flight data and different models of autospectrum of the wall pressure can be found in a NASA report by Robert and Adam [249]. The report indicates that the autospectra predicted by the models of

Table 15.5 Parameters for the Chase model

U_∞	149 m/s		173 m/s		192 m/s	
a_r	0.75		0.78		0.83	
b_r	0.14		0.14		0.14	
b_M	b_T	μ_M	μ_T	γ_M	γ_T	
0.5973	0.3158	0.2531	0.0614	1.2267	1.4186	

Robertson, ESDU, Laganelli, Goodwin are rather similar in a wide frequency range, while the results obtained from the Efimtsov model are approximately 5 dB lower in the low frequency range and less steep at high frequencies as compared to other predictions. However, as suggested by Finnveden, the autospectrum proposed by Robert in Ref. [240] is preferred. Robert estimates the autospectrum of the wall pressure $\Phi_{pp}(\omega)$ as given by Eq. (15.63).

For the prediction of the velocity levels of the plates of the fuselage the wall pressure spectrum, Eq. (15.63), was used for all three cases. Plate dimensions and material parameters are listed in Table 15.3. The flight data are given in Table 15.4.

Predicted velocity levels using the three models are compared in Fig. 15.14 for test condition 1. For this particular aircraft the A-weighted noise level in a fully equipped cabin is determined by TBL-induced noise in the frequency range 500–1250 Hz as discussed in Ref. [247]. In comparison with the Corcos model, the velocity level of the plate elements derived from the Efimtsov model is 3–6 dB lower in this frequency range. The results based on the Chase model are in between the Corcos and Efimtsov predictions in the same frequency region. These results are also supported

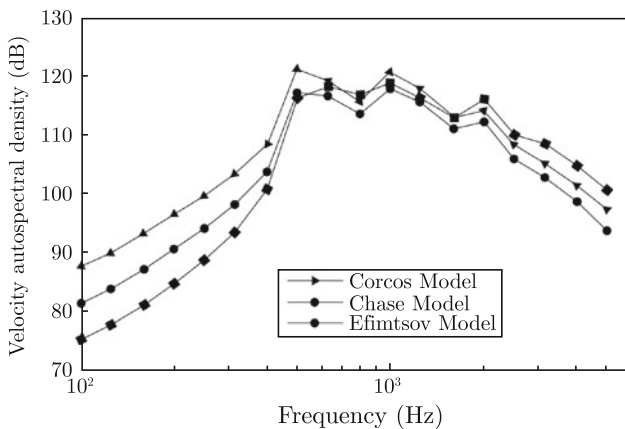


Fig. 15.14 Comparison of predictions based on Corcos, Chase, and Efimtsov models. Predicted velocity autospectrum for the points 2, 7, 12 and 14, test condition 1, velocity 192 m/s, in 1/3 octave band

by Graham's findings as reported in Ref. [238]. The Corcos model shows the better agreement with measurements in the frequency range 200–1500 Hz. Therefore, the Corcos model was used for all predictions.

Figures 15.15, 15.16 and 15.17 compare predicted and measured results using narrow-band analysis and 1/3 octave-band analysis, respectively, for three different flight velocities, test conditions 1, 2 and 3, given in Table 15.4. The Corcos model is used throughout.

The measured velocity levels exclude peaks due to propeller excitation at the propeller harmonics 165, 330 Hz, etc. The TBL-induced noise determines the plate velocity in the frequency range 500–2000 Hz. The noise radiated by the curved plates in this frequency range determines the A-weighted noise level in the cabin. The results justify the assumption that relative differences of plate velocity levels can be predicted by means of the Corcos model as function of flight velocity and plate dimensions.

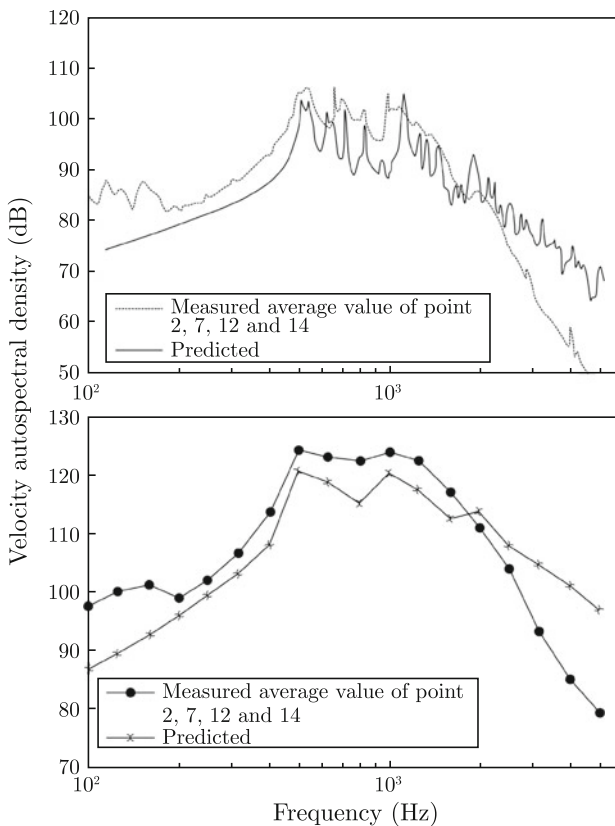


Fig. 15.15 Comparison between predicted and measured velocity autospectral density. (*Upper*) Narrow-band analysis, (*Below*) 1/3 OB analysis. Test condition 1, velocity 192 m/s

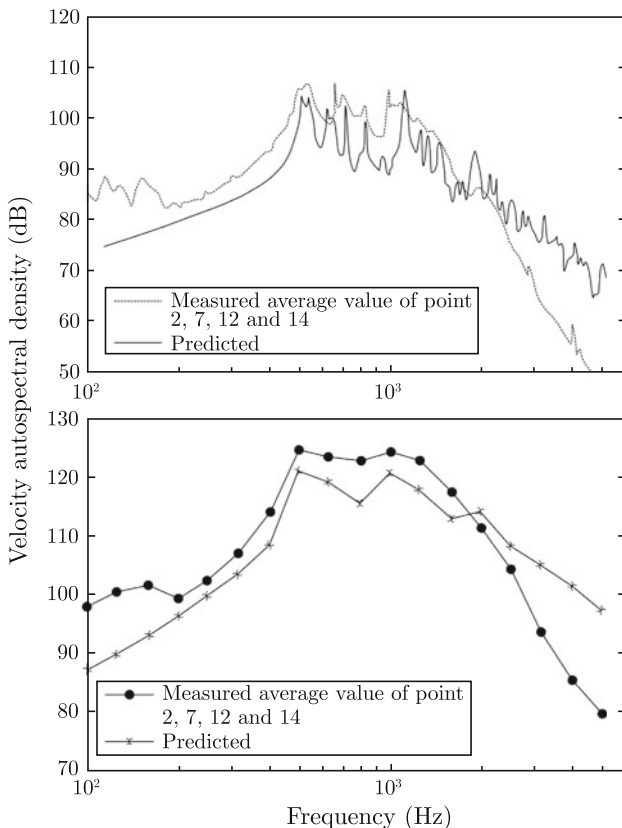


Fig. 15.16 Comparison between predicted and measured average velocity autospectral density. (Upper) Narrow-band analysis, (Below) 1/3 OB analysis. Test condition 2, velocity 173 m/s

Discrepancies between the measured and predicted spectra appear above 2000 Hz. These discrepancies are similar to the results based on wind tunnel experiments reported by Finnveden [241]. The loss factors of the plate elements given in Table 15.3 are based on measurements up to 2500 Hz. In the high frequency region, above 2.5 kHz, the radiation losses would contribute to the total losses of the fuselage. By including radiation losses the discrepancies between measured and predicted velocity levels would somewhat decrease for high frequencies. However, the Corcos model clearly overestimates the velocity levels of the plate elements in the high-frequency region. The agreement between results from the Corcos model and measurements is acceptable, although about 3 dB too low in the important mid-frequency region 200–1500 Hz. The results based on the Efimtsov and Chase models are slightly less accurate in this frequency range and for this particular test case. One possible explanation for the discrepancies between predicted and measured velocity levels in the mid-frequency region might be the influence of the nose wing and the propellers on the thickness of the turbulent boundary layer. If the boundary thickness δ is

increased from 0.06 to 0.1 m the agreement between predicted and measured results is very good (Fig. 15.16).

During the last few years a number of semiempirical models for turbulent boundary layer wall pressure spectra have been published. In Ref. [295] some of these models are compared. The authors, Hwang et al., suggest that the model proposed by Goody [296], provides the best overall prediction of frequency spectra. The Goody model decays more rapidly or as ω^{-5} with increasing frequencies as compared to the Robert model presented in Eq. (15.63) which decays as ω^{-3} . The Goody model would therefore give better agreement than the Robert model when comparisons are made between measured and predicted results as in Figs. 15.15, 15.16 and 15.17.

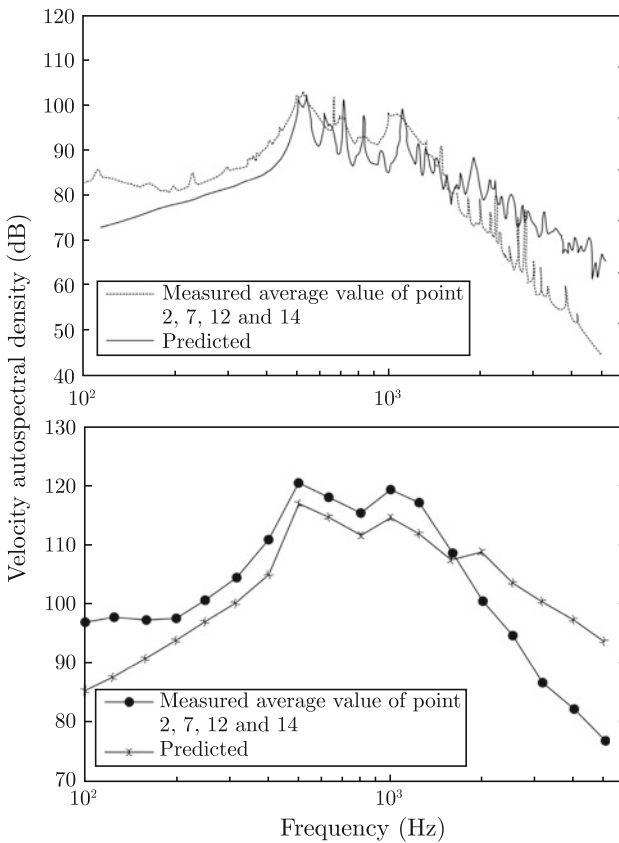


Fig. 15.17 Comparison between predicted and measured average velocity autospectral density. (Upper) Narrow-band analysis, (Below) 1/3 OB analysis. Test condition 3, velocity 149 m/s

The Goody model, double-sided spectrum, can be written as

$$\Phi_{pp}(\omega) = \frac{1.5\tau_w^2 \delta (\omega\delta/U_\infty)^2}{U_\infty \left\{ [0.5 + (\omega\delta/U_\infty)^{3/4}]^{3.7} + [1.1 \cdot R_T^{-0.57} \cdot (\omega\delta/U_\infty)]^7 \right\}} \quad (15.84)$$

For a single-sided spectrum the function Φ_{pp} should be multiplied by a factor 2. The parameter $R_T = (\delta/U_\infty)/(v_f/u_*^2)$ is the ratio of the outer to inner boundary layer timescale. Other notations are given in Sect. 15.5. See also [297].

15.9 Parameter Study

The power spectral density, Eq. (15.73), and thus the velocity level of the plate elements of the fuselage depend on the flow velocity of the TBL disturbance. In turn, the flow velocity depends on the flight velocity of the aircraft. The autospectrum of the wall pressure $\Phi_{pp}(\omega)$, Eq. (15.63), is a function of U_c as $U_c^{15/4}$ in the mid-frequency region and as U_c^6 for high frequencies. In addition, the Λ_m and Γ_n both depend on U_c . However, in-flight measurements on the aircraft, Fig. 15.9, reveal that the A-weighted sound pressure level in the fully equipped cabin depends on the flight velocity v as

$$L_A = C + 80 \log v \quad \text{dB(A)} \quad (15.85)$$

where C is some constant. It is assumed that the altitude of the aircraft is constant, only the velocity is changed. Thus a 20% increase of the speed of the aircraft would increase the interior noise level by approximately 6 dB assuming that all other parameters are kept constant. The expression (15.84) is only valid for moderate variations of the flight velocity.

The response of a plate excited by a TBL was discussed in Sect. 15.6. It was concluded that the response of the plate depends on the geometrical and material parameters and the loss factor of the plate element. Assuming the material parameters to be fixed and the speed and altitude of the aircraft to be constant the parameters which could influence the response of the plate are the radius R_y of the fuselage, the radius R_x of the fuselage in the longitudinal direction of the aircraft, the plate dimensions L_x and L_y , and the plate thickness h as well as the loss factor of the structure.

The loss factor of the plate elements of the fuselage is an important parameter. The frequency average of the power spectral density of the velocity, Eq. (15.78), is inversely proportional to the loss factor of the structure. However, the noise radiated by a plate is not necessarily reduced at the same rate as the plate velocity by adding damping as discussed in Sect. 12.10.

For a plate with a single curvature, the influence of changing the radius of the fuselage is insignificant in the frequency range of importance if the radius is changed by less than $\pm 20\%$.

The effect of the plate thickness on the velocity is demonstrated in Problem 15.8. It can be shown that the power spectral density of the velocity as function of plate thickness is approximately given by

$$S_{vv}(\omega) \propto \frac{1}{h^3} \quad (15.86)$$

However, with respect to the noise radiated into the cabin also the radiation ratio of the plate elements must be considered. The simple result (15.86) gives an indication of the influence of the plate thickness on the autospectrum of the plate velocity. The result also indicates that in the frequency range well above the first natural frequency of the plate, see Eq. (15.79), the autospectrum of the velocity is only moderately dependent on the length and width of the plate. The first natural frequency of the plate elements are determined by the plate parameters as shown in Eq. (15.80). The autospectrum of the plate velocity is more or less independent of the width and length of the plate. These conclusions are supported by Ref. [250].

The power spectrum S_{Π} of the acoustical power radiated by the plate is given by Eqs. (15.81) through (15.83). The modal sound radiation ratio $(\sigma_r)_{mn}$ is a function of the plate dimensions as well as of frequency. Although in the high-frequency range the velocity of the plate is more or less independent of the plate dimensions, the radiation ratio, and thus the radiated power varies very significantly with the plate dimensions. The radiation ratio decreases with increasing plate dimensions. Clearly, the combined effect of plate velocity and radiation ratio must be considered for estimating the noise radiated by a plate structure excited by a TBL.

The acoustic power radiated by a plate not only depends on the plate velocity but also on the radiation ratio of the plate. By increasing the plate thickness the plate velocity is decreased, Eq. (15.86), but at the same time the radiation ratio is increased in the frequency range between the first plate resonance and the critical frequency of the plate. These effects can be counteracting each other. By increasing the plate dimensions, width and length, the radiation ratio is decreased, whereas the plate velocity is more or less constant (Fig. 15.18).

In Ref. [224] it is observed that the influence of stringers on noise radiation from a fuselage depends on the orientation of the frames with respect to the outside airflow. A frame mounted perpendicular to the flow will increase the noise radiated from a plate in the frequency range below the critical frequency and the ring frequency of the panel.

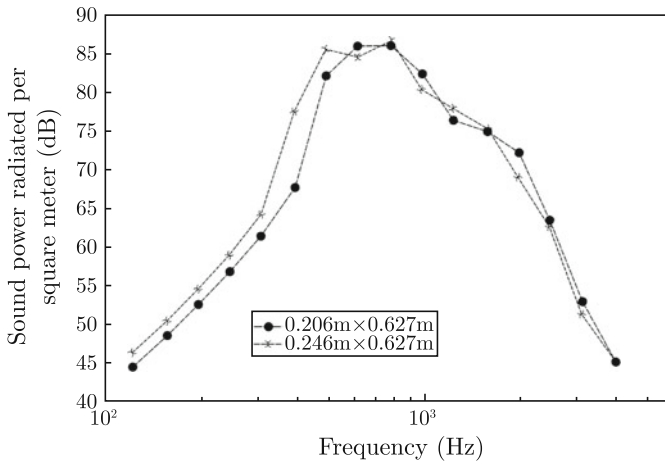


Fig. 15.18 Effect of stringer distance on the predicted sound power radiated by per square meter of the plate in 1/3 octave band 192 m/s. Height of plate is 0.627 m, frame distances are 0.206 and 0.246 m

15.10 Flow Noise Induced in Ships

A turbulent boundary layer—TBL can be developed in a fluid close to a structure at sufficiently high flow velocities as discussed in Sect. 15.4. For a ship traveling through water, the TBL, when developed, excites the hull plates. Part of the acoustic power induced in the hull is transmitted as vibrations in the ship structure to the accommodation spaces. The structures enclosing the accommodations radiate noise into these spaces. The acoustic power radiated due to this effect is proportional to the power induced in the hull structure by the TBL. For fast and comparatively small vessels, water TBL induced noise can be very dominant in the forward part of the ship. For an aircraft, the noise generating mechanism is different. For an aircraft the fuselage excited by the TBL is radiating noise directly into the cabin. On a ship it is essential to determine the relative importance of the TBL effect as compared to the acoustic power induced in the ship structure by other sources like water jets, engines etc. A model describing the effect of a TBL or rather the acoustic power induced in hull plates as function of ship speed, plate geometry, etc., could possibly also be used to minimize the effect of the TBL by changing the hull design. A number of reports have been issued within the project NORMA financed by the European Commission.

The first parameter that determines the nature of turbulence in a boundary layer is the Reynolds number \mathcal{R} in Sect. 15.4 as $\mathcal{R} = U_\infty L / \nu_f$, where U_∞ is the velocity of the fluid well away from a structure, L is the distance of the origin of the boundary layer and ν_f the kinematic viscosity of the fluid. The viscosity for water is $1.284 \cdot 10^{-6} \text{ m}^2/\text{s}$. As discussed in Ref. [162] turbulence can build up spotwise for $\mathcal{R} \approx 2 \cdot 10^6$. For $\mathcal{R} \approx 10^7$ the turbulence is fully developed.

Again, the Corcos model was used for predicting the velocity level of the hull plates. Model-scale measurements determined the autospectrum of the pressure on the hull plates. This type of measurements are described in Ref. [251]. Magienese discusses the scaling laws transforming the model-scale measurement to full scale in Ref. [252]. The pressure spectrum was determined for two different hull shapes, one for a catamaran and one for a slender trimaran. Both hulls were designed for very high velocities.

The fluid loading on a hull plate can be considerable. For a plate in flexure with a fluid loading on one side, the wavenumber κ is according to Eq. (12.13) the solution to

$$\kappa^4 = \kappa_0^4 \left[1 + \frac{\rho_0}{\mu_0 \sqrt{\kappa^2 - k^2}} \right] \quad (15.87)$$

where κ_0 is the wavenumber for the plate in vacuum, k the wavenumber in the fluid, ρ_0 the density of the fluid, and μ_0 the mass per unit area of the unloaded plate. The wavenumber κ for flexural waves is obtained from the expression $\kappa^4 = \mu\omega^2/D$, where D is the bending stiffness of the plate. For $\kappa \gg k$ Eq. (15.87) is written as

$$\mu \approx \mu_0 + \rho/\kappa_0 \quad (15.88)$$

The mass per unit area of the plate with a fluid loading on one side is given by μ whereas μ_0 is the mass per unit area of the unloaded plate. For water $\rho \approx 1000 \text{ kg/m}^3$.

The boundary conditions for the plate elements located between frames can be considered to be clamped or simply supported. In a previous study [163] on the response of hull plates above a cavitating propeller, the plates were assumed as simply supported along the frames. The assumption was based on measured results. The natural frequencies of hull plates were measured and compared to predicted results for various boundary conditions. In Ref. [163] it was found that a good agreement was obtained between predicted and measured results when simply supported boundaries for the plate elements were assumed.

The loss factor η for a fluid loaded plate is modeled as

$$\eta = 0.025 \times f^{-0.275} \quad (15.89)$$

where f is the frequency. The result (15.89) is based on full-scale measurements.

The Corcos model, Eq. (15.55), is again used to describe the wall pressure fluctuations. The flow is in the x direction. The pressure autospectrum Φ_{pp} is the TBL wall pressure autospectrum and taken from model-scale measurements for example Ref. [251]. The convection velocity U_c was approximated from measurement results by $U_\infty/8$, where U_∞ is as before the free-stream velocity. The streamwise and spanwise coherence parameters γ_1 and γ_3 were initially taken as 0.125 and 0.7, respectively, as suggested in Ref. [251].

The hull plates were modeled as simply supported aluminum plates. The plates were assumed to be flat, isotropic, and without prestress. The dimensions were $L_x = 0.7$ m, $L_y = 1.5$ m and thickness 4 mm.

The frequency range investigated was 23–3536 Hz and the main analysis was made in third octave bands. Four free-flow velocities were studied: 25, 30, 35 and 40 knots. Some numerical procedures are discussed in Ref. [250]. The autospectrum $\Phi_{pp}(\omega)$ is shown in Fig. 15.19 for four different ship velocities, 25, 30, 35, and 40 knots. The spectrum is determined from model-scale measurements.

The measured autospectrum is shown in Fig. 15.19 as function of flow velocity. The data is from Ref. [251].

Figure 15.20 compares the autospectral density of the velocity for the four flow speeds. As expected, an increase in speed generally results in an increase in response. The velocity level L_v in dB re 10^{-9} m/s is obtained as (1/3 OB analysis)

$$L_v = 10 \cdot \log(G_{vv}) + 180 \tag{15.90}$$

when G_{vv} is given in SI units. The velocity level of the hull plates is increasing rapidly as function of the flow speed u . In the frequency range 630–1250 Hz the velocity level L_v in dB in 1/3 octave bands is approximately given as

$$L_v = 10 \cdot \log u^{10} + C_1 \tag{15.91}$$

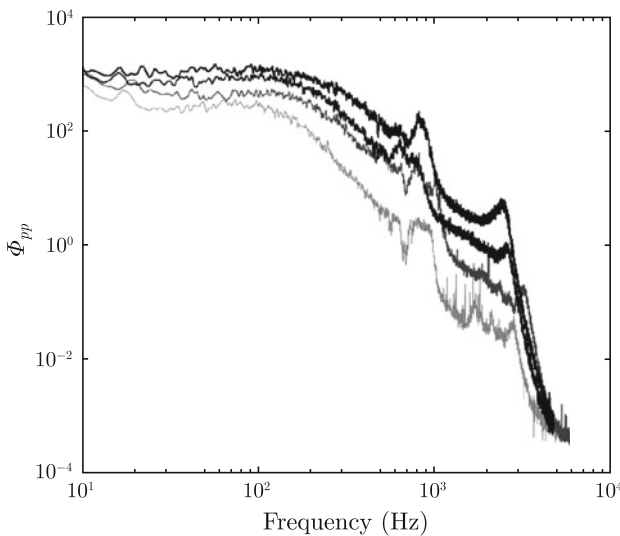


Fig. 15.19 Wall pressure power spectrum Φ_{pp} as function of flow velocity. From *top* to *bottom*; 40, 35, 30, and 25 knots

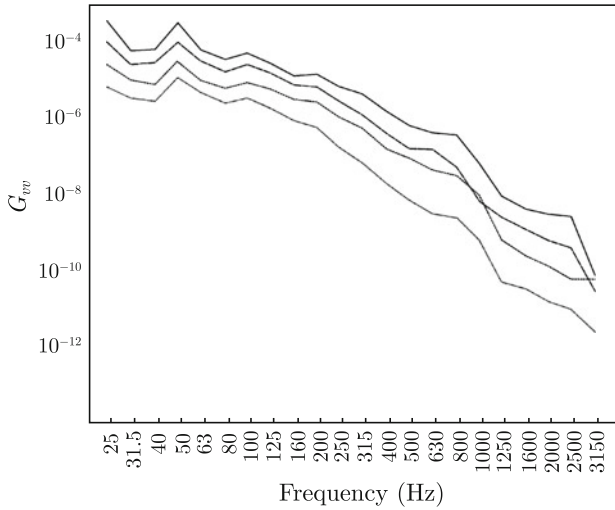


Fig. 15.20 Response S_{vv} as function of flow speed and frequency. From top to bottom: 40, 35, 30 and 25 knots. 1/3 OB analysis

where C_1 is some constant. Thus, by increasing the speed from 25 to 30 knots the velocity level of the plate is increased by 8 dB, from 25 to 35 knots by 14 dB and from 25 to 40 knots by 20 dB. However, some full-scale measurements

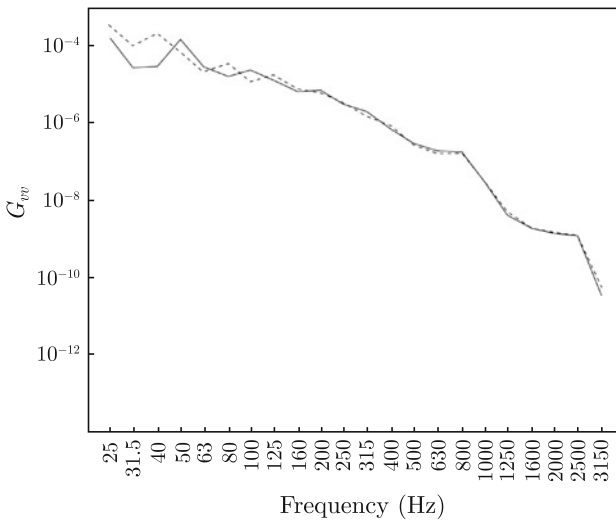


Fig. 15.21 Response as function of length L_x at 40 knots —, 0.7 m; ---, 1 m. 1/3 OB analysis

reported by Det Norske Veritas indicate that the plate velocity can be approximated by $L_v = 10 \cdot \log u^{6.5} + C_1$.

The influence of the frame distance on the plate response is illustrated in Fig. 15.21. At 40 knots the plate response or rather G_{vv} is calculated for L_x equal to 0.7 and 1.0m. The result shows that it is only in the low-frequency region, below 200 Hz, that the frame distance significantly influences the plate response. For frequencies well above the first plate natural frequency the plate dimensions are of minor importance with respect to the plate response.

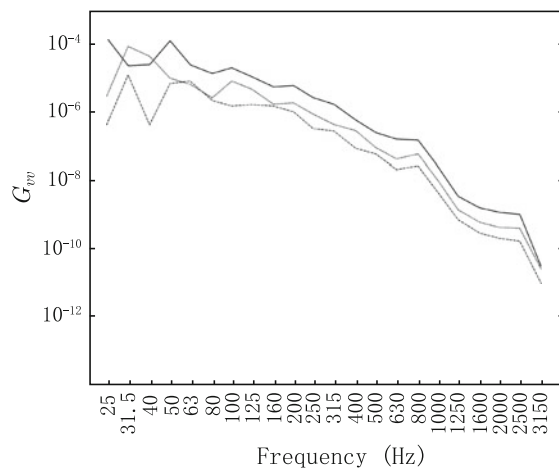
Figure 15.22 shows the plate response S_{vv} for the three different plate thicknesses of 4, 6, and 8 mm. In the high-frequency range, a doubling of the plate thickness gives a reduction of the velocity level by approximately 7 dB. A 50% increase of plate thickness results in a reduction of the velocity level by approximately 4 dB. The velocity level L_v of the hull plate as function of plate thickness h is in the high-frequency region approximately given by

$$L_v = 10 \cdot \log(h^{-9/4}) + C_2 \tag{15.92}$$

where C_2 is some constant. The details are left for Problem 15.9. This result is different from Eq. (15.85) derived for a fuselage. The reason is the effect of the water load on the hull plates.

The main design parameters which influence the velocity level of hull plates excited by a turbulent boundary layer is the speed of the ship, the shape of the hull, and the thickness of the hull plates. A damping layer on the hull plates would decrease the velocity level of the plate but the damping layer does not influence the input power to the plate. A damping layer would therefore have a very limited effect on the noise levels in the accommodation spaces on the main deck and above. The frame distance has a very small effect on the noise levels in the mid- and high-frequency ranges. The shape of the hull is crucial with respect to the acoustic input power to the hull.

Fig. 15.22 Response as function of thickness t at 40 knots. *Top curve*, 4 mm; *middle curve*, 6 mm; *bottom curve*, 8 mm. 1/3 OB analysis



There is a rather strong variation of the hull plate velocity due to the location of the plate in the stern or the bow. The hull of the catamaran was different from the hull of the trimaran used for the tests. The hull section under the water level was much more slender for the trimaran as compared to the catamaran. Although the velocity of the trimaran was 60 knots and the speed of the Catamaran 40 knots the velocity levels of the hull plates were approximately the same for the two ships. This is a clear indication that the shape of a hull is of paramount importance with respect to flow-induced noise.

Problems

15.1 A spatially stationary signal $u(x)$ is defined as $u(x) = A \cdot \cos(k_0 x)$. Determine the spatial autocorrelation function $R_{uu}(\xi)$ defined in Eq. (15.4).

15.2 Determine the spatial spectral density $\tilde{S}_{uu}(k)$ of the signal $u(x) = A \cdot \cos(k_0 x)$.

15.3 A wave, displacement $u(x, t) = A \cdot \sin[\omega_0(t - x/c)]$, is propagating along the positive x -axis in a coordinate system. Determine the autocorrelation function $R_{uu}(\xi, \tau)$ and the corresponding spectral density $\tilde{S}(k, \omega)$.

15.4 Use the expression $\tilde{S}(k, \omega)$ derived in Problem 15.4 to calculate the time and space average of the displacement squared, $\langle \bar{u}^2 \rangle$, for $u(x, t) = A \cdot \sin[\omega_0(t - x/c)]$.

15.5 Show that the time average of the input power to mode (m, n) to a plate is $\bar{P}_{mn} = \omega_{mn} \eta \bar{E}_{mn}$ where \bar{E}_{mn} is the total energy of that mode and η is the loss factor and ω_{mn} the natural angular frequency for that mode. Assume rain on the roof excitation.

15.6 A beam is simply supported at both ends. The beam is excited by a random force per unit length. The autocorrelation function of the force is $R_{F'F'}(\xi, \tau) = S_0 \cdot \delta(\xi) \cdot \delta(\tau)$ where ξ is the separation in space and τ in time of the force function. The bending stiffness of the beam is D' , its mass per unit length m' and its length L . Determine the space and time average of the kinetic energy of the beam.

15.7 Solve Eqs. (15.70) and (15.71).

15.8 Show that the autospectrum of the velocity of a flat plate excited by a TBL is proportional to $1/h^3$ where h is the thickness of the plate.

15.9 Show that the velocity squared of a water loaded plate excited by a water flow is proportional to $h^{-9/4}$.

Chapter 16

Transmission of Sound in Built-Up Structures

Maximum permissible noise and vibration levels are often required for most types of machinery, vehicles, and buildings. These requirements could either be law enforced or indirectly set by consumers. Very often a low-noise product is synonymous with a high-quality product. During the design phase of a manufacturing process of new products the acoustical performance of the products should be considered. It is always difficult, if at all possible, to introduce noise reducing measures once a construction has been manufactured. Consequently, there is a need for reliable noise prediction methods which can be used during the design phase of a new product.

During the design phase it should be ensured that the fundamental frequencies of the main sources, which are part of the construction, do not coincide with some of the first few natural frequencies of the main construction or its substructures. Another major task is the prediction of noise levels, internal as well as external, in the audible frequency range, often in 1/3 or 1/1 octave bands, from 80 to 3150 Hz. This type of prediction is often based on measurements on an existing construction. The purpose of the prediction is to evaluate possible changes and improvements to be implemented in a new construction or model.

There are as yet no general prediction model which can be used for these tasks. Often workable prediction models are developed for a certain class of construction, for example, a building, train, car, or a ship. In the low-frequency region predictions are generally based on the finite element method. In the high-frequency region the so-called Statistical Energy Analysis technique, SEA, is often favored. However, for certain large constructions, for example ships, the waveguide model has been applied for predicting noise levels in accommodation spaces.

In this chapter some basic elements of SEA and some applications are discussed. It is also demonstrated how the waveguide model can be used to predict noise levels in ships and other vehicles.

16.1 Introduction

The noise levels inside a large construction, for example a double-decker train, depend not only on the various noise sources but also on the construction itself. The noise sources like wheel–track interaction vary depending on speed and other running conditions. Variations of noise levels between similar products can also be caused by constructional differences. Even apparently identical structures can acoustically be rather different. Fahy [292] demonstrated that frequency response functions measured in the same way on very simple and presumably identical constructions, beer cans, could vary considerably. The narrow-band frequency plot of the 41 FRFs shows a spread of the order 20 dB in a very wide frequency range. The frequency and amplitudes of FRF peaks are shifted between the various measurements. Similar findings have been reported by Kompella and Bernhard [253], who used 98 vehicles of the same make for their experiment. A force was applied to a wheel and the acoustic response at the position of a driver's ear was recorded. Although the FRF for each car shows the same characteristics, the plot of all the resulting 98 FRFs shows a spread of approximately 20 dB from 50 to 500 Hz.

In practice it is not possible to identify two acoustically identical systems among mass-produced structures. There are many reasons for this. Plate elements used for the manufacturing of many products are slightly different with respect to thickness, material parameters, curvature, and thus also boundary conditions. The dramatic influence of a slight curvature of a plate on its natural frequencies was discussed in Sect. 8.8. A variation of the thickness of a plate by 4% would also shift the natural frequencies of the plate by 4%. A change of width and length by the same amount would shift the natural frequencies by approximately 8% and so on. The boundary conditions of a structure are of critical importance for the natural frequencies of the structure. Boundary conditions depend on the joining of structures. One specific welded joint can hardly be reproduced. The tension in plates can vary with ambient temperature to change a curvature or a boundary condition. A certain manufacturing process can give one result in the morning and another in the afternoon due to varying ambient temperatures. All these effects will influence any FRF in an apparently random way. Any attempt to predict noise levels in narrow frequency bands is therefore in most cases meaningless. Noise levels should preferably be determined in frequency bands, typically 1/3 or 1/1 octave bands, for the result to be representative for a certain type of structure. In general, measurements in 1/1 or 1/3 octave bands can be reproduced quite well. A narrow-band analysis, measurement or predictions, can be used for identifying the dominating natural frequencies of a construction with respect to some excitation. The exact natural frequencies representing a number of seemingly identical products cannot be determined due to structural variations. However, a narrow-band analysis can form the basis for changing the structure in order to shift some natural frequencies.

The degree of detail of any noise prediction scheme should be considered carefully. Certain structural elements could have only a minor influence on the predicted result. A simple example is illustrated in Fig. 16.1. The first natural frequency of a

Fig. 16.1 FEM models for the prediction of the first natural frequency of superstructure on a ship. From Ref. [254]

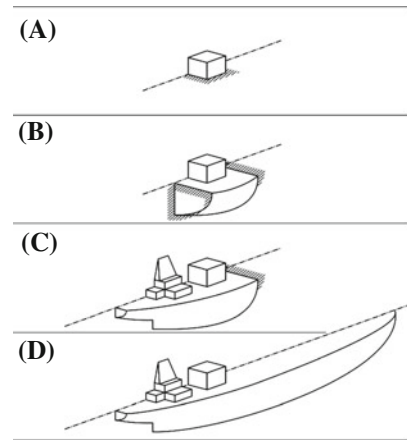


Table 16.1 FEM models and predicted results

Model	Number of elements	Degrees of freedom	First natural frequency (Hz)	Error (%)
A	484	61	11.5	39
B	1190	165	9.0	8
C	1500	315	8.8	6
D	2150	445	8.2	-1

superstructure on a ship should be calculated using a FEM technique. The natural frequency should be well separated from the fundamental frequencies of the main forces induced by propellers and main engines. Four different FEM models were used. The models used were: (A) Superstructure clamped to a solid foundation; (B) Superstructure plus engine room below; (C) Superstructure plus complete model of aft body; (D) Complete ship.

The fundamental frequency was determined by full-scale measurements to be 8.3 Hz. The predicted results are given in Table 16.1. For this type of prediction, Model A is too inaccurate, whereas the result given by Model B is sufficiently precise to determine if the first natural frequency is well separated from the fundamental frequencies of the main sources. Model D is unnecessarily detailed. Clearly, a certain experience of the programmer is required to determine how detailed a model must be made.

The energy flow in any structure is mainly carried by flexural, longitudinal, and transverse waves. Simple measurements on scale models or for that matter full-scale structures can often reveal if any particular wave type is dominating the energy flow. The inclusion of many wave types in a prediction model drastically increases the complexity of any prediction. Certain sources can often be neglected except perhaps very close to their coupling points to the main structure. Any prediction model should be compared to or calibrated against measurements on scale models or real structures. Even if the absolute levels predicted are not quite correct the prediction model might

still be used to estimate level differences due to certain structural changes of the main construction. It should also be possible to use a prediction program for determining the relative importance of the main noise sources and the dominant transmission paths. At the receiving end a prediction should identify the most radiating surfaces facing a particular enclosure. For any prediction to be successful the operator of the prediction program must be experienced and knowledgeable of the general acoustical characteristics of the product being investigated.

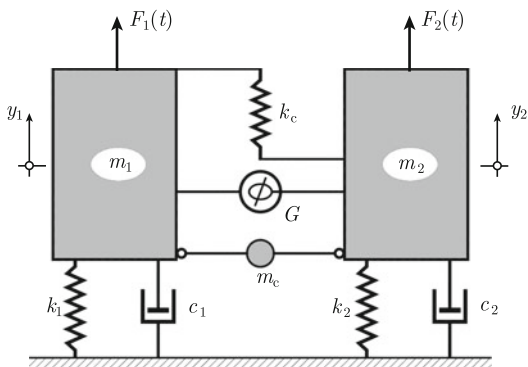
Three methods for the prediction of the propagation of structure borne sound in large structures are discussed in this chapter. The methods could be termed empirical, statistical, or analytical. The prediction schemes discussed are based on Statistical Energy Analysis or SEA, empirical models, and the waveguide model. Empirical methods can be very informative during the acoustical planning of a new construction which is a modification of an existing design. The upper frequency limit for a FEM calculation is too low to make FEM feasible for standard noise predictions. For example, a FEM model of a 2 m section of a Fokker 50 commercial aircraft, required 24,000 degrees of freedom for the prediction of the sound transmission loss of the fuselage up to 120 Hz as reported by Roozen [255]. A full FEM model of the entire 25 m long aircraft would require approximately 6×10^5 degrees of freedom for frequencies up to 125 Hz.

16.2 Statistical Energy Analysis, SEA

The SEA method was introduced in the early 1960s. The method was initially developed for the prediction of the response of space craft structures during take off. Fundamental work was carried out, for example, by Lyon, Scharton, Maidanik, Smith Jr., Heckl, and Fahy. Some basic reports on SEA are given in Refs. [256–269]. Some of the basic results have been summarized by Lyon [258]. As the name of the method implies the SEA procedure is a statistical method. The basic parameter is energy. The method is developed for systems excited by white noise. A system can consist of a number of coupled subsystems. In practice this could mean an assembly of plates and beams which are connected mechanically. The total energy and thus the average velocity of each subsystem is calculated within a frequency band—for example, 1/1 or 1/3 octave bands. Each subsystem should have a large number of natural frequencies within the frequency band of interest. Only the resonant transmission of energy is considered. The SEA formalism is very simple which might be one reason for its popularity and abuse.

The initial concept of SEA was based on the study of the energy flow between two coupled simple linear oscillators. Continuous systems like beams and plates, when excited by external forces, vibrate as an infinite set of simple oscillators as discussed in Chaps. 6, 7 and 8. Each oscillator corresponds to a vibration mode which can be represented as a simple mass–spring system with a certain modal mass, modal stiffness and modal losses and excited by a modal force. The study of the energy flow between continuous systems can therefore be considered as an extension of

Fig. 16.2 Two coupled oscillators excited by two external forces. From Ref. [256]



the problem relating the energy flow between two simple oscillators as proposed by Lyon and Maidanik in their by now classical paper [256].

The starting point for the problem discussed by Lyon and Maidanik and later by Scharton and Lyon [257] is the coupled oscillators shown in Fig. 16.2.

The two oscillators are linear and are mounted on an infinitely stiff foundation. The coupling between the masses of the oscillators is due to a simple spring with a spring constant k_c , a mass coupling m_c , and finally a gyroscopic coupling G . The vertical displacements of the masses are given by y_1 and y_2 as indicated in the figure. The equations of motion for the two systems are most readily derived by means of Lagrange equation (9.99) as demonstrated in Problem 16.1. The equations of motion are

$$(m_1 + m_c/4)\ddot{y}_1 + c_1\dot{y}_1 + (k_1 + k_c)y_1 + (m_c/4)\ddot{y}_2 - G\dot{y}_2 - k_c y_2 = F_1(t)$$

$$(m_2 + m_c/4)\ddot{y}_2 + c_2\dot{y}_2 + (k_2 + k_c)y_2 + (m_c/4)\ddot{y}_1 + G\dot{y}_1 - k_c y_1 = F_2(t) \quad (16.1)$$

A somewhat more simple case can illustrate the energy flow between the two oscillators by assuming that the coupling between the oscillators is only due to the ideal spring between the two masses. The procedure to derive the energy flow between the oscillators shown in Fig. 16.2 is the same as for the simple case, although much more cumbersome. Thus by setting $G = 0$ and $m_c = 0$, the Eq. (16.1) are reduced to

$$m_1\ddot{y}_1 + c_1\dot{y}_1 + (k_1 + k_c)y_1 - k_c y_2 = F_1(t)$$

$$m_2\ddot{y}_2 + c_2\dot{y}_2 + (k_2 + k_c)y_2 - k_c y_1 = F_2(t) \quad (16.2)$$

The time average of the input power induced by the force $F_1(t)$ to the first oscillator is written $\bar{\Pi}_1 = E[F_1\dot{y}_1]$ where $E[F_1\dot{y}_1]$ stands for the expected value of the product within the brackets as defined in Sect. 2.3. The input power to oscillator 1 is obtained by multiplying the first equation of (16.2) by \dot{y}_1 and thereafter forming the expectation values of all the products. Thus the expectation values are

$$m_1 E[\ddot{y}_1 \dot{y}_1] + c_1 E[\dot{y}_1 \dot{y}_1] + (k_1 + k_c) E[y_1 \dot{y}_1] - k_c E[y_2 \dot{y}_1] = E[F_1 \dot{y}_1] \quad (16.3)$$

The forces F_1 and F_2 are assumed to be random and uncorrelated. Consequently, the displacement y_1 is also random. For this type of signal it was shown in Sect. 2.3, Eqs. (2.26) and (2.27) that $E[y \dot{y}] = E[\dot{y} \ddot{y}] = 0$. The expected value or the time average of the input power to the mass 1 induced by the external force F_1 is $\bar{\Pi}_1 = E[F_1 \dot{y}_1]$. The energy flow from oscillator 2 to oscillator 1 across the common spring is $\bar{\Pi}_{21} = E[k_c y_2 \dot{y}_1]$. Inserting these results in Eq. (16.3) the equation is reduced to

$$c_1 E[\dot{y}_1 \dot{y}_1] = \bar{\Pi}_1 + \bar{\Pi}_{21} \quad (16.4)$$

In similar way the energy flow to oscillator 2 is

$$c_2 E[\dot{y}_2 \dot{y}_2] = \bar{\Pi}_2 + \bar{\Pi}_{12} \quad (16.5)$$

Since $\bar{\Pi}_{21} = E[k_0 y_2 \dot{y}_1]$ and $\bar{\Pi}_{12} = E[k_0 y_1 \dot{y}_2]$ it follows from Sect. 2.3 that $E[y_2 \dot{y}_1] + E[y_1 \dot{y}_2] = 0$ which leads to the result

$$\bar{\Pi}_{21} = -\bar{\Pi}_{12} \quad (16.6)$$

For random excitation the kinetic and potential energies of each oscillator are equal as discussed in Sect. 2.7, Eqs. (2.65) and (2.66). Therefore the quantity $c_1 E[\dot{y}_1 \dot{y}_1]$ can also be written as $c_1 E[\dot{y}_1 \dot{y}_1] = \omega \delta_1 \bar{\mathcal{E}}_1$ where $\bar{\mathcal{E}}_1$ is the total energy of oscillator 1 and δ_1 the loss factor of spring 1. Compare Sect. 1.6 and Problem 16.1. Consequently, the Eqs. (16.4) and (16.5) can be reduced to

$$\bar{\Pi}_1 + \bar{\Pi}_{21} = \omega \delta_1 \bar{\mathcal{E}}_1 = \bar{\Pi}_{d1}; \quad \bar{\Pi}_2 + \bar{\Pi}_{12} = \omega \delta_2 \bar{\mathcal{E}}_2 = \bar{\Pi}_{d2} \quad (16.7)$$

The power dissipated due to losses in the spring of oscillator 1 is denoted $\bar{\Pi}_{d1}$. The power lost in oscillator 2 is given by $\bar{\Pi}_{d2}$. By adding the two expressions of Eq. (16.7) and considering the result (16.6), it is found that

$$\bar{\Pi}_1 + \bar{\Pi}_2 = \bar{\Pi}_{d1} + \bar{\Pi}_{d2} \quad (16.8)$$

Thus, the sum of the input power to the oscillators is equal to the sum of the power dissipated in the two systems or rather in the springs supporting the masses. Compare also the discussion of the energy flow between three coupled plates presented in Sect. 8.4.

In order to describe the energy flow between the oscillators the quantities y_1 , \dot{y}_1 , y_2 and \dot{y}_2 must be determined. Using the Fourier transforms of y_1 , y_2 , F_1 and F_2 the basic equations describing the displacements of the oscillators are written in matrix form as

$$[A] \begin{Bmatrix} \hat{y}_1 \\ \hat{y}_2 \end{Bmatrix} = \begin{Bmatrix} \hat{F}_1 \\ \hat{F}_2 \end{Bmatrix}$$

$$[A] = \begin{bmatrix} -\omega^2 m_1 + i\omega c_1 + k_1 + k_c & -k_c \\ -k_c & -\omega^2 m_2 + i\omega c_2 + k_2 + k_c \end{bmatrix} \quad (16.9)$$

The spring constant k_c is real representing a loss-free coupling. The spring constants k_1 and k_2 have losses described by the parameters c_1 and c_2 as discussed in Chap. 1. The FTs of the displacements are given in matrix form as

$$\begin{Bmatrix} \hat{y}_1 \\ \hat{y}_2 \end{Bmatrix} = [B] \begin{Bmatrix} \hat{F}_1 \\ \hat{F}_2 \end{Bmatrix} = \begin{bmatrix} b_{11} & b_{12} \\ b_{21} & b_{22} \end{bmatrix} \begin{Bmatrix} \hat{F}_1 \\ \hat{F}_2 \end{Bmatrix}$$

$$[B] = [A]^{-1} = \begin{bmatrix} -\omega^2 m_2 + i\omega c_2 + k_2 + k_c & k_c \\ k_c & -\omega^2 m_1 + i\omega c_1 + k_1 + k_c \end{bmatrix} / \text{Det} [A] \quad (16.10)$$

The autospectrum of the velocity of oscillator 1 is, following the definitions in Sect. 2.7, given by

$$(G_{vv})_1 = \lim_{T \rightarrow \infty} \frac{\omega^2 |\hat{y}|^2}{T}$$

Consequently

$$\begin{aligned} (G_{vv})_1 &= \omega^2 [|b_{11}|^2 (G_{FF})_1 + |b_{12}|^2 (G_{FF})_2]; \\ (G_{vv})_2 &= \omega^2 [|b_{22}|^2 (G_{FF})_2 + |b_{21}|^2 (G_{FF})_1] \end{aligned} \quad (16.11)$$

The elements b_{ij} of the matrix $[B]$ are defined in Eq. (16.10). The time average of the total energy of oscillator 1 is obtained from (2.49) as

$$\bar{E}_1 = \frac{m_1}{2\pi} \int_0^\infty (G_{vv})_1 d\omega = \frac{m_1 \omega^2}{2\pi} \int_0^\infty [|b_{11}|^2 (G_{FF})_1 + |b_{12}|^2 (G_{FF})_2] d\omega \quad (16.12)$$

For white noise excitation $(G_{FF})_1$ and $(G_{FF})_2$ are constant. For a weak coupling between the oscillators it can be assumed that the total energy of oscillator 1 is the same as if oscillator 2 were stationary, i.e., as if y_2 were equal to zero. Based on these considerations and following the procedure outlined in Sect. 2.7, the time average of the total energy of oscillator 1 is obtained as

$$\bar{E}_1 = \frac{m_1}{2\pi} \int_0^\infty \frac{\omega^2 (G_{FF})_1}{|-m_1 \omega^2 + k_1 + k_c + i\omega c_1|^2} d\omega = \frac{(G_{FF})_1}{4c_1} \quad (16.13)$$

In a similar way the total energy of oscillator 2 is given by

$$\bar{E}_2 = \frac{(G_{FF})_2}{4c_2} \quad (16.14)$$

The energy flow from oscillator 2 to oscillator 1 is defined by its power spectral density

$$\begin{aligned} G_{\Pi_{21}} &= \text{Re} \left\{ -i\omega k_c [(G_{FF})_1 (b_{21} b_{11}^* - |b_{11}|^2) + (G_{FF})_2 (b_{22} b_{12}^* - |b_{12}|^2)] \right\} \\ &= \omega k_c [(G_{FF})_1 \text{Im}(b_{21} b_{11}^*) + (G_{FF})_2 \text{Im}(b_{22} b_{12}^*)] \end{aligned} \quad (16.15)$$

For a weak coupling between the oscillators or for $k_c \ll k_1$ and $k_c \ll k_2$ the elements b_{ij} of Eq. (16.10) can be approximated as

$$\begin{aligned} b_{11} &= \frac{1}{-m_1 \omega^2 + i\omega c_1 + k_1}; & b_{12} &= \frac{k_c}{(-m_1 \omega^2 + i\omega c_1 + k_1)(-m_2 \omega^2 + i\omega c_2 + k_2)} \\ b_{21} &= \frac{k_c}{(-m_1 \omega^2 + i\omega c_1 + k_1)(-m_2 \omega^2 + i\omega c_2 + k_2)}; & b_{22} &= \frac{1}{-m_2 \omega^2 + i\omega c_2 + k_2} \end{aligned}$$

These expressions in combination with Eq. (16.15) yield

$$G_{\Pi_{21}} = \frac{k_c^2}{m_1^2 m_2^2} \cdot \frac{\omega [\omega c_1 (G_{FF})_2 - \omega c_2 (G_{FF})_1]}{[(\omega_1^2 - \omega^2)^2 + (\omega c_1 / m_1)^2][(\omega_2^2 - \omega^2)^2 + (\omega c_2 / m_2)^2]} \quad (16.16)$$

According to Eqs. (16.13) and (16.14) the time average of the total energy of system n is $\bar{E}_n = (G_{FF})_n / (4c_n)$. Inserting this result in Eq. (16.16) gives

$$G_{\Pi_{21}} = \frac{4c_1 c_2 k_c^2}{m_1^2 m_2^2} [\bar{E}_2 - \bar{E}_1] \frac{\omega^2}{[(\omega_1^2 - \omega^2)^2 + (\omega c_1 / m_1)^2][(\omega_2^2 - \omega^2)^2 + (\omega c_2 / m_2)^2]} \quad (16.17)$$

The energy flow from oscillator 2 to oscillator 1 is given as

$$\bar{\Pi}_{21} = \frac{1}{2\pi} \int_0^\infty \text{Re}(G_{\Pi_{21}}) d\omega = \gamma_{21} (\bar{E}_2 - \bar{E}_1) \quad (16.18)$$

where

$$\begin{aligned} \gamma_{21} &= \frac{4c_1 c_2 k_c^2}{2\pi m_1^2 m_2^2} \int_0^\infty \frac{\omega^2 d\omega}{[(\omega_1^2 - \omega^2)^2 + (\omega c_1 / m_1)^2][(\omega_2^2 - \omega^2)^2 + (\omega c_2 / m_2)^2]} \\ &= \frac{k_c^2}{m_1 m_2} \left\{ \frac{c_2}{m_2 [(\omega_1^2 - \omega_2^2)^2 + (\omega_1 c_2 / m_2)^2]} \right. \\ &\quad \left. + \frac{c_1}{m_1 [(\omega_1^2 - \omega_2^2)^2 + (\omega_2 c_1 / m_1)^2]} \right\} \end{aligned} \quad (16.19)$$

It follows from Eq. (16.6) that

$$\bar{\Pi}_{12} = \gamma_{12} (\bar{E}_1 - \bar{E}_2); \quad \gamma_{12} = \gamma_{21} \quad (16.20)$$

The result (16.20) shows that the energy flow between two weakly coupled oscillators, each excited by a random force, white noise, is proportional to the energy difference between the oscillators. The parameter $\gamma_{12} = \gamma_{21}$ is always positive as given by Eq. (16.19). Consequently, the energy flow between the oscillators is always from the oscillator with the highest energy to the oscillator with the lowest energy. A complete analysis [258] of the energy flow between the oscillators shown in Fig. 16.2 gives the same basic result as for the simplified case discussed here. Thus, the energy flow between the oscillators shown in Fig. 16.2 is also proportional to the difference of energy between the two systems. However, the proportionality factor is different for the two cases.

Fahy et al. [270] investigated the energy flow between two oscillators having a nonconservative coupling consisting of a spring and a damper. It was found that the energy between the systems could be written as

$$\bar{\Pi}_{12} = \gamma'_{12} (\bar{E}_1 - \bar{E}_2) + \alpha \bar{E}_1 + \beta \bar{E}_2 \quad (16.21)$$

Consequently, for a nonconservative coupling between the oscillators the simple relationship (16.20) no longer holds.

The results (16.18) and (16.20) were derived based on some very important assumptions. These are:

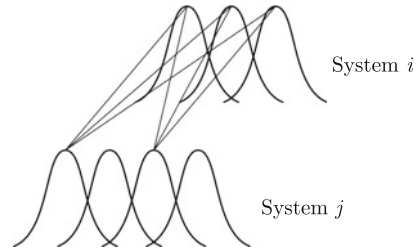
- (i) The forces exciting the oscillators are random, white noise, and thus uncorrelated.
- (ii) The losses of the oscillators are viscous, i.e., the parameters c_1 and c_2 in Eq. (16.2) are constant and thus frequency independent.
- (iii) The coupling parameter k_c is loss free.
- (iv) The energy of an oscillator is assumed to depend on the input power from the external force exciting the oscillator and to a lesser extent to the energy flow from the other system. This requirement can be formulated as $|\bar{\Pi}_1| \gg |\bar{\Pi}_{21}|$ for oscillator 1. Consequently, each oscillator is assumed to vibrate as if almost uncoupled to the other oscillator. This necessitates a weak coupling between the systems. A weak coupling also requires that $k_c \ll k_1$ and k_2 .
- (v) The natural angular frequencies ω_1 and ω_2 of the two systems should be well separated in order to make the coupling factors γ_{12} and γ_{21} small. Whenever the natural frequencies coincide the coupling factors are large as shown by Eq. (16.19). The requirement to weak coupling is no longer satisfied if $\omega_1 \approx \omega_2$.

The result (16.18) forms the basis for the technique referred to as Statistical Energy Analysis or quite simply SEA. In the next section the technique is extended to include energy flow between continuous systems like beams and plates.

16.3 Energy Flow Between Continuous Systems

“Rain on the roof” excitation of structures was discussed in Sects. 8.2 and 15.3. This type of excitation is equivalent to the structure being excited by a large number of sources scattered over its surface. Each source having the same strength or rather the

Fig. 16.3 Coupling between modes in two different systems



same power spectral density. The sources have white noise spectra and are consequently uncorrelated. For a structure excited in this way the time and space averages of the total energy per mode is the same if the losses in the system are viscous. This was demonstrated in Eqs. (6.81), (7.70), (8.39) and again in Eq. (15.50). If in a system each mode has the same energy, there is said to be an equipartition of energy. In a diffuse acoustic field in a closed space, the modal energy is the same assuming random excitation and a certain equivalent absorption area in the enclosed space. This is discussed in Problem 16.2.

If it is assumed that the coupling between any mode in one system and any other mode in a second system is the same, the simple concept of energy flow between two oscillators can be applied to describe the total energy flow between two continuous systems. The coupling between the modes of the two systems is illustrated in Fig. 16.3. Let, within a frequency band Δf , there be N_1 modes in system 1 and N_2 modes in system 2. The space and time average of the total energy of system 1 is $\bar{E}_{1\Delta f}$ and $\bar{E}_{2\Delta f}$ for system 2 within the same frequency band Δf . The modal energies for the two systems are

$$\varepsilon_1 = \bar{E}_{1\Delta f}/N_1; \quad \varepsilon_2 = \bar{E}_{2\Delta f}/N_2 \quad (16.22)$$

By defining the coupling loss factor between a mode of system 1 and a mode of system 2 by γ'_{12} the energy flow $\bar{\pi}_{12}$ between modes is, following the discussion in Sect. 16.2, written as

$$\bar{\pi}_{12\Delta f} = \gamma'_{12}(\varepsilon_1 - \varepsilon_2) \quad (16.23)$$

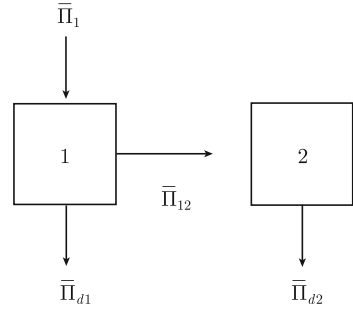
The total flow from N_1 modes in system 1 to N_2 modes in system 2 is consequently,

$$\bar{\Pi}_{12\Delta f} = N_1 N_2 \gamma'_{12}(\varepsilon_1 - \varepsilon_2) = \gamma'_{12}(\bar{E}_{1\Delta f} N_2 - \bar{E}_{2\Delta f} N_1) = \omega \eta_{12} \bar{E}_{1\Delta f} - \omega \eta_{21} \bar{E}_{2\Delta f} \quad (16.24)$$

The parameter η_{ij} is termed the coupling loss factor, or CLF, between the systems i and j . It follows from Eq. (16.24) that

$$\eta_{12}/N_2 = \eta_{21}/N_1 \quad (16.25)$$

Fig. 16.4 Energy flow between two continuous systems



Consider now the coupling between two multimode systems. One of the systems is excited by a force. The input power to system 1 is $\bar{\Pi}_1$. The energy flow between the systems is illustrated in Fig. 16.4.

The energy flows are written

$$\bar{\Pi}_1 = \bar{\Pi}_{d1} + \bar{\Pi}_{12}; \quad \bar{\Pi}_{12} = \bar{\Pi}_{d2} \tag{16.26}$$

The power dissipated in system i is following Eq. (16.7) $\bar{\Pi}_i = \omega \eta_i \bar{\mathcal{E}}_i$. The energy flow $\bar{\Pi}_{12}$ is according to Eq. (16.24) $\bar{\Pi}_{12} = \omega \eta_{12} \bar{\mathcal{E}}_1 - \omega \eta_{21} \bar{\mathcal{E}}_2$. These expressions inserted in Eq. (16.26) give the energies and the ratio between the energies of the systems as

$$\begin{aligned} \bar{\mathcal{E}}_1 &= \bar{\Pi}_1 \frac{\eta_2 + \eta_{21}}{\omega[(\eta_1 + \eta_{12})(\eta_2 + \eta_{21}) - \eta_{12}\eta_{21}]}; \\ \bar{\mathcal{E}}_2 &= \bar{\Pi}_1 \frac{\eta_{12}}{\omega[(\eta_1 + \eta_{12})(\eta_2 + \eta_{21}) - \eta_{12}\eta_{21}]} \\ \frac{\bar{\mathcal{E}}_1}{\bar{\mathcal{E}}_2} &= \frac{\eta_2 + \eta_{21}}{\eta_{12}} \end{aligned} \tag{16.27}$$

For a weak coupling, $\eta_1 \gg \eta_{12}$ and $\eta_2 \gg \eta_{21}$. Thus from Eq. (16.27)

$$\bar{\mathcal{E}}_1 \approx \frac{\bar{\Pi}_1}{\omega \eta_1}; \quad \bar{\mathcal{E}}_2 \approx \frac{\eta_{12} \bar{\Pi}_1}{\omega \eta_1 \eta_2}; \quad \frac{\bar{\mathcal{E}}_1}{\bar{\mathcal{E}}_2} \approx \frac{\eta_2}{\eta_{12}} \tag{16.28}$$

The energies can be reduced by increasing the losses of system 1 or of both systems when the coupling is weak.

For a strong coupling, $\eta_{12} \gg \eta_1$ and $\eta_{21} \gg \eta_2$. Thus

$$\begin{aligned} \bar{\mathcal{E}}_1 &\approx \frac{\bar{\Pi}_1}{\omega(\eta_1 + \eta_2 \eta_{12} / \eta_{21})} = \frac{\bar{\Pi}_1}{\omega(\eta_1 + \eta_2 N_2 / N_1)}; \\ \bar{\mathcal{E}}_2 &\approx \frac{\bar{\Pi}_1}{\omega(\eta_2 + \eta_1 N_1 / N_2)}; \quad \frac{\bar{\mathcal{E}}_1}{\bar{\mathcal{E}}_2} \approx \frac{\eta_{21}}{\eta_{12}} = \frac{N_1}{N_2} \end{aligned} \tag{16.29}$$

The modal energy is the same in both systems when the coupling is strong.

For a lightly damped system any FRF exhibits narrow peaks. As the damping of the system is increased the amplitude of the peaks decreases and the width of the peaks widens and the peaks start to overlap as shown in Fig. 16.3. This overlapping effect improves the coupling between resonant systems. The so-called modal overlap $\mathcal{M}(f)$ is defined as the ratio between the half bandwidth of a resonance peak and the average frequency space between two natural frequencies. The half bandwidth is defined in Eq. (2.87) as $f_1 - f_2 = f_0\eta$ where η is the loss factor of the system at its natural frequency f_0 . The frequencies f_1 and f_2 are the frequencies for which $|H|^2$ has dropped 3 dB from its maximum. The FRF is given by H . The average frequency distance between two natural frequencies is $\Delta f = 1/\mathcal{N}_f$ where \mathcal{N}_f is the modal density of the system. Following these definitions the modal overlap is given as

$$\mathcal{M}(f) = \eta \cdot f \cdot \mathcal{N}_f(f) \quad (16.30)$$

The response of a structure depends strongly on the modal overlap. For $\mathcal{M} \ll 1$ distinct resonances can be observed. The resonant peaks occur at the same frequency irrespective of the observation or measurement point. For $\mathcal{M} \gg 1$ many resonances overlap and no distinct peaks can be recorded. The frequency of a peak can vary depending on the observation point. It is suggested, for example, by Fahy and Mohammed [271] that the modal overlap should be greater than 1 to satisfy the basic assumptions of SEA. Although the study [271] was limited to some simple cases, the requirement $\mathcal{M}_i > 1$ has prevailed. Experience has shown that the modal overlap should exceed unity for SEA to be applicable for estimating the energy distribution between coupled systems.

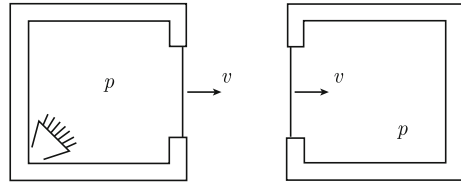
The number of modes within a frequency band is of prime importance for making a successful estimate of the energy of a resonant system. This was discussed in Sect. 6.4. Compare Figs. 16.6 and 16.7. Preferably, there should be more than four modes per frequency band for using SEA for estimating energies of resonant systems.

16.4 Coupling Between Acoustic Fields and Vibrating Structures

One of the first successful applications of the SEA technique was the prediction of plate vibrations induced by strong acoustic fields. This type of problem is of importance for any type of spacecraft. High vibration levels can lead to material fatigue. The coupling between vibrating structures and acoustic fields using the SEA technique is discussed by Lyon [258]. A different approach is used in Sect. 13.2 for the prediction of the response of flat rectangular plates which are excited by acoustic fields. The response of curved plates was discussed in Sect. 15.6.

Another problem is illustrated in Fig. 16.5. A plate is facing an enclosed space. The plate is exposed to “rain on the roof excitation” discussed in Sect. 15.3. The acoustic

Fig. 16.5 Plate excited by an acoustic field, left, and plate radiating sound into a closed space



power $\bar{\Pi}_{\text{rad}}$ radiated by the vibrating panel into the enclosed space is according to Eq. (12.97) given by

$$\bar{\Pi}_{\text{rad}} = \rho_0 c S \bar{\sigma}_r |\bar{v}|^2 \quad (16.31)$$

where $\bar{\sigma}_r$ is the sound radiation ratio discussed in Sect. 12.9 and defined in Eqs. (12.98) through (12.100). The radiated power can also be written as

$$\bar{\Pi}_{\text{rad}} = \omega \eta_{12} \bar{\mathcal{E}}_1 = \omega \eta_{12} \mu S |\bar{v}|^2 \quad (16.32)$$

The Eqs. (16.26) and (16.27) give

$$\eta_{12} = \frac{\rho_0 c \bar{\sigma}_r}{\mu \omega} \quad (16.33)$$

The coupling loss factor η_{21} between the acoustic field and the plate is according to Eq. (16.25) equal to $\eta_{21} = N_1 \eta_{12} / N_2$ where N_1 and N_2 are the number of modes within the frequency band Δf of the plate and the enclosed space respectively. N_1 and N_2 are given in Eqs. (8.18) and (11.137) as

$$N_1 = \Delta f \cdot \frac{S}{2} \sqrt{\frac{\mu}{D_0}} = \Delta f \cdot \frac{\pi f_c}{c^2}; \quad N_2 = \Delta f \cdot \frac{4\pi f^2 V}{c^3} \quad (16.34)$$

The center frequency of the band is f . The critical frequency of the structure is f_c and is according to Eq. (12.18) defined as $f_c = c^2 / (2\pi) \sqrt{\mu / D_0}$. The volume of the closed space is V and the speed of sound in the enclosed fluid is c . Consequently, the coupling loss factor η_{21} is obtained as

$$\eta_{21} = \frac{N_1}{N_2} \eta_{12} = \frac{\rho_0 c^4 \bar{\sigma}_r S}{16\pi^2 f^3 V_1 \sqrt{\mu D_0}} = \frac{\rho_0 c^2 \bar{\sigma}_r f_c S}{8\pi f^3 \mu V_1} \quad (16.35)$$

Following the result (11.155) the average pressure squared in a closed space, volume V , with a diffuse acoustic field, total energy \mathcal{E} , is

$$\langle |\bar{p}|^2 \rangle = \rho_0 c^2 \bar{\mathcal{E}} / V \quad (16.36)$$

For a plate excited by an acoustic field in a closed space the total energy \mathcal{E}_1 of the plate is obtained from

$$\bar{\Pi}_{21} = \omega\eta_{21}\bar{E}_2 = \omega\eta_{d1}\bar{E}_1 = \omega\eta_{d1}S\mu\langle|\bar{v}|^2\rangle$$

Thus,

$$\langle|\bar{v}|^2\rangle = \langle|\bar{p}|^2\rangle \frac{c^2\bar{\sigma}_r}{16\pi^2 f^3\eta_{d1}D_0^{1/2}\mu^{3/2}} = \langle|\bar{p}|^2\rangle \frac{\bar{\sigma}_r \cdot f_c}{8\pi \cdot f^3\eta_{d1}\mu^2} \quad (16.37)$$

However, the response of the structure is not only due to the coupling between resonant modes in the acoustic space and modes of the vibrating structure. There is also a nonresonant coupling between the structures. In the low-frequency region, $f < f_c/2$, the response of the plate is determined by its mass rather than its stiffness as discussed in Sect. 13.1. The velocity v_0 of a mass exposed to a pressure p_w is $v_0 = p_w/(i\omega\mu)$. The pressure squared on the wall is twice as high as the average pressure squared in the enclosure. Thus

$$\langle|\bar{v}_0|^2\rangle = \frac{2\langle|\bar{p}|^2\rangle}{(\mu\omega)^2} \quad (16.38)$$

The total velocity squared is assuming uncorrelated resonant and nonresonant fields are from Eqs. (16.37) and (16.38) obtained as

$$\langle|\bar{v}|^2\rangle = \langle|\bar{p}|^2\rangle \left[\frac{2}{(2\pi f\mu)^2} + \frac{\bar{\sigma}_r \cdot f_c}{8\pi \cdot f^3\eta_{d1}\mu^2} \right] \quad (16.39)$$

In the low frequency region, $f < f_c/2$, the radiation ratio $\bar{\sigma}_r$ is very small resulting in that the first term inside the bracket dominates over the second expression. The response of the plate can for $f < f_c/2$ be written as

$$L_{p/v} = 10 \log \left[\frac{2(\rho_0 c)^2}{(\mu\omega)^2} \right] \approx -9 - R_d \text{ dB for } f < f_c/2 \quad (16.40)$$

The sound transmission loss of structure R_d is defined in Eq. (13.21). The result (16.40) is the same as that previously derived in Sect. 13.2.

In the high-frequency region, $f > f_c$, the radiation ratio $\bar{\sigma}_r > 1$ and the second expression inside the bracket of Eq. (16.39) dominates over the first expression. Consequently, the response of the structure is given by

$$L_{p/v} = 10 \log \left[\frac{(\rho_0 c)^2 \langle|\bar{v}|^2\rangle}{\langle|\bar{p}|^2\rangle} \right] = 10 \log \bar{\sigma}_r - 10 \log \left(\frac{f^3\eta_{d1}\mu^2}{f_c} \right) + 38 \approx -6 - R_d \text{ dB} \quad (16.41)$$

where R_d is the sound transmission loss of the panel for $f \gg f_c$. The result is the same as that presented at the end of Sect. 13.2 for $f > f_c$.

Throughout the discussion it has been assumed that the coupling loss factors between different modes of the plate and the acoustic field are the same. However, in

Sect. 12.9 it was shown that the modal radiation ratio depends on the vibration mode of the panel. In particular this is the case in the low-frequency region. The results of Fig. 16.9 show that the modal radiation ratios converge for $f > f_c/2$ where f_c is the critical frequency of the plate. This would make the result (16.39) valid for $f > f_c/2$ only. However, in the low-frequency region $\bar{\sigma}_r \ll 1$ and the result (16.39) is approximately correct even in this frequency range.

16.5 Prediction of Sound Transmission Through a Panel Using SEA

The sound transmission loss of a panel mounted between two reverberant rooms can be predicted based on the SEA technique as suggested by Crocker and Price in [178]. The problem is illustrated in Fig. 16.6. A loudspeaker is generating acoustic power $\bar{\Pi}_1$ into room 1. The energy flow between the rooms 1 and 3 is caused by resonant and nonresonant transmissions. The acoustic field in room 1 induces reverberant vibrations of the structure. This energy flow is denoted $\bar{\Pi}_{12}$. The resulting resonant vibrations of the plate radiate power $\bar{\Pi}_{23}$ into room 3. The nonresonant transmission between the rooms is given by $\bar{\Pi}_{13}$. The rooms and the structure all have losses denoted $\bar{\Pi}_{dn}$ for $n = 1, 2$ and 3.

The balance of energy between the systems shown in Fig. 16.6 requires that

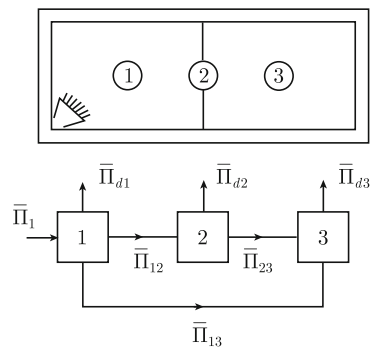
$$\bar{\Pi}_1 = \bar{\Pi}_{12} + \bar{\Pi}_{13} + \bar{\Pi}_{d1}; \quad \bar{\Pi}_{12} = \bar{\Pi}_{23} + \bar{\Pi}_{d2}; \quad \bar{\Pi}_{13} + \bar{\Pi}_{23} = \bar{\Pi}_{d3} \quad (16.42)$$

The total energy of system i is given by \bar{E}_i . The loss factor of system i is η_{di} . The power $\bar{\Pi}_{di}$ dissipated in system i is

$$\bar{\Pi}_{di} = \omega \eta_{di} \bar{E}_i \quad (16.43)$$

The energy flow $\bar{\Pi}_{ij}$ between systems i and j is according to Eqs. (16.24) and (16.25) given by

Fig. 16.6 A panel mounted between two rooms and the corresponding energy flow chart. An acoustic source is operating in room 1



$$\bar{\Pi}_{ij} = \omega \eta_{ij} N_i \left(\frac{\bar{E}_i}{N_i} - \frac{\bar{E}_j}{N_j} \right) \quad (16.44)$$

In addition, from Eq. (16.25) $\eta_{ij}/N_j = \eta_{ji}/N_i$. The Eqs. (16.42) through (16.44) give

$$\frac{\bar{E}_1}{\bar{E}_3} = \frac{(\eta_{d3} + \eta_{31} + \eta_{32})(\eta_{d2} + \eta_{21} + \eta_{23}) - \eta_{32}\eta_{23}}{\eta_{13}(\eta_{d2} + \eta_{21} + \eta_{23}) + \eta_{12}\eta_{23}} \quad (16.45)$$

The derivation is left for Problem 16.3. In most practical cases the dissipated power in a room due to its absorption is much larger than caused by the energy flow from the acoustic field in the room to the panel and to the other room. Thus, $\eta_{d3} \gg \eta_{32}$ and $\eta_{d3} \gg \eta_{31}$. If these conditions are satisfied the coupling is often referred to as being weak. In general, the coupling between resonant acoustic fields and vibration fields are weak. The total loss factor $\eta_{2\text{tot}}$ of the panel is the sum of the internal loss factor η_{d2} and the losses due its radiation to the rooms. Consequently, $\eta_{2\text{tot}} = \eta_{d2} + \eta_{21} + \eta_{23}$. The ratio between the pressure squared in the two rooms is therefore reduced to

$$\frac{\langle |\bar{p}_1|^2 \rangle}{\langle |\bar{p}_3|^2 \rangle} = \left(\frac{\bar{E}_1 V_3}{\bar{E}_3 V_1} \right) \approx \frac{V_3}{V_1} \cdot \frac{\eta_{d3}}{\eta_{13} + \eta_{12}\eta_{23}/\eta_{2\text{tot}}} \quad (16.46)$$

According to Eq. (16.34) the number of modes within the frequency band Δf in room i is

$$N_i = \Delta f \cdot \frac{4\pi f^2 V_i}{c^3} \text{ for } i = 1 \text{ or } 3 \quad (16.47)$$

The number of modes of the structure is given by Eq. (16.34) as

$$N_2 = \Delta f \cdot \frac{\pi f_c S}{c^2} \quad (16.48)$$

The loss factors η_{d1} and η_{d3} in the rooms 1 and 3 can be expressed by means of the equivalent absorption area A_i . Equation (11.159) gives

$$\eta_{di} = \frac{A_i c}{8\pi f V_i} \text{ for } i = 1 \text{ or } 3 \quad (16.49)$$

The coupling loss factors η_{21} and η_{23} determine the resonant sound radiation from the vibrating plate and are given by Eq. (16.34) as

$$\eta_{2j} = \frac{\rho_0 c^2 \bar{\sigma}_r S f_c}{8\pi f^3 \mu V_j} \text{ for } j = 1 \text{ or } 3 \quad (16.50)$$

In the low-frequency region the nonresonant sound transmission through the panel determines the ratio between the pressure squared in the two rooms. In Sect. 11.15 it was shown that for $f \ll f_c$ this ratio is given by

$$\frac{\langle |\bar{p}_1|^2 \rangle}{\langle |\bar{p}_3|^2 \rangle} = \frac{A_3}{\tau_d S} \quad (16.51)$$

where τ_d is the sound transmission coefficient of the panel for nonresonant transmission assuming a diffuse acoustic field in the source room. The sound transmission loss R_d for nonresonant transmission is given in Eq. (13.21) or alternatively in Eq. (13.22). The transmission coefficient can also be written as

$$\tau_d = 10^{-R_d/10}$$

The coupling loss factor η_{13} defining the nonresonant transmission is obtained from Eq. (16.51) as

$$\eta_{13} = \frac{N_3 \tau_d S \eta_{d3}}{N_1 A_3} = \frac{\tau_d S c}{8 \pi f V_1} \quad (16.52)$$

Compare Problem 16.4. Finally, by using Eq. (16.25), i.e., $\eta_{ij}/N_j = \eta_{ji}/N_i$, the expression (16.46) giving the sound pressure level difference between the two rooms is written

$$\Delta L_p = 10 \log A_3 - 10 \log S - 10 \log \left[\tau_d + \frac{(\rho_0 c)^2 \bar{\sigma}_r^2 f_c}{2 \pi \mu^2 f^3 \eta_{2\text{tot}}} \right] \quad (16.53)$$

$$R = -10 \log \tau = -10 \log \left[\tau_d + \frac{(\rho_0 c)^2 \bar{\sigma}_r^2 f_c}{2 \pi \mu^2 f^3 \eta_{2\text{tot}}} \right] \quad (16.54)$$

In high-frequency region for $f > f_c$ the last term inside the bracket of the expression (16.54) dominates. In this frequency region $\bar{\sigma}_r = 1/\sqrt{1 - f_c/f}$ and the sound transmission loss is reduced to

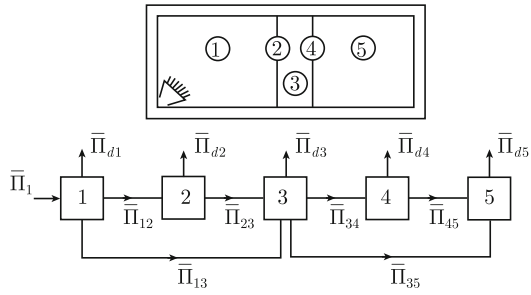
$$\begin{aligned} R &\approx 10 \log \left[\frac{2 \pi \mu^2 f^3 \eta_{2\text{tot}}}{(\rho_0 c)^2 \bar{\sigma}_r^2 f_c} \right] \\ &= 20 \log \mu + 30 \log f + 10 \log \eta_{2\text{tot}} + 10 \log(1 - f_c/f) - 45 \end{aligned} \quad (16.55)$$

This is the same result as presented in Eq. (13.30). It can be noted that $\tau > \tau_d$, consequently $R < R_d$. Thus, the sound transmission loss of an infinite panel can never exceed the sound transmission loss of a limp panel having the same mass. In the low-frequency range, $f < f_c$, the SEA derived sound transmission loss does not quite agree with results based on other models. This is discussed in Sect. 16.7.

16.6 Sound Transmission Through Double Walls

The procedure for the prediction of the sound transmission loss of single leaf panels can be extended also to include double wall constructions as demonstrated by Price and Crocker [272]. Figure 16.7 shows a double wall construction separating two

Fig. 16.7 A double wall mounted between two rooms and the corresponding energy flow chart. An acoustic source is operating in room 1



reverberant rooms. There are no connections between the two panels except along the frame that is assumed to be infinitely stiff. As in the previous case, discussed in Sect. 16.5, the sound pressure level difference between the two reverberant rooms 1 and 5 is determined by both resonant and nonresonant transmissions. The energy flow between the systems is also illustrated in Fig. 16.7.

The nonresonant energy flow from the source room 1 to the cavity 3 between the plates is denoted $\bar{\Pi}_{13}$ and from the cavity to room 5 by $\bar{\Pi}_{35}$. The energy balance for the various systems gives

$$\begin{aligned} \bar{\Pi}_1 &= \bar{\Pi}_{1d} + \bar{\Pi}_{12} + \bar{\Pi}_{13}; & \bar{\Pi}_{12} &= \bar{\Pi}_{2d} + \bar{\Pi}_{23}; & \bar{\Pi}_{13} + \bar{\Pi}_{23} &= \bar{\Pi}_{3d} + \bar{\Pi}_{34} + \bar{\Pi}_{35} \\ \bar{\Pi}_{34} &= \bar{\Pi}_{4d} + \bar{\Pi}_{45}; & \bar{\Pi}_{35} + \bar{\Pi}_{45} &= \bar{\Pi}_{5d} \end{aligned} \tag{16.56}$$

As before

$$\bar{\Pi}_{id} = \omega \eta_{di} \bar{E}_i; \quad \bar{\Pi}_{ij} = \omega \eta_{ij} N_i (\bar{E}_i / N_i - \bar{E}_j / N_j); \quad N_i \eta_{ij} = N_j \eta_{ji} \tag{16.57}$$

The ratio between the pressure squared in the rooms is

$$\frac{\langle |\bar{p}_1|^2 \rangle}{\langle |\bar{p}_5|^2 \rangle} = \left(\frac{\bar{E}_1 V_5}{\bar{E}_5 V_1} \right) \tag{16.58}$$

The ratio \bar{E}_5 / \bar{E}_1 is obtained from Eqs. (16.57) to (16.58) as

$$\begin{aligned} \frac{\bar{E}_1}{\bar{E}_5} &= \frac{\left(\eta_{5\text{tot}} + \frac{\eta_{54} \eta_{35}}{\eta_{34}} \right) \left[\frac{\eta_{4\text{tot}}}{\eta_{34}} \left(\eta_{3\text{tot}} - \frac{\eta_{23} \eta_{32}}{\eta_{2\text{tot}}} \right) - \eta_{43} \right]}{\left(\eta_{45} + \frac{\eta_{4\text{tot}} \eta_{35}}{\eta_{34}} \right) \left(\eta_{13} + \frac{\eta_{12} \eta_{23}}{\eta_{2\text{tot}}} \right)} \\ &\quad - \frac{\left(\eta_{45} + \frac{\eta_{4\text{tot}} \eta_{35}}{\eta_{34}} \right) \left[\frac{\eta_{54}}{\eta_{34}} \left(\eta_{3\text{tot}} - \frac{\eta_{23} \eta_{32}}{\eta_{2\text{tot}}} \right) + \eta_{53} \right]}{\left(\eta_{45} + \frac{\eta_{4\text{tot}} \eta_{35}}{\eta_{34}} \right) \left(\eta_{13} + \frac{\eta_{12} \eta_{23}}{\eta_{2\text{tot}}} \right)} \end{aligned} \tag{16.59}$$

The total loss factor $\eta_{i\text{tot}}$ of system i is the sum of internal plus radiation losses, thus $\eta_{i\text{tot}} = \eta_{di} + \sum_j \eta_{ij}$. The coupling loss factors and modal densities are in principal derived as discussed in the previous sections. However, the volume of the cavity between the plates is very small and the coupling between the cavity and other systems has to be considered. If the distance d between the two plates of the double structure is less than one-half wavelength in the enclosed fluid only modes parallel to the plates can exist. Price and Crocker therefore assumed that the modal density in the cavity is given by

$$\mathcal{N}_3 = \frac{2\pi f S}{c^2} \quad \text{for } f < \frac{c}{2d}; \quad \mathcal{N}_3 = \frac{4\pi f^2 S d}{c^3} \quad \text{for } f > \frac{c}{2d} \quad (16.60)$$

The details are left for Problem 16.5. It is assumed that the part of the cavity not facing the plates, area S_c , is clad by a material with a sound absorption coefficient α_0 . It is assumed that the equivalent absorption area in the cavity is $S_c \alpha_0$ for $f < c/(2d)$ and $2S_c \alpha_0/3$ for $f > c/(2d)$. Thus,

$$\eta_{3\text{tot}} = \frac{S_c \alpha_0 c}{8\pi f V_3} \quad \text{for } f < \frac{c}{2d}; \quad \eta_{3\text{tot}} = \frac{S_c \alpha_0 c}{12\pi f V_3} \quad \text{for } f > \frac{c}{2d} \quad (16.61)$$

It is also assumed by Price and Crocker that the radiation efficiency of a plate facing the cavity is twice the radiation efficiency valid for free field conditions for frequencies below the critical frequency. This is formulated as

$$\eta_{i3} = \frac{\rho_0 c \bar{\sigma}_{ir}}{\pi \mu_i f} \quad \text{for } f < f_{ci}; \quad \eta_{i3} = \frac{\rho_0 c \bar{\sigma}_{ir}}{2\pi \mu_i f} \quad \text{for } f > f_{ci} \text{ and } i = 2 \text{ or } 4 \quad (16.62)$$

The number of modes in the rooms 1 and 5 within the frequency band Δf are

$$N_i = \Delta f \cdot \frac{2f^2 V_i}{c^3} \quad \text{for } i = 1 \text{ and } 5 \quad (16.63)$$

The number of panel modes is

$$N_i = \Delta f \cdot \frac{S f_{ci}}{c^2} \quad \text{for } i = 2 \text{ and } 4 \quad (16.64)$$

The remaining parameters are, as discussed in the previous sections, given by

$$\begin{aligned} \eta_i &= \frac{A_i c}{8\pi f V_i} \quad \text{for } i = 1 \text{ and } 5 \\ \eta_{21} &= \frac{\rho_0 c \bar{\sigma}_{2r}}{2\pi f \mu_2} \quad \eta_{45} = \frac{\rho_0 c \bar{\sigma}_{4r}}{2\pi f \mu_4} \end{aligned} \quad (16.65)$$

The equations (16.59) through (16.65) inserted in the expression (16.58) gives the sound pressure level difference between the rooms separated by the double construction. The resulting sound transmission loss of the double construction is approximately equal to the transmission loss already presented in Sect. 13.10. The main difference between the results depends on how the acoustic field inside the cavity is described. Based on experience the previously discussed formulae (13.127) through (13.129) give satisfactory results as compared to measurements. In addition to problems of modeling the acoustic field inside the cavity also the coupling between the plates via the common frame is a source of error. The acoustic properties of double walls with mechanical couplings between the plates are described by Craik [268] using the SEA technique. The acoustic performances of various types of double constructions are also discussed extensively by Fahy [189], Vigran [149] and Kristensson and Rindel [188]. See also Sect. 16.7.

The sound transmission between two rooms separated by a structure is not only determined by the direct transmission through but also by energy flow, or flanking transmission, via the adjoining structures as discussed in Sect. 13.11. SEA estimates of flanking transmission are discussed by Craik [268], Guyader [273], Kihlman [193], and others. Flanking transmission will increase the transmission between the rooms and thus also decrease the expected measured sound transmission loss of the structure separating the rooms.

16.7 Limitation of SEA-Derived Sound Transmission Loss

A number of different methods for the prediction of the sound transmission loss of single leaf panels have been discussed extensively in Chap. 13, then again in Sect. 14.16, and finally in Sect. 16.5. The models of Chap. 13 and Sect. 14.16 give rather similar results. These models all reveal that the sound transmission loss of even a very large panel or in fact an infinite panel is increasing with frequency as predicted by the simple mass law in the low-frequency region. As the frequency is approaching the critical frequency there is a smooth gradual deviation from the simple mass law curve as given by R_1 and R_2 in Fig. 13.3. The transmission loss, Eq. (16.54), derived from SEA, does not exhibit this tendency. As the panel area becomes very large the radiation ratio $\bar{\sigma}_r$ of Eq. (16.54) tends to zero as given in Eq. (12.98) for $f < f_c$. The radiation ratio for an infinite panel is equal to zero for $f < f_c$, as discussed in Sect. 12.1, Eq. (12.19). The resulting sound transmission loss for a large panel is according to the SEA model, Eq. (16.54) with $\bar{\sigma}_r = 0$ for $f < f_c$, therefore given by R_3 in Fig. 13.3. The curve given by R_3 is increasing more or less linearly up to $f = f_c$. Thereafter R_3 drops sharply at the critical frequency to increase again for $f > f_c$. The reason for this anomaly is that the radiation ratio for a plate excited by an acoustic field is different from and larger than the radiation ratio resulting from free vibrations for $f < f_c$ as previously discussed in Sect. 13.2. The acoustic power radiated from a plate excited by an acoustic field is determined by the velocity of the plate and the radiation ratio $\bar{\sigma}_a$. This parameter $\bar{\sigma}_a$ was first derived for an infinite

panel in Sect. 13.2. It was found that $\bar{\sigma}_a$ approaches 3/2 as the frequency tends to zero. The corresponding radiation ratio for a wall mounted between two rooms was in Eq. (13.126) found to be equal to 2 as the dimensions of the rooms tend to infinity. In an ideal world the results for the two cases should have been the same. In the high-frequency region, $f > f_c$, the radiation ratios $\bar{\sigma}_r$ and $\bar{\sigma}_a$ are equal and given as $\bar{\sigma}_r = \bar{\sigma}_a = 1/\sqrt{1 - f_c/f}$. The modal radiation ratio σ_{mn} , defined in Eq. (12.96) and used in Eq. (14.98) is not equal to $\bar{\sigma}_r$. The parameter $\bar{\sigma}_r$ is a modal average of σ_{mn} . In the expression (14.98) giving the sound transmission coefficient for a wall the modal radiation ratio is weighted with respect to the various modes by means of the denominator. The sound transmission coefficient is given as

$$\tau_d = \sum_{mn} \frac{16\pi\rho_0^2 c^4 \sigma_{mn}^2}{\mu^2 L_x L_y [(\omega_{mn}^2 - \omega^2)^2 + (\eta_{mn} \omega_{mn}^2)^2]} \quad (16.66)$$

For $f > f_c$, $\sigma_{mn} = \bar{\sigma}_a = 1/\sqrt{1 - f_c/f}$. The summation of the expression (16.66) should be made over all the plate modes. According to Eq. (8.19)

$$\frac{\Delta N}{\Delta \omega} = \frac{L_x L_y}{4\pi} \sqrt{\frac{\mu}{D_0}}$$

Thus, $\bar{\tau}_d = \sum_{mn} \tau_{mn} \rightarrow \int d\omega \frac{\Delta N}{\Delta \omega} \tau_{mn}$. By using the expressions (8.19) and (16.66) the result is

$$\bar{\tau}_d = \frac{4\rho_0^2 c^4}{\mu^2} \sqrt{\frac{\mu}{D_0}} \cdot \int_{\omega_{mn} - \Delta\omega/2}^{\omega_{mn} + \Delta\omega/2} \frac{d\omega}{[(\omega_{mn}^2 - \omega^2)^2 + (\eta\omega_{mn}^2)^2](1 - f_c/f)} \quad (16.67)$$

This is by now a standard integral, first discussed in Sect. 2.7. The solution to Eq. (16.67) is

$$\bar{\tau}_d = \frac{2\pi\rho_0^2 c^4}{\mu^2 \eta \omega_{mn}^3 (1 - f_c/f_{mn})} \sqrt{\frac{\mu}{D_0}}$$

By setting $f_c = \frac{c^2}{2\pi} \sqrt{\frac{\mu}{D_0}}$ and $\omega = \omega_{mn}$ the result reads

$$\bar{\tau}_d = \frac{(\rho_0 c)^2 f_c}{2\pi \mu^2 f^3 \eta (1 - f_c/f)} \quad (16.68)$$

This is the same result as that previously given by Eq. (13.29).

Also in the very low-frequency region the modal radiation ratio is constant and independent of the modal numbers or $\sigma_{mn} = \bar{\sigma}_a$. For $f \ll f_c$ Eq. (16.66) is reduced to

$$\tau_d = \sum_{mn} \frac{16\pi\rho_0^2 c^4 \bar{\sigma}_a^2}{\mu^2 L_x L_y \omega^4} \quad (16.69)$$

The number of acoustic modes N exciting the plate is according to Eq. (13.78) equal to $N = L_x L_y k^2 / (4\pi)$ where k is the wavenumber in the fluid. Thus

$$\bar{\tau}_d = \sum_{mn} \frac{16\pi\rho_0^2 c^4 \bar{\sigma}_a^2}{\mu^2 L_x L_y \omega^4} = N \frac{16\pi\rho_0^2 c^4 \bar{\sigma}_a^2}{\mu^2 L_x L_y \omega^4} = \frac{4\rho_0^2 c^2 \bar{\sigma}_a^2}{\mu^2 \omega^2} \quad (16.70)$$

For $\bar{\sigma}_a = 2$ as given by Eq. (13.126) for the plate dimensions approaching infinity the sound transmission loss is obtained as

$$R = 20 \log \mu + 20 \log f - 48 \text{ dB}$$

This is the same result as previously given by Eq. (13.86).

The two examples discussed above illustrate that the parameter $\bar{\sigma}_a$ can be used to calculate the sound transmission loss of a panel. The parameter $\bar{\sigma}_a$ is the sound radiation ratio for a panel excited by an acoustic field. The radiation ratio $\bar{\sigma}_r$ is the result of radiation from resonant vibrations of a plate. For an infinite plate $\bar{\sigma}_a > 0$ and $\bar{\sigma}_r = 0$ for $f < f_c$. For $f > f_c$, $\bar{\sigma}_a = \bar{\sigma}_r = 1/\sqrt{1 - f_c/f}$. It also follows that the radiation ratio $\bar{\sigma}_r$ cannot be used indiscriminately in SEA calculations.

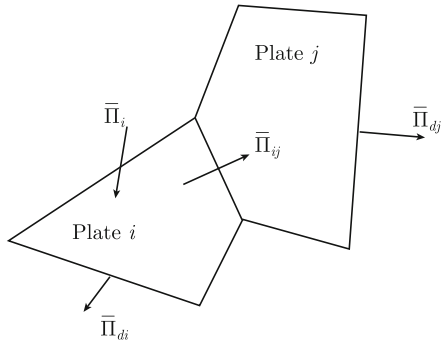
16.8 Coupling Between Vibrating Structures

The applicability of SEA is often based on the assumption that the coupling between the resonant systems of the entire structure is weak. In general the coupling between a structure and an acoustic field is weak. Often a coupling between two systems i and j is referred to as weak if the coupling loss factor η_{ij} between them is much smaller than η_{id} that determines the dissipated power in the system. According to this definition a weak coupling requires $\eta_{ij} \ll \eta_{id}$ as discussed in Sect. 16.3. Further, it is argued in Sect. 16.3 that the modal overlap should exceed unity, i.e.,

$$\mathcal{M}_i = \eta_i f \mathcal{N}_i > 1 \quad (16.71)$$

Over the years a very large number of papers on SEA has been published. There are many numerical comparisons between the energy flow between simple structures using exact methods and the SEA technique. In general fair agreement is obtained in the high-frequency region. However, it is not always possible to define the lower frequency limit for neither the applicability of SEA nor the possible error of a prediction. Despite these fundamental shortcomings the SEA technique in its most primitive form has been used rather successfully to predict the energy flow in complicated structures like buildings, ships, and trains. The ultimate test of any prediction method is a comparison with measured results. This type of comparison would indicate frequency limits, accuracy of the coupling loss factors used, and approximate errors. Once a model has been tested and calibrated the model could be used for parameter

Fig. 16.8 Two plate elements coupled via a junction



studies answering vital questions like; what happens if the material and geometrical parameters of an element in a large construction are changed?

Of primary concern for any SEA calculation is the estimation of the coupling loss factors. The energy flow between coupled plate elements were discussed in Sect. 5.12. The coupling between two elements is illustrated in Fig. 16.8. According to Eq. (5.153) the energy flow across the junction between the plates is for flexural vibrations given by

$$\bar{\Pi}_{ij} = \frac{\bar{E}_i c_{gi} \bar{\tau}_{ij} L_{ij}}{\pi S_i} = \omega \eta_{ij} \bar{E}_i \quad (16.72)$$

The group velocity for flexural waves on plate i is c_{gi} , the length of the junction between the plates is L_{ij} and the average transmission coefficient, assuming a diffuse field on plate i , is $\bar{\tau}_{ij}$. The area of plate i is S_i . The coupling loss factor between the plates is obtained from Eq. (16.72) as

$$\eta_{ij} = \frac{c_{gi} \bar{\tau}_{ij} L_{ij}}{\pi \omega S_i} = \frac{2D_{0i}^{1/4} \bar{\tau}_{ij} L_{ij}}{\pi \omega^{1/2} \mu_i^{1/4} S_i} \quad (16.73)$$

The bending stiffness and mass per unit area of plate i are given by D_{0i} and μ_i , respectively. As discussed in Sect. 5.8, a field incident on a junction between plates can never be completely diffuse. It can therefore be argued, as by Heckl et al. [31], that for many engineering applications it is sufficient to use a transmission coefficient derived for normal incidence between infinite plates. The transmission coefficient for diffuse incidence is slightly lower than the corresponding coefficient for normal incidence. For example, the transmission coefficient for diffuse incidence across a pinned junction between two identical plates is 2/3 of the transmission coefficient for normal incidence as discussed in Sect. 5.8. Corrections for diffuse incidence for a number of joints are discussed in Ref. [268]. Further, the transmission coefficient between two finite systems is set to equal the transmission coefficient between two semi-infinite systems. As a comparison it was found in Sect. 13.5 that the sound transmission through a panel between two irregular finite rooms is the same as for an

infinite panel. The transmission coefficients for flexural waves travelling across some simple junctions are derived in Sect. 5.9. In all cases normal incidence is assumed. The energy flow across the junction is caused by rotation only, i.e., there is no translatory motion of the junction.

The coupling loss factor between two beams i and j are given by

$$\eta_{ij} = \frac{c_{gi}\tau_{ij}}{2\omega L_i} = \frac{(D'_{0i})^{1/4}\tau_{ij}}{\pi\omega^{1/2}(m'_i)^{1/4}L_i} \quad (16.74)$$

The mass per unit length of beam i is m'_i and its bending stiffness D'_{0i} and length L_i . The group velocity in beam i is given by c_{gi} . It is assumed that the translatory motion at the junction of the beams is zero. The transmission coefficient τ_{ij} is again given in Sect. 5.9 for a number of different joints. The derivation of Eq. (16.74) is left for Problem 16.6. The simple coupling loss factors do not apply to the coupling between identical or periodic structures. Compare Sects. 7.7 and 7.8.

Craik has in his book [268] made a catalogue of coupling loss factors across junctions between various types of constructions.

16.9 Energy Flow in Large Structures, SEA

It is suggested by Craik in [268] that the SEA technique outlined in the previous sections can be used for the prediction of velocity-level differences in built-up structures as long as the basic SEA assumptions are satisfied. As an example consider the built-up structure shown in Fig. 16.9. The construction consists of five plate elements. Plate element 1 is excited by an external force, random noise. The power input to plate 1 is $\bar{\Pi}_1$.

The energy flows between the plates in Fig. 16.9 are obtained as

$$\begin{aligned} \bar{\Pi}_1 &= \bar{\Pi}_{d1} + \bar{\Pi}_{12} + \bar{\Pi}_{13}; & \bar{\Pi}_{12} &= \bar{\Pi}_{d2} + \bar{\Pi}_{23}; & \bar{\Pi}_{13} + \bar{\Pi}_{23} &= \bar{\Pi}_{d3} + \bar{\Pi}_{34} + \bar{\Pi}_{35} \\ & & \bar{\Pi}_{34} + \bar{\Pi}_{54} &= \bar{\Pi}_{d4}; & \bar{\Pi}_{35} &= \bar{\Pi}_{d5} + \bar{\Pi}_{54} \end{aligned} \quad (16.75)$$

The energy flow $\bar{\Pi}_{ij}$ is as defined in Eq. (16.24) given as $\bar{\Pi}_{ij} = -\bar{\Pi}_{ji} = \omega(\eta_{ij}\bar{E}_i - \eta_{ji}\bar{E}_j)$. These definitions in combination with Eq. (16.75) give

$$[C] \begin{Bmatrix} \bar{E}_1 \\ \bar{E}_2 \\ \bar{E}_3 \\ \bar{E}_4 \\ \bar{E}_5 \end{Bmatrix} = \begin{Bmatrix} \bar{\Pi}_1 \\ 0 \\ 0 \\ 0 \\ 0 \end{Bmatrix}$$

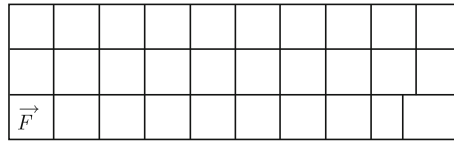


Fig. 16.10 Cross section through a building used for comparisons between measured and predicted noise and velocity levels. An inner wall was excited by a force indicated by F in the *lower left hand corner*

the first floor was excited by a shaker as indicated in Fig. 16.10 which shows a cross section of the building.

Two prediction models were used. In the first case only the energy transfer via flexural waves was considered. In the second case also longitudinal and transverse waves were included. In the last case the building was modeled by means of 1100 subsystems. The predicted and measured sound pressure levels were compared. It was found that the difference between predicted and measured results increased with increasing distance from the source. The full model, F-, L-, and T-waves, gave somewhat better results than the simple model, F-waves only, four or more junctions away from the source. Surprisingly, by comparing the results in the 1/3 OB 125, 500 and 2000 Hz, the apparent prediction errors were increasing with frequency. The difference between measured and predicted results using any of the models was within ± 7 for structures not being more than 4 joints or approximately 10 m from the source. The comparison was made in the 1/3 OB with the center frequencies 125, 250, 500, 1000, and 2000 Hz. Further away the differences could be very large or of the order 10–20 dB. However, it is always of the greatest importance to correctly predict a noise or vibration level close to a source where the levels are the highest. According to Table 4.1, Sect. 4.4, the concrete structures used in the tests cannot be considered as “thin” in an important frequency range. Consequently, the coupling loss factors derived for thin plates should not be used indiscriminately to calculate the energy in a concrete structure.

The application of the SEA method for ship structures is, for example, discussed by Odegaard Jensen [207]. A ship structure and a corresponding flowchart is shown in Fig. 16.11. The coupling loss factor between two adjoining plates is a function of the transmission coefficient τ_{ij} from plate i to plate j . This transmission coefficient is equal to the ratio between the transmitted and incident energy flow over the junction between the structures. The coupling loss factor η_{ij} between two plates coupled along a junction of length L_{ij} is given by Eq. (16.73).

Odegaard compares in Ref. [207] measured and predicted velocity level differences between various deck structures. A model, scale 1:5, was used for the measurements. The width of a plate element was equal to a number of frame distances. The coupling loss factors between the elements were calculated based on the plate dimensions only, i.e., the frames were left out. Only couplings via flexural waves were considered. The agreement between predicted and measured results is quite good as reported in Ref. [207]. In fact the reported discrepancies between measured and predicted results are much smaller in Ref. [207] than given in Ref. [268].

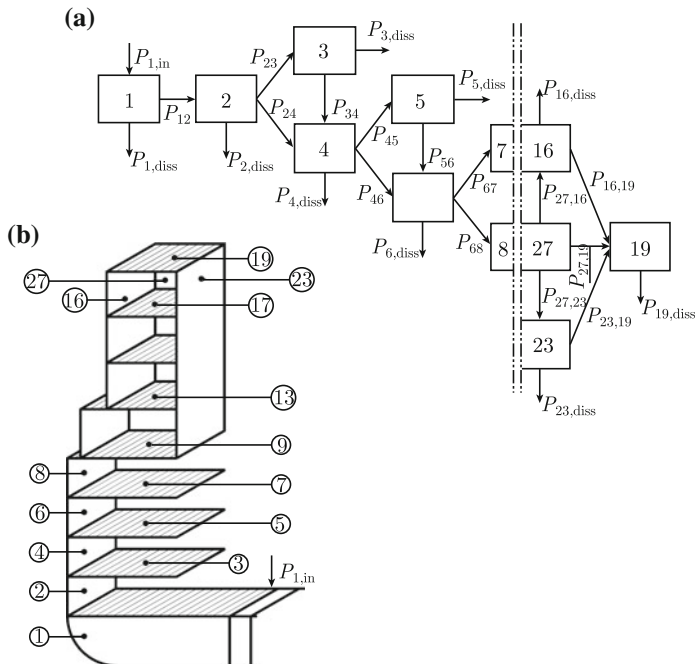


Fig. 16.11 Coupling between plate elements of a ship and the corresponding SEA energy flowchart. From Ref. [207]

Another ambitious attempt to predict velocity levels in ships by using SEA has been presented by Plunt in [164]. In this investigation full-scale measurements carried out on four ships were used for identifying relevant coupling factors for the ship structures. Flexural as well as in plane waves were included in the SEA model. The necessary parameters were determined based on some regression analysis. Consequently, the results from the semi-empirical model agreed quite well with the measured results on which the predictions were based. Other reports on predicting velocity levels on ships using SEA are, for example, reported in Refs. [275, 276]. A number of additional papers on the subject have been published over the years. However, these models are basically the same as that presented by Odegaard [207].

For typical ship structures the requirement to modal overlap defined in Eq. (16.71) is not always met. The same is true for the structures discussed in Sect. 14.4. Consequently, SEA is not applicable for calculating the energy flow in these structures.

An alternative to the SEA technique for predicting ship noise is discussed in Sects. 16.11–16.16.

16.10 SEA Parameters

In deriving the equations governing the energy flow between two simple oscillators a number of assumptions were made. These are listed in Sect. 16.2. For any successful SEA prediction the basic assumptions plus certain other requirements should be satisfied. The following prerequisites should be considered:

- (i) Weak, linear, and non-dissipative coupling between resonant systems.
- (ii) Uncorrelated forces, rain on the roof (white noise) excitation.
- (iii) Well-defined subsystems.
- (iv) Large number of modes in subsystems for each frequency band of interest.
- (v) Well-defined SEA parameters.

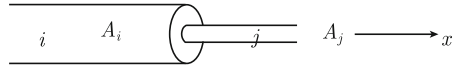
The subsystems should not be identical or rather they should be as different as possible. The transmission coefficients between identical subsystems are different from the corresponding transmission coefficient between irregular systems. In Sect. 7.7 it was shown that the transmission coefficient across a pinned periodic joint was very different from the transmission coefficient across a single pinned joint. The coupling loss factors for the cases are consequently also different. A similar problem was discussed in Chap. 13. It was found that the apparent sound transmission loss of a panel depends on the shape and thus the coupling between the rooms on either side of the panel. For many big constructions like buildings and ships the various elements have dimensions in common due to constant height between storeys and decks. However, to a certain extent even small variations of dimensions, etc., can make apparently identical structures irregular.

Subsystems can sometimes be readily identified. For example, each of the two coupled plates shown in Fig. 16.8 is a subsystem. The coupling is along the common junction. The built-up structure shown in Fig. 16.9 is, in the analysis presented in Sect. 16.8, described as having five subsystems. However, if the plates 1 and 2 are of the same material and have the same thickness and if the plates 4 and 5 also are similar, the number of subsystems could be reduced to three. A large structure like a train carriage, aircraft, ship, or building is not readily described by a number of subsystems. For example, the subsystems identified in the SEA model used by Odegaard and shown in Fig. 16.11 are made up of deck elements with a width of several frame distances. The distance between the parallel frames on a ship is typically of the order 0.6–0.8 m. If instead only the plate elements limited by the frames constitute a subsystem the basic SEA requirements would have been violated with respect to modal density. This particular problem is discussed in Sect. 16.12. Tortaro and Guyader [277] describe a mathematical tool for defining proper subsystems of large constructions, exemplified by a double-decker train carriage.

The modal densities of plates and beam can be estimated by means of mobility measurements. The modal densities and point mobilities for three structures are shown in Table 16.2. In the first two cases, flexural waves are induced by a point force perpendicular to the structure and in the third case longitudinal waves are excited by a force along the axis of the beam as shown in Fig. 16.12.

Table 16.2 Real part of point mobilities and modal densities

Structure	$\text{Re}Y$	\mathcal{N}_f	\mathcal{N}_f
Plate, F-waves	$\frac{1}{8\sqrt{\mu D_0}}$	$\frac{S}{2}\sqrt{\frac{\mu}{D_0}}$	$4S\mu\text{Re}Y$
Beam, F-waves	$\frac{1}{4(m')^{3/4}\omega^{1/2}(D'_0)^{1/4}}$	$\frac{L}{\sqrt{\omega}}\left(\frac{m'}{D'_0}\right)^{1/4}$	$4m' L\text{Re}Y$
Rod, L-waves	$\frac{1}{A\sqrt{\rho E_0}}$	$2L\sqrt{\frac{\rho}{E_0}}$	$2L\rho A\text{Re}Y$
Acoustic cavity	–	$\frac{4\pi f^2 V}{c^3}$	–

Fig. 16.12 Coupling between two semi-infinite rods

The point mobilities are valid for an infinite plate, infinite beam, and semi-infinite rod. The surface of the plate is S , the length of the beam and the rod is L , and the cross-sectional area of the rod is A . The number of modes $N_{\Delta f}$ within a frequency Δf is consequently $N_{\Delta f} = \Delta f \cdot \mathcal{N}_f$ where the modal density can be estimated from the space average of the point mobility and mass of the structure as shown in the right column of Table 16.2. The modal density of an acoustic cavity is given by Eq. (11.138).

The coupling loss factor between two structures can be estimated as discussed in Sect. 16.6. The coupling loss factor between two plates, flexural waves only, is given by Eq. (16.73) as

$$\eta_{ij} = \frac{c_{gi}\bar{\tau}_{ij}L_{ij}}{\pi\omega S_i} = \frac{2D_{0i}^{1/4}\bar{\tau}_{ij}L_{ij}}{\pi\omega^{1/2}\mu_i^{1/4}S_i}$$

The transmission coefficients τ_{ij} are discussed in Sects. 5.8 and 5.9. The coupling loss factor between two beams, flexural waves, is given by Eq. (16.74) as

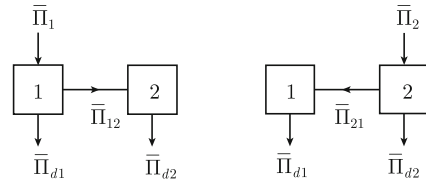
$$\eta_{ij} = \frac{c_{gi}\tau_{ij}}{2\omega L_i} = \frac{(D'_{0i})^{1/4}\tau_{ij}}{\pi\omega^{1/2}(m'_i)^{1/4}L_i}$$

The transmission coefficients τ_{ij} are presented in Sect. 5.8. For coupled rods, Fig. 16.12, longitudinal waves only, the coupling loss factor is

$$\eta_{ij} = \frac{c_{li}\tau_{ij}}{2\omega L_i} = \frac{\tau_{ij}}{2\omega L_i}\sqrt{\frac{E_{0i}}{\rho_i}}; \quad \tau_{ij} = \frac{4A_i A_j \sqrt{\rho_i E_{0i}} \sqrt{\rho_j E_{0j}}}{(A_i \sqrt{\rho_i E_{0i}} + A_j \sqrt{\rho_j E_{0j}})^2} \quad (16.78)$$

The cross-sectional area of rod i is A_i and its density and real part of E -modulus are ρ_i and E_{0i} , respectively. The details are left for Problem 16.7.

Fig. 16.13 Power injected into two coupled systems in two different ways



Coupling loss factors, modal densities, and group velocities can be estimated from FEM calculations as, for example, described in Refs. [278, 279].

The so-called Power Injection Method can be used to estimate the coupling loss factor between two simple systems. First power, $\bar{\Pi}_1^a$, is induced in system 1 as shown in Fig. 16.13. The energies $\bar{\mathcal{E}}_1^a$ and $\bar{\mathcal{E}}_2^a$ in two systems are determined by measuring the velocity levels of the structures. There after the power $\bar{\Pi}_2^b$ is injected in system 2 and the energies $\bar{\mathcal{E}}_1^b$ and $\bar{\mathcal{E}}_2^b$ of the systems 1 and 2 are determined. As shown in Problem 16.8 the loss factors are obtained from the matrix equation

$$\begin{bmatrix} \eta_1 + \eta_{12} & -\eta_{21} \\ -\eta_{12} & \eta_2 + \eta_{21} \end{bmatrix} = \frac{1}{\omega} \begin{bmatrix} \bar{\Pi}_1^a & 0 \\ 0 & \bar{\Pi}_2^b \end{bmatrix} \begin{bmatrix} \bar{\mathcal{E}}_1^a & \bar{\mathcal{E}}_1^b \\ \bar{\mathcal{E}}_2^a & \bar{\mathcal{E}}_2^b \end{bmatrix}^{-1} \quad (16.79)$$

The resulting four equations give the loss factors and the coupling loss factors. The structures should be excited by band-pass white noise. The bandwidth should be wide enough to ensure that a sufficient number of modes is excited in each system.

The loss factor of a subsystem can be measured as discussed in Sect. 2.9. However, the measured loss factor includes also coupling losses to adjoining structures and surrounding fluid. So for example, the measured loss factor η_{measured} for system 1 in Fig. 16.2 is equal to $\eta_{\text{measured}} = \eta_1 + \eta_{12}$. For a weak coupling between the systems $\eta_1 \gg \eta_{12}$ and $\eta_{\text{measured}} \approx \eta_1$. Radiation losses can also contribute to the measured loss factor as discussed by Nijman [160]. Two types of loss factor measurements on a cast iron oil sump for a passenger car are reported in Ref. [160]. In the first case the oil sump was surrounded by air and in the second case the oil sump was submerged in helium gas. The wave impedance of helium is much lower than for air, the ratio being approximately 0.4. In addition, the speed of sound in helium is almost three times the speed of sound in air. The critical frequency of a structure submerged in helium is therefore almost ten times as high as the corresponding critical frequency in air leading to a much reduced radiation ratio in helium. Consequently, the radiation losses are much smaller for the sump being submerged in helium than in air. The average measured loss factor was 19×10^{-4} in air and 3.2×10^{-4} in helium in the frequency range 300–1200 Hz. If the internal losses dominated the measured loss factors would be the same in both cases. The tests clearly demonstrate that radiation losses can exceed internal losses. For small internal losses the weak coupling requirement is not readily satisfied.

In Sect. 16.3 the coupling between modes in different systems was discussed. In SEA it is assumed that the coupling between any mode in one system and any other

mode in another system is the same. This is not always the case. For example, the modal radiation ratio and thus the coupling loss factor between a vibrating structure and an acoustic enclosure depend on the modes of the structure as discussed in Sect. 16.4. The transmission of flexural waves across a junction depends on the thicknesses of the plates. There is no transmission of energy from a thin to a thick plate of the same material if the angle of incidence of the primary wave exceeds a certain value as discussed in Sect. 5.8. Consequently, the coupling loss factor between different modes cannot be the same. This problem has been addressed by Maxit and Guyader [280]. However, despite these and other limitations, basic SEA calculations can yield acceptable results.

16.11 Ship Noise

Noise problems on ships have attracted increasing attention since the beginning of 1970. National and international organizations have issued requirements or recommendations concerning limits for noise levels in sleeping quarters or working areas. Low noise levels in cabins and other public spaces on cruise liners are of paramount importance for attracting customers. Some products like cars, trains, and airplanes are manufactured in very large series. Prototypes are built and tested. During this initial construction phase noise reducing measures can be tested. For the ship building industry the problem is different. Each ship structure is in general individually designed and equipped. Consequently, in the ship industry there is a special need for noise prediction methods. By means of a prediction program the construction and general arrangement can be optimized with respect to noise, economy, weight, etc.

The noise situation on board a ship is determined by many and varied forms of noise sources. Effective shipboard noise control therefore requires identification and knowledge of all significant noise sources. The most important noise sources are main and auxiliary engines, propeller, gear, casing, and exhaust systems including funnel, various pumps, compressors, hydraulic systems, and fan equipment including air intakes and outlets. In spaces containing noise sources such as engines, fans, or pumps the sound pressure level is almost entirely determined by airborne sound. Methods to predict and reduce airborne sound are well known and are extensively treated in the literature. See, for example, the Refs. [281–283]. Typical sound reducing measures are partitions, hoods, screens, and sound absorbing materials. In accommodation spaces other than those mentioned above, with the possible exception of cabins or other spaces directly adjoining a source, the noise level is determined by structure-borne sound. The term structure-borne sound refers to structural vibrations in the frequency range 16–20,000 Hz. High-frequency flexural vibrations of a structure radiate audible noise into a cabin or any other space.

Structure-borne sound is directly induced by any mechanical force. The mechanical power transmitted from a source through its connection to the foundation propagates into the structure. The power can propagate in the structure as flexural, longitudinal, transverse, and torsional waves. The relative importance of these wave

types has been discussed in Refs. [56, 168, 197]. The resulting energy flux in a structure is attenuated as function of the distance from the disturbance. The attenuation depends on losses in the structure and also on the number of obstructions or discontinuities (decks, platforms, frames) in the propagation path. At the receiving end in, for example, a cabin—the acoustical power radiated from a structure depends on the velocity level of the material parameters and dimensions of the structure. To make a prediction of resulting noise levels in an accommodation space possible, the following quantities must be known: (i) source strengths; (ii) transmission properties of steel structure; (iii) radiation properties of structures at the receiving end.

A flowchart for a typical noise prediction procedure is given in Fig. 16.14. Generally, the main problem is the characterization of the acoustical properties of the main sources, their coupling to the ship structure, and the propagation of structureborne

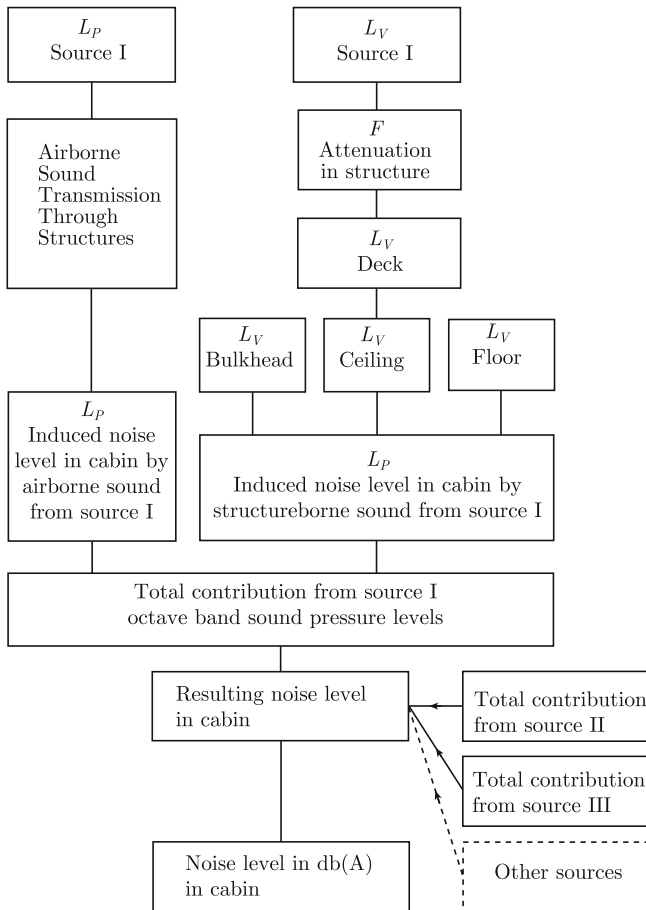


Fig. 16.14 Chart for predicting noise levels in cabins on a ship

sound from a source to a certain deck structure. It is often argued that the acoustical energy flow in a ship structure can be determined by means of empirical methods, finite element methods, statistical energy analysis, or analytical methods.

One of the first empirical methods was introduced by Janssen and Buiten [284] in 1973. The method is very simple but still very informative. Although every ship is individually designed the basic structure must satisfy certain classification rules. This implies a certain conformity between standard ships. In Buiten's model the attenuation of structureborne sound from a source to a deck is assumed to be 5 dB per deck for the first four decks and then 2 dB for each additional deck. The attenuation is assumed to be independent of plate thickness, frame distance, and other design parameters as well as of frequency. For a standard type of ship with a conventional superstructure this simple model gives fairly accurate results.

The outline of Buiten's procedure has been copied in numerous other prediction schemes. The essential difference between these is the description of the attenuation of the energy flow in the steel structure. Another widely used empirical method was published by BSRA [285]. This method is also based on the principles outlined by Buiten. Classification societies and other organizations have access to drawings and noise measurements for a large number of ships. This type of information can be the foundation for a more or less sophisticated database. This is, for example, discussed in [286]. This type of database can be used at the very early design stage so as to avoid any major mistakes with respect to the acoustical planning of the new building.

Very often today yards are mainly interested in the noise prediction for specially designed ships of a type not previously built. This means of course that there is no data available to form the basis for any type of empirical estimates. Other methods used for predicting the energy flow in ship structures are the SEA technique, Sect. 16.8, and the waveguide method discussed in Sects. 14.2 and 14.3.

16.12 Waveguide Model

This approach to the propagation problem was first presented in Ref. [197] and then in a more generalized form in Ref. [168]. The method is based on a technique previously used by Heckl [287] to determine the vibration of grillages. In Refs. [56] and [168] the basic assumptions concerning the adaptation of the method to ship structures have been discussed at length. The waveguide method, which is discussed in Sects. 14.2–14.4, can be used to determine the vibration levels of plate elements in a vertical section of a ship structure, as shown in Figs. 14.5 and 16.18. The plates in the section are restricted by the frames and have junctions with other plates—decks or vertical partitions. The dynamical coupling between the plates in a section can be calculated on the basis of the following assumptions:

- (i) A ship construction can be considered as an acoustical wave guide system; the parallel frames constitute the boundaries for each wave guide; the transverse motion of the plates is negligible at the boundaries;

- (ii) The main power flow from a source propagates as flexural waves in the plate elements within the wave guide system;
- (iii) The coupling between two plate elements is caused by rotation, or a bending moment at the junction between the plates, perpendicular to the frames.

The relative importance of flexural and longitudinal waves has been discussed in Refs. [56, 168]. The results of the study indicated that the main power flow in a ship structure is caused by flexural waves. The test illustrated in Fig. 14.16 and discussed in Sect. 14.4 confirms that the dominating energy flow in a ship structure is within the plate elements and not in the frames. In Refs. [168, 197] model- and full-scale measurements have been compared with predicted results for frequencies above the cutoff frequency for the waveguide system. For a full-scale ship structure this limit corresponds to approximately 100 Hz. In a ship the thicknesses of the plates are greater in the hull and tank top than in the superstructure. Consequently, the cutoff frequencies can be comparatively high for the elements in the tank top. The method described in Ref. [197] therefore has certain limitations with respect to frequency range when its application is extended to include not only superstructures, but also propagation paths all the way from the engine foundations. For this reason it is of importance to determine the propagation pattern even for frequencies below cutoff. This is discussed in Ref. [168]. Coupling factors between plate elements for frequencies below cutoff are presented in Ref. [168].

A detailed knowledge of the mechanism describing the energy flow from the engine foundations could eventually lead to new design criteria for the minimization of the noise levels on a ship and also to the noise radiated out into the water. A low level of water-borne noise is of great importance on e.g., fishing, navy, and geophysical research vessels.

The basic waveguide model is fairly simple as discussed in Sects. 14.2 and 14.3. Initially, a vertical section of a ship construction is considered. One example is shown in Fig. 14.3. The width of the section is determined by the distance between the parallel frames. The plates in the structure are assumed to be excited by a bending moment acting on one element, perpendicular to the frames. The power flow to the adjoining and subsequent elements is then generated by the resulting angular displacement at each junction. The lateral motion of the boundaries is small compared with the displacement of the plates. This has been confirmed by full-scale measurements on typical ship structures. Typically, the velocity level of a plate element is 5 to 10 dB higher than the velocity level of the frames limiting the plate as confirmed by tests described in Sect. 14.4. Therefore the transverse motion of the boundaries and the twisting moments at the junctions has been neglected in the analysis. As a consequence of this, the displacement and thus also the bending moment for any plate element can be derived as functions of the rotation at each junction. However, this is based on the assumption that the angle between two plate elements is not changed by the rotation. The coupling between the elements can then be calculated based on the fact that the sum of the bending moments around each junction should equal zero. This final condition makes it possible to form a system of equations relating all the angular displacements at the junctions of the structure. The solutions to this

set of equations determine the displacement and thus also the velocity of each plate as functions of the initial forcing bending moment. This is discussed in Sect. 14.3.

If plates are assumed to be simply supported along the frames, a simple expansion can be used to determine the plate displacement as discussed in Sect. 14.2. However, for a ship structure with plate elements mounted to parallel frames like in Fig. 14.3 the plate are clamped rather than simply supported along the frames in the frequency range above the first natural frequency of the plate as discussed in Sect. 14.2. This assumption has been confirmed by modal analysis on full-scale ship structures. This is also a criterion generally accepted for similar problems relating to aircraft structures Ref. [288]. For ship structures this problem was discussed in Ref. [56]. No exact solution can be derived by using the expansion theorem for clamped boundary conditions. This difficulty can be overcome if the boundary conditions are somewhat relaxed. However, the main point is that the eigenvalues of the approximate eigenfunctions thus introduced should be reasonably close to the correct eigenvalues of the cross modes. These approximate eigenfunctions are discussed in Sect. 14.2 and defined in Eq. (14.14). The cut-on frequency for the first clamped cross mode is of the order 100 Hz for a typical ship structure. The cut-on frequency for the next symmetric cross mode, $n = 3$ in Eq. (14.14), is of the order 550 Hz. The energy flow carried by the first mode is dominating over the higher modes as discussed in Sects. 14.3 and 14.4. A comparison between predicted and measured results clearly indicates that satisfactory results are obtained if only the first cross mode is considered. In fact, a prediction using one of the higher modes only gives too high attenuations. Therefore the following discussions of all results are based on the concept that the higher modes can be neglected.

In the low-frequency region the boundary conditions are more relaxed. The boundary conditions for the plates along the frames depend on the relative stiffness between the frames and the plates. The moment impedance for a plate is different for frequencies above or below the first plate resonance. This will influence the apparent boundary conditions for the plate. Further, measurements indicate that for frequencies decreasing below the first natural frequency of the plate, the shape of the cross modes is determined by simply supported rather than clamped boundary conditions. For these reasons a different approach is used to calculate the coupling between the plates in the frequency range below the first natural frequency of the plate. This method is based on the Garlekin variational method discussed in Sect. 9.9. The low frequency model is presented in Ref. [168].

When looking at a ship structure from the outside it can be clearly seen that plate elements have a slight curvature even when being part of a flat large section. This is a result of the welding process when plates are mounted to frames. These curvatures of the plates influence the natural frequencies of the plates as discussed in Sect. 8.8. The measured first natural frequency of a plate element is therefore higher than the predicted result for a flat plate. This particular problem introduces a certain error in the frequency bands including the first natural frequencies of the plate elements.

The boundary conditions for the plate along the frames are essential. Various models are discussed in [168]. Once the appropriate boundary conditions along the frames have been established the bending moments acting on the plate element can

be determined. The total bending moment around a junction is equal to zero. This means that the angular displacement at each junction can be solved as function of a force or moment exciting a particular element. In matrix form the resulting system of equations can be written as defined by the Eqs. (14.23) through (14.27). Based on the assumptions made above, the resulting system of equations can be written in matrix form as

$$[A] \begin{Bmatrix} \gamma_1 \\ \gamma_2 \\ \dots \\ \gamma_N \end{Bmatrix} = \begin{Bmatrix} M_1 \\ M_2 \\ \dots \\ M_N \end{Bmatrix} \quad (16.80)$$

The matrix $[A]$ is defined in Eqs. (14.20) and (14.25). The elements M_m are equal to zero except at those junctions where the structure is excited. The velocity level of an element is calculated from the resulting angular displacements as given by Eq. (14.22). The velocity level differences between the elements in the structure and the source element are thereafter calculated. The procedure must be repeated for each source element in the structure. The velocity of a plate element is a rapidly varying function of frequency. The total kinetic energy of a plate element in a certain frequency band must therefore be determined by means of numerical integration: i.e., summation within each frequency band. For a typical noise prediction the nine octave bands with the center frequencies 31.5 Hz to 8 kHz are of interest. In each of these frequency bands the average velocity should be based on 100–250 separate calculations depending on frequency. If, for a typical ship construction, the number of summations within a frequency band is extended from 250 to 500, the resulting velocity level differences between the elements in the structure can change by a few dB. For the predictions discussed in Sect. 16.15 the number of summations within each frequency band was 500.

The model discussed above is valid only for plate elements located in the same vertical plane in between the same two frames. In other words the model describes the energy transmission parallel to the frames from the source. This transmission is very critical and determines the noise levels in the spaces or cabins most exposed to noise. The cabins having the highest noise levels are in general located above the engine room or propeller. It is of great importance that these maximum noise levels can be predicted with a sufficient degree of accuracy so that any necessary noise reducing measures can be properly designed. It is of less importance to predict accurately a noise level which is known to be well below any noise requirement. This is why so little effort has been spent on the investigation of the transmission of structureborne sound in any other than the vertical direction in a ship structure.

The propagation of structureborne sound perpendicular to the frames has been investigated experimentally as reported in Ref. [289]. In that study it was found that this attenuation could be described as function of frequency f and the number r of the frames in between source and receiver. The geometry of the frames was, within certain limits, only of secondary importance. Based on full-scale measurements it was found that in the horizontal direction the transmission loss TL_H in dB across a total of r frames could be written as

$$\begin{aligned}
 TL_H &= \beta_1 r \text{ for } r \leq 20 \\
 TL_H &= 20\beta_1 + (r - 20)\beta_2 \text{ for } 20 \leq r \leq 50 \\
 TL_H &= 20\beta_1 + 30\beta_2 + (r - 50)\beta_3 \text{ for } r \geq 50 \\
 \beta_1 &= 0.7; \quad \beta_2 = 0.10 + 0.161 \cdot \log f; \quad \beta_3 = 0.032 + 0.052 \cdot \log f \quad (16.81)
 \end{aligned}$$

In Ref. [284], the original paper on noise prediction by Janssen and Buiten, the total attenuation TL between a source and a receiving element was given by the expression

$$TL = \left(TL_H^2 + TL_V^2 \right)^{1/2} \quad (16.82)$$

where TL_H and TL_V are the transmission losses in the horizontal and vertical directions, respectively. Despite the lack of any reasonable physical explanation the simple expression (16.82) has been found to yield satisfactory results. The reason is probably that in practice one of the terms TL_H or TL_V dominates.

The method discussed above has certain limitations. The model cannot be used for ship constructions with longitudinal web frames. For ships with frames perpendicular to the center line the frame distance should be the same everywhere. The model can therefore not be used without certain manipulations for ships with additional ice frames. Results based on this model depend on how well the structure can be described. This requires a certain experience. In particular with respect to the modeling of engine foundations.

16.13 Noise Levels in Accommodation Spaces

If in a cabin the noise level is induced by structure-borne sound, then this noise level is a function of the velocity levels, radiation ratios, and dimensions of all the structures facing the cabin. The energy flow or transmission from a deck to a structure, for example, a bulkhead mounted on the deck, can be expressed as a velocity-level difference between the deck and the structure. Henceforth the velocity level of a structure is by means of a coupling factor referred to the corresponding velocity level of the steel deck in the cabin. The strengths of the sources inducing structureborne sound and the transmission losses in the ship construction determine the velocity level of the deck.

Consequently, in order to predict noise levels in accommodation spaces the following quantities must be known: (i) Source strengths; (ii) Transmission losses in structure between sources and deck plates; (iii) Dimensions, radiation ratios, and coupling factors for structures in cabin; (iv) Sound absorption in cabins and other spaces. These statements are readily formulated in a few equations as suggested by Janssen and Buiten [284].

Thus, assume that the rms velocity at the foundation of a source is L_v (source) and the resulting rms velocity of a deck is of a deck is L_v (deck), then

$$L_v(\text{deck}) = L_v(\text{source}) - TL \tag{16.83}$$

The function TL , defined in Eq. (16.82), is the transmission loss in the structure between the source and the receiver or rather the steel deck of the cabin. The structure-borne sound is transmitted from the steel deck to the floor, bulkheads and ceiling in the cabin. The type of mounting of each structure and its connection to the steel construction determine the velocity level difference $(\Delta L_v)_i$ between the steel deck and the radiating surface i . The velocity level L_i of a radiating surface is

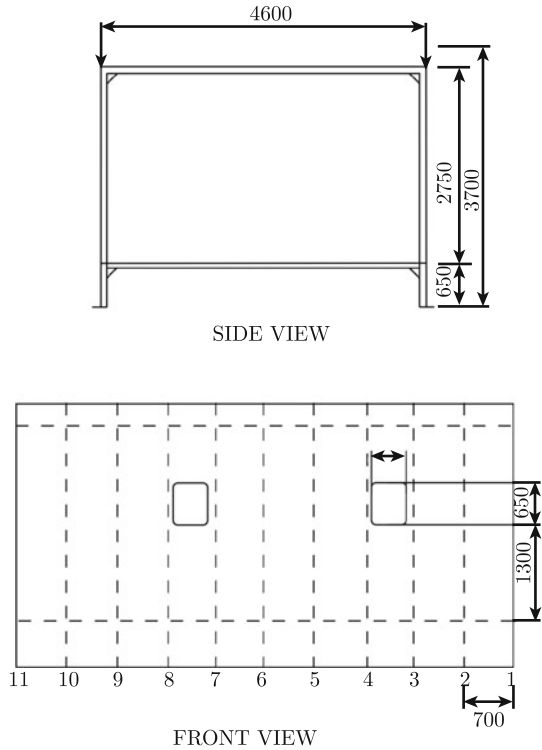
$$L_i = L_v(\text{deck}) - (\Delta L_v)_i \tag{16.84}$$

The sound pressure level L_{pi} induced in a room, equivalent absorption area A (m^2), by a structure i with a velocity level L_i , area S_i , sound radiation ratio σ_i is

$$L_{pi} = L_i + 10 \log(S_i \sigma_i / A) - 28 \text{ dB} \tag{16.85}$$

The sound pressure level and velocity level are referred to 2×10^{-5} Pa and 10^{-9} m/s, respectively. The total noise level L_{tot} in the cabin is obtained by adding logarithmically the contributions from all structures and sources. Thus,

Fig. 16.15 Test rig for measurements of acoustical properties of accommodation systems



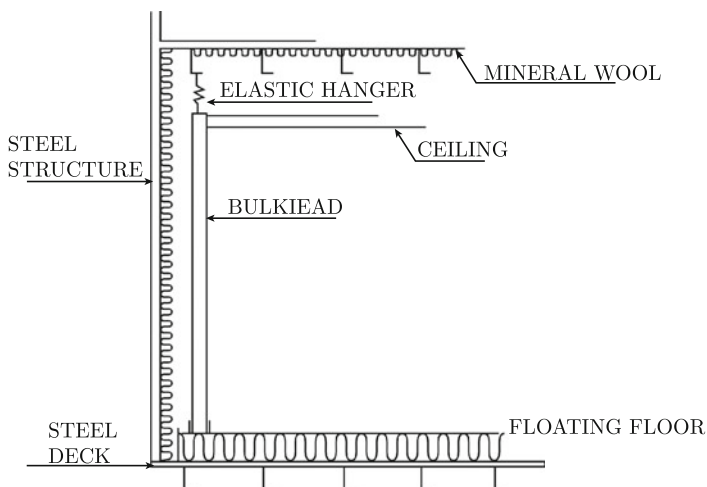


Fig. 16.16 Cross section of a floating accommodation system

$$L_{\text{tot}} = 10 \log \left(\sum_{\text{sources}} \sum_i 10^{L_{pi}/10} \right) \quad (16.86)$$

Any possible contribution from the transmission of airborne sound is added in a similar way. The calculation procedure is typically carried out in the nine octave bands with the center frequencies from 31.5 to 8 kHz. Based on these octave band levels the A-weighted level or a noise rating can be determined.

All acoustical properties of accommodation systems should preferably be measured in situ or else in a special test rig. Figure 16.15 shows a test rig used for these purposes. The rig is quite simply a section of a ship structure extending from the outer bulkhead to the casing. The dimensions of the deck area are in this particular case 7 m × 4.6 m. The structure is excited by a shaker and the resulting vibration levels of the structures facing the cabin and the noise level in the cabin are measured and determined as functions of the velocity level of the deck. A cross section of a floating accommodation system is shown in Fig. 16.16.

16.14 Source Data

For the purpose of a noise prediction it is in general sufficient to determine the velocity level perpendicular to the plating at the foundations of main and auxiliary engines, gears, pumps, etc. Semiempirical formulae for the predictions of these levels have been, for example, presented in Refs. [284, 290]. Various aspects of problems concerning coupling and transmission between engines and foundations have been

discussed in Refs. [116, 291]. See also the discussion in Chap. 10 and in particular Sect. 10.12. The accuracy of a noise prediction is much improved if the input data for the sources are based on direct measurements on similar machinery. Therefore access to a good data bank is essential. Source data for propellers can be determined from model scale measurements or from calculations as discussed in Ref. [195]. For fast vessels flow noise must also be considered, see Sect. 15.10.

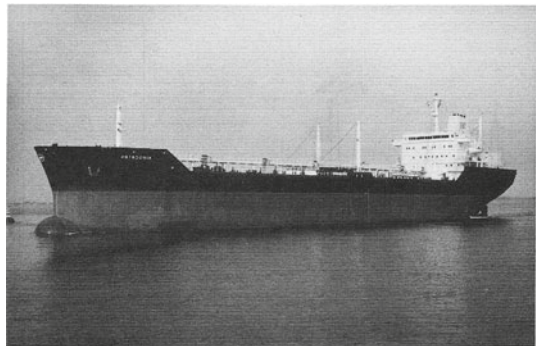
The element model of a ship is shown in Fig. 16.18. Element 28 is the foundation of the main engine. By letting bending moments excite this element the relative velocity levels of all other elements are obtained from Eq. (16.80). The velocity level of element 28 is set to equal the source data for the main engine. Consequently, the velocity levels induced by the main engine can be determined for all elements. The operation is thereafter repeated for all other sources to give the total velocity level for every element.

16.15 Measured and Predicted Results

Predicted and measured velocity levels on a 34,000 tdw conventional tanker are compared in Ref. [168]. The predicted results are based on the waveguide theory. The ship and the corresponding element model are shown in Figs. 16.17 and 16.18. Material parameters plate dimensions, etc., are listed in Appendix C. Measurements of velocity levels were carried out during ordinary service conditions. Measurement positions are indicated in Fig. 16.18. Accelerometers were mounted on the steel plates along the center line between the frames 35 and 36. The distance between two positions was 0.75 m. The standard deviation between individual measurements on a plate element is of the order 1.5 dB in the mid-frequency region, about 0.8 dB in the 4 kHz octave band and 2 dB in the 63 Hz band.

Predicted and measured velocity level differences between element 25 and the elements 2, 8, and 17 are compared in Fig. 16.19a–c, respectively. In general and as indicated in the figures, the attenuation increases as the distance from the sources is

Fig. 16.17 Overall view of ship



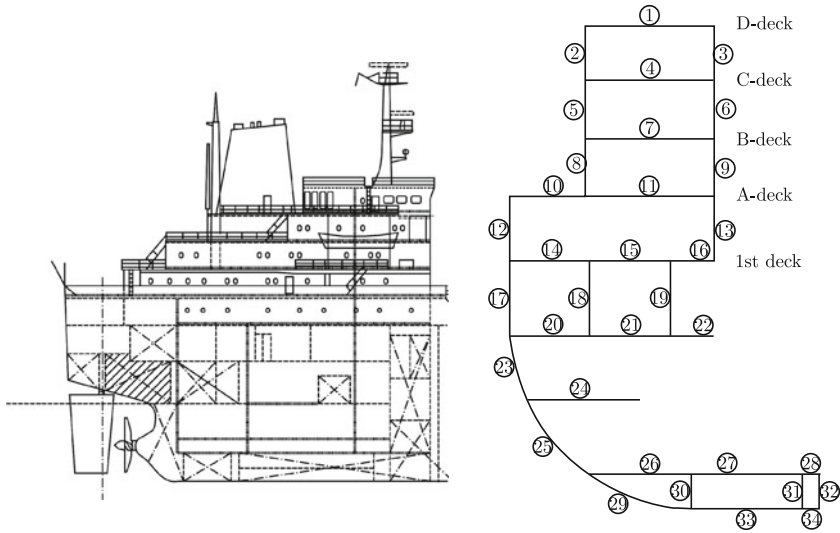


Fig. 16.18 View of the aft body of the ship. Measurement positions located in shaded areas. The corresponding element model is shown on the *right*

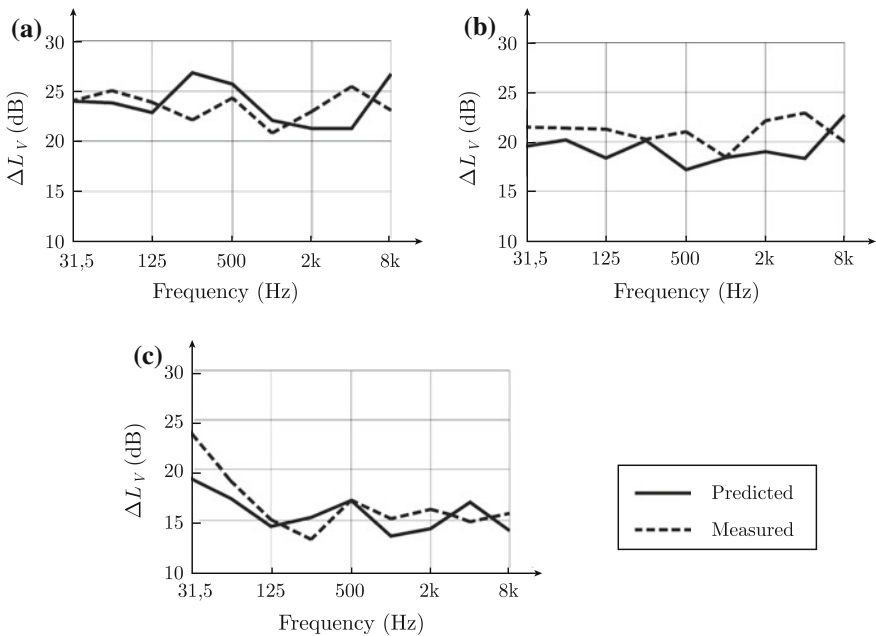
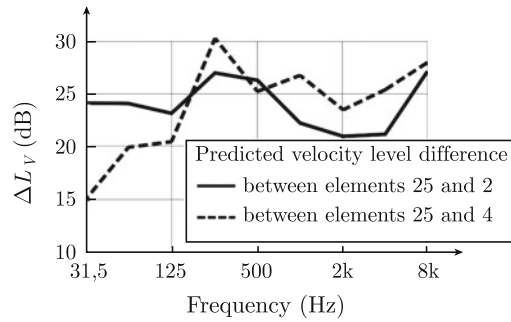


Fig. 16.19 Predicted and measured velocity level differences between the elements, **a** 25 and 2, **b** 25 and 8, **c** 25 and 17. The elements are indicated in Fig. 16.18

Fig. 16.20 Predicted velocity level differences between elements 25 and 2— and 25 and 4 ----



increased. However, the attenuation is not only a function of the location of the plate but also of the plate dimensions.

Predicted velocity level differences between element 25 and the elements 2 and 4 are shown in Fig. 16.20. The last two elements represent the platings between C- and D-deck and the plate structure in C-deck. It is evident that the energy flow to the deck is greater than to the adjoining ship side in the low-frequency region. For high frequencies the opposite is the case. The result—or rather the frequency dependence for the various coupling factors—which is shown in Fig. 16.20 is representative of this type of junction between ship side and deck. The reason for the result is quite simply that the material parameters—total weight, stiffness, etc.—are not the same for a deck construction and a ship side.

The transmission of structureborne sound from the engine foundation to the hull was also investigated. The bottom part of the cross section previously referred to is shown in Fig. 16.21. In this figure L1 denotes the average velocity level on the ship side between the tank top and the platform deck. The positions 2 and 3 correspond to plate elements in the tank top and in the engine foundation. In Fig. 16.22a the predicted and measured velocity level differences between the ship side and tank top elements are compared. In the low-frequency range the velocity level on the ship side is higher than on the tank top. This is mainly due to two reasons. Primarily, the first natural frequency for the water loaded plate is much lower than for a plate in the tank top. The plate in the hull is consequently easier to excite. Secondly, the power flow—from the bottom plates to the ship side is significant in the low frequency range.

In Fig. 16.22b predicted and measured velocity level differences between the ship side and the engine foundation are compared. The difference in stiffness between the elements in the ship side and foundation is here much more pronounced than in the previous case. The result is that the velocity level difference between the elements is much larger than in the previous case for low frequencies. The same observations have been confirmed by other full-scale measurements.

Predicted and measured sound pressure levels, 1/1 octave band analysis, are compared in Fig. 16.23a–d for cabins located on four different decks. In some cases there can be rather large deviations between predicted and measured octave band levels.

Fig. 16.21 Cross section of engine foundation and tank top construction. L_1 , L_2 and L_3 indicate average velocity levels for plate element in the structure

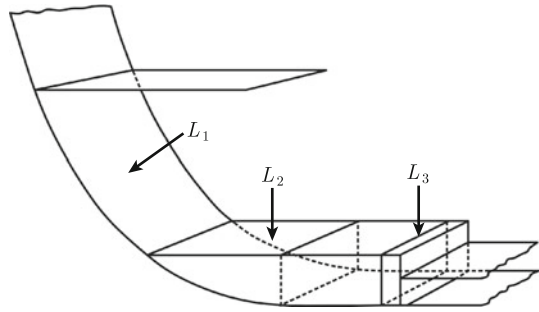
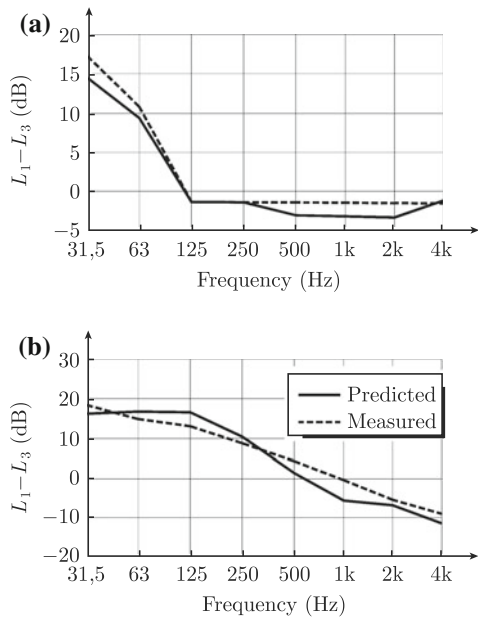


Fig. 16.22 Velocity level difference between ship's side L_1 and **a** element in tank top and **b** engine foundation



This could be due to the effect of a local source not included in the prediction. A more likely explanation could be a rattling door or a squeaking panel. The recorded differences between predicted and measured A-weighted sound pressure levels are shown in Fig. 16.24. The A-weighted noise levels in the cabins were measured twice for the same apparent operating conditions for the ship. The deviations between the two measurement series were of the same order as between predicted and measured results shown in Fig. 16.24. The accuracy of a prediction could never be better than the accuracy of the measurements. It should be noted that additional errors are introduced in the prediction if the data for the main sources have to be estimated rather than measured.

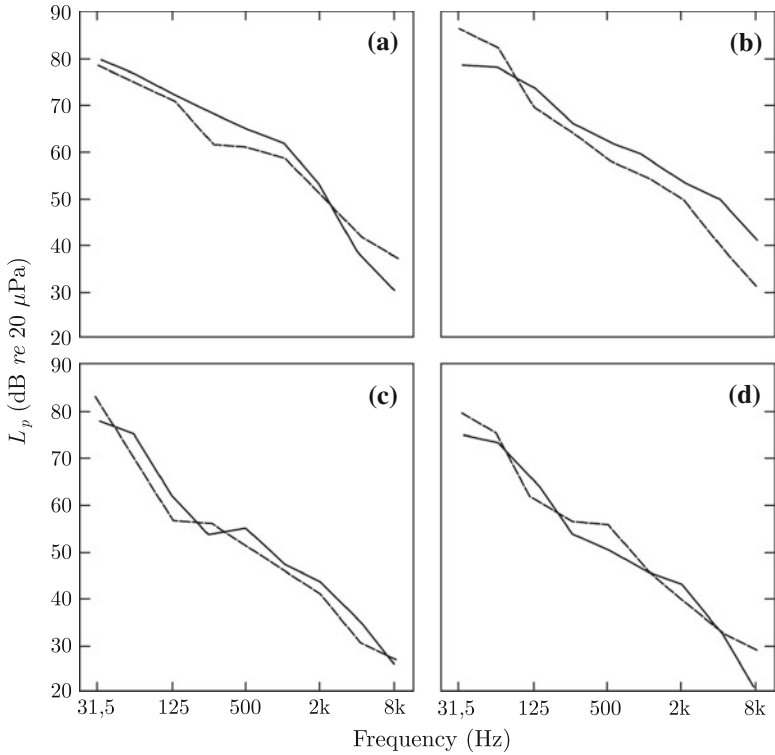
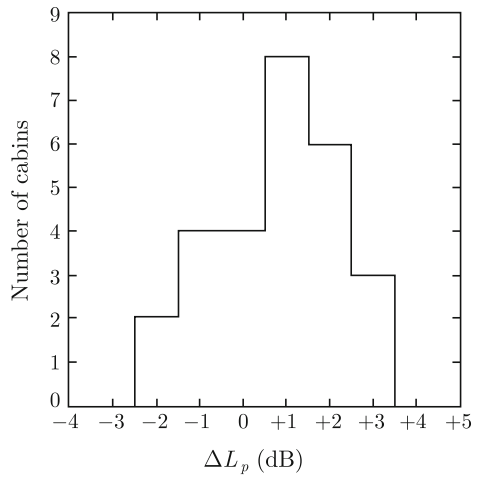


Fig. 16.23 Predicted and measured noise levels in cabins, **a** no. 57 on 1st deck, **b** no. 36 on A-deck, **c** no. 21 on C-deck and **d** no. 10 on C-deck

Fig. 16.24 Distribution of the difference between predicted and measured A-weighted noise levels in cabins



16.16 Conclusions—Noise Prediction on Ships

Empirical methods can be very informative during the acoustical planning of a ship. Predictions based on empirical methods should be limited to standard ships. The upper frequency range for a FEM calculation is much too low to make the model feasible for standard noise predictions. However, FEM calculations could be used for the investigation of the coupling between various substructures in, for example, the tank top structure. Whenever an SEA calculation is attempted it must be verified that the assumptions on which the method is based are not violated. In general ship structures are out of range for SEA calculations. The number of modes for plate elements between frames is much too low. The waveguide model has been verified by a number of measurements on full- and model-scale structures. The waveguide model has been used successfully for the prediction of noise levels on various types of ships from large cruise liners, tankers, research vessels to fast ferries, Ref. [293]. The model has also been used for prediction of the energy flow in railway carriages, Ref. [55].

The basic SEA method was also tested for predicting the attenuation in structures shown in Fig. 14.6. The agreement between measured and predicted results was very poor. The reason is that the basic requirements for the SEA technique to be applicable were not satisfied. The effect of damping layers in the transmission path was investigated by means of the model shown in Figs. 14.6 and 14.14. The SEA technique overestimated the effect of the damping layers quite considerably. The waveguide model yielded acceptable results. This shortcoming of the SEA model is sometimes referred to as the “tunnel effect.” For damped structures not only resonant but also forced transmission are of importance. SEA only includes resonant effects. The waveguide model incorporates both resonant and forced transmission.

The propagation of structureborne sound in steel structures can be predicted by means of fairly simple plate models. In combination with basic acoustical principles the propagation can be used to predict noise levels in accommodation spaces on ships or off-shore structures. The use of a noise prediction program makes it possible already at the design stage to estimate the noise levels in a ship. If for instance the initial design is found to be acoustically unsatisfactory, the effects of improved sound insulation and general arrangement can readily be determined. A noise prediction program can also make it possible to find the most economical solution to achieve certain noise requirements. Ideally, the prediction of noise levels should be standard procedure for every new construction.

The data or type of information necessary for making a noise prediction are as follows: description or type of engines, propellers and other sources, steel drawings and general arrangement, description of accommodation systems and of any sound reducing measures. It is assumed that the necessary acoustical parameters for engines, propellers, and accommodation systems can be obtained from a data bank or otherwise be estimated. However, predictions based on measured source data are always preferred. However, the accuracy of a noise prediction can never be better

than the accuracy of noise measurements. A standard deviation for the difference between measured and predicted A-weighted noise levels cannot be expected to be less than 1.5 dB.

A noise prediction can be made in such a way that the relative importance of the various noise sources and structures facing a cabin is presented. The program can also make it possible to determine the effects of changes of installations such as floating floors, damping layers, resilient mounts for engines, new propeller designs, etc.

Problems

16.1 Derive Eq. (16.1).

16.2 An acoustic source is located in a room. Determine the modal energy of the acoustic field in the room. The equivalent absorption area in the room is A . Assume that the field is induced by a number of sources scattered in the room. The power spectral density of the total volume velocity of the sources is G_Q and is constant.

16.3 Derive the sound pressure level difference between the rooms 1 and 3 shown in Fig. 16.6 by using the appropriate coupling loss factors.

16.4 Derive the coupling loss factor η_{13} between the rooms 1 and 3 shown in Fig. 16.6. The coupling loss factor η_{13} defines the nonresonant transmission through a panel having the sound transmission coefficient τ .

16.5 Derive the modal density in a narrow cavity, height d , having the dimensions L_x and L_y for $f < c/(2d)$. Compare Eq. (16.60).

16.6 Determine the coupling loss factor between two plates. Consider only flexural waves. Only rotation at the junction. Compare Eq. (16.60).

16.7 Determine the coupling loss factor between the two rods shown in Fig. 16.12. Consider only longitudinal waves in the rods. Compare Eq. (16.78).

16.8 Derive the expression (16.74).

Appendix A

Sound Transmission Loss of Single Leaf Panels

Panel parameters; μ -mass per unit area (kg/m^2), l_y -width (m), l_z -height (m), f_c -critical frequency (Hz), η -loss factor. The dimensions of the wall in which the panel is mounted are L_y -width (m) and L_z -height (m).

The sound transmission loss R of a panel is

$$R = 20 \log \mu + 20 \log f - 10 \log[\Gamma \cdot \Lambda(S) + G] - 48 \text{ dB for } f < f_c$$

$$R = 20 \log \mu + 30 \log f - 10 \log f_c + 10 \log \eta + 5 \log(1 - f_c/f) - 47 \text{ dB for } f > f_c$$

$$G = \int_0^{\pi/2} \frac{\sin \varphi d\varphi}{\left[\left(\frac{f}{f_c} \right)^2 \sin^4 \varphi - 1 \right]^2 + \left[\eta \left(\frac{f}{f_c} \right)^2 \sin^4 \varphi \right]^2} - 1 \quad \text{Table A.1}$$

Sliding edges $\Lambda(S) = 1$

Simply supported edges $\Lambda(S) = 1 + \frac{3 \cdot 10^4}{4\eta \cdot f^{1/2} \cdot f_c^{3/2}} \left(\frac{1}{l_y^2} + \frac{1}{l_z^2} \right)$

Clamped edges $\Lambda(S) = 1 + \frac{3 \cdot 10^4}{\eta \cdot f^{1/2} \cdot f_c^{3/2}} \left(\frac{1}{l_y^2} + \frac{1}{l_z^2} \right)$

$$\Gamma(S) = \frac{S}{S_0} [1 + Z(MD)] \cdot [1 + Z(NE)]; \quad S_0 = L_y \cdot L_z \quad ; \quad S = l_y \cdot l_z$$

The function $Z(MD)$ is given in Table A.2

$$Z(MD) = \frac{1}{1 + M_1} \left\{ \sum_{m=1}^{M_1} \left[\left(\frac{\sin(mD)}{mD} \right)^2 + 2\xi_m \frac{\sin(mD)}{mD} \right] + 4 \sum_{m=1}^{M_2} \left(\frac{\sin(mD)}{mD} \right)^2 \right\}$$

Table A.1 Resonant transmission function G

f/f_c	G	f/f_c	G				
			$\eta = 1\%$	$\eta = 2\%$	$\eta = 3\%$	$\eta = 4\%$	$\eta = 5\%$
0	0	0.8	2.53	2.53	2.53	2.52	2.52
0.1	0.01	0.82	2.76	2.76	2.75	2.75	2.74
0.02	0.04	0.84	3.32	3.31	3.31	3.30	3.29
0.03	0.11	0.86	4.08	4.07	4.06	4.04	4.02
0.04	0.21	0.88	5.15	5.14	5.12	5.09	5.05
0.05	0.37	0.90	6.76	6.73	6.69	6.64	6.57
0.55	0.49	0.92	9.39	9.34	9.25	9.13	8.98
0.60	0.65	0.94	14.30	14.15	13.90	13.58	13.19
0.65	0.86	0.96	25.75	25.12	24.15	22–95	21.60
0.70	1.16	0.98	69.35	63.02	55.13	47.41	40.63
0.75	1.60	1.00	791	281	154	100	72

$$+ \frac{2}{1 + M_1} \left\{ \sum_{m=1}^{M_3} \sum_{l=1}^{M_4} \left[\xi_m \frac{\sin[(m+l)D]}{(m+l)D} + \frac{\sin(lD)}{lD} \right]^2 \right\}; \quad D = \frac{\pi l_y}{L_y}$$

$$M = \frac{\sqrt{\pi} L_y f}{c}; \quad M_1 = \text{Integer}(M); \quad M_2 = \text{Integer}(M/2)$$

$$M_3 = \text{Integer}(M - 2); \quad M_4 = \text{Integer}\left(\frac{M - m}{2}\right); \quad \xi_m = (-1)^m$$

$$Z(NE) = \frac{1}{1 + N_1} \left\{ \sum_{n=1}^{N_1} \left[\left(\frac{\sin(nE)}{nE} \right)^2 + 2\xi_n \frac{\sin(nE)}{nE} \right] + 4 \sum_{n=1}^{N_2} \left(\frac{\sin(nE)}{nE} \right)^2 \right\}$$

$$+ \frac{2}{1 + N_1} \left\{ \sum_{n=1}^{N_3} \sum_{l=1}^{N_4} \left[\xi_n \frac{\sin[(n+l)E]}{(n+l)E} + \frac{\sin(lE)}{lE} \right]^2 \right\}; \quad E = \frac{\pi l_z}{L_z}$$

$$N = \frac{\sqrt{\pi} L_z f}{c}; \quad N_1 = \text{Integer}(N); \quad N_2 = \text{Integer}(N/2)$$

$$N_3 = \text{Integer}(N - 2); \quad N_4 = \text{Integer}\left(\frac{N - n}{2}\right); \quad \xi_n = (-1)^n$$

The baffle parameter $Z(MD) = Z(X)$ depends on the ratio between the dimensions of the plate and the dimension of baffle plus plate as well as on the frequency. Once the ratio X is determined the function $Z(X)$ is found in Table A.2 for a frequency f for the product $f \cdot L_y$, where f is the frequency in Hz and L_y the total width of panel plus baffle in m.

Table A.2 Baffle parameter $Z(MD) = Z(X)$

$f \cdot L_y$	$X = 0.05$	$X = 0.10$	$X = 0.15$	$X = 0.20$	$X = 0.25$	$X = 0.30$	$X = 0.35$	$X = 0.40$	$X = 0.45$	$X = 0.50$
100	0	0	0	0	0	0	0	0	0	0
125	0	0	0	0	0	0	0	0	0	0
160	0	0	0	0	0	0	0	0	0	0
200	-0.49	-0.49	-0.49	-0.49	-0.49	-0.49	-0.48	-0.47	-0.45	-0.43
250	-0.49	-0.49	-0.49	-0.49	-0.49	-0.49	-0.48	-0.47	-0.45	-0.43
315	-0.49	-0.49	-0.49	-0.49	-0.49	-0.49	-0.48	-0.47	-0.45	-0.43
400	1.98	1.87	1.72	1.53	1.31	1.08	0.84	0.62	0.42	0.25
500	1.98	1.87	1.72	1.53	1.31	1.08	0.84	0.62	0.42	0.25
630	1.23	1.16	1.07	0.98	0.89	0.82	0.76	0.69	0.61	0.51
800	3.85	3.40	2.80	2.17	1.61	1.18	0.87	0.67	0.55	0.48
1000	3.04	2.71	2.33	2.00	1.72	1.45	1.18	0.91	0.68	0.51
1250	5.57	4.49	3.30	2.35	1.73	1.38	1.16	0.99	0.82	0.63
1600	7.10	5.18	3.51	2.52	2.00	1.66	1.35	1.05	0.82	0.68
2000	8.42	5.58	3.70	2.78	2.23	1.76	1.36	1.11	0.93	0.75
2500	9.53	5.84	3.93	3.00	2.32	1.78	1.45	1.19	0.94	0.77
3150	9.88	6.34	4.28	3.10	2.43	1.88	1.52	1.23	0.99	0.82
4000	12.15	6.71	4.58	3.29	2.54	1.97	1.59	1.28	1.05	0.84
5000	12.90	7.08	4.75	3.41	2.60	2.05	1.62	1.32	1.07	0.87
6300	13.87	7.38	4.85	3.51	2.67	2.09	1.66	1.35	1.10	0.90
8000	14.62	7.67	5.01	3.60	2.72	2.13	1.70	1.38	1.12	0.92
10000	15.38	7.92	5.12	3.67	2.78	2.17	1.73	1.40	1.14	0.93
12500	15.94	8.07	5.21	3.73	2.81	2.20	1.75	1.42	1.15	0.94
16000	16.45	8.24	5.30	3.78	2.85	2.22	1.77	1.43	1.17	0.95
20000	16.90	8.37	5.36	3.81	2.88	2.24	1.79	1.44	1.18	0.96
25000	17.23	8.48	5.41	3.85	2.90	2.26	1.80	1.45	1.18	0.97
31500	17.53	8.57	5.46	3.87	2.91	2.27	1.81	1.46	1.19	0.97

(continued)

Table A.2 (continued)

$f \cdot L_y$	$X = (L_y - 2\Delta L_y)/L_y$	X = 0.55	X = 0.60	X = 0.65	X = 0.70	X = 0.75	X = 0.80	X = 0.85	X = 0.90	X = 0.95
100		0	0	0	0	0	0	0	0	0
125		0	0	0	0	0	0	0	0	0
160		0	0	0	0	0	0	0	0	0
200		-0.41	-0.38	-0.34	-0.30	-0.26	-0.21	-0.16	-0.10	-0.05
250		-0.41	-0.38	-0.34	-0.30	-0.26	-0.21	-0.16	-0.10	-0.05
315		-0.41	-0.38	-0.34	-0.30	-0.26	-0.21	-0.16	-0.10	-0.05
400		0.11	-0.01	-0.09	-0.15	-0.18	-0.18	-0.16	-0.11	-0.06
500		0.11	-0.01	-0.09	-0.15	-0.18	-0.18	-0.16	-0.12	-0.06
630		0.39	0.27	0.14	0.04	-0.05	-0.10	-0.13	-0.11	-0.07
800		0.42	0.35	0.26	0.16	0.06	-0.03	-0.08	-0.10	-0.07
1000		0.40	0.34	0.29	0.22	0.13	0.04	-0.04	-0.08	-0.06
1250		0.46	0.35	0.28	0.23	0.17	0.09	0.00	-0.06	-0.06
1600		0.57	0.45	0.33	0.23	0.18	0.13	0.06	-0.02	-0.05
2000		0.58	0.47	0.39	0.28	0.19	0.14	0.09	.01	-0.04
2500		0.64	0.49	0.39	0.31	0.22	0.14	0.10	.04	-0.03
3150		0.65	0.53	0.42	0.31	0.24	0.17	0.10	.06	-0.02
4000		0.69	0.56	0.44	0.34	0.26	0.18	0.12	.06	0.00
5000		0.72	0.57	0.46	0.36	0.27	0.20	0.13	.06	0.02
6300		0.73	0.59	0.47	0.37	0.28	0.20	0.13	.08	0.03
8000		0.75	0.61	0.49	0.38	0.29	0.21	0.14	.08	0.03
10000		0.76	0.62	0.50	0.39	0.30	0.22	0.15	0.09	0.03
12500		0.77	0.62	0.50	0.40	0.31	0.22	0.16	0.09	0.04
16000		0.78	0.63	0.51	0.40	0.31	0.23	0.16	0.10	0.04
20000		0.79	0.64	0.51	0.41	0.32	0.23	0.16	0.10	0.04
25000		0.79	0.64	0.52	0.41	0.32	0.24	0.16	0.10	0.04
31500		0.80	0.65	0.52	0.41	0.32	0.24	0.16	0.10	0.04

Appendix B

Velocity Level of Single Leaf Panels Excited by an Acoustic Field

Panel parameters; μ -mass per unit area (kg/m^2), l_y -width (m), l_z -height (m), f_c -critical frequency (Hz), η -loss factor. The dimensions of the wall in which the panel is mounted are L_y -width (m) and L_z -height (m).

The response or rather average velocity squared of a plate excited by an acoustic field is discussed in Sect. 13.9. Results are given for different boundary conditions of the plate. The effects of baffles are discussed in ref. [180]. The frequency and space average of the plate velocity are given by the quantity

$$L_{v/p} = 10 \log \left[\frac{(\rho_0 c)^2 \langle \bar{v}^2 \rangle}{\langle \bar{p}_1^2 \rangle} \right]$$

where $\langle \bar{p}_1^2 \rangle$ is the frequency and space average of the pressure squared in the source room. The quantity $L_{v/p}$ is for a baffled rectangular panel given by

1. $f < f_c$

$$L_{v/p} = 39 - 20 \log \mu - 20 \log f + 10 \log [T(S) \cdot \Omega + G] \text{ dB}$$

Sliding clamped edges, Fig. 8.2 $T = 1$

$$\text{Simply supported edges} \quad T = 1 + \frac{50}{\eta \cdot f^{1/2} \cdot f_c^{1/2}} \left(\frac{1}{l_y} + \frac{1}{l_z} \right)$$

$$\text{Clamped edges} \quad T = 1 + \frac{100}{\eta \cdot f^{1/2} \cdot f_c^{1/2}} \left(\frac{1}{l_y} + \frac{1}{l_z} \right)$$

$$\Omega = [1 + U(MD)] \cdot [1 + U(NE)] \text{ where } 1 \geq \Omega > 1/4$$

$$U(MD) = \frac{1}{1 + M_1} \sum_{m=1}^{M_1} \xi_m \cdot \frac{\sin(mD)}{mD}; \quad D = \frac{\pi l_y}{L_y};$$

$$M = \frac{\sqrt{\pi} L_y f}{c}; \quad M_1 = \text{Integer}(M); \quad \xi_m = (-1)^m$$

$$U(NE) = \frac{1}{1 + N_1} \sum_{n=1}^{N_1} \xi_n \cdot \frac{\sin(nE)}{nE}; \quad E = \frac{\pi L_z}{L_y}$$

$$N = \frac{\sqrt{\pi} L_z f}{c}; \quad N_1 = \text{Integer}(N); \quad \xi_n = (-1)^n$$

The function $U(MD)$ is listed in Table B.1. The function G is listed in Table A.1.

2. $f > f_c$

$$L_{v/p} = 41 - 20 \log \mu - 30 \log f + 10 \log f_c - 10 \log \eta$$

The sound radiation ratio for a rectangular plate without a baffle is obtained from (13.124) and (13.125) as

$$\bar{\sigma}_a = \frac{2(\Gamma \cdot \Lambda + G)}{\Omega \cdot T + G} \quad \text{for } f < f_c$$

$$\bar{\sigma}_a = \frac{1}{\sqrt{1 - f_c/f}} \quad \text{for } f > f_c$$

The baffle parameter $U(MD) = U(X)$ depends on the ratio between the dimensions of the plate and the dimension of baffle plus plate as well as on the frequency. Once the ratio X is determined the function $U(X)$ is found in Table B.1 for a frequency f for the product $f \cdot L_y$ where by determining.

f is the frequency in Hz and L_y is the total width of panel plus baffle in m.

Appendix C

Input Data for Noise Prediction on Ships

The prediction model presented in Sects. 16.11 through 16.15 has been used extensively for the prediction of noise levels on various types of ships. One example is discussed in Sect. 16.15 where measured and predicted results are compared. The ship is shown in Fig. 16.17 and the element model in Fig. 16.18

The main particulars of the ship are as follows:

- (1) Hull 33175 TDW, $L_{OA} = 170.7$ m, $T = 11.6$ m
- (2) Main engine (1) 9200 kW, 134 rpm (max.cont.)
- (3) Aux. engines (3) 808 kW, 720 rpm (each)
- (4) Propeller (1) Diameter = 5.6 m, 4-bladed, design rate of revs. = 134 rpm

Main and auxiliary engines were firmly mounted.

On the first deck a floating accommodation system of the type shown in Fig. 16.16 was used. On all other decks, the accommodation system was mounted directly to the steel deck. The radiation ratios and coupling factors for all structures in accommodations are given in Tables C.1 and C.2.

On the decks, layers of levelling compound and vinyl were applied. The additional weight of deck covering system plus furniture, etc., is approximately 20 kg/m². The

Table C.1 Radiation ratio σ given as $10 \log \sigma$ for structures in accommodations

f (Hz)	Deck	Bulkheads	Ceiling	Floating floor
31.5	-10	-10	-22	-20
63	-10	-12	-21	-20
125	-9	-12	-21	-18
250	-7	-9	-19	-16
500	-4	-3	-17	-14
1000	-1	2	-15	-12
2000	0	0	-9	-5
4000	0	0	2	0
8000	0	0	0	0

Table C.2 Coupling factors, ΔL_v , for structures in accommodations

f (Hz)	Bulkheads	Ceiling	Floating floor
31.5	-3	0	4
63	3	0	4
125	3	0	4
250	7	6	10
500	9	8	16
1000	11	9	20
2000	14	11	22
4000	15	13	24
8000	16	16	26

bending stiffness for this type of levelling compound is negligible. The parameters for the elements shown in Fig. 16.18 are given in Table C.3. The loss factor η for the various elements is defined as

Table C.3 Structural model

Element number	L_x (m)	t (mm)	ξ	Added weight (kg/m ²)
1	2.50	6	0.7	
2	2.75	7	0.7	
3	2.75	6	0.7	
4	5.90	6	0.7	20
5	2.75	7	0.7	
6	2.75	7	0.7	
7	5.90	6	0.7	20
8	2.75	6	0.7	
9	2.75	6	0.7	
10	3.50	7.5	0.7	
11	5.90	7.5	0.7	20
12	2.85	11.5	0.7	
13	2.85	6	0.7	
14	3.00	14	0.7	20
15	3.00	14	0.7	20
16	3.30	14	0.7	
17	3.60	15	0.7	
18	3.60	6.5	0.7	
19	3.60	6.5	0.7	
20	3.00	8.5	0.7	

(continued)

Table C.3 (continued)

Element number	L_x (m)	t (mm)	ξ	Added weight (kg/m ²)
21	3.00	8.5	1.0	
22	3.30	8.5	0.7	
23	4.40	14	0.7	
24	3.00	13	0.7	
25*	6.10	14	0.7	
26*	2.00	13.5	1.5	
27*	4.00	13.5	1.5	
28	0.80	45	10	
29**	2.70	15	0.7	
30**	1.40	15.5	0.7	
31*	1.40	20	0.7	
32*	1.40	22	0.7	
33**	4.00	15	0.7	
34*	0.80	18	0.7	

*Fluid loading on one side **Fluid loading two sides (water and oil)

$$\eta = 0.025 \cdot \xi \cdot f^{-0.275}$$

where f is the frequency in Hz and ξ a proportionality factor given in Table C.3. The frame distance L_y is everywhere equal to 0.8m The data for the main sources are presented in Table C.4. The main engine is mounted on element 31 between frames 21 and 43. Auxiliary engines are mounted on element 24 between frames 31 and 40. The propeller is equivalent to a source acting on element 25 between frames 0 and 10. The source strength for the main engine is given as a velocity level of element 25. The actual source strength on the foundation can be calculated using the result shown in Figs. 16.21 and 16.22.

Table C.4 Source data The velocity levels in dB (re 10⁻⁹ m/s) induced by main engine, auxiliary engines, and propeller on the elements 25, 23 and 25 respectively

f (Hz)	Main engine El. 25	Aux. engine El.23	Propeller El.25
31.5	126	109	128
63	128	111	127
125	117	113	122
250	111	117	117
500	108	109	109
1000	100	99	106
2000	90	88	100
4000	84	80	94
8000	74	79	86

References

1. W.T. Thomson, *Theory of Vibration with Applications*, 3rd edn. (Unwin Hyman, London, 1989)
2. A.H. Nayfeh, D.T. Mook, *Nonlinear Oscillations* (Wiley, New York, 1979)
3. J.C. Snowdon, *Vibration and Shock in Damped Mechanical Systems* (Wiley, New York, 1968)
4. W.F. Ames, *Numerical Methods for Partial Differential Equations*, 3rd edn. (Academic Press, San Diego, 1992)
5. E. Kreyszig, *Advanced Engineering Mathematics*, 7th edn. (Wiley, New York, 1993)
6. J.R. Hassal, K. Zaveri, *Acoustic Noise Measurements* (Bruel & Kjaer, Naerum, 1988)
7. R.B. Randall, *Frequency Analysis* (Bruel & Kjaer, Naerum, 1987)
8. J.S. Bendat, A.G. Piersol, *Measurement and Analysis of Random Data* (Wiley, New York, 1968)
9. A. Papoulis, *Signal Analysis* (McGraw-Hill Book Company, New York, 1984)
10. J.D. Robson, *Random Vibration* (Edinburgh University Press, Edinburgh, 1963)
11. D.E. Newland, *Random Vibrations and Spectral Analysis*, 2nd edn. (Longman Group Ltd., Harlow, Essex, 1984)
12. D.J. Ewins, *Modal Testing: Theory and Practice* (Research Studies Press Ltd., Letchworth, 1985)
13. L. Boltzman, Zur Theorie der Elastische Nachwirkung. *Analen der Physik* **7**, 624 (1876)
14. V. Volterra, E. Volterra, *Sur le distortion des corps elastique* (Gauthier-Villars, Paris, 1960)
15. E. Volterra, E.C. Zachmanoglou, *Dynamics of Vibrations* (Charles E. Merrill Books Inc, Columbus, 1965)
16. Y.C. Fung, *Foundations of Solid Mechanics* (Prentice Hall Inc, New Jersey, 1965)
17. K. Dovstam, On material damping modelling and modal analysis in structural dynamics. Doctoral technical thesis, Department of Solid Mechanics, KTH, Stockholm (1998)
18. L. Kari, Structure-borne sound properties of vibration isolators. Doctoral technical thesis, report 98-02, MWL, Department of Vehicle Engineering, KTH, Stockholm, Sweden (1998)
19. G.A. Lesieutre, Finite element modelling of frequency dependent material damping using augmenting thermodynamic fields. Ph.D. dissertation. Aero-space Engineering, University of California, Los Angeles (1989)
20. K. Dovstam, Augmented Hooke's law in frequency domain. A three dimensional, material damping formulation. *J. Solids Struct.* **32**(19), 2835-2852 (1995)
21. F. Odquist, *Hå llfasthetslära* (Natur och Kultur, Stockholm, 1961)
22. S.P. Timoshenko, *Strength of Materials*, 3rd edn. (D. Van Nostrand Company, Inc., New York, 1978)

23. P.M. Morse, K.U. Ingard, *Theoretical Acoustics* (McGraw-Hill Book Company, New York, 1968)
24. B. Sundström (ed.), *Handbok och formelsamling i Hållfasthetslära* (Institutionen Hållfasthetslära, KTH, Stockholm, 1998)
25. R. Szilard, *Theory and Analysis of Plates. Classical and Numerical Methods* (Prentice Hall Inc, Englewood Cliffs, 1974)
26. J. Whitney, *Structural Analysis of Laminated Anisotropic Plates* (Technomic Publishing Company, Lancaster, Basel, 1987)
27. G. Pavic, Energy flow induced by structural vibrations of elastic bodies, in *The American Society of Mechanical Engineers* (Winter Annual Meeting, San Fransisco, 1989)
28. D. Noiseux, Measurements of power flow in uniform beams and plates. *J. Acoust. Soc. Am.* **47**(1), 238 (1970)
29. *3rd International Congress on Intensity Techniques*, CETIM, Senlis, France (1990)
30. *4th International Congress on Intensity Techniques*, CETIM, Senlis, France (1993)
31. L. Cremer, M. Heckl, E. Ungar, *Structure-Borne Sound* (Springer, Berlin, 1973)
32. D. Zenkert, *An Introduction to Sandwich Construction* (EMAS Publishing, Warley, West Midlands, 1997)
33. R.M. Jones, *Mechanics of Composite Materials* (Taylor & Francis, Hemisphere Publishing Corporation, New York, 1975)
34. I.H. Marshall (ed.), *Composite Structures* (Applied Science Publishers, London, 1981)
35. Proceedings of the International Conference on Sandwich Constructions, (1) First Conference, Stockholm, Sweden. 1989. (2) Second Conference, Gainesville, Florida. 1992. (3) Third Conference, Southampton, UK. 1995. (4) Fourth Conference, Stockholm, Sweden. 1998
36. O. Zienkiewicz, R. Taylor, *The Finite Element Method. Vol. 1: Basic Formulation and Linear Problems. Vol. 2: Solid and Fluid Mechanics, Dynamics and Non Linearity* (McGraw-Hill, London, 1991)
37. R. Cook, R. Malkus, M. Plesha, *Concepts and Applications of Finite Element Analysis* (Wiley, New York, 1989)
38. B. Szabo, I. Babushka, *Finite Element Analysis* (Wiley, New York, 1991)
39. A.C. Nilsson, *Description of Structure-borne Sound Transmission in Ship Structures. New Materials* (WEGEMT, 16th Graduate School, Genova, 1992)
40. A.C. Nilsson, Wave propagation in and sound transmission through sandwich plates. *J. Sound Vib.* **138**(1), 73–94 (1990)
41. S. Tavellaey Sander, Wave propagation in sandwich structures. Dr. Tech. thesis, TRITA-FKT 2001:01, MWL, KTH (2001)
42. A.C. Nilsson, Wave propagation in simple hull-frame structures on ships. *J. Sound Vib.* **44**(3), 393–405 (1976)
43. M. Abramowitz, I. Stegun (eds.), *Handbook of Mathematical Functions* (National Bureau of Standards, Washington DC, 1970)
44. U. Carlsson, Mechanical mobility: a tool for the analysis of vibrations in mechanical structures. Doctoral technical thesis, report 93–31, MWL, Department of Vehicle Engineering, KTH, Stockholm (1993)
45. T. Derby, J. Ruzicka, *Loss Factor and Resonant Frequency of Visco Elastic Shear-Damped Structural Composites*. NASA CR-1269, National Aeronautics and Space Administration, Federal Scientific and Technical Information, Springfield, Virginia (1969)
46. SWEDAC Product Catalogue, Göteborg, Sweden (1990)
47. A. Nashif, D. Jones, J. Henderson, *Vibration Damping* (Wiley, New York, 1985)
48. L. Beranek (ed.), *Noise and Vibration Control* (McGraw-Hill Book Company, New York, 1988)
49. L. Cremer, M. Heckl, *Körperschall* (Springer, Berlin, 1995)
50. L. Feng, A. Nilsson, Characterisation methods and ranking of mechanical joints, in *ISMA 25*, Leuven, Belgium (2000)
51. A. Mazelet, Measurement of the reflection and transmission properties of junctions in beams, in *Report 97–28*, MWL, Dept. Vehicle Engineering, KTH, Stockholm (1997)

52. M. Åbom, Measurement of the scattering-matrix of acoustical two-ports, in *Inter-Noise 90*, Göteborg, Sweden (1990)
53. H. Bodén, M. Åbom, Influence of errors on the two-microphone method for measuring acoustic properties in ducts. *J. Acoust. Soc. Am.* **72**(2), 541–549 (1986)
54. L. Feng, Vibration reduction through joints in finite systems, in *Inter-Noise 98*, Auckland (1998)
55. R. Haettel, Propagation in built-up plate structures. Prediction and measurement, in *Report 97–37*, MWL, Dept. Vehicle Engineering, KTH, Stockholm (1997)
56. A.C. Nilsson, Reduction of structure-borne sound in simple ship structures. Results of model tests. *J. Sound Vib.* **61**(1), 45–60 (1978)
57. J. Rongong, Reducing transmitted vibration using "smart joint" concepts, in *ISMA 25*, Leuven, Belgium (2000)
58. R. Courant, D. Hilbert, *Methods of Mathematical Physics* (Interscience Publishers, New York, 1966)
59. A. Nordborg, Vertical rail vibrations. Noise and structure-borne sound generation. Doctoral technical thesis 95–35, MWL, Department of Vehicle Engineering, KTH, Stockholm (1995)
60. D. Thompson, Wheel-rail noise generation. Part III: rail vibration. *J. Sound Vib.* **161**(3), 421–446 (1993)
61. R. Hildebrand, Sound attenuation in railway track, In: *Report 99–15*, MWL, Dept. Vehicle Engineering, KTH, Stockholm (1999)
62. R.D. Blevins, *Formulas for Natural Frequency and Mode Shape* (Van Nostrand, New York, 1979)
63. M. Petyt, *Introduction to Finite Element Vibration Analysis* (Cambridge University Press, Cambridge, 1990)
64. S. Finnveden, Spectral finite element analysis of stationary vibrations in a beam-plate structure. *Acustica/Acta Acustica* **82**, 478–497 (1996)
65. F. Fahy, Statistical energy analysis. A wolf in sheep's clothing? in *Inter-Noise-93*, Leuven, Belgium (1993)
66. B. Jarvis, Simple joint models, in *ISMA 25*, Leuven, Belgium (2000)
67. T. Kihlman, *Transmission of Structure-borne Sound in Buildings* (Swedish Institute of Building Research, Stockholm, 1967)
68. R. Ohayon, C. Soize, *Structural Acoustics and Vibration* (Academic Press, New York, 1998)
69. J. Mathews, R.L. Walker, *Mathematical methods of physics* (W.A. Benjamin, New York, 1965)
70. G.R. Cowper, The shear coefficient in Timoshenko's beam theory. *J. Appl. Mech.* **66**, 335–340 (1966)
71. J.W. Nicholson, J.G. Simmonds, Timoshenko beam theory is not always more accurate than elementary beam theory. *J. Appl. Mech.* **44**, 337–338 (1977)
72. J.W. Nicholson, J.G. Simmonds, Timoshenko beam theory is not always more accurate than elementary beam theory. *J. Appl. Mech.* **44**, 357–360 (1977)
73. R.D. Mindlin, Influence of rotary inertia and shear on flexural motions of isotropic elastic plates. *J. Appl. Mech.* **18**, 31 (1951)
74. A. Nilsson, Some acoustical properties of floating floor constructions. *J. Acoust. Soc. Am.* **61**(6), 1463–1466 (1977)
75. H. Jutulstad, Flytande gulv på fjaerer- lydreduserende konstruksjon for fartyg. MSc- thesis, NTNU, ELAB, Trondheim, Norway (1985)
76. A. Leissa, *Vibration of Plates* (Acoustical Society of America, American Institute of Physics, New York, 1993)
77. R. Weinstock, *Calculus of Variations: With Applications to Physics and Engineering* (Dover Publications, New York, 1974)
78. Y.C. Fung, *Pin Tong Classical and Computational Solid Mechanics* (World Scientific Publishing Company, Singapore, 2005)
79. E. Nilsson, A.C. Nilsson, Prediction and measurement of some dynamic properties of sandwich structures with honeycomb and foam cores. *J. Sound Vib.* **251**(3), 409–430 (2002)

80. D. Backström, A. Nilsson, Modelling the vibration of sandwich beams using frequency-dependent parameters. *J. Sound Vib.* **300**, 589–611 (2007)
81. D. Backström, Vibration of sandwich beams. Doctoral thesis, MWL, KTH, TRITA-AVE 2006:39 (2006)
82. S.V. Sorokin, Analysis of wave propagation in sandwich plates with and without heavy fluid loading. *J. Sound Vib.* **271**, 1039–1062 (2004)
83. E. Ungar, E.M. Kervin, Loss factors of viscoelastic systems in terms of energy concepts. *J. Acoust. Soc. Am.* **34**, 954–957 (1962)
84. E. Ungar, Loss factors of viscoelastically damped beam structures. *J. Acoust. Soc. Am.* **34**, 1082–1089 (1962)
85. S.P. Timoshenko, On the correction for shear of the differential equation for transverse vibrations of prismatic bars. *Phil. Mag. Ser.* **6**(41), 744–46 (1921)
86. S.P. Timoshenko, On the transverse vibrations of bars of uniform cross-section. *Phil. Mag. Ser.* **6**, 125–131 (1922)
87. A. Leissa, *Vibration of Shells* (Acoustical Society of America, New York, 1993)
88. W. Soedel, *Vibrations of Shells and Plates* (Marcel Dekker Inc, New York, 2004)
89. A.E.H. Love, *A Treatise on the Mathematical Theory of Elasticity*, 1st edn. (Cambridge University Press, New York, 1944). (Fourth edition, Dover Publication)
90. Lord Rayleigh, *The Theory of Sound* (Dover, New York, 1945)
91. E.F. Gödel, *Rubber Springs Design* (Newnes-Butterwoths, London, 1974)
92. J.C. Snowdon, Vibration isolation: use and characterization. *J. Acoust. Soc. Am.* **66**(5), 1245–1274 (1979)
93. L. Kari, The non-linear temperature dependent stiffness of precompressed rubber cylinders. *Kautsuk Gummi Kunststoffe* **55**(3), 76–81 (2002)
94. M. Sjöberg, Dynamic behaviour of a rubber component in the low frequency range, in *International Congress on Sound and Vibration*, Garmisch-Partenkirchen, Germany (2000)
95. P.B. Lindley, *Engineering Design With Natural Rubber* (Natural Rubber Producers Research Association, London, 1970)
96. M. Sjöberg, L. Kari, Nonlinear isolator dynamics at finite deformations: an effective hyperelastic, fractional derivative, generalized friction model. *Nonlinear Dyn.* **33**, 323–336 (2003)
97. P.E. Austrell, Modelling of elasticity and damping for filled elastomers. Doctoral thesis, Report TVSM-1009, Lund Institute of Technology, Sweden (1997)
98. M. Heckl, H.A. Muller, *Taschenbuch der Technischen Akustik* (Springer, Berlin, 1994)
99. R.L. Bagley, P.J. Torvik, Fractional calculus—a different approach to the analysis of the viscoelastically damped structures. *Am. Inst. Aeronaut. Astronaut. J.* **21**, 741–748 (1983)
100. L. Kari, On the wave-guide modelling of dynamic stiffness of cylindrical vibration isolators Part I. *J. Sound Vib.* **244**(2), 235–257 (2001)
101. R.E.D. Bishop, Longitudinal waves in beams. *Aeronaut. Q.* **3**, 280–293 (1952)
102. L. Kari, On the wave-guide modelling of dynamic stiffness of cylindrical vibration isolators Part II. *J. Sound Vib.* **244**(2), 211–233 (2001)
103. A.D. Nashif, D.I.G. Jones, J.P. Henderson, *Vibration Damping* (Wiley, New York, 1985)
104. L. Pochhammer, Über Fortpflanzungsgeschwindigkeiten kleiner Schwingungen in Einem unbegrenzten isotropen Kreiszyylinder. *Zeitschrift für die reine und Angewandte Mathematik* **81**, 324–336 (1876)
105. C. Chree, The equation of an isotropic elastic solid in polar and cylindrical coordinate. *Trans. Camb. Philos. Soc.* **14**, 250–369 (1889)
106. D. Bancroft, The velocity of longitudinal waves in cylindrical bars. *Phys. Rev.* **59**, 588–593 (1941)
107. R.M. Davies, Stress waves in solids, in *Survey of Mechanics*, ed. by G.K. Batchelor, R.M. (Cambridge University Press, Cambridge, 1956)
108. S. Ivansson, I. Karasalo, Computation of modal wavenumbers using adaptive winding-number integral method with error control. *J. Sound Vib.* **161**, 173–80 (1993)
109. L. Kari, Dynamic transfer stiffness measurements of vibration isolators in the audible frequency range. *Noise Control Eng. J.* **49**(2), 88–102 (2001)

110. L. Kari, Structure-borne sound properties of vibration isolators. Doctoral technical thesis, report 98-02, MWL, Department of Vehicle Engineering, KTH, Stockholm, Sweden (1998)
111. D.J. Thompson, W.J. van Vliet, J.W. Verheij, Developments of the indirect method for measuring the high frequency dynamic stiffness of resilient elements. *J. Sound Vib.* **213**(1), 169–188 (1998)
112. M. Coja, Effective vibro-acoustical modelling of rubber isolators. Doctoral thesis, 2005:25, MWL, KTH, Stockholm, Sweden (2005)
113. G. Pavic, Noise sources and virtual noise synthesis, in *Internoise-08*, Shanghai, China (2008)
114. C.A. Brebbia, H. Tottenham, G.B. Warburton, J.M. Wilson, R.R. Wilson, *Vibration of Engineering Structures* (Springer, Berlin, 1985)
115. B. Petersson, J. Plunt, On effective mobilities in the prediction of structure-borne sound transmission between a source structure and a receiving structure. Part II. *J. Sound Vib.* **82**(4), 531–540 (1982)
116. J. Plunt, J. Odegaard (eds.). *Noise Sources in Ships. Part II Diesel Engines*. Nordforsk, Publication 1983:2, Stockholm, Sweden (1983)
117. M. Coja, L. Kari, A. Nilsson, *EU-report NORMA*, Deliverable 12, MWL, KTH, Stockholm, Sweden (2004)
118. *International Standards Organisation ISO 9611*, Acoustics-characterisation of sources of structure-borne sound with respect to sound radiation from connected structures-measurement of velocity at the contact points of machinery when resiliently mounted (1996)
119. T. Ten Wolde, G. Gadefelt, Development of standard measurement methods for structure-borne sound emission. *Noise Control Eng. J.* **28**, 5–14 (1987)
120. J. Dobson, E. Rider, A review of the indirect calculation of excitation forces from measured structural response data. *Proc. Inst. Mech. Eng.* **204**, 69–75 (1990)
121. A.S. Elliot, Characterisation of structure borne sound sources, In-situ, PhD thesis, University of Salford, Manchester UK (2009)
122. A.T. Moorhouse, A.S. Elliot, T.A. Evans, In situ measurements of the blocked forces of structure-borne sound sources. *J. Sound. Vib.* **325**, 679–685 (2009)
123. A.T. Moorhouse, B.M. Gibbs, Measurements of structure-borne sound emission from resiliently mounted machines in situ. *J. Sound Vib.* **180**(1), 143–161 (1995)
124. A.T. Moorhouse, B.M. Gibbs, Prediction of the structure-borne noise emission of machines. *J. Sound Vib.* **167**(2), 223–237 (1993)
125. A. Tarantola, *Inverse Problem Theory* (Elsevier, New York, 1987)
126. P. Mas, P. Sas, K. Wyckaert, Indirect force identification based upon impedance matrix inversion. A study on statistical and deterministical accuracy, in *Proceedings ISMA19*, Leuven, Belgium (1994)
127. B. Petersson, B.M. Gibbs, Towards a structure-borne sound source characterization. *Appl. Acoust.* **61**(3), 325–343 (2000)
128. M. Janssens, J. Verheij, A pseudo-forces methodology to be used in characterization of structure-borne sound sources. *Appl. Acoust.* **61**(3), 325–343 (2000)
129. M. Janssens, J. Verheij, D. Thompson, The use of an equivalent forces method for the experimental quantification of structural sound transmission in ships. *J. Sound Vib.* **226**(2), 305–328 (1999)
130. L. Heng-Li, Alternative test methods for measuring structure-borne sound, in *Internoise-06*, Hawaii (2006)
131. G. Arfken, H. Weber, *Mathematical Methods for Physicists* (Harcourt, Academic Press, San Diego, 2001)
132. K.S. Werner, Sound speed in liquid-gas mixtures: water-air and water-steam. *J. Geophys. Res.* **82**(20), 2895–2904 (1977)
133. F. Jacobsen, Sound intensity, in *Hanbook of Acoustics*, ed. by M. Crocker (Springer, New York, 2007)
134. F. Fahy, *Sound Intensity* (Elsevier Applied Science, London, 1989)
135. S. Temkin, *Elements of Acoustics* (Acoustical Society of America, American Institute of Physics, USA, 2001)

136. M.J. Lighthill, On sound generated aerodynamically. I general theory. Proc. R. Soc. A **211**, 564–587 (1954)
137. A. Dowling, W.J.E. Ffowcs, *Sound and Sources of Sound* (Wiley, New York, 1983)
138. M. Åbom, An introduction to flow acoustics. TRITA-AVE 2006:04, KTH, Stockholm, Sweden (2006)
139. W. Nyborg, D. Mintzer, *Review of Sound Propagation in the Lower Atmosphere* (Brown University, USA, 1960)
140. H.H. Hubbard (ed.), *Aeroacoustics of Flight Vehicles. Theory and Practice* (Acoustical Society of America, American Institute of Physics, USA, 1995)
141. American National Standards Institute, *Method for the Calculation of the Absorption of Sound by the Atmosphere*, ANSI S1.26-1995 (1995)
142. E. Torra i Fernández, The influence of tyre air cavities on vehicle acoustics. Doctoral thesis. TRITA-AVE 2006:67, MWL, KTH, Stockholm, Sweden (2006)
143. A. Sommerfeld, The Green's function of the oscillation equation. Jahresber. Disch. Math. Ver. **21**, 309–353 (1912)
144. J.E. Piercy, T. Embleton, L. Sutherland, Review of sound propagation in the atmosphere. J. Acoust. Soc. Am. **61**, 1403–1418 (1977)
145. G.K. Batchelor, *The Theory of Homogeneous Turbulence* (Cambridge University Press, Cambridge, 1967)
146. V.I. Tatarski, *Wave Propagation in a Turbulent Medium* (Dover Publications, New York, 1967)
147. C.F. Eyring, Reverberation time in “dead” rooms. J. Acoust. Soc. Am. **1**, 217–241 (1930)
148. H. Kuttruff, *Room Acoustics* (E&FN Spon, London, 1999)
149. T.E. Vigran, *Building Acoustics* (CRC-Press, Boca Raton, 2008)
150. M. Schröder, The statistical parameters of frequency curves of large rooms. Acustica **4**, 594–600 (1954)
151. M. Schröder, K. Kuttruff, On frequency response curves in rooms. J. Acoust. Soc. Am. **34**, 76–80 (1962)
152. G. Maidanik, E.M. Kerwin, Influence of fluid loading on the radiation from infinite plates below the critical frequency. J. Acoust. Soc. Am. **40**(5), 10234–10238 (1966)
153. D.G. Crighton, The 1988 Rayleigh medal lecture: fluid loading—the interaction between sound and vibration. J. Sound Vib. **133**, 1–27 (1989)
154. D.G. Crighton, Force and moment admittance of plates under arbitrary fluid loading. J. Sound Vib. **20**(2), 209–218 (1972)
155. D.G. Crighton, Point admittance of an infinite thin elastic plate under fluid loading. J. Sound Vib. **54**(3), 389–391 (1977)
156. G. Maidanik, Vibrational and radiative classifications of modes of a baffled finite panel. J. Sound Vib. **34**(4), 447–455 (1974)
157. C.E. Wallace, Radiation resistance of a rectangular plate. J. Acoust. Soc. Am. **51**(3), 946–952 (1970)
158. G. Maidanik, Response of ribbed panels to reverberant acoustic fields. J. Acoust. Soc. Am. **34**(6), 809–826 (1962)
159. F.G. Leppington, E.G. Broadbent, K.H. Heron, The acoustic radiation efficiency of rectangular panels. Proc. R. Soc. Lond. Ser. A **382**(1783), 245–271 (1982)
160. E. Nijman, Simple analytical models for tough mid-frequency range problems, in *EU-project CANTOR*, Course held at CRF, Torino, Italy (2009)
161. K. Andresen, Hydroacoustic radiation from ships hulls. Thesis, TRITA-FKT 9306, MWL, KTH, Stockholm, Sweden (1993)
162. W.K. Blake, *Mechanics of Flow-Induced Sound and Vibration*, vol. 17–1 (Academic Press, Orlando, 1986)
163. A.C. Nilsson, Propeller induced hull plate vibrations. J. Sound Vib. **69**(4), 539–557 (1980)
164. J. Plunt, Methods for predicting noise levels in ships. Part I; Noise level prediction methods for ships based on empirical data. Part II; prediction of structureborne sound transmission in complex structures with SEA method. Doctoral thesis 80–6 and 80–7, Chalmers University of Technology, Göteborg, Sweden (1980)

165. M.C. Junger, D. Feit, *Sound, Structures and Their Interaction* (Acoustical Society of America, American Institute of Physics, New York, 1986)
166. D. Chapman, An improved Kirchhoff formula for reflection loss at a rough ocean surface at low grazing angles. *J. Acoust. Soc. Am.* **73**(2), 520–527 (1983)
167. C. Clay, H. Medwin, Dependence of spatial and temporal correlation of forward scattered underwater sound on surface statistics. *J. Acoust. Soc. Am.* **47**(5), 1414–1429 (1970)
168. A.C. Nilsson, A method for the prediction of noise and velocity levels in ship constructions. *J. Sound Vib.* **94**(3), 411–429 (1984)
169. L. Cremer, M. Heckl, B. Petersson, *Structure-Borne Sound* (Springer, Berlin, 2005)
170. T.W. Wu (ed.), *Boundary Element Acoustics. Fundamentals and Computer Codes* (WIT Press, Southampton, Boston, 2000)
171. M. Crocker (ed.), Encyclopedia of acoustics, Chap. 15, in *Acoustic Modeling. Boundary Element Methods*, ed. by A. Seybert, T. Wu (Wiley, New York, 1997)
172. H.G. Davies, Sound from turbulent boundary layer excited panels. *J. Acoust. Soc. Am.* **49**(3) Part II, 878–889 (1971)
173. H.G. Davis, Low frequency random excitation of water loaded rectangular plates. *J. Sound Vib.* **15**(1), 107–126 (1971)
174. L. Cremer, Theorie der Schalldämmung dünner Wände bei schrägem Einfall. *Akust. Z.* **7**, 81 (1942)
175. L. Beranek, The transmission radiation of acoustic waves by structures. *J. Inst. Mech. Eng.* **6**, 162–169 (1959)
176. E.C. Sewell, Transmission of reverberant sound through a circular panel in a waveguide. *J. Sound Vib.* **12**, 397 (1970)
177. E.C. Sewell, Exact solution for transmission of reverberant sound through a single leaf partition surrounded by an infinite baffle. *J. Sound Vib.* **12**, 21 (1970)
178. M. Crocker, A. Price, Sound transmission using statistical energy analysis. *J. Sound Vib.* **9**, 469–486 (1969)
179. R. Josse, C. Lamure, Transmission du son par une paroi simple. *Acustica* **14**, 266 (1964)
180. A. Nilsson, Sound transmission through single leaf panels, in *Report 74–01*, Applied Acoustics (Chalmers University of Technology, Göteborg, Sweden, 1974)
181. A.S. Nikiforov, Radiation from a plate of finite dimensions with arbitrary boundary conditions. *Sov. Phys. Acoust.* **10**(2), 178 (1964)
182. T. Kihlman, A. Nilsson, The effects of some laboratory designs and mounting conditions on reduction index measurements. *J. Sound Vib.* **24**, 349 (1972)
183. K. Gösele, Über Prüfstände zur Messung der Luftschalldämmung von Wänden und Decken. *Acustica* **15**, 317 (1965)
184. L. Feng, S. Kumar, On application of radiation loss factor in the prediction of sound transmission loss of a honeycomb panel. *Int. J. Acoust. Vib.* **17**(1), 47–51 (2012)
185. G. von Venzke, P. Dämmig, H.W. Fischer, Der Einfluss von Versteifungen auf der Schallabstrahlung Schalldämmung von metallwänden. *Acustica* **29**(1), 29–40 (1973)
186. B. Sharp, Prediction method for the sound transmission of building elements. *Noise Control Eng.* **11**(2), 53–63 (1978)
187. T.D. Northwood, Transmission loss of plasterboard walls, in *Building Research Note 66* (National Research Council of Canada, Ottawa, 1970)
188. J. Kristensson, J.H. Rindel, *Byggningsakustik*, SBI-Anvisning 166 (Statens Byggeforskningsinstitut, Copenhagen, 1989)
189. F. Fahy, *Sound and Structural Vibration* (Academic Press, London, 1985)
190. *EN ISO 140–1*, Acoustics- Measurements of sound insulation in buildings and of building elements- Part 1: Requirements for laboratory test facilities with suppressed flanking transmission
191. *EN ISO 140–3*, Acoustics- Measurements of sound insulation in buildings and of building elements- Part 3: Laboratory measurements of airborne sound insulation between rooms
192. *EN ISO 140–4*, Acoustics- Measurements of sound insulation in buildings and of building elements- Part 4: Field measurements of airborne sound insulation between rooms

193. T. Kihlman, Sound transmission in building structures of concrete. *J. Sound Vib.* **11**, 435 (1970)
194. M. Åbom, Acoustic multi-ports with application to duct acoustic, in *Proceedings International Congress on Sound and Vibration*, Cairo, Egypt (2010)
195. A. Nilsson, P. Tyvand (eds.), *Noise Sources in Ships. Part I: Propellers*. Nordforsk, Miljövärdsserien 1981:2, Stockholm, Sweden (1981)
196. U. Orrenius, S. Finnveden, Calculation of wave propagation in rib-stiffened plate structures. *J. Sound Vib.* **198**(3), 203–224 (1996)
197. A. Nilsson, Attenuation of structure-borne sound in superstructures on ships. *J. Sound Vib.* **55**(1), 71–91 (1977)
198. A. Nilsson, A method for the prediction of noise and velocity levels in ship constructions. *J. Sound Vib.* **94**(3), 411–429 (1984)
199. W. Desmet, B. Pluymers, O. Atak (eds.), “Mid-frequency”. *CAE Methodologies for Mid-frequency Analysis in Vibration and Acoustics*. Katholieke Universiteit Leuven, Faculty of Engineering, Heverlee, Belgium (2012)
200. R. Haettel, Vibration transmission in plate structures. PhD thesis KTH/FKT/DA00/32, KTH, Stockholm, Sweden (2000)
201. J. Aszteley, The uses of viscoelastic materials for noise reduction in ships. *Noise Control Vib. Insul.* 297–299 (1977)
202. T. Kihlman, Noise reduction with constrained viscoelastic layers. A case history, in *Proceedings of the International Symposium on Shipboard Acoustics* (Elsevier Scientific Publishing Company, Amsterdam, 1977)
203. F.H. Van Tol, A model study on the noise reduction effect of damping layers onboard ships, in *TNO report 133S*, Delft, The Netherlands (1970)
204. J. Buiten, Noise reduction on a Rhine-cruise ship due to damping material. *J. Sound Vib.* **21**, 159–167 (1972)
205. A.E. Turner, The use of damping materials for noise reduction on a passenger ship. *J. Sound Vib.* **10**, 187–197 (1969)
206. F. Fahy, E. Lindqvist, Wave propagation in damped stiffened structures characteristic of ship constructions. *J. Sound Vib.* **45**, 115–138 (1976)
207. J. Odegaard-Jensen, Calculation of structure-borne noise transmission in ships using the statistical energy analysis approach, in *Proceedings of the International Symposium on Shipboard Acoustics* (Elsevier Scientific Publishing Company, Amsterdam, 1977)
208. U. Orrenius, Transmission of structure-borne sound in ships: application to a prediction model. PhD thesis, report 9715, MWL, KTH, Stockholm, Sweden (1997)
209. N.J. Hoff, Bending and buckling of rectangular sandwich plates, in *NACA TN 2225* (1950)
210. J. Whitney, *Structural Analysis of Laminated Anisotropic Plates* (Technomic Publication, Basel, 1987)
211. G. Kurtze, B. Watters, New wall design for high transmission loss or high damping. *J. Acoust. Soc. Am.* **31**(6), 739–748 (1959)
212. C. Dym, M. Lang, Transmission of sound through sandwich plates. *J. Acoust. Soc. Am.* **56**(5), 1523–1532 (1974)
213. J.L. Guyader, C. Lesueur, Acoustic transmission through orthotropic multilayered plates. *J. Sound Vib.* **58**(1), 51–68 (1977)
214. S. Timoshenko, *Schwingungsprobleme der Technik* (Springer, Berlin, 1932)
215. E.M. Kervin Jr, Damping of flexural waves by a constrained viscoelastic layer. *J. Acoust. Soc. Am.* **31**(7), 952–962 (1959)
216. D.J. Mead, S. Markus, The forced vibration of a three-layer, damped sandwich beam with arbitrary boundary conditions. *J. Sound Vib.* **10**(2), 163–175 (1969)
217. D.J. Mead, A comparison of some equations for the flexural vibration of damped sandwich beams. *J. Sound Vib.* **83**(3), 363–377 (1982)
218. S. Timoshenko, *Strength of Materials* (Van Nostrand, New York, 1978)
219. E. Nilsson, Some dynamic properties of honeycomb structures, in *TRITA-FKT 2000-30*, MWL, KTH, Stockholm, Sweden (2000)

220. A. Nilsson, E. Piana, Acoustic properties of sandwich and honeycomb panels. in *Medyna, 1st Euro-Mediterranean Conference on Structural Dynamics and Vibro-Acoustics*, Marrakech, Morocco (2013)
221. Lord Rayleigh, Note on the free vibrations on an infinitely long shell. *Proc. R. Soc.* **45**, 443 (1889)
222. A.E.H. Love, On the small free vibrations and deformations of a thin elastic shell. *Philos. Trans. R. Soc. Ser. A* **179**, 491–546 (1888)
223. A.E.H. Love, *A Treatise on the Mathematical Theory of Elasticity*, 4th edn. (Dover Publication, New York, 1944)
224. B. Liu, L. Feng, A. Nilsson, Sound transmission through curved aircraft panels with stringer and ring frame attachments. *J. Sound Vib.* **300**, 949–973 (2007)
225. B. Liu, L. Feng, A. Nilsson, Influence of overpressure on sound transmission through curved panels. *J. Sound Vib.* **302**, 760–776 (2007)
226. T. Wah, Flexural vibrations of ring-stiffened cylindrical shells. *J. Sound Vib.* **3**, 242–251 (1966)
227. *ISO 15186-1:2000 Acoustics—Measurement of sound insulation in buildings and of building elements using sound intensity—Part 1: Laboratory measurements*
228. L.R. Koval, Effect of air flow, panel curvature, and internal pressurization on field-incidence transmission loss. *J. Acoust. Soc. Am.* **59**, 1379–1385 (1976)
229. H. Schlichting, *Boundary Layer Theory* (McGraw-Hill, New York, 1979)
230. M.S. Howe, *Acoustics of Fluid-structure Interactions* (Cambridge University Press, Cambridge, 1998)
231. G.M. Corcos, The structure of the turbulent pressure field in boundary-layer flows. *J. Fluid Mech.* **18**, 353–378 (1963)
232. G.M. Corcos, Resolution of pressure in turbulence. *J. Acoust. Soc. Am.* **35**(2), 192–199 (1963)
233. B.M. Efimtsov, Characteristics of the field of turbulent wall pressure fluctuations at large Reynolds numbers. *Sov. Phys. Acoust.* **28**(4), 289–292 (1982)
234. D.M. Chase, The character of the turbulent wall pressure spectrum at subconvective wavenumbers and a suggested comprehensive model. *J. Sound Vib.* **112**(125–147), 1987 (1987)
235. D.M. Chase, Modelling the wavevector-frequency spectrum of turbulent boundary layer wall pressure. *J. Sound Vib.* **70**, 29–67 (1980)
236. A.V. Smolyakov, V.M. Tkachenko, Model of a field of pseudonic turbulent wall pressure and experimental data. *Sov. Phys. Acoust.* **37**(6), 627–631 (1991)
237. W.J.E. Ffowcs, Boundary-layer pressures and the Corcos model. *J. Fluid Mech.* **125**, 9–25 (1982)
238. W.R. Graham, A comparison of models for the wavenumber-frequency spectrum of turbulent boundary layer pressures. *J. Sound Vib.* **206**, 541–565 (1997)
239. W.W. Willmarth, Measurements of the fluctuating pressure at the wall beneath a thick turbulent layer. *J. Fluid Mech.* **14**, 187–210 (1962)
240. G. Robert, Modelisation et simulation du champ exciteur induit sur une structure par une couche limite turbulente. These no. 84–02, *Ecole Centrale de Lyon*, France (1984)
241. S. Finnveden, F. Birgersson, U. Ross, T. Kremer, A model of wall pressure correlation for prediction of turbulence-induced vibration. *J. Fluids Struct.* **20**, 1127–1143 (2005)
242. D.G. Crighton, A.P. Dowling, W.J.E. Ffowcs, M. Heckl, F.G. Leppington, *Modern Methods in Analytical Acoustics* (Springer, Berlin, 1992)
243. B. Liu, Noise radiation of aircraft panels subjected to boundary layer pressure fluctuations. *J. Sound Vib.* **314**, 693–711 (2008)
244. W.R. Graham, Boundary layer induced noise in aircraft, the flat plate model. *J. Sound Vib.* **192**(1), 101–120 (1996)
245. W.R. Graham, Boundary layer induced noise in aircraft, the trimmed flat plate model. *J. Sound Vib.* **192**(1), 121–138 (1996)
246. N. Totaro, J.L. Guyader, Model of frequency averaged injected power into a plate excited by a turbulent boundary layer. *Acta Acustica/Acustica* **89**, 647–657 (2003)

247. A. Nilsson, L. Feng, Measurements of sound and vibration, in *P1800 Aircraft*, Technical notes MWL, KTH, Stockholm, Sweden (2008)
248. B. Liu, L. Feng, A. Nilsson, M. Aversano, Predicted and measured plate velocities induced by turbulent boundary layers. *J. Sound Vib.* **331**, 5309–5325 (2012)
249. R. Robert, W. Adam, *Modeling of Turbulent Boundary Layer Surface Pressure Fluctuation Auto and Cross Spectra -Verification and Adjustments Based on TU-144LL Data*. NASA/CR-2005-213938 (2005)
250. A. Nilsson, F. Birgersson, Ship hull vibrations induced by turbulent boundary layers, in *International Conference of Sound and Vibration (ICSV)*, Cairns, Australia (2006)
251. E. Ciappi, F. Magionesi, Characteristics of the turbulent boundary layer pressure for high speed vehicles. *J. Fluid Struct.* **21**, 321–333 (2005)
252. F. Magionesi, E. Ciappi, R. Camussi, T. Pagliaroli, A. Di Mascio, B. Imperatore, A. Marino, Measurement and modelling of turbulent boundary layer excitation for naval and aeronautical applications, in *NOVEM 2012*, Sorrento, Italy (2012)
253. M.S. Kompella, R.J. Bernhard, Variation of structural-acoustic characteristics of automotive vehicles. *Noise Control Eng. J.* **44**, 93–99 (1996)
254. K. Skaar (ed.), *Vibration Control in Ships* (Det Norske Veritas, Hovik, Norway, 1985)
255. N.B. Roozen, Sound transmission through aircraft structures. Ph.D. thesis, Technische Universiteit Eindhoven, The Netherlands (1992)
256. R.H. Lyon, G. Maidanik, Power flow between linearly coupled oscillators. *J. Acoust. Soc. Am.* **34**, 623–639 (1962)
257. T.D. Scharton, R.H. Lyon, Power flow and energy sharing in random vibration. *J. Acoust. Soc. Am.* **43**(6), 1332–1343 (1968)
258. R.H. Lyon, *Statistical Energy Analysis of Dynamical Systems: Theory and Applications* (The MIT Press, Cambridge, 1975)
259. R.H. Lyon, R.G. De Jong, *Theory and Applications of Statistical Energy Analysis* (Butterworth-Heinemann, Boston, 1995)
260. P.W. Smith Jr, Concepts and applications of SEA, in *97th Meeting of the Acoustical Society of America*, MIT (June 1979)
261. F. Fahy, Statistical energy analysis: a critical overview. *Philos. Trans. R. Soc. Lond. A* **346**, 431–447 (1994)
262. T.D. Scharton, R.H. Lyon, Power flow and energy sharing in random vibration. *J. Acoust. Soc. Am.* **43**, 1332–1343 (1968)
263. R.S. Langley, A general derivation of the statistical energy analysis equations for coupled dynamic systems. *J. Sound Vib.* **135**, 499–508 (1989)
264. R.S. Langley, The statistical energy analysis of two continuous one-dimensional subsystems. *J. Sound Vib.* **141**, 207–219 (1990)
265. B.R. Mace, A derivation of the coupling loss factor used in statistical energy analysis. *J. Sound Vib.* **166**, 429–461 (1993)
266. P.W. Smith Jr, Statistical models of coupled dynamic systems and the transition from a weak to strong coupling. *J. Acoust. Soc. Am.* **65**, 695–698 (1979)
267. R.S. Langley, A.N. Bercin, Wave intensity analysis of high frequency vibrations. *Philos. Trans. R. Soc. Lond. A* **346**, 489–499 (1994)
268. R.J.M. Craik, *Sound transmission through buildings using Statistical Energy Analysis* (Grower, Vermont, 1996)
269. A.J. Keane, W.G. Price, *Statistical Energy Analysis: An Overview With Applications in Structural Dynamics* (Cambridge University Press, Cambridge, 1997)
270. F.J. Fahy, Y. de-Yuan, Power flow between non-conservatively coupled oscillators. *J. Sound Vib.* **114**(1), 1–11 (1987)
271. F.J. Fahy, A.D. Mohammed, A study of uncertainty in applications of SEA to coupled beam and plate systems. Part I: computational experiments. *J. Sound Vib.* **158**, 45–67 (1992)
272. A.J. Price, M.J. Crocker, Sound transmission through double panels using statistical energy analysis. *J. Acoust. Soc. Am.* **47**(3), 682–693 (1969)

273. J.L. Guyader, C. Boisson, C. Lesueur, Sound transmission by coupled structures: application to flanking transmission. *J. Sound Vib.* **106**(2), 289–310 (1986)
274. R.J.M. Craik, The prediction of sound transmission through buildings using statistical energy analysis. *J. Sound Vib.* **82**, 505–516 (1982)
275. R.J. Sawley, *The Evaluation of a Shipboard Noise and Vibration Problem Using Statical Energy Analysis* (American Society of Mechanical Engineers, New York, 1969)
276. J. Suhara, Analysis and prediction of shipboard noise, in *Proceedings of the International Symposium on Practical Design* (1977)
277. N. Totaro, J.L. Guyader, SEA substructuring using cluster analysis; the MIR index. *J. Sound Vib.* **290**, 264–289 (2006)
278. L. Maxit, J.L. Guyader, Estimation of SEA coupling loss factors using a dual formulation and FEM information. *J. Sound Vib.* **239**, 907–948 (2001)
279. S. Finnveden, Evaluation of modal density and group velocity by a finite element model. *J. Sound Vib.* **273**, 51–75 (2004)
280. L. Maxit, J.L. Guyader, Extension of SEA model to subsystems with non-uniform modal energy. *J. Sound Vib.* **265**(2), 337–358 (2003)
281. J.W.E. Pettersen, J.F. Storm (eds.), *Noise Control in Ships* (Norwegian Council for Technical and Scientific Research (NTNF), Oslo, 1975)
282. L. Beranek (ed.), *Noise and Vibration Control* (McGraw-Hill Book Company, New York, 1971)
283. H. Bodén et al., *Sound and Vibration. Trita-AVE 2008–55*. MWL, KTH, Stockholm, Sweden (2008)
284. J.H. Janssen, J. Buiten, An acoustical design on naval architecture, in *Proceedings Inter-noise-73* (1973)
285. *Acoustic Design Manual for Ships* (The British Ship Research Association, 1976)
286. K. Andresen, Noise prediction and prevention, in *2nd International Symposium on Shipboard Acoustics*, The Hague, The Netherlands (1986)
287. M. Heckl, Investigation on the vibrations of grillages and other simple beam structures. *J. Acoust. Soc. Am.* **36**, 1335–1343 (1964)
288. B.L. Clarkson, R.D. Ford, The response of a typical aircraft structure to jet noise. *J. R. Aeronaut. Soc.* **66**, 31–40 (1962)
289. B.S. Seland, *Propagation of Structure Borne Sound in Stiffened Plates* (DnV-Report, Det norske Veritas, Oslo, 1978)
290. J. Plunt, Methods for predicting noise levels in ships, Part 17, in *Report 17–42*. Chalmers Technical University, Göteborg (1977)
291. J.W. Verheij, *Multi-path Sound Transfer from Resiliently Mounted Shipboard Machinery* (Institute of Applied Physics TNO-TH, Delft, The Netherlands, 1982)
292. F. Fahy, *Foundations of Engineering Acoustics* (Academic Press, London, 2001)
293. K. Andresen, A. Nilsson, E. Brubakk, Noise prediction and prevention, in *2nd International Symposium on Shipboard Acoustics*, The Hague, The Netherlands (Martinus Nijhoff Publishers, 1986)
294. Y. Kou, B. Liu, J. Tian, The radiation efficiency of damped plates. *J. Acoust. Soc. Am.* **137**, 1032 (2015)
295. Y.F. Hwang, W.K. Bonness, S.A. Hambric, Comparison of semi-empirical models for turbulent boundary layer wall pressure spectra. *J. Sound Vib.* **319**, 199–217 (2009)
296. M.C. Goody, Empirical spectral model of surface pressure fluctuations. *J. AIAA* **42**(9), 1788–1794 (2004)
297. D. Lecoq, Identification par probleme inverse vibratoire des bas nombres dnde de precissions parietales turbulentes. These Doctorat, Universit du Maine, France (2013)

Index

A

- Acoustic fields
 - closed rooms, 146
 - near, 155
 - reverberant, 155
- Acoustic impedance, 134
- Acoustic sources
 - cylindrical sources, 126, 128
 - dipole sources, 121
 - moving monopole source, 129
 - multipole sources, 121
 - point source, 113
 - spherical source, 121
 - volume velocity, 116
- Acoustic waves
 - influence of velocity gradients, 143
 - influence of fluid velocity, 143
 - influence of temperature gradients, 144
 - wave equation, 67
- Added weight, fluid loading, 163
- Apparent E -modulus, rubber, 57
- Associated Legendre function, 123
- Attenuation
 - waves in fluids, 103

B

- Beam
 - honeycomb, 294
 - sandwich, 294
- Bessel function, 69
- Boundary conditions
 - beam, constrained viscoelastic layer, 20
 - bending sandwich, 297
 - bending, honeycomb, 14, 298
 - Timoshenko beam, 20
- Boundary layer thickness, 351

Bulk modulus, 54

C

- Coincidence angle, 220
- Constrained viscoelastic layers, 14
- Convective ridge, 352
- Corcos' model, 352
- Corcos' parameters, 354
- Coupling loss factor, 388
- Coupling loss factor, structures, 400
 - measurement of, 408
- Critical frequency, 169, 218
- Cylinders, wave propagation, 316
- Cylindric acoustic source, 117
- Cylindrical shells, 26, 322
 - sound transmission loss, 324

D

- Deflection, rubber mounts, 65
- Dilatation frequency, 8
- Dipole sources, 121
- Donell-Mushtari operator, 31
- Doppler effect, 133
- Double wall resonance, 258
- Driving point stiffness, mounts, 63

E

- Effective stiffness, mounts, 75
- Efimsov models, 355
- Eigenfunctions
 - acoustic fields, rooms, 146
- E -modulus, *see* Young's modulus
- apparent, 55
- Energy

fluids, 109
 Energy flow
 buildings, 403
 SEA, 387, 402
 ships, 405
 Equivalent absorption, 153
 Equivalent mobility
 mounts, 63
 Equivalent stiffness
 measurements, 77
 mounts, 61
 phase, 77
 Eyring's formula, 154

F

Flanking transmission, 260
 Flexural waves, beams, 4
 Flexural waves, plates
 sandwich/honeycomb, 7
 Floating accommodations, 417
 Flow-induced noise, ships, 372
 Fluid loading
 infinite plates, 168
 radiation from plate, 204
 Fluids
 compressibility, 106
 conservation of mass, 104
 conservation of momentum, 104
 losses, 110
 properties, 108
 speed of sound, 108
 wave equation, 103
 Forced response
 simple mass–spring systems, 41
 Fourier transform
 spatial, 174
 Frequency split, 114

G

Garlekin's method, 33
 Geometrical acoustics, 151
 Green's function
 acoustic sources, 118
 Fourier transform of, 175
 rigid plane boundary, 171
 Ground absorption, 141
 Group velocity, 314

H

Hamilton's principle, 1
 Hankel function, 117, 200

Hardness, rubber, 55
 Honeycomb plates, 289
 Honeycomb, *see* Sandwich

I

Impedance
 acoustic, 137
 Impedance matrix, 84
 Intensity
 fluids, 109
 IRH, 55

K

Kinematic viscosity, 350

L

Lagrange's equations, 32
 Lagrangian, 2
 Legendre function, 124
 Longitudinal waves
 Bishop correction, 60
 Love approximation, 60
 rubber mounts, 58
 Lorentz transformation, 130
 Losses
 discrete systems, 46
 fluids, 110
 radiation, 163, 202, 203

M

Mach number, 130
 Mindlin plate, 21
 Mobility matrix, 81, 84
 Mobility, fluid-loaded plates, 184
 Modal density
 acoustic field, rooms, 148
 Modal energy, SEA, 388
 Modal overlap, 390
 Modes, discrete systems, 51
 Moment mobility, 82
 Mounts
 effective stiffness, 75
 rubber, 53
 Multipole sources, 121

N

Natural frequency, 47
 closed rooms, 148
 cylindrical shells, 322

sandwich/honeycomb beam, 300
N-wave, 108

O

Oneo function, 70

P

Particle velocity, 104, 115

Phase velocity

longitudinal waves, 72

Plate

excitation of, 342

excited by acoustic field, 223, 255

excited by TBL, 356

rain on the roof excitation, 346

random excitation, 339

Point mobility

engine foundation, 92

fluid-loaded infinite plate, 181

measurements, 95

Potential

velocity, 107

Q

Quadrupole sources, 122

R

Random excitation, 339

Rayleigh formula, radiation, 173

Reflection

acoustic waves, 133, 139

coefficient, 138

watersurface, 141

Resiliently mounted superstructures, 281

Reverberation time, 154

Reynold's number, 350

Ring frequency, 320

Rubber element

wave propagation, 66

Rubber, material parameters, 55, 56

S

Sandwich plate/beam, 289

bending stiffness, 305

dynamic properties, 302

energy flow, 312

flow across junctions, 314

group velocity, 314

natural frequencies, bending, 299

response, 307

sound transmission loss, 309

Schröder frequency, 155

SEA, 382

buildings, 403

coupling loss factor, 388, 391, 407

energy flow, 387

modal energies, 388

modal overlap, 390

parameters, 405

requirements, 387

ships, 404

sound transmission loss, 393

weak coupling, 389

Shadow zone, 145

Shape function

rubber mounts, 54

Ship noise, 409

measurements of, 418, 420

prediction of, 411, 415

Sound radiation

baffled finite plates, 186

cylinders, 200

fluid-loaded plate, 204

general formulation, 169

induced by acoustic field, 223

infinite plates, 163

losses, 202

modal radiation, 191

point-excited infinite plate, 177, 185

ratios, finite baffled plates, 192

Rayleigh formula, 173

total radiation from plates, 197

Sound reduction index, *see* Sound transmission loss

Sound transmission loss

between equal rooms, 234

between irregular rooms, 236

cylindrical shells, 324

double walls, 257

effect boundary conditions, 237

effect of baffle, 243

effect of niche, 250

flanking transmission, 260

fluid loaded plates, 261

infinite panels, 216

influence of plate tension, 336

loss factors, 253

mass law, 223

measurement of, 157

measurement results, 248, 252, 329

plate with ribs, 257

sandwich/honeycomb plates, 309

- SEA, double wall, 395
- SEA, single wall, 393
- shells with ribs, 328
- total, several wall elements, 159
- wall between rooms, 226

Source strength

- structure-borne sound, 87

Spectral density

- spatial, 340

Spherical Hankel function, 125

Statistical Energy Analysis, *see* SEA

Strouhal number, 354

T

- Test rig, mounts, 75
- Timoshenko beam, 20
- Transfer stiffness
 - magnitude, 76
 - phase, 77
- Transmission through mounts, 84
- Turbulent boundary layers, 350
 - measurements, 362
 - water, 374

V

- Velocity potential, fluids, 105
- Volume velocity, 116

W

- Wave equation
 - fluids, 103
- Wave propagation
 - cylinders, 316
 - cylindrical shells, 322
- Waveguide model, 276, 411
- Waveguides
 - acoustic, 266
 - coupled, 270
 - cut-on frequency, 269
 - general, 267
 - measurement results, 276
 - predictions, 276
 - structural, 267
- Wavenumber
 - honeycomb, 296
 - sandwich, 296

Z

- Zener model, 57